Bitlis Eren Üniversitesi
Fen Bilimleri Dergisi

Bitlis Eren University
Journal of Science

ISSN : 2147-3129
e-ISSN : 2147-3188

Cilt / *Volume*: 12 Sayı / *Number*: 4 Yıl / *Year*: 2023

Yazışma Adresi

Bitlis Eren Üniversitesi
Lisansüstü Eğitim Enstitüsü
13000, Merkez, Bitlis/TÜRKİYE
Tel: 0 (434) 2220071

https://dergipark.org.tr/tr/pub/bitlisfen

BEU FBD

Bitlis Eren Üniversitesi Fen Bilimler Dergisi

Bitlis Eren University Journal of Science

Yıl/*Year:* 2023 - Cilt/*Volume:* 12 - Sayı/*Number:* 4

Editör (Yayın) Kurulu / *Editorial Board*

Danışma Kurulu / *Advisory Board*

Dergi Hakkında / *About Journal*

Bitlis Eren Üniversitesi Fen Bilimleri Dergisi, mühendislik ve temel bilimler alanlarındaki gelişmeleri ve yenilikleri takip etmek, meslek kuruluşlarının, araştırmacıların ve bireylerin ulusal ve uluslararası gelişimlerine katkıda bulunmak ve bu alanlarda elektronik bir kaynak oluşturmak amacıyla yayımlanmaktadır. Derginin yazım dili Türkçe veya İngilizcedir. Fen Bilimleri Dergisi, Bitlis Eren Üniversitesi Lisansüstü Eğitim Enstitüsü yayını olup, 2012 yılından bu yana ücretsiz ve açık erişimli olarak yayın hayatına devam etmektedir. Mühendislik ve temel bilimlerin bilgi tabanına ve teknolojik gelişmelere ışık tutması amacıyla bu alanlarda yapılmış deneysel ve teorik ilerlemeleri konu alan özgün araştırma makalelerine yer verilmektedir. Dergiye gönderilen çalışmaların benzerlik oranı %25'i geçmemelidir. Yazım kurallarına uymayan makaleler, hakemlere gönderilmeden önce düzeltilmek üzere yazara geri gönderilir. Bu nedenle, derginin yazım kuralları dikkate alınmalıdır. Ayrıca, editörlerden yazarlara iletilen düzeltmelere veya taleplere 30 gün içerisinde cevap verilmediği takdirde ilgili makaleler reddedilir. Makaleler şekiller ve tablolar dâhil 20 sayfayı geçmemelidir. Dergiye yayın için gönderilen makaleler en az iki hakem tarafından değerlendirilir. Yazarlardan hakem önerisi talep edilmemektedir. Makalelerin dergide yayımlanabilmesi için hakemler tarafından olumlu görüş bildirilmesi gerekmektedir. Dergi Editör Kurulu, hakem raporlarını (*en aziki hakemin değerlendirmeleri geldikten sonra*) dikkate alarak makalelerin yayımlanmak üzere kabul edilip edilmemesine karar verir. Fen Bilimleri Dergisi, yılda dört defa (*Mart, Haziran, Eylül, Aralık*) yayımlanmaktadır. **Dergimiz Tübitak-Ulakbim Mühendislik ve Temel Bilimler Veri Tabanı Dergi Listesinde taranmaktadır.**

B.E.Ü. Fen Bilimleri Dergisi 12(4), 2023 / *B.E.U. Journal of Science 12(4), 2023*
İÇİNDEKİLER / *CONTENTS*

Bitlis Eren Üniversitesi Fen Bilimleri Dergisi
BİTLİS EREN UNIVERSITY JOURNAL OF SCIENCE
ISSN: 2147-3129/e-ISSN: 2147-3188
VOLUME: 12 NO: 4 PAGE: 941-958 YEAR: 2023
DOI:10.17798/bitlisfen.1264165

Design and Performance Analysis of an Air-Based Photovoltaic/Thermal Collector in Winter

Özer KESTANE[1*], Koray ÜLGEN[2]

[1]*Computer Programming Program, İzmir Vocational School, Dokuz Eylül University, İzmir, Turkiye*
[2]*Solar Energy Institute, Ege University, Izmir,Turkiye*
(ORCID: 0000-0001-6092-2881) (ORCID: 0000-0002-9560-1727)

Keywords: Photovoltaic, Solar air collector, PV/T system, Energy analysis, PV/T collector, Thermal energy.

Abstract

The most basic requirements of the facilities in which we spend nearly all of our time are for electricity and heat. It is critical, especially in cold climate regions, that both electrical energy and heating energy needs are met by the same system. The use of photovoltaic (PV) energy is rapidly expanding. Photovoltaic panels can convert solar energy into electrical energy with less than 20% efficiency. Solar energy applications include photovoltaic-thermal (PV/T) collectors that can be installed on building facades or used as building envelopes. Solar energy is used to generate both electric and thermal energy needs with this collector. Off-grid photovoltaic panels and some types of flat-plate solar air collectors have been considered in our work. An experimental setup and a measurement system have been constructed to investigate the behavior of the air-based photovoltaic-thermal collector. This measurement system, sensors that collect data, and a data storage unit that can communicate temperature, humidity, and radiation data to the computer at the specified frequency comprise the experimental setup. The efficiencies of the PV and the solar air collector were calculated individually to estimate the performance of the air-based PV/T collector. Calculation criteria and a model have been developed to determine the performance of this collector. The problem was viewed as time-dependent under irregular settings when developing this model. The theoretical analytical model developed to determine the performance of the air-based PV/T collector was evaluated using Izmir's, a city in the west of Türkiye, winter climatic conditions. As a result of the studies carried out to determine the experimental performance of the PV/T air collector developed within the scope of the study, the thermal efficiency of the system reached up to 35% and the electrical efficiency reached 19% during the winter months. As a result of comparing the results obtained from theoretical and experimental studies, max. It has been determined that there is an error of 0.12%.

Nomenclature

A	Area [m]
C_p	Specific heat [kJkg^{-1}K^{-1}]
h	Heat transfer coefficient [Wm^{-2}K$^{-1]}$
I	Solar Radiation [Wm^{-2}]
L	Thickness [m]
m	Air mass [kgs^{-1}]
q, Q	Thermal Heat [kJ, W]
T	Temperature [°C, K]
t	time [h]

Greek letter

η	Efficiency [%]
λ	Thermal conductivity [Wm^{-1}K^{-1}]
α	Absorptivity [-]
τ	Transmission [-]

*Corresponding author: ozer.kestane@deu.edu.tr
Received: 12.03.2023, Accepted: 09.10.2023

Subscripts

β	Tilt	PV	Photovoltaic
a	Ambient	rad	Radiation
b	Bottom	ref	Reference
c	Cell	t	Top
conv	Convective	T	Total
f	Fluid	ted	Tedlar
g	Glass	th	Thermal

1. Introduction

PV/T systems have been created in many forms and structures depending on the intended purpose of reducing temperature buildup in solar cells [1]–[4][. PV/T air collector systems, which can be integrated into building solar façades or used as building shells, are a novel type of solar application. In general, the goal of these applications is to create both electrical and thermal energy from solar energy while also meeting the energy demand of buildings [5]–[9].

Solar cells convert some of the solar energy they absorb into electrical energy, but the majority of it turns into heat energy, increasing cell temperature and lowering electrical efficiency. The output power and system efficiency of the solar cells can be enhanced during this photovoltaic conversion by cooling them by removing heat from the absorber surface and the cells using a carrier fluid. In most solar hot water preparation systems, water is employed as the fluid in collectors. To improve the efficiency of the PV/T system, phase-shifting materials capable of operating at low temperatures can be used [10]–[14].

In addition to generating electricity, these double-acting systems can produce hot water or hot air and, alternatively, use it for residential hot water and direct space heating. The use of direct ambient air as a fluid for room heating significantly improves the system's overall efficiency. Furthermore, the heated air from the PV/T collector can be provided to the building's ventilation system as pre-heated fresh air. The creation of these façade-integrated systems, which will be installed on buildings' south, southwest, and west facades, would significantly cut energy consumption. The hot air from the PV/T air collector can be used to heat the building [15], [16].

The number of publications on conventional thermal system design and thermal efficiency modelling is greater than the number of publications on combined solar cell-thermal collector design. The Hottel-Whillier model, established in 1958, is the most well-known modelling method. Later, as dynamic modelling of thermal collectors gained popularity, this was investigated. Klein et al. conducted a study of three distinct dynamic models. [17].

According to the findings, the dynamic impacts cancel each other out over the day. Suzuki and Kitamura's [18] theoretical and experimental work on hybrid PV/T systems provides the main ideas of these systems with the results of employing water or air as a cooling fluid.

The aim of the systems developed within this logic is to provide a combined (hybrid) solution by providing both heat and electricity generation together in the same area. Today, PV/T systems, which produce electricity and heat together, are mostly focused on the systems that are introduced as a result of the integration of solar collectors and solar cells. Today, solar energy is used in two ways: thermal solar systems, in which solar radiation from the earth is converted to heat, and photovoltaic (PV) systems, in which solar energy is transformed into electrical energy. Thermal solar systems are utilized for a variety of purposes, including water heating, space heating, and mechanical power generation. Photovoltaic systems convert solar radiation directly to electrical energy and are utilized to address the electrical energy demands of houses and commercial operations.

Figure 1 shows the comparison of the PV module used in electricity generation and the PV system resulting from the integrated thermal system used in heat generation.

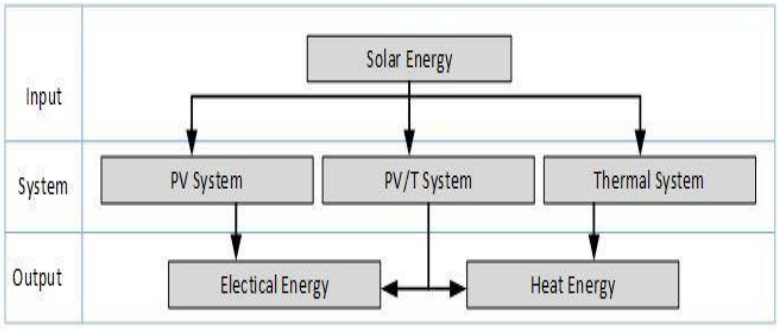

Figure 1. PV system, thermal system, and PV/T system.

Electrical energy and thermal demands are now among the most basic requirements of the structures in which we spend practically all of our time. It is critical, especially in cold areas, to fulfill the electrical energy demand through the same system that meets the high heating energy need. PV/T systems developed for this purpose have two different application types: the roof type and the type integrated into the building. The PV/T systems integrated into the building are mostly used for space heating and are integrated into the building's south, southwest, and west-facing façades, providing an effective solution throughout the day. In this system, the air in the space is used as a fluid, and the need is met by passing it through the PV/T system and returning it directly to the environment. In fact, this system, which acts as an air collector, behaves like a cogeneration system by producing electricity in addition to hot air.

Solar air collectors are generally defined in four different ways: pre-pass, post-pass, double-pass, and matrix pass, depending on the direction of airflow and the location of the flow on the absorber surface (Figure 2).

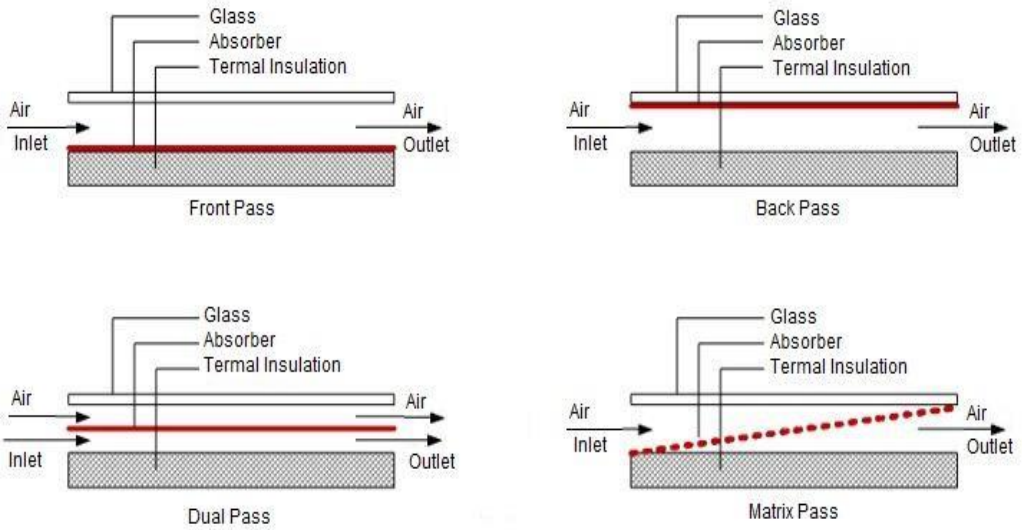

Figure 2. Flow types in air collectors.

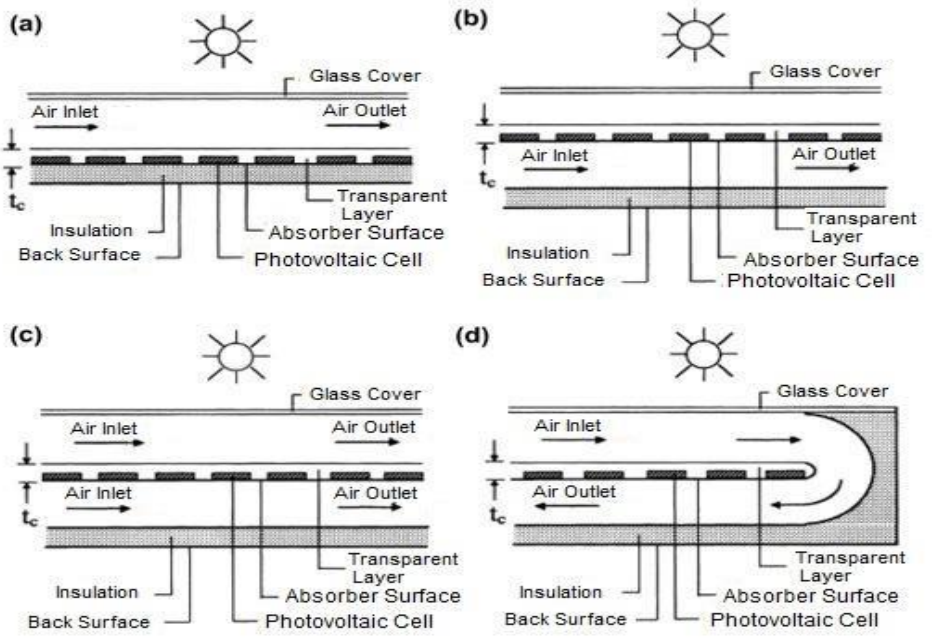

Figure 3. Schematic view of PV/T air collector types [19].

The key elements influencing system efficiency are the location of the flow channel, the velocity of the fluid, and the pressure loss in the flow channel. As a result, while constructing the system, it is critical to design the collector in such a manner that it produces little pressure loss while ensuring maximum flow rate. The most important element influencing the change in the efficiency of solar modules is the temperature of the module's rear surface and the air movement created on this surface. As is well known, some of the solar radiation that reaches the surface of the photovoltaic module is converted into electrical energy, while the remainder is expelled as heat. If a method to lower the rear surface temperature of the solar module is developed, the whole performance of the photovoltaic module will improve. The cross-sections and flow channels of PV/T air collectors designed for this purpose and published in the literature are depicted in Figure 3 [20].

The aim of this study is to determine its performance under the climatic conditions of İzmir province by designing an air source PV/T collector to heat the spaces and meet the partial electricity need, in light of the above information. For this purpose, the design, theoretical analysis, and experimental studies of the system, which are clearly explained in the Method section, were made, and its performance in the winter months was evaluated.

2. Methodology

2.1. Design of PV/T Air Collector

The basic components of the solar-powered air PV/T collector, whose design, application, theoretical, and experimental evaluation were carried out within the scope of this study, consist of a photovoltaic module and solar air collector. The characteristics of the photovoltaic module used in the design of the PV/T air collector are given in Table 1. The photovoltaic module consists of 60 monocrystalline cells, with a peak power of 285 Wp and a module efficiency of 18.2%.

Table 1. Characteristic properties of the PV module.

Nominal Power P_n	Flash Power P_{flash}	Nominal Voltage V_{MPP}	Nominal Current I_{MPP}	Open Circut Voltage V_{oc}	Shortcut Current I_{sc}	Application Class
285 W_p	287 W_p	32,7 V	8,92 A	40,2 V	9,35 A	A Class

The PV/T air collector utilized in the investigation had the following characteristics: The air duct in the PV/T air collector is constructed as a post-pass and has a width of 5 cm. In addition, it is aimed at reducing heat losses and having a smooth

(laminar) flow on the back surface of the air duct by using aluminum foil-coated heat insulation material.

Figure 4 depicts the horizontal section of the designed PV/T air collector, whereas Figure 5 depicts the vertical section. The dimensions in the figures are in cm. The dimensions of the PV/T air collector were established based on the photovoltaic module selected, as shown in the cross-sectional details below.

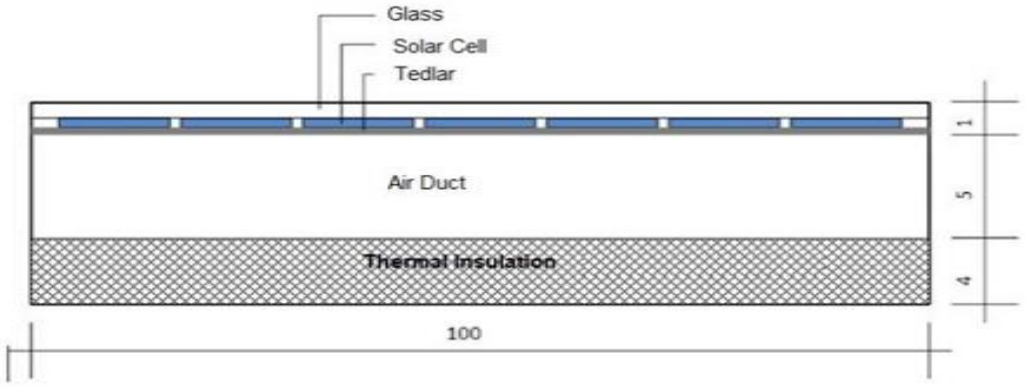

Figure 4. Horizontal section of PV/T air collector.

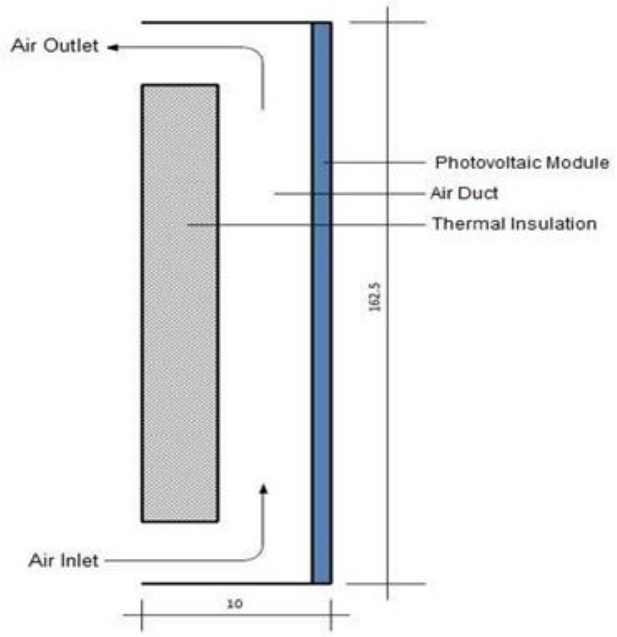

Figure 5. Vertical section of PV/T air collector.

2.2. Theoretical and Experimental Evaluation

The energy balance of the system must be designed in detail in order to determine the theoretical and experimental performance of the PV/T air collector under the climatic conditions of Izmir. Three alternative heat transfer processes are considered when determining the energy balance of the PV/T air collector system (Figures 6 and 7). The thermal study of the PV/T air collector was carried out using the theoretical equations listed below. The heat transfer between the layers of the PV/T air collector is the basis for these equations. When developing the theoretical equations, the following assumptions were made:

- The PV/T air collector system has one-dimensional heat transmission between its layers.
- There is no heat transmission from the PV/T air collector system's edges.
- The materials used to construct the PV/T air collector system have physical and optical qualities that are temperature-independent.

- The contact surfaces of the layers of the PV/T air collection system are all at the same temperature.
- Given the electrical analogy, the heat balance and energy balance equations for different components of the PV/T air collector are shown in Figures 6 and 7.

The energy balance for the solar panel's glass surface can be stated as,

$$m_g C_{p,g} \frac{dT_g}{dt} = q_g(t) - h_{rad,g} A_g (T_g - T_s) - h_{conv,g} A_g (T_g - T_a) - \frac{\lambda_g}{L_g} A_g (T_g - T_c) \quad (1)$$

In this equation, hrad,g expresses the heat transfer from the glass surface of the solar panel to the sky by radiation and is calculated with the help of equation 2, whereas hconv,g denotes heat transfer by convection between the photovoltaic panel's glass surface and the surrounding medium. Furthermore, the quantity qg(t), which is also included in the equation, denotes the amount of solar energy absorbed by the photovoltaic panel's glass and may be determined using equation (3).

$$h_{rad,g} = \frac{\varepsilon \sigma (T_g^4 - T_{sky}^4)}{T_g - T_a} \quad (2)$$

$$q_g(t) = \alpha_g I_\beta(t) A_g \quad (3)$$

The photovoltaic cell's energy balance is as follows,

$$m_c C_{p,c} \frac{dT_c}{dt} = q_c(t) - \frac{\lambda_c}{L_c} A_c (T_c - T_{ted}) - \frac{\lambda_g}{L_g} A_c (T_c - T_g) \quad (4)$$

The term qc(t) in equation (4) relates to the amount of solar energy received by the photovoltaic cell and may be computed using equation (5).

$$q_c(t) = \tau_c \alpha_c (1 - \eta_{PV}) I_\beta(t) A_c \quad (5)$$

The term ηPV in equation (4) refers to the efficiency of a photovoltaic cell as a function of cell temperature and may be computed using equation (6) [21].

$$\eta_{PV} = \eta_{ref} [1 - 0.0054 (T_c - T_{ref})] \quad (6)$$

In this equation, ηref refers to the photovoltaic cell's reference efficiency under 1000 W/m² of radiation, and Tref refers to the cell's reference temperature, which is 25°C as the standard value. The tedlar layer's energy balance is as follows,

$$m_{ted} C_{p,ted} \frac{dT_{ted}}{dt} = -\frac{\lambda_{ted}}{L_{ted}} A_{ted} (T_{ted} - T_c) - h_{rad,ted} A_{ted} (T_{ted} - T_{ins,1}) - h_{conv,ted} A_{ted} (T_{ted} - T_f) \quad (7)$$

The flow channel's energy balance is as follows,

$$m_f C_{p,f} \frac{dT_f}{dt} = -\dot{m} C_{p,f} (T_{f,out} - T_{f,in}) - h_{conv,ted} A_{ted} (T_f - T_{ted}) - h_{conv,ins} A_{ins} (T_f - T_{ins,1}) \quad (8)$$

T_f in this equation represents the average temperature in the flow channel and is calculated by means of equation (9).

$$T_f = \frac{T_{f,in} + T_{f,out}}{2} \quad (9)$$

The insulating layer's energy balance is as follows,

$$m_{ins} C_{p,ins} \frac{dT_{ins}}{dt} = -\frac{\lambda_{ins}}{L_{ins}} A_{ins} (T_{ins,1} - T_{ins,2}) - h_{conv,ins} A_{ins} (T_{ins,1} - T_f) - h_{conv,ins} A_{ins} (T_{ins,2} - T_r) \quad (10)$$

The total heat loss coefficient (UT) is a collector property that has a direct impact on its performance. This coefficient is used to calculate the collector's performance, the quantity of usable heat it creates, and the collector's efficiency. The total heat loss coefficient is determined as the inverse of the thermal resistance using the following equation:

$$U_T = U_t + U_b \quad (11)$$

Ut in this equation shows the heat loss coefficient of the photovoltaic panel, the top layer forming the PV/T collector, and is calculated by means of the equation (12). Ub is the heat loss coefficient in the thermal insulation material, which is the substrate of the PV/T collector, and is calculated by means of equation (13).

$$U_t = \frac{1}{\frac{1}{h_{rad,g} + h_{conv,g}} + \frac{\lambda_g}{L_g} + \frac{\lambda_c}{L_c} + \frac{\lambda_{ted}}{L_{ted}}} \quad (12)$$

$$U_b = \frac{1}{\frac{1}{h_{rad,ins}+h_{conv,ins}}+\frac{\lambda_{ins}}{L_{ins}}} \quad (13)$$

The useful heat to be obtained from the PV/T collector is expressed as follows, depending on the inlet, the outflow temperature, and the flow rate of air in the flow channel.

$$Q_u = \dot{m}C_{p,f}\left(T_{f,out} - T_{f,in}\right) \quad (14)$$

The useful heat of the PV/T collector is expressed as indicated in equation (14), based on the total heat flux.

$$Q_u = \left[\left(\tau_g \alpha_c \tau_{ted} I_\beta A_c\right) - U_T A_c (T_{ted} - T_a)\right] \quad (15)$$

The thermal efficiency of the PV/T collector is calculated as expressed in equation (16).

$$\eta_{th} = \frac{Q_u}{A_c I_\beta} = \frac{\dot{m}C_{p,f}\left(T_{f,out}-T_{f,in}\right)}{A_c I_\beta} \quad (16)$$

In other words, the thermal efficiency of the collector can also be calculated using the following equation.

$$\eta_{th} = \frac{Q_u}{A_c I_\beta} = \frac{\left[\left(\tau_g \alpha_c \tau_{ted} I_\beta A_c\right) - U_T A_c (T_f - T_a)\right]}{A_c I_\beta} = \tau_g \alpha_c \tau_{ted} - \frac{U_T\left(T_{f,out}-T_{f,in}\right)}{I_\beta} \quad (17)$$

The total efficiency of the PV/T totalizer is determined as follows considering the equation (6) and equation (16, 17).

$$\eta = \eta_{th} + \eta_{PV} \quad (18)$$

An iterative technique was employed in the numerical computation with the help of the preceding equations to find the temperature-dependent impacts of the heat transfer coefficient. Temperatures for each layer of the PV/T collector were calculated using Excel-based software and the fourth-order Runga-Kutta method. Table (2) details the accepted physical and thermal parameters of the PV/T collector during these calculations.

Table 2. Physical and thermal properties of the PV/T air collector.

Parameters	Properties	Unit	Parameters	Properties	Unit
A_{PV}	1,6012	m²	σ	5,671 10^{-8}	J/m²sK⁴
A_g	1,6012	m²	$C_{p,g}$	840	J/kgK
A_c	1,4415	m²	$C_{p,c}$	700	J/kgK
A_{ted}	1,6012	m²	$C_{p,ted}$	560	J/kgK
A_{ins}	1,5212	m²	$C_{p,ins}$	880	J/kgK
τ_g	0,90	-	ε_g	0,88	-
τ_{ted}	0,92	-	ε_c	0,35	-
α_g	0,05	-	ε_{ted}	0,95	-
α_c	0,95	-	ε_{ins}	0,05	-
λ_g	1,10	W/mK	ρ_g	2700	kg/m³
λ_c	130	W/mK	ρ_c	2330	kg/m³
λ_{ted}	0,033	W/mK	ρ_{ted}	1200	kg/m³
λ_{ins}	0,040	W/mK	ρ_{ins}	15	kg/m³

There are many experimental studies in the literature developed to determine the experimental performance of PV/T systems [22]–[24]. However, since each study has its own unique setup, a unique experimental setup was created within the scope of this study. The experimental setup formed is shown in Figure 8, the placement of the devices used is given in Figure 9, and the technical features are given in Table 3. According to Figure 9, the measuring points and measuring sensors are as follows:

- Point 1, Solar Radiation (W/m²),
- Point 2, Ambient Temperature (°C) and Humidity (%),
- Point 3, the inlet Temperature (°C) of the PV/T Collector,
- Point 4, the outflow Temperature (°C) of the PV/T Collector,
- Point 5, Room Temperature (°C) and Humidity (%),
- Point 6, Middle Point Temperature (°C) of the Room,
- Point 7, PV panel Current (A), Voltage (V), front and back surface Temperature (°C)

Table 3. Measuring device and sensors.

Main Section	Usage	Specification/description
Sensors	Solar sensor	Type: CMP 11 Pyranometer, Sensivity: ±1% (between -10°C and +40°C), Response time: 12s (between -40°C and +80°C)
	Temperature and Humidity sensor	Type: CS 215 Humidity and Temperature Sensor, Relative Humidity: Measurement Range: 0 to 100%, Error Limit: < 3% Temperature Measurement Range: -40°C to 56°C, Error Limit: <0,5°C
	Temperature sensor	Type: Model 107 , Measurement Range: -40°C to 56°C, Error Limit: <0,5°C
Data-Logger Unit	Use for data storage	Type CR1000 Campbell Data-Logger Capacity: 6MB SRAM, Channels: 16 single-ended or 8 differential,
Electricity Power		The voltage produced: 15,1 V, Peak power: 10 W

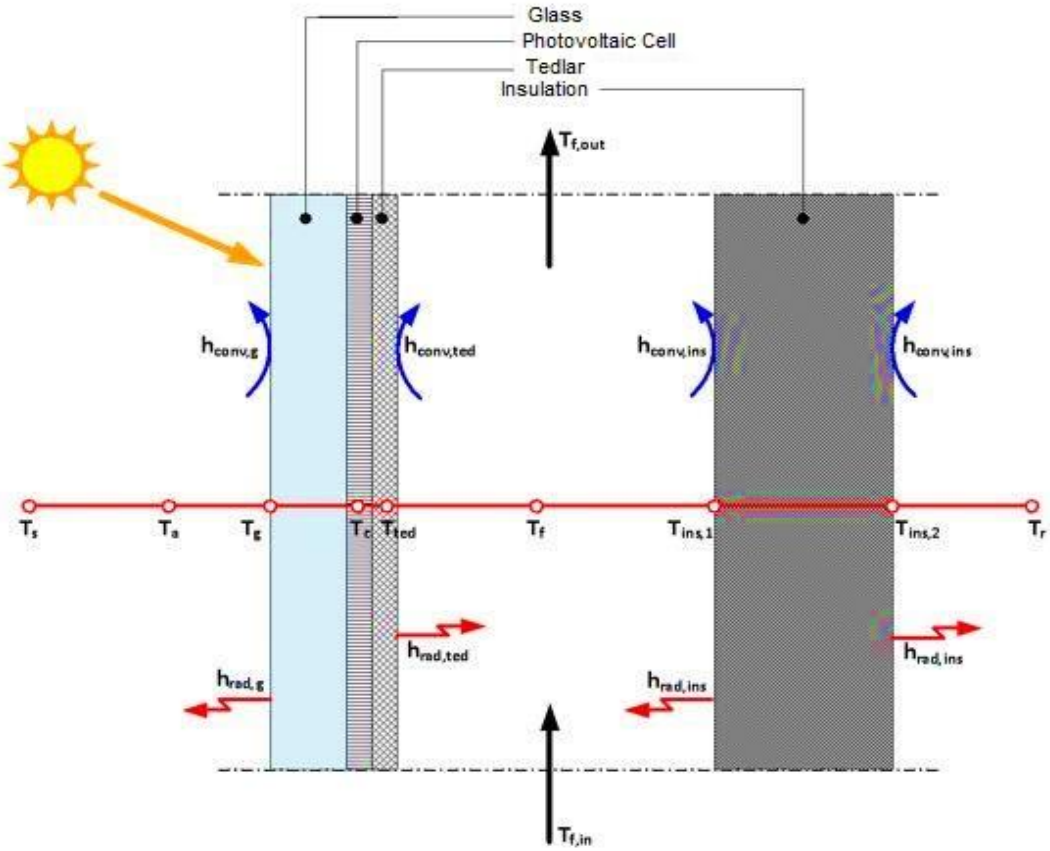

Figure 6. Heat transfer of PV/T air collector.

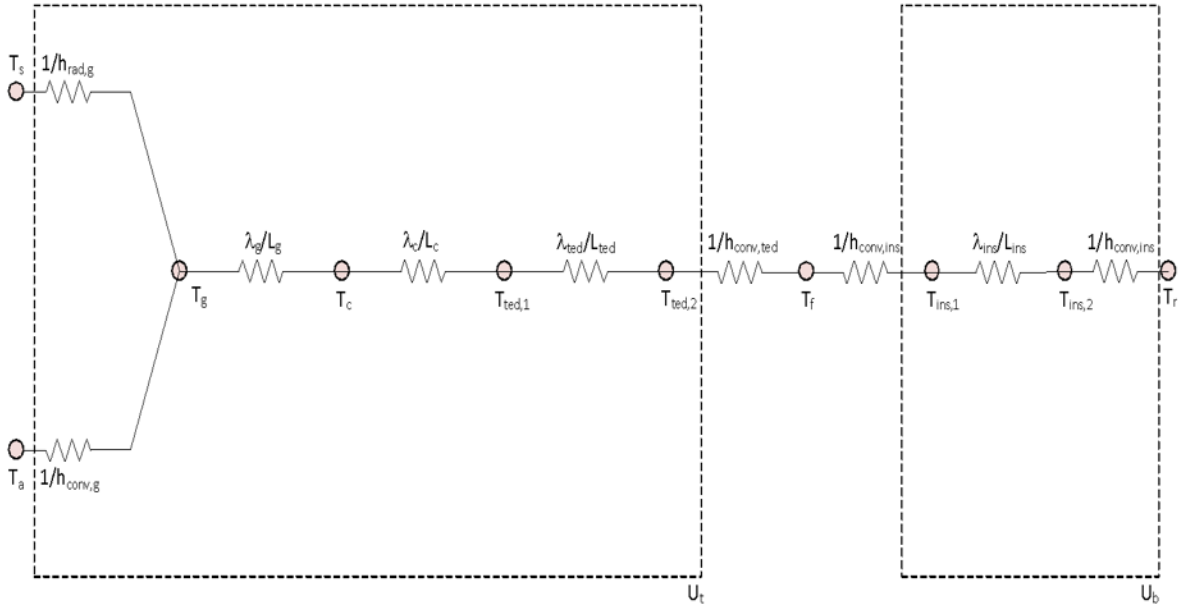

Figure 7. Equivalent circuit diagram of the PV/T air collector.

Figure 8. Mounted view of PV/T air collector.

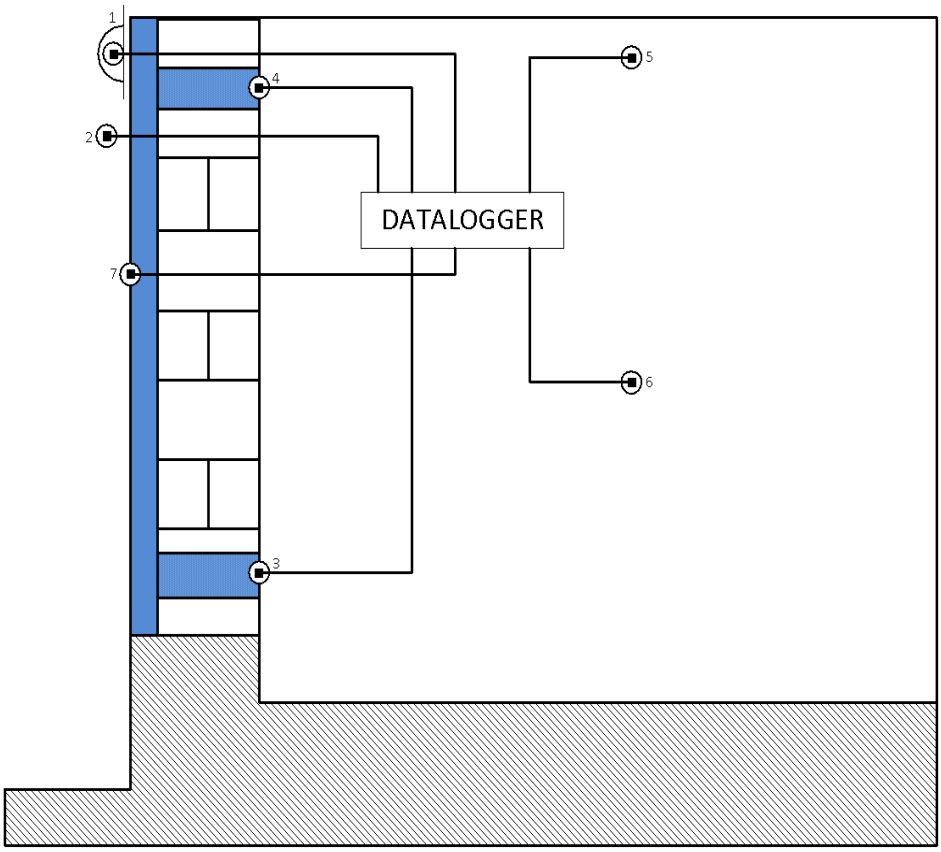

Figure 9. Measuring points in the experimental setup.

3. Analysis and Results

3.1. Analysis

To determine the performance of the designed PV/T solar air collector under İzmir environmental conditions, evaluations were done using data collected from the calculation method and experimental setup. In the experimental studies carried out in December, January, and February, the periodic change of solar radiation from external factors is given in Figure 10, and the change of outdoor temperature and outdoor humidity is shown in Figure 11.

.

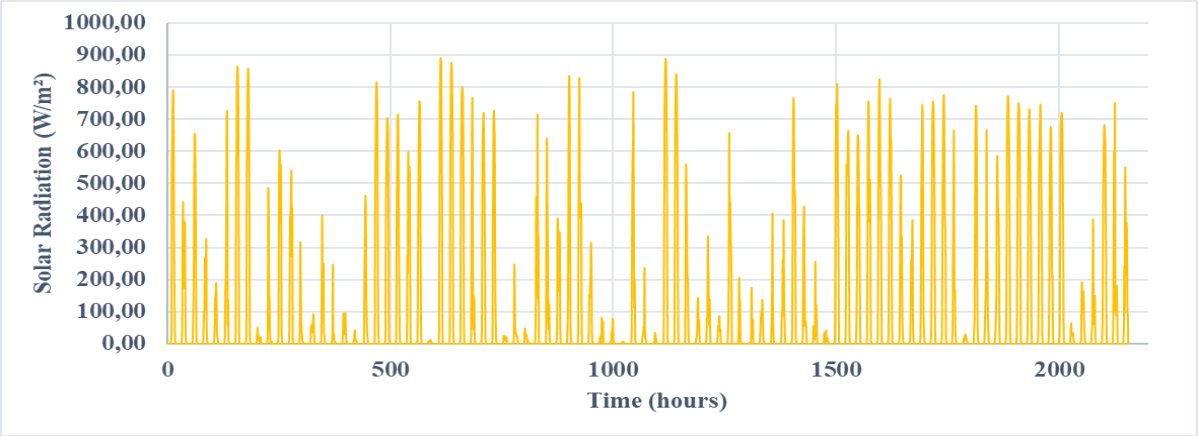

Figure 10. Global solar radiation between December to February.

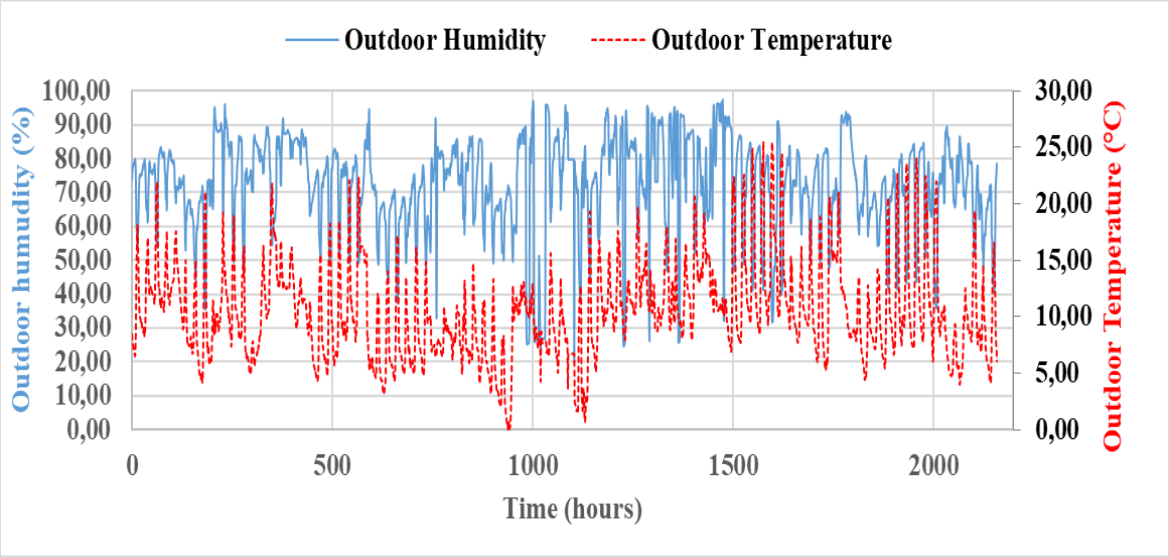

Figure 11. Ambient temperature and relative humidity between December to February.

As a result of the experimental studies performed to determine the performance of the PV/T solar air collector in the winter climatic conditions of Izmir, the results obtained for the average days given in Table 4 are shown in Figure 12.

Table 4. Recommended average days of months (Duffie and Beckman (2013)).

Months	Day of month	For the average day of the month		
		Day	n	δ (°)
January	i	17	17	-20,9
February	31+i	16	47	-13,0
March	59+i	16	75	-2,4
April	90+i	15	105	9,4
May	120+i	15	132	18,8
June	151+i	11	162	23,1
July	181+i	17	198	21,2
August	212+i	16	228	13,5
September	243+i	15	258	2,2
October	273+i	15	288	-9,6
November	304+i	14	318	-18,9
December	334+i	10	344	-23,0

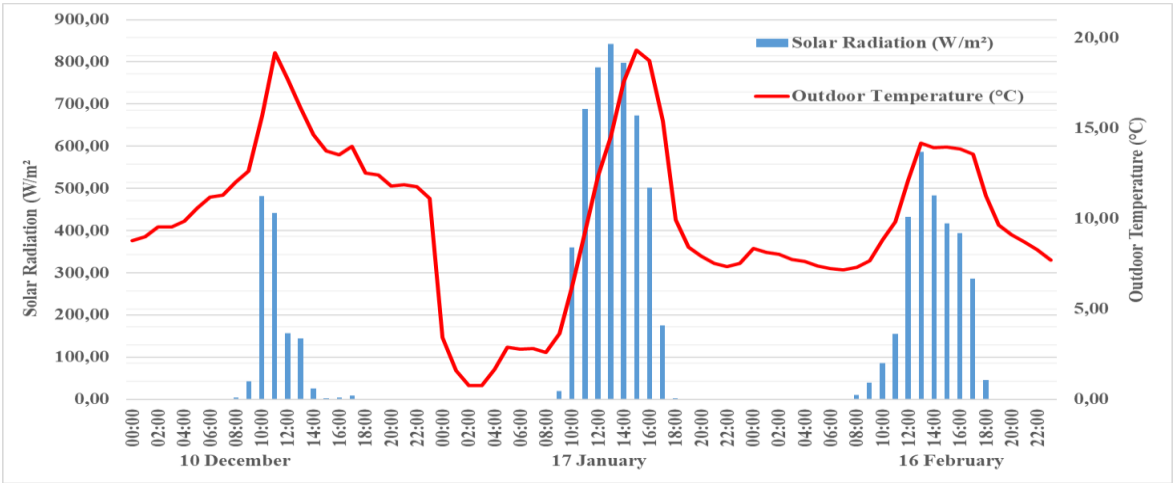

Figure 12. Hourly variation of solar radiation and ambient temperature.

3.2 Results

days mentioned above, the findings obtained from the system are given in detail below. In experimental studies, the system was operated with natural airflow. The findings described in Table 4 for the day representing each month between December and February are given in between Figure 13 and Figure 17.

As a result of the experimental studies carried out during the

In accordance with the experimental studies conducted on December 10th, whose temperature variations are shown in Figure 13, the outdoor temperature change's amplitude is 10.39 °C, while the indoor temperature change's amplitude is 1.60 °C. At the same time, the highest temperature differential between the PV/T collector's inlet and its outflow was 7.87 °C.

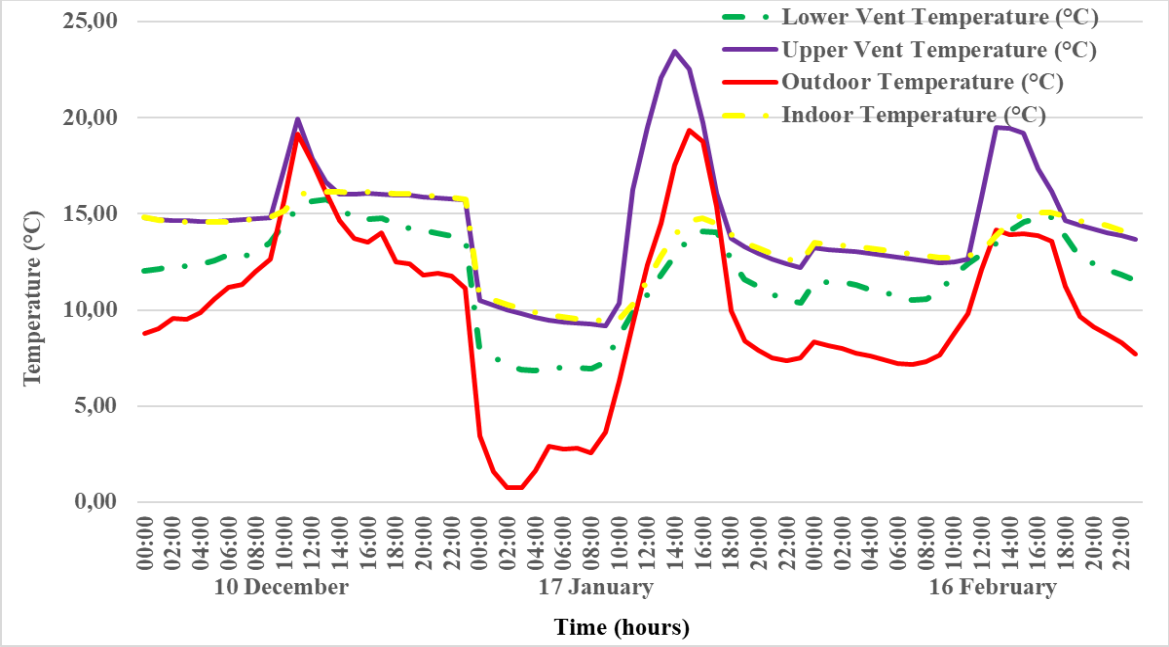

Figure 13. Hourly variation of indoor-outdoor and PV/T collector input-output temperature.

According to experimental studies conducted on January 17, which corresponds to the month of January, the PV/T collector, the inlet and outflow temperatures, and the hourly variation of the outdoor and indoor environments are shown in Figure 13.

Figure 13 indicates that the external temperature change had an amplitude of 18.57 °C and the internal temperature change had an amplitude of 5.35 °C. At the same time, the maximum difference between the inlet and the outflow temperatures of the PV/T collector was 16.59 °C.

The hourly change of the outside and indoor environments, as well as the PV/T collector's inlet and outflow temperatures, are illustrated in Figure 13 in accordance with the experimental studies conducted on February 16, which serves as a representation of the month of February. During the day, the amplitude of the outdoor temperature change was 7.02 °C, while the amplitude of the indoor temperature change was 2.35 °C. At the same time, the difference between the inlet and the outflow temperatures of the PV/T collector was realized to be 8.96 °C.

The change in electrical efficiency obtained from the panel depending on the temperature values formed on the back surface is shown in Figure 14. On December 10, the front surface of the PV panel was observed to rise to a maximum of 26.98 °C, depending on the density of solar radiation, and a minimum of 25.24 °C on the back surface.

Figure 14 illustrates the temperature difference of the PV panel's front and back surfaces on January 17. On the front surface of the PV panel, the temperature increase reached its peak at 43.47 °C, while it was 37.69 °C on the back.

The front and back surface temperatures of the PV panel changed throughout the day of February 16, as shown in Figure 14. The PV panel's front surface experienced a maximum increase of

32,73 °C, while its back surface experienced a maximum increase of 29,42 °C.

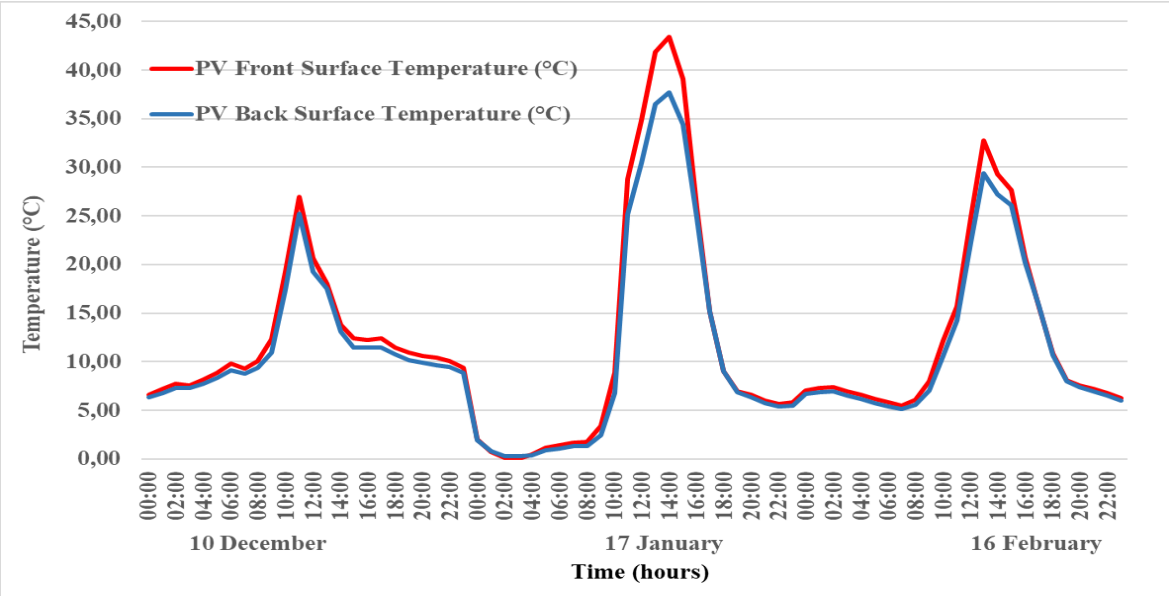

Figure 14. Hourly variation of front and back surface temperature of the PV panel.

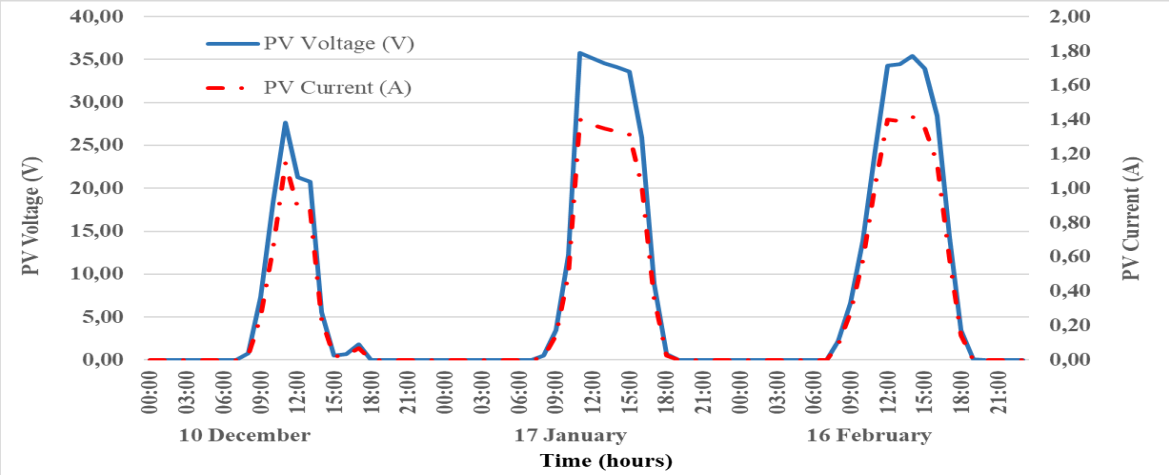

Figure 15. Hourly variation of voltage and current of the PV panel.

As demonstrated in Figure 15, the maximum PV produced on December 10 was 38.94 V, and the current generated was 1.62 A. These results indicate that the PV panel's maximum power of 62.89 W was obtained. Under typical test conditions, the power generated by PV is far less than 285 W. This is due to the vertical orientation of the PV panel. The PV panel's maximum voltage on January 17 was 36.17 V, and the maximum current it could produce was 1.45 A. These results indicate that PV produced a maximum power of 52.30 W. The highest PV value produced during the day on February 16 was 38.48 V, while the current value it produced was 1,61 A. According to these values, the maximum power of 62.03 W was obtained from PV.

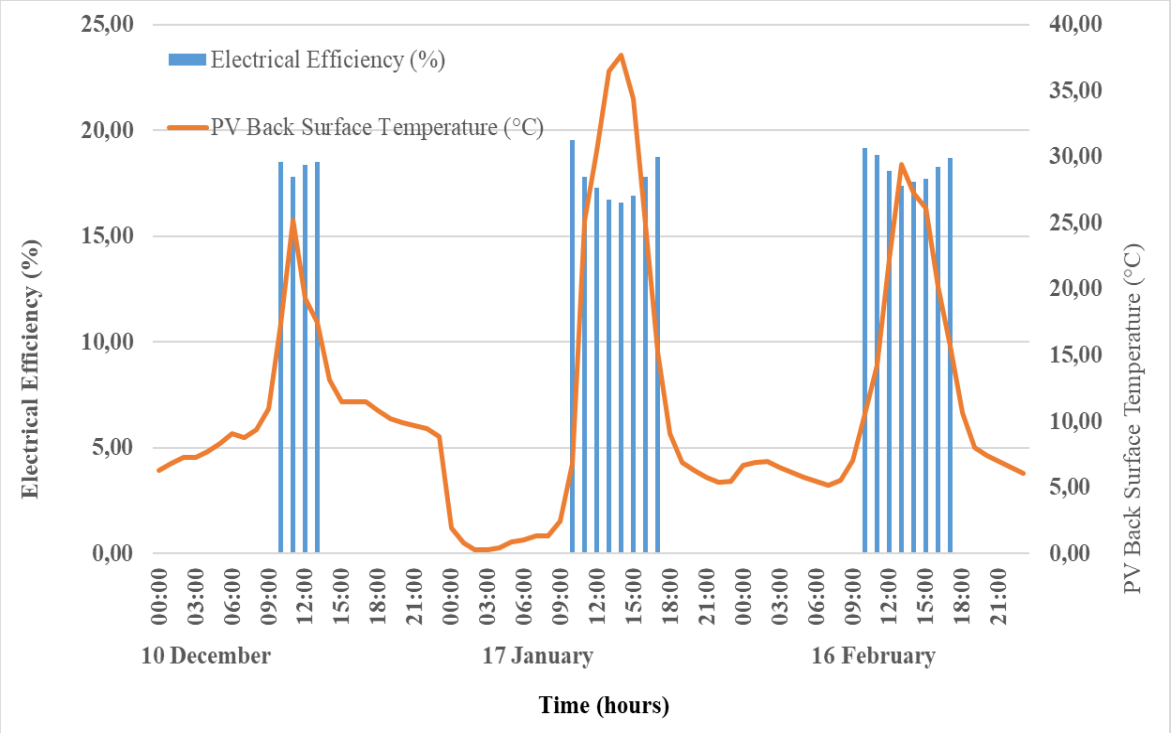

Figure 16. Hourly variation of back surface temperature and electrical efficiency of the PV panel.

According to the temperature values produced on the PV panel's back surface, the electrical efficiency of the panel changes, as illustrated in Figure 16.

The lowest and maximum electrical efficiencies predicted based on the back surface temperature of the PV panel were 17.78% and 18.53, respectively, according to tests taken on December 10. The efficiency of the PV panel is roughly 1.65%, while considering that the project's PV panel has an efficiency of 18.2% under typical test settings. This is because the temperature change behind the PV panel in summer is higher than the standard test temperature of 25 °C.

According to the values obtained on January 17, the calculated lowest electrical efficiency obtained from the PV panel is 16.58%, while the highest is 19.55%, depending on the back surface temperature of the PV panel. According to the yield value of the PV panel under standard test conditions, it has an average yield reduction of around 1.85%.

According to the values obtained on February 16, depending on the back surface temperature of the PV panel during the day, the electrical efficiency obtained from the PV panel was calculated as the lowest (17.38%) and the highest (19.18%). According to the yield value of the PV panel under standard test conditions, the efficiency of the PV panel is approximately 1.59%.

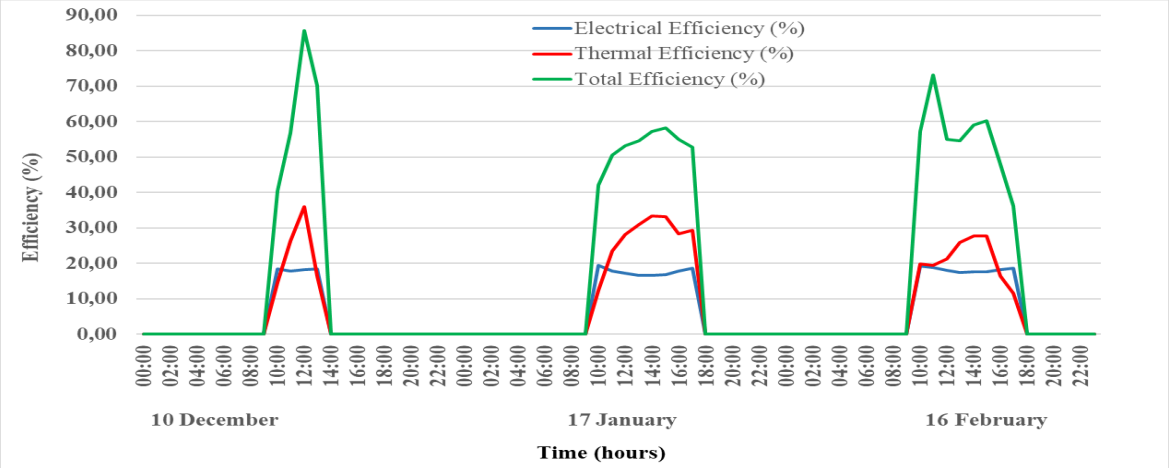

Figure 17. Hourly variation of electrical, thermal and total efficiency of the PV/T collector.

The electrical, thermal, and overall efficiency change of the system was computed in accordance with the results of the experimental study carried out on December 10, January 17, and February 16 and is shown in Figure 17.

The results of the experimental investigation conducted on December 10 showed that, depending on the hourly solar radiation value, the system's thermal efficiency ranged from 14,64% to 35,94%, with 14,64% being the lowest and 35,94% being the greatest. The fluid entering the collector had a temperature range of 12,06 °C to 15,73 °C, which was used to calculate the PV/T collector's change in thermal efficiency. The results of the experimental investigation conducted on January 17 indicated that, depending on the hourly solar radiation value, the system's lowest thermal efficiency was 12,45% and its greatest was 33,39%. The fluid entering the PV/T collector had a temperature value of 6,84 °C when the lowest thermal efficiency change was calculated, and 14,09 °C when the highest. The results of the experimental investigation conducted on February 16 indicated that the system's thermal efficiency ranged from 3,78% to 27,78%, depending on the value of the hourly solar radiation.

The verification method used to compare the results obtained in light of the experimental and theoretical studies carried out within the scope of this study is Root Mean Square Error (RMSE). The equation used in the determination of error analysis is as follows;

$$RMSE = \sqrt{\frac{1}{n}\sum_{i=1}^{n}\left(x_{theo,i} - x_{exp,i}\right)^2} \quad (18)$$

The results of the error analysis performed in light of the data obtained from the experimental and theoretical studies are given in Table 5. Error values calculated depending on ambient conditions are given for PV cell temperature, fluid temperature, thermal, electrical, and total efficiency. According to the error evaluation revealed as a result of the theoretical and experimental studies, the average error rates were calculated as 4.19% according to the PV cell temperature, 5.00% according to the fluid temperature, 0.07% according to the thermal efficiency, 0.03% according to the electrical efficiency, and 0.04% according to the total efficiency.

Table 5. Percentage errors between theoretical and experimental results.

T_a	I_β	Root Mean Square Error (RMSE) (%)				
(K)	(W/m^2)	T_c	T_f	η_{th}	η_{pv}	η
275-280	600-700	3.99	4.56	0.12	0.02	0.04
280-285	200-300	6.06	2.34	0.11	0.03	0.05
	700-800	4.65	4.88	0.08	0.03	0.04
	800-900	4.02	6.76	0.05	0.02	0.03
285-290	400-500	3.23	3.13	0.10	0.04	0.04
	500-600	3.05	3.98	0.07	0.03	0.05

	600-700	2.99	4.12	0.06	0.02	0.03
	700-800	2.76	5.05	0.05	0.02	0.03
	800-900	2.89	7.79	0.04	0.02	0.03
	600-700	4.76	4.22	0.06	0.03	0.04
290-300	700-800	5.18	5.15	0.05	0.03	0.04
	800-900	6.66	8.02	0.04	0.02	0.03
Average		**4.19**	**5.00**	**0.07**	**0.03**	**0.04**

4. Conclusion

The benefit of the PV/T collector system, which serves as the project's foundation, is that the heat created by the PV panel is transported to the air gap established behind the PV panel, allowing the PV module to cool and therefore boost its electrical efficiency. The potential heat generation at the given surface is substantially greater than the electrical performance. In order to ensure the use of PV panels and thermal solar collectors together, it will be more appropriate to use materials that perform heat transfer faster. For this, instead of TEDLER, which is used as a back surface element in traditional photovoltaic panels, the use of materials with high heat transfer coefficients, such as copper or aluminum, will directly contribute to the increase in system performance. PV requires a low temperature for high efficiency; the air solar collector requires a high temperature to produce a high benefit. Current technologies have lower efficiency than 2 separate systems in PV/T collectors, and also because of the initial development step, the PV/T combination is more expensive. However, it is still considered advantageous in terms of aesthetics, future cost reductions (production and installation), and market and consumer needs.

Türkiye, with an average yearly solar energy of 1311 kWh/m² year and a total annual sunlight duration of 2640 hours, is a fortunate country in terms of solar energy potential. If the existing potential is evaluated, the dependence on external energy will be greatly reduced, but the initial installation costs of solar power systems are often quite high. The production of electricity with solar cells is not yet used because it is expensive. The widespread use of electricity, as well as hot water from solar energy in buildings, will significantly reduce environmental pollution. Despite the system's high initial investment cost, its long-term benefit to the national economy and environment will be beneficial. Using these two transducers together reduces costs while increasing system productivity and utilization.

The housing sector consumes 34% of total energy. On a sectoral basis, housing has a large share of energy consumption. In this context, efforts to reduce energy consumption in houses will contribute to the national economy, and at the same time, reduce environmental problems related to fossil fuel consumption.

For this, it is possible to create effective solutions by integrating photovoltaic panels with air solar energy collectors used for heating the spaces. As a result of the studies carried out to determine the experimental performance of the PV/T air collector developed within the scope of the study, the thermal efficiency of the system reached up to 35% and the electrical efficiency reached 19% during the winter months. As a result of comparing the results obtained from theoretical and experimental studies, it has been determined that there is an error of 0.12%.

Acknowledgment

This work was supported by Research Fund of the Dokuz Eylul University. Project Number: 2017.KB.FEN.009

Contributions of the Authors

All authors contributed equally to the study.

Conflict of Interest Statement

There is no conflict of interest between the authors.

Statement of Research and Publication Ethics

The study is complied with research and publication ethics

References

[1] S. C. Solanki, S. Dubey, and A. Tiwari, "Indoor simulation and testing of photovoltaic thermal (PV/T) air collectors," *Appl Energy*, vol. 86, no. 11, pp. 2421–2428, Nov. 2009, doi: 10.1016/J.APENERGY.2009.03.013.

[2] S. R. Reddy, M. A. Ebadian, and C. X. Lin, "A review of PV–T systems: Thermal management and efficiency with single phase cooling," *Int J Heat Mass Transf*, vol. 91, pp. 861–871, Dec. 2015, doi: 10.1016/J.IJHEATMASSTRANSFER.2015.07.134.

[3] A. N. Al-Shamani, K. Sopian, S. Mat, H. A. Hasan, A. M. Abed, and M. H. Ruslan, "Experimental studies of rectangular tube absorber photovoltaic thermal collector with various types of nanofluids under the tropical climate conditions," *Energy Convers Manag*, vol. 124, pp. 528–542, Sep. 2016, doi: 10.1016/J.ENCONMAN.2016.07.052.

[4] C. Babu and P. Ponnambalam, "The role of thermoelectric generators in the hybrid PV/T systems: A review," *Energy Convers Manag*, vol. 151, pp. 368–385, Nov. 2017, doi: 10.1016/J.ENCONMAN.2017.08.060.

[5] A. Makki, S. Omer, and H. Sabir, "Advancements in hybrid photovoltaic systems for enhanced solar cells performance," *Renewable and Sustainable Energy Reviews*, vol. 41, pp. 658–684, Jan. 2015, doi: 10.1016/J.RSER.2014.08.069.

[6] Ömeroğlu G, "Fotovoltaik - Termal (PV / T) Sistemin Sayısal (CFD) ve Deneysel Analizi," *Fırat Üniversitesi Mühendislik Bilimleri Dergisi*, vol. 30, no. 1, pp. 161–167, Mar. 2018.

[7] I. Nardi, D. Ambrosini, T. de Rubeis, D. Paoletti, M. Muttillo, and S. Sfarra, "Energetic performance analysis of a commercial water-based photovoltaic thermal system (PV/T) under summer conditions," *J Phys Conf Ser*, vol. 923, p. 012040, Nov. 2017, doi: 10.1088/1742-6596/923/1/012040.

[8] A. Shukla, K. Kant, A. Sharma, and P. H. Biwole, "Cooling methodologies of photovoltaic module for enhancing electrical efficiency: A review," *Solar Energy Materials and Solar Cells*, vol. 160, pp. 275–286, Feb. 2017, doi: 10.1016/J.SOLMAT.2016.10.047.

[9] P. Xu *et al.*, "A review of thermal absorbers and their integration methods for the combined solar photovoltaic/thermal (PV/T) modules," *Renewable and Sustainable Energy Reviews*, vol. 75, pp. 839–854, Aug. 2017, doi: 10.1016/J.RSER.2016.11.063.

[10] Z. Qiu, X. Ma, X. Zhao, P. Li, and S. Ali, "Experimental investigation of the energy performance of a novel Micro-encapsulated Phase Change Material (MPCM) slurry based PV/T system," *Appl Energy*, vol. 165, pp. 260–271, Mar. 2016, doi: 10.1016/J.APENERGY.2015.11.053.

[11] M. J. Huang, P. C. Eames, and B. Norton, "Phase change materials for limiting temperature rise in building integrated photovoltaics," *Solar Energy*, vol. 80, no. 9, pp. 1121–1130, Sep. 2006, doi: 10.1016/J.SOLENER.2005.10.006.

[12] S. Preet, B. Bhushan, and T. Mahajan, "Experimental investigation of water based photovoltaic/thermal (PV/T) system with and without phase change material (PCM)," *Solar Energy*, vol. 155, pp. 1104–1120, Oct. 2017, doi: 10.1016/J.SOLENER.2017.07.040.

[13] C. S. Malvi, D. W. Dixon-Hardy, and R. Crook, "Energy balance model of combined photovoltaic solar-thermal system incorporating phase change material," *Solar Energy*, vol. 85, no. 7, pp. 1440–1446, Jul. 2011, doi: 10.1016/J.SOLENER.2011.03.027.

[14] Rüstemli S, Dinçer F, Çelik M, and Cengiz M. S, "Fotovoltaik Paneller: Güneş Takip Sistemleri ve İklimlendirme Sistemleri," *Bitlis Eren Üniversitesi Fen Bilimleri Dergisi*, vol. 2, no. 2, pp. 141–147, 2013.

[15] H. M. S. Bahaidarah, "Experimental performance evaluation and modeling of jet impingement cooling for thermal management of photovoltaics," *Solar Energy*, vol. 135, pp. 605–617, Oct. 2016, doi: 10.1016/J.SOLENER.2016.06.015.

[16] H. A. Hasan, K. Sopian, A. H. Jaaz, and A. N. Al-Shamani, "Experimental investigation of jet array nanofluids impingement in photovoltaic/thermal collector," *Solar Energy*, vol. 144, pp. 321–334, Mar. 2017, doi: 10.1016/J.SOLENER.2017.01.036.

[17] S. A. Klein, J. A. Duffie, and W. A. Beckman, "Transient Considerations of Flat-Plate Solar Collectors," *Journal of Engineering for Power*, vol. 96, no. 2, pp. 109–113, Apr. 1974, doi: 10.1115/1.3445757.

[18] A. Suzuki and S. Kitamura, "Combined Photovoltaic and Thermal Hybrid Collector," *Jpn J Appl Phys*, vol. 19, no. S2, p. 79, Jan. 1980, doi: 10.7567/JJAPS.19S2.79.

[19] A. A. Hegazy, "Comparative study of the performances of four photovoltaic/thermal solar air collectors," *Energy Convers Manag*, vol. 41, no. 8, pp. 861–881, May 2000, doi: 10.1016/S0196-8904(99)00136-3.

[20] K. Moradi, M. Ali Ebadian, and C. X. Lin, "A review of PV/T technologies: Effects of control parameters," *Int J Heat Mass Transf*, vol. 64, pp. 483–500, Sep. 2013, doi: 10.1016/J.IJHEATMASSTRANSFER.2013.04.044.

[21] L. M. Candanedo, A. Athienitis, and K.-W. Park, "Convective Heat Transfer Coefficients in a Building-Integrated Photovoltaic/Thermal System," *J Sol Energy Eng*, vol. 133, no. 2, May 2011, doi: 10.1115/1.4003145.

[22] E. Touti, M. Masmali, M. Fterich, and H. Chouikhi, "Experimental and numerical study of the PVT design impact on the electrical and thermal performances," *Case Studies in Thermal Engineering*, vol. 43, 2023, doi: 10.1016/j.csite.2023.102732.

[23] C.-Y. Huang, H.-C. Sung, and K.-L. Yen, "Experimental Study of Photovoltaic/Thermal (PV/T) Hybrid System," *International Journal of Smart Grid and Clean Energy*, vol. 2, no. 2, 2013, doi: 10.12720/sgce.2.2.148-151.

[24] A. Buonomano, F. Calise, and M. Vicidomini, "Design, simulation and experimental investigation of a solar system based on PV panels and PVT collectors," *Energies (Basel)*, vol. 9, no. 7, 2016, doi: 10.3390/en9070497.

Bitlis Eren Üniversitesi Fen Bilimleri Dergisi
BİTLİS EREN UNIVERSITY JOURNAL OF SCIENCE
ISSN: 2147-3129/e-ISSN: 2147-3188
VOLUME: 12 NO: 4 PAGE: 959-968 YEAR: 2023
DOI:10.17798/bitlisfen.1295905

Design, Finite Element Analysis and Optimization of Helical Angular Pressing (HAP) Method as a Novel SPD Technique

Ömer KARABEY*

Bitlis Eren University, Faculty of Engineering and Architecture, Department of Mechanical Engineering, Bitlis, Turkey
(ORCID: 0000-0002-5726-9284)

Keywords: ECAP, SPD, Helical Angular Pressing (HAP), Finite Element Analysis.

Abstract

Severe Plastic Deformation (SPD) processes improve the mechanical properties of materials by obtaining Ultra Fine Grained (UFG) materials, orienting the grains and reforming the grains. Helical Angular Pressing (HAP) is a newly proposed Severe Plastic Deformation (SPD) method. In order to improve the efficiency of the HAP method, its die geometry should be optimized first. In this context, four parameters (helical diameter, helical pitch, helical height and channel radius) were determined for the die channel geometry, each with four levels according to the literature. Then, thanks to Taguchi L16 combinations, 16 Finite Element Analyses (FEA) were carried out using Deform 3D software instead of 256 simulations, and effective strain values and maximum pressing load values were obtained. Later on, using the SPSS 16 software, Taguchi optimization was carried out to obtain the optimum HAP die channel geometries by minimizing the press load and maximizing the effective strain values. Next, the Finite Element Analysis (FEA) was repeated with these determined optimum die channel parameters. Finally, the efficiency of this novel HAP method was compared with conventional Equal Channel Angular Pressing (ECAP) and Twist Extrusion (TE) methods. As a result, HAP method provides effective strain values equivalent to 10 number of passes after processing with ECAP. And it is approximately 4 times higher than that achieved by TE processing. As a result of the Taguchi optimization, it is concluded that the values in the combination of diameter (d)=60 mm, height (h)=50 mm, radius (r)=4 and pitch (p)=1.25 are the optimum die geometry. In conclusion, these results indicate that the proposed novel HAP method is an efficient and applicable SPD technique.

1. Introduction

In the field of materials science, the development of novel processing techniques to customize the microstructure and properties of metals and alloys is a major area of research. Among these techniques, Severe Plastic Deformation (SPD) have emerged as promising methods to produce ultra fine grained (UFG) materials with exceptional mechanical properties [1]–[5]. UFG materials produced by ECAP and SPD have shown excellent mechanical properties, such as high strength, ductility, and fatigue resistance, making them promising candidates for structural and load-bearing components. Additionally, SPD-processed materials have shown improved wear resistance and corrosion resistance, making them suitable for various tribological and corrosion-resistant applications [2], [6]–[10]. Thanks to these enhancements, SPD has been extensively investigated for their potential applications in various industries, including aerospace, automotive, biomedical, and energy.

SPD techniques involve subjecting a material to high pressure and shear forces, leading to severe plastic deformation. SPD can produce materials with ultrafine grains and a high density of defects, such as

*Corresponding author: okarabey@beu.edu.tr
Received: 11.05.2023, Accepted: 15.12.2023

dislocations, stacking faults, and twins. The mechanical properties of SPD-processed materials are generally superior to those of conventionally processed materials due to the refinement of the microstructure and the high density of defects [11]–[13]. Some of the frequently preferred SPD techniques are Equal Channel Angular Pressing (ECAP), High-Pressure Torsion (HPT), Accumulative Roll Bonding (ARB), Cyclic Extrusion Compression (CEC), Multi-Directional Forging (MDF), Vortex Extrusion (VE) and Twist Extrusion (TE) [14]–[21]. In order to improve the efficiency of the SPD techniques some modifications also applied. Some of the well-known of these modifications are Expansion Equal-Channel Angular Pressing (Exp.-ECAP) and Hybrid Equal-Channel Angular Pressing (Hybrid-ECAP), Twist Channel Angular Pressing (TCAP), Twisted Variable Channel Angular Pressing (TV-CAP) [22]–[25]. Moreover, all these techniques are generally applied to billets or cylindrical shaped geometries. For tubular workpieces, Thin-Walled Open Channel Angular Pressing (TWO-CAP) and Parallel Tubular Channel Angular Pressing (PTCAP) methods have been developed as modified SPD technique [26], [27]. Besides, for sheet materials Repetitive Corrugation and Straightening (RCS) method is another developed as modified SPD technique [28]. Equal Channel Angular Pressing (ECAP) involves pressing a metal or alloy through a channel with two intersecting channels, where the material undergoes intense plastic deformation. The process results in a significant reduction in the grain size of the material and the formation of a homogeneous microstructure with a high density of dislocations. The grain size reduction is a result of the repetitive shearing and bending of the material as it passes through the channel, leading to an increase in the number of grain boundaries and a decrease in the average grain size. ECAP has been shown to be effective in refining the microstructure of a wide range of materials, including aluminium, copper, magnesium, titanium, and their alloys [24], [29]–[31].

The main objective of this study is to propose a new SPD technique that can be an alternative to conventional SPD methods and to examine the efficiency, applicability and processability of this proposed technique. In this context, the effective strain parameter results were obtained with Deform 3D software for efficiency analysis and compared with conventional SPD methods. In addition, to verify the applicability and processability of this novel method, maximum press load values were obtained using Deform 3D software and compared with literature results. Furthermore, apart from the improvement of the novel die geometry, it is aimed to optimize the die channel geometry of the HAP method using the Taguchi optimization method in order to further increase the efficiency and improve the applicability and processability of the method. Finally, it is aimed to obtain effective strain and maximum press load values by FEA using the obtained optimum die channel geometry.

2. Material and Method

2.1. Material

In this paper, AA5083 aluminium alloy was studied for a novel SPD technique. In this technique, both angular and helical channels are used together. Thus, a novel method that improves the efficiency of ECAP and TE methods is proposed. This new method is called Helical Angular Pressing (HAP). For this method, 4 different design parameters are considered. For each of these parameters, 4 different values were determined. Taguchi method was used for the determined parameters. SolidWorks software was used for the design with the 16 determined parameter combinations. For 16 different cases, finite element analyses were performed with Deform 3D software for AA5083 aluminium alloy material and optimum parameters were determined. The chemical composition of AA5083 alloy is given in Table 1. Finally, the best parameters were decided according to the results of the finite element analysis.

Table 1. Chemical Composition of AA5083 Alloy.

Alloy	Element (mass%)						
	Al	**Mg**	**Mn**	**Fe**	**Cr**	**Si**	**Cu**
AA5083	Bal.	4.73	0.71	0.26	0.17	0.14	0.03

AA5083 is generally used for all kinds of welded joints, tanks, and marine components where max. joint strength and high weld efficiency are required. This material finds application in various industries, such as in pressure vessels operating up to 65°C (150°F) and in a wide array of cryogenic uses. Additionally, it is utilized in constructing bridges, drilling rigs, marine components, freight cars, transportation equipment, TV towers, dump truck bodies, and missile components, showcasing its versatility. Moreover, it exhibits commendable resistance against corrosion [32].

2.2. Die Design and Dimensional Parameters

The new designed die has both angular and helical channel for SPD process. The channel diameter was specified as 10 mm. The variables in die design are helical diameter (d), helical height (h), helical pitch

(p) and die channel radius (r). Table 2 shows these four levels with their four factors for the HAP die channel.

Table 2. Design parameters for the HAP die channel.

d (mm)	h (mm)	r (mm)	p
40	40	0	0.5
60	50	1	0.75
80	60	2	1
100	70	4	1.25

CAD models of these 16 different cases, punch and workpiece were created with SolidWorks software. Figure 1 shows the 3D model and dimensional details of the die channel. For the analyses to be performed, the workpiece was designed with a diameter of 10 mm and a length of 470 mm. These values have been determined through the analysis of detailed studies in the literature.

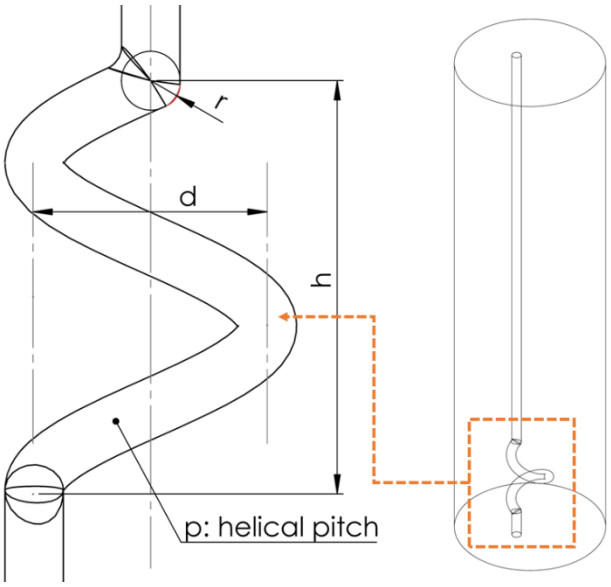

Figure 1. 3D model and dimensional details of the die.

2.3. Finite Element Analysis (FEA)

In this study, the finite element analysis method Deform 3D software was used for the simulation of the HAP method. This software is frequently preferred in SPD studies. The CAD modelling of die, workpiece and punch were designed and, were imported into the Deform 3D software. In the analysis, the die and punch are modelled as rigid and the workpiece is modelled as a plastic material. The parameters used for all analyses are listed in Table 3 in details.

In order to verify the FEA, a hexa-ECAP die model was used and analysed by Deform 3D software. The obtained effective strain value is first compared with analytically calculated value found by Iwashi and given in Equation 1 [36]. In addition, the effective strain and maximum press load values obtained are compared with literature results using the same parameters. Finally, a comparison will be made between the sample output images as a result of the FEA in this study and the reference study.

Studies have demonstrated a relationship between alterations in the mechanical characteristics of a specimen in severe plastic deformation methods and the effective plastic strain experienced by the sample during the process. The variation of the effective strain values obtained as a result of the studies in the transverse plane of the sample is also important. This is called strain homogeneity. In order to evaluate the homogeneity, effective strain values were obtained from 56 different points in the transverse plane as shown in Figure 2.

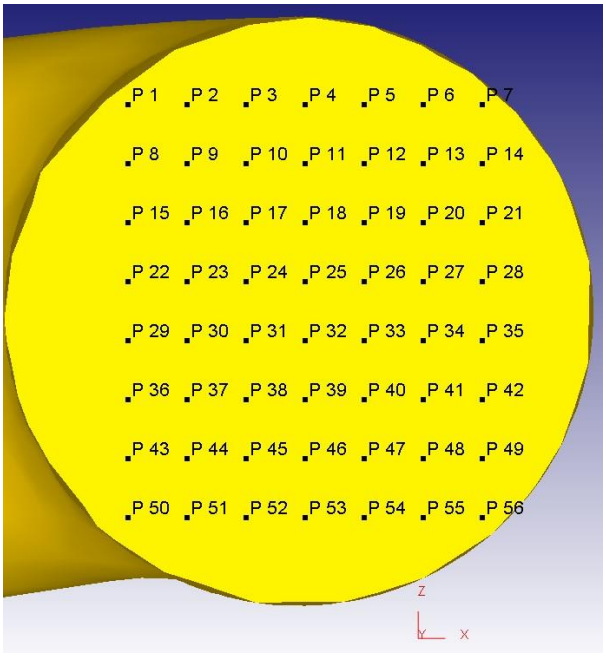

Figure 2. Pattern of points used to determine the effective strain values.

Table 3. Parameters for Deform 3D software.

Process Type	Warm forming
Temperature Calculation	Constant temperature (Isothermal)
Shape Complexity/Accuracy	Moderate/Moderate
Workpiece Shape	Whole part
Workpiece Geometry	Plastic
Top and Bottom Die Geometry	Rigid
Number of Objects	1 workpiece + 2 dies
Material	Aluminium -5083 [70-900F(40-480C)]
Temperature	200 °C
Number of Mesh	55000
Mesh type	Tetrahedron
Pressed (Movement) Speed:	1.5 mm/s
Shear Friction Coefficient	0.12

2.4. Taguchi Optimization

Traditional experimental designs are difficult to use especially when dealing with a large number of experiments and when the number of process parameters is increased. Therefore, the Taguchi method allows multiple factors to be taken into account at the same time, and it also allows the optimum result to be obtained with fewer experiments. Taguchi experimental design method is to analyses the relationship between specified parameters and output responses. With this analysis, it offers the best parameter combination according to the desired output. Thus, the number of experiments to be performed is considerably reduced and profits are made. Taguchi utilizes Orthogonal Arrays (OA) to perform multivariate experiments with a few numbers of tests. The use of OA significantly reduces the number of experiments to be performed [33]–[35].

In this study, the input processing parameters included the four-level helical diameter (d), helical height (h), helical pitch (p) and die channel radius (r). Also output responses are effective strain (ES) and maximum pressing load (ML). The ultimate goal with this method is the high ES value and low ML value of the specimen. For each input processing parameter, 4 different values were specified. Thus, using the Taguchi method with the L16 orthogonal array, the optimum processing parameters were determined with the SPSS 16 statistical software. The parameter combinations obtained by Taguchi method are given in Table 4.

Table 4. Parameter combinations determined from Taguchi.

Cases	d (mm)	h (mm)	r (mm)	p
Case 1	40	40	0	0.5
Case 2	40	50	1	0.75
Case 3	40	60	2	1
Case 4	40	70	4	1.25
Case 5	60	40	1	1
Case 6	60	50	0	1.25
Case 7	60	60	4	0.5
Case 8	60	70	2	0.75
Case 9	80	40	2	1.25
Case 10	80	50	4	1
Case 11	80	60	0	0.75
Case 12	80	70	1	0.5
Case 13	100	40	4	0.75
Case 14	100	50	2	0.5
Case 15	100	60	1	1.25
Case 16	100	70	0	1

3. Results and Discussion

3.1. Finite Element Analyses (FEA) Results

The verification of FEA were firstly carried out by comparing effective strain results with analytical calculation. For one number of pass after ECAP process when channel angle Ψ=90° and corner angle Φ=0° the effective strain value was calculated as 1.15 mm/mm (Equation 1). After FEA results with hexa-ECAP die, it is acquired as 1.12 mm/mm. So, the relative error is calculated as 2% which is acceptable for verifications. In addition, same effective strain value is obtained when comparing with the reference study. Finally, the verification is done by comparing the final shape of the workpieces after FEA results [10]. The Figure 3 illustrates the acquired workpiece geometries from carried out for this study and the reference study. When the figures are compared especially the exit shapes and accumulated areas are very similar. These similarities verify the FEA done in the scope of this study.

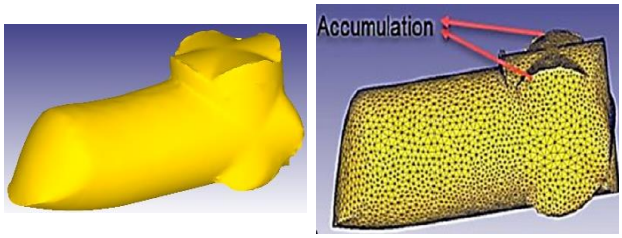

a) b)

Figure 3. FEA results a) caried out for this study, b) carried out by reference study [10].

The literature studies indicate that the required pressing load is maximum while the flow of the sample through the die channel is more difficult [25], [26], [30]. Therefore, it is predicted that the maximum pressing load in the HAP study will occur for the combination where the diameter (d) value is the largest, height (h) is the smallest, radius (r) is the smallest, and pitch (p) is the largest. This combination represents the most challenging flow conditions in the die channel for the HAP process. Although it is possible to predict the maximum pressing load combinations for the HAP process, predicting the effective strain value is not feasible. In general, it is thought that forcing the sample flow through the die channel leads to increased stress on the particles constituting the sample, but this forced flow does not always result in high effective strain.

L16 combinations determined by Taguchi and, FE analyses were carried out with the help of Deform 3D software and the results were analysed by acquiring the effective strain and maximum pressing

load parameters. It is known that the improvement amounts of material properties as a result of SPD processes correlate with effective strain [10], [25]. The analytical calculation of effective strain for the ECAP method is given in Equation 1 [36]. Additionally, the examination of the maximum pressing load parameter shows the experimental applicability and ease of processing of the SPD process.

$$\varepsilon_N = \frac{N}{\sqrt{3}}\left[2\cot\left(\frac{\Phi}{2}+\frac{\Psi}{2}\right)+\Psi\csc\left(\frac{\Phi}{2}+\frac{\Psi}{2}\right)\right] \qquad (1)$$

The obtained effective strain and maximum pressing load values are given in Table 5. When the table is analysed, it is seen that the highest effective strain value is 12 mm/mm. This value is approximately ten times higher than the analytically calculated value (1.15 mm/mm) for ECAP with one pass, obtained using Equation 1 [36]. In other words, the improvement amount obtained from a sample processed with 10 number of passes with ECAP can be achieved with a single pass with the proposed HAP method. On the other hand, the lowest effective strain value was calculated as 0.7 mm/mm. Although the proposed HAP method aimed to increase the efficiency of the traditional ECAP method, this calculated value is even worse than the traditional ECAP method. When the results obtained are compared with the Twist Extrusion (TE) method, which is another frequently studied SPD method, it is seen that the acquired effective strain value after HAP method is higher than the TE method. The study conducted by Found and colleagues suggests that for the TE method, the effective strain per pass is approximately 0.5 mm/mm when β=30°, and with their special design, a value of 3.6 mm/mm is achievable for the AA1100 material after 3 number of passes. Even this value is about one-fourth of the value obtained with the HAP process [37], [38]. Therefore, considering the material improvements, the proposed novel SPD technique has the potential to be an efficient method, but if the correct values for die geometry are not chosen, it can be less efficient than traditional methods too. In this study, this possibility led to make optimization of the die channel geometry first for the HAP method proposed.

The results given in Table 5 are compared with other methods in terms of applicability and workability with the maximum press load parameter, it is observed that it varies between 16 tons and 44.4 tons within the determined combinations. In conventional ECAP and TE methods, this value is around 6-8 tons per each pass [39], [40]. Although the pressing load values in the HAP method are about six times higher than traditional methods, this load is applied in a single pass instead of over ten passes. Therefore, while the total energy expenditure is roughly equivalent, the HAP method provides a shorter production time. As a result, it is concluded that the HAP method does not have a significant disadvantage in terms of applicability and processability compared to traditional methods and even has an advantage due to potential time savings.

In the FEA result for Case 6 parameters determined by the Taguchi combinations, it was observed that the sample could enter the first helix turn and flow was able to be achieved, but the material flow did not occur from the exit turn while continuing to compress the sample. This situation is accepted as an indication that the sample would not flow through the channel under these conditions in a real physical environment. The reason is thought to be the bending moment caused by the force applied to the sample not being in the exact center of the channel, making the flow through the die channel more difficult. Therefore, only the pitch (p) value was changed to 1.25 in the Taguchi combination, and the die drawings were redrawn then, FEA repeated as Case 6.1. But then again, a similar situation occurred in Case 6.1. Hence, the pitch (p) value had to be changed to 1 and the radius (r) value had to be changed to 2 in the Taguchi combination. These parameters were recorded as Case 6.2 and the FEA results were obtained and given in Table 5. These results were accepted as Case 6 results in Taguchi optimization.

Table 5. Finite element analyses results.

Cases	d (mm)	h (mm)	r (mm)	p	Effective Strain (mm/mm)	Max. Pressing Load (ton)
Case 1	40	40	0	0.5	12	25
Case 2	40	50	1	0.75	2.03	26.2
Case 3	40	60	2	1	2.36	31.1
Case 4	40	70	4	1.25	3.24	30.9
Case 5	60	40	1	1	5.3	32.8
Case 6	60	50	**0**	**1.25**	****	****
Case 6.1	60	50	**0**	**1**	****	****
Case 6.2	60	50	**2**	**1**	4.43	32.43
Case 7	60	60	4	0.5	2.3	33.4
Case 8	60	70	2	0.75	0.7	16.1
Case 9	80	40	2	1.25	6	31.3
Case 10	80	50	4	1	5.15	30.6
Case 11	80	60	0	0.75	11	28.5
Case 12	80	70	1	0.5	0.75	21
Case 13	100	40	4	0.75	2.7	33.3
Case 14	100	50	2	0.5	0.91	44.4
Case 15	100	60	1	1.25	7.3	34.9
Case 16	100	70	0	1	5.6	16

3.2. Taguchi Optimization Results

The signal to noise ratios values obtained as a result of Taguchi optimizations are given in Table 6. The results reveal that the most influential parameter in the optimization process is the height (h) with a delta value of 3.412, indicating its significant impact on the results. The least influential parameter is found to be the diameter (d), with a delta value of 1.448. It is concluded that the other parameters are radius and pitch parameters respectively according to the order of influence. As a result, when the priority ranking of the effective parameters is examined, it is seen that d and h values balance each other and r and p values balance each other.

Table 6. Response table for signal to noise ratios.

Level	d	h	r	p
1	5.699	5.627	4.307	6.102
2	6.879	8.076	6.201	5.209
3	5.431	6.120	6.652	5.906
4	6.476	4.664	7.326	7.268
Delta	1.448	3.412	3.019	2.059
Rank	4	1	2	3

Analysing the signal-to-noise ratio graph in Figure 4, it can be seen that the combination that gives the best result among the Taguchi L16 combinations is defined as a diameter (d) value of 60 mm, a height (h) value of 50 mm, a radius (r) value of 4 mm, and a pitch (p) value of 1.25. When calculating the optimization result, the effective strain value is a more effective output variable for decision making. Because signal-to-noise ratio was obtained at a higher level for all four parameters as illustrated in Figure 4. As the load value is related to the application, it was the second level decision maker in calculating the optimum die geometry as predicted.

When the results here are analysed in terms of HAP process, it is seen that the effective strain value is not maximum for the most difficult flow conditions. However, when the results in Table 6 are analysed, it is noted that the increase in pitch, which extends the flow path, does not necessarily lead to a significant gain in effective strain as expected, but rather increases the maximum pressing load. The actual gains in values seem to occur at the entrance and exit of the helical channel. Despite the highest pitch value being used, the radius (r) is also chosen to be the largest to facilitate flow.

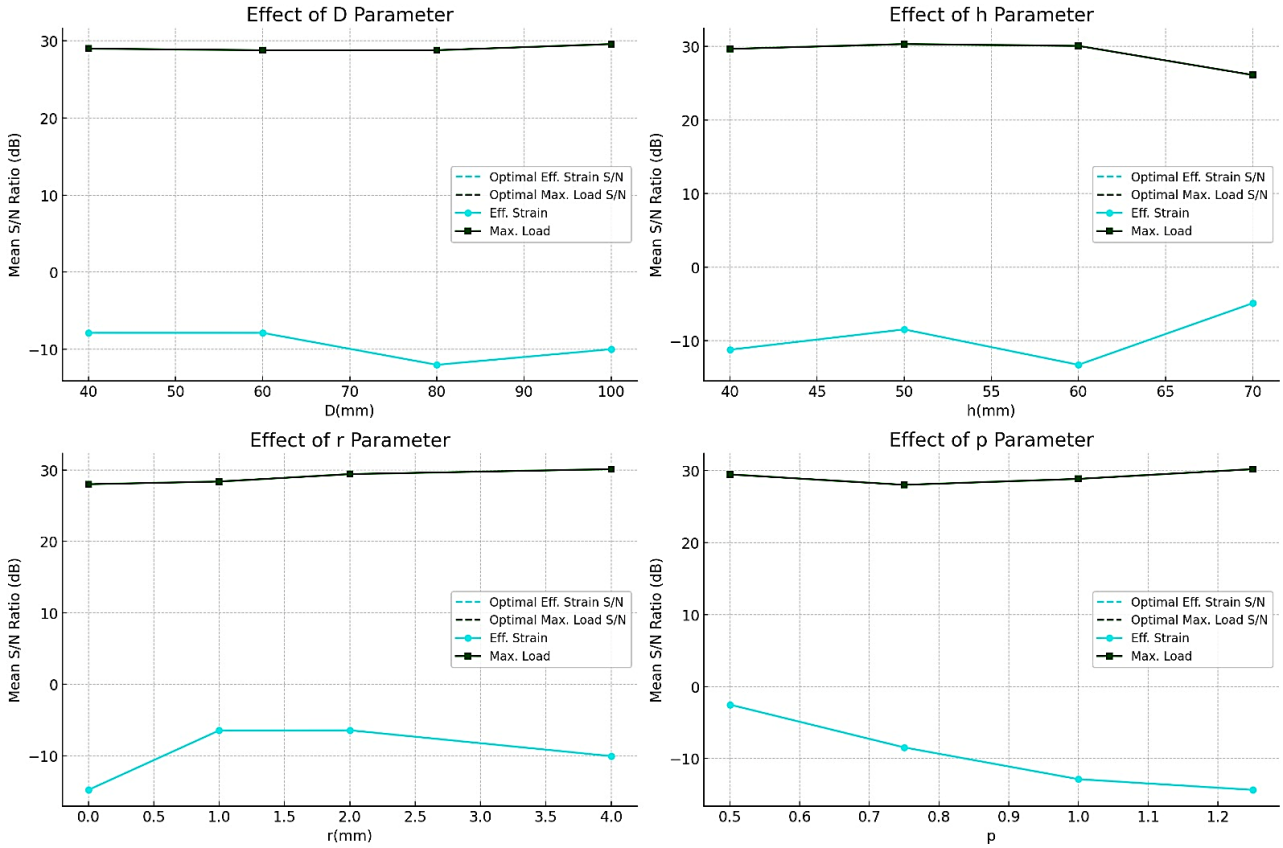

Figure 4. Signal to noise graphs after Taguchi optimization by using SPSS 16 software.

.

After finding the optimum parameters through the Taguchi optimization method, the design of the HAP die was revised accordingly. Subsequently, FEA was conducted again using the Deform 3D software with the same material and parameters as shown in Figure 5. The FEA results with the optimized die geometry showed an effective strain value of 9.34 mm/mm and a maximum pressing load of 31.82 tons.

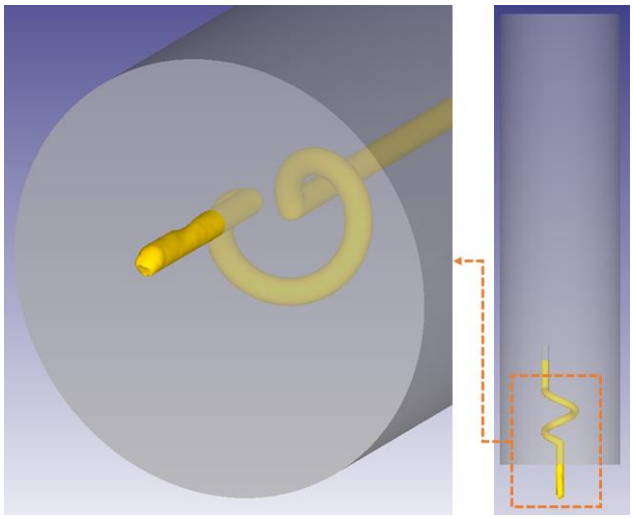

Figure 5. FEA results for optimum die channel geometry.

4. Conclusion and Suggestions

Within the scope of this study, a novel SPD method called Helical Angular Pressing (HAP) has been proposed to the literature. The efficiency, applicability, and workability of this novel method were investigated. The die channel geometries were analysed using FEA, and optimized for maximum effective strain and minimum pressing load through Taguchi optimization technique.

The obtained results can be summarized as follows:

- The maximum effective strain value was achieved as 12 mm/mm, comparable to the results of 10 passes through ECAP method. In addition, when this result is compared with TE, it is approximately 4 times higher than the value obtained as a result of TE processing.
- The minimum effective strain value was calculated as 0.7 mm/mm. This value is even worse than the conventional ECAP method. The HAP method has the potential to be more efficient than the conventional ECAP or TE methods. For this reason, it is crucial for its efficiency to optimize the geometry of the die channel firstly.
- The average pressing load obtained (around 30 tons) is approximately four times higher than ECAP and TE methods (around 8 tons), but the gains with HAP are achieved in a single pass, which potentially reduces total energy expenditure and processing time.
- As a result of the Taguchi optimization, the order of the effect of the die channel geometries on the optimization result is as h, r, p and d respectively.
- When the signal-to-noise ratios resulting from the Taguchi optimization were investigated, the combination of diameter = 60 mm, height = 50 mm, radius= 4 mm and pitch= 1.25 were found to be the optimal die channel geometry for HAP method. Repeating the FEA with these optimum values, the effective strain value was achieved as 9.34 mm/mm and the maximum press load value was acquired as 31.82 tons.

In summary, the HAP method, as a new SPD technique, is found to be more efficient, applicable, and workable compared to traditional ECAP and TE methods. It's expected to contribute significantly to future research and applications in this field.

Future Works

1. Within the scope of this study, only 16 analyses were performed for the parameters determined by Taguchi combination. Therefore, the effects of die geometries on effective strain and maximum press load were not discussed. In future studies, these effects can be investigated by performing analyses with FEA and/or experimentally with different die geometries.
2. Within the scope of this study, only FEA was performed for the HAP method proposed for the first time. It is obvious that it is very difficult to produce die channel geometry with today's technology. However, it is thought that the HAP die in question can be produced more easily, especially as a result of rapid developments in additive manufacturing methods. Therefore, experimental validation of this study's findings may be feasible in the future.

Acknowledgment

The author would like to thank Dr. Mehmet Akif YERLİKAYA for his helps during optimization process of this study.

Statement of Research and Publication Ethics

The study is complied with research and publication ethics.

References

[1] T. Langdon, 'The processing of ultrafine-grained materials through the application of severe plastic deformation', *Journal of Materials Science*, vol. 42, pp. 3388–3397, May 2007, doi: 10.1007/s10853-006-1475-8.

[2] G. Faraji, H. S. Kim, and H. T. Kashi, 'Severe Plastic Deformation Methods, Processing and Properties', in *Severe Plastic Deformation*, Elsevier, 2018, pp. 1–315. doi: 10.1016/B978-0-12-813518-1.00020-5.

[3] R. Z. Valiev, R. K. Islamgaliev, and I. V. Alexandrov, 'Bulk nanostructured materials from severe plastic deformation', *Progress in Materials Science*, vol. 45, no. 2, pp. 103–189, Mar. 2000, doi: 10.1016/S0079-6425(99)00007-9.

[4] R. Z. Valiev and T. G. Langdon, 'Principles of equal-channel angular pressing as a processing tool for grain refinement', *Progress in Materials Science*, vol. 51, no. 7, pp. 881–981, Sep. 2006, doi: 10.1016/j.pmatsci.2006.02.003.

[5] H. Gleiter, 'Nanostructured materials: basic concepts and microstructure', *Acta Materialia*, vol. 48, no. 1, pp. 1–29, Jan. 2000, doi: 10.1016/S1359-6454(99)00285-2.

[6] T. Lowe and R. Valiev, 'Investigations and applications of severe plastic deformation'. Accessed: May 31, 2023. [Online]. Available: https://www.semanticscholar.org/paper/Investigations-and-applications-of-severe-plastic-Lowe-Valiev/5fb98bd57db1c90daeb3a4a24191e189901fe4e9

[7] C. Haase, O. Kremer, W. Hu, T. Ingendahl, R. Lapovok, and D. A. Molodov, 'Equal-channel angular pressing and annealing of a twinning-induced plasticity steel: Microstructure, texture, and mechanical properties', *Acta Materialia*, vol. 107, pp. 239–253, Apr. 2016, doi: 10.1016/j.actamat.2016.01.056.

[8] H. Shahmir, T. Mousavi, J. He, Z. Lu, M. Kawasaki, and T. G. Langdon, 'Microstructure and properties of a CoCrFeNiMn high-entropy alloy processed by equal-channel angular pressing', *Materials Science and Engineering: A*, vol. 705, pp. 411–419, Sep. 2017, doi: 10.1016/j.msea.2017.08.083.

[9] A. Esmaeili, M. H. Shaeri, M. T. Noghani, and A. Razaghian, 'Fatigue behavior of AA7075 aluminium alloy severely deformed by equal channel angular pressing', *Journal of Alloys and Compounds*, vol. 757, pp. 324–332, Aug. 2018, doi: 10.1016/j.jallcom.2018.05.085.

[10] S. Öğüt, H. Kaya, A. Kentli, K. Özbeyaz, M. Şahbaz, and M. Uçar, 'Investigation of Strain Inhomogeneity in Hexa-ECAP Processed AA7075'.

[11] R. Z. Valiev, A. V. Korznikov, and R. R. Mulyukov, 'Structure and properties of ultrafine-grained materials produced by severe plastic deformation', *Materials Science and Engineering: A*, vol. 168, no. 2, pp. 141–148, Aug. 1993, doi: 10.1016/0921-5093(93)90717-S.

[12] Y. Estrin and A. Vinogradov, 'Extreme grain refinement by severe plastic deformation: A wealth of challenging science', *Acta Materialia*, vol. 61, no. 3, p. 782, 2013.

[13] R. Z. Valiev, I. V. Alexandrov, and R. K. Islamgaliev, 'Processing and Properties of Nanostructured Materials Prepared by Severe Plastic Deformation', in *Nanostructured Materials: Science & Technology*, G.-M. Chow and N. I. Noskova, Eds., in NATO ASI Series. , Dordrecht: Springer Netherlands, 1998, pp. 121–142. doi: 10.1007/978-94-011-5002-6_7.

[14] V. M. Segal, 'Materials processing by simple shear', *Materials Science and Engineering: A*, vol. 197, no. 2, pp. 157–164, Jul. 1995, doi: 10.1016/0921-5093(95)09705-8.

[15] A. P. Zhilyaev and T. G. Langdon, 'Using high-pressure torsion for metal processing: Fundamentals and applications', *Progress in Materials Science*, vol. 53, no. 6, pp. 893–979, Aug. 2008, doi: 10.1016/j.pmatsci.2008.03.002.

[16] Y. Ito, K. Edalati, and Z. Horita, 'High-pressure torsion of aluminum with ultrahigh purity (99.9999%) and occurrence of inverse Hall-Petch relationship', *Materials Science and Engineering A*, vol. 679, pp. 428–434, Jan. 2017, doi: 10.1016/j.msea.2016.10.066.

[17] A. Fattah-alhosseini, A. R. Ansari, Y. Mazaheri, and M. K. Keshavarz, 'Effect of immersion time on the passive and electrochemical response of annealed and nano-grained commercial pure titanium in Ringer's physiological solution at 37 °C', *Materials Science and Engineering: C*, vol. 71, p. 771, 2017.

[18] M. Shahbaz, N. Pardis, R. Ebrahimi, and B. Talebanpour, 'A novel single pass severe plastic deformation technique: Vortex extrusion', *Materials Science and Engineering: A*, vol. 530, pp. 469–472, Dec. 2011, doi: 10.1016/j.msea.2011.09.114.

[19] R. Z. Valiev, Y. Estrin, Z. Horita, T. G. Langdon, M. J. Zechetbauer, and Y. T. Zhu, 'Producing bulk ultrafine-grained materials by severe plastic deformation', *JOM*, vol. 58, no. 4, pp. 33–39, Apr. 2006, doi: 10.1007/s11837-006-0213-7.

[20] M. Richert, R. Hubicki, and P. Łebkowski, 'Perspectives of Microstructure Refinement of Aluminum and Its Alloys by the Reciprocating Extrusion (Cyclic Extrusion Compression—CEC)', *Materials*, vol. 15, p. 4006, Jun. 2022, doi: 10.3390/ma15114006.

[21] G. A. Manjunath, S. Shivakumar, S. P. Avadhani, and P. C. Sharath, 'Investigation of mechanical properties and microstructural behavior of 7050 aluminium alloy by multi directional forging technique', *Materials Today: Proceedings*, vol. 27, pp. 1147–1151, Jan. 2020, doi: 10.1016/j.matpr.2020.02.001.

[22] R. Kocich, G. Miroslav, M. Kursa, I. Szurman, and A. Macháčková, 'Twist channel angular pressing (TCAP) as a method for increasing the efficiency of SPD', *Materials Science and Engineering: A*, vol. 527, pp. 6386–6392, Sep. 2010, doi: 10.1016/j.msea.2010.06.057.

[23] S. Sepahi-Boroujeni and F. Fereshteh-Saniee, 'The influences of the expansion equal channel angular extrusion operation on the strength and ductility of AZ80 magnesium alloy', *Materials Science and Engineering: A*, vol. 636, pp. 249–253, Jun. 2015, doi: 10.1016/j.msea.2015.03.073.

[24] S. Öğüt, H. Kaya, A. Kentli, and M. Uçar, 'Applying hybrid equal channel angular pressing (HECAP) to pure copper using optimized Exp.-ECAP die', *Int J Adv Manuf Technol*, vol. 116, no. 11, pp. 3859–3876, Oct. 2021, doi: 10.1007/s00170-021-07717-9.

[25] K. Özbeyaz, H. Kaya, and A. Kentli, 'Novel SPD Method: Twisted Variable Channel Angular Extrusion', *Met. Mater. Int.*, vol. 28, no. 5, pp. 1290-1305, May 2022, doi:10.1007/s12540-021-01086-4.

[26] M. Şahbaz, H. Kaya, and A. Kentli, 'A new severe plastic deformation method: thin-walled open channel angular pressing (TWO-CAP)', *Int J Adv Manuf Technol*, vol. 106, no. 3, pp. 1487–1496, Jan. 2020, doi: 10.1007/s00170-019-04748-1.

[27] G. Faraji, A. Babaei, M. M. Mashhadi, and K. Abrinia, 'Parallel tubular channel angular pressing (PTCAP) as a new severe plastic deformation method for cylindrical tubes', *Materials Letters*, vol. 77, pp. 82–85, Jun. 2012, doi: 10.1016/j.matlet.2012.03.007.

[28] N. Thangapandian, S. Balasivanandha Prabu, and K. A. Padmanabhan, 'Effect of Temperature on Grain Size in AA6063 Aluminum Alloy Subjected to Repetitive Corrugation and Straightening', *Acta Metall. Sin. (Engl. Lett.)*, vol. 32, no. 7, pp. 835–844, Jul. 2019, doi: 10.1007/s40195-018-0866-6.

[29] H. Kaya, K. Özbeyaz, A. Kentli, M. Şahbaz, and S. Öğüt, *Mechanical Properties and Electrical Conductivity Performance of ECAP Processed Al2024 Alloy*. 2019.

[30] S. Öğüt, H. Kaya, and A. Kentli, 'Comparison of the Effect of Equal Channel Angular Pressing, Expansion Equal Channel Angular Pressing, and Hybrid Equal Channel Angular Pressing on Mechanical Properties of AZ31 Mg Alloy', *J. of Materi Eng and Perform*, vol. 31, no. 4, pp. 3341–3353, Apr. 2022, doi: 10.1007/s11665-021-06430-8.

[31] X. Zhao, X. Yang, X. Liu, C. T. Wang, Y. Huang, and T. G. Langdon, 'Processing of commercial purity titanium by ECAP using a 90 degrees die at room temperature', *Materials Science and Engineering: A*, vol. 607, pp. 482–489, Jun. 2014, doi: 10.1016/j.msea.2014.04.014.

[32] J. R. Davis, *Aluminum and Aluminum Alloys*. ASM International, 1993.

[33] A. Mashhuriazar, A. Ebrahimzadeh Pilehrood, H. Moghanni, A. H. Baghdadi, and H. Omidvar, 'Finite Element Analysis and Optimization of Equal-Channel Angular Rolling Process by Using Taguchi Methodology', *J. of Materi Eng and Perform*, vol. 32, no. 1, pp. 176–184, Jan. 2023, doi: 10.1007/s11665-022-07100-z.

[34] C. Obara, F. M. Mwema, J. N. Keraita, H. Shagwira, and J. O. Obiko, 'A multi-response optimization of the multi-directional forging process for aluminium 7075 alloy using grey-based taguchi method', *SN Appl. Sci.*, vol. 3, no. 6, p. 596, May 2021, doi: 10.1007/s42452-021-04527-2.

[35] C. Hamzaçebı and F. Kutay, 'Taguchi Metodu: Bir Uygulama: Taguchi Method: An Application.', *Teknoloji*, vol. 6, no. 3/4, pp. 7–17, Jul. 2003.

[36] Y. Iwahashi, Z. Horita, M. Nemoto, and T. G. Langdon, 'An investigation of microstructural evolution during equal-channel angular pressing', *Acta Materialia*, vol. 45, pp. 4733–4741, Jan. 1997, doi: 10.1016/S1359-6454(97)00100-6.

[37] D. M. Fouad, A. Moataz, W. H. El-Garaihy, and H. G. Salem, 'Numerical and experimental analysis of multi-channel spiral twist extrusion processing of AA5083', *Materials Science and Engineering: A*, vol. 764, p. 138216, Sep. 2019, doi: 10.1016/j.msea.2019.138216.

[38] S. A. A. Akbari Mousavi and A. R. Shahab, 'Influence of Strain Accumulation on Microstructure of Aluminum 1100 in The Twist Extrusion', *Int. J. Mod. Phys. B*, vol. 22, no. 18n19, pp. 2858–2865, Jul. 2008, doi: 10.1142/S0217979208047687.

[39] R. Kulagin, M. I. Latypov, H. S. Kim, V. Varyukhin, and Y. Beygelzimer, 'Cross Flow During Twist Extrusion: Theory, Experiment, and Application', *Metall Mater Trans A*, vol. 44, no. 7, pp. 3211–3220, Jul. 2013, doi: 10.1007/s11661-013-1661-7.

[40] 'Twist Extrusion as a Potent Tool for Obtaining Advanced Engineering Materials: A Review - Beygelzimer - 2017 - Advanced Engineering Materials - Wiley Online Library'. Accessed: May 31, 2023. [Online]. Available: https://onlinelibrary.wiley.com/doi/full/10.1002/adem.201600873

Bitlis Eren Üniversitesi Fen Bilimleri Dergisi
BİTLİS EREN UNIVERSITY JOURNAL OF SCIENCE
ISSN: 2147-3129/e-ISSN: 2147-3188
VOLUME: 12 NO: 4 PAGE: 969-977 YEAR: 2023
DOI:10.17798/bitlisfen.1306633

Phenolic Characterization and *in vitro* Biological Activities of *Ranunculus Cornutus* DC.

Ahmet SAVCI[1*], Serap DİCLE[2]

[1]*Muş Alparslan University, Faculty of Science and Literature, Department of Molecular Biology and Genetics*
[1]Muş Alparslan University, *Graduate School of Natural and Applied Sciences*
(ORCID: 0000-0002-9609-785X) (ORCID: 0000-0001-7642-0405)

Keywords:
Antioxidant, DNA,
DPPH, FRAP,
Metal Chelating, *Ranunculus*.

Abstract
In this study, *Ranunculus cornutus* DC. (Evlimemedotu) content analysis and some biological activities were investigated. For this purpose, methanol and water extracts of the plant were taken and their phenolic analyzes were determined by LC-MS-MS. Total antioxidant method, FRAP, CUPRAC, iron chelation method, DPPH and ABTS methods were used for antioxidant studies. According to LC-MS-MS results, the highest amounts of phenolic substances were determined as fumaric acid (3261.43 µg/L), vanillic acid (1217.70 µg/L) and ferulic acid (769.40 µg/L), respectively. According to the antioxidant results, it was determined that water and methanol extracts exhibited lower activity than standard antioxidants. It can be said that the reason for this is the amount of phenolic they contain. However, it was observed that the methanol extract generally had better antioxidant activity than the water extract. Finally, according to the DNA study results, it was determined that water and methanol extracts alone did not have a negative effect on the stable structure of DNA. Since there are no studies with *R. cornutus* DC., it is thought that this study will make a very important contribution to the literature and provide important data for future studies.

1. Introduction

Ranunculaceae family, which has approximately 50 genera and 2000 species in the world, has about 85 species in our country. 15 of these species are endemic [1]. *Ranunculus* species, which are annual or perennial herbaceous, rarely shrub-like or climbing plants, are also known by the names of "buttercup, hemlock and evlimemedotu" among the people [2]. These plants are used in the treatment of various diseases among people in many parts of our country. It is used in the treatment of diseases such as constipation, rheumatic diseases, hemorrhoids, edema, abscess, healing of wounds and jaundice [1], [3], [4].

Several compounds isolated from Ranunculus species have previously undergone clinical trials. Some are used in the treatment of various conditions such as cancer, cardiac dysfunctions, severe hemostasis, and various types of inflammation [5]–[7]. Numerous reports have been made of the traditional use of members of the Ranunculaceae family in the treatment of various oxidative stress-related diseases. Despite this fact, as far as we know, studies on the antioxidant properties of these plants are limited [8]–[11].

It has been reported by various studies that oxidative stress, which occurs as a result of excessive accumulation of reactive oxygen species in the organism, causes various diseases [12], [13]. In recent years, there have been various studies on the interaction of compounds with DNA. It is known that DNA damage occurs as a result of excessive accumulation of free radicals in the organism [14]–[16]. For this reason, it is important whether the DNA remains stable as a result of the interaction of plants with plasmid DNA.

*Corresponding author: a.savci@alparslan.edu.tr
Received: 31.05.2023, Accepted: 24.08.2023

In our literature search, no study on the biological activities of *R. Cornutus* (RC) was found. Therefore, in this study, phenolic content analysis was performed by preparing methanol and water extracts of RC. The total antioxidant method according to thiocyanate method, ferric reducing antioxidant power (FRAP), cupric reducing antioxidant capacity (CUPRAC), iron chelation activity, 1,1-diphenyl-2-picrylhydrazil (DPPH), 2,2'-azino -bis(3-ethylbenzothiazoline-6-sulfonate) methods were used for the antioxidant analysis of extracts. PBR322 plasmid DNA was used to determine the interaction of extracts on DNA. Since no previous studies on this plant have been found, this study will make a very important contribution to the literature and will be a reference for future studies.

2. Material and Method

2.1. Plant material

R. cornutus DC. was collected from Eastern Anatolia, Muş, Çöğürlü Village and the species were determined by Murat Kurşat from the Biology Department of the Faculty of Arts and Sciences at Bitlis University. Chemical processes were carried out in the laboratories of Muş Alparslan University.

2.2. Preparation of Extracts

After the plants were collected during the vegetation period, they were left to dry. After species determination, water (RcWtr) and methanol (RcMetOH) extracts were obtained. For extracts, approximately 50 g of plant samples were dissolved in 300 mL of solvent. The extracts prepared with the help of the Soxhlet Extraction Device were filtered with the help of filter paper and lyophilized in the Laboratories of the Chemistry Department of Muş Alparslan University. It was stored in colored bottles at +4 ºC until analysis.

2.3. Phenolic Compound Analysis by LC-MS/MS

Detection of phenolic compounds was performed with Agilent 6460 Triple Quadrupole LC-MS/MS (Liquid Chromatography-Tandem Mass/Mass Spectrometer, Agilent Technologies) equipped with a Zorbax SB-C18 (4.6x100mm; 3.5 Micron) column. Analysis mode is multiple reaction monitoring mode (MRM). The mobile phase was filtered with a 0.45 µm Millipore membrane filter before use. The total run time was 7.0 minutes. The injection volume for sample extracts was 5 µl. Mobile phase A consisted of 0.1% (v/v) formic acid in water (solvent A) and mobile phase B consisted of 0.1% formic acid in acetonitrile (solvent B). LC-MS/MS analyzes were performed in the laboratories of the Eastern Anatolia Advanced Technologies Research and Application Center (DAYTAM).

2.4. Total Antioxidant Activity Assay

According to the thiocyanate method [17], the volumes of the extracts at 15µl, 30µl and 45µl concentrations were made up to 500 µl with phosphate buffer and 500 µl of linoleic acid was added to each. The extracts were incubated at 37 °C. Every eight hours, 20 µl of the extract was taken and placed in test tubes containing ethanol. 20 µl of Fe^{2+} and SCN^- solutions were added to each. The absorbance of the samples at 500 nm was read on a Microvolume Spectrophotometer (Thermo Scientific Multiscan Go).

2.5. FRAP Assay

Distilled water was used to make the volumes of the extracts of different concentrations (15, 30 and 45 µg/ml) to 200 µl. 500 µl of phosphate buffer and potassium ferricyanide [$K_3Fe(CN)_6$] were added to the extracts. After 20 min incubation at 50ºC, 500 µl of trichloroacetic acid (TCA) was added. The same amount of distilled water and 100 µl of $FeCl_3$ were added to the 500 µl mixture taken from the upper phase, and the absorbance values at 700 nm were recorded [18].

2.6. CUPRAC Assay

For the test, extracts of different concentrations and standard antioxidants were placed in the sample cups and their volumes were completed to 1 ml with distilled water. After adding 250 µl of $CuCl_2$ solution, ethanolic neocuprine and acetate buffer, they were incubated at room temperature for 30 minutes. Finally, absorbances at 450 nm were recorded [19].

2.7. Metal Chelating Ability

Iron chelating activities of extracts and standard antioxidants (BHA, BHT and Ascorbic acid) were performed according to the previous method [20]. For this process, 2 mM solution containing 100 µL of $FeCl_2.4H_2O$ and 70 µL of distilled water was added to 50 µL of solution containing samples at concentrations of 15, 30 and 45 µg/ml. The total volume was made up to 1 ml by adding distilled ethanol. The reaction was initiated by adding 50 µL of 5 mM ferrozine solution. After mixing the solution

in a vortex, it was incubated at room temperature for 10 minutes. After incubation, the absorbance of the solutions at 562 nm was recorded using a UV-Vis spectrophotometer.

2.8. DPPH Radical Scavenging Assay

The DPPH free radical scavenging capacities of the samples were determined according to the method of Blois [21]. Samples (15, 30 and 45 µg/µl) were taken into test tubes and their total volume was made up to 600 µl with ethyl alcohol. After adding 200 µl of DPPH• solution on them, they were incubated for 30 minutes. Finally, their absorbances at 517 nm were recorded.

2.9. ABTS Radical Scavenging Assay

According to the method of Re et al., the ABTS solution was first diluted with phosphate buffer (pH 7.4) to obtain an absorbance of 0.750 ± 0.025 at 734 nm. Then, 15, 30, and 45 µL of stock solutions were taken and their volumes were made up to 100 µL with distilled water. 1 mL of $ABTS^{\bullet+}$ solution prepared on them was added and vortexed. Radical scavenging activity was measured at 734 nm [22].

2.10. Plasmid DNA Interaction Assay

The possible effect of *R. cornutus* DC. on DNA was determined by agarose gel electrophoresis method using pBR322 plasmid DNA [23]. For this purpose, the main stock materials were prepared by dissolving 10 mg of the substance sample in 1 ml of DMSO. These stocks were diluted to use substances with concentrations of 1, 0.5 and 0.25 mg/ml. Amounts to 16 PCR tubes, respectively; 1. pBR322 DNA (50 ng) 10 µl, Hydrogen peroxide (H_2O_2) 5 µl, 3. DMSO 10 µl and 4. *R. cornutus* DC. It was prepared to be completed to 25 µl in total with concentrates. 5 µl of deionized distilled water was used to make up the tubes without adding H_2O_2 to 25 µl. The effect of each sample on DNA was determined by agarose gel electrophoresis. PCR tubes were incubated in the dark (24 hours at 37 ºC). After incubation, 5 µl of the DNA mixture was mixed with loading buffer and loaded onto a 1% agarose gel. Then electrophoresis was performed in TBE buffer at 40 V for 2-3 hours. After electrophoresis, the gels were stained with ethidium bromide and the gel photographs were viewed with the aid of the CemiDoc XRS BIORAD imaging device.

3. Results and Discussion

3.1. Phenolic compound analysis

The phenolic compound composition of *R. cornutus* DC. analyzed by LC-MS/MS method was evaluated with the phenolic compounds introduced as standard. As seen in Table 1, fumaric acid (3261.43 µg/L), vanillic acid (1217.70 µg/L), ferulic acid (769.40 µg/L), caffeic acid (509.10 µg/L), The amount of chlorogenic acid (311.90 µg/L) and p-Coumaric Acid (136.60 µg/L) were higher than the others (Sinapic Acid, Cyanidin-3-O-Glucoside, Quinic Acid, Rosmarinic Acid, etc.).

In the literature search, no study was found on the phenolic contents of *R. cornutus*. However, there are studies on phenolic substance analyses of different *Ranunculus* species. In a study conducted by Bhatti et al. in 2015, the presence of caffeic acids (0.017%) in the methanol extract of the *R. arvensis* plant was shown. In addition, it was determined that there was less caffeic acid (0.008%) in the water extract compared to the methanol extract [24]. In another study; The presence of quercetin-7-O-glucoside and rutin in R. peltatus extracts was determined [25]. It has been reported by Noor et al. that *R. repens* contains many flavonoids and phenolics [26]. In another study conducted by Campos et al in 1996, the phenolic profiles of pollen belonging to the *R. sardous* Crantz species were examined. It has been stated that all pollens analyzed contain flavonol glycosides, usually quercetin, kaempferol, herbacetin or isorhamnetin derivatives, and some contain myricetin, tricetin, luteolin and 3-O-methylquercetin. Significant levels of phenolic acid derivatives were also detected in some pollen [27]. In the study conducted by Wang et al., it was reported that the extract of the *R. japonicus* species contains Chaphthoside, Apigenin-7-O- β-D-glucoside, Yangonin, Luteolin-7-O- β-D-glucoside and Berberine [28]. In a study by Deghima et al, it was reported that *R. macrophyllus* ethyl acetate extract contains high amounts of gallic acid, dihydroxybenzoic acid and hesperidin [29].

Table 1. Quantitative determination of phenolic compound content of *R. cornutus* DC by LC-MS/MS method

Phenolic Compounds	RT	Concentration (µg L^{-1})
4-OH-Benzoic Acid	11,269	33,8778
Apigenin	14,033	ND
Ellagic acid	12,073	ND
Epigallocatechin Galate	11,518	ND
Epicatechin	11,233	ND
Ferulic Acid	12,571	769,4048
Fumaric Acid	3,597	3261,4255
Galanjin	15,672	ND
Gallic acid	5,451	ND
Hesperidin	11,937	26,9232
İsorhamnetin	14,160	ND
Caffeic Acid	11,571	509,1006
Catechin	11,174	ND
Keracyanin Chloride	10,385	0,5261
Quinic Acid	2,390	36,3593
Chlorogenic Acid	10,896	311,8981
Chrysin	15,586	ND
Quercetin	13,494	ND
Curcumin	15,682	ND
Luteolin	13,423	ND
Myricetin	12,753	ND
Naringenin	14,062	ND
Naringin	11,909	ND
Peonidin-3-O-Glucoside	11,039	9,3682
Pyrogalol	6,570	ND
p-Coumaric Acid	12,312	136,5990
Resveratrol	13,107	10,6104
Rosmarinic Acid	12,520	35,0895
Sinapic Acid	12,367	50,1630
Syringic Acid	11,657	ND
Cyanidin-3-O-Glucoside	10,706	38,8923
Taxifolin	12,391	ND
Vanillic Acid	11,877	1217,7027
Vanillin	12,617	11,3878
Vitexin	11,736	ND

ND: not detected, RT: Retention time

3.2. Antioxidant Activity

Six different tests were used to determine the antioxidant properties of RCWtr and RCmetOH. FRAP and CUPRAC results were calculated as µg TE/ml and other test results were calculated by taking the IC50 value (Table 2).

Ferric thiocyanate method was used for the total antioxidant activity measurements of the extracts. For this purpose, the lipid peroxide removal percentages of the extracts were calculated using the equation below.

According to the total antioxidant results, it was observed that standard antioxidants scavenge lipid peroxides better, however, the activities of the samples generally increased depending on the increase in concentration. In addition, it was determined that water extract (IC50:106,79) exhibited stronger activity than methanol extract (IC50:146,41). The lipid peroxide removal powers of the samples were respectively as follows: BHT (IC50: 24.96) > BHA (IC50: 26.13) > AA (IC50: 46.72) > RcWtr (IC50: 106.79) > RcMetOH (IC50: 146.41).

Iron ions (Fe^{3+}) reduction analysis (FRAP) can be defined as an electron transfer. It can be defined as an electron transfer-based assay that measures the reducers (antioxidants) present in a sample based on a spectrophotometric redox reaction [30]. According to the FRAP results, it was observed that BHA, BHT and AA used as standard were stronger reducing agents than extracts. According to

the table, BHA (90.34 µg TE/ml) showed the best effect, while AA (38.71 µg TE/ml), BHT (18.16 µg TE/ml), RcMetOH (6.01 µg TE/ml) and RcWtr (5.03 µg TE/ml) followed.

$$\text{Lipid peroxidation scavenging } (\%) = 100 - (\frac{As}{Ac} x100) \quad (1)$$

Table 2. Antioxidant activity results from extracts and standard antioxidants (BHA, BHT and AA)

Samples	Total antioxidant activity (IC50)	FRAP (µg TE/ml)	CUPRAC (µg TE/ml)	Metal chelating (IC50)	DPPH (IC50)	ABTS (IC50)
Rc-Wtr	106.79±0.12	5.03±0.01	6.21±0.01	128.2±0.77	152.67±0.06	155.23±0.22
Rc-MetOH	146.41±0.04	6.01±0.02	7.88±0.01	124.1±1.98	121.24±0.02	125.43±0.15
BHA	26.13±0.02	90.34±0.01	101.47±0.03	38.29±0.81	20.14±0.01	18.29±0.08
BHT	24.96±0.02	18.16±0.01	72.81±0.04	38.1±0.43	26.86±0.04	24.65±0.02
AA	46.72±0.01	38.71±0.02	21.33±0.01	32.41±0.91	19.4±0.01	20.19±0.03

TE: Trolox equivalent

According to the results of the Kuprak method, it was observed that BHA, BHT and AA reduced Cu^{+2} ions better than the extracts. According to the table, BHA (101.47 µg TE/ml) exhibits the best effect, while BHA (72.81 µg TE/ml), AA (21.33 µg TE/ml), RcMetOH (7.88 µg TE/ml) and RcWtr (6.21 µg TE/ml) followed.

The metal chelating activity results were in line with the FRAP results. The results showed that BHA, BHT and AA chelated iron ions more strongly than extracts. According to Table 2, AA (IC50: 32.41) showed the best effect, while RcWtr (IC50: 128.2) showed the lowest activity.

The antiradical activities of the extracts and standard antioxidants were investigated by two different methods and it was observed that the results supported each other. According to the DPPH radical scavenging results, it was observed that BHA, BHT and AA scavenged radicals more powerfully than the extracts. According to the table, AA (IC50: 19.4) showed the best effect, while BHA (IC50: 20.14), BHT (IC50: 26.86), RcMetOH (IC50: 121.24) and RcWtr (IC50: 152.67) followed. Similarly, BHA, BHT, and AA were found to scavenge $ABTS^{\bullet+}$ radicals more strongly than extracts. According to the table, AA (IC50: 20.19) showed the best effect, while RcWtr (IC50: 155.23) showed the lowest activity.

In the literature, no study was found on the antioxidant properties of the *Rc* DC. However, there are various studies on different species of the same family. In a study, it was determined that *R. macrophyllus* ethyl acetate extract had better antioxidant capacity than chloroform, hexane and water extracts. It has also been reported that the ethyl acetate extract exhibits stronger performance than the standard antioxidants of BHA and quercetin [29]. In another study, it was stated that *R. repens* methanol extract showed the best antioxidant activity [31].

Shadid et al. [32] reported that *R. sceleratus* ethyl acetate extract reduced iron ions most strongly, while Say et al. [33] reported that *R. constantinopolitanus* methanol extract reduced Cu^{+2} ions better than hexane, ethyl acetate, water and trolox extracts.

When metal chelating activities of different extracts were examined in previous studies, it was observed that some extracts formed strong chelates with ferrous metal, while some extracts had very weak activities [34], [35].

According to the results of DPPH and ABTS radical scavenging activity of n-hexane, ethyl acetate, methanol and water extracts prepared from *R. marginatus* and *R. sprunerianus* species, it was observed that methanol extract performed stronger than other extracts [34]. In another study, it was stated that *R. sceleratus* ethyl acetate extract scavenged DPPH radicals better than other extracts [35]. Solanki et al. [35] reported that R. sceleratus ethanol extract scavenges ABTS radicals better than chloroform extract.

While this study has similar aspects to previous studies, it also has different aspects. This situation is thought to be caused by the difference in

of factors such as different species, climatic conditions, different solvents, phenolic content, etc.

3.3. Interaction with plasmid DNA

pBR322 plasmid DNA was used to determine the interaction of the extracts with DNA (Figure 1).

DNA can be found in different forms in organisms, and these forms are shaped according to the genetic character of the organisms. When any molecule interacts with this DNA, it can cause these forms to degrade or turn into each other. The double-stranded superhelix structure of DNA is known as form I. After one of the strands forming the Form I structure is broken, Form II, which moves more slowly in the agarose gel and has a looser structure than Form I, occurs. In addition, after the other strand is broken, the DNA becomes linear and this structure is known as Form III [36].

According to the results of the study, it was observed that H_2O_2 and H_2O_2+DMSO disrupted Form I, making it more unstable. It was observed that water and methanol extracts alone did not have a negative effect on the stable structure of DNA and kept it in Form I and Form II structures. In addition, it was determined that the increase in concentration did not have a significant effect on DNA, however, a decrease in the Form III structure occurred with the increase in concentration in the water extract. When the activities of water and methanol extracts to reduce the harmful effects of peroxide on DNA were compared, it was determined that the water extract was more effective. When water extract was used together with peroxide, it was determined that DNA remained in Form I and Form II structures, but methanol extract did not show a significant effect.

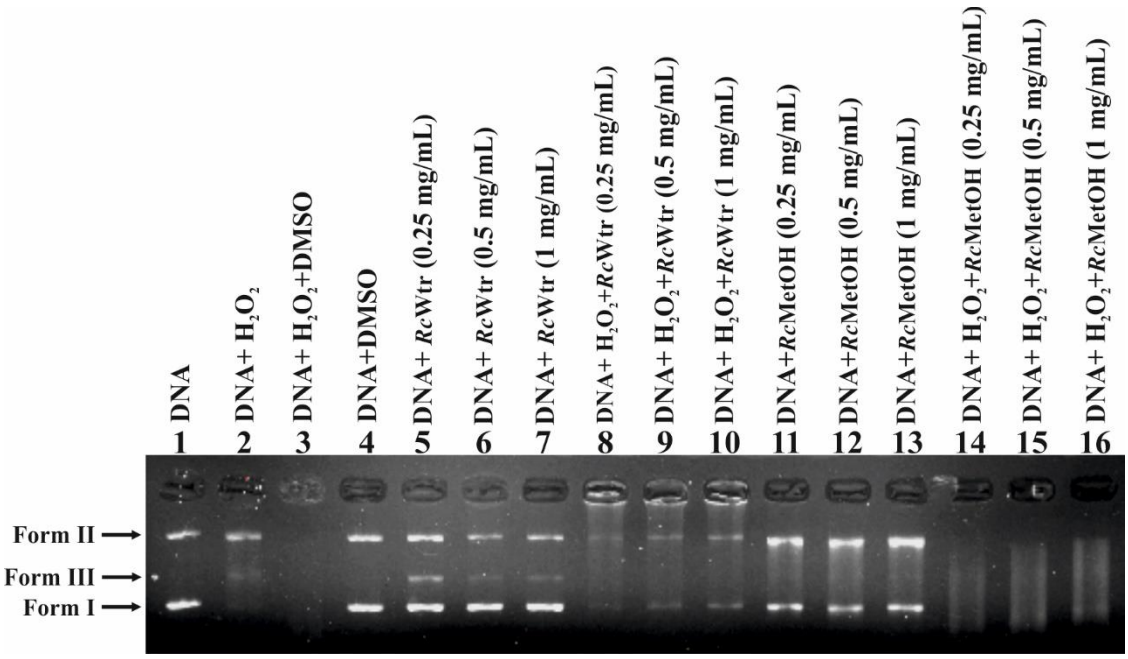

Figure 1. Comparison of the effects of *R. cornutus* DC. extracts on DNA

Studies on the plasmid DNA interaction of *Ranunculus* species are very limited. In a study, it was reported that the ethanol extract of *R. japonicus* Thunb was able to inhibit the replication of Hepatitis B Virus (HBV) in more than one step and showed inhibitory effects, especially on CCC DNA formation and capsid formation. This indicates that *R. japonicus* Thunb as a source of antiviral agents against HBV specifically targets viral CCC DNA, which is the molecular basis of HBV chronic infection [37].

4. Conclusion and Suggestions

In this study, the content and biological activities of *R. cornutus* grown in Muş province were investigated. In the literature review, no study was found about the biological activities of this plant species. For this reason, after the secondary metabolite content of the plant was determined by LC-MS-MS, different methods were used to determine in vitro antioxidant activities. The results were compared with the standard antioxidants (BHA, BHT and AA). Finally, pBR322 plasmid DNA was used to determine the effects of the plant on DNA. When the phenolic content results were examined, it was determined that

the plant contained fumaric acid, vanillic acid, ferulic acid, caffeic acid, chlorogenic acid and p-Coumaric Acid metabolites more than the others, but overall the total phenolic content was at an average value. When the antioxidant results were evaluated, it was seen that the water and methanol extracts of the plant exhibited lower activity than the standard antioxidants. It can be said that the reason for this is related to the amount of phenolics they contain. However, it was observed that the methanol extract generally had better antioxidant activity than the water extract. According to the results of the effects of the extracts on DNA, it was determined that the water extract was more effective. When water extract was used together with peroxide, it was determined that DNA remained in Form I and Form II structures, but methanol extract did not show a significant effect. Considering all the results, we believe that this study will make very important contributions to the literature and will shed light on the studies to be done with this plant.

Acknowledgment

Conflict of Interest Statement

There is no conflict of interest between the authors.

Statement of Research and Publication Ethics

The study has complied with research and publication ethics

References

[1] *Flora of Turkey and the East Aegean Islands, Volume 1*, c. 1. Edinburgh University Press, 1965. accessed: 26 May 2023. [online]. Access adress: https://www.jstor.org/stable/10.3366/j.ctvxcrdfg

[2] A. Baytop, içinde *Farmasötik botanik*, İ.Ü. Eczacılık Fakültesi Yayınları, Baha Matbaası: İstanbul Üniversitesi, 1996, ss. 166-169.

[3] E. Sezik, E. Yeşilada, G. Honda, Y. Takaishi, Y. Takeda, ve T. Tanaka, "Traditional medicine in Turkey X. Folk medicine in Central Anatolia", *J. Ethnopharmacol.*, vol. 75, no 2-3, pp. 95-115, May. 2001, doi: 10.1016/s0378-8741(00)00399-8.

[4] G. Gürhan ve N. Ezer, "Halk Arasında Hemoroit Tedavisinde Kullanılan Bitkiler-I", *Hacet. Univ. J. Fac. Pharm.*, no. 1, Art. sy 1, Oca. 2004.

[5] S. Darshan ve R. Doreswamy, "Patented antiinflammatory plant drug development from traditional medicine", *Phytother. Res.*, vol. 18, pp. 343-357, May. 2004, doi: 10.1002/ptr.1475.

[6] M. L. Salem, "Immunomodulatory and therapeutic properties of the Nigella sativa L. seed", *Int. Immunopharmacol.*, vol. 5, no 13-14, pp. 1749-1770, Ara. 2005, doi: 10.1016/j.intimp.2005.06.008.

[7] P. M. Dewick, *Medicinal Natural Products*. Chichester, UK: John Wiley & Sons, Ltd, 2009. doi: 10.1002/9780470742761.

[8] M. J. Cuéllar, R. M. Giner, M. C. Recio, S. Máñez, ve J. L. Ríos, "Topical anti-inflammatory activity of some Asian medicinal plants used in dermatological disorders", *Fitoterapia*, vol. 72, no 3, pp. 221-229, Mar. 2001, doi: 10.1016/s0367-326x(00)00305-1.

[9] N. Erdemoglu, E. Küpeli, ve E. Yeşilada, "Anti-inflammatory and antinociceptive activity assessment of plants used as remedy in Turkish folk medicine", *J. Ethnopharmacol.*, vol. 89, no 1, pp. 123-129, Kas. 2003, doi: 10.1016/s0378-8741(03)00282-4.

[10] R. W. Li, G. David Lin, S. P. Myers, ve D. N. Leach, "Anti-inflammatory activity of Chinese medicinal vine plants", *J. Ethnopharmacol.*, vol. 85, no 1, pp. 61-67, Mar. 2003, doi: 10.1016/s0378-8741(02)00339-2.

[11] P. Landa, P. Marsik, J. Havlik, P. Kloucek, T. Vanek, ve L. Kokoska, "Evaluation of antimicrobial and anti-inflammatory activities of seed extracts from six Nigella species", *J. Med. Food*, vol. 12, no 2, pp. 408-415, Nis. 2009, doi: 10.1089/jmf.2007.0600.

[12] A. Savcı, N. Turan, K. Buldurun, M. Eşref Alkış, ve Y. Alan, "Schiff base containing fluorouracil and its M(II) complexes: Synthesis, characterization, cytotoxic and antioxidant activities", *Inorg. Chem. Commun.*, vol. 143, no. 109780, Eyl. 2022, doi: 10.1016/j.inoche.2022.109780.

[13] E. F. Koçpinar, M. Kürşat, A. Savci, ve Y. Alan, "Some biological properties of ethanol extract prepared from the aerial parts of Scutellaria albida L. subsp. condensata (Rech.f.) J.R. Edm.", *Bitlis Eren Univ. J. Sci. Technol.*, vol. 10, no 2, pp. 43-48, Ara. 2020, doi: 10.17678/beuscitech.805013.

[14] A. Savci, E. F. Koçpinar, Y. Alan, ve M. Kürşat, "Nepeta transcaucasica Grossh. (kaf pisikotu) Estraktının HPLC ile Fenolik Madde İçeriğinin Tayini, Antimikrobiyal, Antioksidan ve DNA Koruyucu Aktivitelerinin Belirlenmesi", *Muş Alparslan Üniversitesi Fen Bilim. Derg.*, vol. 8, no 2, pp. 797-803, Ara. 2020, doi: 10.18586/msufbd.797056.

[15] A. Savci, E. koçpınar, Y. Alan, ve M. Kurşat, "Antioxidant, antimicrobial, and DNA protection activities of some Tanacetum species and phenolic richness in their ethanolic extracts", *Int. Food Res. J.*, vol. 27, pp. 160-170, Oca. 2020.

[16] A. Savci, "Eryngium Billardieri F. Dolaroche'den (Boğa Dikeni) Hazırlanan Ekstraktlarin Fenolik İçerikleri Ve Biyolojik Özellikleri,", *İnönü Üniversitesi Sağlık Hizmetleri Mesl. Üksek Okulu Derg.*, vol. 9, no. 3, pp.785-795, 2021, doi: 10.33715/inonusaglik.904506.

[17] H. Mitsuda, K. Yasumoto, ve K. Iwami, "Antioxidative Action of Indole Compounds during the Autoxidation of Linoleic Acid", *Eiyo Shokuryo*, vol. 19, no. 3, pp. 210-214, 1966, doi: 10.4327/jsnfs1949.19.210.

[18] M. Oyaizu, "Studies on Products of Browning Reaction Prepared From Glucose Amin", *Jpn. J. Nutr. Diet.*, vol. 44, no. 6, pp. 307-315, 1986, doi: 10.5264/eiyogakuzashi.44.307.

[19] R. Apak, K. Güçlü, M. Ozyürek, ve S. E. Karademir, "Novel total antioxidant capacity index for dietary polyphenols and vitamins C and E, using their cupric ion reducing capability in the presence of neocuproine: CUPRAC method", *J. Agric. Food Chem.*, vol. 52, no. 26, pp. 7970-7981, Ara. 2004, doi: 10.1021/jf048741x.

[20] A. Alhafez, A. Savci, Y. Alan, R. Söylemez, ve A. Kilic, "Preparation of Cu(II), Ni(II), Ti(IV), VO(IV), and Zn(II) Metal Complexes Derived from Novel vic-Dioxime and Investigation of Their Antioxidant and Antibacterial Activities", *Chem. Biodivers.*, vol. 19, no 3, Mar. 2022, doi: 10.1002/cbdv.202100768.

[21] M. S. Blois, "Antioxidant Determinations by the Use of a Stable Free Radical", *Nature*, vol. 181, no. 4617, pp.1199-1200, 1958, doi: 10.1038/1811199a0.

[22] R. Re, N. Pellegrini, A. Proteggente, A. Pannala, M. Yang, ve C. Rice-Evans, "Antioxidant activity applying an improved ABTS radical cation decolorization assay", *Free Radic. Biol. Med.*, vol. 26, no 9-10, pp. 1231-1237, May. 1999, doi: 10.1016/s0891-5849(98)00315-3.

[23] T. L. Siddall *vd.*, "Synthesis and herbicidal activity of phenyl-substituted benzoylpyrazoles", *Pest Manag. Sci.*, vol. 58, no 12, pp. 1175-1186, 2002, doi: 10.1002/ps.588.

[24] M. Z. Bhatti, A. Ali, A. Ahmad, A. Saeed, ve S. A. Malik, "Antioxidant and phytochemical analysis of Ranunculus arvensis L. extracts", *BMC Res. Notes*, vol. 8, no 1, 2015, doi: 10.1186/s13104-015-1228-3.

[25] J. M. Prieto, M. C. Recio, R. M. Giner, G. R. Schinella, S. Máñez, ve J. L. Ríos, "In vitro and in vivo effects of Ranunculus peltatus subsp. baudotii methanol extract on models of eicosanoid production and contact dermatitis", *Phytother. Res. PTR*, vol. 22, no 3, pp. 297-302, Mar. 2008, doi: 10.1002/ptr.2309.

[26] W. Noor, R. Gul, ve M. Choudhary, "Isolation and antibacterial activity of the compound from Ranunculus repens L.", *J. Chem. Soc. Pak.*, vol. 28, pp. 271-274, Haz. 2006.

[27] M. Campos, K. Markham, K. Mitchell, ve A. Cunha, "An approach to the characterization of bee pollens via their flavonoid/phenolic profiles", *Phytochem. Anal.*, vol. 8, pp. 181-185, Tem. 1997, doi: 10.1002/(SICI)1099-1565(199707)8:4<181::AID-PCA359>3.0.CO;2-A.

[28] Z.-Y. Wang *vd.*, "Integrated strategy of LC-MS and network pharmacology for predicting active constituents and pharmacological mechanisms of Ranunculus japonicus Thunb. for

treating rheumatoid arthritis", *J. Ethnopharmacol.*, vol. 271, no. 113818, p.113818, May. 2021, doi: 10.1016/j.jep.2021.113818.

[29] A. Deghima *vd.*, "Bioactive polyphenols from Ranunculus macrophyllus Desf. Roots: Quantification, identification and antioxidant activity", *South Afr. J. Bot.*, vol. 132, pp. 204-214, Ağu. 2020, doi: 10.1016/j.sajb.2020.03.036.

[30] D. Huang, B. Ou, ve R. L. Prior, "The chemistry behind antioxidant capacity assays", *J. Agric. Food Chem.*, vol. 53, no. 6, pp. 1841-1856, Mar. 2005, doi: 10.1021/jf030723c.

[31] M. P. Kähkönen *vd.*, "Antioxidant Activity of Plant Extracts Containing Phenolic Compounds", *J. Agric. Food Chem.*, vol. 47, no. 10, pp. 3954-3962, Eki. 1999, doi: 10.1021/jf990146l.

[32] S. Shahid, T. Riaz, ve M. N. Asghar, "Screening of Ranunculus sceleratus for enzyme inhibition, antibacterial and antioxidant activities", *Bangladesh J. Pharmacol.*, vol. 10, no. 2, p. 436, 2015, doi: 10.3329/bjp.v10i2.22805.

[33] D. Say, P. Tastan, ve T. Fafal, "Fatty Acid Composition and Antioxidant Activity of Ranunculus constantinopolitanus", *Chem. Nat. Compd.*, vol. 58, no. 3, pp. 527-530, May. 2022, doi: 10.1007/s10600-022-03725-7.

[34] G. İ. Kaya *et al.*, "Antioxidant and Antibacterial Activities of Ranunculus marginatus var. trachycarpus and R. sprunerianus", *Turk. J. Biol.*, 2010, doi: 10.3906/biy-0809-13.

[35] A. K. Singh, S. Solanki, ve D. Prasad, "Antioxidant Determination And Thin Layer Chromatography Of Extract Withania Somnifera, Terminalia Arjuna, Bacopa Monnieri, Ranunculus Sceleratus And Acalypha Indica.", *Eur. J. Mol. Clin. Med.*, vol. 7, no 11, pp. 4394-4408, Oca. 2021.

[36] H. Zhang *vd.*, "Human mitochondrial topoisomerase I", *Proc. Natl. Acad. Sci.*, vol. 98, no. 19, pp. 10608-10613, Eyl. 2001, doi: 10.1073/pnas.191321998.

[37] M. Luo *vd.*, "Inhibitory activities of Ranunculus japonicus Thunb. ethanol extract against hepatitis B virus", *J. Med. Virol.*, vol. 94, no. 6, pp. 2727-2735, Haz. 2022, doi: 10.1002/jmv.27621.

Bitlis Eren Üniversitesi Fen Bilimleri Dergisi
BİTLİS EREN UNIVERSITY JOURNAL OF SCIENCE
ISSN: 2147-3129/e-ISSN: 2147-3188
VOLUME: 12 NO: 4 PAGE: 978-984 YEAR: 2023
DOI:10.17798/bitlisfen.1305017

Healing Effect of Ascorbic Acid against Genetic and Epigenetic Changes Caused by Pendimethalin in Wheat

Nalan YILDIRIM DOĞAN[1*], Muhammed Semih DARTAR[2]

[1]*Erzincan Binali YILDIRIM University, Faculty of Science , Department of Biology, Erzincan, Turkey*
(ORCID: 0000-0002-5344-5367) **(***ORCID:0000-0003-3618-7295***)**

Keywords: Genotoxicity, Herbicide, IRAP, ISSR, *Triticum aestivum* Vitamin C.

Abstract
Because of the increasing need for agricultural products in the world, the use of pesticides, which are used to increase yield, is increasing day by day. Herbicides constitute a large part of the total amount of pesticides used, such as 20%. It is known that herbicides have toxic effects and irreversibly disrupt DNA and gene expression. Pendimethalin is a widely used herbicide against weeds in the production of grains, legumes, and vegetables. Ascorbic acid has an antioxidant effect. Molecular markers are frequently used to determine genotoxic and mutagenic effects at the DNA level. It was aimed to determine the curative effect of ascorbic acid on the negative effects of pendimethalin. IRAP and ISSR molecular markers were used. It was found that the Genomic Template Stability (GTS) ratio decreased as a result of increasing the dose of pendimethalin applied in wheat, resulting in DNA damage and the positive effect of applied ascorbic acid on DNA damage.

1. Introduction

Because of the rapid increase in the world population, the gradual decrease in agricultural lands, urbanization, unconscious resource use, climate changes and similar factors, it has become more and more difficult to meet the increasing demand for food. Physical and chemical applications are carried out to increase the yield in agricultural production and to obtain products equivalent to the need. Some of these are the use of quality seeds, tillage, irrigation, fertilization. Besides these to these applications, pesticides are used to combat harmful factors [1]. Unconscious application of pesticides used in chemical control produces negative effects in non-target organisms. Mutagenic, carcinogenic, teratogenic effects are the most well-known effects of pesticides [2], [3], [4]. When exposed to pesticides for a certain period, disorders in the liver, reproductive and nervous systems cause toxicity that causes allergic reactions [5].

Pendimethalin is a selective herbicide belonging to the dinitroaniline group, targeting single-year-old grasses and broad-leaved wild shrubs. In grain, legume, vegetable cultivation it is also used to remove unwanted weeds from decorative ornamental plants used for landscaping. [6], [7], [8]. Pendimethaline affects the mitotic division of root tips in the *Vigna mungo* plant by disrupting microtubule formation, preventing chromosome separation and cell wall formation [9]. Pendimethaline, which has high efficiency and long duration of action, medium and high soil permanence and low leakage property, increase the risk of polluting the environment [10]. There are studies in the literature on the cytotoxic and genotoxic effects of pendimethaline in different animal organisms [11], [12], [13] and studies in plant organisms are very limited [14], [2], [15].

Ascorbic acid, a water-soluble glucose derivative, has significant antioxidant activity *in*

*Corresponding author: nyildirim@erzincan.edu.tr
Received: 01.06.2023, Accepted: 30.10.2023

vitro, in part because of its ease of oxidation and the low reactivity of the semide-hydroascorbate radical derived from it [16]. Ascorbic acid has shown antioxidant effects in many test, systems such as human lymphocyte cells, eukaryotic tissues, *Drosophila* [17], [18], [19], [20].

This study, it was aimed to determine the genetic and epigenetic changes caused by pendimethalin in wheat with ISSR and IRAP techniques and the curative effects of ascorbic acid after pendimethalin treatment.

2. Material and Method

2.1. Chemicals Example

Pendimethalin (CAS 40487-42-1. Molecular Weight 281.31) and ascorbic acid (CAS Number: 50-81-7; Molecular Weight: 176.12) are commercially available from Sigma-Aldrich.

2.2. Treatment of Triticum aestivum L. seeds with pendimethalin and ascorbic acid

Triticum aestivum L. seeds were selected and kept in 5% sodium hypochlorite (NaOCl) solution for 10 minutes. The sterilized seeds were placed in petri and germinated with distilled water at 25 ^{0}C. Increased doses (0, 0.033, 0.044, 0.055 and 0.066 g kg−1) applied to germinated wheat germs and taken to pots and left to grow. Pendimethalin concentrations used in the study were determined according to Verna et al. [21]. Wheat leaves that reached sufficient maturity were treated with ascorbic acid in 2 different doses (50 and 100 ppm) by spraying and watered with pure water for 7 days. Ascorbic acid concentrations used in the study were determined according to Barakat [22]. The control group was treated only with distilled water. For molecular examination, samples were stored at -80^o C.

Table 1. Pendimethalin, ascorbic acid, control groups and administered doses

No	Group	Pendimethalin	Ascorbic Acid
1	Control	-	-
2	Control	-	50 ppm
3	Control	-	100 ppm
4	1.Group	0.033 g kg^{-1}	-
5	1.Group	0.033 g kg^{-1}	50ppm
6	1.Group	0.033 g kg^{-1}	100 ppm
7	2.Group	0.044 g kg^{-1}	-
8	2.Group	0.044 g kg^{-1}	50ppm
9	2.Group	0.044 g kg^{-1}	100 ppm
10	3.Group	0.055 g kg^{-1}	-
11	3.Group	0.055 g kg^{-1}	50ppm
12	3.Group	0.055 g kg^{-1}	100 ppm
13	4.Group	0.066 g kg^{-1}	-
14	4.Group	0.066 g kg^{-1}	50ppm
15	4.Group	0.066 g kg^{-1}	100 ppm

2.3. DNA isolation

It implemented the isolation of genomic DNA from plant samples with minor changes to the protocol of Shagai-Maroof et al. [23]. It carried the quantity determination of DNA samples out using the Epoch Microplate Spectrophotometer instrument.

2.4. ISSR analysis

We used 8 primers for ISSR analysis. The protocol followed for the ISSR PCR process; 3µL 10x PCR buffer, (10 mg mL^{-1}), 0.3 µL dNTP (10 mM), 1.15 µL MgCl2 (25 mM), 1µL DNA (100 ngm L -1), 1 µL primary (25 pmol), 0.5 µL 5 Unit mL L -1 Taq DNA polymerase was placed in the 0.2 ml PCR tube. By adding pure water, the volume is completed to 20 µL. Samples denatured for 4 minutes at 94 ºC are then processed for each cycle for 34 cycles; It is arranged so that there are 40 seconds at 94 ºC, different annealing temperatures for each primer for 45 seconds and 2 minutes at 72 ºC. Then, at the end of 1 cycle lasting 6 minutes at 72 ºC, the samples were removed to +4 ºC. The PCR procedure, the samples were loaded into the pre-prepared 0.8% agarose gel and executed in 1 X TBE (Tris Borat Edta) buffer [24].

2.5. IRAP analysis

I used 5 primers for IRAP analysis. Protocol followed for IRAP PCR processing; 3 µL 10xPCR buffer, (10 mg ml-1), 0.3 µL dNTP (10 mM), 1.15 µL MgCl2 (25 mM), 1 µL DNA (100 ng ml -1), 0.5 µl 5 Unit mL L -1 Taq DNA polymerase was placed in the 0.2 ml PCR tube. By adding pure water the volume is completed to 20µl. Samples denatured at 95 ºC for 2 minutes are then 41 cycles for each cycle; It is arranged so that it is 30 seconds at 95 ºC,

different annealing temperatures for each primer for 60 seconds and, 2 minutes at 72 ºC. Then, at the end of 1 cycle lasting 5 minutes at 72 ºC, the samples were removed to +4 ºC [24].

2.6. Determination of genomic pattern stability (GTS*)*

The presence and absence of amplified DNA bands in all samples for each primer, decreases and increases in band densities according to negative control ISSR AND IRAP profiles were determined by agarose gel imaging device and Total LAB TL 120 (Nonlinear Dynamics) software. Genomic pattern stability (%) for all primary products; It was calculated using the formula 100 x 1-a/b. Formula; a; the ISSR and IRAP polymorphic profiles detected for each application sample, n; DNA obtained in the relevant primary and negative control group was selected as the total band number. The polymorphism observed in the ISSR and IRAP profiles of the application groups included the emergence of a new band or the loss of an existing band according to the negative control group [25].

3. Results and Discussion

Triticum aestivum L. in the samples, 8 primers were used in the ISSR analysis and 129 polymorphic bands were detected. Some observe that the size of these bands varies between 1630 bp and 224 bp. Polymorphism was detected in all samples where pendimethalin was applied. The rate of polymorphism is between 6.06% and 24.24%. In the evaluation of the samples with regarding to the control group**,** we observed an increase parallel with the dose increase. It was found that the samples treated with pendimethalin showed an increase inversely proportional to the dose increase where the GTS values were between 77.27% and 93.93%. Some observe that ascorbic acid applied in two different doses to pendimethalin groups reduces the polymorphism occurring and increases the GTS value (Table 1.)

Triticum aestivum L. in the samples, 5 primers were used in the IRAP analysis and 75 polymorphic bands were detected. Some observed that the size of these bands varies between 1189 bp and 27 bp. Polymorphism was detected in all samples where pendimethalin was applied. The polymorphism rate is between 31.57% and 73.68%. In the evaluation of the samples with reference to the control group, an increase in polymorphism was observed in parallel with the dose increase. We found the samples treated with pendimethalin showed an increase inversely proportional to the dose increase in GTS values between 26.32% and 63.16%. It was determined that ascorbic acid applied in two different doses to pendimethalin groups reduced the polymorphism and increased the GTS value (Table 2).
the environment and acute or chronic toxic effects in organisms. In addition, the inducing of DNA damage by herbicides leads to potentially adverse reproductive outcomes in humans, such as cancer and many other acute or chronic diseases. The negative impact of genetically damaged crops, potentially on both natural ecosystems and human health, has been reported. The genotoxic effects of most herbicides on agricultural crops are unknown [7], [11], [12].

There are many studies on the harmful effects of pendimethalin on non-target organisms. There are studies showing that pendimethalin has a significant toxic effect, especially on aquatic life [26], [13]. In studies conducted in animal organisms, it has been determined that pendimethalin causes toxicological effects, oxidative stress and DNA damage [27], [12], [11]. Alavanja et al. [28], it was determined that the herbicide pendimethalin showed a statistically significant exposure-response relationship with pancreatic cancer. Arici et al. [29], examined the effect of pendimethalin on inflammation caused by pancreatic cancer and drew attention to the use and toxic effect of pendimethalin because of oxidative damage in the results obtained.

In the literature, there are the limited number of studies investigating the cytotoxic and genotoxic effects of pendimethalin in plant organisms [15], [8]. In their of growth and DNA damage at the root ends of the Allium cepa, they determined that pendimethalin caused DNA damage at all concentrations compared to the control group [30]. Akbulut [15], determined that gene expression levels decreased depending on pendimethalin concentration and revealed that salicylic acid application had an effect on reducing the toxic effect caused by pendimethalin. Promkaew et al. [31]; found a significant increase in chromosome aberrations and mitotic index because of the increase in the amount of pendimethalin administered in Allium cepa and three Zea mays varieties. Anghel et al. [32]; we found that the increased dose of pendimethalin in the Allium test system induced a mitodepiric effect and caused an abnormal cell increase.

Table 2. ISSR analysis results of the wheat samples

Primer name	K	A1	A2	P1	P1/ A1	P1/A2	P2	P2/ A1	P2/ A2	P3	P3/ A1	P3/A2	P4	P4/ A1	P4/ A2
UBC 816	6	-	-	+1093 -330	-330	-330	+1152 -330	+1137 -330	+1137 -330	+1079 -330	+1107	+1112	+1093 -330	+1065	+1093
UBC 817	12	-803	-	+1269	+1269	-	- +1269	+1269	+1269	+1269 +552	+1269 +418	+1269	+1269 +413 -650	+1269	+1269
UBC 824	5	-	-	-	-	-	-	-	-	+1162 +698	+1142	+1159	+1154 +947	+1165 +987	+1148
UBC 825	9	-	-440	+775 +242	+812	-	-	-	-	+1348 -317	-394 -317	-394 -317	-394 -317	-394 -317	-394 -317
UBC 840	8	-	+256	-655 -485 -351	-485 -351	-	+1230 -485 -351	-351	+1230 -351	+1230 -485 -351 -310	+1630 +1214 -351 -310	+1290 -351 -310	+1306 -485 -440 -351 -310	-485 -440 -351 -310	-485 -440 -351 -310
UBC 841	11	-	-	-	+950 -230	-	-230	-230	-	+638	+605 -230	-	-	-733 -465 -415	-733
UBC 856	15	-	-	-367 -224	-1330 -1198	-1330 -1198 -790	-367 -224	-367 -224	-367 -224	-367 -224	-367 -224	-367 -224	-367 -224	-	-367 -224
Total Band	66	1	2	10	9	4	9	7	7	15	14	10	16	13	12
% Pol.		1,51	3,03	15,15	13,63	6,06	13,63	10,60	10,60	22,72	21,21	15,15	24,24	19,69	18,18
GTS		98,4	96,9	84,84	86,36	93,93	86,36	89,39	89,39	77,27	78,78	84,84	75,75	80,30	81,81

Table 3. IRAP analysis results of the wheat samples

Primer name	K	A1	A2	P1	P1/ A1	P1/ A2	P2	P2/ A1	P2/ A2	P3	P3/ A1	P3/ A2	P4	P4/ A1	P4/ A2
Nikita	4	-	-	+734 +613 -143	+718 +605 -361 -143	-361 -143	+753 +627 -143	-491 -143	+618 -143	+1163 +637 -143	+1169 +640	+613	+1189 +783 +670 -143	+812 +685 -143	+670 -143
LTR 6150	5	-	-	+300	+308	-	+500 +443	-	-	+1070 +982	-	-	+1062 +450 +291	+449 +294	+498 +392
5LTR1	3	+164	+351	-	-	-	-	-	-	+447 +389	+362	+383	+527 +457 +394	+517 +451 +398	+531
3LTR5	2	-	-	+358	-	-	+354	-	-	+428 +351	+432	+437	+435 +390	+387	+411
Sukkula	4	-	+27	+202 +38	-	+47	-	-	-	-	-	-	+584 +486	+393	+396
Total Band	19	1	2	7	5	3	6	2	2	9	4	3	14	10	7
% Pol.		5,26	10,52	36,84	26,31	15,78	31,57	10,52	10,52	47,36	21,05	15,78	73,68	52,63	36,84
GTS		94,74	89,48	63,16	73,69	84,22	68,43	89,48	89,48	52,64	78,95	84,22	26,32	47,43	63,16

Using high-dose herbicides causing contamination in

4. Conclusion and Suggestions

One of our most basic needs is nutrition. Sales of agricultural products are increasing at a rapid pace worldwide and are shrinking. In this case, methods such as breeding methods and removing pests are used to increase productivity. Although the use of pesticides is aimed at the target organism, these studies have negative effects on nontarget organisms. Today, chemicals used unconsciously cause environmental pollution and negatively effect the vital activities of organisms in many ecosystems. It is stated in the literature that the widespread use of herbicides causes genotoxic effects on plant and animal organisms, it was also detected in our study. Here, it would be appropriate to restrict the use of herbicides and raise awareness among users**.**

Acknowledgment

This study was supported by Erzincan University Scientific Research Coordination Units (Project number: FYL-2022-815).

Contributions of the authors

Muhammed Semih Dartar carried out the molecular genetic studies and drafted the manuscript. Nalan Yıldırım Doğan participated in the design of the study and helped to draft the manuscript.

Conflict of Interest Statement

There is no conflict of interest between the authors.

Statement of Research and Publication Ethics

The study is complied with research and publication ethics.

References

[1] G. Beker Akbulut, "Atrazin ve asetoklor herbisitlerinin *Zea mays* L. (mısır) ve *Pisum sativum* L.(bezelye) bitkilerinde biyokimyasal ve fizyolojik parametreler üzerine etkileri," İnönü Üniversitesi Fen Bilimleri Enstitüsü, 2008.

[2] P. Gupta, and S. K. Verma, "Evaluation of genotoxicity induced by herbicide pendimethalin in fresh water fish *Clarias batrachus* (linn.) and possible role of oxidative stress in induced DNA damage, "*Drug and Chemical Toxicology*, vol. 45, no. 2, pp. 750–759, 2020.

[3] S. Sciacca and G. O. Conti. "Mutagens and carcinogens in drinking water," *Mediterranean Journal of Nutrition and Metabolism*, vol. 2, pp. 157–162, 2009.

[4] G. Andreotti, L.E.B. Freeman, L. Hou, J. Coble, J. Rusiecki, J.A Hoppin, D.T. Silverman and M.C. R. Alavanja, "Agricultural pesticide use and pancreatic cancer risk in the Agricultural Health Study Cohort, " *International Journal of Cancer*, vol. 124, no. 10, pp. 2495-2500, 2009.

[5] S. S. Sternberg, "The carcinogenesis, mutagenesis and teratogenesis of insecticides. Review of studies in animals and man," *Pharmacology & Therapeutics*, vol. 6, no. 1, pp. 147-166, 1979. doi.org/10.1016/0163-7258(79)90059-7.

[6] N. S. Hammok and F. A. Al-mandeel, "Effect of Different application methods for pendimethalin herbicide on growth and productivity of green pea plant (*Pisum sativum* L.)," *Current Applied Scince and Technology*, vol. 2, no.3, pp. 528-536, 2020.

[7] Ü. Ündeğer, M. Schlumpf and W. Lichtensteiger, "Effect of the herbicide pendimethalin on rat uterine weight and gene expression and in silico receptor binding analysis." *Food and Chemical Toxicology*, vol. 48, no. 2, pp. 502-508, 2010, doi.org/10.1016/j.fct.2009.11.001.

[8] S. Verma and A. Srivastava, "Morphotoxicity and cytogenotoxicity of pendimethalin in the test plant *Allium cepa* L.-A biomarker based study," *Chemosphere*, vol. 206, pp. 248-254, 2018, doi.org/10.1016/j.chemosphere.2018.04.177.

[9] N. Singh and A. Srivastava, "Biomonitoring of genotoxic effect of glyphosate and pendimethalin in *Vigna mungo* populations." *Cytologia, v*ol. 79, no. 2, pp. 173-180, 2014.

[10] Y. Lv, Y. Li, X. Liu and K. Xu, "Toxicity and tissue accumulation characteristics of the herbicide pendimethalin in ginger (*Zingiber officinale* Roscoe)," *Environmental Science and Pollution Research*, vol. 29, pp.25263–25275, 2022.

[11] M. I. Ahmad, M. F. Zafeer, M. Javed and M. Ahmad, "Pendimethalin-induced oxidative stress, DNA damage and activation of anti-inflammatory and apoptotic markers in male rats." *Scientific Reports*, vol. 8, no. 1, pp. 17139, 2018.

[12] S. M. Ansari, Q. Saquib, S. M. Attia, E. M. Abdel-Salam, H. A. Alwathnani, M. Faisal and J. Musarrat, "Pendimethalin induces oxidative stress, DNA damage, and mitochondrial dysfunction to trigger apoptosis in human lymphocytes and rat bone-marrow cells," *Histochemistry and Cell Biology*, vol. 149, no. 2, pp. 127-141. 2018, doi.org/10.1007/s00418-017-1622-0.

[13] H. Park, J. Y. Lee, W. Lim and G. Song, "Assessment of the *in vivo* genotoxicity of pendimethalin via mitochondrial bioenergetics and transcriptional profiles during embryogenesis in zebrafish: Implication of electron transport chain activity and developmental defects." *Journal of Hazardous Materials*, vol. 411, 125153, 2021.

[14] B. D. Dimitrov, P. G. Gadeva, D. K. Benova and M. V. Bineva, "Comparative genotoxicity of the herbicides Roundup, Stomp and Reglone in plant and mammalian test systems." *Mutagenesis*, vol. 21, no. 6, pp. 375-382, 2006.

[15] E. Akbulut, "Pendimethalin ve salisilik asit uygulamalarının *Carthamus tinctorius* l. cv. "remzibey" yağ asidi desatüraz genlerinin anlatımı üzerine etkisi," *Journal of the Institute of Science and Technology*, vol. 10, no. 4, pp. 2915-2925, 2020.

[16] B. Halliwell, "Vitamin C and genomic stability," *Mutation Research/Fundamental and Molecular Mechanisms of Mutagenesis*, vol. 475(1-2), pp. 29-35. 2001.

[17] K. Premkumar and C. L. Bowlus, "Ascorbic acid reduces the frequency of iron induced micronuclei in bone marrow cells of mice." *Mutation Research/Genetic Toxicology and Environmental Mutagenesis*, vol. 542, pp. 99-103, 2003.

[18] B. Kaya, A. Creus, A. Velázquez, A. Yanikoğlu and R. Marcos, "Genotoxicity is modulated by ascorbic acid: Studies using the wing spot test in *Drosophila*, *Mutation Research/Genetic Toxicology and Environmental Mutagenesis*, vol. 520, pp. 93-101, 2002, doi.org/10.1016/S1383-5718(02)00173-0.

[19] P. Banerjee, S. S. Bhattacharyya, N. Bhattacharjee, S. Pathak, N. Boujedaini, P. Belon and A. R. Khuda-Bukhsh, "Ascorbic acid combats arsenic-induced oxidative stress in mice liver." *Ecotoxicology and Environmental Safety*, vol. 72, pp. 639-649, 2009, doi.org/10.1016/j.ecoenv.2008.07.005.

[20] I. C. Ozturk, F. Ozturk, M. Gul, B. Ates and A. Cetin, "Protective effects of ascorbic acid on hepatotoxicity and oxidative stress caused by carbon tetrachloride in the liver of Wistar rats. " *Cell Biochemistry and Function: Cellular biochemistry and its modulation by active agents or disease,* vol. 27, no. 5, pp. 309-315, 2009, doi.org/10.1002/cbf.1575.

[21] S. Verma, A.Srivastava, "Morphotoxicity and cytogenotoxicity of pendimethalin in the test plant Allium cepa L. - A biomarker based study." *Chemosphere,* vo. 206, pp. 248-254, 2018.

[22] H. Barakat, "Interactive effects of salinity and certain vitamins on gene expression and cell division," *Internatıonal Journal of Agrıculture & Bıology,* vol. 5, no. 3, pp. 219–225, 2003.

[23] M. A. Saghai-Maroof, K. M. Soliman, R. A. Jorgensen and R. W. Allard, "Ribosomal DNAsepacer-length polymorphism in barley: mendelian inheritance, chromosomal location, and population dynamics," *Proceedings of The National Academy Sciences*, vol. 81, pp. 8014-8019, 1984.

[24] H. Bulut, N. Y. Doğan and M. Korkmaz, "Tıbbi ve aromatik bitki olarak kullanılan *Tanacetum sp*. (pire otu) türlerinin genetik benzerliğinin moleküler yöntemler ile belirlenmesi**.**" *Manas Journal of Agriculture Veterinary and Life Sciences,* vol. 9, no.1, pp. 22-29, 2019.

[25] F. A Atienzar, M. Conradi, A. J. Evenden, A. N. Jha and M. H. Depledge, "Qualitative assessment of genotoxicity using random amplified polymorphic DNA: comparison of genomic template stability with key fitness parameters in *Daphnia magna* exposed to benzo pyrene." *Enviromental Toxicology Chemistry,* vol. 18, pp. 2275-2282, 1999. doi.org/10.1002/etc.5620181023.

[26] P. Gupta and S.K. Verma, "Evaluation of genotoxicity induced by herbicide pendimethalin in fresh water fish *Clarias batrachus* (linn.) and possible role of oxidative stress in induced DNA damage," *Drug Chemical Toxicology,* vol.45, no. 2, pp. 750-759, 2020, doi.org/10.1080/01480545.2020.1774603.

[27] S. Patel, M. Bajpayee, A. K. Pandey, D. Parmar and A. Dhawan, "*In vitro* induction of cytotoxicity and DNA strand breaks in CHO cells exposed to cypermethrin, pendimethalin and dichlorvos," *Toxicology In Vitro,* vol. 21, no. 8, pp. 1409-1418, 2007.

[28] M. C. Alavanja, M. Dosemeci, C. Samanic, J. Lubin, C. F. Lynch, C. Knott and A. Blair, "Pesticides and lung cancer risk in the agricultural health study cohort," *American Journal Of Epidemiology*, **v**ol. 160, no. 9, pp. 876-885, 2004.

[29] M. Arici, M. Abudayyak, T. Boran, G. Özhan, "Does pendimethalin develop in pancreatic cancer induced inflammation? " *Chemosphere*, vol. 252, pp. 126644, 2020.

[30] B. Taşdemir, R. Liman, S. Gökçe, E. Amaç, İ. H. Ciğerci and S. E. Korcan, "Cytogenotoxic and forced degradation studies of pendimethalin using root growth, comet assay and LC-MS/MS, " *Annals of Clinical and Analytical Medicine*, vol. 12, no. 1, pp. 96-100, 2021.

[31] N. Promkaew, P. Soontornchainaksaeng, S. Jampatong and P. Rojanavipart, "Toxicity and genotoxicity of pendimethalin in maize and onion" *Agriculture and Natural Resources*, vol. *44, no.* 6, pp. 1010-1015, 2010.

[32] A. M. Anghel, A. G. G. Sîrbu, S. Ostan, C. Ianăş, and M. Corneanu, "The assessment of pendimethalin cytotoxity by *Allium* assay," *Research Journal of Agricultural Science*, vol. 51, no. 2, pp. 3-10, 2019.

Bitlis Eren Üniversitesi Fen Bilimleri Dergisi
BİTLİS EREN UNIVERSITY JOURNAL OF SCIENCE
ISSN: 2147-3129/e-ISSN: 2147-3188
VOLUME: 12 NO: 4 PAGE: 985-993 YEAR: 2023
DOI:10.17798/bitlisfen.1308493

Non-Destructive Prediction of Bread Staling Using Artificial Intelligence Methods

Mustafa Samil ARGUN[1], Fuat TURK[2], Abdullah KURT[1*]

[1]*Selçuk University, Akşehir Faculty of Engineering and Architecture, Food Engineering Department, Akşehir, Konya, Türkiye, 42550*
[2]*Kırıkkale University, Faculty of Engineering and Architecture, Computer Engineering Department, Kırıkkale, Türkiye, 71450*
(ORCID: 0000-0001-8209-3164) (ORCID: 0000-0001-8159-360X) (ORCID: 0000-0003-1452-3278)

Keywords: Bread image processing, Bread staling, Deep learning, Machine learning

Abstract

In foods with limited shelf life and in new product development studies, it is important for producers and consumers to estimate the degree of staling with easy methods. Staling of bread, which has an essential role in human nutrition, is an important physicochemical phenomenon that affects consumer preference. Costly technologies, such as rheological, thermal, and spectroscopic approaches, are used to determine the degree of staling. This research suggests that an artificial intelligence-based method is more practical and less expensive than these methods. Using machine learning and deep learning algorithms, it was attempted to predict how many days old breads are, which provides information on the freshness status and degree of staling, from photos of whole bread and pieces of bread. Among the machine learning algorithms, the highest accuracy rate for slices of bread was calculated as 62.84% with Random Forest, while the prediction accuracy was lower for all bread images. The training accuracy rate for both slices and whole bread was determined to be 99% when using the convolutional neural network (CNN) architecture. While the test results for whole breads were around 56.6%, those for sliced breads were 92.3%. The results of deep learning algorithms were superior to those of machine learning algorithms. The results indicate that crumb images reflect staling more accurately than whole bread images.

1.Introduction

Bread staling is characterized by an increase in crumb firmness and a loss of loaf freshness, in which the bread flavor has degraded, and the aroma has disappeared [1]. It contains the interplay of two major events: the migration of water from the crumb to the crust and the retrogradation of starch molecules, both of which cause economic losses in the baking industry and also negatively affect consumers' preferences [2]. Starch retrogradation, the gradual transition of starch components from amorphous to crystalline form, plays an important role in the bread staling process by causing gluten dehydration and the redistribution of water molecules throughout the bread [3, 4]. A growing number of studies have concentrated on reducing the retrogradation of starch in bread and improving its shelf life by adjusting the manufacturing formulation, packaging technique, and storage conditions. Accordingly, timely monitoring of bread staleness is necessary to improve control of the staleness process, limit the bread's quality deterioration, and advance the industrialization process. Traditional methods for determining bread staling, such as texture profile analysis, water content/activity, and differential scanning calorimetry, may be reliable,but their sample preparation and analysis procedures are time-consuming, destructive and laborious requiring highly skilled operators [5]. For the food industry, it is important to establish techniques and methods for quickly and accurately identifying and analyzing food quality and safety. To predict bread quality characteristics, there is a significant need for efficient and automated techniques. Several spectroscopic approaches, such as near-infrared (NIR)

* Corresponding author: *abdullah.kurt@selcuk.edu.tr*
Received:01.06.2023, Accepted: 21.08.2023

spectroscopy, Raman spectroscopy, and fluorescence spectroscopy, have been investigated and developed for the qualitative and quantitative study of food matrices as a result of recent technological advancements in photonics and optics [6].

NIR, MIR, and Raman spectroscopy were also employed to determine the staling region of wheat bread as well as its retrogradation behavior [7]. To observe and clarify the process of bread staling in the presence of maltogenic amylases over time, machine learning techniques using near infrared hyperspectral imaging were employed by Amigo, et al. [8].

Digital imaging systems have been used to evaluate the quality features of various foods, such as the size and shape, surface color, appearance, and surface defects, using computer vision and machine learning-based methodologies that are non-invasive, non-destructive, and objective with reduced human errors [9]. Deep learning uses artificial neural networks to create the visual neural network of the human brain to analyze and process enormous amount of data and automatically extract hierarchical data representations. The convolutional neural network (CNN), the most widely used deep learning architecture, has recently emerged as an effective and viable method for extracting features for detecting and analyzing complex food matrices, such as meat and aquatic products, cereals and cereal products and fruits and fruit products [10]. The browning degree of bread crust during seven different baking periods was identified by the CNN model with computer vision systems with the accuracy of 98.8% [11]. Image-processing techniques facilitate the extraction of quantitative features based on the shape, size, color, and texture of food products. These features can be utilized for training classifiers, as well as to provide objective data for decision-making or characterization of food products, such as the distribution of cell sizes in a slice of bread. Researchers have employed various statistical, machine, and deep learning methods to assess the diverse quality characteristics of baked products [9]. Artificial neural networks (ANN) and convolutional neural networks (CNN), in addition to efficient fuzzy-based classifiers, such as Random Forest (RF), Decision Tree (DT), and Support Vector Machine (SVM) methods, are examples of general techniques that simulate human decision-making processes and produce uniform outcomes [12]. The convolutional neural network (CNN) is an effective tool for extracting features with more accurate and stable and is considered to be the most popular architecture in deep learning. It has been increasingly used for detecting and analyzing complex food matrices [10]. CNN have recently demonstrated satisfactory results in evaluating the freshness of fish and meat products [13]. The purpose of this research was to establish a CNN architecture for the estimation of the bread's freshness over a period of four days under ordinary consumption conditions.

2. Material and Methods

2.1. Material

For image analysis, whole bread and slices of bread were employed. Five different breads were purchased from a local bakery. A loaf of bread was sliced from the same oven. The thickness of the slices was about 2 cm. Five randomly selected slices were used for image analysis. The samples were stored at room temperature in sealed bags. Top, side, and bottom images of fresh and stale breads were taken on each day of storage (1st, 2nd, 3rd, and 4th days). Only the top and bottom images of the slices were taken.

2.2. Methods

2.2.1. Recommended architectural structure and workflow

In the proposed architectural structure (Figure 1), the images were first pre-processed. At this stage, the same procedures were carried out for whole bread and sliced bread. First, after the image pre-processing stage, machine learning and deep learning algorithms were applied separately. As a result of both methods, the number of days the breads were stored was estimated with a multiple classifier.

2.2.2. Image pre-processing

Photographs of whole and sliced bread were taken with an iPhone 7 mobile phone from a height of 45 cm. A total of 468 images were preprocessed for five classes. Firstly, unnecessary areas were removed, and resizing operations were performed on the images. As a result of this process, all images were reduced to 224*224 size. Later, Contrast, Sharpness, Brightness, and Color improvements were made using Python PILLOW library commands. Image preprocessing results for whole and sliced breads are shown in Figure 2. Images of the same five slices of bread were captured and analyzed each day.

2.2.3. GLCM future extraction

The feature extraction method consists of data acquisition steps to find a subset of useful image-

based variables. In this study, seven textural features based on gray level co-occurrence matrix (GLCM) were obtained from each image. GLCM has been calculated for four directions: 0º, 45º, 90º, and 135º [14, 15].

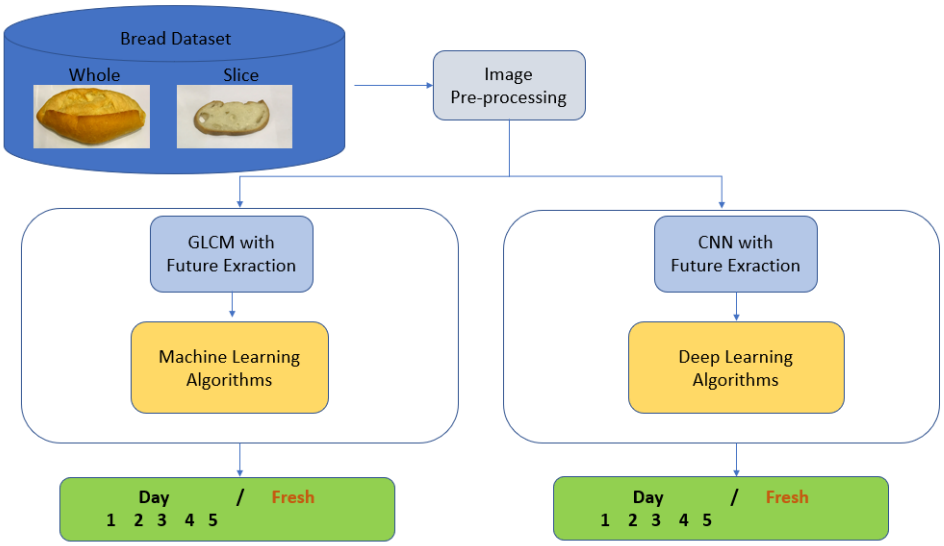

Figure 1. Recommended workflow model

With this method, the properties calculated for each of the four angles are as follows;

Energy

Energy is another name for "uniformity" or "angular second moments". It is the sum of the values of the square elements in the GLCM matrix. It is the transition from homogeneous regions to non-homogeneous regions.

Entropy

Calculates the randomness of the image. As a result, a homogeneous image will result in lower entropy values.

Contrast

It measures the intensity that connects the contrast between a pixel and its neighbor across the entire image.

Correlation

It is a measure of grayscale linear dependencies in an image. Specifies how a pixel is associated with its neighbor.

Homogeneity

Explains the similarity of pixels. The GLCM matrix of the homogeneous image gives the value 1. Image texture is very low if it requires minimal changes [16].

2.2.4. Machine learning algorithms

Decision Tree

Decision Trees (DT) are trees that classify samples by ordering them according to their feature values. Classification is carried out on the samples in the data set, and each sample is classified according to its properties starting from the root node [16, 17]. Decision tree learning, used in data mining and machine learning, uses a decision tree as a predictive model that matches observations about an item with the item's results [18].

Support Vector Machine (SVM)

SVM is a type of supervised learning algorithm used for classification and regression [18-20]. The goal of SVM is to get the highest margin individual hyperplane that can divide classes linearly. SVM is most commonly used when identifying datasets where the number of training data is limited and the optimal solution cannot be obtained with the normal use of many statistics [21-24].

K-nearest neighbors (KNN)

In KNN, the main idea is to determine the category

of a given query not only by the document closest to it in the document area but also by the categories of the k documents closest to it. With this in mind, the Vector method can be viewed as an example of the KNN method where k = 1. It can be predicted that as the K value increases, it will increase in the samples [25].

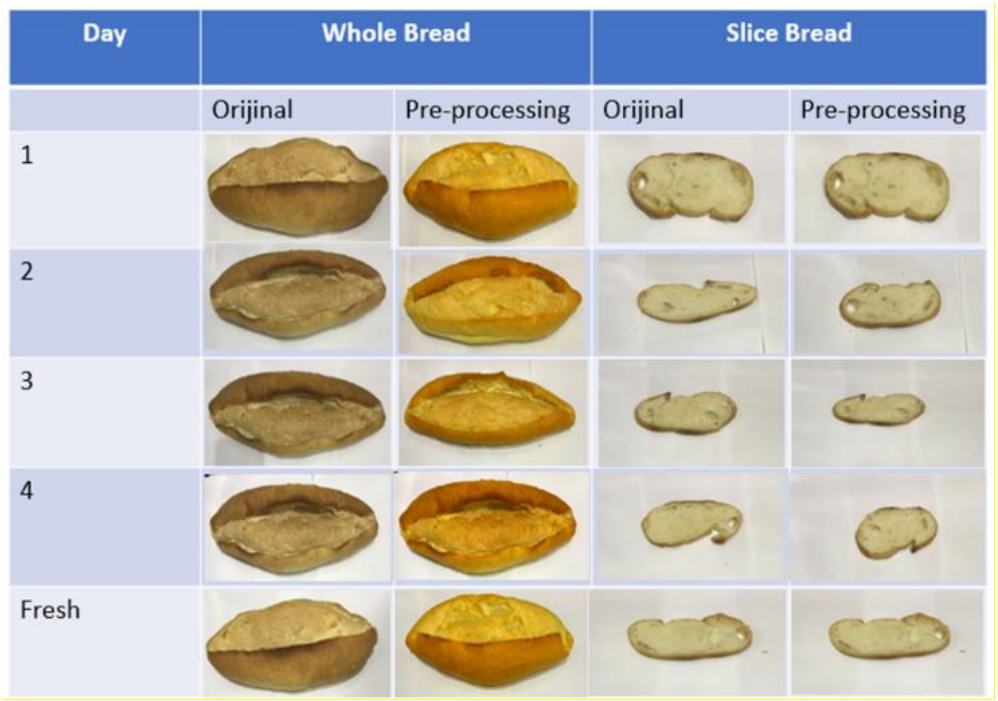

Figure 2. Pre-processed whole and sliced breads

Random Forest

Random Forest (RF) is a regression method that combines the performance of multiple Decision Trees algorithms to classify or predict the value of a variable [26, 27]. In other words, it is the process of constructing an input vector (x) obtained from the values of different features analyzed for a training domain, with a set of K regression trees, and averaging the results [28].

2.2.5. Deep learning algorithms

In classification problems, Convolutional Neural Network (CNN) networks are most commonly used among deep learning algorithms [29]. CNNs can achieve the highest results based on performance results. In the early stages of CNNs, they extract local features from images or numerical data. In subsequent layers, features are combined to detect objects or feature symbols. These processes repeat until the input image is created. CNN architecture is a structure that continues with the Convolution layer, the pooling layers, the activation functions used, and the fully connected layer. Finally, according to the classification problem, the output is tried to be estimated with the binary or multiple softmax function. The model proposed for this study is shown in Figure 3. After the input image was set to 224*224*3, convolutional layers were created with filters with a size of 32, 64, 128, 256, 512 respectively. Following each convolutional layer, the max pooling layer and dropout layers were added. The maximum pooling layer and 3*3 filters ensured that the features with the greatest value were taken into account. The dropout layer was preferred at a rate of 0.2 and the last two layers at a rate of 0.1 to simplify the intermediate layers. ReLU was chosen as the activation function. With the Flatten layer, the matrix values were converted to one dimension. Then the architectural structure is followed by 256, 512, and 5-element dense layers. Finally, with the softmax function, the output is set to 5 classes.

2.2.6. Performance evaluation criteria

Accuracy indicates the proportion of correct predictions;

$$Accuracy = (TN + TP)/(TP + FP + TN + FN) \quad (1)$$

(True Positive (TP); Cases where both the predicted and actual values are positive; True Negative (TN);

cases where the predicted and actual values are negative; False Positive (FP); cases where the predicted value is positive but the true value is negative; False Negative (FN); cases where the predicted value is negative but the true value is positive.)
Precision shows how many of the positively predicted values are actually relevant;

$$Precision = TP / (TP + FP) \quad (2)$$

Sensitivity is a true positive rate that expresses the probability of a positive test if it actually happens;

$$Sensitivity = TP/(TP + FN) \quad (3)$$

The F1-Score takes into account both precision and precision as the harmonic mean [30];

$$F1 - Score = 2 * (Recall * Precision) / (Recall + Precision) \quad (4)$$

For machine learning and deep learning, images are divided into 80% training and 20% testing. The training and testing phases were fixed at 100 steps and were run with Tensorflow-GPU version 2.2 with a GTX 1050 Ti graphics card.

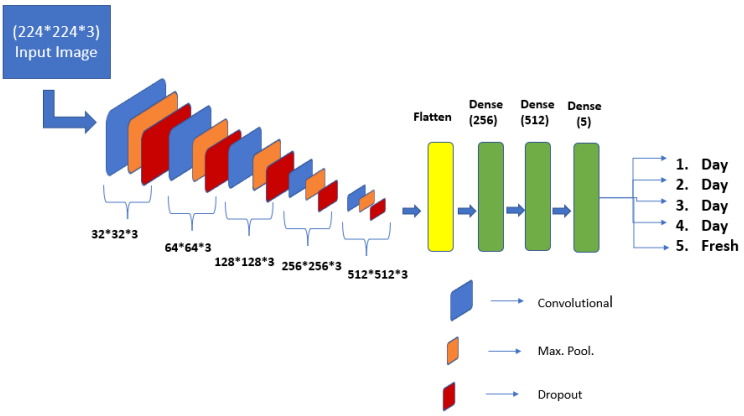

Figure 3. The designed CNN model architectural structure

3. Results and Discussion

Freshness is a key factor in determining the quality of a loaf of bread when it is consumed, and it is necessary to determine its freshness on a daily basis since consumers may mistake changes in freshness for a lack of quality. Thus, it is essential to monitor the bread's freshness during storage. Machine learning and deep learning results are shown in Table 1. The highest accuracy rate among machine learning algorithms was calculated with Random Forest for slice breads with a rate of 62.84%. In the images obtained from different combinations of whole breads, four machine learning algorithms could not perform very well with an accuracy of almost 50%. With an accuracy ranging from 86.75% to 87.25%, the SVM approach is used to categorize biscuits into eight unique groups [31]. The SVM algorithm has been used to accurately categorize biscuits moving on a conveyor belt at a high speed of 9 meters per minute [32]. Archandani, et al. [33] utilized a multilevel SVM classifier to classify bread samples into five fault categories. These categories comprise fractures, cuts, folds, non-uniformity, blackened or burnt areas during baking, deformity, color, and size. Despite the algorithm having a simple construction, the authors claimed that it achieved a 97% classification success rate. The authors concluded that the system's speed ensures its usability in a machine vision system.

Table 1. Machine learning and deep learning algorithms for accuracy results

Test Accuracy	Machine Learning			
	All Bread Images Included	No Side Shots Images	No Bottom Taken Images	Slice Bread Images
SVM	50.45%	52.33%	52.57%	60.87%
KNN	47.46%	43.12%	45.49%	54.64%
Decision Tree	50.12%	41.37%	49.83%	52.39%
Random Forest	52.17%	54.76%	53.46%	62.84%
	Deep Learning			
Train Accuracy	99%	99%	99%	99%
Test Accuracy	56.67%	59.04%	56.99%	92.37%

Using CNN with a limited training dataset is a highly active area of study that can be implemented in real-time manufacturing [34]. Considering the results obtained with CNN architecture in Table 2, the training accuracy rate was found to be 99% for both slice breads and whole breads. However, the test results remained around 56.67% for whole breads. This can be explained by the fact that the image samples are few and similar. In addition, with a more comprehensive data set, training and test results can be optimized to a closer value. However, the most remarkable result was seen in the test results for slice breads. The test results of 92.37% revealed the success of the architectural structure. This is a natural result of extracting more features from the dense layers of the CNN architecture that we have built inside each other.

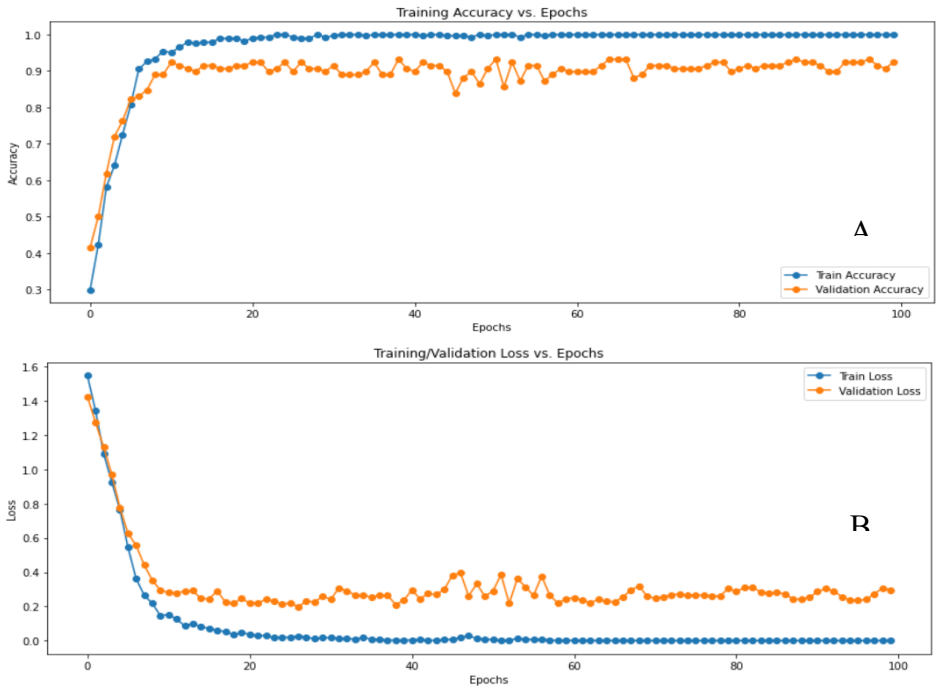

Figure 4. Accuracy (A) and loss (B) graphs for training and validation result

Figure 4 shows the accuracy and loss functions obtained as a result of the 100-step operation of the CNN architecture. When the graphs are examined, it is calculated that the accuracy and loss functions are at an acceptable level, even if they are not very close to the training results. Today, deep learning is recognized as an algorithm that can be applied to the surface of bread. A simple neural network was used to classify the surface color of baked bread with 93% accuracy [35]. In another study of changes in the color of cereal product, with an accuracy of 98.8%, short-CNN was able to predict the level of bread crust browning during baking, which was directly related to customer purchase decisions. This model was found to be superior to AlexNet and

VGGNet-16 models [36].

In their study, Zhang, et al. [37] investigate two techniques for identifying tea quality, utilizing deep convolutional neural networks and transfer learning. Building CNN models based on a small input size can result in a high-quality identification effect for tea and attain superior performance comparable to transfer learning models while consuming less computing power and memory.

Wang, et al. [38] proposed a portable computer vision system to assess the freshness of crayfish, based on a convolutional neural network (CNN), which captures microscopic images of crayfish with different degrees of freshness. The use of optimized networks resulted in freshness prediction accuracy reaching 86.5% and 83.3%.

Figure 5 shows the confusion matrix graph calculated as a result of the test process. When the class results are examined, while 23 data points are known correctly for the 1st day, for the other days, 22, 21, and 22 images respectively and 21 images for fresh bread, were correctly recognized. It was observed that incorrectly labeled data was often confused with the class closest to it. This kind of mislabeling is normal, as there is little variation between fresh bread and day 1, or between day 1 and day 2 or day 3.

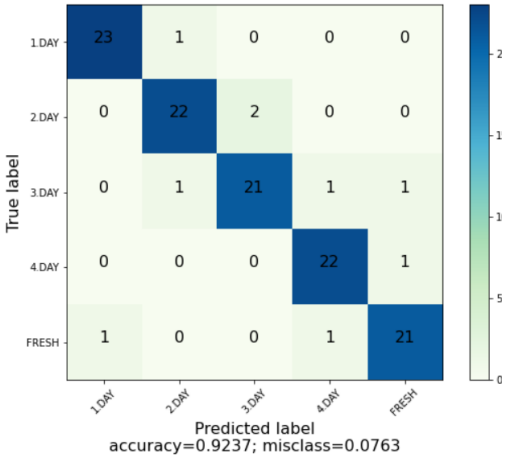

Figure 5. Confusion matrix graph obtained as a result of the test process

4. Conclusion

In this study, a method was proposed to predict the staling process of bread under storage conditions without damaging the bread. In this study, we have shown that the staling level of bread can be determined by utilizing these changes in the appearance of bread in the first few days of consumption. The images of the bread crumbs better reflect staling than the whole bread. In general, when the proposed artificial intelligence algorithms are evaluated, it is revealed that deep learning algorithms perform better than machine learning algorithms if sufficient data is available. The proposed methods and techniques have been encouraging in the food industry, especially in a critical phenomenon such as the detection of problems caused by staling of bread. In addition, it is thought that the current algorithms can be developed for other bread types in future studies and important results can be obtained. In the near future, CNN models are expected to be applied to mobile devices for real-time detection and analysis of food matrices and used to monitor the degree of staling of bread and also to develop effective food spoilage monitoring systems to maintain food quality requirements.

Contributions of the Authors

The authors confirm that the contribution is equally for this paper.

Conflict of Interest Statement

There is no conflict of interest between the authors.

Statement of Research and Publication Ethics

The study is complied with research and publication ethics.

References

[1] G. M. Bosmans, B. Lagrain, E. Fierens, and J. A. Delcour, "The impact of baking time and bread storage temperature on bread crumb properties," *Food chemistry*, vol. 141, no. 4, pp. 3301-3308, 2013.

[2] I. Demirkesen, O. H. Campanella, G. Sumnu, S. Sahin, and B. R. Hamaker, "A Study on Staling Characteristics of Gluten-Free Breads Prepared with Chestnut and Rice Flours," *Food and Bioprocess Technology*, vol. 7, no. 3, pp. 806-820, 2014/03/01 2014, doi: 10.1007/s11947-013-1099-3.

[3] J. Gray and J. Bemiller, "Bread staling: molecular basis and control," *Comprehensive reviews in food science and food safety*, vol. 2, no. 1, pp. 1-21, 2003.

[4] L. Wang et al., "Effect of buckwheat hull particle-size on bread staling quality," *Food Chemistry*, vol. 405, p. 134851, 2023/03/30/ 2023, doi: https://doi.org/10.1016/j.foodchem.2022.134851.

[5] H. An et al., "Quantitative analysis of Chinese steamed bread staling using NIR, MIR, and Raman spectral data fusion," *Food Chemistry*, vol. 405, p. 134821, 2023/03/30/ 2023, doi: https://doi.org/10.1016/j.foodchem.2022.134821.

[6] K. Wang, D.-W. Sun, and H. Pu, "Emerging non-destructive terahertz spectroscopic imaging technique: Principle and applications in the agri-food industry," *Trends in Food Science & Technology*, vol. 67, pp. 93-105, 2017.

[7] T. Ringsted, H. W. Siesler, and S. B. Engelsen, "Monitoring the staling of wheat bread using 2D MIR-NIR correlation spectroscopy," *Journal of Cereal Science*, vol. 75, pp. 92-99, 2017.

[8] J. M. Amigo, A. d. Olmo, M. M. Engelsen, H. Lundkvist, and S. B. Engelsen, "Staling of white wheat bread crumb and effect of maltogenic α-amylases. Part 3: Spatial evolution of bread staling with time by near infrared hyperspectral imaging," *Food Chemistry*, vol. 353, p. 129478, 2021/08/15/ 2021, doi: https://doi.org/10.1016/j.foodchem.2021.129478.

[9] S. J. Olakanmi, D. S. Jayas, and J. Paliwal, "Applications of imaging systems for the assessment of quality characteristics of bread and other baked goods: A review," *Comprehensive Reviews in Food Science and Food Safety*, vol. 22, no. 3, pp. 1817-1838, 2023, doi: https://doi.org/10.1111/1541-4337.13131.

[10] Y. Liu, H. Pu, and D.-W. Sun, "Efficient extraction of deep image features using convolutional neural network (CNN) for applications in detecting and analysing complex food matrices," *Trends in Food Science & Technology*, vol. 113, pp. 193-204, 2021/07/01/ 2021, doi: https://doi.org/10.1016/j.tifs.2021.04.042.

[11] W. da Silva Cotrim, V. P. R. Minim, L. B. Felix, and L. A. Minim, "Short convolutional neural networks applied to the recognition of the browning stages of bread crust," *Journal of Food Engineering*, vol. 277, p. 109916, 2020.

[12] C.-J. Du and D.-W. Sun, "4 - Object Classification Methods," in Computer Vision Technology for Food Quality Evaluation, D.-W. Sun Ed. Amsterdam: Academic Press, 2008, pp. 81-107.

[13] A. Taheri-Garavand, S. Fatahi, M. Omid, and Y. Makino, "Meat quality evaluation based on computer vision technique: A review," *Meat science*, vol. 156, pp. 183-195, 2019.

[14] J. Joshi and M. Phadke, "Feature extraction and texture classification in MRI," *Energy*, vol. 1, no. 0, 2010.

[15] D. Kumar, "Feature extraction and selection of kidney ultrasound images using GLCM and PCA," *Procedia Computer Science*, vol. 167, pp. 1722-1731, 2020.

[16] S. B. Kotsiantis, I. Zaharakis, and P. Pintelas, "Supervised machine learning: A review of classification techniques," *Emerging artificial intelligence applications in computer engineering*, vol. 160, no. 1, pp. 3-24, 2007.

[17] T. Hastie, R. Tibshirani, J. H. Friedman, and J. H. Friedman, *The elements of statistical learning: data mining, inference, and prediction*. Springer, 2009.

[18] C. Wang, Y. Zhang, J. Song, Q. Liu, and H. Dong, "A novel optimized SVM algorithm based on PSO with saturation and mixed time-delays for classification of oil pipeline leak detection," *Systems Science & Control Engineering*, vol. 7, no. 1, pp. 75-88, 2019.

[19] M. Fan, L. Wei, Z. He, W. Wei, and X. Lu, "Defect inspection of solder bumps using the scanning acoustic microscopy and fuzzy SVM algorithm," *MiRe*, vol. 65, pp. 192-197, 2016.

[20] S. Long, X. Huang, Z. Chen, S. Pardhan, and D. Zheng, "Automatic detection of hard exudates in color retinal images using dynamic threshold and SVM classification: algorithm development and evaluation," *BioMed research international*, vol. 2019, 2019.

[21] I. S. Abd Elkarim and J. Agbinya, "A Review of Parallel Support Vector Machines (PSVMs) for Big Data classification," *Australian Journal of Basic and Applied Sciences*, vol. 13, no. 12, pp. 61-71, 2019.
[22] Q. Li, X. Du, H. Zhang, M. Li, and W. Ba, "Liquid pipeline leakage detection based on moving windows LS-SVM algorithm," in *2018 33rd Youth Academic Annual Conference of Chinese Association of Automation (YAC)*, 2018: IEEE, pp. 701-705.
[23] C. Dai, J. Yang, Y. Qin, and J. Liu, "Physical layer authentication algorithm based on SVM," in *2016 2nd IEEE International Conference on Computer and Communications (ICCC)*, 2016: IEEE, pp. 1597-1601.
[24] D. M. Abdullah and A. M. Abdulazeez, "Machine Learning Applications based on SVM Classification A Review," *Qubahan Academic Journal*, vol. 1, no. 2, pp. 81-90, 2021.
[25] V. Bijalwan, V. Kumar, P. Kumari, and J. Pascual, "KNN based machine learning approach for text and document mining," *International Journal of Database Theory and Application*, vol. 7, no. 1, pp. 61-70, 2014.
[26] L. Breiman, J. Friedman, R. Olshen, and C. Stone, "*Classification and Regression Trees. 1st Editio*," ed: Routledge, 1984.
[27] V. F. Rodriguez-Galiano, B. Ghimire, J. Rogan, M. Chica-Olmo, and J. P. Rigol-Sanchez, "An assessment of the effectiveness of a random forest classifier for land-cover classification," *ISPRS journal of photogrammetry and remote sensing*, vol. 67, pp. 93-104, 2012.
[28] V. Rodriguez-Galiano, M. Sanchez-Castillo, M. Chica-Olmo, and M. Chica-Rivas, "Machine learning predictive models for mineral prospectivity: An evaluation of neural networks, random forest, regression trees and support vector machines," *Ore Geology Reviews*, vol. 71, pp. 804-818, 2015.
[29] A. Yılmaz, "Diagnosing COVID-19 from X-Ray images with using multi-channel CNN architecture," *Journal of the Faculty of Engineering and Architecture of Gazi University*, vol. 36, no. 4, pp. 1761-1774, 2021.
[30] T. Fuat and Y. Kökver, "Application with deep learning models for COVID-19 diagnosis," *Sakarya University Journal of Computer and Information Sciences*, vol. 5, no. 2, pp. 169-180, 2022.
[31] S. Nashat and M. Z. Abdullah, "Multi-class colour inspection of baked foods featuring support vector machine and Wilk's λ analysis," *Journal of Food Engineering*, vol. 101, no. 4, pp. 370-380, 2010/12/01/ 2010, doi: https://doi.org/10.1016/j.jfoodeng.2010.07.022.
[32] S. Nashat, A. Abdullah, S. Aramvith, and M. Z. Abdullah, "Support vector machine approach to real-time inspection of biscuits on moving conveyor belt," *Computers and Electronics in Agriculture*, vol. 75, no. 1, pp. 147-158, 2011/01/01/ 2011, doi: https://doi.org/10.1016/j.compag.2010.10.010.
[33] R. B. Archandani, F. Mohanna, and M. J. Ahsani, "Introducing an automatic bread quality assessment algorithm using image processing techniques," *European Journal of Electrical Engineering and Computer Science*, vol. 6, no. 6, pp. 31-38, 2022.
[34] P. Tantiphanwadi and K. Malithong, "Bread Browning Stage Classification Model using VGG-16 Transfer Learning and Fine-tuning with Small Training Dataset," *Engineering Journal*, vol. 26, no. 11, pp. 1-12, 2022.
[35] O. Paquet-Durand, D. Solle, M. Schirmer, T. Becker, and B. Hitzmann, "Monitoring baking processes of bread rolls by digital image analysis," *Journal of Food Engineering*, vol. 111, no. 2, pp. 425-431, 2012/07/01/ 2012, doi: https://doi.org/10.1016/j.jfoodeng.2012.01.024.
[36] W. d. S. Cotrim, V. P. R. Minim, L. B. Felix, and L. A. Minim, "Short convolutional neural networks applied to the recognition of the browning stages of bread crust," *Journal of Food Engineering*, vol. 277, p. 109916, 2020/07/01/ 2020, doi: https://doi.org/10.1016/j.jfoodeng.2020.109916.
[37] C. Zhang, J. Wang, G. Lu, S. Fei, T. Zheng, and B. Huang, "Automated tea quality identification based on deep convolutional neural networks and transfer learning," *Journal of Food Process Engineering*, vol. 46, no. 4, p. e14303, 2023/04/01 2023, doi: https://doi.org/10.1111/jfpe.14303.
[38] C. Wang et al., "Convolutional neural network-based portable computer vision system for freshness assessment of crayfish (Prokaryophyllus clarkii)," *Journal of Food Science*, vol. 87, no. 12, pp. 5330-5339, 2022, doi: https://doi.org/10.1111/1750-3841.16377.

Bitlis Eren Üniversitesi Fen Bilimleri Dergisi
BİTLİS EREN UNIVERSITY JOURNAL OF SCIENCE
ISSN: 2147-3129/e-ISSN: 2147-3188
VOLUME: 12 NO: 4 PAGE: 994-1005 YEAR: 2023
DOI:10.17798/bitlisfen.1312188

The Antioxidant Capacities and Antimicrobial Activities of Some *Salvia* L. Seeds

Murat KURSAT[1*], Sevda KIRBAG[2], Irfan EMRE[3], Pınar ERECEVIT SONMEZ[4], Mustafa Yunus EMRE[5], Okkeş YILMAZ[3], Şemsettin CIVELEK[3]

[1]*Bitlis Eren University, Faculty of Science and Arts, Department of Biology, Bitlis, Turkey;*

[2]*Firat University, Faculty of Science, Department of Biology, Elazığ, Turkey;*

[3]*Firat University, Faculty of Education, Department of Basic Education, Elazığ, Turkey*

[4]*Munzur University, Pertek Vocational Higher School, Department of Food Processing, Tunceli, Turkey;*

[5]*Mardin Artuklu University, Vocational Higher School of Health Services, Mardin, Turkey*

(ORCID: 0000-0002-0861-4213) (ORCID: 0000-0002-4337-8236) (ORCID:0000-0003-0591-3397) (ORCID:0000-0003-2389-0694) (ORCID:0000-0001-6602-8872) (ORCID:0000-0002-8276-4498) (ORCID:0000-0002-6868-4125)

Keywords: Antimicrobial Activity, Antioxidant Capacity, Phenolics, *Salvia* L

Abstract

The goal of the present study is to find the penolic contents, antioxidant activities and antimicrobial capacities in the seeds of five *Salvia* L. taxa two of which are endemics (*Salvia euphratica* var. *leiocalycina* and *Salvia euphratica* var. *euphratica*). The flavonoid and phenolic acid are determined by using HPLC while the antioxidant activities are determined based on different methods. Also, the antimicrobial activities of some *Salvia* species are determined by using the well agar method. The current study found that the studied *Salvia* species have low flavonoids. It has been found that *Salvia euphratica* var. *euphratica* has high vanillic acid, ferulic acid and rosmarinic acid among the studied taxa. Similarly, it has been found that *Salvia euphratica* var. *euphratica* has high DPPH and ABTS radical scavening capacity in all concentrations. It has been also found that *Salvia euphratica* var. *euphratica* has the highest total phenolic content (372,63±0,87 µgGAE/mg) while *Salvia tricholoda* has low total phenolic content (46,41±1,71 µgGAE/mg). In addition, this study demonstrated that *Salvia tricholoda* has the lowest metal chelating activity (37,35±0,51%). Furthermore, the present study found that the lipid peroxidation levels of the studied Salvia taxa are between 18,21±0,37 mg/kg and 21,03±0,22 mg/kg while it has been found that the antibacterial properties of the *Salvia* taxa under study are altering.

.

1. Introduction

The Latin word Salvare which means health or heal was where the name *Salvia* originates [1]. The genus contains 1000 species distributed throughout the world including Asia, Africa and Europe [2, 3, 4]. In Turkey, the genus is represented by 100 taxa with a 57% endemism ratio [5]. Anatolia is a main centre of gene for the genus *Salvia* [6]. In Turkey, the *Salvia* species are known as adaçayı and are used to make herbal tea [7, 8]. *Salvia* species are exported to different regions of the world from Turkey [2].

In traditional medicine, *Salvia* species are used all throughout the world and they are employed in the management of several diseases such as rheumatism, aches, epilepsy, bronchitis, cold

* Corresponding author:botanikkursat@gmail.com and mkursat@beu.edu.tr *Received: 09.06.2023, Accepted: 23.11.2023*

improver, and tuberculosis [9, 10]. Also, it has been reported that *Salvia* has a strong antioxidant capacity which is directly correlated with phenolic content [11]. The current study's objective is to assess the radical scavenging abilities of DPPH, ABTS, flavonoids, phenolic acids, lipid peroxidation capacity, Fe chelating, total phenolics and antimicrobial activities in mature seeds of the *S. suffruticosa* Montbret & Aucher ex Bentham; *S. trichoclada* Bentham; *S. euphratica* Montbret & Aucher ex Bentham var. *leiocalycina* (Rech. Fil.) Hedge; *S. euphratica* Montbret & Aucher ex Bentham var. *euphratica* (Rech. Fil.) Hedge; *S. multicaulis* Vahl grown in Elazig.

2. Material and Method

2.1. Plant Materials

In this investigation, plants were used that were gathered from their native environments. The Firat University Herbarium (FUH) is where the plant samples are kept. Table 1 lists the locations of the examined *Salvia* taxa.

Table 1. Localities of studied *Salvia* L. taxa

Taxa	Locality
S. suffruticosa Montbret & Aucher ex Bentham	Elazig Baskil district, marble factory around, railway near, 1330 m.
S. trichoclada Bentham	Elazig Baskil district, 1450m.
S. euphratica var. Montbret& Aucher ex Bentham *leiocalycina* (Rech. Fil.) Hedge	Elazig Baskil district, marble factory around, railway near, 1330 m.
S. euphratica var. Montbret& Aucher ex Bentham *euphratica* (Rech. Fil.) Hedge	Elazig- Malatya road, Komurhan district,755 m.
S. multicaulis Vahl	Elazig Baskil district, Bolucuk village, 1490 m.

2.2. Microbial Strain

4 bacteria (*Escherichia coli* ATCC 25922, *Klebsiella pneumoniae* FMC 5, *Staphylococcus aureus* COWAN 1, *Bacillus megaterium* DSM 32), 2 yeasts (*Candida albicans* FMC 17, *Candida glabrata* ATCC 66032) and 2 dermatophyte species (*Trichophyton sp*., *Epidermophyton sp*.) are employed in this inquiry. Microorganisms are supplied by the Department of Biology, Firat University, Microbiology Labarotory, Elazig-Turkey.

2.3. Extraction of Dried Seed Materials

To analyze the phenolic compounds, including flavonoids and phenolic acids, 2 g of seed material is homogenized in 5 ml of 80% methanol. Centrifuging the homogenates at 5000 rpm and +4 °C. Rotary evaporation is used to treat the supernatant. Finally, to create a stock solution, extracts are suspended in dimethyl sulphoxide (DMSO) [12]. Three times the experiment is conducted.

2.4. Determination of Bioactive Properties

2.4.1. Chromatographic Conditions for Flavonoids and Phenolic Acids

A PREVAIL C18 reversed-phase column (15x4.6mm, 5m, USA) isused for the chromatographic analysis. The mobile phase is composed of methanol, water, and acetonitrile (46/46/8, v/v/v), and contains 1.0% acetic acid [12,13]. A Millipore 0.45 m membrane filter is used to filter the mobile phase. Morin, kaempferol, quercetin, naringin, catechin, resveratrol, rutin, myricetin, naringenin, erulic acid, caffeic acid, vanillic acid, cinnamic acid, and rosmarinic acid have been determined by DAD following RP-HPLC. Flow rate and injection volume are 1.0 ml/min and l0 µL, respectively. By comparing the samples' retention periods to those of the reference standards, the chromatographic peaks of the samples are confirmed. At 25°C, the entire chromatographic process is completed.

2.4.2. Antioxidant Assay by DPPH Radical Scavenging Activity

The Liyana-Pathiranan and Shahidi [14] approach is used to assess the radical scavenging abilities of the study's seed materials. Shortly, 4.0 ml of a daily 25 mg/L DPPH in methanol solution are mixed with 25, 50, 100, 150, and 250 µL of extract in DMSO. The samples are maintained at room temperature for 30 minutes in the dark. At 517 nm, the mixture's absorbance is spectrophotometrically analyzed. As a benchmark, quercetin at 1 M is employed.

The ability to scavenge DPPH radicals was calculated by the following formula: DPPH radical scavenging activity (%) = [(Abs control – Abs sample)]/ (Abs control)] x 100. where Abs control is the absorbance of DPPH radical + methanol; Abs sample is the absorbance of DPPH radical + sample extract /standard.

2.4.3. Antioxidant Assay by ABTS [2,2-azinobis-(3-ethylbenzothiazoline-6-sulfonic acid) diammonium salt]

The ABTS radical cation decolorization assay is used to investigate another free radical-scavenging action [15]. The ABTS radical cation (ABTS•+) was created by combining 2.45 mM potassium persulphate with 7 mM ABTS. At room temperature, the solution was incubated for 12–16 hours. Water is used to dissolve the (ABTS•+) solution, resulting in an absorbance of 0.700±0.020 at 734 nm. The decrease in absorption is then observed over the course of six minutes after three ml of diluted ABTS cation solution has been treated with 25, 50, 100, 150, and 250 µL of extract. Three experiments are conducted [16]. The absorbance of the control (3.0 mL (ABTS•+) solution with 30 L water) is recorded as Acontrol.

The ability to scavenge ABTS radicals (734 nm) was calculated by the following formula: ABTS radical scavenging activity (%) = [(Abs control – Abs sample)]/ (Abs control)] x 100

2.4.4. Determination of Total Phenolic

The Folin-Ciocalteu technique is used to assess total phenolics [17]. Following the treatment of the 100 ml extracts with 200 ml of Folin-Ciocalteu reagent and 3.16 ml of water, the samples are left at room temperature for 3 minutes. The mixture is then supplemented with anhydrous sodium carbonate (20% w/v), and the total phenolic content is determined two hours later at room temperature. At 765 nm, the samples' absorbance is measured [18]. Gallic acid equivalents per gram of dry weight (gGAE/mg) have been used to calculate the total phenolic content.

2.4.5. Metal Chelating Activity

This methodology was utilized by Dinis et al. [19] to ascertain the chelating abilities of the studied taxa. 50 µl of 2 mM FeCl2 is added to extracts at different concentrations (50, 100, 250, and 500 µg/mL). The reaction was started by adding 0.2 mL of 5 mM ferrozine to the mixture. After a vigorous shake, the combinations are left at room temperature for 10 minutes. At 562 nm, sample absorbances are determined.

The percentage blocking of of ferrozine–Fe2+ complex was measured based on following formula: Ferrous ion chelating activity (%) = [1 - (As /Ac)] × 100 where Ac was the absorbance of the control, and As was the absorbance of the extract/ standard (Kızılpınar et al., 2017). Na2EDTA was used as positive control.

2.4.6. Determination of Antioxidant Activity by MDA/TBARS Formation

The Shimoi et al. [20] method is used to measure the antioxidant activity of the samples. The sample extracts are extracted using dimethyl sulfoxide, or DMSO. In the experiments, hydrogen peroxide and solutions of Fe2+ (FeCl2.2H2O) are utilized. Additionally, DMSO is used to dissolve oleic acid (3.35 mM), linoleic acid (9.01 mM), and linolenic acid (2.30 mM). The groups of controls, sage extracts, and the Fenton reagent are established. The fenton group is treated with 0.5 mL of fatty acid, a buffer solution, FeCl2.2H2O (50 µM), and hydrogen peroxide (0.01 mM), whereas the control group is treated with 0.5 mL of fatty acid, a buffer solution, 0.2% Tween 20, 0.05 M Tris HCl, and 0.15 M KCl, pH=7.4. 0.5 mL of fatty acid, a buffer, 50 µM FeCl2, 0.01 mM hydrogen peroxide, and 0.25 mL of all sage extract are added to the sample extracts as a treatment. To stop further oxidation, 0.1 mL of 4% (w/v) BHT is added to each group and all groups are incubated at 37 °C for 24 hours of incubation. After that, the reaction mixture is added 1 mL of 0.6% TBA, and it is then incubated at 90 °C for 30 min using 1 mL of samples from each of the three groups. The tubes are then filled with 4 mL butan-1-ol, mixed, and centrifuged at 4250 rpm for 10 min. Using a Shimadzu UV mini-1240 spectrophotometer, the absorbance of the supernatant is measured at 532 nm. Tetraethoxyopropane is used to create MDA standard curves, and TBARS are represented as mg MDA/kg dry matter [21].

2.5. Antimicrobial Activity

The well agar method is used to conduct antimicrobial tests, and 100 µL of suspension containing, according to the McFarland standard, 106 cells/mL of bacteria, 104 cells/mL of yeast, and cells/mL of dermatophyte

fungi is inoculated into Mueller Hinton Agar (Difco), Malt Extract Agar (Difco), and Sabouroud Dextrose Agar (Oxoid), respectively. Wells are furnished with plates and a 0.85-cm cork-borer. The flavonoids from the seed materials are poured into the well in a volume of 10 µl. 9 cm diameter sterile Petri dishes are kept at 4 °C for two hours. The infected plates are then incubated for 24 hours at 37±1°C for bacterial strains and for 72 hours at 25±1°C for yeast and dermatophyte fungus. By analyzing the zone of inhibition against the test organisms, antimicrobial activity is evaluated [22]. Methanol and hexane injection wells were employed as negative controls. Three times experimental experiments are conducted.

2.6. Statistical Analysis

Using the SPSS 21.0 package program, all analyses are carried out. The relationship between total phenolic content and antioxidant capacity (ABTS, DPPH, and metal chelating) is determined using a simple linear regression model. The data from the current investigation is shown as mean values±S.D. Additionally, the significance of variations between antimicrobial activity is assessed using the LSD (least significant difference). The results are presented as mean ± S.D. and $p<0.0001$, $p<0.001$, $p>0.05$ are conceived as significant compare to the control group (ampicillin sulbactam, mikostatin). Each sample is examined three times.

3. Results and Discussion

Scientific research on *Salvia* species is drawn to them due to their significant therapeutic value. The present study demonstrated that the flavonoid content of *Salvia* seeds are low amounts (Table 2). It has been detected that the rutin amount is relatively higher than the other studied flavonoids. *S. euphratica* var. *euphratica* has high rutin contents (61,67±1,27 µg/mg) while *S. tricholoda* has low rutin content (1,21±0,07 µg/mg). Besides, catechin content has been only found in *S. euphratica* var. *leicalycina* (90,4±1,27 µg/mg). The naringenin is not determined in the present study. In addition, it has been shown that the other studied flavonoids are absent or in trace amounts (Table 2). Similarly, Kivrak et al. [23] suggested that in *Salvia* species other than this study don't have myricetin, resveratrol and quercetin contents.

Also, a current study showed that vanillic acid contents of studied *Salvia* taxa have been found between 9,97±0,34 µg/mg (*S. tricholoda*) and 56,32±0,99 µg/mg (*S. euphratica* var. *euphratica*) except for *S. multicaulis* has trace amount (0,2±0,01 µg/mg) (table 3). Cinnamic acid is only found in trace amounts in *S. multicaulis* (0,4±0,01 µg/mg). In addition, it has been determined that caffeic acid content is between 2,23±0,06 µg/mg and 12,64±0,41 µg/mg and *S. euphratica* var. *euphratic*a, *S. euphratica* var. *leicalycina* and *S. multicaulis* have higher ferulic acid and rosmarinic acid contents than the other taxa in this study. And also, the present study showed that *S. euphratica* var. *euphratica* has high vanillic acid (56,32±0,99 µg/mg), ferulic acid (82,45±0,65 µg/mg) and rosmarinic acid (145,27±1,55 µg/mg) contents (Table 3).

It has been demonstrated that *S. euphratica* var. *euphratica* has the highest rutin (61,67±1,27 µg/g), vanillic acid (56,32±0,99 µg/g), ferulic acid (82,45±0,65 µg/g) and rosmarinic acid (145,27±1,55 µg/g) contents (Table 2, 3). Kocak et al. [11] found that rosmarinic acid is in high amounts in *Salvia* taxa. Likewise, it has been found that *S. euphratica* var. *leicalycina* has the second major vanillic acid (33,2±0,3 µg/g) content. Moreover, *S. euphratica* var. *leicalycina* and *S. multicaulis* have high ferulic acid and rosmarinic acid contents (Table 3). Similarly, Francik et al. [24] found that Salvia species have significant ferulic acid amounts. Also, Zengin et al. [25] and Kivrak et al. [23] found that *Salvia* species including *S. euphratica* var. *leiocalycina* have apigenin, kaempferol, luteolin, naringenin, rutin, caffeic acid, protocatechuic acid, vanillic acid, rosmarinic acid, ferulic acid and 3-O-caffeoylquinic acid. Yumrutas et al. [26] found that major phenolic acids are rosmarinic and caffeic acid in *S. euphratica* var. *euphratica* and *S. euphratica* var. *leiocalycina*. On the other hand, the present study showed that cinnamic acid is absent or in trace amounts (Table 3). In a study done by Erdogan et al [27] supported that cinnamic acid contents of Salvia taxa are trace amounts.

The present study demonstrated that all of the studied taxa showed highest DPPH activities in 150 and 250 µl except for *S. suffruticosa* (57,8±0,43%) and *S. tricholoda* (23,7±0,41%) (Table 4). *S. euphratica* var. *leicalycina* and *S. euphratica* var. *euphratica* have shown high radical scavening activity in 100 µl (81,47±0,87% and 94,84±1,14%, respectively). Generally, it has been measured that the DPPH radical scavenging activity of studied taxa are low in 25 µl and 50 µl except for *S. euphratica* var. *euphratica* has 91,11±0,49% and 90,73±1,54%, respectively. Besides, *S. euphratica* var. *euphratica*

has represented the highest DPPH radical scavenging activity among the studied Salvia taxa. Similarly, Tepe et al. [28] found that the most active herb is *S. euphratica* var. *euphratica*, with an IC50 value of 20.7±1.22 g/ml. Further, Orhan et al. [29] and Zengin et al. [25] indicated that the Salvia species exhibited significant antioxidant properties. Also, Svydenko et al. [30] and Onder et al. [31] suggested that the Salvia species under investigation is a source of polyphenol chemicals with high antioxidant activity. However, it has been determined that *S. tricholoda* has the lowest radical scavenging activity in the present study. (Table 4). Similarly, Culhaoglu et al. [32] showed that *S. tricholado* has weak DPPH activity.

In addition, it has been found that the studied *Salvia* taxa have the highest ABTS radical scavenging apart from *S. suffruticosa* in 25 µl and *S. tricholoda* in 50 and 100 µl (Table 5). The several literatures showed that *Salvia* species strong DPPH and ABTS radical scavenging activities [33,34,35].

Table 2. The results of flavonoid contents of *Salvia* taxa (µg/mg)

Taxa	Rutin	Myricetin	Morin	Quercetin	Kaempferol	Catechin	Naringin	Naringenin	Resveratrol
Salvia suffruticosa	24,04±1,06	-	-	-	-	-	-	4,61±0,18	-
Salvia tricholoda	1,21±0,1	0,19±0,01	0,21±0,02	0,21±0,02	0,2±0,01	-	-	-	0,59±0,02
Salvia euphratica var. *leicalycina*	32,62±1,17	1,41±0,08	1,02±0,08	-	0,39±0,01	90,4±1,27	-	-	-
Salvia euphratica var. *euphratica*	61,67±1,27	-	-	-	-	-	-	-	-
Salvia multicaulis	32,15±0,68	-	-	-	-	-	-	2,05±0,04	-

Table 3. The results of phenolic acid contents of *Salvia* taxa (µg/mg)

Taxa	Vanillic acid	Cinnamic acid	Caffeic acid	Ferulic acid	Rosmarinic acid
Salvia suffruticosa	20,78±0,54	-	12,64±0,41	3,43±0,03	25,81±1,17
Salvia tricholoda	9,97±0,34	-	2,23±0,06	3,32±0,04	3,39±0,12
Salvia euphratica var. *leicalycina*	33,2±0,3	-	4,02±0,06	36,64±0,79	61,2±1,4
Salvia euphratica var. *euphratica*	56,32±0,99	-	10,65±0,43	82,45±0,65	145,27±1,55
Salvia multicaulis	0,2±0,01	0,4±0,01	8,82±0,78	28,66±0,45	79,37±0,64

Table 4. The DPPH results of *Salvia* species (%)

Taxa	25 µl	50 µl	100 µl	150 µl	250 µl
Salvia suffruticosa	14,98±0,98	54,37±0,76	20,1±0,71	57,8±0,43	92,1±0,53
Salvia tricholoda	23,48±0,72	20,57±0,47	20,92±0,74	88,32±1,17	23,7±0,41
Salvia euphratica var. *leicalycina*	45,38±1,03	40,92±0,57	81,47±0,87	93,14±1,27	93,24±0,64
Salvia euphratica var. *euphratica*	91,11±0,49	90,73±1,54	94,84±1,14	92,1±0,57	92,68±0,28
Salvia multicaulis	34,49±0,63	38,58±0,43	75,49±0,78	92,3±0,64	94,06±1,15

Table 5. The results ABTS of *Salvia* taxa (%)

Taxa	25 µl	50 µl	100 µl	150 µl	250 µl
Salvia suffruticosa	39,54±0,81	64,48±0,53	98,87±0,73	95,11±0,62	98,55±1,14
Salvia tricholoda	81,14±0,48	15,86±0,41	48,13±0,51	62,04±0,64	90,71±0,49
Salvia euphratica var. *leicalycina*	65,68±1,04	98,69±0,92	98,47±0,76	98,61±1,17	98,78±1,1
Salvia euphratica var. *euphratica*	98,75±0,71	98,37±0,84	98,73±1,16	98,4±0,84	98,85±0,76
Salvia multicaulis	64,51±0,36	98,6±1,21	98,54±0,88	98,61±1,14	98,68±0,84

Besides, this study found that studied *Salvia* species have similar lipid peroxidation values (18,21±0,37 mg MDA/kg-21,03±0,22 mg MDA/kg) (Table 6). Works of literatures displayed that *Salvia* species have considerable potent to protection of TBARS formation [7, 36]. In addition, It has been found that *S. euphratica* var. *euphratica* has high total phenolic content (372,63±0,87 µgGAE/mg) and *S. tricholoda* has low total phenolic content (46,41±1,71 µgGAE/mg) (table 6). In a study done by Kocak et al. ([11] found that sage has rich in total phenolics which is measured as 64,98 mol GAEs/g dry plants. Another study done by Zengin et al. [25] found that *S. euphratica* var. *leicalycina* has 108,00±0,11 mg GAE/g total phenolic content. However, the results of Firuzia et al. [37] conflict with current study. Because they determined that *S. multicaulis* has 13.0±2.3 mg CE/g DW total phenolics [37]. Kivrak et al. [23] claimed that the total phenolic contents are responsible for the antioxidant capacity of *Salvia*. On the contrary, Jeshvaghani et al. [38] don't find a high correlation between total phenolic and antixodant capacity. Further, it has been determined that *S. multicaulis* has the highest metal chelating activity (76,25±0,69%) whilst *S. tricholoda* has the lowest metal chelating activity (37,35±0,51%) in the present study (Table 6). Zengin et al. [25] found that *S. euphratica* var. *leicalycina* has significant metal chelating activity. And also, Orhan et al. [29] showed that *Salvia* taxa represented the finest metal chelating activity. However, Orhan et al. [39] found that *Salvia* taxa displayed low metal chelating activity (92 ± 1.17% and 24.19 ± 3.28% at 1000 lg ml-1) and Senol et al. [40] found that the methanol extracts of fifty-five *Salvia* taxa comprising *S. euphratica* var. *euphratica, S. euphratica* var. *leicalycina, S. russellii* and *S. tricholoda* showed weak chelation activity. Additionally, this study shows that there is a poor association between total phenolics and metal chelating (r2:,158), but an important relationship

between total phenolics and DPPH (r2:,959) and ABTS (r2:,803). Also, Svydenko et al. [30] suggested that the *Salvia* species under investigation is a source of polyphenol chemicals with high antioxidant activity. In addition, According to Adımcılar et al. (2019), there was a strong correlation between the bioactivities and the rosmarinic acid levels in the samples. Furthermore, Onder et al. (2022) demonstrated that *Salvia* species, including *S. sclarea*, and *S. palaestina*, have the potential to be rich sources of interesting bioactive chemicals.

Additionally, the findings of this investigation revealed that *Trichopyton sp.*, *Epidermophyton sp.*, and *C. glabrata* did not show any antimicrobial action against the examined *Salvia* species (Table 7). Also, the studied *Salvia* taxa showed low antimicrobial activity against *K. pneumoniae*. On the contrary, it has been found that *Salvia* taxa apart from *S. suffruticosa* have high antimicrobial capacity against *E. coli* (Table 7). In a study done by Gulcin et al. [43] showed that *S. tricholoda* had no antimicrobial activity against fungal and bacterial strains. Similarly, another study by done Guzel et al. [44] demonstrated that the extracts of *S. euphratica* extracts don't represent antifungal activity against *C. glabrata*, *S. aureus* and *E. coli*. However, a study by done Norouzi-Arasi et al. [45] found that S. *suffruticosa* represented significant antimicrobial activity

Table 6. The lipid peroxidation inhibition (mg MDA/kg), total phenolic contents (µgGAE/mg) and metal chelating (%) results of *Salvia* taxa

Taxa	Lipid Peroxidation Inhibition	Total Phenolics	Metal Chelating %
Salvia suffruticosa	20,67±0,49	125,14±1,29	75,52±0,77
Salvia tricholoda	19,61±0,47	46,41±1,71	37,35±0,51
Salvia euphratica var. *leicalycina*	18,21±0,37	195,08±0,9	68,12±1,03
Salvia euphratica var. *euphratica*	19,67±0,22	372,63±0,87	63,29±0,54
Salvia multicaulis	21,03±0,22	223,32±1,13	76,25±0,69

Table 7. The disc diffusion assay results of the antimicrobial susceptibility tests for growing reference microorganisms

Microorganisms	1	2	3	4	5	Standart antibiotics
			Inhibition *zone*			
E. coli	8.33±0.3^{c}	13.33±0.3^{d}	11.00±0.0^{d}	13.33±0.3^{d}	13.33±0.3^{d}	11.66±0.3*
S. aureus	8.33±0.3^{c}	8.33±0.3^{c}	13.33±0.3^{d}	11.00±0.0^{d}	12.33±0.3^{d}	9.66.±0.3*
K. pneumoniae	8.33±0.3^{c}	8.33±0.3^{c}	8.33±0.3^{c}	9.66±0.3^{d}	9.66±0.3^{d}	11.66±0.3*
B. megaterium	9.33±0.3^{c}	14.33±0.3^{d}	8.33±0.3^{c}	8.33±0.3^{c}	11.00±0.0^{d}	11.66±0.3 **
C. albicans	-	13.66±0.3^{d}	8.33±0.3^{c}	8.66±0.3^{c}	-	11.66±0.3 **
C.glabrata	-	-	-	-	-	8.66±0.3**
Epidermophyton sp.	-	-		-	-	8.33±0.3**
Trichopyton sp.	-	-	-	-	-	8.33±0.3**

The positive control; ampicillin sulbactam (*) and mikostatin (**) (120 µL and 20µg/disc Inhibition zone> 15 mm (highly significant effect; p<0.0001; cd), 14 – 10 mm (significant effect; p<0.001;d), 10-8 mm (moderate effect; c: p<0.01), not inhibited (-) (a: p>0.05) 1: *S. suffruticosa*, 2: *S. trichoclada* Bentham, 3: *S. euphratica* var. *leicalycina*, 4: *S. euphratica* var. *euphratica*, 5:*S. multicaulis*

4. Conclusion and Suggestions

The current investigation demonstrated the low flavonoid concentration of Salvia taxa. Additionally, it was discovered that the investigated Salvia has no or very little cinnamic acid. It has been found that the phenolic acid content of *S. tricholoda* has the lowest among the studied *Salvia* taxa. *S. euphratica* var. *euphratica* has high rosmarinic acid, vanillic acid, and ferulic acid. Also, it has been found that the rosmarinic acid content of studied *Salvia* taxa are high apart from S. tricholoda. In addition, *S. euphratica* var. *euphratica* has high DPPH and ABTS radical scavenging capacity. Similarly, *S. euphratica* var. *euphratica* has the highest total phenolic content whilst *S. tricholoda* has the lowest total phenolic content and metal chelating activity. On the other hand, current study showed that lipid peroxidation inhibition levels of studied *Salvia* are changed from 18,21±0,37 mg/kg to 21,03±0,22 mg/kg. This study showed that the studied *Salvia* taxa represented different antimicrobial activities.

Acknowledgment

The Firat University Scientific Research Unit is funding this study (Project Number: FUBAP 2041). We gratefully acknowledge the Scientific Research Unit of Firat University. Additionally, certain study data are presented orally, and an abstract of the study is included in the National Botanical Science Congress Abstract Book (25-28 October 2014).

Conflict of Interest Statement

The authors declare no conflicts of interest.

Statement of Research and Publication Ethics

The study has complied with research and publication ethics

References

[1] A. Ulubelen, H. Birman, S. Oksuz, G. Topcu, U. Kolak, A. Barla, and W. Voelter, "Cardioactive diterpenes from the roots of *Salvia eriophora," Planta Medica,* vol. 68, no. 9, pp.818-821, 2002.

[2] E. Kupeli-Akkol, F. Goger, M. Kosar, and K. H. C. Baser, "Phenolic composition and biological activities of *Salvia halophila* and *Salvia virgate*, "*Food Chemistry*, vol.108, pp.942-949, 2008.

[3] M. B. Bahadori, B. Asghari, L. Dinparast, G. Zengin, C. Sarikurkcu, M. Abbas-Mohammadi, and S. Bahador, "*Salvia nemorosa* L. A novel source of bioactive agents with functional connections," *Lwt-Food Science annd Technology*, vol.75, pp.42-50, 2017.

[4] K. Aktas, C. Ozdemir, M. Ozkan, and P. Baran, "Pollen morphology of some Turkish *Salvia* L. (Lamiaceae: Mentheae) species," *Planta Daninha*, vol. 38, pp. 1-12, 2020.

[5] H. Maral, "Chemical and antioxidant diversity of essential oils of some *Salvia* species from Turkey, " *Biochemical Systematics and Ecology*, vol.106, pp.104575, 2023.

[6] A. Kaya, M. Dinc, S. Dogu, and B. Demirci, "Compositions of essential oils of *Salvia adenophylla*, *Salvia pilifera*, and *Salvia viscosa* in Turkey, " *Journal of Essential Oil Research*, vol. 29, no. 3, pp.233-239, 2017.

[7] M. Kosar, F. Goger, and K. H. C. Baser, "In vitro antioxidant properties and phenolic composition of *Salvia halophila* Hedge from Turkey, " *Food Chemistry*, vol.129, pp.374-379, 2011.

[8] S. D. Hatipoglu, N. Zorlu, T. Dirmenci, A. C. Goren, T. Ozturk, and G. Topcu, "Determination of volatile organic compounds in fourty five *Salvia* species by thermal desorption-GC-MS Technique, " *Records of Natural Products*, vol.10, no.6, pp. 659-700, 2016.

[9] G. Topcu, "Bioactive triterpenoids from *Salvia* species," *Journal of Natural Products*, vol. 69, pp. 482-487, 2006.

[10] G. P. P. Kamatou, N. P. Makunga, W. P. N. Ramogola, A. M.Viljoen, "South African *Salvia* species: a review of biological activities and phytochemistry, " *Journal of Ethnopharmacology*, vol. 119, pp. 664–672, 2008.

[11] M. S. Kocak, C. Sarikurkcu, M. Cengiz, S. Kocak, M. C. Uren, and B. Tepe, "*Salvia cadmica*: Phenolic composition and biological activity," *Industrial Crops and Products*, vol. 85, pp. 204-212, 2016.

[12] M. Kursat, I. Emre, O. Yilmaz, and P. Erecevit. "Antioxidant and antimicrobial activity in the seeds of *Origanum vulgare* L. subsp. *gracile* (C. Koch) Ietswaart and *Origanum acutidens* (Hand.-Mazz.) Ietswaart from Turkey, " *Grasas y Aceites*, vol. 62, no. 4, 410-417, 2011.

[13] Y. G. Zu, C. Y. Li, Y. J. Fu, and C. J. Zhao, "Simultaneous determination of catechin, rutin, quercetin kaempferol and isorhamnetin in the extract of sea buckthorn (*Hippophae rhamnoides* L.) leaves by RP-HPLC with DAD," *Journal of Pharmaceutical and Biomedical Analysis*,vol. 41, pp. 714-719, 2006.

[14] C. M. Liyana-Pathiranan, and F. Shahidi, "Antioxidant activity of commercial soft and hard wheat (*Triticum aestivum* L.) as affected by gastric pH conditions," *Journal of Agricultural and Food Chemistry*, vol. 53, pp. 2433–2440, 2005.

[15] R. Ree, N. Pellegrini, A. Proteggente, A. Pannala, M. Yang, and C. Rice-Evans, "Antioxidant activity applying an improved ABTS radical cation decolorization assay, " *Free Radical Biology and Medicine*, vol. 26, pp.1231–1237, 1999.

[16] E. Skotti, E. Anastasaki, G. Kanello, M. Polissiou, P. A.Tarantilis, "Total phenolic content, antioxidant activity and toxicity of aqueous extracts from selected Greek medicinal and aromatic plants, " *Industrial Crops and Products*, vol. 53, pp. 46-54, 2014.

[17] V. L. Singleton, R. Orthofer, and R. M. Lamuela-Raventos, "Analysis of total phenols and other oxidation substrates and antioxidants by means of Folin-Ciocalteu reagent, " *Methods Enzymol*, vol. 299, pp. 152–178, 1999.

[18] H. H. Robya, M. A. Sarhana, K. A. Selima, K. I. Khalel, "Evaluation of antioxidant activity, total phenols and phenolic compounds in thyme (*Thymus vulgaris* L.), sage (*Salvia officinalis* L.), and marjoram (*Origanum majorana* L.) extracts, " *Industrial Crops and Products*, vol. 43, pp. 827–831, 2013.

[19] T. C. P. Dinis, V. M. C. Madeira, and M. L M. Almeida, "Action of phenolic derivates (acetoaminophen, salycilate and 5-aminosalycilate) as inhibitors of membrane lipid peroxidation and as peroxyl radical scavengers, " *Archives of Biochemistry and Biophysics*, vol. 315, pp. 161-169, 1994.

[20] K. Shimoi, S. Masuda, M. Furugoru, S. Esaki, N. Kinae, "Radioprotective effect of antioxidative flavonoids in X-ray irradiated mice, " *Carcinogenesis*, vol. 15, pp. 2669-2672, 1994.

[21] S. Keser, E. Demir, and O. Yılmaz, "Phytochemicals and Antioxidant activity of the almond kernel (*Prunus dulcis* Mill.) from Turkey", *Journal of the Chemical Society of Pakistan*, vol. 36, pp.534-541, 2014.

[22] C. M. Collins and P. M. Lyne, *Microbiological Methods*, Buttermorths & Co (Publishers) Ltd. Pp. 450. London, 1987.

[23] S. Kivrak, T. Gokturk, I. Kivrak, E. Kaya, and E. Karababa, "Investigation of phenolic profiles and antioxidant activities of some *Salvia* species commonly grown in southwest Anatolia using UPLC-ESI-MS/MS," *Food Science and Technology*, pp. 1-9, 2018.

[24] S. Francik, R. Francik, U. Sadowska, B. Bystrowska, A. Zawislak, A. Knapczyk, A. Nzeyimana, "Identification of phenolic compounds and determination of antioxidant activity in extracts and ınfusions of *Salvia* leaves," *Materials*, vol. 13, pp. 1-15, 2020.

[25] G. Zengin, E. J. Llorent-Martinez, M. L. Fernandez-de Cordova, M. B. Bahadoric, A. Mocand, M. Locatellif, and A. Aktumsek, "Chemical composition and biological activities of extracts from three *Salvia* species: *S. blepharochlaena, S. euphratica* var. *leiocalycina*, and *S. verticillata* subsp. *amasiaca*, " *Industrial Crops and Products*, vol. 111, pp.11-21. 2018.

[26] O. Yumrutas, A. Sokmen, H. A. Akpulat, N. Ozturk, D. Daferera, M. Sokmen, and B.Tepe, "Phenolic acid contents, essential oil compositions and antioxidant activities of two varieties of *Salvia euphratica* from Turkey, " *Natural Product Research*, vol. 26, no.19, pp. 1848-1851, 2012.

[27] S. S. Erdogan, U. Karik, K. H. C. Baser, "The Determination of antioxidant activity of some sage populations of in the Marmara region," *Turkish Journal of Agricultural and Natural Sciences*, vol .2, pp. 1877-1882, 2014.

[28] B. Tepe, M. Sokmen, H. A. Akpulat, and A. Sokmen, "Screening of the antioxidant potentials of six *Salvia* species from Turkey," *Food Chemistry*, vol. 95, pp.200–204, 2006.

[29] I. E. Orhan, F. S. Senol, T. Ercetin, A. Kahraman, F. Celep, G. Akaydin, B. Sener, M. Dogan, "Assessment of anticholinesterase and antioxidant properties of selected sage (*Salvia*) species with their total phenol and flavonoid contents, " *Industrial Crops and Products*, vol. 41, pp. 21-30.

[30] L. Svydenko, O. Vergun, E. Ivanišová, O. Korablova, and K. F. Šramková, "Polyphenol compounds and antioxidant activity of *Salvia officinalis* L. and *Salvia sclarea* L., " *Agrobiodiversity for Improving Nutrition, Health and Life Quality*, vol. 6, no. 2, pp.139–148, 2022.

[31] A. Onder, M. N. Izgi, A. S. Cinar, G. Zengin, and M. A. Yilmaz, "The characterization of phenolic compounds via LC-ESI-MS/MS, antioxidant, properties enzyme inhibitory activities of *Salvia absconditiflora*, *Salvia sclarea*, and *Salvia palaestina*: A comparative analysis, " *South African Journal of Botany*, vol.150, pp. 313-322, 2022.

[32] B. Culhaoglu, S. D. Hatipoglu, A. A. Donmez, G. Topcu, "Antioxidant and anticholinesterase activities of lupane triterpenoids and other constituents of *Salvia trichoclada*, " Medicinal Chemistry Research, vol. 24, pp. 3831–3837, 2015.

[33] M. Ben Farhat, R. Chaouch-Hamada, J. A. Sotomayor. et al., "Antioxidant potential of *Salvia officinalis* L. residues as affected by the harvesting time", Industrial Crops and Products, vol. 54, pp.78-85, 2014.

[34] S. Duletic-Lausevic, A. Alimpic, D. Pavlovic, P. D. Marin, and D. Lakusic, "*Salvia officinalis* of different origins Antioxidant activity, phenolic and flavonoid content of extracts. *Agro Food Industry Hi Tech*, vol. 27, no.1, pp. 52-55, 2016.

[35] G. Yilmaz, N. Eruygur, G. Eksi Bona, M. Bona, M. Akdeniz, M. A. Yilmaz, A. Ertas, "Phytochemical analysis, antioxidant, and enzyme inhibition activity of five Salvia taxa from Turkey", *South African Journal of Botany*, vol. 152, pp. 212-221, 2023.

[36] R. S. Marinel, E. A. Moraes, S. A. Lenquiste, A. T. Godoy, M. N. Eberlin, M. R. Marostica, "Chemical characterization and antioxidant potential of chilean chia seeds and oil (*Salvia hispanica* L. ,". *LWT - Food Science and Technology*, vol. 59, pp.1304-1310, 2014.

[37] O. Firuzia, K. Javidniaa, M. Gholamia, R. Soltania Mir, "Antioxidant activity and total phenolic content of 24 Lamiaceae species growing in Iran," *Natural Product Communications*, vol. 5, no.2, pp. 261-264, 2010.

[38] Z. A. Jeshvaghania, M. Rahimmalek, M. Talebi, S. Amir, H. Golli, "Comparison of total phenolic content and antioxidant activity in different *Salvia* species using three model systems, " *Industrial Crops and Products*, vol. 77, pp. 409-414, 2015.

[39] I. E. Orhan, F.S. Senol, N. Ozturk, G. Akaydin, B. Sener, "Profiling of in vitro neurobiological effects and phenolic acids of selected endemic *Salvia* species, " *Food Chemistry*, vol.132: pp. 1360-1367, 2012.

[40] F. S. Senol, I. Orhan, F. Celep, A. Kahraman, M. Dogan, G. Yılmaz, B. Sener, "Survey of 55 Turkish *Salvia* taxa for their acetylcholinesterase inhibitory and antioxidant activities," *Food Chemistry*, vol. 120, pp. 34–43, 2010.

[41] V. Adımcılar, Z. Kalaycıoğlu, N. Aydoğdu, T. Dirmenci, A. Kahraman, F.B. Erim, "Rosmarinic and carnosic acid contents and correlated antioxidant and antidiabetic activities of 14 *Salvia* species from Anatolia", Journal of Pharmaceutical and Biomedical Analysis, vol. 175, 112763, 2019.

[42] A. Onder, M.N. Izgi, A.S. Cinar, G. Zengin, M.A.Yilmaz, "The characterization of phenolic compounds via LC-ESI-MS/MS, antioxidant, properties enzyme inhibitory activities of *Salvia absconditiflora, Salvia sclarea,* and *Salvia palaestina*: A comparative analysis" South African Journal of Botany, vol. 150, 313-322, 2022.

[43] I. Gulcin, M. T. Uguz, M. Oktay, S. Beydemir, I. O. Kufrevioglu, "Evaluation of the antioxidant and antimicrobial activities of clary sage (*Salvia sclarea* L.), " Turkish Journal of Agriculture and Forestry, vol. 28, pp. 25-33, 2004.

[44] S. Guzel, Y. Ozay, M. Kumas, C. Uzun, E. Gokal Ozkorkmaz, Z. Yıldırım, M. Ulger, G. Guler, A. Celik, Y. Camlıca, A. Kahraman, "Fito (Wound healing properties, antimicrobial and antioxidant activities of *Salvia kronenburgii* Rech. f. and *Salvia euphratica* Montbret, Aucher & Rech. f. var. *euphratica* on excision and incision wound models in diabetic rats", *Biomedicine & Pharmacotherapy*, vol. 111, pp. 1260-1276, 2019.

[45] H. Norouzi-Arasi, I. Yavari, F. Chalabian, P. Baghaii, V. Kiarostami, M. Nasrabadi, A. Aminkhani, "Volatile constituents and antimicrobial activities of *Salvia suffruticosa* Montbr. & Auch. ex Benth. from Iran," *Flavour and Fragrance Journal*, vol. 20, no. 6, pp. 633-636, 2005.

Bitlis Eren Üniversitesi Fen Bilimleri Dergisi
BİTLİS EREN UNIVERSITY JOURNAL OF SCIENCE
ISSN: 2147-3129/e-ISSN: 2147-3188
VOLUME: 12 NO: 4 PAGE: 1006-1014 YEAR: 2023
DOI:10.17798/bitlisfen.1299867

The Effect of Conductivity on Surface Leakage Currents on Iced-Covered Insulators

Muhammed Buğracan ÖZKÜÇÜK[1*], Muhsin Tunay GENÇOĞLU[2]

[1]*Malatya Turgut Ozal University, Faculty of Engineering and Natural Sciences, Department of Civil Engineering, Malatya/Turkey*
[2]*Firat University, Faculty of Engineering, Department of Electrical-Electronics Engineering, Elazig/TURKEY*
(ORCID: 0000-0002-1466-2502) (ORCID: 0000-0002-1774-1986)

Keywords: Ice-covered insulator, Surface conductivity, Leakage current, AC voltage, LabVIEW.

Abstract
Insulators on power transmission systems today are vital to ensuring high-voltage lines' reliable and effective operation. However, insulators will inevitably encounter problems such as contamination and icing due to natural environmental conditions and environmental factors. Pollution layers and ice buildup that have developed on insulator surfaces harm insulation performance, increase surface leakage currents, and result in power line failures or interruptions. This article focuses on understanding the phenomena of contamination and icing in insulators, evaluating their effects, and investigating methods that can be taken to prevent or reduce these problems. For this purpose, solutions with different conductivity values (1000–4000 µS/cm) were sprayed on the insulators in the laboratory environment, and ice covering the insulator surface was provided. An alternating voltage (5–20 kV) with the frequency of the mains was applied to the insulators to study leakage currents. Data were obtained with the help of the LabVIEW program, and the relationship between leakage currents of porcelain, glass, and silicone insulators and conductivity was compared. The amplitude of leakage current increases with the increase in conductivity in all three types of insulators. The increase in leakage current with conductivity is most observed in the glass insulator, while the least affected element is the silicon insulator.

1. Introduction

Bridging of the insulator surface brought on by the supercooled water droplets landing on the insulator surface results in the transmission line icing problem, which is brought on by the worsening of the electric field distribution of the insulator sheds. A key danger factor for the dependability of insulators in areas with cold climates has been recognized as atmospheric ice formation combined with pollution. A number of interrelated variables cause the flashovers that happen on ice and snow-covered insulators. Flashovers caused by icing in the insulators are influenced by a variety of climatic and meteorological parameters, including changes in air temperature, the type of ice, and the structure of the ice. Icing of insulators, which can happen at normal operating voltage under the worst circumstances, depends on a number of factors, including the presence of surface contamination during the freezing and melting processes and the status of ions at the time of the transition from solid to liquid layers [1].

The conductivity of the ice accumulated on the insulator surface seriously affects the insulation property of the insulator, along with the applied voltage. The effects of ice with different conductivities and ion contents in frozen water have been studied by a number of researchers. For various researchers, the consequences of ice with varying conductivity and ion content in freezing water have

*Corresponding author: bugracan.ozkucuk@ozal.edu.tr
Received: 11.06.2023, Accepted: 18.12.2023

been studied. The conductivity of ice increased seven times between -15 and 0 degrees Celsius. The relatively restricted temperature range between -2 °C and 0 °C is where the majority of this alteration has taken place. Decembers of the change have been observed. However, ice sample conductivities at 0 °C remained, on average, 187 times lower than solution conductivities at 20 °C. The resistance per unit length of the ice sheet, which is utilized in pollutant flow modeling, cannot be determined using the electrical conductivity of ice alone. Using the length and width of the ice sheet has been effective in providing better modeling results [2]-[6].

Flashover performance in a soiled and icy insulator is related to the level of contamination as well as the level of icing. ISP was used as a characteristic metric to assess the impact of ice accumulations and pollutants on the flashover voltage of an ice-covered insulator. ISP is calculated as the product of ice sheet conductivity and ice sheet weight per centimeter of dry arc distance. As the ISP characteristic parameter increased, the flashover voltage of an insulator covered in ice decreased. The flashover voltage in the ice-covered insulator has increased linearly with the increase in insulator length due to the resistance property of ice formation on the insulator, such as the fouling flashover performance of an insulator [7].

The effect of salt accumulation density (SDD) and the average diameter of insulators on flashover performance shows that the flashover voltage decreases with an increase in SDD. When the icing state is the same, a larger insulator diameter correlates to a larger icing area, which has led to a smaller resistance on the insulator's surface. For this reason, the flashover voltage also decreased with an increase in the average diameter of a fixed SDD. However, the leakage current before the flashover is larger, and this situation is identified with Ohm's law [8]-[9].

On iced porcelain, glass, and composite insulators, it has been shown that the flashover voltage of all three types of insulators decreases with an increase in ice thickness, pollution, and pressure. In comparison to the porcelain and glass insulators, the composite insulator showed a more obvious effect of ice thickness and ambient pressure on the icing flashover voltage. It was determined that, under the same conditions, the value describing the impact of pollution on the flashover voltage is smaller for composite insulators than it is for porcelain and glass insulators covered with ice [10].

The equivalent salt deposit density (ESDD) and the flashover voltage are independent of each other in both rime ice and dry-iced insulators. However, there is a negative power function relationship between the flashover voltage and ESDD on insulators covered with glazed ice with contamination. In addition, when the power function is compared with the exponential function, the relationship between flashover voltage and ice weight is more favorable. The flashover behavior of insulators in different circumstances diverges significantly. When the level of pollution is the same across all natural habitats, the pollution flashover has the biggest arc diameter, followed by the flashover of an insulator covered in glazed and dried ice [11]–[12].

Insulators that have been iced with and without energy have different results from liquid conductivity on icing. When used for spray, melted water has a higher conductivity than frozen water. The salt concentration on the insulator surface rises when icing is produced under electrified conditions because of the heat impact. As a result, during the flashover test, the meltwater conductivity sprayed was higher than it was under de-energized conditions [13].

Pollution and icing are related conditions that affect flashover voltage, together with seasonal conditions. Therefore, the flashover voltage has been studied both in dirty and icy insulators and only in dirty insulators. At the same degree of pollution, the flashover voltage of the insulator in the non-ice-contaminated state is larger than that of the icy insulators. When there is icing or pollution, the composite insulator's leakage current progressively rises as the applied voltage rises. A continuous film of water is formed due to the melting of the ice layer on the insulator surface. This circumstance offers the essential conditions for the creation of a leakage current. As a result, as the voltage is applied, the leakage current that passes through the ice-covered insulator's surface steadily increases [14].

In this study, he focuses on understanding the phenomena of contamination and icing in insulators, evaluating their effects, and investigating methods that can be taken to prevent or reduce these problems. Conductivity values of 1000, 2000, 3000, and 4000 μS/cm were obtained by adding salt to water. The liquid sprayed on the porcelain, glass, and silicone insulators is iced in the cabinet. Voltage was applied to the insulators at 15-minute intervals until the ice melted under 5, 10, 15, and 20 kV values. The relationship between surface leakage currents and conductivity was investigated for all three insulators.

2. Material and Method

The issue of environmental contamination becomes increasingly important as society and the economy

evolve. One of the main reasons for insulation mishaps on transmission lines is the issue of insulator flashover brought on by pollution. Global warming has led to an increase in the frequency of extremely cold weather, including ice and snow. Therefore, one of the biggest hazards to the safe operation of the electrical grid is pollution and the icing flashover of insulators brought on by the change in operating conditions.

In this study, solutions were prepared by adding salt to water. The solution sprayed on the surface of insulator types made of different substances was subjected to an icing process in the icing cabinet. Voltages were applied to the iced insulators in the experimental setup schematized in Figure 1.

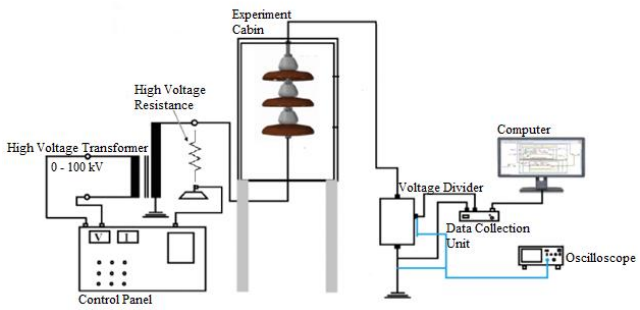

Figure 1. Experimental scheme.

The connection diagram provided in the LabVIEW application, as shown in Figure 2, was utilized to get the data on leakage currents on the insulator surface.

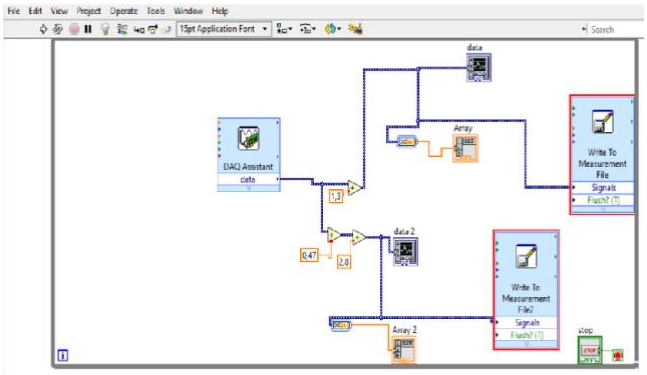

Figure 2. LabVIEW connection diagram.

Sections of porcelain, glass and silicon insulator used in the experiment are given in Figure 3.

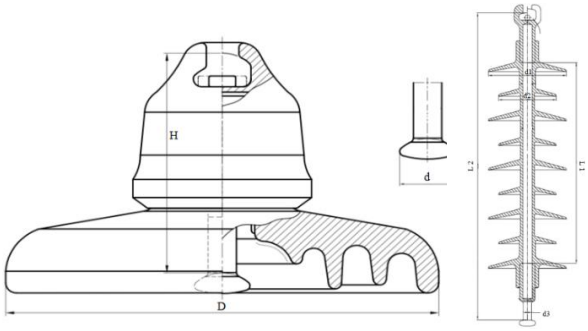

(a) **(b)**

Figure 3. (a) Porcelain and glass insulator section (b) Silicone insulator section.

The characteristic values of one element of the glass and porcelain insulator are shown in Table 1.

Table 1. Characteristic values of porcelain and glass insulator.

Insulator Variety	Diameter (D) (mm)	Height (H)	Pin diameter (d)	Leakage current path length
U100 BL (K3) Porcelaın	255	146	16	280
U100 Glass	255	146	16	280

The sizes of the silicon insulator used in the experiments are shown in Table 2.

Table 2. Characteristic values of the silicone insulator.

Insulator Variety (mm)	L1	L2	d1	d2	d3	Leakage current path length
Silicone (K2)	248.8	440	120	90	17	900

2.1. Estimation of Flashover Voltage

The most basic model for calculating the flashover voltage of icy insulators makes the assumption that the effective resistance of the ice sheet is described by multiplying the weight of ice (w) by the conductivity of melted ice (σ20) [15]. The icing voltage product

(ISP) is represented by (w·σ20). The critical flashover voltage E_{50} is given as in equation (1):

$$E_{50\,ac} = 396(\mathrm{ISP})^{-0.19} \quad (1)$$

Flashovers are described by equation (1), which describes the accumulation of ice at normal line voltage and during a phase of AC melting. The critical flashover voltage is defined as equation (2) for experiments utilized in numerous DC flashovers on an ice sheet generated without line voltage [16]:

$$E_{50\,dc-} = 1174(\mathrm{ISP})^{-0.26} \quad (2)$$

Basic modeling of the ice flashover process using the Obenaus model of a serial arc with a distributed resistive layer has been successful [5]. According to equation (3), the flashover model adds the voltage drop along the arc and the voltage drop brought on by the current flow through the remaining ice sheet.

$$V_m = A.x.I_m^{-n} + I_m R(x) \quad (3)$$

Where V_m (V) is the peak value of the applied voltage, x (cm) is the total arc length. A and n are the derived arc constant and R(x) is the residual resistance of the ice sheet. The expression R(x) is defined as in equation (4).

$$R(x) = \frac{1}{2\pi\gamma_e}\left[\frac{4(L-X)}{D+2t} + \ln\left(\frac{D+2t}{4r}\right)\right] \quad (4)$$

Where L is the length of the half cylinder of ice along the dry arc distance (cm), D is the diameter of the insulator (cm), γe is the equivalent surface conductivity of the ice sheet (μS), t is the thickness of the ice sheet, and r is the radius of the effective arc root.

The effective arc root radius in equation (4) is taken as constant with the square root of the current and varies depending on the type of voltage. The values r=0.7√I are valid for DC and r=0.6√Ipk AC arc currents.

2.2. Effect of Contamination on Ice-Covered Insulators

The pre-contamination levels on high voltage DC insulators can be at least 20% higher in insulators with positive polarity compared to negative polarity. This raises the issue of how to account for insulator surface pre-contamination when calculating the DC^+ and DC^- flashover voltages during ice conditions [15].

Equation (5) gives the amount of salt that enters the ice sheet, accumulates in the insulator, and is retained there.

$$m = F.\mathrm{ESDD}.A_{top} \quad (5)$$

Where; F is the insulator properties split into ice layers factor, ESDD, perfect salt deposit density, Atop is the total area of the insulating surfaces and m is the near salt weight.

The amount of ice in contact with the insulator depends on the degree to which the insulator is fully bridged, which is determined by the deposition thickness t, insulator diameter D, and dry arc or leakage distance L. The water volume is calculated as in equation (6).

$$V_{water} = 0.9.\frac{\pi}{4}((D+2t)^2 - D^2).L \quad (6)$$

It is estimated that the DC+ flashover voltage for contaminated insulators remains well above the DC- flashover voltage for clean insulators [15].

3. Results and Discussion

In the study carried out, conductivity values of 1000, 2000, 3000, and 4000 μS/cm were obtained in four separate solutions by means of a conductivity meter. The solution prepared for porcelain, glass, and silicone insulators was sprayed in the icing cabinet, and ice formation was ensured on the insulator surface. Voltages of 5, 10, 15, and 20 kV were applied to the iced insulators at 15-minute intervals until the ice on the insulator surface melted. When applying voltage, with the help of the data acquisition unit, the voltage value on the resistor connected to the output of the voltage divider was measured, and leakage currents were obtained with periods of 100 ms using the LabVIEW program. It has been examined how leakage currents and leakage currents depending on the conductivity state depend on the type of insulator.

Figure 4 shows the leakage currents obtained with a voltage of 5 kV applied to the porcelain, glass, and silicone insulators iced for a conductivity of 1000 μS/cm immediately after removal from the icing cabinet.

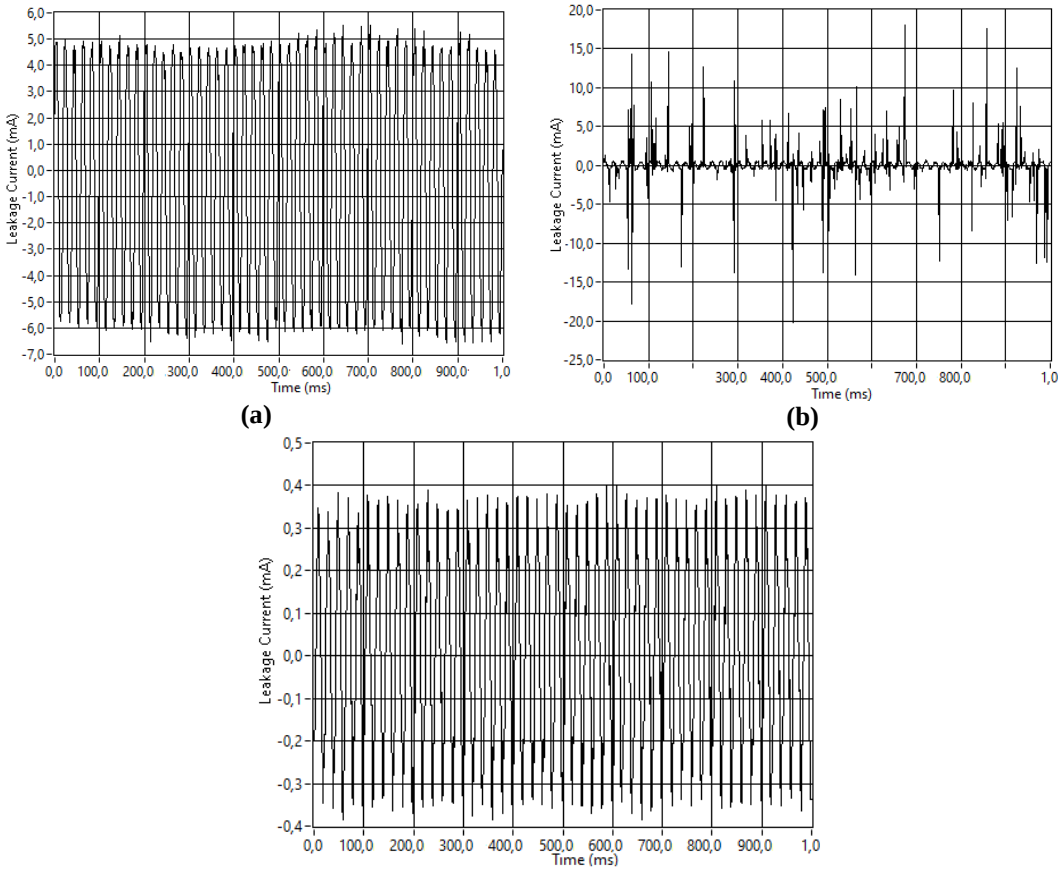

Figure 4. Leakage currents obtained under 5 kV voltage for iced (a) porcelain, (b) glass, (c) silicone insulator with a conductivity of 1000 µS/cm.

Figure 5 shows the leakage currents with a voltage of 5 kV applied to the iced porcelain, glass, and silicon insulators for a conductivity of 1000 µS/cm near melting.

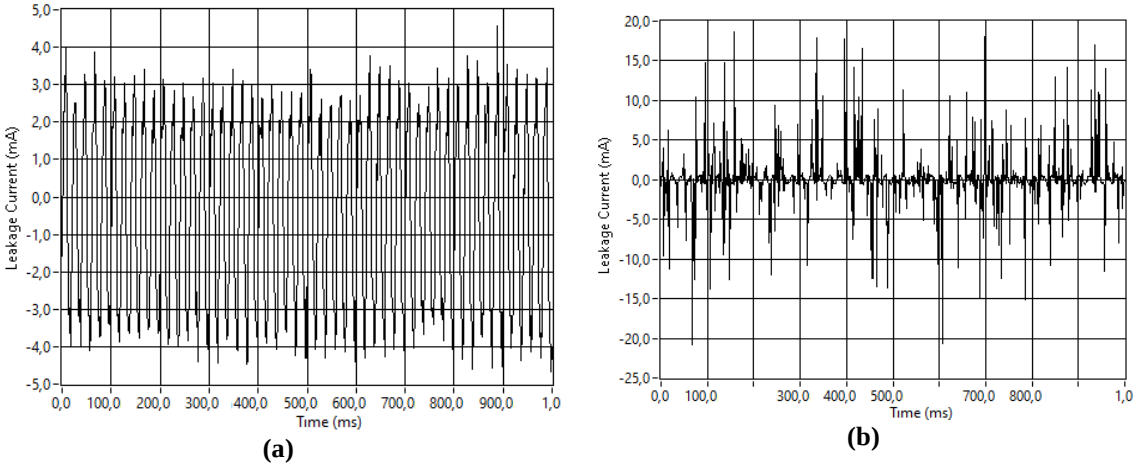

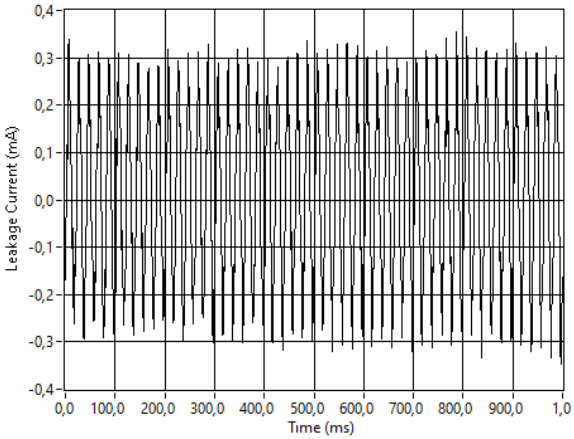

(c)

Figure 5. For a ıced (a) porcelain, (b) glass, (c) silicone insulator with a conductivity of 1000 µS/cm, the leakage currents obtained under a voltage of 5 kV just before the ice liquefies.

Figure 6 shows the leakage currents obtained with a voltage of 20 kV applied to the porcelain, glass and silicone insulator iced for a conductivity of 4000 µS/cm immediately after removal from the icing cabinet

.

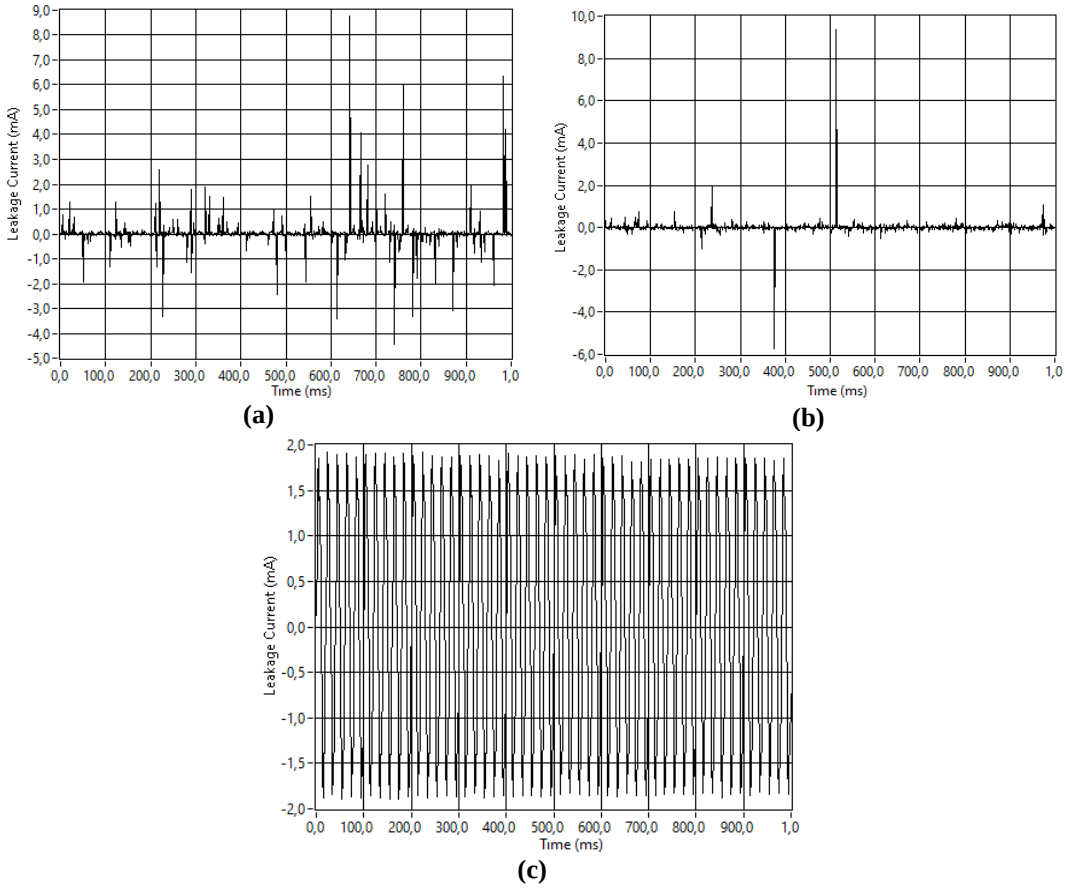

(a) **(b)**

(c)

Figure 6. Leakage currents obtained under 20 kV voltage for ıced (a) porcelain, (b) glass, (c) silicone insulator with a conductivity of 4000 µS/cm.

Figure 7 shows the leakage currents with a voltage of 20 kV applied to the iced porcelain, glass, and silicon insulators for a conductivity of 4000 µS/cm near melting

.

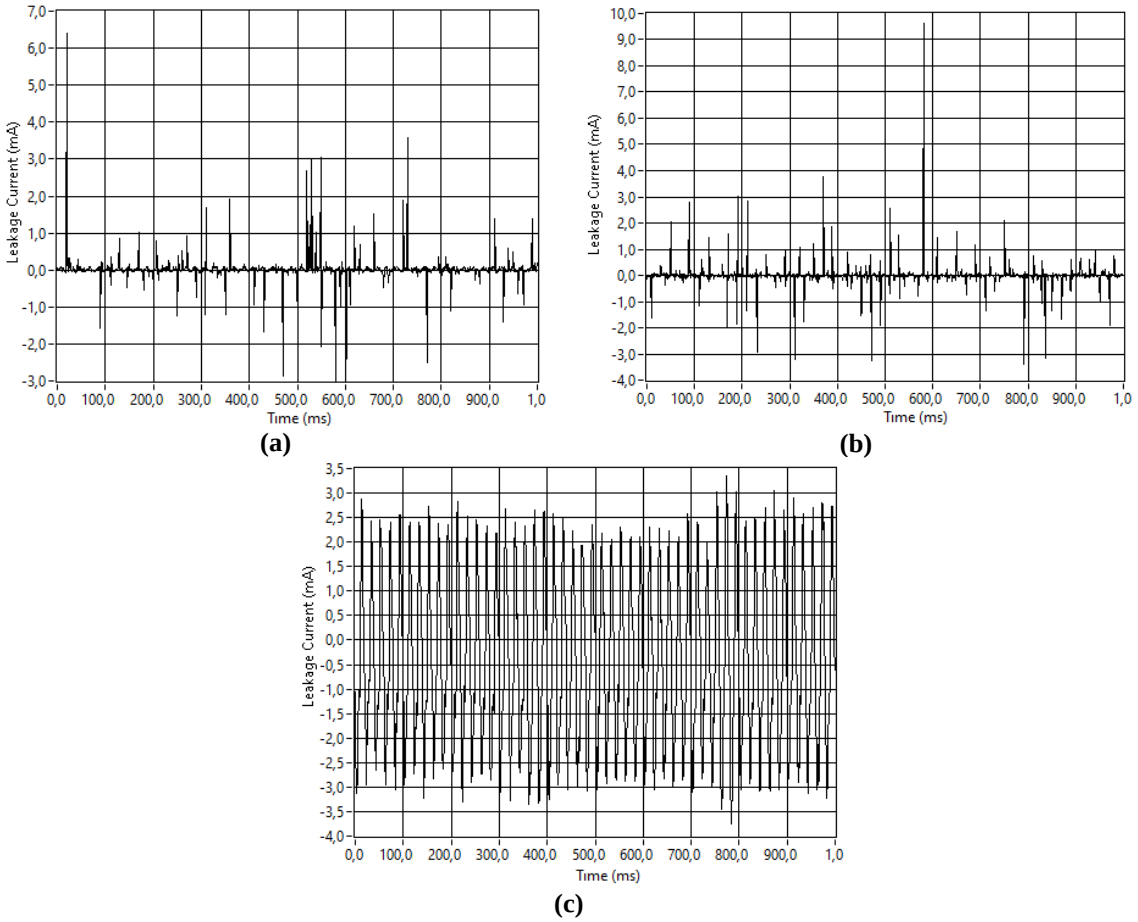

Figure 7. For an iced (a) porcelain, (b) glass, (c) silicone insulator with a conductivity of 4000 µS/cm, the leakage currents obtained under a voltage of 20 kV just before the ice liquefies.

Leakage currents partially increase with the liquid conductivity in the porcelain insulator. This is due to the fact that the resistance is inversely proportional to the surface conductivity, as can be seen in equation (4). An increase in surface conductivity will reduce the resistance of ice, and with a decrease in resistance, the leakage current will increase. As can be seen from the instantaneous jumps in the graphs, partial arcs were formed on the insulator surface along with increasing the applied voltage when the liquid conductivity was 4000 µS/cm, and the length of these arcs was longer than in low conductivity cases.

Leakage currents in the glass insulator have approached 25 mA levels from time to time. With the increase in liquid conductivity, arcs were formed on the insulator surface. Compared to the porcelain insulator, the glass insulator is more sensitive to increasing the conductivity and applied voltage.

Leakage currents in the silicon insulator did not exceed 4 mA. In general, the leakage current did not exceed the levels of 0.4 mA at 5 kV, 0.8 mA at 10 kV, 1.2 mA at 15 kV, and 2 mA at 20 kV. However, at a conductivity value of 4000 µS/cm, it approached the level of 4 mA at the moment when the ice began to melt on the insulator surface. According to the glass and porcelain insulators, the insulator that is least affected by liquid conductivity is the silicone insulator. However, since the leakage path length of the silicone insulator used in the experiments is much longer than that of the glass and porcelain insulators, it would be more accurate to compare the glass and porcelain insulators among themselves.

The relationship between leakage currents of porcelain, glass, and silicone insulators and conductivity is shown in Figure 8.

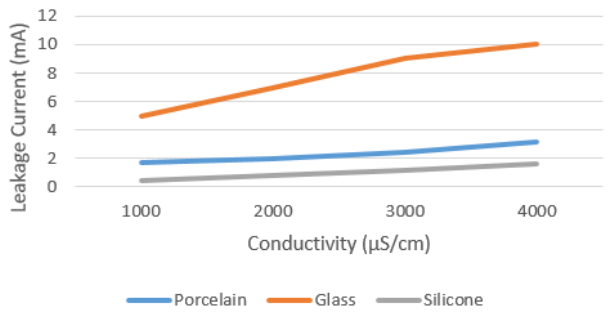

Figure 8. Relationship between conductivity and leakage current of porcelain, glass, and silicone insulators.

The amplitude of the leakage current increases with the increase in conductivity in all three types of insulators. The increase in leakage current with conductivity is most observed in the glass insulator, while the least affected element is the silicon insulator.

With the artificial icing used in the study, the leakage currents also differ, since the ice that the cabin will accumulate on the insulator surface may differ according to the ice that naturally accumulates on the insulator surface. However, the examination of leakage currents at December intervals of 100 milliseconds reduced this situation as much as possible. Considering the continental climate and high regions of our country, it is the insulators that are one of the transmission and distribution line elements where the most failures occur. For this reason, the icing event is one of the issues that needs to be studied in more detail. But there are almost no studies on this topic in our country. This study will guide future studies.

4. Conclusion and Suggestions

Wind, air pressure, pollution, temperature, humidity, etc., which are effective against the icing event in insulators and the flashover event with them, have been studied in many studies in which environmental events have been simulated. The studies carried out focused more on the voltage value at which the flashover occurred, and the flashover event in insulators could not be completely solved. In this study, taking into account the icing situation along with pollution, leakage currents were studied in detail for very short time intervals, and more data were obtained.

Liquid conductivity is an important parameter in the effect of icing events on surface leakage currents in insulators. Increasing the conductivity of the liquid is very effective in losing the insulating property of the iced insulator surface. When the sensitivity of leakage currents to liquid conductivity is compared in porcelain and glass insulators, it is concluded that glass insulators are more affected than porcelain.

When designing the insulators, taking into account the icing level and the pollution level according to the climatic conditions of the region and the mechanical properties, such as the material from which they are made, will help to reduce the problems that may occur due to pollution and icing.

In our country, which is covered with seas on three sides, the conductivity of the liquid formed on the insulator surface increases with the effect of sea water along with humidity and precipitation. The impact of natural events on the environment on Earth is being felt more and more with increasing global warming. Together with this, considering the geographical situation of our country and the rural areas where the continental climate is intense, the failures caused by icing and the conductivity of the iced liquid in the insulators are quite high. It is possible to minimize the effects of adverse conditions that will occur. In future studies, signal processing or image processing techniques can be used more effectively together with artificial intelligence techniques, which are one of the most popular topics today. With the early warning system, the occurrence of malfunctions can be prevented by timely intervention with the insulators.

Acknowledgment

This work was supported by the Management Unit of Scientific Research projects of Firat University (FÜBAP) (Project Number: MF.21.68).

Conflict of Interest Statement

There is no conflict of interest between the authors.

Statement of Research and Publication Ethics

The study is complied with research and publication ethics.

References

[1] M. B. Özküçük "İzolatörlerde Buzlanmanın Yüzey Kaçak Akımları Üzerine Etkisi," *Yüksek Lisans Tezi, Fırat Üniversitesi, Fen Bilimleri Enstitüsü*, Elazığ, 2022.

[2] M. M. Khalifa and R. M. Morris, "Performance of Line Insulators Under Rime Ice," in *IEEE Transactions on Power Apparatus and Systems*, vol. PAS-86, no. 6, pp. 692-698, June 1967, doi: 10.1109/TPAS.1967.291880.

[3] R. Wilkins, "Flashover voltage of high-voltage insulators with uniform surface-pollution films," *Proceedings of the Institution of Electrical Engineers*, vol. 116, no. 3, p. 457, 1969, doi: 10.1049/piee.1969.00.

[4] J. Vlaar, "Thermal and electrical properties of icicles", University of Waterloo, *2B Honours Physics Report* SN 88104434, 1991.

[5] M. Farzaneh, J. Zhang and X. Chen, "Modeling of the AC arc discharge on ice surfaces," in *IEEE Transactions on Power Delivery*, vol. 12, no. 1, pp. 325-338, Jan. 1997, doi: 10.1109/61.568256.

[6] M. Farzaneh, J. Zhang and X. Chen, "A laboratory study of leakage current and surface conductivity of ice samples," *Proceedings of IEEE Conference on Electrical Insulation and Dielectric Phenomena* - (CEIDP'94), Arlington, TX, USA, 1994, pp. 631-638, doi: 10.1109/CEIDP.1994.592040.

[7] X. Jiang, S. Wang, Z. Zhang, S. Xie and Y. Wang, "Study on AC Flashover Performance and Discharge Process of Polluted and Iced IEC Standard Suspension Insulator String," in *IEEE Transactions on Power Delivery*, vol. 22, no. 1, pp. 472-480, Jan. 2007, doi: 10.1109/TPWRD.2006.876705.

[8] Z. Xu et al., "Flashover performance of UHV&EHV post insulators under icing conditions," *2014 IEEE Conference on Electrical Insulation and Dielectric Phenomena (CEIDP)*, Des Moines, IA, USA, 2014, pp. 295-298, doi: 10.1109/CEIDP.2014.6995754.

[9] Z. Zhang, J. You, D. Wei, X. Jiang, D. Zhang, and M. Bi, "Investigations on AC pollution flashover performance of insulator string under different non-uniform pollution conditions," *IET Generation, Transmission & Distribution*, vol. 10, no. 2, pp. 437–443, Feb. 2016, doi: 10.1049/iet-gtd.2015.0691.

[10] X. Jiang, Z. Xiang, Z. Zhang, J. Hu, Q. Hu, and L. Shu, "Comparison on ac icing flashover performance of porcelain, glass, and composite insulators," *Cold Regions Science and Technology*, vol. 100, pp. 1–7, Apr. 2014, doi: 10.1016/j.coldregions.2013.12.010.

[11] X. Qiao, Z. Zhang, X. Jiang, R. Sundararajan, X. Ma, and X. Li, "AC failure voltage of iced and contaminated composite insulators in different natural environments," *International Journal of Electrical Power & Energy Systems*, vol. 120, p. 105993, Sep. 2020, doi: 10.1016/j.ijepes.2020.105993.

[12] M. Farzaneh, "Insulator flashover under icing conditions," in *IEEE Transactions on Dielectrics and Electrical Insulation*, vol. 21, no. 5, pp. 1997-2011, Oct. 2014, doi: 10.1109/TDEI.2014.004598.

[13] F. Yin, Xingliang Jiang and M. Farzaneh, "Electrical performance of composite insulators under icing conditions," in *IEEE Transactions on Dielectrics and Electrical Insulat*ion, vol. 21, no. 6, pp. 2584-2593, December 2014, doi: 10.1109/TDEI.2014.004571.

[14] M. Bi, Z. Yang, T. Jiang, X. Chen and Y. Wang, "Study on Flashover Characteristic and Critical Flashover Current of icing and polluted 110kV Composite Insulators," *2018 IEEE International Conference on High Voltage Engineering and Application (ICHVE)*, Athens, Greece, 2018, pp. 1-4, doi: 10.1109/ICHVE.2018.8642223.

[15] M. Farzaneh and W. A. Chisholm, *Insulators for Icing and Polluted Environments*. Wiley-IEEE Computer Society Press, 2009.

[16] X. Jiang, L. Chen, Z. Zhang, C. Sun and J. Hu, "Equivalence of Influence of Pollution Simulating Methods on DC Flashover Stress of Ice-Covered Insulators," in *IEEE Transactions on Power Delivery*, vol. 25, no. 4, pp. 2113-2120, Oct. 2010, doi: 10.1109/TPWRD.2009.2032329.

Bitlis Eren Üniversitesi Fen Bilimleri Dergisi
BİTLİS EREN UNIVERSITY JOURNAL OF SCIENCE
ISSN: 2147-3129/e-ISSN: 2147-3188
VOLUME: 12 NO: 4 PAGE: 1015-1027 YEAR: 2023
DOI:10.17798/bitlisfen.1312360

Multi Deep Learning Based Approaches for COVID-19 Diagnosis Using Class Resampling on Chest X-Ray Images

Talha Burak ALAKUŞ[1*], Muhammet BAYKARA[2]

[1]*Kırklareli University, Engineering Faculty, Department of Software Engineering, Kırklareli, Turkey*
[2]*Fırat University, Technology Faculty, Department of Software Engineering, Elazığ, Turkey*
(ORCID: 0000-0003-3136-3341) (ORCID: 0000-0001-5223-1343)

Keywords: Deep learning, Artificial intelligence, Medical imaging, Transfer learning, Classification

Abstract

Nowadays, current medical imaging techniques provide means of diagnosing disorders like the recent COVID-19 and pneumonia due to technological advancements in medicine. However, the lack of sufficient medical experts, particularly amidst the breakout of the epidemic, poses severe challenges in early diagnoses and treatments, resulting in complications and unexpected fatalities. In this study, a CNN (Convolutional Neural Network) model, VGG16 + XGBoost and VGG16 + SVM hybrid models, were used for three-class image classification on a generated dataset named Dataset-A with 6,432 chest CXR (Computed X-Ray) images (containing Normal, Covid-19, and Pneumonia classes). Then, pre-trained ResNet50, Xception, and DenseNet201 models were employed for binary classification on Dataset-B with 7,000 images (consisting of Normal and Covid-19). The suggested CNN model achieved a test accuracy of 98.91%. Then the hybrid models (VGG16 + XGBoost and VGG16 + SVM) gained accuracies of 98.44% and 95.60%, respectively. In our experiments, accuracy rates of 98.90%, 99.14%, and 99.00% were achieved for the fine-tuned ResNet50, Xception, and DenseNet201 models, respectively. Finally, the models were further evaluated and tested, yielding impressive results. These outcomes demonstrate that the models can aid radiologists with robust tools for early lungs related disease diagnoses and treatment.

1. Introduction

Just recently, the entire world was in a state of extreme fear and trepidation due to the outburst of the novel COVID-19 (Corona Virus Disease 2019) epidemic that started in Wuhan, Hubei province of China, in December 2019 [1], [2]. This virus, also known as SARS-CoV-2 or the severe acute respiratory syndrome coronavirus 2, holds an unknown etiology and is zoonotic, meaning it can propagate from animals to human beings [3]. Because of the novel virus's airborne nature, any infected person can spread it to people around them by merely breathing, speaking, sneezing, or coughing [4]. The above-mentioned nature of the virus made it easy to circulate rapidly. Seeing the rate at which the virus spread, the WHO (World Health Organization) assessed and characterized it all together as a global epidemic on March 11, 2020 [5]. The virus poses serious illness, particularly to the elderly, children, and persons with underlying medical conditions [6–8]. According to WHO, Worldometer, and Statista websites, there have been over 6.5 million reported deaths and over 635 million documented cases of SARS-CoV-2 infections worldwide [9]–[11].

The most effective means of combating such diseases being early testing and diagnosis are challenging, especially in the event of a worldwide epidemic, when the number of infected people exceeds the capacity of hospitals and healthcare professionals. Moreover, most of the widely accepted methods of testing the COVID-19 virus are not without caveats, making them unsuited for application in early testing and diagnosis. Even the

*Corresponding author: talhaburakalakus@klu.edu.tr
Received: 12.06.2023, Accepted: 11.10.2023

widely used and validated method, RT-PCR (Reverse Transcription - Polymerase Chain Reaction), is not entirely effective, especially in patients with low viral loads. Also, the cost of running laboratories that require expensive instruments, affirmative examinations, and trained personnel remains a significant drawback [12]. Due to the advancement and diversity of various medical imaging and CAD (Computer Aided Diagnoses) techniques, mainly in the field of radiology and oncology, AI-based models provide a quick and inexpensive means of diagnosing COVID-19 and other related diseases [13]. The primary cause of this significant milestone is the remarkable breakthrough these models have accomplished, particularly in image classification and segmentation tasks for both binary and multi-class with high accuracy [14]. It is now simpler to employ the power of these models to support radiologists with early diagnostic techniques even amid a global pandemic, because of the abundance of medical images from technologies like MRI (Magnetic Resonance Imaging), CT (Computed Tomography) scans, and X-ray [15]. Because of their improved classification performance, robustness, and enormous data processing power, various artificial intelligence algorithms significantly reduce the limitations of human medical experts, thereby mitigating the occurrence of severe illnesses and deaths [16].

Several recent studies employed deep learning models based on conventional CNN to class medical chest images into various classes. In study [17], researchers proposed a CNN model that classified CXR images as either COVID-19 cases or normal, achieving 96.71% accuracy. In another study researchers proposed other sets of CNN models for image segmentation and classification, reaching the highest accuracy of 93.2% [18]. Also, fine-tuning pre-trained models for detecting COVID-19 from several medical images is another widely deployed method by many researchers. In study [19] researchers utilized the ResNet18 model on CXR to identify COVID-19 with 93% accuracy. In study [20] ResNet50V2, DenseNet201, and InceptionV3 models were employed on CXR images attaining an accuracy of 91.62%. The hybridization of deep learning models with machine learning classifiers provides a fast and efficient means of classifying medical images, particularly in the presence of limited training data. In another study authors combined DenseNet201 with a Random Forest (RF) classifier to detect COVID-19 on CXR images with an accuracy of 94.55% [21]. Lastly, in study [22] researchers applied a hybrid of several pre-trained models with the SVM (Support Vector Machine) classifier to detect COVID-19 with 94.7% accuracy.

This study aims to demonstrate the performance of three categories of AI-based models on CXR images for binary and three-class image classification tasks utilizing two openly accessible datasets from Kaggle [23]-[24]. After applying random oversampling to address class-imbalance, a CNN and two hybrid models (using VGG16 to extract deep-level features followed by XGBoost and SVM classifiers to categorize the obtained features) were employed for three-class image classification on our generated Dataset-A. There are 6,342 images in total in Dataset-A, and there are three classes in this dataset: normal, pneumonia and COVID-19. Then, Dataset-B was used for binary image classification using three pre-trained models: Xception, ResNet50, and DenseNet201, using transfer learning and fine-tuning techniques. There are 7,000 images in total in the Dataset-B, of which 3,500 are normal and 3,500 are COVID-19. In this data set, there are two class labels. Finally, the study's outcome was analyzed and compared with recent works on this area. To fully appreciate the relevance of this study, we precisely summarized its contributions as follows:

- Employing the random oversampling technique to handle the issue of class imbalance and limited input data significantly improves the performance of the models. High test accuracies on unseen images, indicating less overfitting and more generalizable models, are evidence of these improvements.
- Utilizing proper image pre-processing techniques, like resizing and cropping the images to remove unnecessary features and enable the models to learn the appropriate ones, has significantly improved their performance and conserved memory and resources during training.
- Training different models, including standard convolutional neural networks, hybrid models, and pre-trained models that achieve high test accuracies, demonstrates that this research can undoubtedly aid radiologists in making accurate early diagnoses, even during pandemics. In turn, this could reduce severe illness and save lives.

The remainder of the article is organized as follows. In the second section, information about the data sets and methods used in the study were given. Moreover, the study encompassed an examination of the deep learning models that were considered for evaluation. In the third section, the results of the classifiers were given, and the evaluations of the classifiers were made. This section also involved the examination and comparison of studies from existing

literature with the findings obtained in this current study. In the fourth section, the advantages and disadvantages of this study were mentioned by discussion. In the last section, the study was summarized and its contributions to the literature were mentioned.

2. Material and Method

In this section, the data set, the image processing steps, and the deep learning models were mentioned.

2.1. Dataset A

Dataset-A consists of 6,432 CXR images from the following categories: Normal, pneumonia, and COVID-19 [23]. Table 1 illustrates the image allocation in the train and test folders. As shown in Table 1, the dataset comprises 1,266 and 317 normal images, 3,418 and 855 pneumonia-infected images, and 460 and 116 COVID-19 positive images in the train and test folders, respectively.

Table 1. Distribution of the unprocessed and unbalanced CXR images in Dataset A

Data	Normal	Pneumonia	COVID-19	Total
Train	1,266	3,418	460	5,144
Test	317	855	116	1,288
Total	1,583	4,273	576	6,432

2.2. Dataset B

The initial dataset is created in partnerships between medical professionals and researchers from various universities from Qatar, Bangladesh, Malaysia, and Pakistan [24]. Dataset-B, our created dataset in this study, is composed by randomly selecting 3,500 CXR images from the COVID-19 positive and the normal CXR image folders. A total of 7,000 images were formed and used for training and validation after applying several data augmentation techniques like rescaling, zooming, rotation, etc. Table 2 and Table 3 show the breakdown of the fully pre-processed and balanced data distributed among the classes for the binary and three-class image classifications for Dataset-A and Dataset-B in train, test, and validation categories.

Table 2. Distribution of the preprocessed and balanced CXR images in Dataset-A

Data	Normal	Pneumonia	COVID-19	Total
Train	3,418	3,418	3,418	10,254
Test	428	428	428	1,284
Val.	427	427	427	1,281
Total	4,273	4,273	4,273	12,819

Table 3. Distribution of the preprocessed and balanced CXR images in Dataset-B

Data	Normal	COVID-19	Total
Train	2,800	2,800	5,600
Test	350	350	700
Val.	350	350	700
Total	3,500	3,500	7,000

2.3. Random Oversampling

The random oversampling technique offers a naive and straightforward approach to harmonizing the class allocations of the imbalanced dataset. The Random Over Sampler [25] is employed in this study to generate new samples of the under-represented classes by arbitrarily sampling and replacing the existing images. The issue of overfitting is appropriately addressed by using data augmentation, dropout, batch normalization, and callbacks. Also, the data were adequately distributed into training, validation, and testing, with the testing data being withheld and then utilized to evaluate the performance of the models on the never-before-seen data.

2.4. Data Augmentation

Data augmentation involves creating additional data samples from existing data to boost the extent and diversity of the training data. Augmentation may include making minimal modifications to data or utilizing machine learning models to create extra data samples in the underlying space of the initial data to augment the dataset and reduce overfitting. Several geometric transformations, like translation, flipping, rescaling, rotation, and so on, are used on the original images to generate numerous variations of each image. These rendered images will appear different to the classifying algorithms, thereby increasing the volume of data and curtailing the over-memorization issue that learning algorithms fall short of due to imbalance or limited available data. It differs from synthetic data generation, in which data is created artificially. Several geometric transformations were made to these images. These transformations consist

of a horizontal flip, the nearest fill mode, a channel shift range of 10, a rotation range of 40 degrees, and a width shift, height shift, shear, and zoom range values of 0.2. Data augmentation was carried out by considering geometric transformations. These formations cover the meta learning. Meta learning is also an effective approach in convolution based neural networks [26]. For this reason, geometric transformations were employed in this study. Figure 1 provides random samples of images that were created because of using numerous data augmentation approaches in the study.

Figure 1. A random sample of the augmented images.

In the study, the original data was first augmented and then separated as training, validation, and test data. To construct effective deep learning models, it is vital that the validation error consistently diminishes along with the training error. Data augmentation stands as a potent technique for accomplishing this objective. By generating augmented data, a broader array of potential data instances is captured, thereby reducing the gap between the training and validation sets, as well as any subsequent test sets. In this way, the problem of overfitting can be avoided [26].

2.5. The Proposed CNN Model

After applying the random oversampling and necessary data pre-processing to Dataset A, the data types were converted from 8 bits unsigned integers to 32 bits floating point numbers using the assign-type python command. This step is crucial because all the mathematical operations in the deep learning process involve continuous rather than discrete values. Then these values were further normalized to the range [0, 1] by dividing by the highest image pixel value of 255 to aid with faster computations and reduce exhausting unnecessary computer resources. The final step before building the proposed model involved splitting the pre-processed and normalized images into 80:10:10 ratios for training, validation, and testing. These ratios signify that the model will use 80 % of the input images during the training phase, 10 % for the validation phase, and the remaining 10 % for the testing phase. Figure 2 shows a visualized depiction of the proposed architect to aid with the quick assimilation.

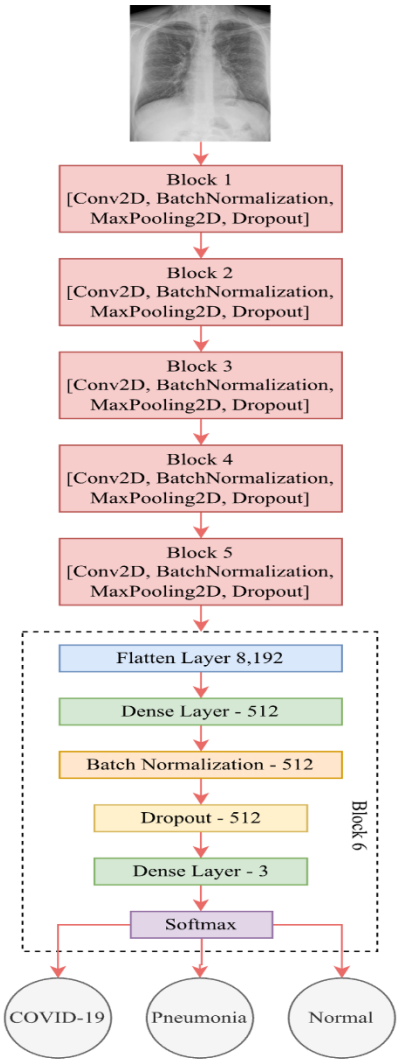

Figure 2. The proposed CNN architecture.

The model was later compiled by an RMSprop optimizer with a 0.001 learning rate, sparse categorical cross-entropy loss function since the input data were not hot encoded, and an accuracy metric. The compiled model generated 6,571.651 parameters due to the weights and biases, of which only 3,840 are not trainable. Furthermore, two callback functions, namely early stopping and reduced learning rate, were used during the training process to aid with quick convergence and mitigate the overfitting of the suggested model. In Table 4, the tune parameters of the CNN model proposed in the study are given.

Table 4. Hyperparameters of the proposed CNN model

Hyperparameters	Value
Number of epoch	60
Learning rate	0.001
Batch size	32
Loss function	Sparse categorical cross entropy (multi-class), binary cross entropy (binary class)
Optimizer	RMSProp

2.6. Hybrid Models

The second sets of architecture proposed in the paper is the hybrid model. These hybrid models are an example of the late fusion method of deep hybrid learning techniques. Late fusion because only at the last part of the process a particular classifier is used to make predictions. Deep learning methods, like the pre-trained models have remarkable feature-extracting power (VGG16 in this case), which are leveraged to perform automatic feature extraction, where classical machine learning classifiers are employed to make predictions from the generated features of Dataset A. Initially, the VGG16 pre-trained model was loaded without the top fully connected layers with an input shape of 150 × 150 × 3 using the ImageNet weights and making the loaded layers non-trainable to allow exclusively feature extraction and avoid retraining the model from scratch. Then the same images from Dataset A in the earlier CNN model were passed through the VGG16 feature extractor. Two classifiers, XGBoost and SVM, were utilized to provide predictions for three-class image categorization based on the derived features from the training and validation sets of data. Figure 3 reveals a graphical illustration of the proposed model architecture for more comprehension of the whole process. Later, the test set of images was utilized to evaluate the implementation of the classifiers, resulting in more accurate classifications. Other performance indicators were applied for further analysis, including the confusion matrix, F1-score, precision, and recall.

2.6.1. VGG16

This architecture is a prominent CNN model presented by [27], which enhances its predecessor, the AlexNet model, by substituting the 11 × 11 and 5 × 5 kernels in the first two convolution layers with several 3 × 3 ones in succession. The model is about 528 MB in size with a recorded 90.1% top-5 accuracy on ImageNet data and about 138.4 million parameters. The ImageNet dataset possesses around 14 million images from 1,000 categories. VGG16 was trained on powerful GPUs over a period of several weeks.

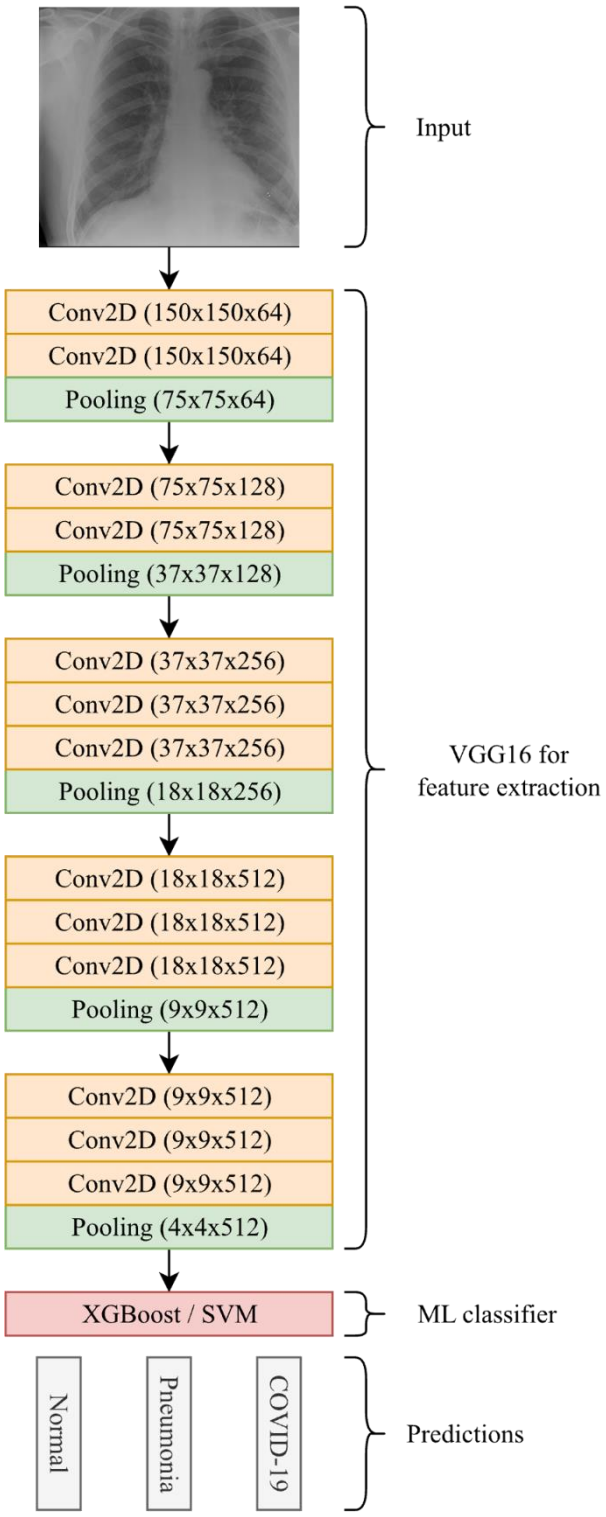

Figure 3. The architecture of the hybrid model.

2.6.2. XGBoost

Coined after extreme gradient boosting, it is a collection of scalable and distributed gradient boosting that are prominent for their high efficiency, flexibility, and portability, which executes machine learning algorithms under the gradient-boosted frameworks. XGBoost presents a similar tree-boosting approach known as GBDT (Gradient-Boosted Decision Tree) or GBM (Gradient Boosting Machine) that efficiently and precisely solves classification and regression problems involving billions of cases or more [28].

2.6.3. SVM

SVM is among the most prominent algorithms for classification and regression issues along with outlier detection in supervised learning circumstances. SVM is a machine learning technique that strives to classify data points operating a hyperplane in the space of N-dimensions with N as the number of features. It is a memory-efficient method of applying varying kernel operations for the decision function to solve issues where the number of dimensions surpasses the number of samples [29].

2.7. The Pre-Trained Models

Like the pre-processing steps conducted in the first dataset, the images in Dataset B were also reshaped, normalized, augmented, and split into an 80:10:10 ratio for training, validation, and testing. Then ResNet50, Xception, and DenseNet201 models were loaded with the ImageNet pre-trained weights without their respective top layers. The same layers comprising global average pooling, dropout with the probabilities of 0.2, batch normalization, and dense layers with two units using the Softmax activation functions were later added to the models to aid with the classification. Then we compiled them using the Adam optimizer, each with a learning rate of 0.00001 and a decay of 0.00001/60. Other hyperparameters used in the compilation process include categorical cross-entropy loss function and accuracy metrics. The model's training process involves using epochs of 60, a batch size of 128, along with early stopping and reduced learning rate callbacks. The models were evaluated individually using accuracy, F1-score, precision, recall, and confusion matrix.

2.7.1. ResNet50

It is a kind of ANN (Artificial Neural Network) that produces networks by piling blocks of residual connections, as demonstrated by the 50-layer ConvNet featuring 48 convolution layers, a maximum, and an average pooling layer [30]. Trained on ImageNet data, the 224 × 224 input-sized networks can categorize images into a thousand object groups.

2.7.2. Xception

This architecture was created to improve the fundamentals of the Inception model, where 1 × 1 convolution operations were used to compress input data and further utilize varying filters on each data's depth space. Extreme Inception, short for Xception, essentially reverses this mentioned process. Conversely, it applies the filters to each depth map before performing the exact convolution processes across the depth to shrink the input space. This technique is known as the depth-wise separable convolution operation [31].

2.7.3. DenseNet201

This network has a 201-layer design in which directly linked channels form dense connections. Each layer obtains extra inputs from previous ones and sends its feature maps to succeeding layers utilizing a concatenated strategy. Splitting the 3 × 3 convolution operation into a 1 × 1 and a 3 × 3 minimizes the quantity of the model parameters since each layer gets feature maps from subsequent ones. The growth rate denoted by *k* signifies that the amount of feature maps rises by *k* each moment the dense block is traversed, which helps to lower the parameters. The dense blocks are joined by a transitional layer that significantly minimizes the number of features and nets out the most effective ones in each layer [32].

With the mentioned models and designed models, chest x-ray images were used in the study and the classification process was carried out. The flow chart of the study is given in Figure 4.

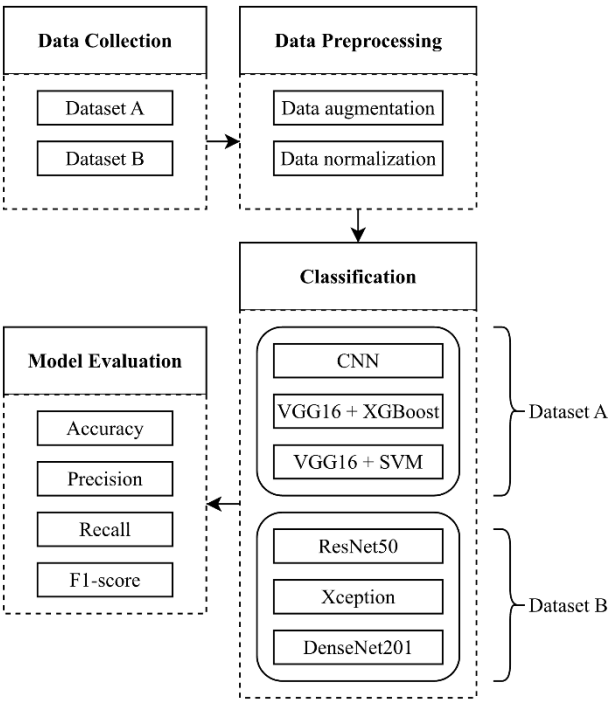

Figure 4. Flow chart of the study.

As can be seen in Figure 4, the study consists of four stages. In the first stage **(Data Collection)**, two different data sets containing CXR images were obtained, and the data sets were named as Data Set A and Data Set B. In the second stage **(Data Preprocessing)**, data augmentation was performed on the images in the data sets and the size of the data sets was increased. Afterwards, the normalization process was performed, and the pixels of the images were reduced to the range of [0, 1]. In the third stage **(Classification)**, classification was carried out according to the data sets. For Data Set A CNN, VGG16+XGBoost and VGG16+SVM classifiers were employed. On the Data Set B, deep learning models ResNet50, Xception and DenseNet201 were considered, and the images were classified. In the last stage **(Model Evaluation)**, the performances of the classifiers were evaluated and for this, accuracy (acc), precision (pre), recall (rec) and F1-score (f1s) values were calculated.

3. Results and Discussion

3.1. Experimental Results

After training the models in this study with the two distinct datasets, we evaluated them using test portions of the preserved data to measure their test loss and accuracy. The plots of these losses and accuracies against the number of training epochs are known as learning curves. Figure 5 (a) and (b), and Figure 6 (a) and (b) depict the learning curves for our suggested ConvNets model, ResNet50, Xception, and DenseNet201 deep learning models, respectively. Moreover, Table 5 and Table 6 contain the summary of overall results of the experimental analysis.

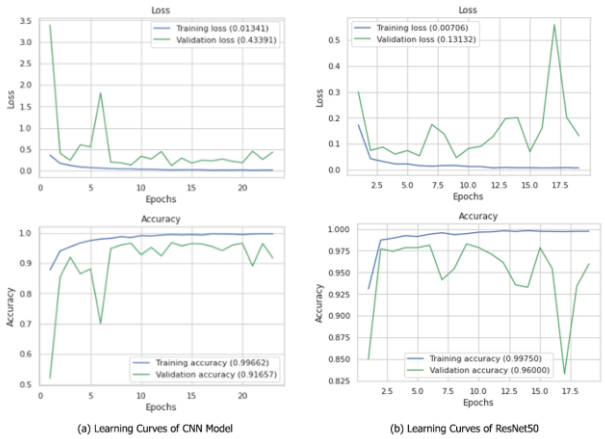

Figure 5. Learning curves of losses and accuracies of (a) CNN model, (b) ResNet50 model.

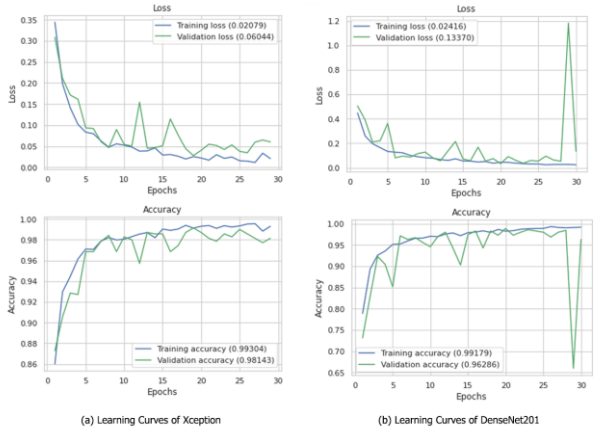

Figure 6. Learning curves of losses and accuracies of (a) Xception model, (b) DenseNet201 model.

Table 5. Results of the models on Dataset A

Models	Pre	Rec	F1s	Acc
CNN	98.92%	98.90%	98.90%	98.91%
VGG16 + XGBoost	96.00%	96.00%	96.00%	98.44%
VGG16 + SVM	96.00%	96.00%	96.00%	95.60%

Table 6. Results of the models on Dataset B

Models	Pre	Rec	F1s	Acc
ResNet50	98.86%	98.86%	98.86%	98.90%
Xception	99.14%	99.14%	99.14%	99.14%
DenseNet201	99.00%	99.00%	99.00%	99.00%

3.2. Evaluation Metrics

The metrics employed for evaluating the obtained results include accuracy, precision, recall, and F1-score. The accuracy of an artificial intelligence model is represented as the proportion of accurate predictions to all other classifications generated by the model using the input data. Precision is the ratio of the correct predictions to all the positive predictions in its dataset. The recall is expressed as the ratio of the correct predictions to the complete number of accurate entities in the given dataset. Finally, F1-score is the weighted harmonic mean of the recall and precision, ranging between zero (0) and one (1). When the value of the f-measure is increased, the model's classification performance also increases [33]. The formulas of the evaluation metrics used in the study are given between Equation 1 and Equation 4.

$$Accuracy = \frac{TP + TN}{TP + TN + FP + FN} \quad (1)$$

$$Precision = \frac{TP}{TP + FP} \quad (2)$$

$$Recall = \frac{TP}{TP + FN} \quad (3)$$

$$F1 - score = 2 * \left(\frac{precision * recall}{precision + recall}\right) \quad (4)$$

The equations portrayal of TP expression signifies True Positive values, whereas the TN expression represents True Negative values. FN corresponds to False Negative values, while FP corresponds to False Positive values.

3.3. Confusion Matrix

A confusion matrix is a table-like plot that is widely employed to describe the performance of classification models on a collection of known-true test data. It offers far more information than a straightforward accuracy score. For the multi-class case, it illustrates how inaccurate a prediction maybe when the output classes are ordinal. When dealing with imbalanced data, where there is a considerable gap between the different categories of groups, accuracy alone is insufficient. Figure 7 (a), (b), and (c) presents the confusion matrices for the ConvNet and hybrid models obtained using Dataset A.

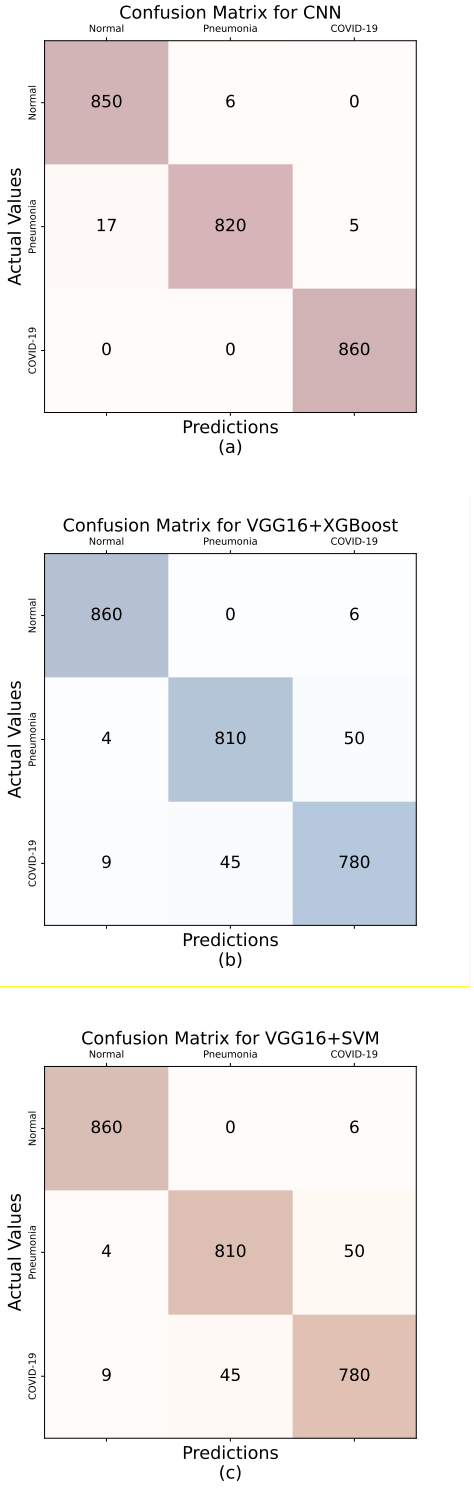

Figure 7. The confusion matrices of (a) CNN model, (b) VGG16+XGBoost model and (c) VGG16+SVM model on Dataset A.

Figure 8 (a), (b), and (c) shows the confusion matrices for the pre-trained models acquired from Dataset B. Moreover, Table 7 compares the performances of our proposed models with recent state-of-the-art studies from the literature.

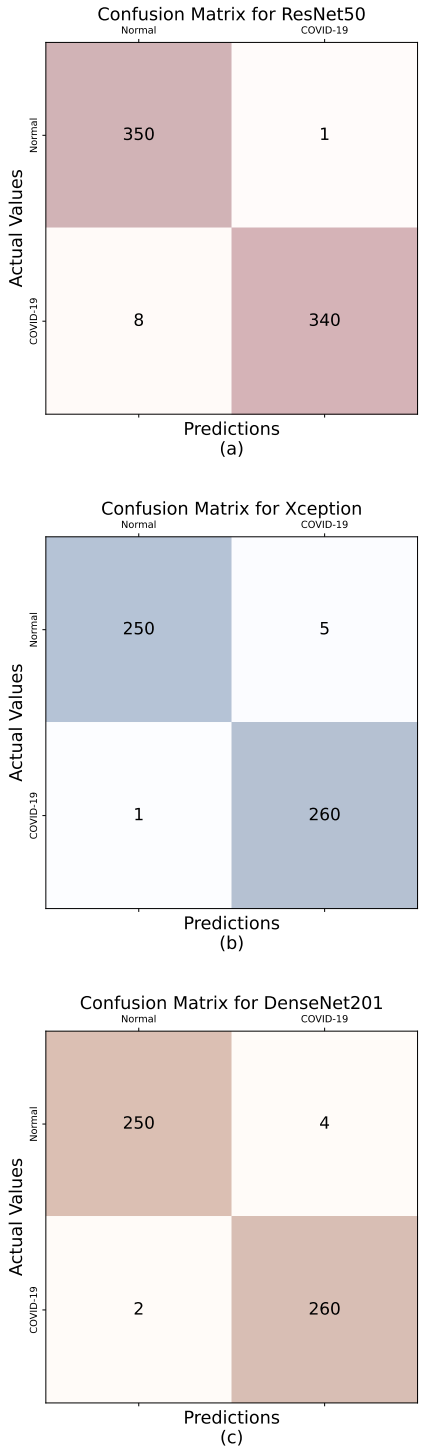

Figure 8. The confusion matrices of (a) ResNet50 model, (b) Xception model and (c) DenseNet201 model on Dataset B.

Table 7. Performance comparisons with some state-of-the-art studies from the literature

Reference	Top Accuracy
[34]	95.00%
[35]	96.00%
[36]	96.56%
[37]	87.00%
[38]	96.68%
[39]	97.40%
[40]	96.33%
[41]	97.00%
[42]	97.00%
[43]	98.05%
[44]	99.69%
[45]	96.73%
[46]	95.00%
[47]	97.00%
[48]	98.23%
This study	**99.10%**

The results of the experimental analysis conducted in this paper begins with the learning curves shown by Figure 5 and Figure 6. These plots are very significant as they indicate the performance of the models in terms of training and validation losses and accuracies. Typically, they are used to detect overfitting and underfitting in models. Based on these curves, the models perform well since the gap between average losses and accuracies is minimal. The variation in the number of epochs shown by various plots is another factor worthy of consideration concerning these graphs. These differences are due to the early stopping and reduced learning rate callback methods used during model training. These callbacks continuously monitor the models convergence to determine the optimal learning rates. Consequently, training was terminated early with epochs between 17 and 30, demonstrating the quality of the models. These factors also cause large models such as the ResNet50 and DensNet201 to have non-smooth learning curves while producing excellent results.

After obtaining the plots of the individual deep learning models learning curves, the average precision, recall, F1-score, and accuracy metrics from the test data was calculated. Table 5 and Table 6 show the summary of the experimental results obtained from the proposed models conducted on the two datasets for the three-class and binary-class image classification. The proposed CNN model achieved an estimated accuracy of 98.91%. It also attained an average precision value of 98.92%, 98.90% recall,

and 98.90% F1-score for COVID-19, pneumonia, and normal images. The VGG16 + XGBoost and VGG16 + SVM hybrid models obtained 98.44% and 95.60% accuracies, respectively. However, they recorded similar average precision, recall, and F1-score value of 96.00%. For the fine-tuned pre-trained models, the Xception model performed the best, reaching a test accuracy of 99.14%. The precision, recall, and F1-score values all showed consistent results at 99.14%. Following that, the DensNet201 model achieved an accuracy of 99.00%, with precision, F1-score, and recall also at 99.00%. Lastly, the pre-trained ResNet50 model achieved an accuracy of 98.90%, with identical values for precision, recall and F1-score, all at 98.86%.

The adoption of several essential image pre-processing techniques, such as reshaping, resizing, and cropping, as well as the class resampling techniques described previously, are among the main contributing factors for these vast models to achieve such performance with minimal computer resource consumption. In addition, the inclusion of callback functions has significantly aided in the prevention of overfitting and early convergence, as the reduced learning rate class, for instance, monitors the loss and decreases the learning rate when there is no discernible improvement. Moreover, these results are very impressive in comparison to many recent published state-of-the-arts work. Performance comparison presented by Table 7 is the evidence of this assertion since it was created by picking the best accuracies of some work conducted in the literature to the best of our knowledge and compared with the ones obtained by our proposed models. The comparison is organized into three sections to represent performance of the studies. The first section comprises [34] – [38] studies using the conventional CNN models to detect lungs diseases. The second category of studies [39] – [43] are the ones performed by fine-tuning the pre-trained models. Lastly, these studies [44] – [48] were based on the various hybrid models for COVID-19 and pneumonia detection. For the ConvNet and pre-trained models, our proposed models have the best accuracies compared to these novel studies to the best of our knowledge. Also, our proposed hybrid models are the second best in terms of accuracy. These accomplishments are only feasible due to the time and effort devoted to meticulously scrutinizing each experimental stage, including data collection, in-depth literature review, conceptualization, model training, experimental result gathering, etc. The adoption of this strategy stems from a desire to build upon recent work to create robust tools that will benefit the scientific community.

Several further studies have leveraged the might of deep learning algorithms to diagnose the novel COVID-19 disease using other techniques with high performances. For instance, to aid with fast and inexpensive methods in combating the recent pandemic, researchers developed a software that integrates the web design approach to create an interactive GUI (Graphical User Interface (GUI) [49]. Their software, CoviExpert, involves making combined independent predictions by training on 1,584 CXR images to detect COVID-19 cases with high classification accuracy. In another study, researchers aimed to minimize the performance reduction of models posed by obtaining datasets from various sources in image classification problems [50]. To achieve that, they offered a self-supervised block for feature standardization and optimization on three pre-trained models, VGG, Xception, and DenseNet, as a baseline to extract features from four CXR lung disease classification datasets and observed improved classification outcomes. Lastly, researchers in [51] suggested a hybrid multimodal framework that fused two separate models employing the weighted sum-rule fusion approach to segment and classify CXR images and collected cough samples. After using the necessary signal processing and Mel frequency cepstral coefficient to pre-process the cough samples, the fused model attained high classification accuracies for the CXR images and the cough samples. These alter-native methods to COVID-19 detection are a solid indication that one has no limit in employing deep learning approaches to develop robust models that can quickly and efficiently diagnose diseases in biomedical data with less cost and human errors.

4. Conclusion

The deep learning-based methods provide an efficient way of diagnosing chest-related diseases, particularly the recent COVID-19 virus. Three categories of models namely, conventional CNN, hybrid, and pre-trained models proposed in this study to classify CXR images into normal, pneumonia or COVID-19 and normal or COVID-19 classes. The suggested CNN and hybrid models achieved test accuracies of 98.91%, 98.44% and 95.60%, respectively. Also, the fine-tuned ResNet50, Xception, and DenseNet201

models achieved test accuracies of 98.90%, 99.14%, and 99.00%, respectively. These outcomes showed the significance of the study and, without a doubt, maked us confident that the models can indeed be deployed in real-life scenarios to aid radiologist with robust tools for early disease detection and diagnosis. For future research, we aim to use alternative resampling methods, such as combinations of under sampling and oversampling or synthetic minority oversampling techniques called SMOTE to address the class imbalance. We also wish to use additional hybrid models, such as merging CNN with ELM (Extreme Learning Machine) or convolution auto-encoders with deep learning classification using the encoded features to classify the images. Research in these domains will allow exploring other boundaries in image classification to create robust models for aiding medical experts in quick diagnoses and treatment of ailments.

This research work was supported by grants given to the MSc. dissertation project by the Scientific Research Projects Administration Unit of Fırat University, Elazığ, Turkey [grant number: TEKF.22.32]. The authors would like to express immense gratitude for this unit's financial support throughout the research study.

Contributions of the authors

The authors contributions to the paper are equal.

Conflict of Interest Statement

There is no conflict of interest between the authors.

Statement of Research and Publication Ethics

The study is complied with research and publication ethics.

Acknowledgment

References

[1] L. Qun et al., "Early transmission dynamics in Wuhan, China, of novel coronavirus-infected pneumonia," *N Engl J Med.,* vol. 382, pp. 1199-1207, March 2020.
[2] M. A. Alah, S. Abdeen, and V. Kehyayan, "The first few cases and fatalities of corona virus disease 2019 (COVID-19) in the Eastern Mediterranean Region of the World Health Organization: a rapid review," *J Infect Public Health,* vol. 13, pp. 1367-1372, October 2020.
[3] J. S. Mackenzie, and D. W. Smith, "COVID-19: a novel zoonotic disease caused by a coronavirus from China: what we know and what we don't," *Microbiol Aust.,* pp. 1-14, March 2020.
[4] A. R. Rahmani et al., "Sampling and detection of corona viruses in air: a mini review," *Sci Total Environ.,* vol. 740, pp. 1-7, October 2020.
[5] J. She, L. Liu, and W. Liu, "COVID-19 epidemic: Disease characteristics in children," *J Med Virol.,* vol. 92, pp. 747-754, April 2020.
[6] L. Baroiu et al., "COVID-19 impact on the liver," *World J Clin Cases.,* vol. 9, pp. 3814-3825, June 2021.
[7] P. Sirohiya et al., "Airway management, procedural data, and in-hospital mortality records of patients undergoing surgery for mucormycosis associated with coronavirus disease (COVID-19)," *J Mycol Med.,* vol. 32, pp. 1-6, November 2020.
[8] Y. Rolland et al., "Coronavirus disease-2019 in older people with cognitive impairment," *Clin Geriatr Med.,* vol. 38, pp. 501-507, August 2022.
[9] M. Sachdeva et al., "Cutaneous manifestations of COVID-19: report of three cases and a review of literature," *J Dermatol Sci.,* vol. 98, pp. 75-81, May 2020.
[10] M. Bansal, "Cardiovascular disease and COVID-19," *Diabetes Metab Syndr.,* vol. 14, pp. 247-250, May 2020.
[11] B. P. Goodman et al., "COVID-19 dysautonomia," *Front Neurol.,* vol. 12, pp. 1-5, April 2021.
[12] L. Falzone et al., "Current and innovative methods for the diagnosis of COVID-19 infection (review)," *Int J Mol Med.,* vol. 47, pp. 1-23, June 2021.
[13] A. Barragan-Montero et al., "Artificial intelligence and machine learning for medical imaging: a technology review," *Phys Med.,* vol. 83, pp. 242-256, March 2021.
[14] M. Aljabri and M. AlGhamdi, "A review on the use of deep learning for medical images segmentation," *Neurocomputing,* vol. 506, pp. 311-335, September 2022.

[15] P. Asha et al. "Artificial intelligence in medical Imaging: An analysis of innovative technique and its future promise," *Mater Today Proc.*, vol. 56, pp. 2236-2239, December 2021.
[16] A. Singhal et al., "Study of deep learning techniques for medical image analysis: a review," *Mater Today Proc.*, vol. 56, pp. 209-214, January 2022.
[17] M. E. Sahin, "Deep learning-based approach for detecting COVID-19 in chest X-rays," *Biomed Signal Process Control.*, vol. 78, pp. 1-10, September 2022.
[18] S. Hassantabar, M. Ahmadi, and A. Sharifi, "Diagnosis and detection of infected tissue of COVID-19 patients based on lung X-ray image using convolutional neural network approaches," *Chaos Solitons Fractals.*, vol. 140, pp. 1-11, November 2020.
[19] R. Malhotra, H. Patel, and B. D. Fataniya," Prediction of COVID-19 disease with chest X-Rays using convolutional neural network," in *Proc of the 3rd Int. Conf. on Inventive Research in Computing Applications, ICIRCA 2021, Coimbatore, India, September 2-4, 2021.*
[20] A. K. Das et al., "Automatic COVID-19 detection from X-ray images using ensemble learning with convolutional neural network," *Pattern Anal Appl.*, vol. 24, pp. 1111-1124, March 2021.
[21] A. Banerjee et al., "COVID-19 chest X-ray detection through blending ensemble of CNN snapshots," *Biomed Signal Process Control.*, vol. 78, pp. 1-9, September 2022.
[22] A. M. Ismael and A. Şengür, "Deep learning approaches for COVID-19 detection based on chest X-ray images," *Expert Syst Appl.*, vol. 164, pp. 1-11, February 2021.
[23] P. Patel, "Chest X-ray (Covid-19 & Pneumonia)," kaggle.com, 2020. [Online]. Available: https://www.kaggle.com/datasets/prashant268/chest-xray-covid19-pneumonia. [Accessed: Oct. 4, 2023].
[24] T. Rahman, M. Chowdhury, and A. Khandakar, "COVID-19 Radiography Database," Kaggle.com, 2021. [Online]. Available: https://www.kaggle.com/datasets/tawsifurrahman/covid19-radiography-database. [Accessed: Oct. 4, 2023].
[25] R. Mohammed, J Rawashdeh, and M. Abdullah, "Machine learning with oversampling and undersampling techniques: overview study and experimental results," in *Proc of the 11th Int. Conf. on Information and Communication Systems, ICICS 2020, Irbid, Jordan, April 7-9, 2020,* pp. 243-248.
[26] C. Shorten and T. M. Khoshgoftaar, "A survey on image data augmentation for deep learning," *J Big Data*, vol. 6, pp. 1-48, July 2019.
[27] K. Simonyan and A. Zisserman, "Very deep convolutional networks for large-scale image recognition," in *Proc of the 3rd Int. Conf. on Learning Representations, ICLR 2015, San Diego, USA, May 7-9, 2015.*
[28] R. Mitchell and E. Frank, Accelerating the XGBoost algorithm using GPU computing," *PeerJ Comput Sci.*, vol. 3, pp. 1-37, July 2017.
[29] Y. Shihong, L. Ping, and H. Peiyi, "SVM classification:Its contents and challenges," *Appl Math J Chin Univ.*, vol. 18, pp. 332-342, September 2003.
[30] K. He et al., "Deep residual learning for image recognition," in *Proc of the Conf. on Computer Vision and Pattern Recognition, CVPR 2016, Las Vegas, USA, June 27-30, 2016,* pp. 770-778.
[31] F. Chollet, "Xception: deep learning with depthwise separable convolutions", in *Proc of the Conf. on Computer Vision and Pattern Recognition, CVPR 2017, Honolulu, USA, July 21-26, 2017,* pp. 1800-1807.
[32] G. Huang et al., "Densely connected convolutional networks," in *Proc of the Conf. on Computer Vision and Pattern Recognition, CVPR 2017, Honolulu, USA, July 21-26, 2017,* pp. 2261-2269.
[33] T. Y. Chen, FC. Kuo, and R. Merkel, "On the statistical properties of the f-measure," in *Proc of the 4th Int. Conf. on Quality Software, QSIC 2004, Washington, USA, September 8-10, 2004,* pp. 146-153.
[34] G. Caseneuve et al., "Chest X-ray image preprocessing for disease classification," *Procedia Comput Sci.*, vol. 192, pp. 658-665, October 2021.
[35] G. Hussain and Y. Shiren, "Recognition of COVID-19 disease utilizing -ray imaging of the chest using CNN," in *Proc of the Int. Conf. on Computing, Electronics & Communications Engineering, iCCECE 2021, Southend, UK, August 16-17, 2021,* pp. 71-76.
[36] A. S. Musallam, A. S. Sherif, and M. K. Hussein, "Efficient framework for detecting COVID-19 and pneumonia from chest X-ray using deep convolutional network," *Egypt Inf J.*, vol. 23, pp. 247-257, July 2022.

[37] S. Singht et al., "CNN based Covid-aid: Covid 19 detection using chest X-ray," in *Proc of the 5th Int. Conf. on Computing Methodologies and Communication, ICCMC 2021, Erode, India, April 8-10, 2021,* pp. 1791-1797.

[38] G. Gilanie et al., "Coronavirus (COVID-19) detection from chest radiology images using convolutional neural networks," *Biomed Signal Process Control,* vol. 66, pp. 1-6, April 2021.

[39] T. Mahmud, A. Rahman, and S. A. Fattah, "CovXNet: A multi-dilation convolutional neural network for automatic COVID-19 and other pneumonia detection from chest X-ray images with transferable multi-receptive feature optimization," *Comput Biol Med.,* vol. 122, pp. 1-10, July 2020.

[40] S. Dilshad et al., "Automated image classification of chest X-rays of COVID-19 using deep transfer learning," *Results Phys.,* vol. 28, pp. 1-10, September 2021.

[41] P. A. Vieria et al., "Classification of COVID-19 in X-ray images with genetic fine-tuning," *Comput Electr Eng.,* vol. 96, pp. 1-8, December 2021.

[42] A. Abbas, M. M. Abdelsamea, and M. M. Gaber, "4S-DT: self-supervised super sample decomposition for transfer learning with application to COVID-19 detection," *IEEE Trans Neural Netw Learn Syst.,* vol. 32, pp. 2798-2808, July 2021.

[43] D. M. Ibrahim, N. M. Elshennawy, and A. M. Sarhan, "Deep-chest: multi-classification deep learning model for diagnosing COVID-19, pneumonia, and lung cancer chest diseases," *Comput Biol Med.,* vol. 132, pp. 1-13, May 2021.

[44] M. Toğaçar, "Disease type detection in lung and colon cancer images using the complement approach of inefficient sets," *Comput Biol Med.,* vol. 137, pp. 1-13, October 2021.

[45] D. K. Sharma et al., "Classification of COVID-19 by using supervised optimized machine learning technique," *Mater Today Proc.,* vol. 56, pp. 2058-2062, November 2021.

[46] S. S. Verma, A. Prasad, and A. Kumar, "CovXmlc: high performance COVID-19 detection on X-ray images using multi-model classification," *Biomed Signal Process Control,* vol. 71, pp. 1-7, January 2022.

[47] B. Prabha et al., "Intelligent predictions of Covid disease based on lung CT images using machine learning strategy," *Mayer Today Proc.,* vol. 80, pp. 3744-3750, July 2021.

[48] H. Nasiri and S. Hasani, "Automated detection of COVID-19 cases from chest X-ray images using deep neural network and XGBoost," *Radiography,* vol. 28, pp. 732-738, August 2022.

[49] A. Arivoli, D. Golwala, and R. Reddy, "CoviExpert: COVID-19 detection from chest X-ray using CNN," *Measur Sens.,* vol. 23, pp. 1-8, October 2022.

[50] X. Li et al., "A self-supervised feature-standardization-block for cross-domain lung disease classification," *Methods.,* vol. 202, pp. 70-77, June 2022.

[51] S. Kumar et al., "Chest X ray and cough sample based deep learning framework for accurate diagnosis of COVID-19," *Comput Electr Eng.,* vol. 103, pp. 1-19, October 2022.

Bitlis Eren Üniversitesi Fen Bilimleri Dergisi
BİTLİS EREN UNIVERSITY JOURNAL OF SCIENCE
ISSN: 2147-3129/e-ISSN: 2147-3188
VOLUME: 12 NO: 4 PAGE: 1028-1040 YEAR: 2023
DOI:10.17798/bitlisfen.1316881

Prediction of Lake Van Water Level Using an Artificial Neural Network Model with Meteorological Parameters and Multiple Linear Regression Analysis: A Comparative Study

Furkan SİDAL[1], Yener ALTUN[1*]

[1]*Department of Statistics, Institute of Science, Yüzüncü Yıl University,Van, Türkiye (ORCID: 0000-0002-9670-2618) (ORCID: 0000-0003-1073-5513)*

Keywords: Artificial Neural Network, Comparative Study, Lake Water Level Prediction, Modeling, Multiple Linear Regression Analysis.

Abstract

The water level of Lake Van has shown changes over time. This study encompasses a statistical investigation conducted to understand the reasons behind the variation in the lake's water level. In this study, an attempt has been made to establish a predictive model by determining the effects of meteorological factors on the lake's water level. Artificial neural networks have been utilized to predict the water level of Lake Van using meteorological parameters such as precipitation, temperature, evaporation, wind speed, relative humidity, and atmospheric pressure. Furthermore, a model equation has been formulated by examining the relationship between independent variables and the changes in the water level of Lake Van through multiple linear regression analysis. The two models have been compared, and the results have been evaluated. The obtained results indicate that the artificial neural network model can provide more realistic predictions for the water level of Lake Van compared to the multiple regression analysis method, demonstrating that artificial neural networks serve as a tool for both temporal and spatial predictions.

1. Introduction

Van Lake, one of the largest lakes in Turkey, holds significant ecological and socioeconomic importance. In recent years, noticeable fluctuations have been observed in the water level of Van Lake. These fluctuations have had significant impacts on both the lake ecosystem and the lives of the people residing in its vicinity. Therefore, understanding the causes behind these changes in the water level of Van Lake and predicting future fluctuations are of great importance. Numerous studies have been conducted to identify the reasons behind the rise and fall of the water level in Van Lake. These studies not only focus on determining the physical factors responsible for these changes but also employ statistical approaches to analyze the lake's water level.

This study presents a statistical approach to investigate the changes in the water level of Van Lake. With the rapid advancement of technology, an innovative method utilizing artificial neural networks (ANNs) has been employed for predicting the lake's water level. Artificial neural networks (ANNs) are widely and effectively used in various fields today, and water level prediction is one of these areas.

Artificial neural networks (ANNs) are systems designed to analyze and process information similar to humans. They combine multiple neurons (cells) according to a specific rule to perform a task and provide solutions to statistical, mathematical, structural, and philosophical problems. ANNs have recently emerged and have gained wide acceptance across various disciplines for solving many real-world problems [1].

In this study, an attempt was made to establish a prediction model by determining the effects of meteorological factors on the water level of Van Lake. Artificial neural networks (ANNs) were used in this model to predict the Van Lake water level using meteorological parameters such as precipitation (P), temperature (T), evaporation (E), wind speed (WS), relative humidity (RH), and actual pressure (AP). Monthly average water level data of Van Lake from 2004 to 2022 obtained from the 17th Regional

[*]Corresponding author: yeneraltun@yyu.edu.tr
Received:19.06.2023 , Accepted:26.11.2023

Directorate of State Hydraulic Works (DSI) and monthly average meteorological parameter data (precipitation, temperature, evaporation, wind speed, relative humidity, and actual pressure) collected from various stations in the Van region from 2004 to 2022 obtained from the General Directorate of Meteorology were used to create a model and predict the impact of these meteorological variables on the lake level using ANNs. After completing the training of the model, it was tested using data from 2022. Additionally, another focus of the study is multiple linear regression analysis. With this analysis method, the relationship between the independent variables (precipitation, temperature, evaporation, wind speed, relative humidity, and actual pressure) and the dependent variable, Van Lake water level changes, was examined, and a model equation was formed. These two methods were compared, and the results obtained were evaluated.

In the literature, there are numerous studies focusing on the prediction of groundwater levels, where various models have been established.

In [2], Çobaner and others applied a novel genetic programming approach called multi-gene genetic programming (MGGP) to predict groundwater levels using meteorological data and historical groundwater levels. The construction of this model involved the use of four years of daily data from the Karacaviran observation well, covering the period from 2007 to 2010, as well as daily meteorological data from the Develi meteorology station. The accuracy of these models was evaluated and compared with conventional rating curve analysis (RCA). The results of the MGGP models were found to be superior to RCA based on four different criteria.

In [3], Yalova Gökçe Dam water levels were predicted for the year 2019 using artificial neural networks (ANNs) based on data from 2000 to 2019, including the flow rate of Selimandıra stream, evaporation and precipitation values, dam water discharge, seepage water quantity, and dam level. The developed models utilized the Levenberg-Marquardt algorithm with a multi-layered ANN function to evaluate monthly datasets. The prediction data showed a close approximation to the actual water level with a determination coefficient of 94.14%. In summary, the average predicted water level in the dam for 2019 was 73.77 m, while the actual average water level in the dam was 72.13 m. These results suggest that the ANN model yielded successful outcomes in predicting the water levels of Yalova Gökçe Dam.

In [4], Ispir conducted a study in the sandy region of Hatay Amik Plain. In this study, monthly measurements of groundwater levels were obtained from an observation well belonging to the General Directorate of State Hydraulic Works (DSI) between 2000 and 2015. Additionally, monthly measurements of total precipitation and average temperature were included to predict groundwater levels. Autoregressive (AR) and Artificial Neural Network (ANN) models were developed in the study, and the performance of groundwater level prediction was evaluated. As a result of the study, it was observed that the ANN model yielded better results in predicting groundwater levels in the region compared to the AR and AR models.

Artificial Neural Networks (ANNs) were used to model the temporal changes in water levels of Lake Van. The backpropagation algorithm was employed to train the developed model. This study aimed to evaluate the dynamic variations in the lake's water level. As a result, the study demonstrated that ANNs can successfully model the complex relationship between precipitation and consecutive water levels [5].

In [6], Panyadee and others modeled the water level fluctuations of Lake Drwęckie using Artificial Neural Network (ANN) techniques. Meteorological data from the Olsztyn meteorological station for the years 1980-2012 were used for modeling purposes. The study concluded that predicting lake water level changes using ANN yielded accurate results.

This study contributes to the literature by developing a statistical model that examines the relationship between meteorological factors and the water level changes in Lake Van. While some studies in the existing literature focus on the physical causes of water level variations in Lake Van, others analyze the lake level using statistical approaches. This study extensively investigates the effects of meteorological factors on the lake water level and provides a model that can predict future changes.

2. Material and Method

In this section of the study, the structure of the Artificial Neural Network (ANN), the functioning of neurons, its components, and the training of the network, as well as the significance of Regression Analysis (RA), Multiple Linear Regression (MLR), the study area, and the dataset are explained to describe the methods used. The modeling techniques employed in the study are also outlined.

2.1. Artificial Neural Networks (ANNs)

Artificial Neural Networks (ANNs) are systems that enable computers to learn from data and generate new

information by mimicking the learning process of the human brain. They are based on a mathematical modeling of the biological and cognitive properties of the human brain. ANNs are models created by imitating the biological neural structure of living organisms [7].

The recognition that the computations performed by the human brain are significantly different from those of digital machines has been a driving force behind research on ANNs since their inception [8].

In humans, the process of learning occurs through synaptic connections between neurons. Neurons receive input signals through numerous dendrites. The input received by dendrites can be excitatory or inhibitory. Inputs are integrated into the neuron's cell body. When the combined input exceeds a certain threshold, the neuron transmits an output signal to other cells through its axon. This basic description forms a model for artificial neurons [9].

Table 1. Comparison of biological and artificial neurons

Biological Neuron Structure	Artificial Neuron Structure
Neuron	Input Value
Dendrite	Summation Function
Cell Body	Activation Function
Akson	Output Value
Synapse	Weights

The basic elements of ANNs are artificial neurons inspired by the functioning of biological neurons. These neurons form connections among themselves, which are grouped into layers to construct ANNs. Figure 1. depicts a graphical representation of how the cellular structure of a brain is mathematically modeled [8].

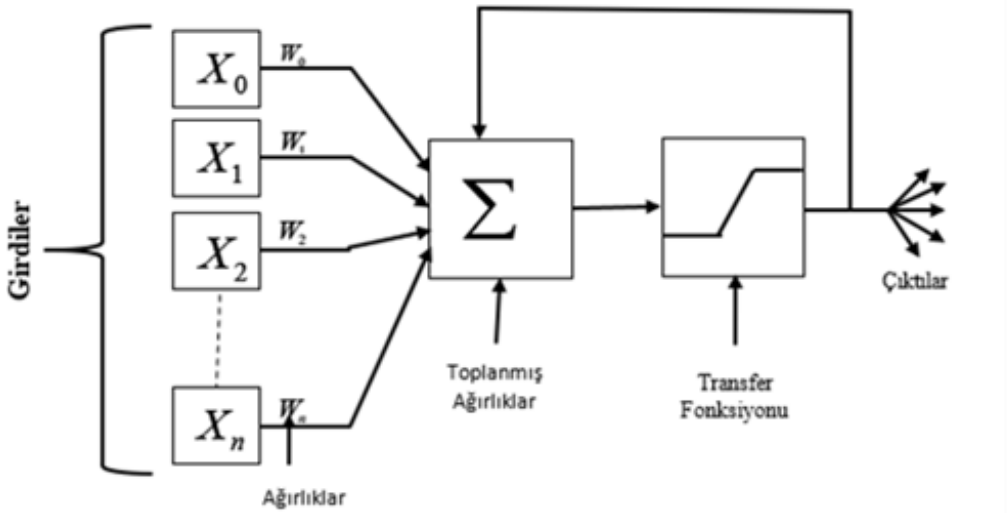

Figure 1. For captions, please use the figure description style.

The information from the external world (x_i) is gathered and fed into the input layer. In other words, the desired learning information for the network is collected at the input layer. For example, data such as precipitation, temperature, wind speed, relative humidity, cloud cover, and atmospheric pressure that affect the water level of Lake Van are gathered as inputs in this layer, and there is a corresponding neuron for each input.

The weight values (w_i) represent the importance and impact of the incoming inputs on the neuron. This effect can be positive or negative [10].

The weights of the presented inputs in the network are not fixed. As the ANN is presented with new examples, it adjusts the weight values to achieve the most suitable result for itself. At the beginning of the training, the weights are assigned randomly. If the output value reaches an acceptable error level at the end of the process, the training of the network is considered complete. Otherwise, the process is repeated and the weights are adjusted again. Minimizing the error between the actual values and the predicted output values of the model is crucial [11].

The Net Input (s) value of the cells in the hidden layer is obtained by combining (summing) the inputs with their corresponding weights. Several methods can be used to calculate this value.

$$s = \sum_{i=1}^{n} x_i * w_i \quad (1)$$

In Equation (1), x_i represents the values of the inputs, and w_i represents their corresponding weights. Each input is multiplied by its randomly assigned weight, from the first input to the last input, and the results are summed to obtain the value of *s*.

After the computation of the activation function, the resulting *s* value is passed through an activation function. The output of the pooling function is transformed into the final output through the activation function. The activation function determines the output value produced by the cell based on the net input value received by the cell. If we consider an artificial neural network without an activation function, the network would resemble a simple linear regression. Different activation functions can be used depending on the problem type and network structure.

The resulting value after the computation of the activation function becomes the output of the cell. This value can serve as input to another cell or be directly used as information. A single cell obtains only one output value. The information that passes to other process elements remains consistent throughout the process. When the process is completed, the artificial neural network has fulfilled its task and generated the required information [11].

To train an ANN and enable it to produce results, several steps need to be taken. These steps are as follows:

- Presenting Data to the Network and Determining the Network Structure
- Determining the Number of Hidden Neurons
- Selecting Activation Functions for Combination
- Determining Stopping Criteria
- Performance (Error) Measures for Models
- Error Reduction

By following these steps, the ANN can be trained and utilized to produce the desired results.

2.2. Regression Analysis (RA)

Regression is the process of expressing the relationship between at least two variables through an equation [12]. Similarly, in Regression Analysis (RA), when variables are considered dependent and independent, their relationship is expressed through an equation.

The term 'regression' was first introduced by Francis Galton. Regression is the first technique that comes to mind when examining the relationship between variables. From a statistical perspective, the relationship between two variables is interpreted as a dependence that exists between the varying values of these variables. If the value of variable '*x*' changes and this change is accompanied by a change in the value of variable '*y*' that is dependent on '*x*', it can be said that there is a relationship between these variables [13]. There are various types of regression analysis found in the literature.

Linear regression is an approach aimed at modeling the relationship between a numerical dependent variable (*y*) and one or more independent variables (*x*) [14].

In regression analysis, instead of analyzing the entire set of data (population), the analysis is performed with samples selected from this data. Due to the large number of data points in the population, statistical analyses are conducted using a specific number of randomly selected data points from the population, taking into account time and research costs. The results obtained with the sample data are then used to predict the relationship in the population [15].

Simple linear regression analysis is used when there is a linear relationship between a single explanatory (independent) variable, denoted as *x*, and a response (dependent) variable, denoted as *y*. It is employed to predict the value of the *y* variable based on the *x* variable.

$$y = \beta_0 + \beta_1 x + \varepsilon \quad (2)$$

The equation (2) represents the equation for building a linear model. In this model, β_0 is the intercept term of the linear function, representing the point where the regression line intersects the vertical axis when $X = 0$. β_1, on the other hand, describes the slope of this function and is also known as the regression coefficient, indicating how much change in the dependent variable is associated with a one-unit change in the independent variable *x* in regression analysis. The error term ε is represented by ε [16].

When the dependent variable consists of two-choice categorical data, logistic regression analysis can be used to reveal the cause and effect relationship between the independent variables and the dependent variable [17]. The relationship between a dependent variable and independent variables is analyzed using

simple regression analysis. However, in some analyses, multiple independent variables can influence a dependent variable. In cases where multiple independent variables affect a dependent variable, a multiple regression model should be constructed [18]. Multinomial models in which one independent variable takes more than two discrete variables often deal with more complex models, such as multivariate models with many independent variables [19]. Multiple linear regression has two general purposes. One is to predict the value of the dependent variable through variables identified to affect the dependent variable. The other is to determine which independent variable or variables, believed to influence the dependent variable, have a greater impact on it and describe the relationship between them.

$$Y = b_0 + b_1 X_{i1} + b_2 x_{i2} + \ldots\ldots + b_n x_{in} + e_i \quad (3)$$

$$Y = b_0 + \sum_{k=1}^{p} b_k X_{ik} + e_i \quad (4)$$

In equations (3) and (4), the estimation of the dependent variable is calculated in multiple linear regression analysis. Here, b_0, b_1,..., b_n represent the regression coefficients [20].

2.3. Research Field

Van Lake, located in the lowest part of the closed basin, is a soda lake with a salinity rate of 2.6%. It has a surface area of 3,626 km², a volume of 607 km³, a drainage area of 12,470 km², a pH value of 9.7, and a maximum depth of 451 meters, making it the largest body of water in Turkey. Van Lake is situated within the boundaries of Van and Bitlis provinces. The borders of Van Lake are indicated in Figure 2.

Figure 2. Map of Lake Van

As Lake Van is a closed basin, the water level of the lake usually varies according to climate and seasons. Observable changes in the lake's water level are noticeable fluctuations that occur at different times, resulting in both rising and falling levels. It can be said that such changes are largely influenced by factors such as rainfall, temperature, and evaporation control [21].

2.4. Data Set

The data used in the study were obtained from various measurement stations belonging to the Meteorology 14th Regional Directorate and the General Directorate of State Hydraulic Works (DSI) 17th Regional Directorate, located within the boundaries of Van province.

Table 2. Comparison of biological and artificial neurons

Parameter	Unit	Type of Use	Institution
Rainfall	mm=kg÷m²	Independent variable	General Directorate of Meteorology
Temperature	ºC	Independent variable	General Directorate of Meteorology
Evaporation	mm	Independent variable	General Directorate of Meteorology
Wind Speed	m/sn	Independent variable	General Directorate of Meteorology
Relative Humidity	%	Independent variable	General Directorate of Meteorology

In Table 2, the parameters of rainfall, temperature, evaporation, wind speed, relative humidity, atmospheric pressure, and Lake Van water level, along with their respective units of measurement (mm for millimeters, °C for degrees Celsius, m/s for meters per second, % for percentage, hPa for hectopascals, m for meters), their purpose in the model, and their sources of acquisition are specified. These parameters were measured using stations belonging to the institutions obtained between the years 2004 and 2022, and they cover monthly data.

2.5. Data Preparation

Model development, training, comparison of obtained output values with the defined target values, and evaluation of results primarily started with the collection of input and output values from past records. The data consists of monthly measurements taken from various measurement stations belonging to the General Directorate of Meteorology in the 14th Region and the General

Directorate of State Hydraulic Works in the 17th Region, covering the years 2004-2022 within the boundaries of Van province.

In Table 3, the results of the normal distribution tests for these data are presented. The Kolmogorov-Smirnov and Shapiro-Wilk tests have been applied. According to the results of these tests, since the p-value is less than 0.05, the water level variable does not follow a normal distribution.

Table 3. Tests of normality

	Kolmogorov-Smirnov	Shapiro-Wilk
Water Level	0.001	0.004

$$P_{(avg.parameter)} = \frac{1}{n}\sum_{i=1}^{n} P_{(parameter)} \quad (5)$$

The values measured by multiple stations have been transformed into a single value as shown in Equation (5).

Here, P(parameter) represents the monthly measured values of the respective parameter, n represents the total number of stations where this parameter is measured, and $P_{(avg.parameter)}$ represents the monthly average value of this parameter. After this process, a total of 225 data points covering the years 2004-2022 were obtained. Among them, 216 data points from 2004 to 2021 were used for model development, while 9 data points from 2022 were separated to test the established models, forming two distinct groups.

Lastly, before constructing the models, the data was normalized using the adjusted minimum-maximum method to enhance the efficiency of the models, as shown in Equation (6). This normalization process ensured that the data set takes on a dimensionless form within the range of

0.1 to 0.9, aiming to improve the effectiveness of the models.

$$X_i = 0.8\frac{(X - X_{min})}{(X_{max} - X_{\min}\ )} + 0.1 \quad (6)$$

Here, X_i represents the value to be normalized, X represents the measured value, X_{min} represents the minimum value for X, and X_{max} represents the maximum value for X. The equation is used to normalize X_i within the range of 0.1 to 0.9 using the minimum and maximum values of X.

Table 4. Descriptive statistics of the data

	Mean	Median	Std. Deviation	Minimum	Maximum
Rainfall	0.2977	0.2812	0.1416	0.1000	0.9000
Temperature	0.5355	0.5510	0.2381	0.1000	0.9000
Evaporation	0.3750	0.2938	0.2436	0.1000	0.9000
Wind Speed	0.4306	0.4114	0.1448	0.1000	0.9000
Relative Humidity	0.5050	0.5227	0.1903	0.1000	0.9000
Actual Pressure	0.4932	0.4856	0.1516	0.1000	0.9000
Water Level	0.4694	0.5339	0.2386	0.1000	0.9000

In Table 4, descriptive statistics such as mean, median, standard error, and other measures have been provided for the normalized data.

3. Results and Discussion

3.1. Results of the ANN Model

In order to develop and train an ANN model in the MATLAB environment, the data needs to be classified into training, testing, and validation sets.

This classification process is generally done randomly. Out of the total 216 data points allocated for training the ANN model, 70% are assigned for learning, 15% for testing, and 15% for validation purposes.

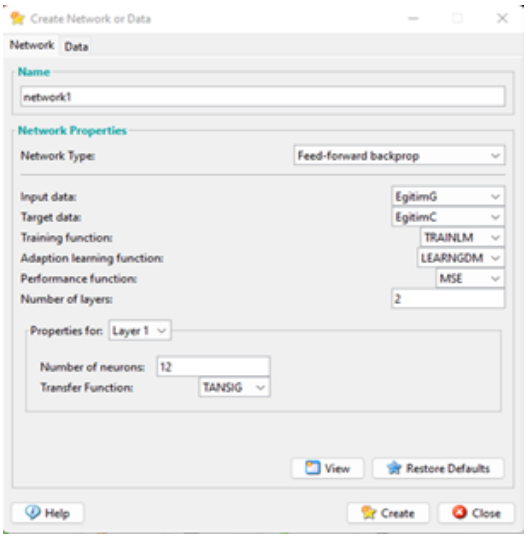

Figure 3. The characteristics of an Artificial Neural Network (ANN) structure

Figure 3 illustrates the characteristics of the network structure. Due to the nonlinear relationship between the data, a feedforward backpropagation multilayer network, which is widely used, has been preferred. In the weight determination for prediction, the "TANSIG" function, which provided the most successful results through trial and error, was selected as the activation function. Various training functions available in Matlab were tested, and it was observed that the network learned best using the "TRAINLM (Levenberg-Marquardt)" function, which was consequently chosen.

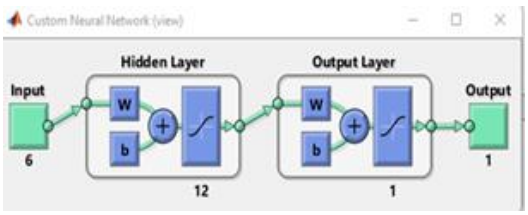

Figure 4. The structure of the ANN

The network architecture is depicted in Figure 4. It consists of 6 input data points and 1 output data point. The number of layers and hidden cells is determined as 2 and 12, respectively. These values were chosen through trial and error as they yielded the most successful results.

The network achieved a low error value of 0.0131, which indicates a high level of accuracy. The fact that this value is close to zero implies that the network has performed well. It took approximately 11 seconds for the network to reach its best result and complete the training process. The performance graph in Figure 5 illustrates how the training, validation, and testing data evolved during each iteration. According to this result, the completed model achieved its best performance at iteration 4.674.

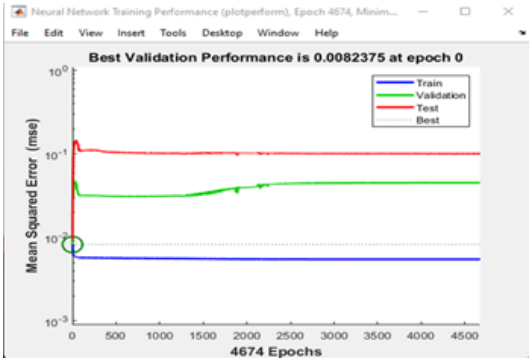

Figure 5. Performance Graph after YSA Training

Figure 6 illustrates the relationship between the input values entered into the model and the predictions made by the model. In this context, the regression (R) values for training, validation, and testing, as well as their overall value, are observed to be 0.88. Since these values are close to 1, the learning process has been successfully carried out.

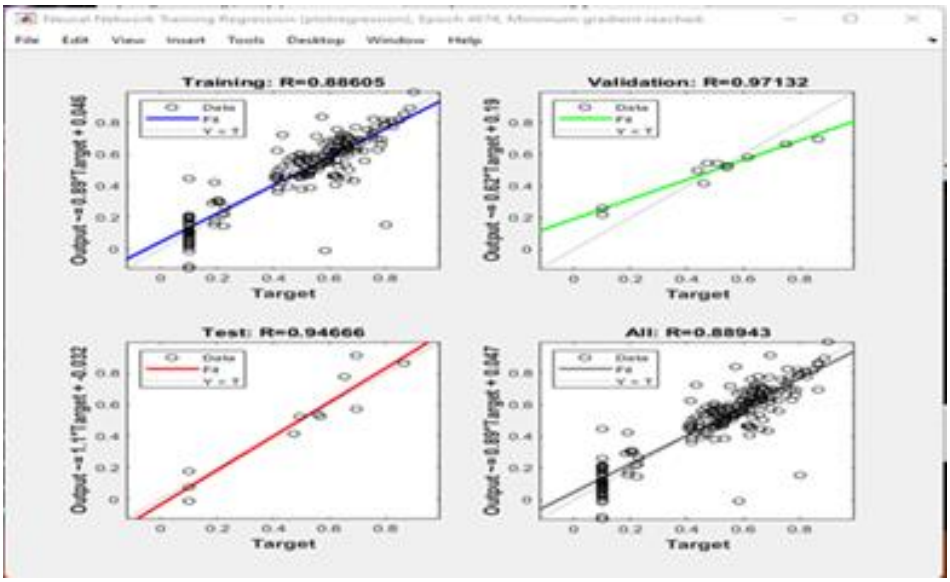

Figure 6. YSA training regression results

The water level prediction using YSA was achieved with an accuracy of 99%. The Mean Absolute Percentage Error (MAPE) was found to be very close to 0, specifically 0.34, indicating a 0.34% margin of error. The Mean Absolute Deviation (MAD) value was found to be 0.05. Having MAPE and MAD values close to 0 in predictions signifies that the network provides more realistic results.

Table 5 presents real data that has not been introduced to the model before. These data were used as input for testing the generated model. Table 6 shows the actual and predicted water levels for these data, along with the deviations between them. It is observed that the predicted values by the YSA model are very close to the actual values. For example, if the actual water level measured during a certain period is 1648.59, the YSA model predicts it as 1648.56 based on the meteorological parameters of that period. The difference between this predicted value and the actual water level is determined to be 0.0297.

Table 5. Test data

AB (hPa)	B (mm)	NN (%)	RH (m÷sn)	S (°C)	D (mm=kg÷m²)
819.62	8.90	78.44	1.83	-6.51	61.68
821.83	14.60	79.65	1.57	-3.02	22.87
818.33	38.15	77.17	2.43	-1.65	61.29
821.54	24.80	58.82	2.39	8.39	24.80
821.22	115.30	66.83	2.37	10.50	47.77
820.56	189.30	45.02	2.33	18.51	12.17
819.34	255.20	35.76	2.30	22.11	1.34
820.90	298.70	30.34	2.21	23.26	0.26
822.86	230.20	35.15	2.11	18.46	0.64

Table 6. Actual and predicted water level values

Actual Water Level (m)	Predicted Water Level (m)	|Actual - Predicted| (m)
1648.49	1648.41	0.0713
1648.49	1648.42	0.0721
1648.52	1648.46	0.0650
1648.58	1648.57	0.0120
1648.67	1648.59	0.0733
1648.66	1648.53	0.1341
1648.59	1648.56	0.0276
1648.59	1648.56	0.0297
1648.33	1648.36	0.0284

3.2. Results of the MRA Model

The 216 data points used in the training of the ANN model were analyzed using Multiple Linear Regression techniques. The independent variables chosen were precipitation, temperature, evaporation, wind speed, relative humidity, and actual pressure, while the dependent variable was the lake water level.

Table 7. Regression analysis results

Regression Statistics	
R	0.50
R^2	0.25
R-squared (Coefficient of determination)	0.23
Standard deviation	0.21
Number of observations	216

The summary of the model created using regression analysis is presented in Table 7. The R-value is observed as 0.50. The proximity of this value to 1 indicates the strength of the relationship between the variables. The coefficient of determination (R-squared) is calculated as 0.23, meaning that the independent variables can explain 23% of the variation in the dependent variable. This value is relatively low, indicating that the model's fit to the data is considered inadequate.

Table 8 presents the information regarding the p-values. The variables of actual pressure, relative humidity, wind speed, temperature and precipitation have p-values smaller than 0.05, indicating that they significantly influence the water level.

Table 8. The analysis results of the regression analysis

	p-Values
Intercept	0.000
Actual Pressure (hPa)	0.000
Evaporation (mm)	0.246
Relative Humidity (%)	0.002
Wind Speed (m/s)	0.000
Temperature (°C)	0.021
Precipitation (mm=kg/m²)	0.028

Table 9. The weight coefficients of the regression analysis

	Coefficients
Intercept Coefficient (Q)	1.185
AB	-0.631
B	-0.205
NN	-0.575
RH	-0.438
S	0.104
Y	0.321

The coefficients of the variables obtained from the regression analysis are shown in Table 9. These calculated coefficients indicate how much the respective parameters affect the water level.

$$Y = Q + (-0.631 * AB) + (-0.205 * B) + (-0.575 * NN) + (-0.438 * RH) + (0.104 * S) + (0.321 * Y) \quad (7)$$

Table 10. The prediction results of the regression analysis

Actual Water Level (m)	Predicted Water Level with CRA (m) |	|AWL- PWL|(m)
1648.49	1648.07	0.4168
1648.49	1647.98	0.5093
1648.52	1648.00	0.5157
1648.58	1647.95	0.6343
1648.67	1647.95	0.7183
1648.66	1647.99	0.6721
1648.59	1648.03	0.5577
1648.59	1648.01	0.5712
1648.33	1647.97	0.3603

The CRA equation is formulated as Equation (7). In this equation, the effects of independent variables on the dependent variable are determined. For example, a unit change in the temperature variable will result in a 0.104 change in the water level. By substituting the parameter values into the equation, the water level value is calculated. Using the test data in Table 5, the water level is predicted using this equation. Table 10 shows the actual and predicted water levels for these data, along with the deviations. For instance, if the measured water level in a certain period is 1648.49, the CRA model predicts it as 1648.07 based on the meteorological parameters for that period. The difference between the predicted and actual water level values is determined as 0.4168.

3.3. Comparison of ANN and MRA Models

In this study, two different models, ANN and MRA, were developed using the same dataset of 216 samples. Table 11 presents the performance results of the two models. Upon completion of model development, the R-squared values for ANN and MRA were found to be 0.88 and 0.50, respectively. The MAPE values were 0.34 for ANN and 3.34 for MRA, while the MAD values were 0.57 for ANN and 0.10 for MRA. Based on these results, the error rate of the ANN model was calculated as 0.34%, while the error rate of the MRA model was 3.34%. The mean absolute deviation (MAD) was found to be 0.05 for ANN and 0.10 for MRA. According to the MAD results, it was observed that the ANN model provided predictions closer to the actual water levels compared to the MRA model. The R-squared results of both models were compared to measure the level of relationship between variables. The comparison results indicated that the ANN model had a significantly higher level of relationship between variables compared to the MRA model. This value is expected to be close to 1 at all times.

Table 11. The performance results of the YSA and MRA models

Performance	ANN	MRA
R	0.88	0.50
MAPE (%)	0.34	3.34
MAD	0.05	0.10

The developed models were tested by predicting the water level using 9 identical datasets. The predicted water level values obtained from the test results were compared with the actual water level values.

Table 12. YSA and MRA Comparison

Actual Water	Level ANN Water	Level MRA Water	|AW-ANN|	|AW-MRA|
1648.49	1648.41	1648.07	0.0713	0.4168
1648.49	1648.42	1647.98	0.0721	0.5093
1648.52	1648.46	1648.00	0.0650	0.5157
1648.58	1648.57	1647.95	0.0120	0.6343
1648.67	1648.59	1647.95	0.0733	0.7183
1648.66	1648.53	1647.99	0.1341	0.6721
1648.59	1648.56	1648.03	0.0276	0.5577
1648.59	1648.56	1648.01	0.0297	0.5712
1648.33	1648.36	1647.97	0.0284	0.3603

Table 12 displays the actual water level values, the predicted values from both models, and the absolute differences between the actual and predicted values. For example, for a specific period, if the actual water level is 1648.49, the YSA model predicts it as 1648.41, and the MRA model predicts it as 1648.07. The absolute difference between the YSA prediction and the actual value is 0.0713, while the absolute difference between the MRA prediction and the actual value is 0.4168. When comparing these two differences, it can be observed that the YSA model provides predictions that are closer to the actual values compared to the MRA model.

4. Conclusion and Suggestions

One of the sciences developed to study phenomena in nature and solve existing or potential problems is the science of data analysis. The science of data analysis aims to explain the subject with a certain probability and a limited number of observations using methods and theories appropriate to the data structure and to shed light on future research. In nature, there is a lot of data in every field of science, but it is important to know how to use these data and produce new information from them by analyzing them [22]. In this study, the relationship between changes in lake water level and some meteorological parameters was analyzed using ANN and MRA models, which are machine learning methods.

The results of the study indicate a close relationship between changes in the lake water level and meteorological parameters. The analyses conducted have shown that meteorological factors such as precipitation, temperature, evaporation, wind speed, relative humidity, and atmospheric pressure play a significant role in explaining the variations in the lake water level. The artificial neural network model used in this study has yielded highly accurate results in predicting the lake water level. With its ability to model complex relationships, the artificial neural network has achieved high levels of accuracy in predicting the lake water level. Additionally, it has been observed that artificial neural networks can be applied not only for temporal but also for spatial predictions of the lake water level. Furthermore, multiple linear regression analysis has been employed in the study to examine the relationship between independent variables and changes in the lake water level. This analysis has provided a more detailed understanding of the effects of meteorological parameters on the lake water level. However, it has been observed that the predictions obtained through the artificial neural network model offer more realistic results compared to multiple linear regression analysis.

The findings of this study demonstrate that changes in the water level of Lake Van are associated with meteorological factors and can be accurately predicted. These results will contribute to a better understanding of lake water level variations for decision-makers and researchers in

areas such as sustainable water resource management, environmental planning, and climate change. They will also assist in forecasting future scenarios related to lake water level changes.

In conclusion, this study examined the relationship between the lake's water level and meteorological parameters, and this relationship was evaluated through specific statistical analyses. Statistical power can be assessed based on the results of these analyses. Specifically, it has been demonstrated how accurate the artificial neural network model's predictions are and how it outperforms multiple linear regression analysis. This can be a significant factor in demonstrating the statistical strength of the study.

Contributions of the authors

The authors' contributions to the study are equal.

Conflict of Interest Statement

There is no conflict of interest between the authors.

Statement of Research and Publication Ethics

The study is complied with research and publication ethics

This study was conducted with the aim of examining and predicting the changes in the water level of Lake Van. The main objective of the study was to determine the effects of meteorological factors on the lake water level and to create a prediction model using these effects.

References

[1] M. F. Keskenler and E. F. Keskenler, "Geçmişten Günümüze Yapay Sinir Ağları," *Takvimi Vakiye*., vol. 5, no. 2, pp. 8–18, 2017.

[2] M. Çobaner, E. Babayiğit, and B. Babayiğit, "Meteorolojik Veriler Kullanılarak Yeraltı Su Seviyesinin Genetik Programlama ile Tahmini," *Ömer Halisdemir Üniv. Mühendis. Bilim. Derg.*, vol. 5, no. 2, pp. 177–187, 2016.

[3] Y. Damla, T. Temiz, and E. Keskin, "Yapay Sinir Ağı Kullanılarak Su Seviyesinin Tahmin Edilmesi: Yalova Gökçe Barajı Örneği," *Kırklareli Üniversitesi Mühendislik ve Fen Bilimleri Dergisi*, vol. 6, no. 1, pp. 32–49, 2020.

[4] E. İspir, "Hatay Amik Ovası Kumlu Bölgesindeki Yeraltı Suyu Seviyesinin Yapay Sinir Ağları Yöntemi ile Tahmini," Iskenderun Technical University, Turkey, 2017.

[5] A. Altunkaynak and Z. Şen, "Fuzzy logic model of lake water level fluctuations in Lake Van, Turkey," *Theor. Appl. Climatol.*, vol. 90, no. 3–4, pp. 227–233, 2007.

[6] P. Panyadee, P. Champrasert, and C. Aryupong, "Water level prediction using artificial neural network with particle swarm optimization model," in *2017 5th International Conference on Information and Communication Technology (IcoIC7)*, 2017.

[7] V. Nabiyev and A. K. Erümit, Eds., *Eğitimde Yapay Zeka Kuramdan Uygulamaya*. Ankara Pegem Akademi Yayıncılık, 2020.

[8] S. Haykin, *Neural networks: Comprehensive foundation*, 2nd ed. Piscataway, NJ: I.E.E.E. Press, 1999.

[9] E. Ersoy and Ö. Kartal, "Yapay Sinir Ağları ve İnsan Beyni," *İnsan ve Toplum Bilimleri Araştırmaları Dergisi II*, vol. 1, no. 2, pp. 188–205, 2012.

[10] M. Caner and E. Akarslan, "Mermer Kesme İşleminde Spesifik Enerji Faktörünün ANFIS ve YSA Yöntemleri ile Tahmini," *Pamukkale Üniversitesi Mühendislik Bilimleri Dergisi*, vol. 15, no. 2, pp. 221–226, 2009.

[11] F. Sönmez Çakır, *Yapay Sinir Ağları Matlab Kodları ve Matlab Toolbox Çözümleri*. Turkey: Nobel Akademik Yayıncılık, 2020.

[12] B. Çil, *İstatistik*. Ankara: Detay Yayıncılık, 2014.

[13] B. A. Köksal, *İstatistik Analiz Metotları*. Istanbul: Çağlayan Kitapevi, 2013.

[14] S. Kılıç, "Doğrusal Regresyon Analizi," *İstatistiki İfadeyle*, vol. 3, no. 2, pp. 90–92, 2013.

[15] F. Yüzük, "Çoklu Regresyon Analizi ve Yapay Sinir Ağları ile Türkiye Enerji Talep Tahmini," Cumhuriyet University Institute of Social Sciences, Turkey, 2019.

[16] G. James, D. Witten, T. Hastie, and R. Tibshirani, *An introduction to statistical learning: With applications in R*, 1st ed. New York, NY: Springer, 2013.

[17] H. Eygü, "Covid-19 Sürecinde Üniversite Öğrencilerinin Uzaktan Eğitim Eğiliminin Araştırılması," *Mehmet Akif Ersoy Üniversitesi İktisadi ve İdari Bilimler Fakültesi Dergisi*, vol. 10, no. 2, pp. 882-903, 2023.

[18] C. Okutkan, "Borsa İstanbul Şirketlerinin Hisse Senedi Getirilerinin Yapay Sinir Ağları ve Çoklu Regresyon Yöntemleri Kullanarak Analizi," Kocaeli University Graduate School of Natural and Applied Sciences, Turkey, 2014.

[19] H. Eygü, *Çözümlü güncel örneklerle olasılık ve istatistik*. Ankara: Nobel Yayınları, 2020.

[20] M. Öztürkcan, *Regresyon analizi*. 2009.

[21] M. Z. Yıldız, "Kapalı Havza Göllerinde Seviye Değişimlerinin Kıyı Yerleşmelerine Etkisi: Van Gölü Örneği," *Fırat Üniversitesi Sosyal Bilimler Dergisi*, vol. 15, no. 1, pp. 15–31, 2005.

[22] G. A. A. Mulla, Y. Demir, and M. M. Hassan, "Combination of PCA with SMOTE Oversampling for Classification of High-Dimensional Imbalanced Data," *BEU Journal of Science*, vol. 10, no. 3, pp. 858-869, 2021.

Bitlis Eren Üniversitesi Fen Bilimleri Dergisi
BİTLİS EREN UNIVERSITY JOURNAL OF SCIENCE
ISSN: 2147-3129/e-ISSN: 2147-3188
VOLUME: 12 NO: 4 PAGE: 1041-1053 YEAR: 2023
DOI:10.17798/bitlisfen.1317696

Parameter Extraction of PV Solar Cells Using Metaheuristic Methods

Seyit Alperen CELTEK[1], Seda KUL[2*]

[1]*Department of Energy Systems Engineering, Karamanoglu Mehmetbey University, Karaman, Türkiye*
[2]*Department of Electrical Electronics Engineering, Karamanoglu Mehmetbey University, Karaman, Türkiye*
(ORCID: 0000-0002-7097-2521) (ORCID: 0000-0001-8278-4723)

Keywords: Solar energy, PV parameter, Meta-heuristic, Single Diode PV, Improved Grey Wolf Optimizer.

Abstract

Due to the increasing crises in energy and environmental factors, the importance of renewable energy is increasing. However, it is gaining importance in developing photovoltaic energy systems. Therefore, great efforts are made to maximize success in accurately modeling PV parameters. Parameter estimation is a complex problem and requires advanced design tools such as optimization techniques because the current voltage (I–V) characteristics of PVs are nonlinear. This study investigates the best technique to estimate the parameters obtained in single-diode and double-diode cases. The Grey Wolf Optimization (GWO), Improved Grey Wolf Optimization (IGWO), Sine Cosine Algorithm (SCA), Whale Optimization Algorithm (WOA), and Multi-Verse Optimizer (MVO) are the algorithms used in this paper. Apart from the literature, this study considers that the PV parameter extraction problem is not just an offline optimization problem but also a real-time optimization issue. The performance of all methods has been compared with experimental data. The lowest error on minimum iteration and highest convergence accuracy have been achieved for offline optimization by using IGWO. The results clearly state that the IGWO is not usable in real-time applications even though IGWO is the best optimizer in offline optimization.

1. Introduction

The reasons such as the energy and climate crisis in recent years, the limited use of fossil fuels, acid rain, carbon emission, and negative ozone changes have highlighted the importance of renewable and clean energy. Long-term solutions and research are needed before environmental problems become more serious and irreversible problems. For this reason, renewable energy sources such as the sun [1], water [2], and wind [3] and their sustainable application areas are increasing daily. In addition to the increasing use of clean energy in industry, it is becoming increasingly common in rural and urban areas. This widespread using makes solar systems more and more popular due to their potential advantages, ease of installation, and efficiency.

Solar systems are one of the growing systems in the renewable energy sector. Solar energy systems are one of the most common methods of generating electricity through photovoltaic (PV) modules. Besides, PV systems are preferred due to low pollution, noiseless operation, and widespread distribution. Sunlights are converted into electricity using semiconductor systems [4]. The correct modeling and optimization processes of these systems are the factors that directly affect the efficiency and operating characteristics of the systems.

Photovoltaic systems have nonlinear characteristics depending on variables such as semiconductor material characteristics and environmental factors such as temperature. Therefore, in PV studies, it is essential to compute the correct circuit values to obtain the correct cell characteristics and operate the system efficiently [5]. In recent

*Corresponding author: sedakul@kmu.edu.tr
Received: 20.06.2023, Accepted: 23.11.2023

studies on this subject, optimization methods are used seriously as well as numerical methods. The reason for this is that in addition to the values such as open circuit voltage (V_{oc}), maximum power (P_{mpp}), short circuit current (I_{sc}), the current and voltage temperature coefficients (K_v; K_i) given in the datasheet, the actual circuit parameters used in the system are determined. It is expected to be calculated by the manufacturers. These parameters are photocurrent (I_{ph}), the ideality coefficients of diode (n), saturation current (I_0), shunt resistance (R_{sh}) and series resistance (R_s) [6].

Models used to show the behavior characteristics of PV models are single-diode (SDM) and double-diode (DDM) models [7], [8]. In the estimation and optimization processes, there are five values in the SDM and seven values for the DDM [6]. Many methods have been used in finding these parameters and obtaining the optimum parameter values by determining a particular objective function, and studies have been applied on this subject.

Different optimization studies on the PV module have been carried out with different methods in recent studies in the literature. Due to the weaknesses of deterministic methods, optimization algorithms have started to be used to determine unknown values of PV modules in studies. These are maximum power point tracking (MPPT), parameter estimation, maximum efficiency, and minimum cost optimization studies. In [6], the flexible particle swarm optimization (FPSO) based approach is used to extract the values of PV cell models to arrive the maximum power point. It is compared with known methods to demonstrate the proposed adequacy of the approach. In another parameter estimation study [9], the Stochastic Fractal Search (SFS) technique was used. The SFS-based method has been tested for different situations using the SDM and DDM to evaluate its performance. Whippy Harris Hawks Optimization (WHHO) [10] was preferred because of its effectiveness in practical application. According to the literature research, the optimization approaches used to extract the PV parameters are Harmony Search-based Algorithm (HS) [11], Simulated Annealing (SA) [12], Bird Mating Optimizer (BMO) [13], Genetic Algorithm (GA) [14], Teaching Learning Based Optimization (TLBO) [15], [16], Artificial Bee Colony Algorithm (ABC) [17], Mine Blast Algorithm (MBA) [18], Moth–Flame Optimizer (MFO) [19], Whale Optimizer [20], Flower-Pollinating Optimization (FPO) [21], Cat Swarm Optimization (CSO) [22], water cycling optimization [23], Wind Driven Optimization (WDO) [24], Jaya optimization [25], Sunflower Optimization (SFO) [26], Enriched HHO (EHHO) [27], Improved Opposition-Based Whale Optimization Approach (IWOA) [28], Slime Mould Optimization (SMA) [29], Springy whale optimization (SWOA) [30], Bald Eagle Search (BES) Algorithm [31], Improved Marine Predators Algorithm [32], Jellyfish Search Optimizer [33], War Strategy Optimization [34], Improved Honey Badger Algorithms [35], Musical chairs algorithm [36], Honey Badger Algorithm [37], Artificial Ecosystem Optimization Algorithm [38], Tuna Swarm Optimization [39], respectively.

Nowadays, where renewable energy is essential, the role of photovoltaic (PV) systems in energy production is increasing. However, optimizing accurate parameters is of great value for these systems to work effectively and efficiently. In this context, getting the PV module design with optimized parameters increases energy and minimizes system costs. Extracting this output from the traditional method is complex and time-consuming, so using metaheuristic techniques in this field has great potential.

When the methods and performance evaluations used in studies on obtaining the parameters of PV models in the literature are examined, it is seen that there are still unused methods for obtaining values in SDM and DDM. Moreover, along with the literature, this study investigates the best method for real-time estimation of PV parameters.

This study aims to examine five different metaheuristics to extract the release of PV module design: GWO, IGWO, MVO, WOA, and SCA. Additionally, whether these techniques are suitable for real-time applications will be evaluated within the scope of this study. The main contributions of this study are listed below:

- IGWO was first used to solve SDM (five unknown parameter extraction) and DDM (seven unknown parameter extraction).
- The PV unknown parameter extraction problem is considered a real-time problem.
- For this problem, IGWO, GWO, SCA, WOA, and MVO calculation time is calculated.
- The method that provides the best results in the shortest time is investigated among the five methods.

The rest of the paper has these sections: The SDM and DDM is explained in Section 2. The meta-heuristic methods that are implemented is described in material and methods which is Section 3. Section 4 demonstrates the results and discussion of the

optimization data. Section 5 concludes the paper with discussion and future works.

2. Problem Formulation

Since PV modules are semiconductor structures, I-V structures are characteristically similar to diodes. Therefore, the parameters are found as different values over time due to the nonlinear characteristic of the PV structure. Therefore, SDM and DDM are the most preferred models in equivalent circuit modeling [40].

2.1. Single Diode

Figure 1 shows the equivalent circuit of the SDM. This circuit includes the following circuit elements, respectively: a current source, a diode in parallel with the current source, a semiconductor, and a shunt ($\boldsymbol{R_{sh}}$) and a series ($\boldsymbol{R_s}$) resistor that models the ohmic losses in leakage current [41].

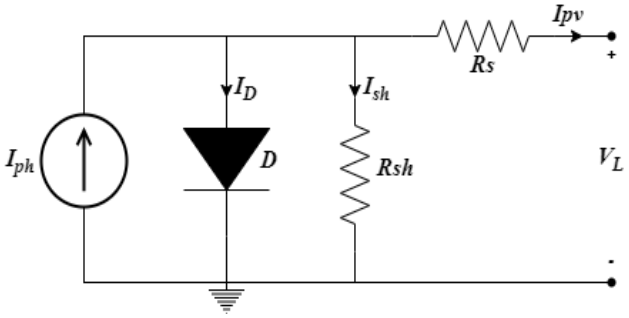

Figure 1. Single diode model of PV equivalent circuit.

The output current (I_{pv}) can be formulated as in Eq.1 [42]:

$$I_{pv} = I_{ph} - I_D - \left(\frac{V_{pv} + I_{pv}R_s}{R_{sh}}\right) \quad (1)$$

where V_{pv} is the output voltage. The current (I_D) flowing through the diode is expressed as in Eq.2 [42]:

$$I_D = I_0\left[exp\left(\frac{V_{pv} + I_{pv}R_s}{V_t\alpha}\right) - 1\right] \quad (2)$$

α is the ideality coefficient of diode. The thermal voltage (V_t) used in Eq.2 is calculated as in Eq.3 [42]:

$$V_t = \frac{N_s kT}{\mathrm{q}} \quad (3)$$

where k, q, and T are the Boltzmann constant, electron charge, and operating temperature, respectively. The photo-generated current (I_{ph}) is shown as Eq.4 [42]:

$$I_{ph} = I_{ph-STC} + K_i(T - T_{STC}) \times \left(\frac{G}{G_{STC}}\right) \quad (4)$$

where T_{STC}, I_{ph-STC} and G_{STC} are the temperature at standard test condition, photocurrent at standard test condition, and irradiance at standard test condition ($1000W/m^2$), respectively. I_{ph-STC} is calculated as Eq.5 [42]:

$$I_{ph-STC} = I_{sc-STC}\left(\frac{R_s + R_{sh}}{R_s}\right) \quad (5)$$

The reverse saturation current (I_0) is calculated as follows [42]:

$$I_0 = \frac{I_{ph-STC} - (V_{oc-STC}/R_{sh})}{exp\left(\frac{V_{oc-STC}}{\alpha V_{t-STC}}\right) - 1} \quad (6)$$

Based on all these calculations, five parameters (I_{ph}, I_0, α, R_s and R_{sh}) requires optimization for the single-diode model.

2.2. Double Diode

The SDM does not give good results, especially in low irradiance [37]. Therefore, the DDM is preferred to increase the calculation accuracy. Figure 2 shows the equivalent circuit of DDM. As illustrated in the figure, the first of the two diodes acts as a rectifier and the second account for the current effect from recombination effects. In this way, more precise I-V characteristics are obtained.

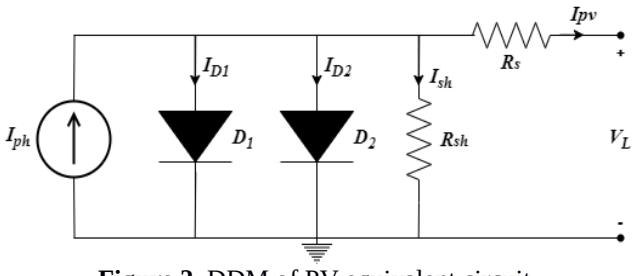

Figure 2. DDM of PV equivalent circuit.

The output current of the system (I_{pv}) is shown as:

$$I_{pv} = I_{ph} - I_{D1} - I_{D2} - \left(\frac{V_{pv} + I_{pv}R_s}{R_{sh}}\right) \quad (7)$$

Here I_{D1}, I_{D2} are diode currents and calculated like Eq.8 and Eq.9:

$$I_{D1} = I_{01}\left[exp\left(\frac{V_{pv} + I_{pv}R_s}{V_t\alpha_1}\right) - 1\right] \quad (8)$$

$$I_{D2} = I_{02}\left[exp\left(\frac{V_{pv} + I_{pv}R_s}{V_t\alpha_2}\right) - 1\right] \quad (9)$$

where V_t, V_{pv} are the same in Eq.2. The reverse saturation currents in each diode are calculated as follows:

$$I_{01} = \frac{I_{ph-STC} - (V_{oc-STC}/R_{sh})}{exp\left(\frac{V_{oc-STC}}{\alpha_1 V_{t-STC}}\right) - 1} \quad (10)$$

$$I_{02} = \frac{I_{ph-STC} - (V_{oc-STC}/R_{sh})}{exp\left(\frac{V_{oc-STC}}{\alpha_2 V_{t-STC}}\right) - 1} \quad (11)$$

Based on all these calculations, seven parameters (I_{ph}, I_{01}, I_{02}, α_1, α_2, R_s and R_{sh}) requires optimization for the double-diode model.

2.3. Real Time Optimization for PV

The optimization time must be short in the PV panel production process for several reasons. This can both reduce costs and increase production capacity and product quality. The first reason is that PV production consists of certain stages, and correct optimization of each stage can increase the production speed. A rapid optimization process reduces delays on the production line and shortens the overall production time.

The second reason is that the materials used to manufacture solar panels are generally costly. Rapid optimization can minimize material waste, which in turn can reduce costs by optimally optimizing material usage. The third reason is that during the production process, it is essential to control the quality of the panels. Fast optimization processes enable immediate intervention when a production error is detected, thus reducing the number of defective products. Another reason is that solar panel demand may vary depending on technological developments or economic factors. Rapid optimization allows the production process to adapt to such demand changes quickly. Any delay or disruption in the production process can result in additional costs, from energy usage to labor. A fast and effective optimization process can avoid these extra costs.

3. Material and Methods

Section 3 discusses the algorithms used in this paper with their mathematical model.

3.1. Grey Wolf Optimizer (GWO)

The GWO is a heuristic algorithm developed in 2014 [40]. The hunting behavior of grey wolves inspires the GWO algorithm. They are hierarchically classified into alpha, beta, delta, and omega groups. The alpha team is a dominant species responsible for making decisions such as hunting, sleeping places, and waking time. The beta group, the second layer of the hierarchy, assists the alpha wolves in making decisions and other activities. The delta group and the omega group represent the lowest-ranked grey wolves.

The hunting is a fascinating social behavior of grey wolves alongside the social interactions of wolves. To design GWO, First, we need to define the social hierarchy of wolves. The best, second, third, and worst candidate solutions are alpha, beta, delta, and omega. There are three main parts of the hunting method, the encircling prey, the hunting, and the attacking prey.

The grey wolf can randomly update its position around its hunt using Eq. 12 and 13. The encircling prey can be formulated as below:

$$D = \left|CX_p(t) - X(t)\right| \quad (12)$$

$$X(t+1) = \left|X_p(t) - AD\right| \quad (13)$$

Here, t symbolizes the iteration value, A and C represent the coefficients, Xp the location of the hunt, X the location of an agent. The A and C are calculated as follows:

$$A = |2ar_1 - a| \quad (14)$$

$$C = |2ar_2| \quad (15)$$

The a is the parameter that linearly decreases from 2 to 0 by the iterations. The r_1 and r_2 are random values in the range of [0, 1].

α, β and δ species of grey wolves have extraordinary hunting abilities. They know the current location of their prey. Therefore, the best three solution candidates are recorded, and the other wolves are allowed to update their locations relative to the positions of the best search wolves using below Eq. 16-18:

$$\begin{aligned} D_a &= |C_1X_a - X| \\ D_\beta &= \left|C_1X_\beta - X\right| \end{aligned} \quad (16)$$

$$D_\delta = |C_1 X_\delta - X|$$

$$\begin{aligned} X_1 &= |X_a - A_1 D_a| \\ X_2 &= |X_\beta - A_2 D_\beta| \\ X_3 &= |X_\delta - A_3 D_\delta| \end{aligned} \quad (17)$$

$$X(t+1) = \frac{X_1 + X_2 + X_3}{3} \quad (18)$$

At the exploitation (attacking prey) stage, a value is reduced, and therefore the limit of variation of A is reduced. When A has random values in the [-1,1] range, the search agent's next position will be anywhere between its current location and the hunt. Detailed coverage of GWO can be found in [40].

3.2. Improved Grey Wolf Optimizer (IGWO)

IGWO is designed to minimize the imbalance between the exploration and exploitation of the GWO method. The IGWO algorithm is inspired by the dimension-learning-based-hunting (DLH) wolves in nature.

In the beginning, wolves (N: number of agents) are randomly distributed in the search space in the limit of $[l_i, u_j]$.

$$X_{ij} = I_j + rand_j\,[0,1]\left(u_j - l_j\right) \quad i \in [1, N] \quad , \quad j \in [1, D] \quad (19)$$

$X_i(t) = \{X_{i1}, X_{i2}, \dots, X_{iD}\}$ represents the i^{th} position in the t^{th} iteration (D=dimension). The population is recorded in a matrix with N rows and D columns. In the movement phase, The IGWO computes the next position of the wolf $X_i(t)$. For this computation, IGWO uses the wolf's different neighbors and a randomly selected agent from the matrix. The $R_i(t)$ is indicates the radius between the current location $X_j(t)$ and the location of the candidate $X_{j_{GWO}}(t+1)$. The $R_i(t)$ is computed by Eq. 20.

$$R_i(t) = \left|\left| X_j(t) - X_{j_{GWO}}(t+1) \right|\right| \quad (20)$$

$$N_i(t) = \left\{ X_j(t) \middle|\, D_i(X_j(t), X_j(t)) \le R_i(t),\ X_j(t) \in Matrix \right\} \quad (21)$$

The $N_i(t)$ is the neighbor of $X_j(t)$. It is calculated by Eq. 21. Here, D_i is the Euclidean interval between $X_j(t)$ and $X_i(t)$.

$$X_{i_{DLH},d}(t+1) = X_{i,d} + rand[0,1]\left(X_{n,d}(t) - X_{r,d}(t)\right) \quad (22)$$

$X_{i_{DLH},d}(t+1)$ is the new position of DLH based model, calculated using Eq. 23. Here, n is the number of wolves, and d is the dimension.

$$X_i(t+1) = \begin{cases} X_{i_{GWO}}(t+1), & if\ f\left(X_{i_{GWO}}(t+1)\right) < f\left(X_{i_{DLH}}(t+1)\right) \\ X_{i_{DLH}}(t+1), & otherwise \end{cases} \quad (23)$$

Detailed coverage of IGWO can be found in [41].

3.3. Multi-Verse Optimizer (MVO)

MVO is an optimization method inspired by multi-verse theory [42]. According to multi-verse theory, it is believed that there is more than one big bang theory [43] that accepts the universe started with a explosion and each explosion causes the birth of a universe [44]. The MVO method considers each solution candidate as a universe. Also, MVO assumes that each parameter in the solution candidate is a member in that universe. The MVO method assigns each solution a value called the inflation rate. The inflation parameter is a value to the fitness function of the solution candidate.

There are three concepts in the MVO method: white holes, black holes, and wormholes. These three concepts are used in order to explore search spaces by MVO. If the inflation rate is high, the white hole probability is high, and the black hole probability is low. The wormholes are used for the random movement of objects toward the best universe.

The white/black hole tunnels are modeled by the roulette wheel mechanism. In each iteration, the universes are ranked according to their inflation parameter, and one is chosen as a white hole. The solution matrix (Universe-U) is calculated as Eq. 24:

$$U = \begin{matrix} X_1^1 & \dots & X_1^d \\ \vdots & \vdots & \vdots \\ X_n^1 & \dots & X_n^d \end{matrix} \quad (24)$$

where d and n symbolise the amount of variables and universes. X_i^j symbolizes the j^{th} parameter of the i^{th} universe. Ui: universe i, NI: normalized inflation rate.

$$X_i^j = \begin{cases} X_k^j r_1 < NI(Ui) \\ X_k^j r_1 \ge NI(Ui) \end{cases} \quad (25)$$

The random number is symbolized by r_1 [0,1]. $X_k^j r_1$ is the solution candidate by the roulette wheel mechanism method.

Wormhole tunnels are assumed to be between a universe and the best universe created to provide local varies for each universe and have a high probability of improving the inflation parameter. The formulation of this mechanism is as follows:

$$X_i^j = \begin{cases} X_j + TDR\left((ub_j - lb_j)r_4 + lb_j\right) r_3 < 0.5 & r_2 < WEP \\ X_j - TDR\left((ub_j - lb_j)r_4 + lb_j\right) r_3 \geq 0.5 & r_2 < WEP \\ X_i^j & r_2 < WEP \end{cases} \quad (26)$$

X_j shows the j^{th} parameter of the best universe, *TDR* and *WEP* are coefficients, lb_j and ub_j indicate the minimum limit of j^{th} variable X_i^j indicates the j^{th} parameter of i^{th} universe, and r_2, r_3, and r_4 are random values in the range of [0, 1].

$$WEP = min + l\left(\frac{max - min}{L}\right) \quad (27)$$

where *min*=0.2 and *max*=1, *l*=iteration, and *L*= the maximum iteration.

$$TDR = 1 - \left(\frac{l^{1/p}}{L^{1/p}}\right) \quad (28)$$

where p=6 represents the exploitation accuracy. Detailed coverage of MVO can be found in [42].

3.4. Whale Optimization Algorithm (WOA)

The WOA approach is inspired by humpback whales (Megaptera novaeangliae) [45]. Megaptera novaeangliae have specific hunting techniques called bubble-net feeding [46]. They prefer to hunt little prey by creating bubbles [47]. There are three main stages in the WOA; encircling prey, spiral bubble-net feeding maneuver, and search for prey.

The WOA algorithm assumes that the optimum value is the prey in the encircling prey stage. Thus, every search agent tries to reach the optimal value by Eq. 29.

$$D = \left|CX_p(t) - X(t)\right| \quad (29)$$

$$X(t+1) = \left|X_p(t) - AD\right| \quad (30)$$

where X_p the location of the best solution candidate, $X(t)$ is the location of a search agent in the t^{th} iteration. The A and C values are coefficients calculated in Eq. 31 and 32, respectively. In these equations, a is the value linearly decreased from 2 to 0, and r is the random value between 0 and 1.

$$A = |2ar_1 - a| \quad (31)$$

$$C = |2ar_2| \quad (32)$$

The second main step of WOA is the bubble net attacking stage, which is an exploitation phase. The humpback whale attacks prey by using a Shrinking encircling mechanism. The shrinking encircling mechanism is mathematically formulated as Eq. 33.

$$X(t+1) = D'e^{bl}cos(2\pi l) + X(t), \quad D' = X_p(t) - X(t) \quad (33)$$

where b indicates the constant value, the b value defines the size of the logarithmic spiral. The l is a random value range of [−1,1]. In the WOA, there is a probability of 50% for updating the location of whales. WOA chooses between the shrinking encircling mechanism or the spiral model as Eq. 34. (p: random number)

$$X(t+1) = \begin{cases} X_p(t) - AD & if\ p < 0.5 \\ D'e^{bl}\ cos(2\pi l) + X(t) & if\ p \geq 0.5 \end{cases} \quad (34)$$

The last step of WOA is the search for the hunt stage, which is the exploration phase. The WOA explores the search spaces using Eq. 29-30. Detailed coverage of WOA can be found in [45].

3.5. Sine Cosine Algorithm (SCA)

The SCA is a metaheuristic method proposed by [48]. Initial, the SCA produces a random set of solutions. Then, according to its objective function value, it chooses the best individual solution as a target for other solutions. Then, each individual in the first population updates their location concerning the best solution using Eq. 35-36.

$$X_i^{t+1} = X_i^T + r_1 \sin r_2 \left|r_3 P_i^t - X_i^T\right| \quad (35)$$

$$X_i^{t+1} = X_i^T + r_1 \cos r_2 \left|r_3 P_i^t - X_i^T\right| \quad (36)$$

where X_i^T is the candidate solution of the population on the t^{th} iteration and P_i^t is the best solution obtained. The r_1, r_2 and r_3 are the random values.

$$X_i^{t+1} = \begin{cases} X_i^T + r_1 \sin r_2 \ |r_3 P_i^t - X_i^T|, r_4 < 0.5 \\ X_i^T + r_1 \cos r_2 \ |r_3 P_i^t - X_i^T|, r_4 \geq 0.5 \end{cases} \quad (37)$$

The parameter r_1 determines the updated direction in the gap between or outside the best solution. The r_2 parameter determines the update distance based on the best solution. The r_3 parameter introduces a random weight to emphasize stochastically ($r_3 > 1$) or lessen ($r_3 < 1$) the impact of the target in defining distance. The parameter r_4 switches equally between the sine and cosine values in Eq. 37.

$$r_1 = a - t\,\frac{a}{T} \quad (38)$$

The sine and cosine spacing is reduced during optimization using Eq. 38 to achieve a proper balance between exploration and exploitation in SCA. The t, T, and a symbolize the current iteration, maximum iteration, and constant. Detailed coverage of SCA can be found in [45], [48].

3.5. Sine Cosine Algorithm (SCA)

This section introduces the fitness function and solution clusters for the PV parameter extraction issue. The unknown PV module parameters are computed using a fitness function defined based on the solution cluster. The solution cluster consists of unknown PV module parameters and affects the fitness function value.

There are five parameters in the solution cluster for the SDM $\{I_{ph},\ I_0,\ N_s,\ R_s,\ R_{sh}\}$ while double diode cluster $\{I_{ph},\ I_1,\ I_2,\ N_1,\ N_2,\ R_s,\ R_{sh}\}$ consists of seven parameters. This paper uses an error function to extract the parameters correctly. An error function depicts the difference between the computed and measured data. This paper considers the error function as the fitness function (objective function). The objective function of PV parameter estimation could be described like the mean square error between the computed and measured currents, as shown in Eq. 39. (N: number of measured points, FF: fitness function)

$$FF = \frac{\sum_{k=1}^{N} (I_{measured} - I_{computed})^2}{N} \quad (39)$$

The measured data used in this study is referred from [49].

4. Experiment and Results

Section 4 presents the case studies to evaluate the IGWO based PV parameter extraction model performance. The cases of the SDM and the DDM are investigated. The real measurement data is used to compare the results. The output is explained with graphs and tabular forms.

This study has written all optimization methods on the MATLAB platform. The accuracy of each method has been evaluated with CEC benchmark (Congress of Evolutionary Computation) functions [50]. The simulations have been performed using an I7 7500U Intel 2.7 GHz and 16 GB RAM. Each code has run 25 times to obtain the main results.

4.1. Case 1: Single Diode

Figure 3 shows the fitness function graph of the optimization methods for extracting PV values. In addition, it concluded that the IGWO algorithm converges faster than others. The IGWO achieves the best value of 0.0416 in the 15^{th} iteration, while the GWO, the second-best method, reaches the best value in the 28^{th}. Five methods reach the best result (0.0416). Figure 3 shows that the MVO is the worst convergence method for this model. The MVO reaches the best value in about the 375^{th} iteration. The SCA and WOA achieve the results on the 140^{th} and 105^{th} iterations.

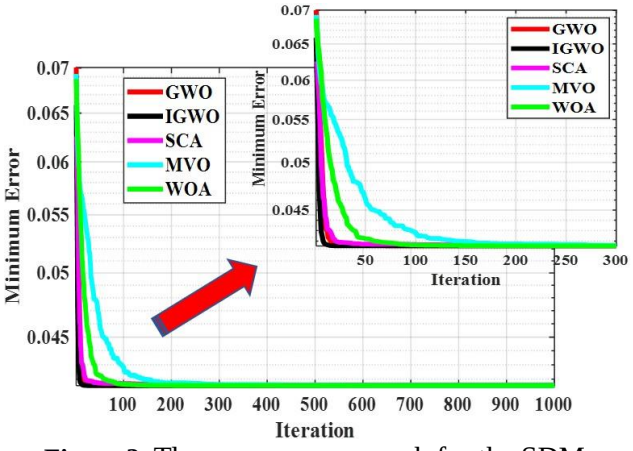

Figure 3. The convergence graph for the SDM.

One of the exciting outputs of this study is the computation time results. Figure 4 shows the comparison of the calculation time results of each method. Although Figure 3 clearly shows that the IGWO is the best convergence method among the

others, the results of Figure 4 state that The IGWO is the slowest method, with 2.3708 seconds.

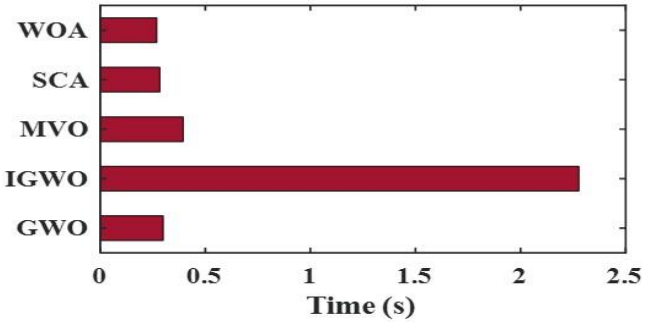

Figure 4. The computation time for single diode model.

For real-time optimization analysis, getting the best value in the minimum time [51]. Each algorithm runs with 1000 iterations. One iteration of IGWO spent 2.37 ms time. IGWO reach the best results on the 15^{th} iteration, which equals 35,55 ms (15×2.37). If the same calculation is done for GWO, SCA, MVO, and WOA, the results are 9.4977 ms (0.3392×28), 41.6488 ms (0.2228×140), 155.4196 ms (0.4145×375) and 30.0418 ms (0.2861×105), respectively. Thus, in real time, the GWO and WOA solve this problem faster than IGWO.

Figure 5 shows the I-V polarization curve of SDM for further validation of IGWO success. The blue colored curve is the curve of the experiment data gathering from [49]. The red circle represents the IGWO results. It can be concluded from Figure 5 that there is an exact match between the IGWO results and the measurement results in the I-V curve.

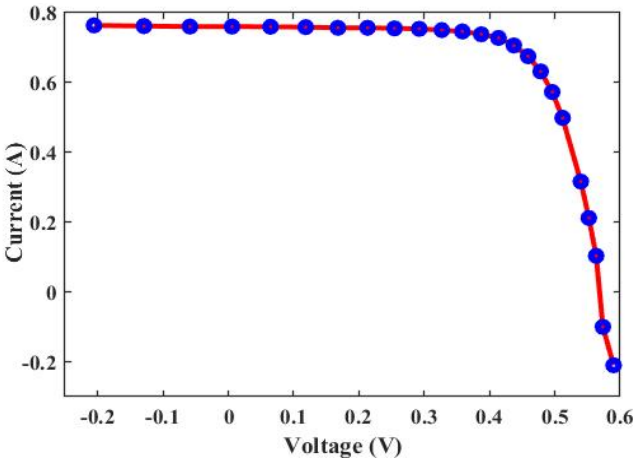

Figure 5. The I-V Polarization curve for SDM.

A comparison between the optimal unknown parameter output for the single diode case has been presented for more validation. Table 1 indicates the outputs of five methods that extract the PV parameters for a SDM.

Table 1. The unknown parameter results in the single diode.

Parameters	GWO	IGWO	MVO	SCA	WOA
R_{sh}	1.237515	1.236925	1.237425	1.235133	1.236917
R_s	0.421066	0.421976	0.140933	0.424598	0.422377
α	1.630063	1.04896	1.99602	1.000001	1.999988
I_0	0.605225	0.007517	0.876953	0.00001	0.24931
I_{ph}	0.999276	0.999833	0.886133	0.999999	0.999994

Table 2. Friedman ranking test results for SDM.

Algorithms	GWO	IGWO	MVO	SCA	WOA
Friedman Rankings	2	1	5	4	3

Table 2 shows the Friedman ranking test for SDM. The Friedman rank test is a non-parametric statistical test that compares differences between two or more dependent groups [52]. Table 2 shows that the IGWO algorithm is clearly better than other algorithms regarding convergence ability and accuracy, with IGWO securing first rank, followed by GWO, WOA, SCA, and MVO.

4.2. Case 2: Double Diode

Figure 6 shows the convergence graph of the techniques used to extract the DDM parameters. It also shows that the IGWO algorithm has a fast convergence. The IGWO achieves the best value, 0.041569, in the 12^{th} iteration. The second best is GWO with the 21^{th} iteration. These results are logical because the IGWO is an improved variant of the GWO method and has the advantage of high convergence speed over the original algorithm. The SCA and MVO achieve the best value on 125^{th} and 87^{th} iterations. Figure 6 demonstrates that the WOA is the worst convergence method for this problem with the 219^{th} iteration.

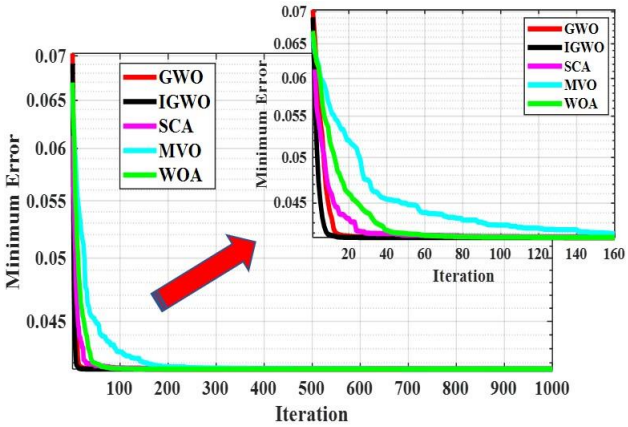

Figure 6. The convergence graph for DDM.

According to the computation time outputs, the situation for the DDM is really interesting, like a single-diode model. Figure 7 compares the calculation time results for the DDM. Although the convergence trend in Figure 6 indicates that the IGWO is the best convergence method, the time outputs of Figure 7 state that The IGWO is the slowest method, with 2.7615 seconds.

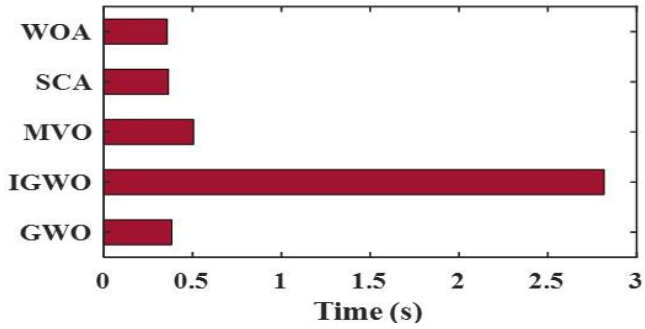

Figure 7. The computation time for DDM.

According to the computation time outputs, the situation for the DDM is really interesting, like a single-diode model. Figure 7 compares the calculation time results for the DDM. Although the convergence trend in Figure 6 indicates that the IGWO is the best convergence method, the time outputs of Figure 7 state that The IGWO is the slowest method, with 2.7615 seconds.

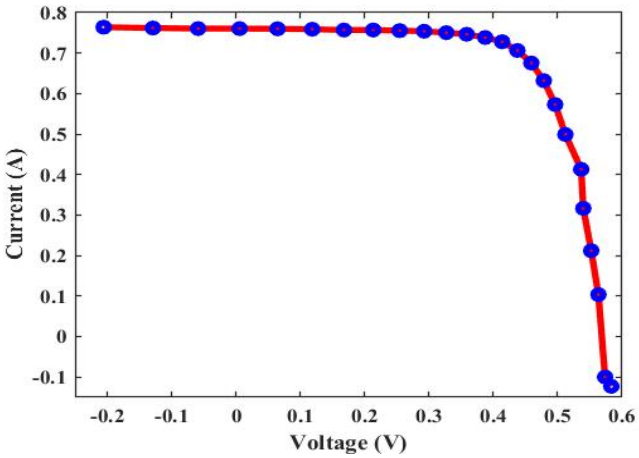

Figure 8. The I-V Polarization curve for DDM.

Figure 8 demonstrates the polarization plot of the DDM that emphasizes the success of the IGWO. The blue colored curve is the curve of the experiment data gathering from [49]. The red circle represents the IGWO results. As seen in Figure 7, there is a precise match on the I-V graph between calculated output and measurement results.

Table 3. The unknown parameter results in the double diode.

Parameters	GWO	IGWO	MVO	SCA	WOA
R_{sh}	1.237112	1.237378	1.237186	1.255711	1.237312
R_s	0.111071	0.002382	0.238979	0.00001	0.422831
α_1	1.212469	1.995611	1.996953	1.676885	1.77301
α_2	1.200126	1.992697	1.887299	1.984556	1.111419
I_{01}	0.122898	0.093894	0.700794	0.00001	0.024884
I_{02}	0.000523	0.008832	0.640783	0.62012	0.14825
I_{ph}	0.874122	0.830082	0.92585	0.826977	0.99999

Table 4. Friedman ranking test results for DDM.

Algorithms	GWO	IGWO	MVO	SCA	WOA
Friedman Rankings	2	1	3	4	5

For validation, the comparison between the unknown parameters obtained from methods for the double diode case has been presented for more validation. Table 3 shows the output of all methods used to extract the PV parameters for a DDM.

The Friedman ranking test for DDM is given Table 4. According to the ranking results on Table 4, the IGWO algorithm performs better than other methods regarding convergence ability and accuracy,

with IGWO securing first rank, followed by GWO, MVO, MVO, and WOA.

4.3. An Overview of The Results

The SDM and DDM results show that different optimization algorithms have unique advantages and limitations for this application. IGWO offers rapid convergence for both SDM and DDM. The fast convergence ability of IGWO maybe because this algorithm is an improved version of GWO. As an improved algorithm, IGWO can explore the search space more effectively. Although IGWO offers fast convergence for both SDM and DDM, it is the slowest in computation time. IGWO tends to approach the best result by doing more detailed research.

On the other hand, the fact that GWO has good performance for both SDM and DDM shows that this algorithm's basic features and structure are quite suitable for the nature of the PV parameter extraction problem. SCA and MVO may offer better results in DDM than SDM because the convergence process of these algorithms may be more conducive to investigating different combinations of parameters in a more complex model. The fact that WOA performs lower than other methods may suggest that the algorithm does not have an optimal search and convergence process for this particular problem set.

5. Conclusion and Discussion

In this paper, five different meta-heuristic optimization techniques have been implemented to extract PV module design parameters. These methods include GWO, IGWO, MVO, WOA), and SCA. These algorithms have been implemented in the SDM case and the DDM case. An error function has been used to calculate the difference between the computed and measured current values. Different from the literature, the unknown parameter estimation is not just considered an offline optimization problem but also a real-time optimization problem in which the calculation time matters. Thus, the computation times for each method used in this paper are calculated. The inferences obtained from the study can be listed as follows;

1) The IGWO, GWO, SCA, MVO, and WOA algorithms can successfully extract PV module design parameters. The fitness function results can be given as proof of this inference.
2) For offline optimization, the IGWO is more successful than the other system in both cases, SDM and DDM. The convergence trends in Figure 3 and Figure 6 can be proven. In SDM, IGWO reaches 0.0416 in the 15^{th} iteration, and in DDM, it comes to 0.041569 in the 12^{th} iteration, supporting this claim.
3) The unknown PV parameters extraction problem is an offline optimization issue. However, if we want a real solution for the solar PV industry, it needs to be real-time optimization solved quickly. The computed time results are really interesting. The IGWO, the most successful method, is also the slowest among the five methods. The GWO, SCA, and WOA methods are more usable for real-time application. Figure 4 and Figure 7 can be given as proof.
4) The IGWO is used for the five unknown SDM parameter estimation and the seven unknown DDM parameter estimation issues for the first time in the literature. This study provided the first literature contribution in this field, with IGWO's successful results of 0.0416 for SDM and 0.041569 for DDM. The success of IGWO for these problems has been shown with this study for the first time.

The limitation of this paper is that this study was conducted only on a specific set of PV module design parameters. This study assumes that the mathematical modeling used fully reflected PV module structures. For future work, we will try the solve optimum parameters for the three-diode / four-diode model. Also, we will run this problem with other heuristic based optimization methods.

Contributions of the authors

SAC: Conceptualization,Methodology, Software, Validation, Analysis,Visualization, Writing,
SK: Conceptualization,Methodology, Software, Validation,Visualization, Investigation,Writing.

Conflict of Interest Statement

There is no conflict of interest between the authors.

Statement of Research and Publication Ethics

The study is complied with research and publication ethics.

References

[1] V. V. S. N. Murty and A. Kumar, "Multi-objective energy management in microgrids with hybrid energy sources and battery energy storage systems," *Protection and Control of Modern Power Systems*, vol. 5, no. 1, 2020, doi: 10.1186/s41601-019-0147-z.

[2] H. Zhang, Z. Lu, W. Hu, Y. Wang, L. Dong, and J. Zhang, "Coordinated optimal operation of hydro–wind–solar integrated systems," *Appl Energy*, vol. 242, 2019, doi: 10.1016/j.apenergy.2019.03.064.

[3] J. Liu et al., "Impact of Power Grid Strength and PLL Parameters on Stability of Grid-Connected DFIG Wind Farm," *IEEE Trans Sustain Energy*, vol. 11, no. 1, pp. 545–557, Jan. 2020, doi: 10.1109/TSTE.2019.2897596.

[4] M. Abdel-Basset, R. Mohamed, M. Sharawi, L. Abdel-Fatah, M. Abouhawwash, and K. Sallam, "A comparative study of optimization algorithms for parameter estimation of PV solar cells and modules: Analysis and case studies," *Energy Reports*, vol. 8, pp. 13047–13065, Nov. 2022, doi: 10.1016/j.egyr.2022.09.193.

[5] B. Aboagye, S. Gyamfi, E. A. Ofosu, and S. Djordjevic, "Investigation into the impacts of design, installation, operation and maintenance issues on performance and degradation of installed solar photovoltaic (PV) systems," *Energy for Sustainable Development*, vol. 66, 2022, doi: 10.1016/j.esd.2021.12.003.

[6] S. M. Ebrahimi, E. Salahshour, M. Malekzadeh, and Francisco Gordillo, "Parameters identification of PV solar cells and modules using flexible particle swarm optimization algorithm," *Energy*, vol. 179, pp. 358–372, Jul. 2019, doi: 10.1016/j.energy.2019.04.218.

[7] D. Kler, Y. Goswami, K. P. S. Rana, and V. Kumar, "A novel approach to parameter estimation of photovoltaic systems using hybridized optimizer," *Energy Convers Manag*, vol. 187, 2019, doi: 10.1016/j.enconman.2019.01.102.

[8] S. Kumar Patro and R. P. Saini, "Mathematical modeling framework of a PV model using novel differential evolution algorithm," *Solar Energy*, vol. 211, 2020, doi: 10.1016/j.solener.2020.09.065.

[9] H. Rezk, T. S. Babu, M. Al-Dhaifallah, and H. A. Ziedan, "A robust parameter estimation approach based on stochastic fractal search optimization algorithm applied to solar PV parameters," *Energy Reports*, vol. 7, 2021, doi: 10.1016/j.egyr.2021.01.024.

[10] M. Naeijian, A. Rahimnejad, S. M. Ebrahimi, N. Pourmousa, and S. A. Gadsden, "Parameter estimation of PV solar cells and modules using Whippy Harris Hawks Optimization Algorithm," *Energy Reports*, vol. 7, 2021, doi: 10.1016/j.egyr.2021.06.085.

[11] A. Askarzadeh and A. Rezazadeh, "Parameter identification for solar cell models using harmony search-based algorithms," *Solar Energy*, vol. 86, no. 11, 2012, doi: 10.1016/j.solener.2012.08.018.

[12] K. M. El-Naggar, M. R. AlRashidi, M. F. AlHajri, and A. K. Al-Othman, "Simulated Annealing algorithm for photovoltaic parameters identification," *Solar Energy*, vol. 86, no. 1, 2012, doi: 10.1016/j.solener.2011.09.032.

[13] A. Askarzadeh and A. Rezazadeh, "Extraction of maximum power point in solar cells using bird mating optimizer-based parameters identification approach," *Solar Energy*, vol. 90, 2013, doi: 10.1016/j.solener.2013.01.010.

[14] M. S. Ismail, M. Moghavvemi, and T. M. I. Mahlia, "Characterization of PV panel and global optimization of its model parameters using genetic algorithm," *Energy Convers Manag*, vol. 73, 2013, doi: 10.1016/j.enconman.2013.03.033.

[15] S. J. Patel, A. K. Panchal, and V. Kheraj, "Extraction of solar cell parameters from a single current-voltage characteristic using teaching learning based optimization algorithm," *Appl Energy*, vol. 119, 2014, doi: 10.1016/j.apenergy.2014.01.027.

[16] X. Chen, B. Xu, C. Mei, Y. Ding, and K. Li, "Teaching–learning–based artificial bee colony for solar photovoltaic parameter estimation," *Appl Energy*, vol. 212, 2018, doi: 10.1016/j.apenergy.2017.12.115.

[17] D. Oliva, E. Cuevas, and G. Pajares, "Parameter identification of solar cells using artificial bee colony optimization," *Energy*, vol. 72, 2014, doi: 10.1016/j.energy.2014.05.011.

[18] A. El-Fergany, "Efficient tool to characterize photovoltaic generating systems using mine blast algorithm," *Electric Power Components and Systems*, vol. 43, no. 8–10, 2015, doi: 10.1080/15325008.2015.1014579.

[19] D. Allam, D. A. Yousri, and M. B. Eteiba, "Parameters extraction of the three diode model for the multi-crystalline solar cell/module using Moth-Flame Optimization Algorithm," *Energy Convers Manag*, vol. 123, 2016, doi: 10.1016/j.enconman.2016.06.052.

[20] O. S. Elazab, H. M. Hasanien, M. A. Elgendy, and A. M. Abdeen, "Parameters estimation of single- and multiple-diode photovoltaic model using whale optimisation algorithm," *IET Renewable Power Generation*, vol. 12, no. 15, pp. 1755–1761, Nov. 2018, doi: 10.1049/iet-rpg.2018.5317.

[21] D. F. Alam, D. A. Yousri, and M. B. Eteiba, "Flower Pollination Algorithm based solar PV parameter estimation," *Energy Convers Manag*, vol. 101, 2015, doi: 10.1016/j.enconman.2015.05.074.

[22] L. Guo, Z. Meng, Y. Sun, and L. Wang, "Parameter identification and sensitivity analysis of solar cell models with cat swarm optimization algorithm," *Energy Convers Manag*, vol. 108, 2016, doi: 10.1016/j.enconman.2015.11.041.

[23] D. Kler, P. Sharma, A. Banerjee, K. P. S. Rana, and V. Kumar, "PV cell and module efficient parameters estimation using Evaporation Rate based Water Cycle Algorithm," *Swarm Evol Comput*, vol. 35, 2017, doi: 10.1016/j.swevo.2017.02.005.

[24] M. Derick, C. Rani, M. Rajesh, M. E. Farrag, Y. Wang, and K. Busawon, "An improved optimization technique for estimation of solar photovoltaic parameters," *Solar Energy*, vol. 157, 2017, doi: 10.1016/j.solener.2017.08.006.

[25] K. Yu, B. Qu, C. Yue, S. Ge, X. Chen, and J. Liang, "A performance-guided JAYA algorithm for parameters identification of photovoltaic cell and module," *Appl Energy*, vol. 237, 2019, doi: 10.1016/j.apenergy.2019.01.008.

[26] M. H. Qais, H. M. Hasanien, and S. Alghuwainem, "Identification of electrical parameters for three-diode photovoltaic model using analytical and sunflower optimization algorithm," *Appl Energy*, vol. 250, 2019, doi: 10.1016/j.apenergy.2019.05.013.

[27] H. Chen, S. Jiao, M. Wang, A. A. Heidari, and X. Zhao, "Parameters identification of photovoltaic cells and modules using diversification-enriched Harris hawks optimization with chaotic drifts," *J Clean Prod*, vol. 244, 2020, doi: 10.1016/j.jclepro.2019.118778.

[28] M. Abd Elaziz and D. Oliva, "Parameter estimation of solar cells diode models by an improved opposition-based whale optimization algorithm," *Energy Convers Manag*, vol. 171, 2018, doi: 10.1016/j.enconman.2018.05.062.

[29] C. Kumar, T. D. Raj, M. Premkumar, and T. D. Raj, "A new stochastic slime mould optimization algorithm for the estimation of solar photovoltaic cell parameters," *Optik (Stuttg)*, vol. 223, 2020, doi: 10.1016/j.ijleo.2020.165277.

[30] N. Pourmousa, S. M. Ebrahimi, M. Malekzadeh, and F. Gordillo, "Using a novel optimization algorithm for parameter extraction of photovoltaic cells and modules," *Eur Phys J Plus*, vol. 136, no. 4, 2021, doi: 10.1140/epjp/s13360-021-01462-4.

[31] N. F. Nicaire, P. N. Steve, N. E. Salome, and A. O. Grégroire, "Parameter Estimation of the Photovoltaic System Using Bald Eagle Search (BES) Algorithm," *International Journal of Photoenergy*, vol. 2021. 2021. doi: 10.1155/2021/4343203.

[32] M. Abdel-Basset, D. El-Shahat, R. K. Chakrabortty, and M. Ryan, "Parameter estimation of photovoltaic models using an improved marine predators algorithm," *Energy Convers Manag*, vol. 227, 2021, doi: 10.1016/j.enconman.2020.113491.

[33] R. Bisht and A. Sikander, "A novel way of parameter estimation of solar photovoltaic system," COMPEL, vol. 41, no. 1, 2022, doi: 10.1108/COMPEL-05-2021-0166.

[34] T. S. L. V. Ayyarao and P. P. Kumar, "Parameter estimation of solar PV models with a new proposed war strategy optimization algorithm," *Int J Energy Res*, vol. 46, no. 6, 2022, doi: 10.1002/er.7629.

[35] T. Düzenli, F. Kutlu Onay, and S. B. Aydemir, "Improved honey badger algorithms for parameter extraction in photovoltaic models," *Optik (Stuttg)*, vol. 268, p. 169731, Oct. 2022, doi: 10.1016/j.ijleo.2022.169731.

[36] A. M. Eltamaly, "Musical chairs algorithm for parameters estimation of PV cells," *Solar Energy*, vol. 241, pp. 601–620, Jul. 2022, doi: 10.1016/j.solener.2022.06.043.

[37] D. M. Djanssou, A. Dadjé, and N. Djongyang, "Estimation of Photovoltaic Cell Parameters using the Honey Badger Algorithm," *Int J Eng Adv Technol*, vol. 11, no. 5, pp. 109–124, Jun. 2022, doi: 10.35940/ijeat. E3552.0611522.

[38] T. T. Nguyen, T. T. Nguyen, and T. N. Tran, "Parameter estimation of photovoltaic cell and module models relied on metaheuristic algorithms including artificial ecosystem optimization," *Neural Comput Appl*, vol. 34, no. 15, 2022, doi: 10.1007/s00521-022-07142-3.

[39] C. Kumar and D. Magdalin Mary, "A novel chaotic-driven Tuna Swarm Optimizer with Newton-Raphson method for parameter identification of three-diode equivalent circuit model of solar photovoltaic cells/modules," *Optik (Stuttg)*, vol. 264, p. 169379, Aug. 2022, doi: 10.1016/j.ijleo.2022.169379.

[40] S. Mirjalili, S. M. Mirjalili, and A. Lewis, "Grey wolf optimizer," *Advances in engineering software*, vol. 69, pp. 46–61, 2014.

[41] M. H. Nadimi-Shahraki, S. Taghian, and S. Mirjalili, "An improved grey wolf optimizer for solving engineering problems," *Expert Syst Appl*, vol. 166, p. 113917, 2021.

[42] S. Mirjalili, S. M. Mirjalili, and A. Hatamlou, "Multi-verse optimizer: a nature-inspired algorithm for global optimization," *Neural Comput Appl*, vol. 27, no. 2, pp. 495–513, 2016.

[43] J. Khoury, B. A. Ovrut, N. Seiberg, P. J. Steinhardt, and N. Turok, "From big crunch to big bang," *Physical Review D*, vol. 65, no. 8, p. 086007, 2002.

[44] M. Tegmark, Barrow, JD Davies, PC Harper, CL, Jr eds," *Science and Ultimate Reality* Cambridge University Press Cambridge, 2004.

[45] S. Mirjalili and A. Lewis, "The whale optimization algorithm," *Advances in engineering software*, vol. 95, pp. 51–67, 2016.

[46] W. A. Watkins and W. E. Schevill, "Aerial observation of feeding behavior in four baleen whales: Eubalaena glacialis, Balaenoptera borealis, Megaptera novaeangliae, and Balaenoptera physalus," *J Mammal*, vol. 60, no. 1, pp. 155–163, 1979.

[47] J. A. Goldbogen, A. S. Friedlaender, J. Calambokidis, M. F. McKenna, M. Simon, and D. P. Nowacek, "Integrative approaches to the study of baleen whale diving behavior, feeding performance, and foraging ecology," *Bioscience*, vol. 63, no. 2, pp. 90–100, 2013.

[48] S. Mirjalili, "SCA: a sine cosine algorithm for solving optimization problems*," Knowl Based Syst*, vol. 96, pp. 120–133, 2016.

[49] S. Gao, K. Wang, S. Tao, T. Jin, H. Dai, and J. Cheng, "A state-of-the-art differential evolution algorithm for parameter estimation of solar photovoltaic models," *Energy Convers Manag*, vol. 230, p. 113784, 2021.

[50] S. A. Çeltek and A. Durdu, "An Operant Conditioning Approach For Large Scale Social Optimization Algorithms," *Konya Mühendislik Bilimleri Dergisi*, vol. 8, pp. 38–45, 2020.

[51] S. A. Celtek, A. Durdu, and M. E. M. Alı, "Real-time traffic signal control with swarm optimization methods," *Measurement*, vol. 166, p. 108206, 2020.

[52] López-Vázquez, C., & Hochsztain, E. "Extended and updated tables for the Friedman rank test". *Communications in Statistics-Theory and Methods*, vol. 48, no. 2, pp. 268-281, 2019.

Bitlis Eren Üniversitesi Fen Bilimleri Dergisi
BİTLİS EREN UNIVERSITY JOURNAL OF SCIENCE
ISSN: 2147-3129/e-ISSN: 2147-3188
VOLUME: 12 NO: 4 PAGE: 1054-1068 YEAR: 2023
DOI:10.17798/bitlisfen.1325877

AMFC: A New Approach Efficient Junctions Detect via Maximum Flow Approach

Furkan ÖZTEMİZ*

Software Engineering Department, Faculty of Engineering, Inonu University, Malatya, TURKEY (ORCID: 0000-0001-5425-3474)

Keywords: Maximum Flow, Ford-Fulkerson Algorithm, Maximum Road Capacity, Transport Network, Graph Theory

Abstract

In this study, max flow analysis processes are carried out with a graph theory-based approach that can be used in optimizing the traffic load in transportation networks. The data used in the study consists of 2 years of vehicle number data consisting of 438 million vehicle passes of a real city. Bottleneck points affecting traffic flow, maximum flow values, and effectiveness values of traffic generating and attracting locations were determined in the uniquely created transportation network. The Ford-Fulkerson algorithm was used to determine the maximum flow and bottleneck road connections in the designed transportation network. According to the maximum traffic flow to the junction point, the most effective junction points were determined by the PageRank algorithm. In addition, a unique algorithm is presented in the study that determines the effective intersection points that transfer vehicle traffic at maximum capacity to all junction points according to the maximum demand capacity data. The analysis results produced by the proposed method constitute an important decision support system for traffic management and transportation network design.

1. Introduction

One of the most important factors in making a city livable is a developed and sustainable transportation system [1]. The transportation network must be manageable and developable for this sustainable structure to continue. The measurability and manageability of the transportation network depend on converting the traffic data into digital form and processing it with data mining techniques. In this way, determining the vehicle carrying capacity of the roads and junction points, which constitute the important parts of the transportation networks, enables many different optimization processes to be performed on the urban transportation system [2]. Studies in the literature show that transportation networks modeled based on graph theory give very successful results [3, 4]. Calculating the maximum vehicle traffic at determined locations in transportation systems is a significant problem. In computer science, this type of problem is solved with the max flow approach. The determination of max flow is expressed as an NP-Complete problem that cannot be solved in polynomial time [5]. The max flow approach calculates all flow values between the two specified locations and detects the connections with the weakest flow despite the maximum flow potential in the network. The places with the weakest flow are called bottleneck points [6]. In this study, the transportation network in the city was designed by using the real vehicle count data of a city. This weighted graph is used to determine the transportation network's bottleneck points and the most effective intersection point under the maximum flow. In addition, with the proposed Average Maximum Flow Closeness (AMFC) algorithm, the efficiency of the points producing vehicle traffic according to the maximum demand capacity has been determined.

2. Related Work

There are studies in the literature that use various approaches to determine maximum flow values and bottleneck points. The maximum flow approach,

*Corresponding author: furkan.oztemiz@inonu.edu.tr
Received: 11.07.2023, Accepted: 23.10.2023

which is very popular in transportation, has often been used to balance and optimize the traffic load [7]. Studies on the determination of the maximum flow value in the transportation network [8] and the determination of the speed ratios [9] at which maximum safe flow will be provided have provided significant benefits. In particular, maximum flow calculations were carried out for the optimization of green light flashing times in signaling systems, which is one of the important criteria affecting the management of the transportation network [10]. In addition, there are effective methods developed to detect bottleneck points that will cause interruptions in the transportation network [11, 12]. By designing transportation networks of real cities, analyses such as determining the bottleneck points and determining air pollution with travel speed data [13], bottleneck cost [14], and PMFA [15] were carried out. Maximum flow is used to highlight the importance of bottlenecks in high-scale networks [16] and to correlate traffic carrying capacity with signal timing parameters [17]. Maximum flow approaches have a very wide area of use outside of transportation networks. By determining the capacity flexibility of the passenger transportation network, it is possible for individuals to have route selection [18]. In power networks, critical capacity values have been determined for each situation where the network is resistant to failures [19]. Ford Fulkerson method has been applied to determine the maximum electrical carrying capacity in electrical transmission lines [20]. In another study, it is aimed to determine the maximum production rate that the network can reach when a production flow network with known edge capacity is given [21]. To support flow latency control in TDMA-based wireless networks, a flexible bandwidth allocation and uncoordinated scheduling scheme called two-stage link scheduling (2SLS) [22] have been proposed. The fragility analysis of the carrying capacity of the natural gas pipeline network [23] is carried out, and the capacity differences are explained from the perspective of graph theory [24].

When the studies in the field of transportation are examined, it is seen that the data sets used in most studies are limited or randomly generated. In this study, an important analysis of traffic flow has been carried out by using vehicle count data from a real city. The data used consists of vehicle count data passing through 161 road connections connected to 41 junction points. The dataset, which includes 438 million vehicle passes, consists of 2-year vehicle count data. The data consisting of approximately 56 million rows of SQL data was filtered and transformed into 1-hour count data. The transportation network graph is weighted according to the maximum number of vehicles obtained (Realized Demand capacity). The dataset specially prepared for this study makes the study unique in this respect. Maximum traffic flow values and bottleneck points were determined between the locations determined according to the scenarios created in line with the needs of the city. Ford-Fulkerson algorithm has been applied to determine the network's maximum flow and bottleneck edges. In the study, the most efficient junction points were determined according to the incoming traffic load by using the PageRank algorithm. Furthermore, a unique method for determining the effectiveness values of traffic-generating points that are thought to contribute to the literature has been proposed. The proposed AMFC algorithm evaluates the transfer potential of the traffic load arriving at the intersection at maximum capacity and determines the efficiency values of the intersection points accordingly. Important outputs were obtained by applying the AMFC algorithm on real field data. This way, the order of importance of the traffic-generating locations has been determined and explained comparatively. Another feature that distinguishes the study is that the road's vehicle carrying capacity is not physically used while the transportation network is weighted. Instead, the transportation network was weighted by determining the maximum demand values based on traffic flow in 1-hour periods over a city's two-year period. The fact that the data set is inclusive of the city and consists of big detailed data has increased the success and quality of the employee.

3. Material and Method

The development process of the study is explained in 5 primary stages with the graphical summary given in Figure 1. In Stage 1, the junction and road relations of the city to be analyzed (Malatya city in Turkey) were determined, and the transportation network graph was designed. The generated transportation network graph has 41 junction points and 161 road connections. In Stage 2, vehicle count data consisting of approximately 56 million rows of SQL data, (The data consists of time, green time, vehicle count, direction and junction columns), belonging to 161 roads taken from the city's signaling system was processed through data preprocessing processes. The vehicle count data used covers a period of 24 months. During this period, approximately 438 million vehicles passed through the designed transportation network. In Stage 3, the vehicle count data of 24 months were grouped at 1-hour intervals, and the vehicle count data at the peak point was determined. This process was carried out separately for 161 different road

connections. In Stage 4, the entire transportation network is weighted with the peak pass data. This way, the transportation network is weighted with the road's realized maximum capacities by using the maximum demand value according to the real traffic data. In Stage 5, three important analyses were carried out, namely maximum flow, bottleneck location detection, and node efficiency, using the transportation network designed using the original data set. In the next stage of the study, extra explanations about these summarized stages are given. In this study, MS SQL Server was used for vehicle count data preprocessing, and R programming language was used for the development and implementation of algorithms. In addition, the igraph and visnetwork libraries were used to visualize and perform graph-based operations on the transportation network.

Figure 2 zooms in on a sample area in the red square and provides a visual representation of transforming signalized junction points into a graph. The green circles in the image represent the junction points, and the blue lines represent the road connections connecting the junction points.

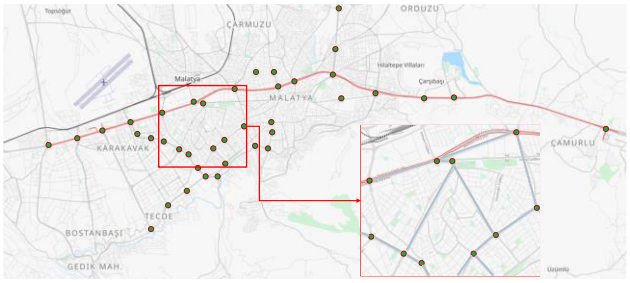

Figure 2. The designed transportation network graph.

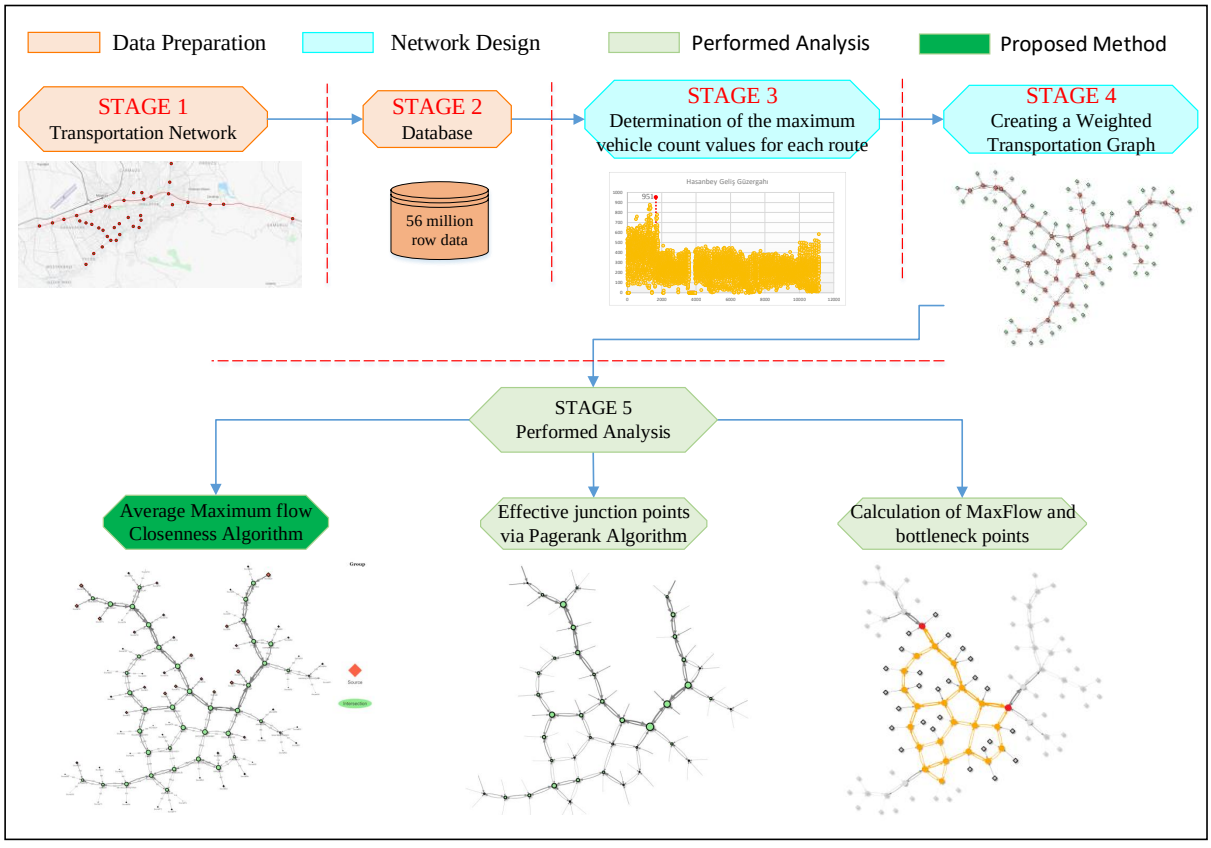

Figure 1. Analysis process

Let's explain how road connections are weighted for an example intersection in Figure 3. Figure 3 shows the weighting of 4 different roads connected to the Temelli junction point. These roads are Mezarlık Geliş, Feyzullah Taşkınsoy, Dede Korkut, and Hasanbey arrival routes. When the Dede Korkut arrival route is examined, the vehicle count data in 2 years, approximately 11,500 different (1-hour intervals) time zones, can be seen. Each yellow dot in the graph represents the vehicle count data in the 1-hour interval. The maximum number of vehicles in the Dede Korkut Geliş direction within these time zones was 1277 (peak point). Each point on the yellow graph is the vehicle count data in the 1-hour interval. As indicated in the graph, the road edge related to the 1277 value at the peak point has been

weighted. The process performed is indicated on Figure 3 with a red arrow.

Like the Temelli arrival, direction operation was carried out for all 161 road connections in the transportation network. And all the edges of the transportation network are weighted. Figure 4 gives the visual for the final weighted transportation network diagram. While the red nodes in the image represent the source points (traffic-generating nodes), the green circular nodes indicate the junction points where the roads intersect. The edges expressing the roads are sized according to the vehicle count data. Edges with a high vehicle count are thicker, while edges with a low vehicle count are thinner. The area indicated by the red borders on the image is given in a zoomed form.

The most basic step of the analysis process is determining the maximum flow values in the network. The maximum flow value represents the vehicle traffic capacity that the transportation network will carry between 2 different locations [25]. Maximum flow is one of the fundamental parameters in this study's analysis. Ford-Fulkerson algorithm was used to detect bottleneck points(Maximum Flow) in the network. Considering the maximum vehicle crossing densities, the most effective junction points were determined according to the vehicle traffic coming to the junction points with the PageRank algorithm. One of the original outputs of the study is to determine the efficiency value of traffic-generating points.

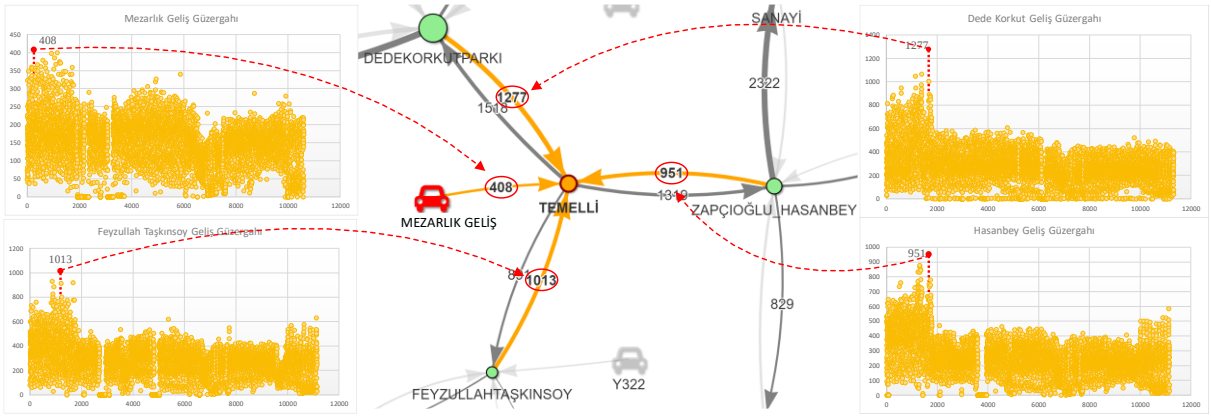

Figure 3. The weighting of the transport network

This original proposed method is named the Average Maximum Flow Closeness Algorithm (AMFC). The method's main goal is to determine the potential of the points that generate vehicle traffic to distribute the traffic they generate to the entire network. The proposed algorithm includes the maximum flow approach and the approach of reaching the nodes of the closeness centricity algorithm. The following sections provide detailed information about the methods used and developed during the analysis process.

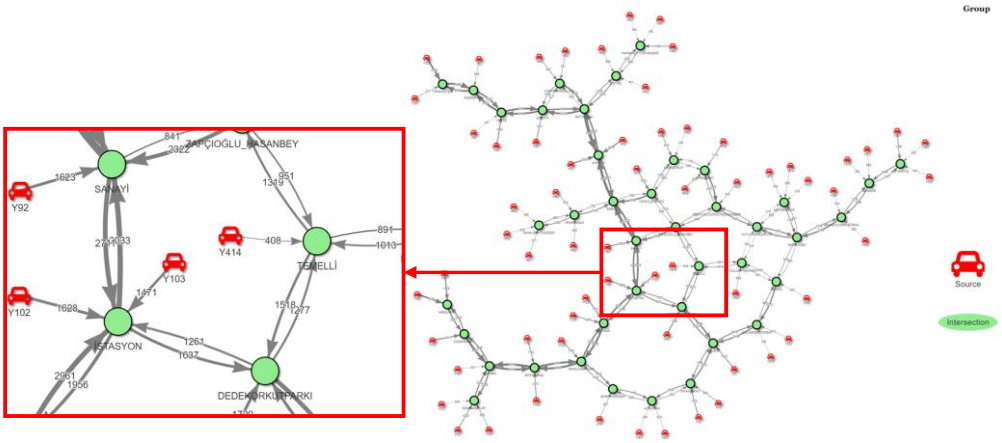

Figure 4. Transportation network weighted with maximum flow values

3.1. Maximum Flow

The purpose of the maximum flow problem is to find the maximum flow from a single source to a single sink in a given flow network [26]. This problem is defined in graph theory as the NP-Complete problem type that cannot be solved in polynomial time [27]. In Figure 5, the vertex labeled S represents the source point, and the vertex labeled T represents the target point or sink point. The edge weights on the graph give the capacity information of the relevant edge points. As understood from the graph, the graph given is a directional graph. The indicated directions represent the direction of the flow in the graph. In order to find the maximum amount to be transferred from the S node to the T node in the example graph, it is essential to identify the bottleneck points.

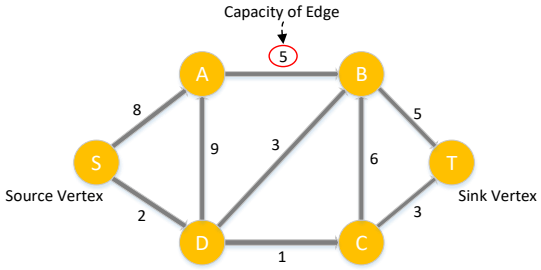

Figure 5. Maximum Flow Network [28].

G = (V, E) is defined as a directed graph. E denotes the edges in the graph, while V denotes the nodes. Each edge e in the flow network has a capacity c_e, which is a non-negative number. The network also consists of a single source node $s \in V$ and a single sink $t \in V$ [29].

For every $e \in E$, $0 \leq f(e) \leq c_e$.

for every node v except s and t, [30]

$$\sum_{e\ into\ v} f(e) = \sum_{e\ out\ of\ v} f(e) \quad (1)$$

Flow conservation: At each $v \in V\{s,t\}$ node, incoming streams are offset by outgoing streams. That is, all flows through v must be limited, as in equation 1 [31].

$$\left(\sum_{e_n \in N(v)} p(e_n)\right) - p_s(v) + p_t(v) = 0 \quad (2)$$

In Equation 2, $N(v) \subset E$ is the set of edges connecting v to neighboring nodes. The maximum flow problem tries to find the largest amount of flow allowed from the source.

$$\max_{p_s} \sum_{v \in V\{s,t\}} p_s(v) \quad (3)$$

As given in Equation 3, when a flow p(e) on edge $e \in E$ reaches the corresponding capacity $C(e)$, it is said to be saturated, otherwise unsaturated [31].

3.2. Ford-Fulkerson algorithm

The Ford-Fulkerson algorithm is a greedy approximation algorithm that calculates the maximum flow value in a flow network. L. R. Ford Jr. and D. R. Fulkerson developed the algorithm in 1956 [32]. The idea behind the algorithm is briefly as follows: As long as there is a path from the source (start node) to the pool (end node), flow is sent along one of the paths with usable capacity on all edges of the path. A path with available capacity is called augmenting path. The formula for the algorithm is given in equation 4 [33].

$$c(V,E) = \sum_{u \in S, u \in T | (u,v) \in E} c(u.v) \quad (4)$$

$G(V,E)$ is a finitely directional graph. (u,v) denotes the edges, while $c(u,v)$ denotes the capacity value of the relevant edge. Nodes s and t represent the source and sink points, respectively. Cut işlemi S ve T düğümlerinin iki kümeye ayrılma işlemidir. The cut operation is the process of separating S and T nodes into two clusters. Therefore, $2^{|V|-2}$ possible cuts occur on the graph. $c(V,E)$ gives the maximum capacity of interrupts in the graph [33].

In other words, each edge correlation in the network is associated with a positive number called capacity. In this context, the flow amount f_{ij} on one side must meet the condition of not exceeding the flow capacity c_{ij} determined for the edge, as stated in equation 5. This expression is called the capacity constraint or boundary condition. In addition, as given in equation 6, it must be ensured that the inflow (f_{ki}) equals the output (f_{ij}) for every vertex except the s and t nodes. Given these conditions, the algorithm's goal is to maximize the flow between s and t as much as possible [20].

$$0 \leq f_{ij} \leq c_{ij} \;\; (i = 1,2, \dots \dots, n;\; j = 1,2, \dots . . n) \tag{5}$$

$$\sum_k f_{ki} - \sum_j f_{ij} = 0 \begin{cases} f & ,if\ i = s \\ -f & ,if\ i = t \\ 0 & ,otherwise \end{cases} \quad ,i = 2, \dots \dots, N-1 \tag{6}$$

3.3. Pagerank algorithm

It was developed by Lary Page and Sergey Brin in 1998 [34]. It has been used to prioritize web pages in order to deliver the most suitable web pages on the Internet to users [35]. If we consider the related web pages as nodes, a centrality value is generated according to the importance of the incoming links to the nodes. By means of this centrality value, the priority of displaying web pages in search engines is realized [36]. The formula of the algorithm is given in equation 7.

$$PR(A) = (1-d) + d\left(\frac{PR(t1)}{C(t1)} + \cdots + \frac{PR(tn)}{C(tn)}\right) \tag{7}$$

tn: the relevant source node, PR(tn): the values of the source nodes, C(tn): the number of connections that each node gives to other nodes, d: the dumping factor coefficient [36]. In this study, the PageRank algorithm is used to determine the junction points that can meet the maximum demand.

4. Average Maximum Flow Closeness Algorithm (Proposed Method)

Average Maximum Flow Closeness (AMFC) algorithm has been developed to determine the potential of traffic-generating points (Nodes) to transfer traffic at the maximum rate to the entire transportation network. The average flow values obtained by the AMFC algorithm are a unique method recommended to determine the potential of traffic-generating points in the city. The proposed algorithm realizes the maximum flow value to all nodes in the transportation network, which is weighted with the maximum vehicle count data, in a structure similar to the approach of reaching all nodes of the closeness algorithm. The maximum flow value of a traffic-generating node to the remaining 160 nodes is calculated one by one. The average flow of the calculated maximum flow values for each node is calculated. The maximum flow value to the obtained medium will give information about how high a node can transfer the vehicle traffic load it has produced to the overall network. In the study carried out for all nodes, the nodes that produce the best demand at maximum capacity and distribute it the best are determined. In optimizing the transportation network, successful results have been produced about the efficiency order of junction and source points. The formula of the algorithm is specified in equation 8.

$$\frac{\sum_{V_s,\ V_s \neq V_i} c(V_i,V_s)}{n}, |\mathrm{V}| = \mathrm{n}, 1 \leq \mathrm{s} \leq \mathrm{n} \tag{8}$$

V_i is the source vertex with the number i. V_s represents the sink node in the graph. $c(V_i, V_s)$ i. th source vertex represents the maximum flow value to the sink vertex in the graph. n is the number of all vertices in the graph. In the given formula, the average maximum flow value of the i.th source point to all vertexes in the graph is calculated. This calculation is performed for all vertexes for analysis of the entire network. The flow diagram and pseudocode of the proposed algorithm are shown in Figure 6 and Table 1.

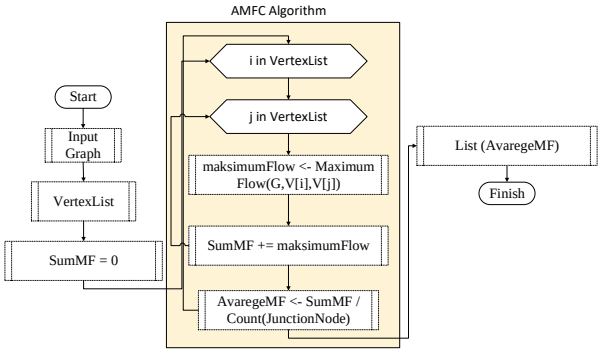

Figure 6. AMFC flowchart

Bottleneck points in transportation networks are an important criterion that directly affects the flow situation in the network. The detection of bottleneck points in the transportation network in certain regions or throughout the network gives important results about the flow. We can express the formation of bottleneck points in 4 stages.

V_i^{in}, It is the vertex that expresses the traffic flow coming to the i junction point in the transportation network. $c(V_i^{in})$, i is the maximum flow amount calculated according to the traffic load arriving at the junction. V_j is the neighboring vertex of vertex i. In other words, they are neighboring junction points connected to junction point i. $c(V_j^{out})$ is the maximum vehicle traffic from neighboring junction. k represents the roads coming out of the neighboring junction points.

Table 1. AMFC Pseudocode

	Average Maximum flow Closeness Algorithm
1	G:(V,E)
2	VertexList <- c(V(G))
3	JunctionNode: Production and attraction points (junctions in the transport network)
4	u <- Source Node
5	v <- Sink Node
6	MaximumFlow(G,u,v){ // Method to detect Max Flow value between Source and Sink nodes in G graph
7	flow = 0
8	for each edge (u, v) in G:
9	flow(u, v) = 0
10	while there is a path, p, from s -> t in residualnetwork G_f:
11	residualcapacity(p) = minimum(residualcapacity(u, v) : for (u, v) in p)
12	flow += residualcapacity(p)
13	for each edge (u, v) in p:
14	if (u, v) is a forward edge:
15	flow(u, v) += residualcapacity(p)
16	else:
17	flow(u, v) -= residualcapacity(p)
18	return flow }
19	SumMF <- 0
20	for (i in VertexList){ // Calculates maximum flow from each node to all nodes
21	for(j in VertexList){
22	maximumFlow = MaximumFlow(G,VertexList[i],VertexList[j])
23	SumMF += maximumFlow }
24	AvarageMaksimumFlow = ToplamMF / Count(JunctionNode) } // detects the average
25	maximum flow of the related node to all nodes.

Theorem 1

Suppose the maximum vehicle traffic arriving at the i junction is higher than the exit traffic volume at the j neighboring junction of the i junction point. In that case, the potenatial of occuring traffic bottleneck problem on the roads connected to i is possible (Eq.9).

$$\sum_{V_i} c(V_i^{in}) - \sum_{V_j \in N(V_i)} \sum_{k=1}^{|N(V_j,k)^{max}|} c(V_j^{out}) \; > 0 \tag{9}$$

Proof: The volume of traffic arriving i junction is $\sum_{V_i} c(V_i^{in})$ and the volume of traffic leaving j junction which is the neighbour of i junction, is $\sum_{V_j \in N(V_i)} \sum_{k=1}^{|N(V_j,k)^{max}|} c(V_j^{out})$. If the difference between volume of arriving traffic and volume of leaving traffic is greater that zero, this means that some vechiles remain in i junction. This case causes traffic problem ■

Theorem 2

If the maximum vehicle traffic arriving at any junction point i is less than the exit traffic volume at the j neighboring junction points connected to the junction point i, it can be said that there is no possibility of a bottleneck on the roads belonging to the junction point j (Eq.10).

$$\sum_{V_i} c(V_i^{in}) - \sum_{V_j \in N(V_i)} \sum_{k=1}^{|N(V_j,k)^{max}|} c(V_j^{out}) \; < 0 \tag{10}$$

Proof: The volume of traffic arriving i junction is $\sum_{V_i} c(V_i^{in})$ and the volume of traffic leaving j junction which is the neighbour of i junction, is $\sum_{V_j \in N(V_i)} \sum_{k=1}^{|N(V_j,k)^{max}|} c(V_j^{out})$. If the difference between volume of arriving traffic and volume of leaving traffic is less than zero, this means that there is no vechiles in j junction. This case has more traffic volume ■

Theorem 3

If the maximum vehicle traffic arriving at any junction point i is equal to the exit traffic volume at the j neighboring junction points connected to the junction point i, it can be said that there is no possibility of a bottleneck on the roads belonging to the junction point j (Eq.11).

$$\sum_{V_i} c(V_i^{in}) - \sum_{V_j \in N(V_i)} \sum_{k=1}^{|N(V_j,k)^{max}|} c(V_j^{out}) \; = 0 \tag{11}$$

Proof: The volume of traffic arriving i junction is $\sum_{V_i} c(V_i^{in})$ and the volume of traffic leaving j junction which is the neighbour of i junction, is $\sum_{V_j \in N(V_i)} \sum_{k=1}^{|N(V_j,k)^{max}|} c(V_j^{out})$. If the difference between volume of arriving traffic and volume of leaving traffic is equal to zero, this means that there is no vechiles in j junction. This case has no traffic problem ■

Theorem 4

The previous theories focused on bottleneck scenarios for a certain vertex point. The maximum flow value of the entire transportation network is given in Equation 12. It is the case when the vehicle traffic arriving at all i junction points is equal to the sum of the k exits of all j junction points connected to the forwards. In this case, it can be said that the traffic flows with the maximum flow for the whole transportation network and is at the saturation limit.

$$\sum_{V_{ij}}^{V_{all}} \left(\sum_{V_i} c(V_i^{in}) - \sum_{V_j \in N(V_i)} \sum_{k=1}^{|N(V_j,k)^{max}|} c(V_j^{out}) \right) = 0 \tag{12}$$

Proof: The proofs of Theorem 1, Theorem 2, and Theorem 3 illustrate the traffic volumes at a specific junction. This theorem states the ideal case for no traffic problems on highway (roads). The incoming traffic volumes for all junctions chould be equal to the outgoing traffic volumes for all junctions. This is the best case (ideal case) for highways (roads) traffic arrangement efforts. The main aims of all traffic arrangement/planning is to get ideal case of traffic volume ■

5. Experimental Results

The analysis processes in the study were carried out under three headings. First, the maximum flow value on the specified route in the transportation network, which is weighted with the real vehicle count data, is calculated. Afterward, the bottleneck points that cause the maximum flow value are determined. In this way, considering the improvement for maximum capacity on the determined route, it is aimed to determine the routes to be intervened first in the transportation network. In the second analysis, the most effective junction points of the city were determined according to the maximum capacity values by using the PageRank centrality algorithm, which is very popular in graph theory. These efficiency

values give information about the ability of the junction points to meet the traffic load coming to them. Finally, in the last analysis study, a unique method named Average Maximum flow Closeness Algorithm has been proposed. This method produces results on the capacity of the traffic generating points to spread this traffic to the whole city. In this way, it creates a centrality value on the capacity to distribute the traffic density they produce for the entire city. These results generate efficiency values according to the traffic data from the junction points or the traffic-generating source points themselves.

5.1. Detection of maximum flow and bottlenecks of roads

In this section, the maximum flow value between a determined route was calculated, and bottleneck points on this route were determined. In Figure 7, two junction points located in the west-east direction of the city are determined. These points are marked in red. 'Bostanbaşı' junction was chosen as the source point, and 'Emeksiz' junction point was chosen as the sink point. Road connections highlighted in yellow in the figure represent road connections between Bostanbaşı and Emeksiz, where all vehicle flow can take place. The yellow circular nodes represent the junction points where the roads connect, and the gray diamond shape represents the locations that generate one-way vehicle traffic. The enlarged version of the area indicated by the rectangle on the figure on the left in Figure 7 is given in the right part.
Ford-Fulkerson algorithm was applied for the Bostanbaşı-Emeksiz route, and the maximum flow value was determined as 3555 (number of vehicles).

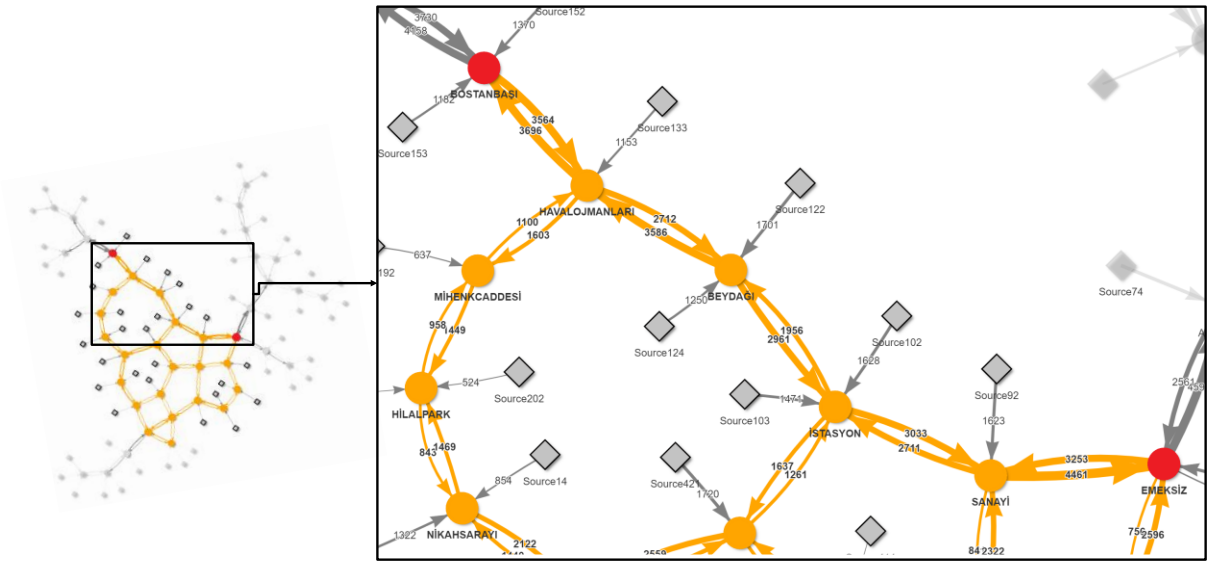

Figure 7. Flows between Source and Sink nodes

Figure 8 shows the edges where the bottleneck occurs on the determined route. The maximum flow value is the sum of the bottleneck edges. When Figure 8 is examined, the Havalojmanları-Beydağı road constitutes the bottleneck points with a maximum of 2712 and Hilalpark-Nikahsarayı road with a maximum of 843 vehicles in 1 hour.
The location of bottleneck points plays a crucial role in increasing traffic capacity. Considering the Bostanbaşı-Emeksiz route, if it is desired to increase the maximum flow here, the first place to focus should be the roads connecting the junction points of Havalojmanları-Beydağı and Hilalpark-Nikahsarayı. By increasing the capacities of these roads, the maximum flow value of the route will also increase.

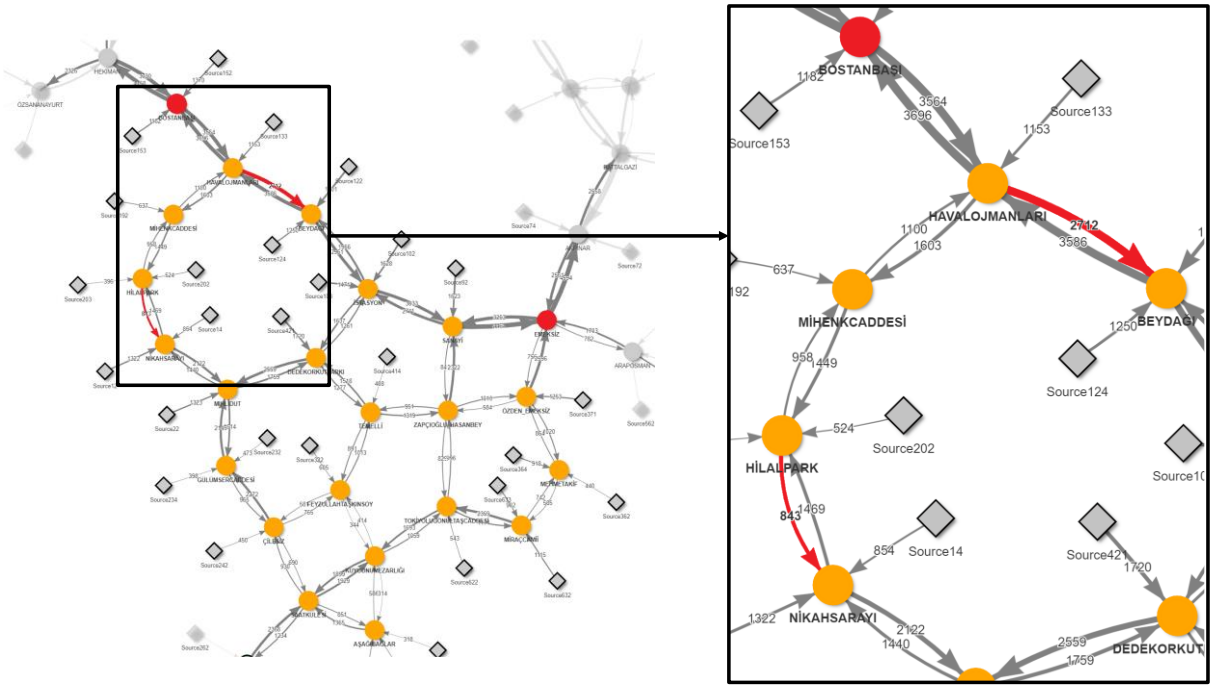

Figure 8. Bottleneck points between Source and Sink nodes

5.2. Junctions efficient value via pagerank algorithm

The PageRank algorithm is applied on the graph to determine the junction points with the maximum demand in the transportation network. In Table 2, the pagerank centrality values of the ten junction points with the highest density and the least density in the transportation network are given. When the values are examined, the Point of Emeksiz junction can be expressed as the junction point that best transfers the traffic flow with the value of 0.05255. The junction point named KonferansSalonu is the junction point with the lowest dominance value with a PageRank centrality value of 0.00858.

In Figure 9, images of the junction points with the highest and lowest PageRank values are given. In the area indicated by the square in the image, the location of the junction points named Emeksiz and Konferans Salonu on the transportation network is provided by zooming in. The edge relations expressed in yellow in the image contain vehicle traffic information coming and going to the relevant junction points. Nodes in green indicate junction points. The sizes of these nodes are visualized in proportion to their PageRank centrality values.

Table 2. Pagerank values of the most effective and most ineffective junction nodes

Ten nodes with the highest centrality value		Ten nodes with the lowest centrality value	
Junction	Pagerank values	Junction	Pagerank values
Emeksiz	0,052559766	Konferanssalonu	0,008583588
Akpınar	0,046014059	Mehmetakif	0,009004943
Battalgazi	0,043730462	Havalimanı	0,009074974
Hekiman	0,041337738	Hanımınçiftliği	0,010827013
Mıhlıdut	0,037891714	Feyzullahtaşkınsoy	0,011039468
Sanayi	0,034062546	Sanayibent	0,011324006
Saatkulesi	0,033643565	Miraççamii	0,011645474
Bostanbaşı	0,032104338	Aşağıbağlar	0,011781241
Havalojmanları	0,030274251	Altınkayısı	0,011921711
Mişmişpark	0,028772595	Özden_Emeksiz	0,013283945

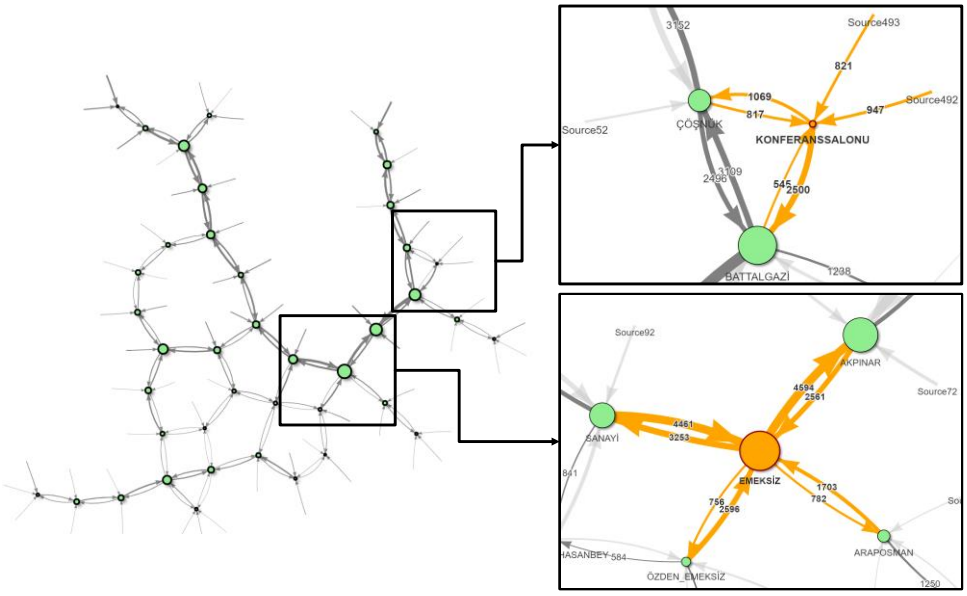

Figure 9. Junction centrality according to PageRank Algorithm

5.3. Determination of efficient nodes via AMFC algorithm (Proposed method's implementation)

By using the maximum flow values, the Average MaxFlow Closeness algorithm calculates how much of this traffic, on average, can be transferred by the locations that generate vehicle traffic to other locations. In Figure 10, the maximum amount of vehicles that the Bostanbaşı junction point can transfer to other junction points in a 1-hour period is given. When the graph is examined, the highest traffic flow with 4158 vehicle flow in 1 hour is between Bostanbaşı and Hekiman junction points. The lowest vehicle flow was realized at the junction named SanayiBent, with 782 vehicles. In other words, a maximum of 782 vehicles can cross in an hour from the Bostanbaşı junction to the junction point called SanayiBentCaddesi. The orange line indicated in Figure 10 is the AMFC (average maximum flow to all junction points) value of the Bostanbaşı junction point.

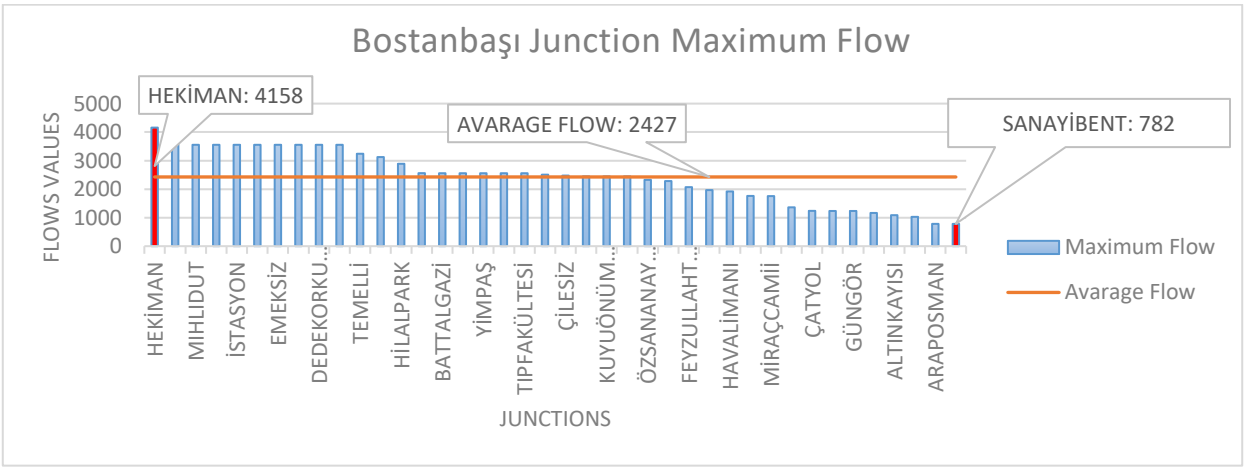

Figure 10. Bostanbaşı junction's AMFC value calculation

As a result of the application of the proposed algorithm to the entire transportation network, the AMFC values of the highest and lowest 10 locations are given in Table 3. When the results are examined, Zapçıoğlu_Hasanbey junction point is the junction point that transfers the traffic density it has to other junction points in the city most efficiently. The AMFC value determined as 2547

for the Zapçıoğlu_Hasanbey junction means that this junction point can transfer 2547 vehicles on average to all junction points of the city without any problems, in line with the maximum flow values calculated by considering the city's 2-year vehicle count data. When the lowest 10 AMFC values are examined, it is seen that these points are not junction points but low-traffic generating nodes. These nodes have been determined as the most ineffective nodes in terms of both the traffic load they produce and their position in the transportation network. The Source541 node is the location that generates the least traffic in the transportation network and transfers the least traffic to other locations at maximum capacity.

Table 3. AMFC values of the most and least effective source nodes

Maximum average flow ten highest nodes		Minimum average flow lowest ten nodes	
Source Node	AMFC values	Source Node	AMFC values
Zapçıoğlu_Hasanbey	2547	Source541	160
İstasyon	2490	Source293	255
Sanayi	2489	Source723	264
Beydağı	2485	Source543	292
Dedekorkutparkı	2477	Source672	318
Özsansanayi	2468	Source42	357
Bostanbaşı	2427	Source262	385
Emeksiz	2423	Source602	385
Havalojmanları	2419	Source273	392
Hekiman	2416	Source203	396

In Figure 11, the most effective and ineffective junction and source points according to the proposed AMFC algorithm are given by zooming in. In the image, the nodes are proportionally sized according to the AMFC value. When the figure is examined, the effectiveness value of both source points and junction points decreases as they move away from the main arteries.

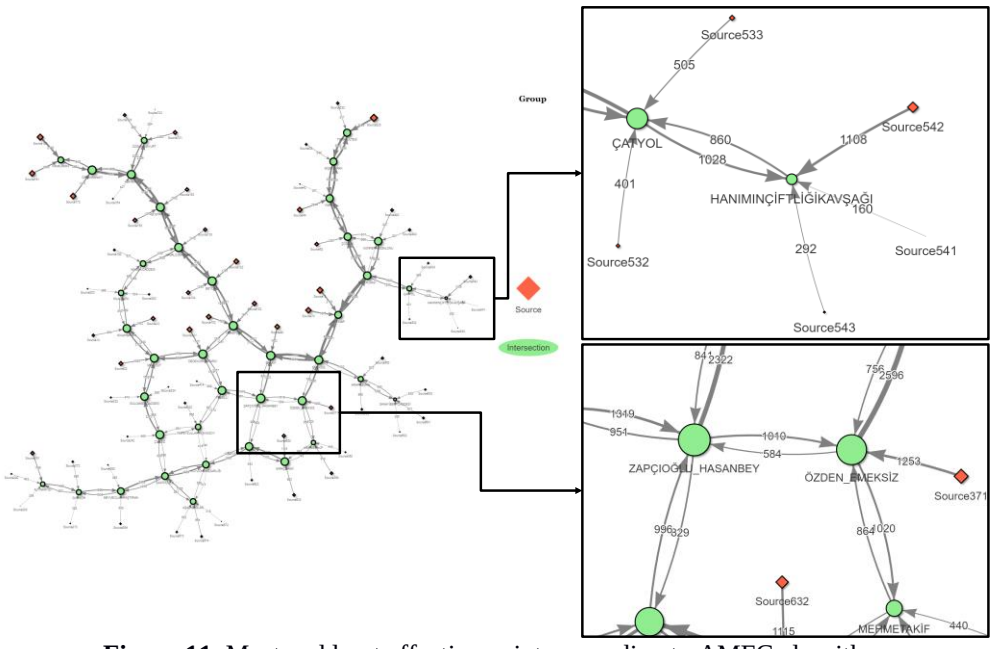

Figure 11. Most and least effective points according to AMFC algorithm

6. Conclusion and Results

In the presented study, a series of analyzes were carried out on the maximum flow approach on the designed transportation network. The designed network is weighted using a city's approximately 24 monthly vehicle count data. The network consisting of 41 junction points and 161 road connections was designed specifically for this study. Vehicle count data on all road connections in the transportation network were filtered in 1-hour intervals, and the maximum vehicle pass value was determined within 1 hour. In light of these data, the entire transportation network has been transformed into a weighted network with the maximum vehicle count data. The vehicle count data at the peak point provides important information about the capacities of the relevant roads. Three different analysis processes were carried out, which will be an important decision support system for managing the transportation system with maximum capacity information. First of all, 2 locations were selected in the east-west regions of the city, and the roads with the maximum vehicle pass value and bottleneck were determined on this route. It is important to identify bottleneck points in regulating vehicle traffic on a route. To increase this route's capacity, the bottleneck roads should be optimized first. Another analysis process, it was carried out on the junction points with the highest vehicle density. According to the maximum traffic load in the transportation network, the most effective junction points were determined by the PageRank algorithm. In this way, the performance of the junction points according to the traffic load they have been determined. The PageRank algorithm and most other centrality algorithms work according to the traffic load that comes to it. When the results of the PageRank algorithm are examined, it is seen that the efficiency value of the junction points on the main streets is high, while the centricity value decreases as you move away from the main street. There is no theory-based graph method for how well the intersection or source (traffic generating locations) points can distribute the maximum traffic load they produce to the entire transportation network. AMFC algorithm, which is an effective method to overcome this deficiency, is proposed in this study. It is presented as a centrality method that determines how much vehicle traffic the traffic-generating node can transfer to the nodes in the entire network at maximum capacity with the AMFC algorithm. When the results are examined, it has been determined that the locations close to the city center and on the main streets have higher flow values. As the distance from the city center increased and the distance from the highway increased, the average maximum flow value decreased. These values obtained as a result of the AMFC algorithm will be an important decision support system in many studies, from routing the traffic in the city to the creation of new road connections. The study has made several unique contributions to the literature. The first significant contribution is the design of a city-specific transportation network based on real-time vehicle counts. Vehicle Count data were obtained from vehicle count cameras in the city's signaling system, and the data were preprocessed. Another unique contribution was presented as the AMFC method by evaluating the maximum flow approach from a different perspective. It is thought that the developed method will provide important conveniences for those who work on transportation systems and graph theory due to its easy-to-apply structure. In the following stages, this analysis will be carried out in a real-time system, and studies will be carried out to optimize the transportation network instantly. Especially with the detection of bottleneck points, estimation processes can be carried out to determine at which intersection point the solution of the problems here can create a bottleneck again.

Acknowledgment

This study was supported by Malatya Inönü University Scientific Research Projects Management Department (BAP) fund under project ID, 3136 project code, FBG-2023-3136.

Statement of Research and Publication Ethics

The study is complied with research and publication ethics.

References

[1] S. Siddiqui and Ş. G. Eren, “The analysis of the sustainability pillars of Karachi city’s transportation system,” *Mimar. Bilim. ve Uygulamaları Derg. (MBUD)*, pp. 181–190, 2022.

[2] F. Öztemiz and A. Karci, “Topluluk Tespiti Yöntemi ile Ulaşım Ağında Verimli Yeşil Dalga Koridorlarının Belirlenmesi,” *Politeknik Dergisi*, pp. 1–1, 2023.

[3] A. Erath, M. Löchl, and K. W. Axhausen, "Graph-theoretical analysis of the Swiss road and railway networks over time," *Netw. Spat. Econ.*, vol. 9, no. 3, pp. 379–400, 2009.

[4] Z. Yi, X. C. Liu, N. Markovic, and J. Phillips, "Inferencing hourly traffic volume using data-driven machine learning and graph theory," *Comput. Environ. Urban Syst.*, vol. 85, no. 101548, p. 101548, 2021.

[5] D. Granata, R. Cerulli, M. G. Scutellà, and A. Raiconi, "*Maximum flow problems and an NP-complete variant on edge-labeled graphs*," in Handbook of Combinatorial Optimization, New York, NY: Springer New York, 2013, pp. 1913–1948.

[6] D. Blazek, O. Blazekova, and M. Vojtekova, "Analytical model of road bottleneck queueing system," *Transp. Lett.*, vol. 14, no. 8, pp. 888–897, 2022.

[7] A. R. Mahlous, R. J. Fretwell, and B. Chaourar, "MFMP: Max Flow Multipath Routing Algorithm," *in 2008 Second UKSIM European Symposium on Computer Modeling and Simulation*, 2008.

[8] A. Akhmediyarova, D. Kassymova, A. Utegenova, and I. Utepbergenov, "Development and research of the algorithm for determining the maximum flow at distribution in the network," *Open Comput. Sci.*, vol. 6, no. 1, pp. 213–218, 2016.

[9] E. J. Moore, W. Kichainukon, U. Phalavonk, "Maximum flow in road networks with speed-dependent capacities – application to Bangkok traffic," *Songklanakarin Journal of Science and Technology (SJST)*, vol. 35, 489-499, 2013.

[10] A. Ngaosai and J. Chawachat, "Traffic signal management using maximum flow approach for consecutive intersections," *in 2018 15th International Conference on Electrical Engineering/Electronics, Computer, Telecommunications and Information Technology (ECTI-CON)*, 2018.

[11] X. Sun, Z. Bai, K. Lin, P. Jiao, and H. Lu, "Optimization model of traffic sensor layout considering traffic big data," *J. Adv. Transp.*, vol. 2020, pp. 1–11, 2020.

[12] M. G. H. Bell, F. Kurauchi, S. Perera, and W. Wong, "Investigating transport network vulnerability by capacity weighted spectral analysis," *Trans. Res. Part B: Methodol.*, vol. 99, pp. 251–266, 2017.

[13] V. Torrisi, M. Ignaccolo, and G. Inturri, "Analysis of road urban transport network capacity through a dynamic assignment model: validation of different measurement methods," *Transp. Res. Procedia*, vol. 27, pp. 1026–1033, 2017.

[14] C. Li, W. Yue, G. Mao, and Z. Xu, "Congestion propagation based bottleneck identification in urban road networks," *IEEE Trans. Veh. Technol.*, vol. 69, no. 5, pp. 4827–4841, 2020.

[15] S. Kamishetty, S. Vadlamannati, and P. Paruchuri, "Towards a better management of urban traffic pollution using a Pareto max flow approach," *Transp. Res. D Transp. Environ.*, vol. 79, no. 102194, p. 102194, 2020.

[16] N. Abdullah, T. Hua, "Traffic Congestion Problem In Kota Kinabalu, Sabah Using Ford-Fulkerson Algorithm And Max Flow-Min Cut Theorem," *International Conference on Business, Tourism & Technology, Port Dickson*, Negeri SembilanVolume: 2, 2017.

[17] Y. Gao, Z. Qu, X. Song, and Z. Yun, "Modeling of urban road network traffic carrying capacity based on equivalent traffic flow," *Simul. Model. Pract. Theory*, vol. 115, no. 102462, p. 102462, 2022.

[18] A. Chen and P. Kasikitwiwat, "Modeling capacity flexibility of transportation networks," *Transp. Res. Part A Policy Pract.*, vol. 45, no. 2, pp. 105–117, 2011.

[19] R. Ghanbari, M. Jalili, and X. Yu, "Analysis of cascaded failures in power networks using maximum flow based complex network approach," in *IECON 2016 - 42nd Annual Conference of the IEEE Industrial Electronics Society*, 2016.

[20] M. Bulut and E. Özcan, "Optimization of electricity transmission by Ford–Fulkerson algorithm," *Sustain. Energy Grids Netw.*, vol. 28, no. 100544, p. 100544, 2021.

[21] Y. M. Omar and P. Plapper, "Maximum flow of complex manufacturing networks," *Procedia CIRP*, vol. 86, pp. 245–250, 2019.

[22] Y.-C. Tu, M. C. Chen, and Y. S. Sun, "A two-stage link scheduling scheme for variable-bit-rate traffic flows in wireless mesh networks," *IEEE Trans. Wirel. Commun.*, vol. 13, no. 11, pp. 6232–6244, 2014.

[23] W. Wang, Y. Zhang, Y. Li, C. Liu, and S. Han, "Vulnerability analysis of a natural gas pipeline network based on network flow," *Int. J. Pressure Vessels Piping*, vol. 188, no. 104236, p. 104236, 2020.

[24] H. Su, E. Zio, J. Zhang, and X. Li, "A systematic framework of vulnerability analysis of a natural gas pipeline network," *Reliab. Eng. Syst. Saf.*, vol. 175, pp. 79–91, 2018.

[25] T. Werho, V. Vittal, S. Kolluri, and S. M. Wong, "Power system connectivity monitoring using a graph theory network flow algorithm," *IEEE Trans. Power Syst.*, vol. 31, no. 6, pp. 4945–4952, 2016.

[26] M. Du, X. Jiang, and A. Chen, "Identifying critical links using network capacity-based indicator in multi-modal transportation networks," *Transp. B Transp. Dyn.*, vol. 10, no. 1, pp. 1126–1150, 2022.

[27] İ. Akgün, B. Ç. Tansel, and R. Kevin Wood, "The multi-terminal maximum-flow network-interdiction problem," *Eur. J. Oper. Res.*, vol. 211, no. 2, pp. 241–251, 2011.

[28] Maksimum Flow, Retrieved from https://www.scaler.com/topics/data-structures/ford-fulkerson-algorithm-for-maximum-flow-problem/. January 3, 2023.

[29] J. Kleinberg, and É. Tardos, *Algorithm Design. Pearson Education*, 337–411. isbn: 0-321-29535-8, 2006.

[30] S. Långström, E. Frıdsäll, "Optimizing Traffic Flow On Congested Roads," Stockholm, Degree Project In Electronics And Computer Engineering, Fırst Cycle, 2019.

[31] J. Yuan, E. Bae, and X.-C. Tai, "A study on continuous max-flow and min-cut approaches," in *2010 IEEE Computer Society Conference on Computer Vision and Pattern Recognition*, 2010.

[32] T. Mukherjee, I. Sangal, B. Sarkar, and T. M. Alkadash, "Mathematical estimation for maximum flow of goods within a cross-dock to reduce inventory," *Math. Biosci. Eng.*, vol. 19, no. 12, pp. 13710–13731, 2022.

[33] A. R. Mahlous, R. J. Fretwell, and B. Chaourar, "MFMP: Max Flow Multipath Routing Algorithm," in *2008 Second UKSIM European Symposium on Computer Modeling and Simulation*, 2008.

[34] F. Öztemiz, "Sinyalizasyon Verileri Ile Malatya Kenti Ulaşim Aği Kavşak Noktalarinin Merkezlilik Analizi," *Computer Science*, 2021.

[35] F. Öztemiz and A. Karci, "Bağlı Graflarda Etkili Düğümlerin Belirlenmesinde Yeni Bir Yaklaşım," *Deu Muhendis. Fak. Fen Ve Muhendis.*, vol. 24, no. 70, pp. 143–155, 2022.

[36] F. Öztemiz and A. Karci, "Malatya İli ulaşım ağı kavşak noktalarının merkezlilik analizi," *Gazi Üniv. Mühendis.-Mimar. Fak. Derg.*, 2021

Bitlis Eren Üniversitesi Fen Bilimleri Dergisi
BİTLİS EREN UNIVERSITY JOURNAL OF SCIENCE
ISSN: 2147-3129/e-ISSN: 2147-3188
VOLUME: 12 NO: 4 PAGE: 1069-1082 YEAR: 2023
DOI:10.17798/bitlisfen.1328893

Assessing the Effects of Water Content on the Unconfined Compression Strength of Egg White-Stabilized Khorasan Mortar

Emrah DAĞLI[1], Murat ÇAVUŞLU[1*]

[1]*Zonguldak Bulent Ecevit University, Civil Engineering, Zonguldak, Türkiye*
(ORCID: 0000-0002-5744-8151) (ORCID: 0000-0002-2285-8513)

Keywords: Brick ballast, Egg white, Khorasan mortar, Lime, Sand, Unconfined compression strength.

Abstract
Khorasan mortar, a traditional, durable, and environmentally friendly building material, has been utilized for centuries in the Khorasan region of Türkiye. Its composition, which is based on natural hydraulic lime, imparts exceptional strength, breathability, and workability, making it suitable for diverse construction projects. Consequently, investigating the mechanical properties of Khorasan mortar, specifically its interaction with stone elements in historical buildings, in various mixing ratios, can provide valuable insights into the preservation and future of these architectural treasures. This study focuses on researching Khorasan mortar as a material of interest, utilizing brick ballast, lime, standard sand, water, and egg white, with a particular emphasis on egg white-stabilized Khorasan mortar. Four different water contents (70%, 80%, 90%, and 100%) were carefully selected, based on the dry mass of the egg white, to prepare a total of 12 samples (three identical samples for each water content) for testing. Prior to testing, the samples were cured for seven days in a desiccator. Unconfined compression strength tests were conducted, and axial strain-stress graphs were plotted to determine the unconfined compression strength (UCS) of the mixtures. The results revealed that the mixtures containing 80% water content exhibited the highest UCS values, while the samples with 90% and 100% water content demonstrated similar UCS values. The minimum UCS was approximately 0.518 times the maximum value, suggesting the importance of optimizing the water amount in Khorasan mortar formulations.

1. Introduction

The preservation of cultural heritage stands as a powerful testament to a nation's strength, with the imperative for enduring structures resonating across the globe. This demand has compelled engineers to explore and investigate materials that can withstand the pressures exerted on buildings, emerging as a significant global concern. Khorasan mortar, historically employed in civil engineering structures by various empires such as the Ottoman, Roman, Byzantine, and Seljuk [1], epitomizes a traditional mortar that has thrived for centuries in the Khorasan region of Türkiye, encompassing present-day Iran, Afghanistan, and Central Asia. Celebrated for its exceptional durability, strength, and distinctive composition, Khorasan mortar relies primarily on natural hydraulic lime (NHL) or hydraulic lime derived from quicklime obtained by burning limestone with clayey impurities. The utilization of NHL endows the mortar with the ability to set and harden even in the presence of moisture, rendering it particularly suitable for construction in humid or wet environments. A fundamental hallmark of Khorasan mortar lies in its dependence on natural materials and sustainable production methods, effectively reducing the environmental impact associated with the production of conventional Portland cement-based mortars. This alignment corresponds with the mounting global emphasis on eco-friendly and sustainable building practices. Furthermore,

*Corresponding author: murat.cavusli@beun.edu.tr
Received: 17.07.2023, Accepted: 23.09.2023

Khorasan mortar offers several practical advantages. Its exceptional breathability facilitates the efficient transfer of moisture vapor, mitigating the risk of trapped moisture within the masonry. This attribute holds particular value for historic restoration projects and regions with high humidity, averting damage caused by moisture accumulation. Moreover, Khorasan mortar showcases superior workability and adhesion properties, empowering skilled craftsmen to achieve intricate and precise detailing in masonry construction, while its flexibility accommodates the natural movements of buildings, diminishing the likelihood of cracks or structural damage. Overall, Khorasan mortar represents a sustainable and high-performance alternative to conventional mortars, rendering it a favored choice for a wide spectrum of construction projects, spanning from the preservation of historical landmarks to contemporary sustainable architecture. The recent devastating earthquakes that struck the southeastern part of Türkiye brought the use of Khorasan mortar to the forefront once again. Historical structures constructed with this mortar have proven their resilience due to the strength conferred by lime [1]. Notably, Khorasan mortar exhibits remarkable resistance to seawater, making it highly suitable for cities in close proximity to the seaside, where moisture content is substantial. Various studies have examined the usage of different admixtures in Khorasan mortar [2-9]. For instance, egg white can be incorporated in a mixture at a ratio between 5% and 25%, with 10% appearing to be the optimum ratio in terms of maintaining strength [2]. The addition of polypropylene fiber admixture reduces mortar shrinkage by approximately 35% compared to control samples [3]. The investigation of lime/aggregate and lime/brick aggregate ratios revealed that a 1:1 ratio yielded the maximum compressive strength [4]. Calcium-rich fly ashes prove effective in mixtures due to their significant CaO content. When fly ash was added to the mixture, along with tile ballast, at varying ratios (10%, 20%, 30%, and 40%), compressive strength was notably enhanced by up to 75% [7]. The optimization of lime/aggregate and lime/brick aggregate ratios in Khorasan mortar demonstrated that ratios of 0.67 and 0.75, respectively, yielded the best results [8]. Additionally, the inclusion of a low percentage (between 2.5 and 10) of bentonite improved the unconfined compression strength (UCS) of the mortar, with 5% being the optimum ratio, resulting in an approximate 20% enhancement in UCS values [9]. The extended setting time and relatively lower strength of Khorasan mortar in comparison to cement can be addressed by modifying additives or adjusting water content in the mortar. Canbaz and Güler [11] examined the effect of lime type on the properties of Khorasan mortar. According to analysis results, they revealed that lime type had significant effects on the strength of Khorasan mortar. In this study, the effect of water content on the unconfined compression strength value was investigated, with egg white serving as an additive. The water content of any mixture containing clayey materials can provide insights into its strength and durability. Given the paucity of research on this subject, this study aims to contribute to the body of knowledge surrounding Khorasan mortar.

2. Material and Method

2.1. General Information

This section provides a comprehensive account of the experimental investigation conducted on Khorasan mortar, delving into the effects of varying water contents. The materials employed in the study comprised brick ballast, lime, and standard sand, all derived from the Khorasan clay. These materials were procured from Ekşioğlu Ltd. Şti., a local company located in the center of Zonguldak. Additionally, eggs were obtained from a local market. Brick ballast was used as a powder form. Fig. 1 illustrates all the materials utilized in the study, which were stored in a controlled room environment devoid of any direct exposure to sunlight. During the preparation of Khorasan mortar, the materials were mixed with the help of a special tray at certain mixing ratios until they became homogeneous. The chemical compositions of materials were presented in Table 1. Then, the aggregate gradations were shown in Figs. 2-4

Figure 1. Materials used for the Khorasan mortar a) brick ballast b) standard sand c) lime d) egg white.

Table 1. The chemical composition of materials

Chemical composition (%)	SiO_2	Al_2O_3	Fe_2O_3	TiO_2	CaO	MgO	K_2O	Na_2O	SO_3	Free CaO	L.O.I.	Water Absorption Rate (%)
Brick ballast	62.1	17.9	10.31	0.38	1.46	1.41	1.93	NA	0.03	NA	10.2	14
Lime	1.51	1.63	0.76	NA	91.90	2.55	0.18	NA	1.26	NA	NA	13
Powder	98.03	NA	NA	NA	1.15	NA	NA	NA	NA	NA	NA	2.8

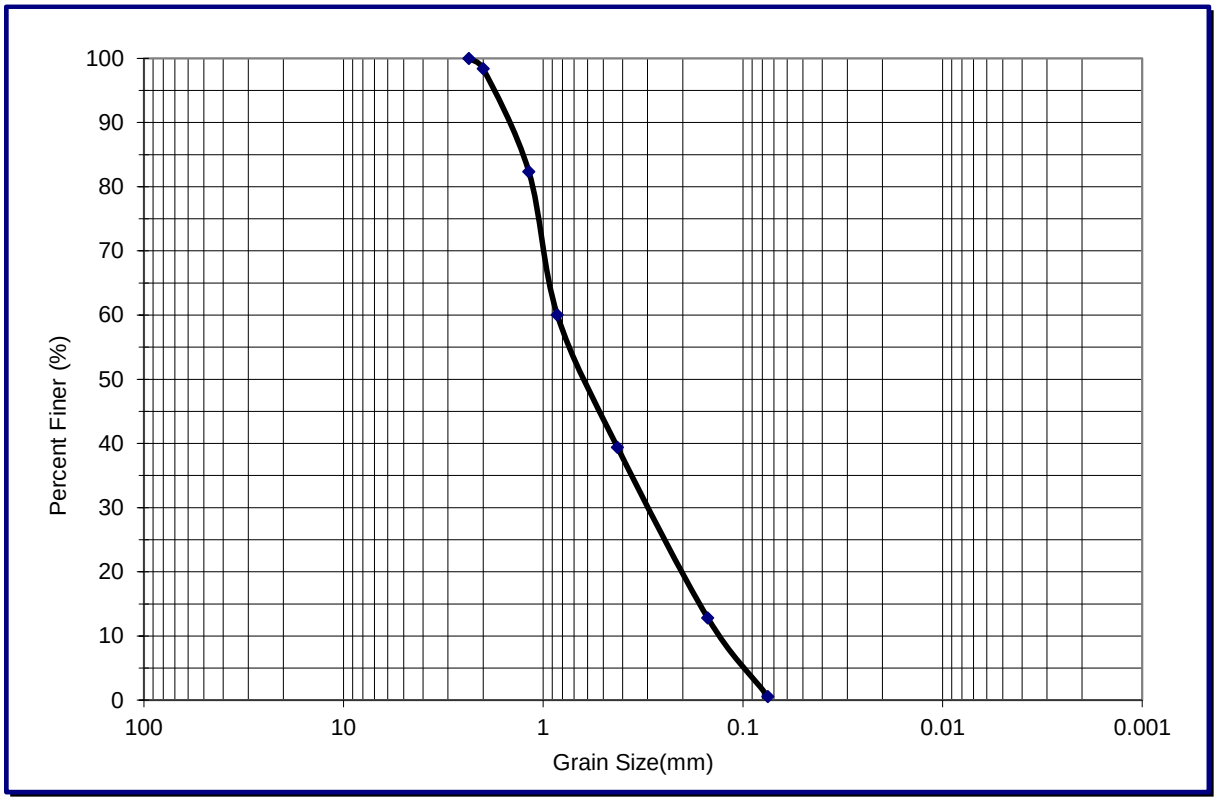

Figure 2. The aggregate gradation of sand.

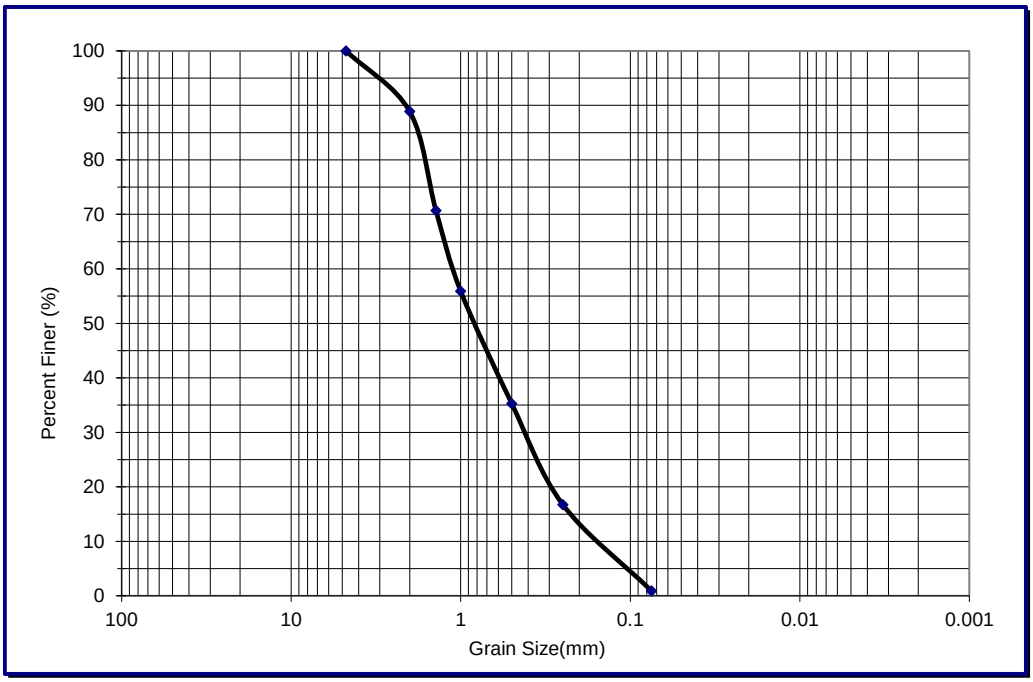

Figure 3. The aggregate gradation of brick ballast.

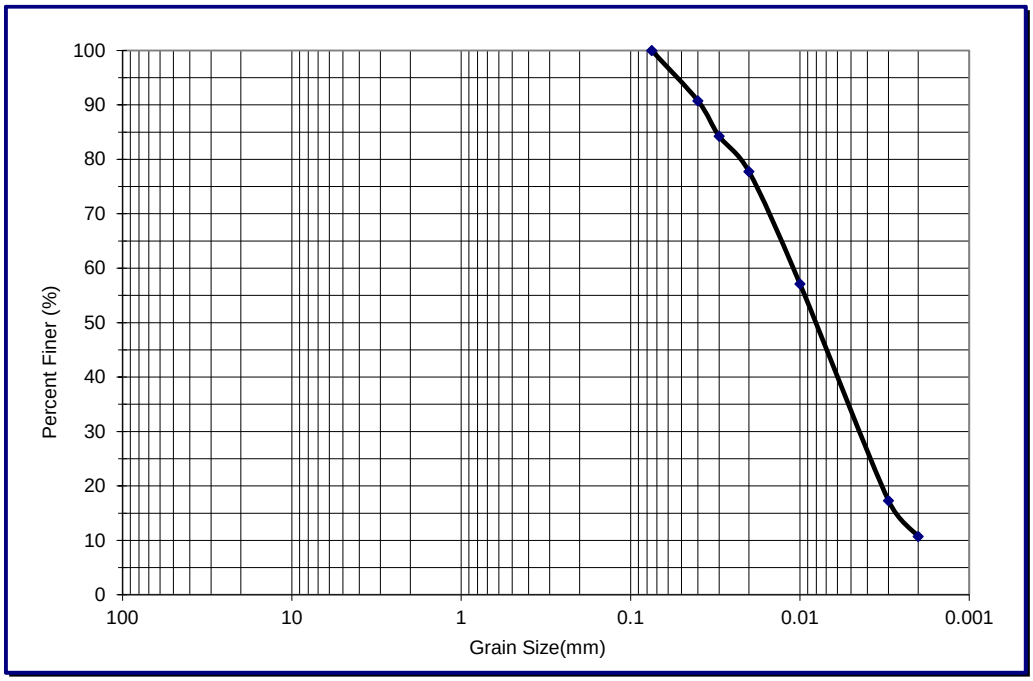

Figure 4. The aggregate gradation of lime.

This study encompassed the utilization of four different water content levels, namely 70%, 80%, 90%, and 100%. The determination of water content was based on the formula "water amount * 100/egg white," thereby expressing the water percentage relative to the dry mass of the egg white. For each water content level, three identical samples were meticulously prepared, ensuring consistency in both water amount and additive quantity. The primary constituents of Khorasan mortar, namely brick ballast, standard sand, and lime, were combined in a ratio of 9:3:4, respectively, within the mixture. Notably, a 60% water content level was initially attempted numerous times; however, the samples

proved fragile and lacked cohesion during preparation, leading to their exclusion from the study. To facilitate better comprehension, the mixtures were assigned unique codes. For instance, the mixture code EW70C7-1 signifies "EW" as egg white, "70" representing the water percentage relative to the egg white amount, "S" denoting the sample, and "1" indicating the sample number. There were prepared 3 identical (same additive ratio and same water content) samples. Therefore, samples were numbered as 1, 2 and 3. The admixture ratio within the mixture mirrors that of the lime component. Further details regarding the mixture compositions can be found in Table 2.

Table 1. Mixture details

Mixture Code	Sample Number	Water (g)	Egg White (g)	Brick Ballast (g)	Standard Sand (g)	Lime (g)
EW70S1	1	28	40	90	30	40
EW70S2	2	28	40	90	30	40
EW70S3	3	28	40	90	30	40
EW80S1	1	32	40	90	30	40
EW80S2	2	32	40	90	30	40
EW80S3	3	32	40	90	30	40
EW90S1	1	36	40	90	30	40
EW90S2	2	36	40	90	30	40
EW90S3	3	36	40	90	30	40
EW100S1	1	40	40	90	30	40
EW100S2	2	40	40	90	30	40
EW100S3	3	40	40	90	30	40

2.2. Specimen Preparation

Brick ballast was prepared for use by grinding it with a Los Angeles abrasion test device. A total of 1500 revolutions were performed to attain a finer material suitable for testing purposes. Additionally, egg white was exclusively incorporated after being broken and mixed in a porcelain dish. The materials comprising Khorasan mortar were meticulously blended to ensure homogeneity. To achieve smooth and uniform compaction, equal amounts of the sample were poured for each layer. The compaction process was carried out using specialized Harvard compaction test equipment, as illustrated in Fig. 5a.

a) b) c)

Figure 5. Harvard test equipment **a)** full set **b)** compaction mould **c)** compaction with hammer.

2.2. Unconfined Compression Strength (UCS) Test

Unconfined compression strength test is one of the most important signs of the change in strength and it is not a time-consuming test. Usage of low number of materials (because of the preparation of test with Harvard miniature compaction test equipment) make this test also favorable. There is no study that research the unconfined compression strength of Khorasan mortar stabilized soils with various water content. ASTM D2166D2160M-16 [10] standard was used for unconfined compression strength. The cured samples were carefully positioned on an automated triaxial

compression test device, as depicted in Fig. 6. Pertinent information regarding each sample, such as diameter, height, and mixture code, was recorded during the initial stage. A data saving interval of 1 data point per second was selected for precise data acquisition. The approximate dimensions of the samples were measured to be approximately 33 mm in diameter and 71 mm in height.

Figure 6. Automated triaxial compression test device for unconfined compression strength.

To ensure compliance with the standard requirements [10], a loading rate of 0.71 mm/min was selected, as this would facilitate the attainment of a 10% axial strain within a 10-minute duration of the test. The lower part of the device was gradually elevated until it made contact with the sample, while the top part was positioned accordingly. The efficacy of this alignment was verified by monitoring the load variation displayed on the program screen. The automated triaxial compression test device provided comprehensive results pertaining to the axial stress and strain of the samples.

3. Results and Discussion

This section provides a concise summary of the stress-strain graphs obtained from the automated triaxial compression test device for the various mixtures. For instance, in the case of the EW70S1 sample (Fig 7a), the unconfined compression strength (UCS) is determined to be 606.26 kPa, with the axial strain (ε) reaching a value of 2.95% at the maximum stress (UCS). The stress increase during the first 60 seconds of the test (ε = 0 - 1) for the EW70S1 sample was relatively slow, followed by a rapid enhancement beyond ε = 1% until the maximum stress was attained. Similar stress-axial strain behavior is observed for the EW70S2 and EW70S3 samples, as evident from Fig 7b and 7c. The axial strain (ε) values at the maximum stress are found to be closely distributed between 2.23% and 3.02%. The maximum UCS value being 1.13 times the minimum UCS value is within an expected range. The average UCS of the three samples is determined to be 646.88 kPa, which closely aligns with the value of the third sample (EW70S3). Regarding failure behavior, EW70S1 and EW70S3 exhibit similarities, as illustrated in Fig 8a and 8c, while EW70S2 showcases a slightly different failure pattern. The failure image of EW70S2 presents a characteristic 45° angle from the top of the sample to the peak, which is further validated by the axial strain-stress graph in Fig 8b

The EW80S1 sample exhibits an unconfined compression strength (UCS) of 792.33 kPa, with an ε value of 2.42% at the maximum stress, as depicted in Fig. 9a. During the initial 30 seconds of the test (ε = 0 – 0.5) for the EW80S1 sample, stress enhancement was relatively gradual, followed by a rapid increase between ε = 0.5% and 1%. The graph slope exhibited a slower rate during the axial strain range of 1% to 1.5% compared to the first part. The speed of the graph for the third segment, from ε = 1.5% to 2.42%, resembled the behavior observed in the initial part. Notably, the graph behavior for the EW80S1 sample differs slightly from that of EW80S2 and EW80S3, as illustrated in Fig. 9b and 6c. The axial strain (ε) values at the maximum stress are closely distributed between 2.03% and 3.02%. The difference between the maximum and minimum UCS values is 119.63 kPa, which is considered acceptable for this level of UCS, as one value is only 1.15 times that of the other. The average UCS of the three samples is determined to be 853.98 kPa, closely aligning with the value of the second sample (EW80S2). Regarding failure behavior, EW80S1 and EW80S2 demonstrate similarities when observed in Figs. 10a and 10b. Conversely, EW80S3 exhibits failure initiation from the bottom part, while the other samples fail from the top. EW80S2 exhibits a well-known failure pattern characterized by a 45° angle. The axial strain-stress graph in Fig. 10b further supports this observation, as a rapid stress reduction is observed after reaching the UCS value compared to the other samples.

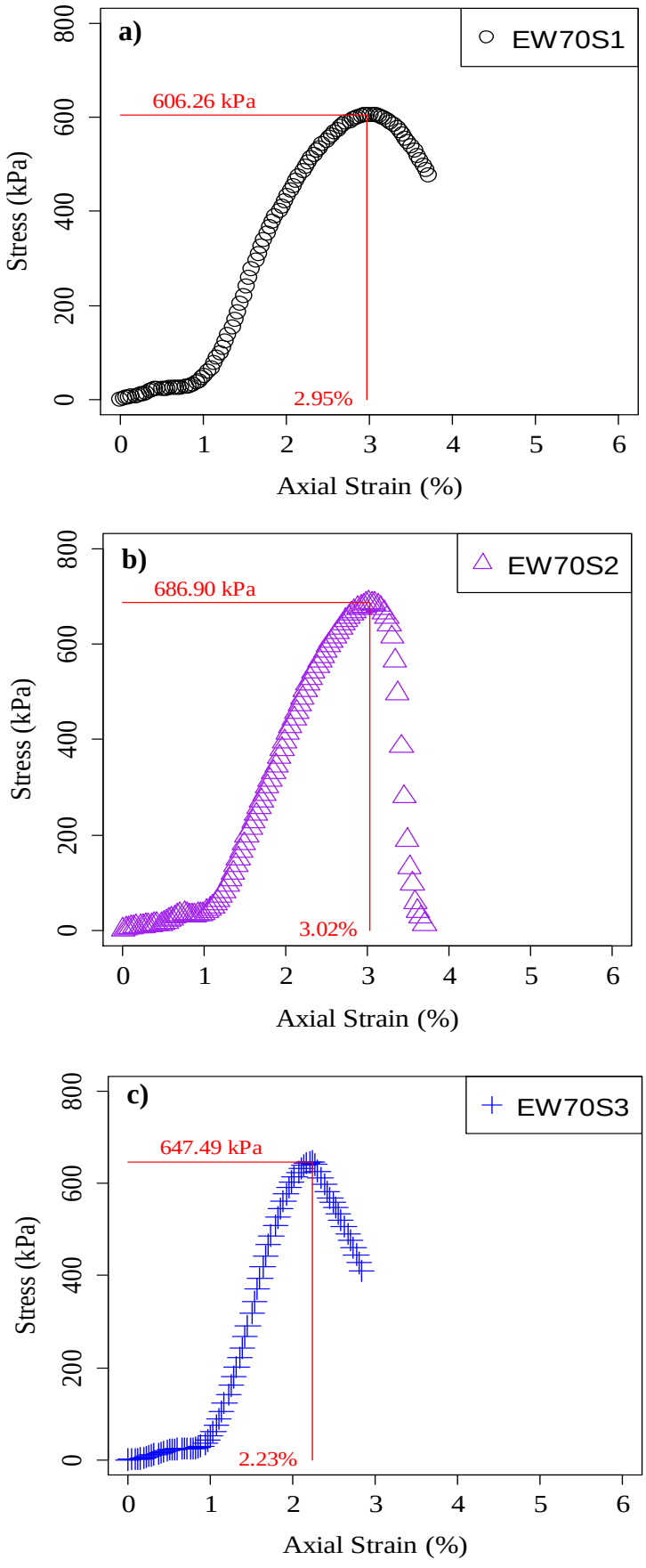

Figure 7. Stress-axial strain graphs for mixtures having 70% water content.

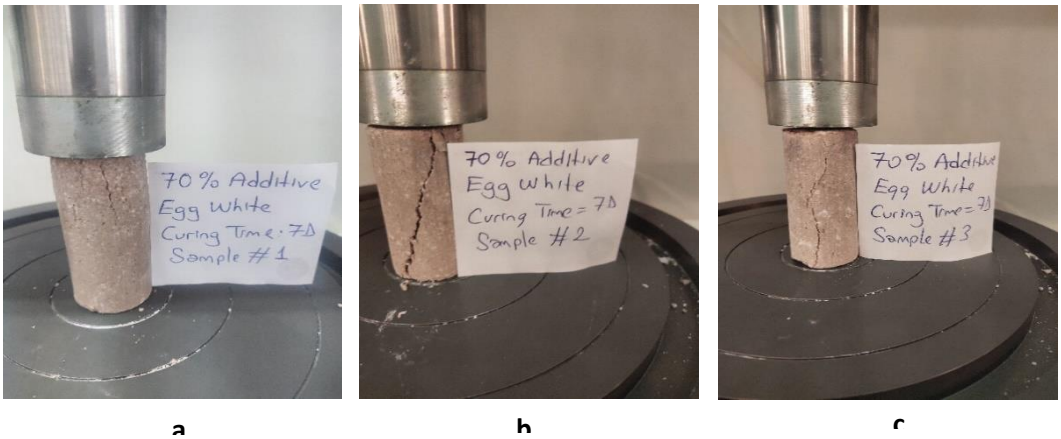

Figure 8. Failure views for samples **a)** EW70S1 **b)** EW70S2 **c)** EW70S3.

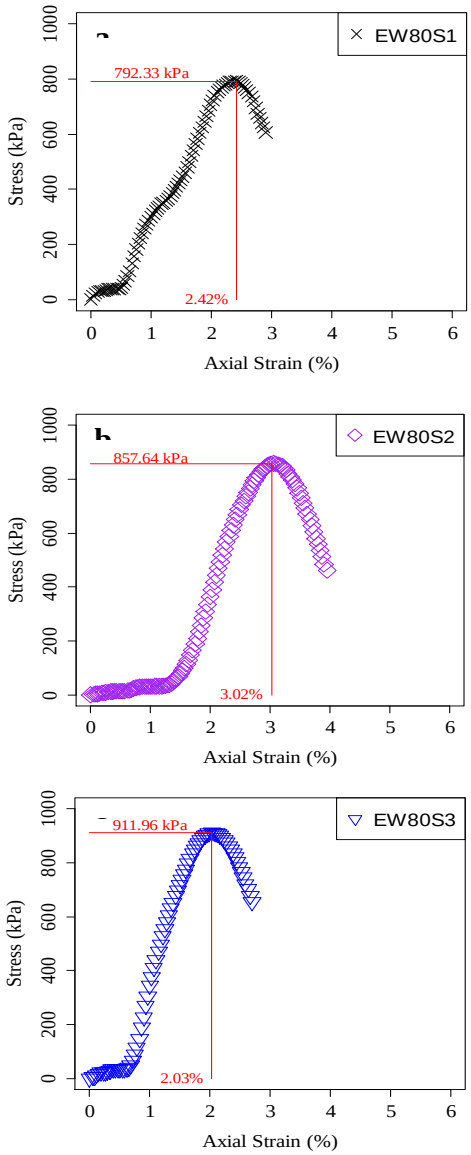

Figure 9. Stress-axial strain graphs for mixtures having 80% water content.

a) **b)** **c)**

Figure 10. Failure views for samples **a)** EW80S1 **b)** EW80S2 **c)** EW80S3.

The EW90S1 sample exhibits an unconfined compression strength (UCS) of 792.33 kPa, with an ε value of 2.42% at the maximum stress, as depicted in Fig. 9a. During the initial 30 seconds of the test (ε = 0 – 0.5) for the EW80S1 sample, stress enhancement was relatively gradual, followed by a rapid increase between ε = 0.5% and 1%. The graph slope exhibited a slower rate during the axial strain range of 1% to 1.5% compared to the first part. The speed of the graph for the third segment, from ε = 1.5% to 2.42%, resembled the behavior observed in the initial part. Notably, the graph behavior for the EW80S1 sample differs slightly from that of EW80S2 and EW80S3, as illustrated in Fig. 9b and 6c. The axial strain (ε) values at the maximum stress are closely distributed between 2.03% and 3.02%. The difference between the maximum and minimum UCS values is 119.63 kPa, which is considered acceptable for this level of UCS, as one value is only 1.15 times that of the other. The average UCS of the three samples is determined to be 853.98 kPa, closely aligning with the value of the second sample (EW80S2). Regarding failure behavior, EW80S1 and EW80S2 demonstrate similarities when observed in Figs. 10a and 10b. Conversely, EW80S3 exhibits failure initiation from the bottom part, while the other samples fail from the top. EW80S2 exhibits a well-known failure pattern characterized by a 45° angle. The axial strain-stress graph in Fig. 10b further supports this observation, as a rapid stress reduction is observed after reaching the UCS value compared to the other samples. The unconfined compression strength (UCS) of the EW90S1 sample is determined to be 516.78 kPa, with an ε value of 2.42% at the maximum stress, as illustrated in Fig. 11a. During the initial 45 seconds of the test (ε = 0 – 0.75) for the EW90S1 sample, stress enhancement was relatively gradual, followed by a rapid increase between ε = 0.75% and 2.42%. The behavior of the second graph for the EW90S2 sample differs from that of EW90S1 and EW90S3, as evident in Figs. 11a, 11b, and 11c. The graphs for EW90S1 and EW90S3 indicate ductile behavior, whereas the graph for EW90S2 exhibits brittle behavior. After reaching the maximum stress, there is a rapid reduction in stress for the EW90S2 sample compared to the graphs of EW90S1 and EW90S3. The axial strain (ε) values at the maximum stress exhibit slight variations between the samples, ranging from 2.42% to 4.65%. The difference between the maximum and minimum UCS values is 89.56 kPa, which is considered acceptable given that one value is only 1.21 times that of the other. The average UCS of the three samples is determined to be 465.18 kPa, which is close to the value of the second sample (EW90S2). Regarding failure behavior, all samples exhibit distinct characteristics when observed in Figs. 12a, 12b, and 12c. The EW90S1 sample appears to be nearly split in half (Fig 12a), while the axial strain-stress graph indicates a ductile behavior. EW90S2 showcases a similar failure pattern (Fig 12b), with a sharp decrease in stress after reaching the maximum value, as observed in Fig. 12b. The bottom part of the EW90S3 sample is observed to have undergone significant breakage, as depicted in Fig. 12c, with a stress value of approximately 380 kPa even when the ε value reaches 6.25%.

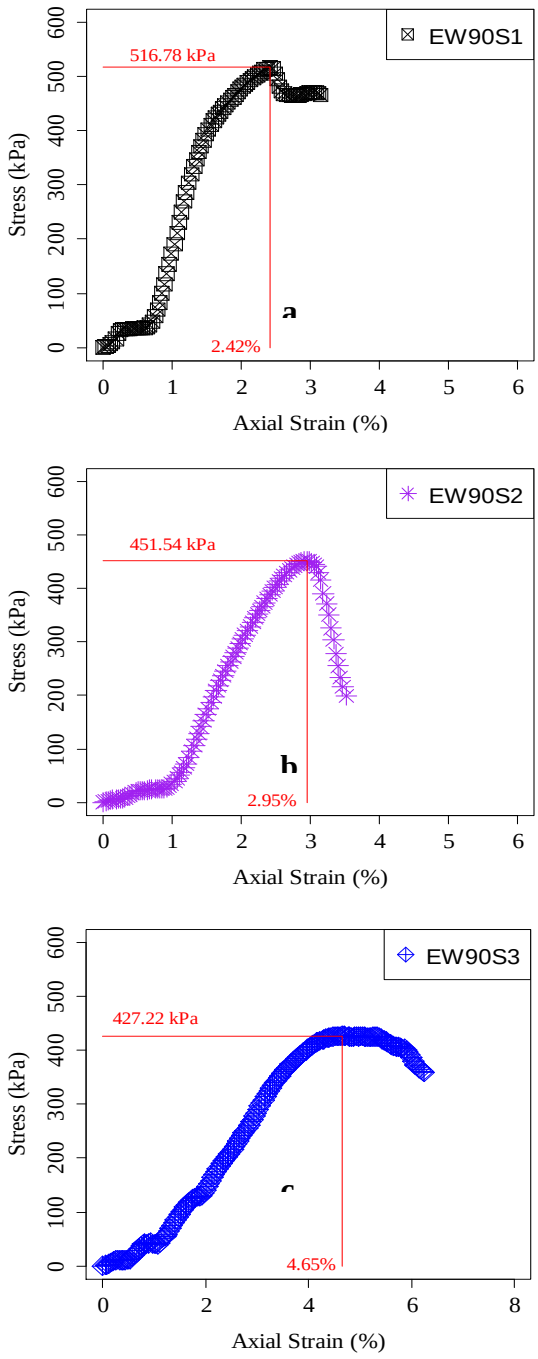

Figure 11. Stress-axial strain graphs for mixtures having 90% water content.

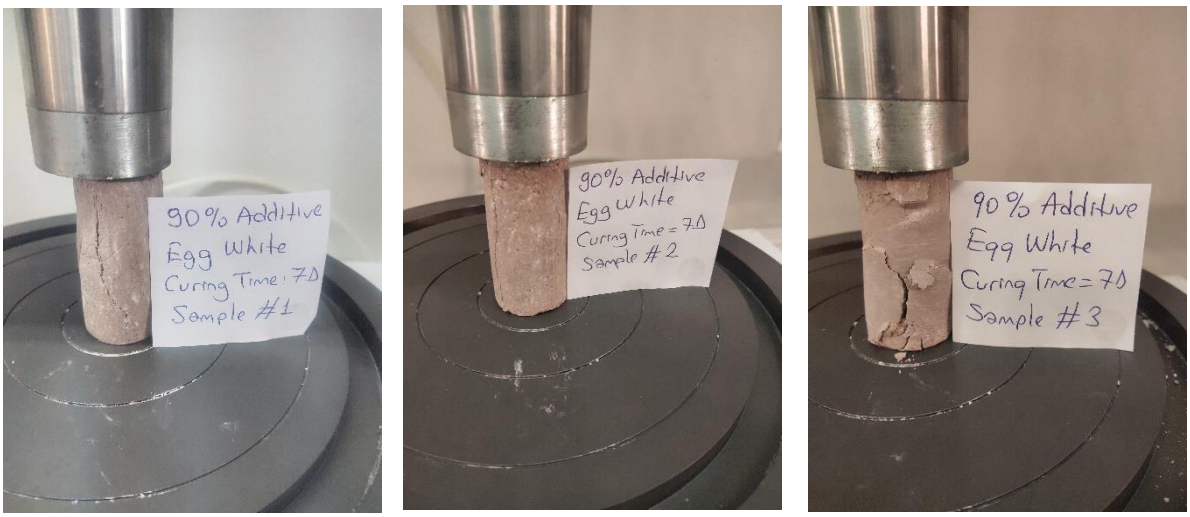

a) **b)** **c)**

Figure 12. Failure views for samples **a)** EW90S1 **b)** EW90S2 **c)** EW90S3.

The unconfined compression strength (UCS) of the EW100S1 sample is determined to be 412.14 kPa, with an ε value of 2.17% at the maximum stress, as depicted in Fig. 13a. During the initial 45 seconds of the test (ε = 0 – 0.75) for the EW100S1 sample, stress enhancement was relatively gradual, followed by a rapid increase between ε = 0.75% and 2.17%. The behavior of the graphs for the EW100S1, EW100S2, and EW100S3 samples appeared similar, as observed in Figs. 13a, 13b, and 13c. However, the graphs for EW100S3 exhibit a slightly more brittle behavior compared to EW100S1 and EW100S2. There is a significant stress reduction of 200 kPa within a small ε range (between 3.6% and 4%) after reaching the maximum stress for EW100S3. This reduction occurs more rapidly compared to EW100S1 and EW100S2, as indicated by their respective graphs. The axial strain (ε) values at the maximum stress exhibit slight variations between the samples, ranging from 2.17% to 4.05%. The difference between the maximum and minimum UCS values is 72.76 kPa, which is considered acceptable given that one value is only 1.18 times that of the other. The average UCS of the three samples is determined to be 442.51 kPa, which is close to the value of the second sample (EW100S2). Regarding failure behavior, EW100S1 and EW100S2 samples exhibit similar characteristics, with the breaking initiating from the bottom and displaying a comparable shape, as depicted in Figs. 14a and 14b. In contrast, EW100S3 demonstrates a typical failure behavior (Fig. 14c) when considering the axial stress-strain graph (Fig. 13c) in conjunction. A significant decrease in stress (approximately 180 kPa within an ε range between 3.60% and 4%) is observed after the occurrence of maximum stress.

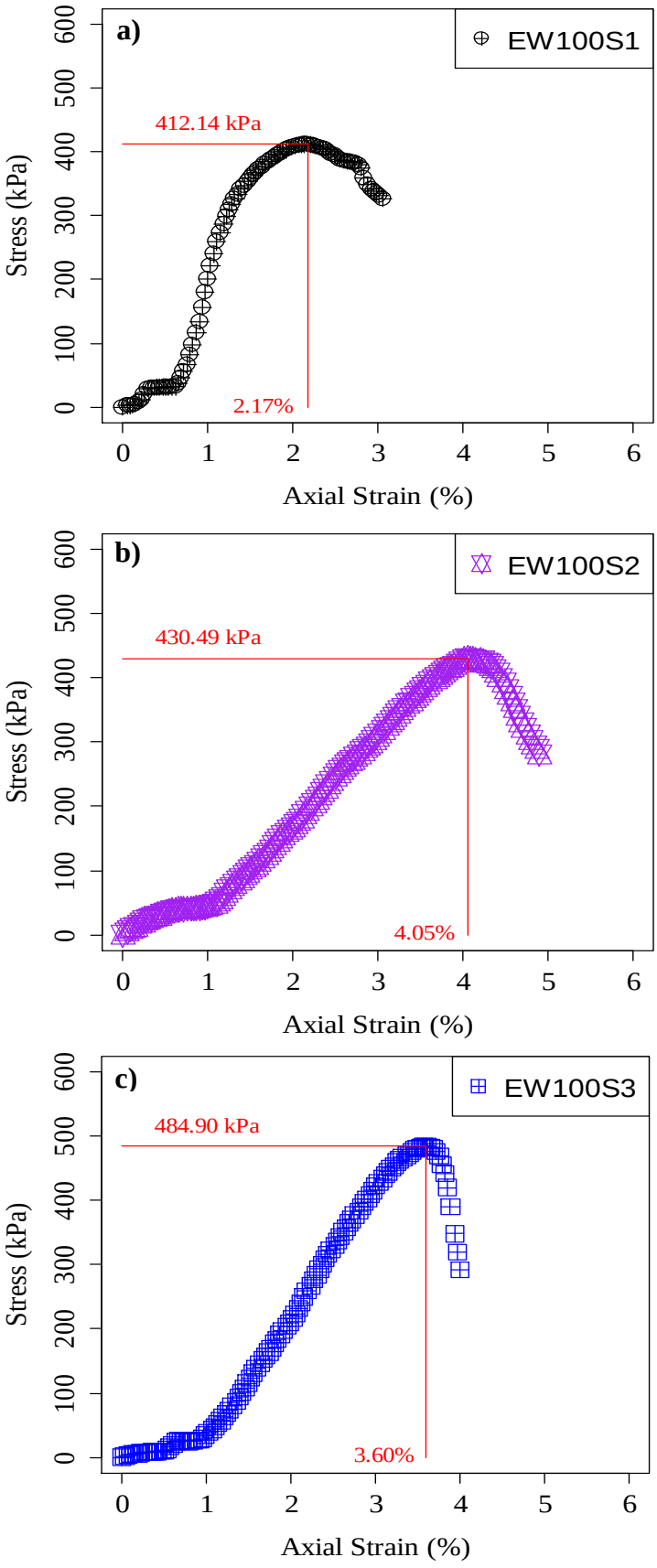

Figure 13. Stress-axial strain graphs for mixtures having 100% water content.

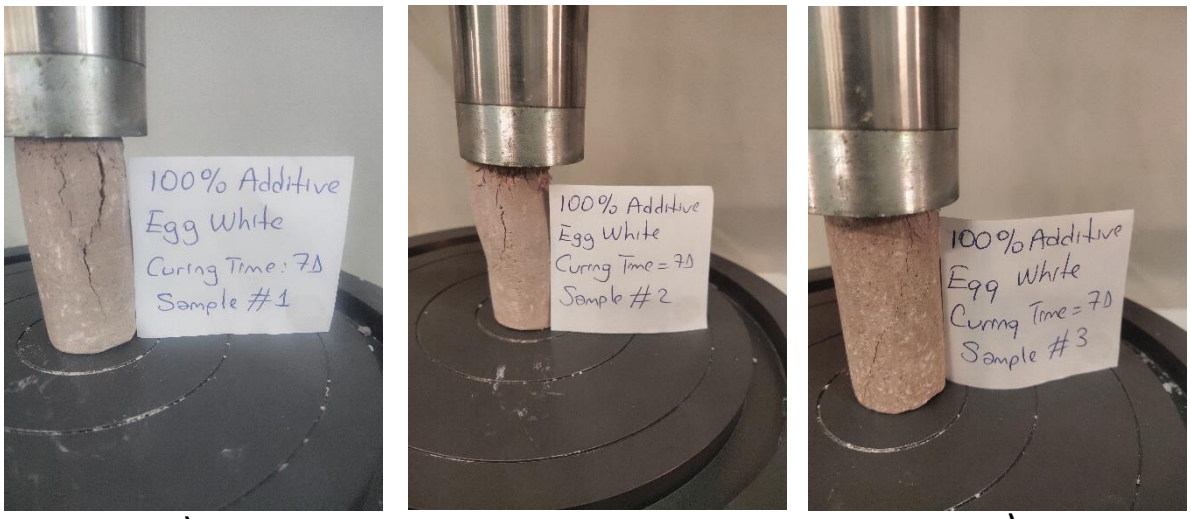

Figure 14. Failure views for samples **a)** EW100S1 **b)** EW100S2 **c)** EW100S3.

Table 3. Results of unconfined compression strength tests.

Mixture Code	Sample Number	ε (%)	UCS (kPa)
EW70S1	1	2.95	606.26
EW70S2	2	3.02	686.90
EW70S3	3	2.23	647.49
EW80S1	1	2.42	792.33
EW80S2	2	3.02	857.64
EW80S3	3	2.23	911.96
EW90S1	1	2.42	516.78
EW90S2	2	2.95	451.54
EW90S3	3	4.65	427.22
EW100S1	1	2.17	412.14
EW100S2	2	4.05	430.49
EW100S3	3	3.60	484.90

All the results have been compiled and presented in Table 3. It is noteworthy that the axial strain (ε) values corresponding to the attainment of UCS for the mixtures do not exceed 4.65%. The overall average of ε is calculated to be 2.98%. These strain values at maximum stress suggest that the mixtures have been effectively stabilized with lime. The increase in water content from 80% to 90% results in a significant reduction of approximately 45.43% in the average UCS value. Further increasing the water content up to 100% does not bring about any significant change in the UCS. The EW70 and EW80 samples exhibit ε values that do not surpass 3.02%, whereas the EW90 and EW100 samples demonstrate axial strains of 4.05% and 4.65% respectively. This observation may serve as an indication of the comparatively lower strength of the EW90 and EW100 samples when compared to the EW70 and EW80 samples.

4. Conclusion and Suggestions

In this study, the optimization of water content for Khorasan mortar samples was thoroughly investigated, leading to the following conclusions:

- The unconfined compression strength (UCS) test results revealed that mixtures containing 80% water content exhibited the highest UCS values, indicating their optimal composition.
- The samples with EW100 mixtures, which had the highest water content, exhibited the lowest UCS values. This suggests that increasing the water content beyond a certain threshold does not have a positive effect on the strength of the mixtures. On average, the UCS of these mixtures was approximately 0.518 times lower than that of the EW80 mixtures.
- Water contents lower than 70% were also experimented with, but the lack of sufficient moisture resulted in poor cohesion between particles. As a consequence, the samples were dry and prone to breakage upon extrusion from the sample extractor.
- These findings highlight the importance of considering the water content when preparing Khorasan mortar. Insufficient water content, without proper research, may be responsible for the lower unconfined compression strength observed in the samples.

These conclusions offer valuable insights for the preparation of Khorasan mortar, emphasizing the

significance of optimizing the water content to achieve the desired strength and quality in the mortar.

Acknowledgment

The authors wish to express their thanks to the authors of the literature for the supplied scientific aspects and ideas for this study.

Conflict of Interest Statement

There is no conflict of interest between the authors.

Statement of Research and Publication Ethics

The study is complied with research and publication ethics.

References

[1] M. S. Akman, A. Güner, and İ. H. Aksoy, "The history and properties of khorasan mortar and concrete," *II. Uluslararası Türk-İslam Bilim ve Teknoloji Tarihi Kongresi, İstanbul, Türkiye, April 28- May 2, 1986*, pp. 1-11.

[2] İ. Kılıç, "Horasan harcında yumurta akı kullanımının incelenmesi" *Kırklareli Üniversitesi Journal of Engineering and Science*, vol. 7-1, pp. 122-134, June 2021.

[3] T. İsafça-Kaya, K. Karakuzu, S. Özen, A. Mardani, and A. Doğangün, "Effects of shrinkage reducing admixture and polypropylene fiber utilization on some fresh state, mechanical and durability properties of khrosan mortar" *International Journal of Architectural Heritage*, July 2022, https://doi.org/10.1080/15583058.2022.2100295..

[4] H. S. Şengel, M. Canbaz, and E. Güler, "Utilization of ceramic waste in the production of Khorasan mortar" *Challenge Journal of Structural Mechanics*, vol. 5, no. 3, pp. 80-84, 2019, https://doi.org/10.20528/cjsmec.2019.03.001.

[5] N. Arıoğlu, and S. Acun, "A research about a method for restoration of traditional lime mortars and plasters: A staging system approach" *Building and Environment*, vol. 41, no. 9, pp. 1223-1230, September 2006, https://doi.org/10.1016/j.buildenv.2005.05.015.

[6] H. Böke, S. Akkurt, and B. İpekoğlu, "Tarihi yapılarda kullanılan horasan harcı ve sıvalarının özellikleri [The properties of Khorasan mortar and plasters used in historical buildings]" *Yapı Dergisi*, 2004.

[7] B. Işıkdağ, and İ. B. Topçu, "Improvement of Khorasan mortar with fly ash for restoration of historical buildings" *Science and Engineering of Composite Materials*, vol. 21, no. 3, pp. 359-367, 2014, https://doi.org/10.1515/secm-2013-0065.

[8] A. Bilal, "Investigation of hydraulic binding characteristics of lime based mortars used in historical masonry structures" *IOP Conf. Series: Materials Science and Engineering*, vol. 245, 022081, 2017, https://doi.org/10.1088/1757-899X/245/2/022081

[9] C. B. Emrullahoğlu Abi, and E. Abi, "Bentonite doped Khorasan mortar" *Academic Journal of Science*, vol. 08, no. 02, pp. 43-54, 2018.

[10] ASTM D2166/D2166M-16. Standard test method for unconfined compressive strength of cohesive soil, 2016. pp. 1-7.

[11] M. Canbaz and E. Güler, "The Effect of Lime Type on the Properties of Khorasan Mortar" *6th Symposium on Conservation and Strengthening of Historical Buildings*, Trabzon, 2017.

Bitlis Eren Üniversitesi Fen Bilimleri Dergisi
BİTLİS EREN UNIVERSITY JOURNAL OF SCIENCE
ISSN: 2147-3129/e-ISSN: 2147-3188
VOLUME: 12 NO: 4 PAGE: 1083-1093 YEAR: 2023
DOI:10.17798/bitlisfen.1335217

Work Accidents: A Bibliometric Analysis of International Literature and the Situation in Turkey

Ali AĞAR[1*]

[1]*Artvin Çoruh University, Şavşat Vocational School Health Care Services Department, Artvin, Türkiye*
(ORCID: 0000-0003-2771-9587)

Keywords: Bibliometric Analysis, Work Accident, Occupational Health and Safety, VOSviewer, Web of Science.

Abstract
With scientific and technological developments, people's welfare levels have increased. However, occupational accidents still continue to be an important problem in workplaces around the world. The aim of this study is to examine the necessary articles about the active journals, the most publishing countries, the most used keywords and research areas in the international and Turkish literature on occupational accidents. In this study, bibliometric analysis techniques were used to realize the purpose of the research and to find answers to the research questions. Research data were obtained from the Web of Science (WoS) database in November 2023. VOSviewer and Excel software program were used in the analysis of the data. While the most publications on work accidents in the world were made in 2022, they were made in 2021-2022 in Turkey. While the most publications were made in the field of public, environmental and occupational health as a research subject in the world, the most publications were made in the field of engineering in our country. While United States of America is the most broadcasting country in the world, Turkey ranks third. It has been determined that the most widely published journal in the world is Safety Science magazine and the most frequently used keyword is occupational accident. In addition, it has been determined that most of the publications addressing Turkey were made in Istanbul University. As a result, preventing work accidents should be the first priority in order to increase the productivity of workplaces and the efficiency of employees. Therefore, increasing and supporting research on occupational accidents is of great importance for the awareness of the global community and employees.

1. Introduction

People spend most of their life in working life. Working is one of the most important determinants of a person's living conditions and health. Also, work is necessary for human beings as it is the way to gain respect, integration, socialization, recognition and bonds of friendship [1].

With scientific and technological developments, people's welfare levels have increased. However, occupational accidents still continue to be an important problem in workplaces around the World [2]. The International Labor Organization (ILO) defines an occupational accident as an unexpected and unplanned work-related event, including acts of violence that causes injury, illness or death to one or more workers [3].

Occupational accidents are one of the phenomena that have become widespread with technological developments and threaten employee health, causing financial losses to human communities [4]. Occupational accidents directly affect the construction of social reality. It poses a serious public health problem, primarily because it leaves youth and working-age adults disabled or even fatally injured [5].

Every year, countless employees suffer material and moral damage due to work accidents. Occupational accidents not only damage work activities, but also cause significant economic, social

*Corresponding author: aliagar828@gmail.com
Received: 31.07.2023, Accepted: 19.12.2023

and environmental effects [6]. Every year, millions of occupational accidents occur in the world that cause injuries and economic losses [2]. According to the ILO, approximately 4% of the world's gross domestic product (GDP) is lost every year as a result of work accidents and occupational diseases. The exact number of deaths from occupational accidents and occupational diseases worldwide is not available because most countries do not have reliable sources to obtain these figures [5]. In addition, 588 thousand 823 employees will have work accidents in Turkey in 2022, and 1517 of them died [7]. While a total of 2 million 607 thousand 900 employees had work accidents in the USA in 2021, 5 thousand 190 people died as a result of work accidents [8]. In Canada, a total of 253 thousand 397 employees had a work accident in 2020, while 924 employees died as a result of a work accident [9]. ILO states that every year there are approximately 340 million work accidents worldwide and 2.3 million workers lose their lives. The ILO periodically updates these estimates and the updates show that accidents and health problems are increasing [10]. The financial burden of occupational accidents is greater than costly diseases such as cancer, Alzheimer's, human immunodeficiency virus (HIV) and cardiovascular diseases [4], [11].

For this reason, occupational accidents are an important burden for society [12]. Various studies have been conducted to investigate the causes of accidents, including the well-known Heinrich's domino theory. After Heinrich's work in 1931 and the presentation of the domino model, the idea that the most critical role in the occurrence of the accident was formed. According to his study, 88%, 10% and 2% of the causes of accidents, respectively, are related to unsafe behavior, unsafe conditions and unpredictable factors [13].

No study has been found in the literature on the bibliometric analysis of publications in the field of occupational accidents. This study is especially for researchers; It will shed light on the active journals in the international literature on occupational accidents, the countries with the most publications, the most used keywords and the necessary articles about the research areas. In addition, this study will contribute to researchers who want to study work accidents in Turkey by revealing the deficiencies in the literature and preserving originality in the path they will follow. In line with the purpose of the research, the research questions are as follows:

- In which years were the most publications made on occupational accidents in the world?
- Which countries publish the most publications on occupational accidents?
- What are the most studied topics or concepts according to the keywords of the publications on occupational accidents?
- In which years were the most publications about work accidents made in Turkey?
- What are the most published research areas regarding work accidents in Turkey?
- Which institutions publish the most on work accidents in Turkey?

2. Material and Method

In this study, bibliometric analysis techniques were used to realize the purpose of the research and to find answers to the research questions.

Bibliometric analysis is widely used in qualitative and quantitative research to evaluate and compare the trends and academic impact of journals [14]. Bibliometric analysis is a field of scientific study that aims to create research performance indicators of studies that represent a topic based on the quantitative analysis of academic documents [15] – [17]. Bibliometric studies analyze a particular scholarly journal and publications in a particular field to map the most prolific authors, institutions, countries, and journals by their scientific productivity and citation rates [18]. In addition, the bibliometric analysis method relies on specific articles to identify publications, citations, authors, countries and keywords. The results of these studies have shown that bibliometric analysis can reveal the status and global trend of a particular journal and further improve its quality on this basis [14].

Bibliometric analysis was performed using VOSviewer (Version 1.6.19, Center for Science and Technology Studies of Leiden University), a mapping and visualization software tool. The VOSviewer program, on the other hand, has been used for data visualization among many existing software due to its free accessibility and ease of use. VOSviewer provides researchers with the opportunity to analyze a wide variety of bibliometric networks consisting of publications, authors, journals, organizations or countries [18].

2.1. Data Collecting

Research data were obtained from the Web of Science (WoS) database in November 2023. Study data in bibliometric studies can be obtained from WoS, Scopus and Google Scholar databases. Each database has its own unique functionality. Compared to WoS, Scopus and Google Scholar, it offers a rich publication and citation history and includes only high-impact factor journals and provides efficient

access to bibliographic data [18]. For this reason, research data were obtained from the WoS database.

By using the search button in the WoS database, the literature was scanned with the keywords "work accident" or "occupational accident" or "workplace injuries" or "fatal and non-fatal work accidents" for all fields, and a total of 1751 studies constituted the universe of the research. The sample of the research was included in the studies that met the criteria for participation in the research. The criteria for inclusion in the research are as follows.

1. Published only in English
2. Emerging sources citation index (ESCI), Science Citation Index Expanded (SCI-EXPANDED) and Social Sciences Citation Index (SSCI) have been published
3. Studies conducted between 2003 and 2023 (studies conducted in the last 20 years)
4. Only research articles were included, while other types of publications (e.g. proceedings, meeting abstracts, retracted publications, and book chapters) were not included.

As a result of these inclusion criteria, 143 publications were not included because they were not published between 2003 and 2023, 116 were not published because they were not research articles, 291 studies were not included because the publication language was not English, and 170 publications were not included in the specified indexes. 1031 publications that met the inclusion criteria for the research were reached. The titles, abstracts or full texts were read and evaluated to determine whether they met the research topic. In addition, the effectiveness of bibliometric analyzes in the field of work accidents in Turkey's international literature was also evaluated. Figure 1 shows the research flow chart.

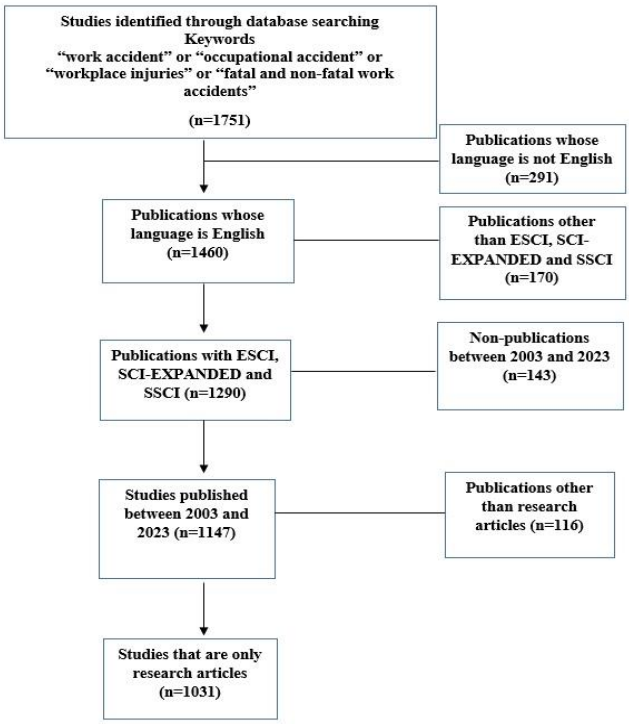

Figure 1. Flow chart of literature search and selection process

2.2.Data Analysis

Data were analyzed using descriptive content and bibliometric content analysis. Descriptive features (distribution of publications by years, type of publication, research area and journals) were analyzed using Excel program. Descriptive analysis consists of three stages. First, by entering the keywords determined on the WoS database, studies in the field of work accidents were accessed and some studies were excluded within the scope of the inclusion criteria. Then, the obtained data were classified using the Excel program and tables and figures were created.

3.Results

The findings of the research include the distribution of studies on occupational accidents in the world according to their years, journals in which they were published, research areas, publishing countries and the most used keywords in publications in this field. In addition, the years of publications on occupational accidents in Turkey, universities that publish, research areas and the most frequently used keywords in the studies are included.

When Figure 2 is examined, it is seen that the most publications on work accidents in the world were made in 2022 (101 publications), followed by 2020 (93 publications) and 2019 (87 publications). The fewest publications were made in 2004 (10 publications), followed by 2003 (16 publications), 2005 (18 publications) and 2006 (18 publications).

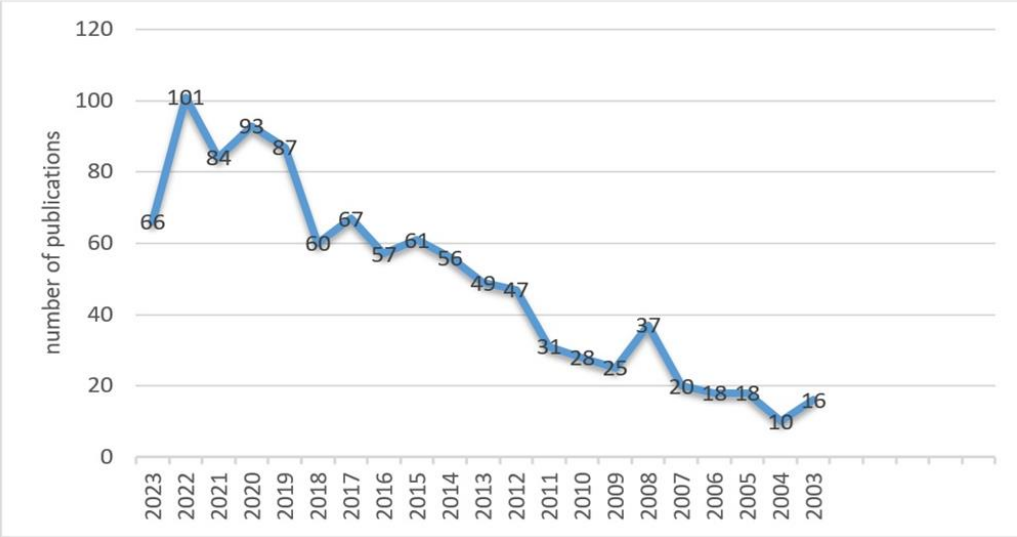

Figure 2. Flow chart of literature search and selection process [19]

Table 1 lists the 10 journals in which studies on work accidents are most frequently published in the world. It is seen that the journal with the most publications is "Safety Science" with 78 publications, followed by "American Journal Of Industrial Medicine" with 43 publications and "Journal of Safety Research" with 31 publications.

Table 1. The 10 journals in the world where studies on work accidents are most published [19]

Publication Titles	Record Count
Safety Scıence	78
Amerıcan Journal of Industrıal Medıcıne	43
Journal of Safety Research	31
Work a Journal of Preventıon Assessment Rehabılıtatıon	29
Internatıonal Journal of Occupatıonal Safety and Ergonomıcs	21
Journal of Occupatıonal And Envıronmental Medıcıne	20
Internatıonal Journal of Envıronmental Research and Publıc Health	18
Accıdent Analysıs and Preventıon	15
Internatıonal Journal of Occupatıonal And Envıronmental Health	13
Occupatıonal and Envıronmental Medıcıne	13

Figure 3 shows the 10 most frequently conducted research areas on work accidents in the world. Most publications were made in the fields of "Public Environmental Occupational Health" (404 publications), "Engineering" (251 publications) and "Operations Research Management Science" (89 publications). The

research fields with the least publications are "Nursing" (34 publications), "Psychology" (47 publications) and "Transportation" (52 publications), respectively.

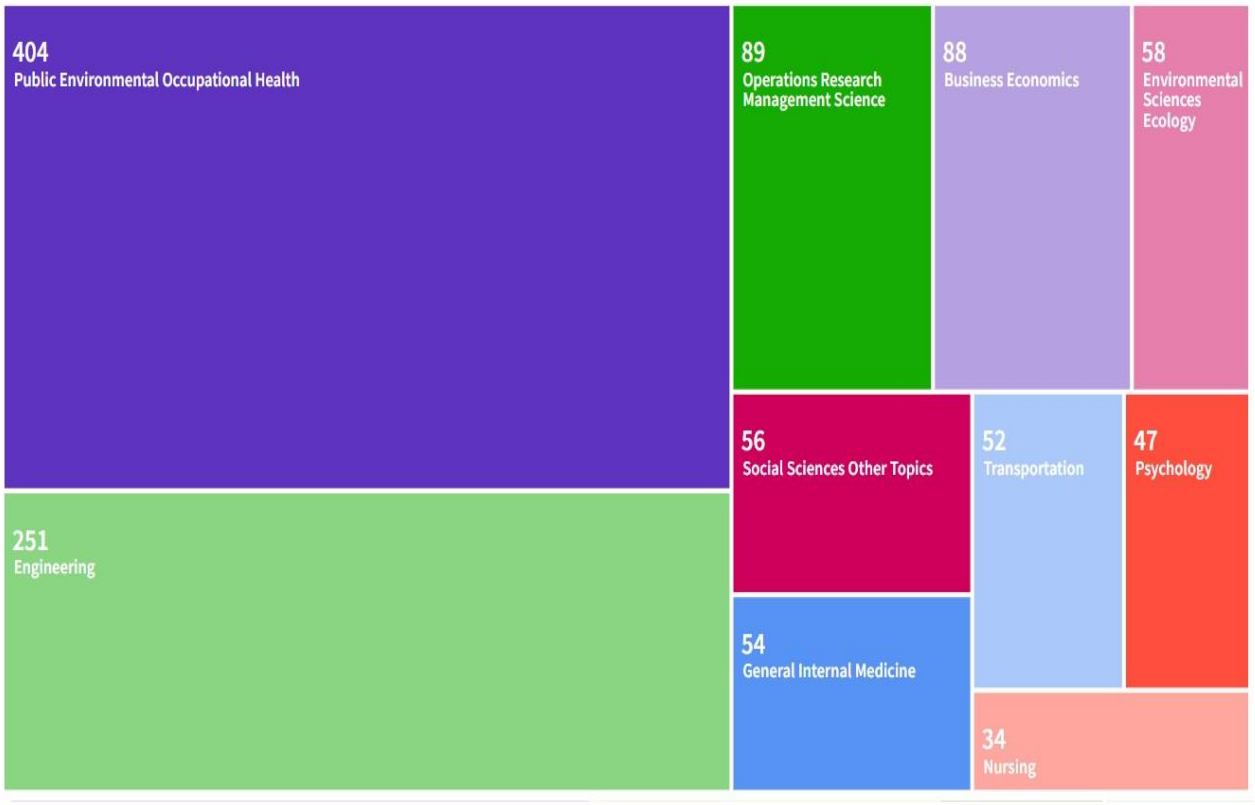

Figure 3: The 10 most published research areas on work accidents in the world [19].

Figure 4 shows the distribution of the 10 countries that publish the most on work accidents in the world. It was determined that most of the publications were made in the United States (280 publications), followed by Canada (86 publications) and Turkey (80 publications). It is seen that the countries with the least publications are France (33 publications), South Korea (34 publications) and Germany (39 publications).

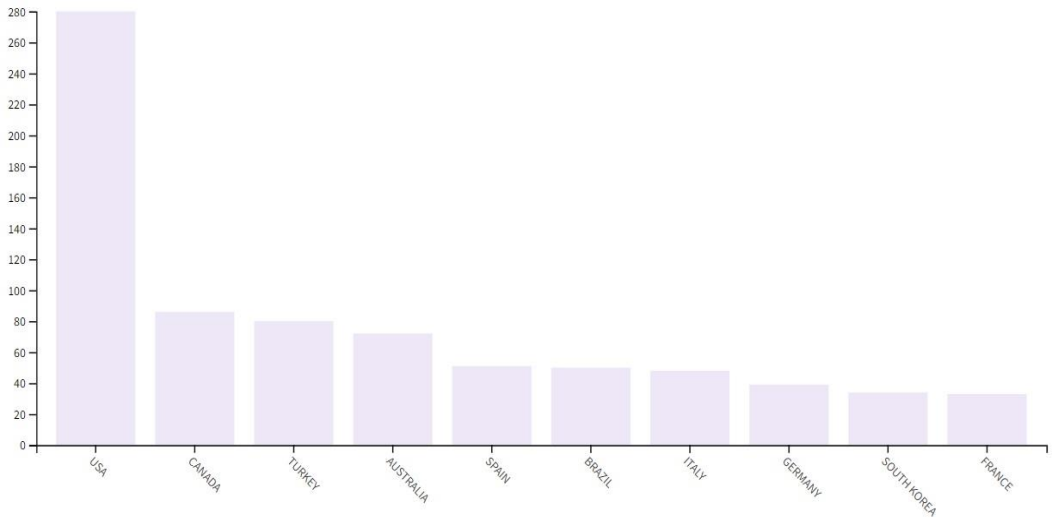

Figure 4: The 10 countries that publish the most about work accidents in the world [19].

Figure 5 shows the keywords used in studies on work accidents in the world. In the studies, the authors used 2791 different keywords. Keywords used two or more times were included in the word cloud analysis. The size of the circle shows the frequency of use of the keyword, colors show the clustering of keywords, and lines show the usage of keywords together. The most frequently used keywords were found to be Occupational Accident (140 times), Work Accidents (53 times) and Occupational Accidents (51 times).

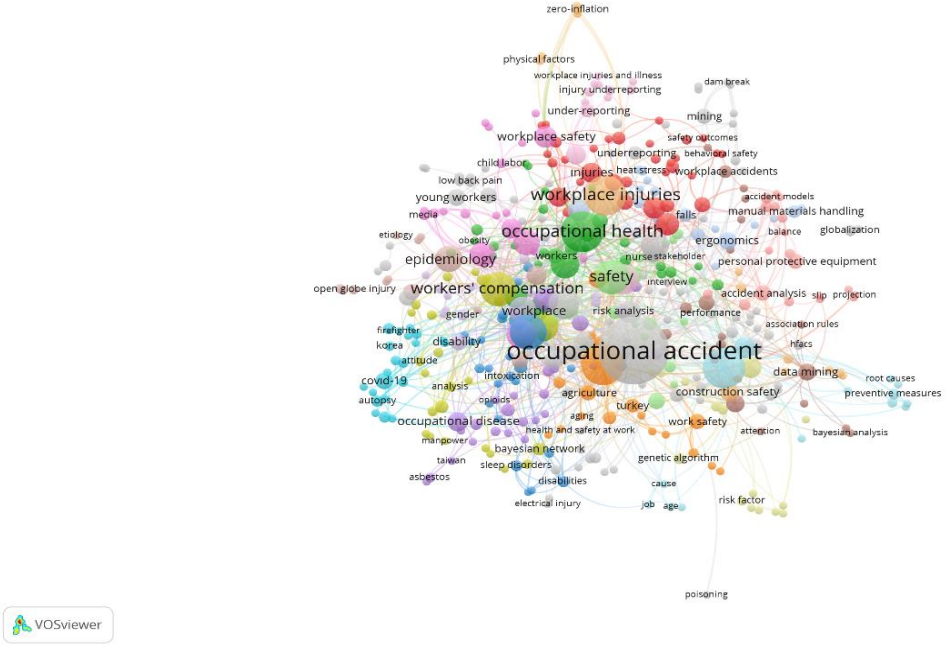

Figure 5: Keywords used in studies on work accidents in the world [19].

3.1. Publications From Türkiye

In the next part of our research, a total of 100 publications related to work accidents, addressed to Turkey, were analyzed. The distribution of the number of publications by years is shown in Figure 6. It is noteworthy that especially in 2021 and 2022, the number of publications addressing Turkey is higher than in other years. Additionally, the number of publications in 2019 and 2015 is higher than in other years. In 2023, the number of publications appears to be 0. This may be due to the fact that 2023 has not yet been completed.

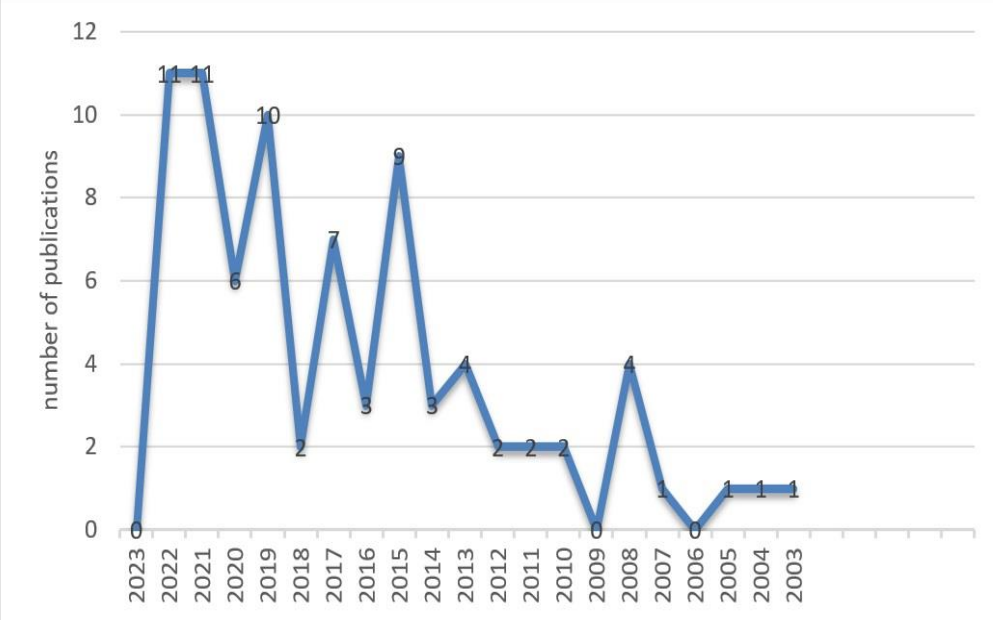

Figure 6: Distribution of studies on work accidents in Turkey by years [20].

In the table, the distribution of publications regarding work accidents from Turkey according to universities is shown for the top 10 most active universities. When the figure is examined, it can be seen that the most active contributors to the literature are Istanbul Technical University (7 publications), Yıldız Technical University (6 publications) and Istanbul University (5 publications).

Table 2: Distribution of studies on work accidents in Turkey according to universities [20].

Affiliation with Department	Record Count
Istanbul Technıcal Unıversıty	7
Yıldız Technıcal Unıversıty	6
Istanbul Unıversıty	5
Ankara Numune Traınıng Research Hospıtal	4
Dokuz Eylul Unıversıty	4
Ege Unıversıty	3
Hacettepe Unıversıty	3
Karadenız Technıcal Unıversıty	3
Kırıkkale Unıversıty	3
Mınıstry Of Justıce Turkey	3

Figure 7 shows the 10 most published research areas in the field of occupational accidents in Turkey. The most common ones are "Engineering" (20 publications), "Public Environmental Occupational Health" (17 publications) and "Emergency Medicine" (12 publications).

Figure 7. The 10 most published research areas in the field of work accidents in Turkey [20].

Figure 8 shows the keywords used in studies on work accidents in Turkey. In the studies, the authors used 260 different keywords. Keywords used two or more times were included in the word cloud analysis. The size of the circle shows the frequency of use of the keyword, colors show the clustering of keywords, and lines show the usage of keywords together. The most frequently used keywords were found to be Occupational Accident (22 times), Work Accidents (11 times) and Occupational Health and Safety (9 times).

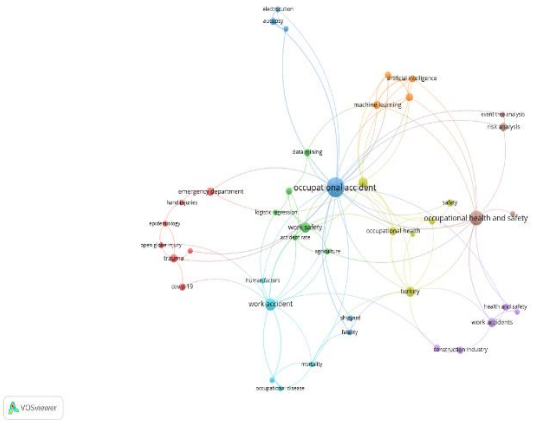

Figure 8. Keywords used in studies on work accidents in Turkey [20].

4. Conclusion and Suggestions

In this research, studies in the field of occupational accidents were examined by bibliometric analysis method. Studies in this area were accessed from the Web of Science Core Collection database. Other databases were not used. By using VOSviewer software and excel application, the publication year, research areas, the most publishing journals and word mining analyzes of the studies on occupational accidents were made.

In our research, the number of work accidents by year is given. The number of publications is a descriptive indicator that shows the productivity in the relevant field [21]. While the number of publications in this field was 16 in 2003, it is seen that it increased to 101 in 2022. Even if there is not a regular increase every year, there is an increase in the number of publications made over the last 20 years. This may be thought to be due to the fact that the importance given by countries and researchers to occupational accidents is increasing every year. In addition, legislators have to develop various policies regarding work accidents in order to increase the development levels of their countries. This situation has led to research on work accidents.

Analysis of the countries or journals that publish the most on the subject provides information about their productivity. Therefore, the one who publishes the most is considered the most productive [22]. It is seen that the journal that contributes the most to the work accident literature in the world is Safety Science. Therefore, this shows that the most productive journal contributing to the work accident literature is Safety Science. It may be important for a healthy research process for researchers who will work in this field to start their studies after reviewing the publications in the Safety Science journal. In addition, this journal is a journal with a high impact factor [23], and therefore, publication of work accident-related publications in high-impact journals will increase the motivation of researchers and positively affect the quality of future studies.

It has been determined that the countries that contribute the most to the work accident literature in the world are the United States, Canada and Turkey. It can be interpreted that these countries are the most productive countries contributing to the literature on work accidents. It can also be considered that the USA and Canada have an absolute advantage in this area due to their better economy and scientific research expenditures. In Turkey, the high number of publications on occupational accidents can be interpreted as a positive finding as it indicates that the body of knowledge on this subject will continue to increase. However, although studies on work accidents on a global scale seem sufficient, it can be interpreted that the publications have no effect on work accidents in the country.

In the international literature, it is seen that the most publications about work accidents are in the field of Public Environmental Occupational Health. Thanks to this study, it will be better for researchers who want to publish on work accidents to see which field there is a gap in and focus on that field. Turning to other research areas will provide a versatile perspective on the field of work accidents in international literature. It was determined that the most used keyword was Occupational Accident. Using the right keywords when researchers scan the literature will lead them to the right path. Additionally, the frequency of keywords shows the most researched topics [24].

When the publications addressed to Turkey were examined, it was determined that 80 publications were produced between 2003 and 2023 and the number of publications increased over the years. It can be seen that between 2003 and 2012, a maximum of 4 publications were made only in 2008. With the occupational health and safety law no. 6331 coming into force in 2012, a gradual increase in the number of publications was observed. This may be an indication that Turkey attaches more importance to work accidents after 2012.

When we look at the institutions that publish the most in this field, we see that Istanbul University is at the forefront. This situation can be thought to be due to the interest of researchers at Istanbul University in the subject or to the fact that the university supports researchers in every field. When looking at the research areas, it is seen that most publications are made in the field of Public Environmental Occupational Health. There is great interest in this field of research in Turkey, as in the world. Likewise, the gap in other research areas in Turkey can also be evaluated by researchers. It seems that the most used keyword in publications is Occupational Accident. It can be thought that the publications made from Turkey are mostly related to the Occupational Accident.

As a result, preventing work accidents should be the first priority in order to increase the productivity of workplaces and the efficiency of employees. Therefore, increasing and supporting research on occupational accidents is of great importance for the awareness of the global community and employees. Our results provided insights and valuable information regarding occupational accident research. These findings will guide researchers to guide new researchers by examining and analyzing the gaps in the literature, journals publishing on occupational accidents, and trends in research areas in a timely manner. In addition, Turkey ranks 3rd among the countries that publish on work accidents. However, although this is considered a good result in the international literature, it is not sufficient. Supporting publications about occupational accidents and creating financial resources are important in preventing occupational accidents and increasing awareness in Turkey.

Limitations

The most critical limitation of the study is that databases such as scopus and pubmed, as well as sources that are not online, were not included in the analyzes made on the studies listed in the wos care collection.

Statement of Research and Publication Ethics

Ethical approval is not required for this study.

References

[1] L. M. C. A. Magalhães, K. T. da Silva Costa, G. N. Capistrano, M. D. Leal, and F. B. de Andrade, "A study on occupational health and safety," *BMC Public Health*, vol. 22, no. 1, pp. 1–9, Dec. 2022.

[2] B. Saranjam, I. Shirinzadeh, K. Davoudi, Z. Moammeri, A. Babaei-Pouya, and A. Abbasi-Ghahramanloo, "Latent class analysis of occupational accidents patterns among Iranian industry workers," *Sci. Rep.*, vol. 12, no. 1, p. 7512, Dec. 2022.

[3] "ILO," 2023. [Online]. Available: https://ilostat.ilo.org/resources/concepts-and-definitions/description-occupational-safety-and-health-statistics/. [Accessed: 22-Feb-2023].

[4] A. Barkhordari, B. Malmir, and M. Malakoutikhah, "An Analysis of Individual and Social Factors Affecting Occupational Accidents," *Saf. Health Work*, vol. 10, no. 2, pp. 205–212, Jun. 2019.

[5] C. Melchior and R. R. Zanini, "Mortality per work accident: A literature mapping," *Safety Science*, vol. 114. Elsevier, pp. 72–78, 01-Apr-2019.

[6] S. B. B. Gonçalves, T. M. Sakae, and F. L. Magajewski, "Prevalence and factors associated with work accidents in a metal-mechanic company," *Rev. Bras. Med. do Trab.*, vol. 16, no. 1, pp. 26–35, 2018.

[7] SGK, 2022. [Online]. Available: https://www.sgk.gov.tr/Istatistik/Yillik/fcd5e59b-6af9-4d90- a451-ee7500eb1cb4/

[8] "U.S. Bureau of Labor Statistics," 2023. [Online]. Available: https://www.bls.gov/iif/home.htm. [Accessed: 08-Nov-2023].

[9] "2022 Report on Work Fatality and Injury Rates in Canada,"2022. [Online]. Available: www.uregina.ca/business/faculty-staff/faculty/file_download/2022-Report-on-Workplace-Fatalities-and-Injuries-April-28-FINAL.pdf. [Accessed: 10-Nov-2023].

[10] "ILO World Statistic," 2023. [Online]. Available: http://www.ilo.org/moscow/areas-of-work/occupational-safety-and-health/WCMS_249278/lang--en/index.htm. [Accessed: 05-Apr-2023].

[11] A. H. Khoshakhlagh, S. Yazdanirad, M. M. Kashani, E. Khatooni, Y. Hatamnegad, and S. Kabir, "A Bayesian network based study on determining the relationship between job stress and safety climate factors in occurrence of accidents," *BMC Public Health*, vol. 21, no. 1, pp. 1–12, Dec. 2021.

[12] H. Alali, M. A. Wahab, T. Van Hecke, and L. Braeckman, "Work accident victims: A comparison between non-standard and standard workers in Belgium," *Int. J. Occup. Environ. Health*, vol. 22, no. 2, pp. 99–106, Apr. 2016.

[13] J. Jehring and H. W. Heinrich, "Industrial Accident Prevention: A Scientific Approach," *Ind. Labor Relations Rev.*, vol. 4, no. 4, p. 609, 1941.

[14] M. del C. Giménez-Espert and V.J. Prado-Gascó, "Bibliometric analysis of six nursing journals from the Web of Science, 2012–2017," *J. Adv. Nurs.*, vol. 75, no. 3, pp. 543–554, Mar. 2019.

[15] P. Chen *et al.*, "Brain-gut axis and psychiatric disorders: A perspective from bibliometric and visual analysis," *Front. Immunol.*, vol. 13, Nov. 2022.

[16] X. Zhu *et al.*, "Bibliometric and Visual Analysis of Research on the Links Between the Gut Microbiota and Depression From 1999 to 2019," *Front. Psychiatry*, vol. 11, p. 587670, Jan. 2021.

[17] B. Martín-Del-Río, Á. Solanes-Puchol, F. Martínez-Zaragoza, and G. Benavides-Gil, "Stress in nurses: The 100 top-cited papers published in nursing journals," *Journal of Advanced Nursing*, vol. 74, no. 7. John Wiley & Sons, Ltd, pp. 1488–1504, 01-Jul-2018.

[18] H. Yesilbas and F. Kantek, "Trends and hot topics in nurse empowerment research: A bibliometric analysis," *Japan J. Nurs. Sci.*, vol. 19, no. 2, p. e12458, Apr. 2022.

[19] Web of Science Core Collection. [Online]. Available: https://www.webofscience.com/wos/woscc/summary/d669e79e-9c21-4bd3-aa81-bc879199ef55-b2148639/relevance/1

[20] Web of Science Core Collection. [Online]. Available: https://www.webofscience.com/wos/woscc/summary/dc2178a5-d178-4d5a-9358-5f4b5605a8a8-b2153b3f/relevance/1

[21] H. Yesilbas and F. Kantek, "Trends and hot topics in nurse empowerment research: A bibliometric analysis", *Japan Journal of Nursing Science*, vol. 19, no.2, 2022.

[22] A. Çiçek Korkmaz, S.A. Altuntaş, "bibliometric analysis of COVID-19 publications in nursing by visual mapping method", *J Nurs Manag*, vol. 30, no.6, pp.1892-1902, sep.2022. doi: 10.1111/jonm.13636. Epub 2022 May 2. PMID: 35429086; PMCID: PMC9115144.

[23] "Elsevier," 2023. [Online]. Available: https://www.sciencedirect.com/journal/safety-science. [Accessed: 08-Nov-2023].

[24] S. Liu, R. Y. Zhang, and T. Kishimoto, "Analysis and prospect of clinical psychology based on topic models: Hot research topics and scientific trends in the latest decades", *Psychology, Health & Medicine*, vol.26, no.4, pp.395–407, 2021. Doi: 10.1080/13548506.2020.1738019

Bitlis Eren Üniversitesi Fen Bilimleri Dergisi
BİTLİS EREN UNIVERSITY JOURNAL OF SCIENCE
ISSN: 2147-3129/e-ISSN: 2147-3188
VOLUME: 12 NO: 4 PAGE: 1094-1104 YEAR: 2023
DOI:10.17798/bitlisfen.1337326

Development of Chip Temperature and Cost-Based Optimum Design for a Radial Heat Sink Cooling High Power LEDs

Orhan KALKAN[1*]

[1]*Erzincan Binali Yıldırım University, Faculty of Engineering and Architecture, Department of Mechanical Engineering, Erzincan, Turkey*
(ORCID: 0000-0002-9664-1819)

Keywords: High power LEDs, thermal management, optimization, numerical analysis

Abstract
High-power Light Emitting Diodes (LED)s are preferred in places that produce intense light output and have overheating problems because they work with high currents. Therefore, efficient thermal management is essential to ensure optimal performance and longevity. In the present study, a numerical analysis is conducted on a high-power Light Emitting Diode (LED) circuit with a Circuit on Board (COB) design featuring a radial heat sink. Additionally, a multi-objective optimization approach using the Desirability Function Approach (DFA) is introduced for the modeled radial heat sink. Two performance parameters, namely the maximum junction temperature and the cost of the radial heat sink, are defined as the objective functions, and the aim is to minimize both of these parameters. The independent variables for the objective functions are the geometrical parameters of the radial heat sink, namely the base radius (R), fin length (L), and heat sink height (H). The Response Surface Method (RSM) is applied to minimize sample numbers in the Design of Experiment (DOE) while still obtaining accurate response values. Furthermore, Analysis of Variance (ANOVA) is utilized to assess the fit of the real response equations with the representative answer equations. The minimum prediction R^2 is calculated to be 0.9748%, indicating a good agreement between the models. A cost-based, realistic optimum design for radial heat sinks, which are frequently used for COB HPLEDs, is presented in the study. The response values for this optimal design are validated with a low error rate of 0.25% using numerical analysis.

1. Introduction

Light Emitting Diodes, abbreviated as LED, are semiconductor elements that emit light when an electric current is passed through them. They are a type of solid-state lighting technology that is highly preferred in industry and daily life due to their efficiency, durability, and versatility in various applications. LEDs have revolutionized lighting technology and are used in a wide range of devices and systems, from small indicator lights to large outdoor displays. [1]. Chip-on-Board (COB) LEDs are a type of high-power LED technology that offers several advantages over traditional discrete LEDs. In a COB LED package, multiple LED chips are mounted directly onto a single substrate, forming a single module, or "chip," that acts as a single light source [2]. COB LEDs are generally more energy-efficient than traditional lighting sources like incandescent bulbs, making them an attractive option for various applications [3], [4].

COB LEDs need improved thermal performance compared to traditional discrete LEDs. Because the LED chips are mounted close together, they can share a larger heat sink area, requiring more effective heat dissipation to achieve lower operating temperatures. LEDs are energy-efficient light sources, but they still produce heat when converting

*Corresponding author: orhan.kalkan@erzincan.edu.tr
Received: 03.08.2023, Accepted: 17.11.2023

electricity into light. If this heat is not effectively removed, it can negatively impact the LED's performance, reliability, and lifespan. A heat sink is often used to dissipate the heat produced by light-emitting diodes (LED)s during operation. Some current studies about cooling LEDs are summarized as follows:

Song et al. focused on analyzing the cooling capabilities of a heat sink that has perforated fins. They aimed to enhance the cooling performance by investigating the impact of varying the size and number of perforations. The results revealed that a higher number of perforations with smaller sizes contributed to better cooling performance. Additionally, the research involved a numerical analysis of the heat-dissipation performance, considering factors such as fin number, fin angle, heat sink angle, and the Rayleigh number. [5]. Xu introduced a rectangular radial fin-equipped heat sink designed for high power LEDs (HPLED)s cooling. The optimization study, which aims to minimize maximum temperature and mass, considers the number of fins and fin length as parameters. The multi-objective optimization study identifies a solution with a maximum temperature of 67.7°C, a thermal resistance of 0.45 K/W, and a mass of 1.74 kg. This optimal solution corresponds to 23 fins and a fin length of 59 mm, effectively dissipating 92 W of heat [6]. Azarifar et al. explored the enhancements in both optical and thermal aspects achieved through a novel package-level liquid coolant encapsulation designed to specifically target heat generation. As a result of the study, the potential of this new cooling method for optoelectronic components was demonstrated. A remarkable minimization of 15% in thermal resistance was obtained [7]. Jiu et al. proposed a novel heat sink design equipped with a mini heat pipe array (MHPA), addressing the existing challenges in heat dissipation. The heat sink's thermal performance was thoroughly evaluated through experimental testing. With an input power of 100 W, the substrate temperature can be effectively reduced below 70 °C. The MHPA exhibits excellent temperature uniformity, with maximum temperature drops of only 0.6 °C and 1.1 °C in the vertical direction for input powers of 100 W and 200 W, respectively [8]. Ben Hamida et al. aimed to provide effective thermal management for the efficient removal and dissipation of the heat produced by an LED, thus ensuring its efficient and safe operation. The study explored a cost-effective solution to reduce the maximum LED temperature at junction points. The focus was on investigating the effects of square and circular holes in the heat sink. The findings indicated that two square or cylindrical holes lead to a decrease in the maximum temperature of the LED chips under different input powers. [9]. Rammohan studied to estimate the service life of High-Power Light Emitting Diodes (HPLED)s through an experimental approach. A real-time algorithm based on the Arrhenius model was employed to monitor HPLED failure. The results showed that at a junction temperature (T_j) of 25 °C, the lifetime of the HPLED was approximately 120,000 hours. However, when the maximum T_j of the HPLED reached 125 °C, the lifetime reduced significantly to 4796 hours at a maximum current of 0.45 A [10]. Moon et al. presented the development of a U-shaped single unit cooling fin aluminum flat heat pipe (AFHP) for a 100 W COB LED lamp with small dimensions (120 mm×120 mm×170 mm) and an electric connection using a socket. The U-shaped AFHP module did not exceed 900 g, is cost-effective due to the extrusion method used in its production, and was designed to be used in socket-type lamps. The junction temperature of the COB LED module was evaluated to be within 85 °C at an input power of 100 W [11]. Shin et al. introduced a novel active cooling method for Light LED applications using the ionic wind. Through analysis, it was presented that the center pole within the heat sink has no appreciable thermal effect. The optimum radius of the wire curvature and input voltage for the ionic wind were identified as 110 mm and 7.5 kV, respectively. Results demonstrated a significant improvement in the heat transfer coefficient of the heat sink by 37%, from 96.7 to 133 W/m²K, due to the ionic wind, which was confirmed experimentally [12]. Lazarov et al. highlighted the exceptional performance of topology-optimized heat sinks when compared to lattice designs, proposing more straightforward and manufacturable pin-fin design interpretations. To address manufacturing costs, a simplified version of the optimized design is created and validated. Both numerical and experimental results show excellent agreement, confirming that the obtained designs outperform lattice geometries by over 21%. As a result, the optimized heat sinks offer a doubled life expectancy and a 50% decrease in operational costs compared to traditional lattice designs [13].

When we look at the studies in the literature on LED cooling, the researchers mostly focus on the heat sink design that provides effective cooling. The cooling performances of many different configurations of the heat sinks have been examined. In addition, geometric optimization of heat sink is also discussed. However, it seems that studies on cost-based optimization of heat sinks, which are frequently used for COBLEDs, are quite limited. This

is evident in the literature on the subject. It is obvious that there is a gap in the literature on this subject.

In this study, a COB HPLED consisting of a radial heat sink is modeled and numerically analyzed. Then, a multi-objective optimization for the modeled radial heat sink is performed using the Desirability Function Approach (DFA). Studies in the literature also show that geometric parameters, maximum LED junction temperature, and mass are important criteria for finned heat emitters used for LEDs. The mass of the heat sink is an important criterion because aluminum material is generally used, and it is meaningful in terms of cost. Therefore, maximum junction temperature and radial heat sink cost are two performance parameters defined as objective functions. The goal of the multi-objective optimization procedure is to reduce both chosen performance parameters. The geometrical parameters of radial heat sink base radius, fin length, and heat sink height are defined as the independent variables of both objective functions. The Response Surface Method (RSM) is employed to reduce the number of Design of Experiment (DOE) samples while still obtaining an acceptable estimation of the response values. Then, Analysis of variance (ANOVA) is used to find out how well the real and representative answer equations fit together. Finally, a cost-based, realistic optimum design for radial heat sinks, which are frequently used for COB HPLEDs, is assessed in the present study.

2. Numerical Modeling

The cooling performance of the modeled COB HPLED and radial heat sink is numerically investigated using the ANSYS-Fluent package program. A COB HPLED is modeled with components such as an aluminum heatsink, GaN-based chips, silver paste, a silicon ring, thermal grease, and an aluminum heat slug. The geometric models and computational domains are generated using SolidWorks CAD software. Then, the mesh model of the domains is built up using the ANSYS Mesh module, and thereafter, the numerical model set-up and solutions are performed step by step. The thermophysical properties of the COB HPLED components are given in Table 1 [14]. LEDs have a 9.92 W electrical power supply. It has been calculated by Wu et al. that 80% of the electrical energy in LEDs is converted into thermal energy [14]. Therefore, 7.936 W heat generation is defined for LED domains when boundary conditions are set. Throughout thermal simulations, the scalar temperature field will be governed by the convection-diffusion equation. For this particular case, the following notation is frequently employed [15].

$$\left(\rho c_p\right)\frac{\partial T}{\partial t} = \left(\rho c_p\right)\nabla.\left(uT\right) - \nabla.\left(k\nabla T\right) + \dot{Q}_v \quad (1)$$

where ρ is material density, c_p is specific heat capacity, T is temperature, k is thermal conductivity, and $\dot{\mathbf{Q}}_\mathbf{v}$ is volumetric heat flux.

Table 1. Thermophysical properties of the components.

Component	Density	Component	Density
Heat sink (Al)	2707	896	204
GaN-based chips	6150	417	130
Silver paste	2300	671	8
Silicon ring	980	1173	0.2
Thermal grease	1180	1044	3.6
Heat slug (Al)	2707	896	204

Considering that the ambient temperature is 25 °C, a heat convection boundary condition is defined for all domain walls. Besides, the initial temperature of all domains is also 25 °C. On the other hand, the energy equation convergence criteria are set to 10^{-10}.

2.1. Geometric Model and Parameters

Radial heat sinks have fins that radiate outward from a central base, creating a circular or cylindrical shape. This design allows for efficient heat dissipation in all directions, as heat is conducted from the device to the base and then transferred to the fins, which increases the surface area for better heat transfer to the surrounding air. Radial heat sinks are commonly found in various electronic devices, including computers, laptops, HPLEDs, and other consumer electronics, where effective cooling is essential to maintain the device's performance and prolong its lifespan. The representation of the COB LED and radial aluminum heat sink geometric model and the used optimization parameters are shown in Figure 1. There are three geometrical optimization parameters for the radial heat sink. These are heat sink height (H), heat sink base radius (R), and heat sink fin length (L). The COB LED has a dimension of 33 mm×33 mm×2.1 mm. The size of the chips emitting heat and light in the COB LED is 1 mm×1 mm and has a 3×3 array. The distance between the chips is 0.5 mm.

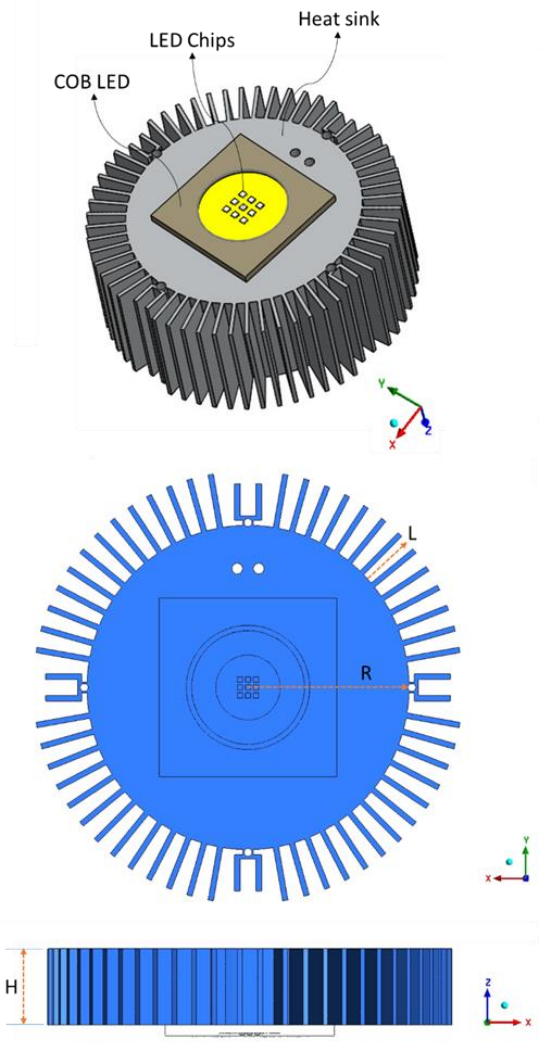

Figure 1. COB LED and heat sink model with optimization parameters.

2.2. Meshing Step

The polyhedral mesh structure is generated for the COB LED and heat sink computational domains, as depicted in Figure 2. Polyhedral meshes can require fewer elements to achieve comparable accuracy compared to traditional meshes. This can result in reduced computational effort and memory requirements for simulations. Due to the fewer element interfaces and increased geometric flexibility, polyhedral meshes may lead to improved solver behavior and convergence in some simulation scenarios [16]. While generating the mesh for the domains, the minimum element quality is not reduced below 0.2.

Mesh independency analysis is a crucial step in numerical simulations and finite element analysis to ensure that the results obtained from the simulation are not significantly affected by the size or type of the computational mesh. The purpose of this analysis is to determine the appropriate level of mesh refinement required to achieve accurate and reliable simulation results without unnecessarily increasing computational cost and time. The aim of mesh independence analysis is to strike a balance between accuracy and computational cost. If the results converge to a consistent solution as the mesh is refined, the simulation is said to be mesh-independent for the specific problem and mesh type used. Considering the present study, the maximum junction temperature ($T_{j,max}$) is selected for the mesh independency analysis parameter. Therefore, the variation of $T_{j,max}$ according to the mesh number is presented in Table 2. The mesh model has 380892 mesh numbers selected for the numerical analysis.

Table 2. Mesh independency analysis.

Mesh number	Maximum junction temperature, $T_{j,max}$ (°C)
9453	93.57
176602	88.63
380892	88.05
516841	88.04

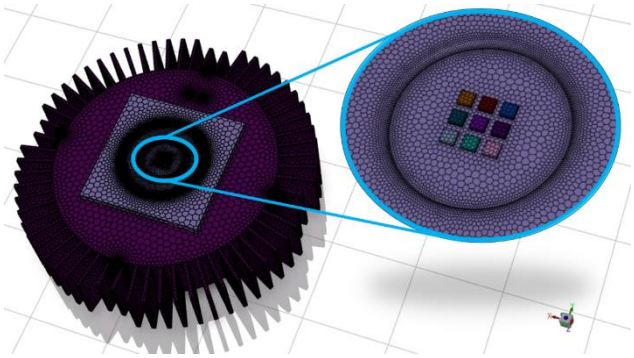

Figure 2. Mesh model of the COB LED and heat sink domains.

2.3. Validation of the Numerical Solutions

In this section, the numerical solution results of the open literature and the current study are compared for the model with the same geometric parameters and COB LED. Figure 3 shows the comparison of the temperature contours of COB LED and radial heat sinks introduced by Wu et al. and the present study [14]. H is 15 mm, R is 30 mm, and L is 10 mm for both studies. When both the chips with maximum temperatures and the heat sink temperatures are compared, it is seen that suitable results are obtained. Besides, Wu et al. validated their numerical results with an experimental study.

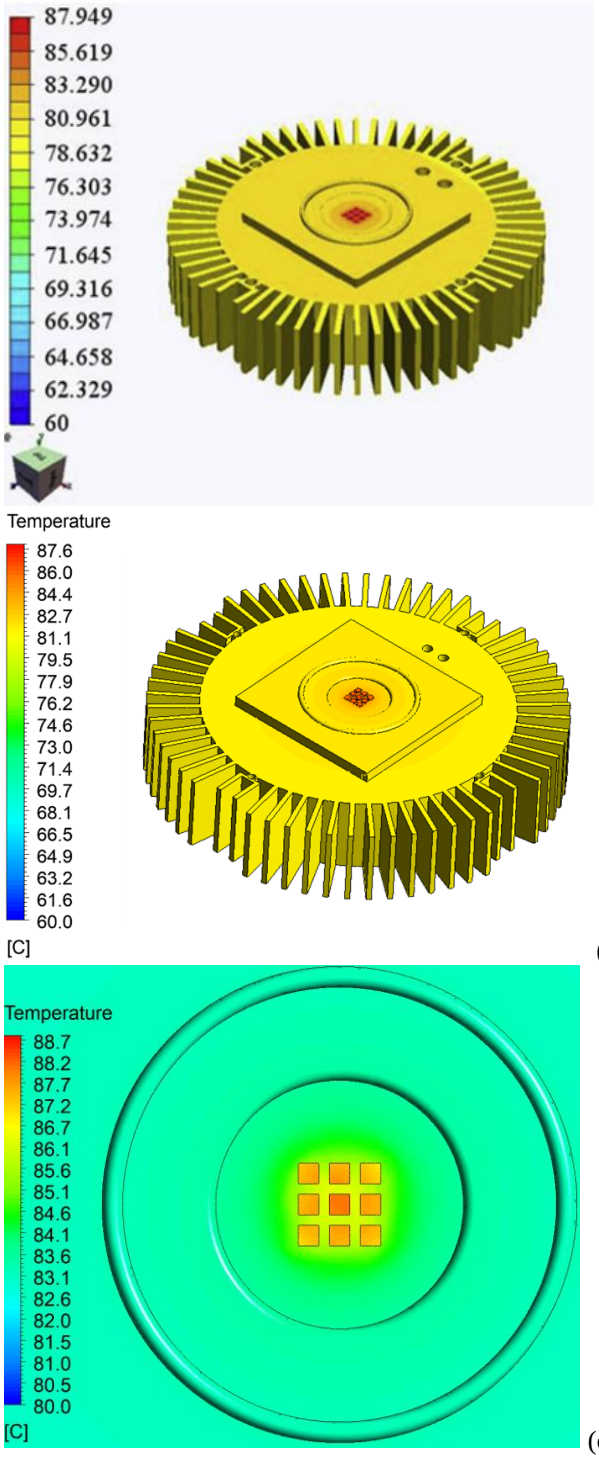

Figure 3. Temperature distributions of COB LED and heat sink presented by a) Wu et al. [14], b) this study, and c) COB LED detail in the present study.

3. Multi-Objective Optimization

In this section, $T_{j,max}$ and heat sink cost (C_{hs}) are two performance parameters defined as objective functions. The goal of the multi-objective optimization procedure is to reduce both of these chosen performance parameters. The previously defined geometrical parameters of R, L, and H are the independent variables of both objective functions. These independent variables are also optimization parameters. The optimization parameters and their levels are given in Table 3.

For a full factorial DOE, 33=27 different solutions must be performed. The RSM is employed to reduce the number of DOE samples while still obtaining an acceptable estimation of the response values. The core principle of this method involves creating a simplified mathematical representation of computationally intensive analysis and simulation codes. This surrogate model replaces the original code to facilitate multi-objective design optimization [17], [18].

Configuring the response surface aims to strike a balance between accuracy and computational cost. Achieving an acceptable level of accuracy while minimizing computational effort is the primary objective. The accuracy of the response surface depends on two key factors. The first factor is the selection of the appropriate approach function, and the second factor is determining the specific design points within the design area, often referred to as DOE. Quadratic Central Composite Design is one of the most preferred methods for generating mathematical model functions. This method relies on a quadratic polynomial that establishes a straightforward correlation between the design variables and their corresponding responses. The unknown coefficients in this mathematical model are determined through the least squares method. The actual response function (g) and the approximation function (G) are given by the following equations, respectively.

Table 3. Independent variables and their levels.

Independent variables	Optimization Parameters (mm)	Levels		
		-1	0	1
I_1	R	25	30	35
I_2	L	5	10	15
I_3	H	10	55	100

$$g = f(I_1, I_2, \dots, I_n) + E \tag{2}$$

$$G = \beta_0 + \sum_{i=1}^{m} \beta_i I_i + \sum_{i=1}^{m} \beta_{ii} {I_i}^2 + \sum_{i=1}^{m-1} \sum_{j=i+1}^{m} \beta_{ij} I_i I_j + E \tag{3}$$

Analysis of variance (ANOVA) is used to find out how well the real and representative answer equations fit together. ANOVA is a statistical technique used to compare the means of two or more

groups to determine if there are any significant differences between them. ANOVA is particularly useful when comparing means from multiple groups simultaneously, making it a powerful tool for DOE and research [19], [20].

Prior to the optimization process, the interrelationship between the objective functions and the independent variables is assessed, leading to the formation of approximation equations. To evaluate the compatibility between the approximation functions and the actual objective functions, ANOVA employs several measurement tools, including the R2, adjusted R^2, adjusted R^2 ($\mathbf{R^2_a}$), predicted R^2 ($\mathbf{R^2_p}$) and Adequate Precision (AP). The relevant equations for these measurement tools are provided below.

$$R^2 = 1 - SS_e/SS_t \tag{4}$$

$$R^2{}_a = 1 - (1 - R^2)\frac{n-1}{n-p-1} \tag{5}$$

$$R^2{}_p = (1 - \sum_{i=1}^{n} e_{-i}{}^2)/SS_t \tag{6}$$

$$AP = \frac{\max(\hat{J}) - \min(\hat{J})}{\sqrt{\frac{p\varepsilon}{n}}} \tag{7}$$

here ε is the residual mean square, p is predictors number, $\hat{\boldsymbol{J}}$ is the prediction at the run, SSt is the sum of squares total, SS_e is the sum of squares error. AP value greater than 4 indicates an adequate signal. The present model can be used to navigate the design space.

The composite desirability function (CDF) approach is performed to select optimum DOE sample. A composite desirability function is a technique used in multi-objective optimization to combine multiple individual objective functions into a single overall desirability function. The purpose of using a composite desirability function is to simultaneously optimize multiple conflicting objectives by transforming them into a unified goal. The basic idea behind the composite desirability function is to assign a desirability value to each objective function based on its importance and desired target. The desirability value typically ranges from 0 to 1, where 0 represents the worst outcome (undesirable) and 1 represents the best outcome (fully desirable). Intermediate values between 0 and 1 indicate partial desirability. The individual objective functions are usually normalized to a common scale before assigning desirability values. This normalization ensures that objectives with different units or scales can be combined effectively. Once the desirability values are assigned, the composite desirability function is computed by combining the individual desirability values. There are several methods to combine these desirability values, such as taking the geometric mean, the arithmetic mean, the product of desirability values, or the minimum value among the desirability values. By maximizing the composite desirability function, the optimization process aims to find the optimal set of input variables that simultaneously satisfy the desired targets for all individual objectives. Composite desirability functions are widely used in engineering, manufacturing, and other fields where multiple conflicting objectives need to be considered simultaneously. They provide a powerful approach to handling multi-objective problems and making informed decisions when facing trade-offs between different criteria. [21]. The following desirability function handles the multi-objective optimization.

$$D = \prod_{i-1}^{n} d_i{}^{w_i^{\frac{1}{\sum_{i=1}^{n} w_i}}} \tag{8}$$

4. Results and Discussion

A total of 15 samples are randomly generated for DOE based on the CCF approach. A separate geometry is generated for each sample, and the numerical analysis procedure is followed. The optimization parameters in each sample are calculated numerically using ANSYS-Fluent. DOE has 15 randomly generated samples, and their response values are shown in Table 4.

Then, the multi-objective optimization procedure is run to determine the optimum parameters. Quadratic approximation equations are generated for $T_{j,max}$, and C_{hs} objective functions. Next, an ANOVA is performed for both the objective function and its independent variables, which are also optimization geometric parameters. Data transformations are preferred when the range between the maximum and minimum values of the objective functions is excessively large. Data transformations are techniques used to modify the original data in order to meet specific requirements or improve the quality of the data for analysis or modeling purposes. Data transformation is a common step in data preprocessing and is often employed to address issues like data skewness and heteroscedasticity or normalize the data for certain statistical tests [22]. It is seen that the $T_{j,max}$, and C_{hs} value ranges are far from each other. Therefore, it would be logical to transform the data for $T_{j,max}$ and bring it to close value ranges with C_{hs}. Considering the present DOE dataset, an

inverse data transformation for $T_{j,max}$ is generated. It is understood from Figure 4 that the actual and estimated values for both objective functions are in good agreement with each other.

Table 4. Optimization parameters and response values.

Sample no	Optimization parameters (mm)			Response values	
	R	L	H	$T_{j,max}$ (°C)	C_{hs} ($)
1	35.00	15.00	10.00	88.581	0.283
2	25.00	5.00	10.00	155.259	0.138
3	25.00	5.00	100.00	47.581	1.381
4	30.00	10.00	109.69	39.727	2.254
5	35.00	5.00	100.00	45.711	2.514
6	35.00	15.00	100.00	37.668	2.828
7	25.00	15.00	10.00	95.444	0.169
8	25.00	15.00	100.00	38.109	1.694
9	23.92	10.00	55.00	49.395	0.791
10	30.00	16.08	55.00	42.935	1.235
11	36.08	10.00	55.00	47.641	1.549
12	30.00	10.00	0.31	321.249	0.006
13	30.00	3.92	55.00	62.193	1.025
14	30.00	10.00	55.00	48.385	1.130
15	35.00	5.00	10.00	132.183	0.251

Table 5 and Table 6 represent the ANOVA test summary and fit statistics for both regression approximation equations derived for $T_{j,max}$, and C_{hs}, respectively. Model equations can estimate the response values with a minimum prediction R^2 of 0.9748%, which indicates a good fit. Besides, AP values for both objective functions are greater than 4. This also indicates good navigation for the design space.

Table 5. ANOVA test summary.

Response Model	DF	SS	MS	F-value	p-value
$T_{j,max}$	3	0.0008	0.0003	293	<0.0001
C_{hs}	6	11.41	1.90	3573	<0.0001

Table 6. ANOVA fit statistics.

Response Model	R^2	R^2_a	R^2_p	AP
$T_{j,max}$	0.9876	0.9843	0.9748	43.8384
C_{hs}	0.9996	0.9993	0.9987	178.2252

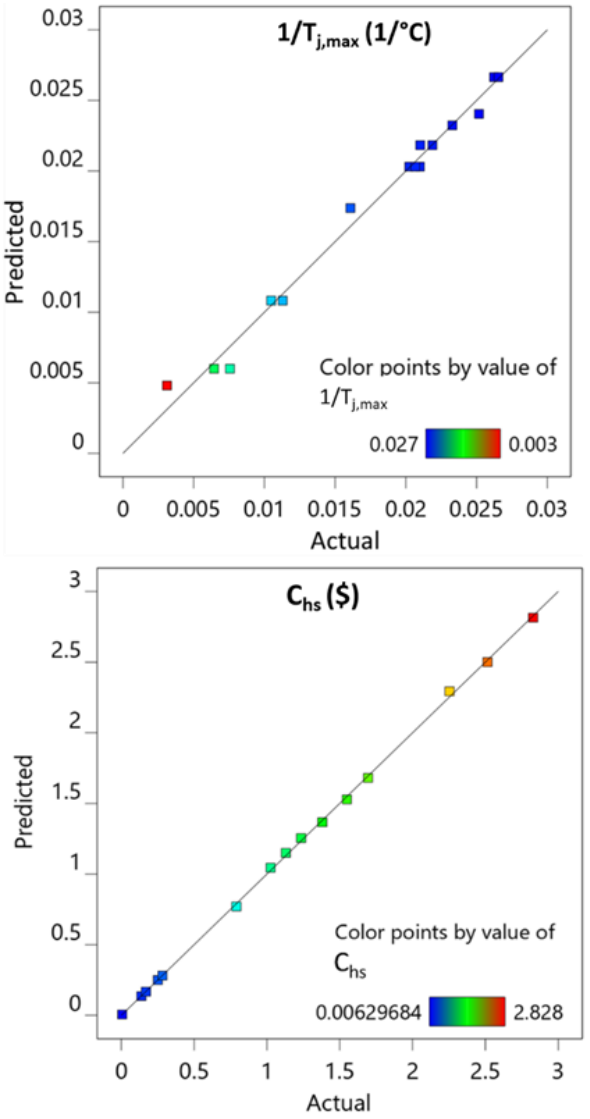

Figure 4. Actual and predicted value comparison for the objective functions.

Finally, an optimal solution set is generated using the CDF approach, as given in Table 7. The dataset in the first row with the maximum desirability value is selected as the optimum design. The heat sink with a 25 m base radius, 15 mm fin length, and 55.36 mm height is selected as the optimum radial heat sink design.

Table 7. Optimal data set.

#	R (mm)	L (mm)	H (mm)	$T_{j,max}$ (°C)	C_{hs} ($)	Desirability
1	**25**	**15**	**55.36**	**43.891**	**0.931**	**0.751**
2	25	15	55.681	43.784	0.936	0.751
3	25	15	54.998	44.014	0.924	0.751
4	25	15	54.642	44.136	0.918	0.751
5	25.008	15	56.306	43.579	0.947	0.751
6	25	15	53.764	44.444	0.904	0.751
7	25	14.967	55.81	43.771	0.937	0.751
8	25	14.962	55.444	43.899	0.931	0.751
9	25	14.935	55.048	44.058	0.924	0.751
10	25.043	15	56.125	43.638	0.946	0.751
11	25	15	52.336	44.968	0.88	0.751
12	25	14.887	56.275	43.692	0.944	0.751
13	25	14.798	56.481	43.707	0.946	0.75
14	25	15	59.823	42.511	1.006	0.75
15	25.103	15	52.683	44.838	0.892	0.75
16	25.104	15	57.903	43.076	0.98	0.75
17	25.166	15	55.229	43.935	0.939	0.749
18	25	15	61.022	42.179	1.026	0.749
19	25	14.459	53.971	44.89	0.898	0.748
20	25	14.365	55.735	44.361	0.926	0.748

The optimum design of the selection is remodeled and numerically analyzed to ensure that the response values of the optimum design parameters truly reflect the correct data. Figure 5 depicts the temperature distribution of the COB LED with a heat sink, which has an optimum design. When $T_{j,max}$ response value, and the confirmation analysis results are compared, it is seen that they are in good agreement with a 0.25% error rate.

Table 8 compares some related previous studies and the present study in terms of LED power, heat sink material, $T_{j,max}$ and cost. Many previous studies on LED cooling show that LED power, distances between LED chips, heat sink material, geometric parameters of the heat sink, and cooling method are effective parameters in the design of heat sinks. Copper and aluminum are the most preferred heat sink materials due to their good thermal conductivity. However, it can be said that aluminum is preferred more because it is cost effective. The maximum junction temperature of an LED is a critical parameter that defines the highest temperature the LED's semiconductor junction can reach without causing damage or negatively affecting its performance. It's essential to manage the junction temperature to ensure the LED operates within its specified limits for optimal efficiency and longevity. It is always necessary to take into account the data sheet or specifications provided by the LED manufacturer for the specific $T_{j,max}$ value of a particular LED model; because this value can vary significantly. Operating the LED within the recommended temperature range ensures reliable and efficient performance. In this study, an optimum point was selected in terms of heat sink cost and maximum led junction temperature, and an improvement was performed for the radial heat sink designed for COB LEDs.

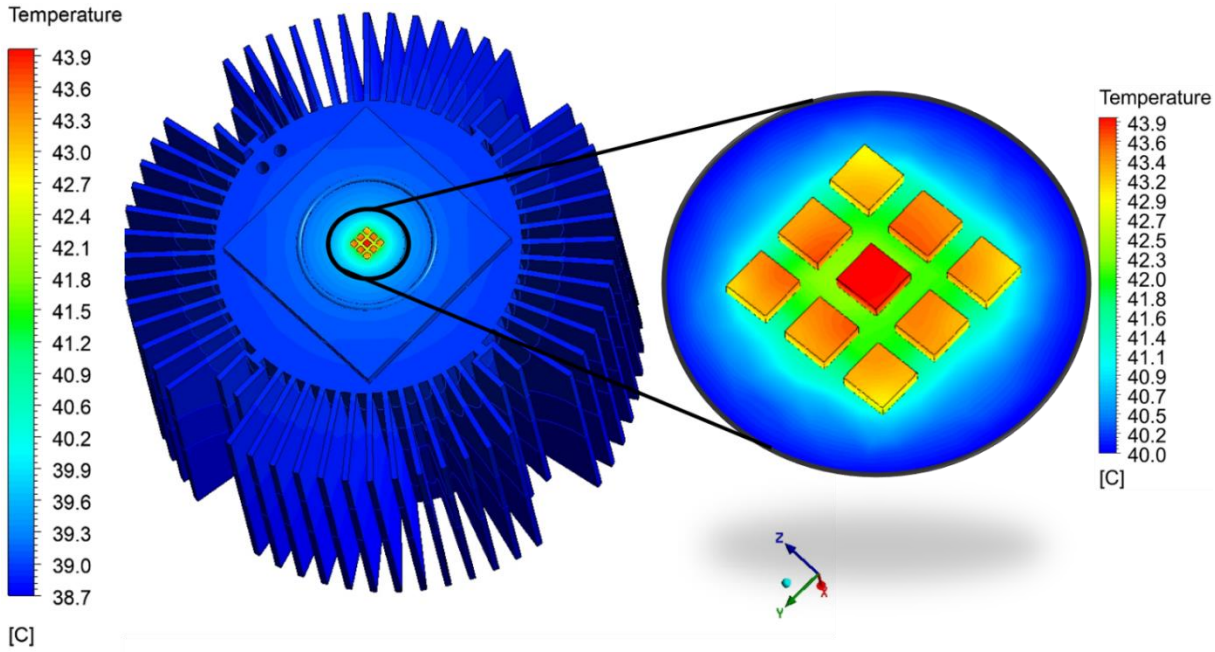

Figure 5. Validation of the optimum design.

Table 8. Comparison of the present study with some previous studies.

	LED power (W)	Heat sink material	$T_{j,max}$ (°C)	Cost ($)
Yu et al. [23]	12.37	Aluminum	64.5	N/A
Xu [6]	92	Aluminum	67.7	3.92
Wu et al. [14]	7.94	Aluminum	75.09	N/A
This study	7.94	Aluminum	43.89	0.93

4. Conclusion and Suggestions

In the present study, a Circuit on Board (COB) high power Light Emitted Diode (LED) with a radial heat sink is modeled and numerically analyzed. Besides, a multi-objective optimization for the modeled radial heat sink is introduced using the Desirability Function Approach (DFA). Maximum junction temperature ($T_{j,max}$) and radial heat sink cost (C_{hs}) are two performance parameters defined as objective functions. The goal of the multi-objective optimization procedure is to reduce both chosen performance parameters. The geometrical parameters of radial heat sink base radius (R), fin length (L), and heat sink height (H) are defined as the independent variables of both objective functions. The Response Surface Method (RSM) is employed to reduce the number of Design of Experiment (DOE) samples while still obtaining an acceptable estimation of the response values. Then, Analysis of variance (ANOVA) is used to find out how well the real and representative answer equations fit together. The minimum prediction R^2 is calculated as 0.9748%, which represents a good agreement. Finally, the optimum radial heat sink design is obtained as R=25 mm, L=15 mm, and H=55.36 mm. Besides, the response values of the optimum design are validated with a 0.25% error rate using the numerical analysis method.

In future work, a more comprehensive optimization study can be done by detailing the optimization parameters. Different optimum design proposals can be presented as a result of the analyzes to be made in different environmental conditions, such as forced air flow and natural convection.

Statement of Research and Publication Ethics

The study is complied with research and publication ethics

References

[1] M. Ha and S. Graham, "Development of a thermal resistance model for chip-on-board packaging of high power LED arrays," *Microelectron. Reliab.*, vol. 52, no. 5, pp. 836–844, 2012.

[2] H. Yang, B. Yang, J. Li, and P. Yang, "Failure analysis and reliability reinforcement on gold wire in high-power COB-LED under current and thermal shock combined loading," *Appl. Therm. Eng.*, vol. 150, pp. 1046–1053, 2019.

[3] C.-Y. Kang, C.-H. Lin, T. Wu, P.-T. Lee, Z. Chen, and H.-C. Kuo, "A novel liquid packaging structure of deep-ultraviolet light-emitting diodes to enhance the light-extraction efficiency," *Crystals (Basel)*, vol. 9, no. 4, p. 203, 2019.

[4] Z. Xia, S. Liang, B. Li, F. Wang, and D. Zhang, "Influence on temperature distribution of COB deep UV LED due to different packaging density and substrate type," *Optik (Stuttg.)*, vol. 231, no. 166392, p. 166392, 2021.

[5] G. Song, D.-H. Kim, D.-H. Song, J.-B. Sung, and S.-J. Yook, "Heat-dissipation performance of cylindrical heat sink with perforated fins," *Int. J. Therm. Sci.*, vol. 170, no. 107132, p. 107132, 2021.

[6] Z. Xu, "Thermal performance and multi-objective optimization of thermosyphon heat sinks with rectangular radial fins for high power LED lamps cooling," *Case Stud. Therm. Eng.*, vol. 30, no. 101778, p. 101778, 2022.

[7] M. Azarifar, C. Cengiz, and M. Arik, "Thermal and optical performance characterization of bare and phosphor converted LEDs through package level immersion cooling," *Int. J. Heat Mass Transf.*, vol. 189, no. 122607, p. 122607, 2022.

[8] Y. Jiu, H. Fan, and W. Wang, "Investigation of a novel natural convection heat sink for LEDs based on U-shaped mini-heat pipe arrays," *Appl. Therm. Eng.*, vol. 204, no. 118000, p. 118000, 2022.

[9] M. B. Ben Hamida, M. A. Almeshaal, K. Hajlaoui, and Y. A. Rothan, "A three-dimensional thermal management study for cooling a square Light Edding Diode," *Case Stud. Therm. Eng.*, vol. 27, no. 101223, p. 101223, 2021.

[10] Rammohan, R. Kumar, and Chandramohan, "Experimental analysis on estimating junction temperature and service life of high power LED array," *Microelectron. Reliab.*, vol. 120, no. 114121, p. 114121, 2021.

[11] S.-H. Moon, Y.-W. Park, and H.-M. Yang, "A single unit cooling fins aluminum flat heat pipe for 100 W socket type COB LED lamp," *Appl. Therm. Eng.*, vol. 126, pp. 1164–1169, 2017.

[12] D. H. Shin, D. K. Sohn, and H. S. Ko, "Analysis of thermal flow around heat sink with ionic wind for high-power LED," *Appl. Therm. Eng.*, vol. 143, pp. 376–384, 2018.

[13] B. S. Lazarov, O. Sigmund, K. E. Meyer, and J. Alexandersen, "Experimental validation of additively manufactured optimized shapes for passive cooling," *Appl. Energy*, vol. 226, pp. 330–339, 2018.

[14] H.-H. Wu, K.-H. Lin, and S.-T. Lin, "A study on the heat dissipation of high power multi-chip COB LEDs," *Microelectronics*, vol. 43, no. 4, pp. 280–287, 2012.

[15] W. J. Minkowycz, E. M. Sparrow, and J. Y. Murthy, Eds., *Handbook of numerical heat transfer*, 2nd ed. Nashville, TN: John Wiley & Sons, 2008.

[16] M. Sosnowski, J. Krzywanski, K. Grabowska, and R. Gnatowska, "Polyhedral meshing in numerical analysis of conjugate heat transfer," *EPJ Web Conf.*, vol. 180, p. 02096, 2018.

[17] T. W. Simpson, A. J. Booker, D. Ghosh, A. A. Giunta, P. N. Koch, and R.-J. Yang, "Approximation methods in multidisciplinary analysis and optimization: a panel discussion," *Struct. Multidiscipl. Optim.*, vol. 27, no. 5, 2004.

[18] O. Kalkan, A. Celen, and K. Bakirci, "Multi-objective optimization of a mini channeled cold plate for using thermal management of a Li-Ion battery," *Energy*, vol. 251, no. 123949, p. 123949, 2022.

[19] N. R. Smalheiser, *Data literacy: How to make your experiments robust and reproducible*. San Diego, CA: Academic Press, 2017.

[20] O. Kalkan, "Multi-objective optimization of a liquid metal cooled heat sink for electronic cooling applications," *Int. J. Therm. Sci.*, vol. 190, no. 108325, p. 108325, 2023.

[21] M. Mobin, M. Mobin, and Z. Li, "Multi-response optimisation of cavitation peening parameters for improving fatigue performance using the desirability function approach," *Int. J. Appl. Decis. Sci.*, vol. 9, no. 2, p. 156, 2016.

[22] T. Zhang and B. Yang, "Box–cox transformation in big data," *Technometrics*, vol. 59, no. 2, pp. 189–201, 2017.

[23] S.-H. Yu, K.-S. Lee, and S.-J. Yook, "Optimum design of a radial heat sink under natural convection," *Int. J. Heat Mass Transf.*, vol. 54, no. 11–12, pp. 2499–2505, 2011.

Bitlis Eren Üniversitesi Fen Bilimleri Dergisi
BİTLİS EREN UNIVERSITY JOURNAL OF SCIENCE
ISSN: 2147-3129/e-ISSN: 2147-3188
VOLUME: 12 NO: 4 PAGE: 1105-1116 YEAR: 2023
DOI:10.17798/bitlisfen.1338180

SkinCNN: Classification of Skin Cancer Lesions with A Novel CNN Model

İbrahim Çetiner[1*]

[1]*Vocational School of Technical Sciences, Burdur Mehmet Akif Ersoy University, Burdur, Türkiye (ORCID: 0000-0002-1635-6461)*

Keywords: MobileNet V3, CNN, Skin cancer, Transfer learning, Classification.

Abstract

Recently, there has been an increase in the number of cancer cases due to causes such as physical inactivity, sun exposure, environmental changes, harmful drinks and viruses. One of the most common types of cancer in the general population is skin cancer. There is an increase in exposure to the sun's harmful rays due to reasons such as environmental changes, especially ozone depletion. As exposure increases, skin changes occur in various parts of the body, especially the head and neck, in both young and old. In general, changes such as swelling in skin lesions are diagnosed as skin cancer. Skin cancers that are frequently seen in the society are known as actinic keratosis (akiec), basal cell carcinoma (bcc), bening keratosis (bkl), dermatofibroma (df), melanoma (mel), melanocytic nevi (nv), and vascular (vasc) types. It is not possible to consider all possible skin changes as skin cancer. In such a case, the development of a decision support system that can automatically classify the specified skin cancer images will help specialized healthcare professionals. For these purposes, a basic model based on MobileNet V3 was developed using the swish activation function instead of the ReLU activation function of the MobileNet architecture. In addition, a new CNN model with a different convolutional layer is proposed for skin cancer classification, which is different from the studies in the literature. The proposed CNN model (SkinCNN) achieved a 97% accuracy rate by performing the training process 30 times faster than the pre-trained MobileNet V3 model. In both models, training, validation and test data were modelled by partitioning according to the value of cross validation 5. MobileNet V3 model achieved F1 score, recall, precision, and accuracy metrics of 0.87, 0.88, 0.84, 0.83, 0.84, and 0.83, respectively, in skin cancer classification. The SkinCNN obtained F1 score, recall, precision, and accuracy metrics of 0.98, 0.97, 0.96, and 0.97, respectively. With the obtained performance metrics, the SkinCNN is competitive with the studies in the literature. In future studies, since the SkinCNN is fast and lightweight, it can be targeted to run on real-time systems.

1. Introduction

The world population is expected to increase substantially in the next quarter century [1]. It is noted that with the increase in the number of people, there has been a rapid increase in the number of human diseases [2]. As the world's population grows, so too does the damage done to the environment, especially to nature. The main reason for this is that people unconsciously cause water, air and soil pollution. The damage to the main material of nature returns as an increase in human diseases. It is observed that there is a great increase in cancer cases due to various environmental factors, especially chemicals, tobacco and radiation [2].

Five years ago today, in 2018, nearly ten million people are reported to have died from cancer [3]. There has been a serious increase in cancer cases

*Corresponding author: icetiner@mehmetakif.edu.tr
Received: 05.08.2023, Accepted: 20.11.2023

in recent years due to various reasons such as constant work, constant exposure to blue rays, physical inactivity, harmful sun rays and radiation [4]. Although there are many different types of cancer, skin cancer is one of the most common and deadly cancers [5]. It is reported that the pollution caused by UV-B rays emitted by the sun is directly linked to the depletion of the ozone layer. As a result, a large increase in skin cancer cases has been observed [6]–[8]. Skin cancer of the melanoma type is affected by 86% of ultraviolet radiation, while other types of skin cancer are affected by 90% of ultraviolet radiation [9].

Dermatology is an important department in the medical field with cases of serious diseases. It is common in countries such as the United States, regardless of age, gender, or culture. So much so that at least 1 out of 3 patients has serious skin disease [10]. Due to the reasons and reasons stated, skin diseases are accepted as a global health problem [11].

Skin diseases should be comprehensively scanned with medical imaging devices and lesions should be defined. Variable-sized skin growths that occur on the skin should be examined under observation [12]. Analyzes are carried out with different techniques according to changes in skin structure, irregularities on the border, asymmetrical structure, and uniform color structure [13]. These techniques support the analysis of skin diseases via medical images. In this context, akiec, nv, df, bcc, mel, bkl, and vasc, which are the most common types of skin cancer in the world, are examined. Several factors, including sun exposure and population longevity, may be contributing to the increasing incidence of this cancer [14]. Mendes et al. report that although skin cancer is widespread, its treatment is successful thanks to early detection and treatment. However, if the disease is detected late, the chance of survival drops to around 15% [14].

As with other health problems, early diagnosis of skin cancer saves lives. With early detection, there is a good chance of preventing the disease from spreading to other organs. There are studies that classify melanoma, one of the deadliest skin cancers. According to Barata et al, two different systems are proposed to detect melanoma skin type in dermoscopy images. The first system uses local features and pockets to group skin lesions. This article reports that color images provide more detailed information than textural features in the detection of skin lesions [15]. In line with this finding, operations were performed to analyze data on color images. In another study, a decision support system is proposed using different inputs to obtain the characteristic features of melanoma [16], [17]. Pomponi et al. developed a CNN model with multiple convolution and fully connected layers [18]. In the first of the convolutional layers of their model, they apply 96 kernels of size 11x11x3 to a color skin image. The second convolutional layer applies filtering to the normalized and pooled image with 256 kernels of 5x5x48 dimensions. The other convolutional layers are linked together without any normalization or pooling. In the sixth and seventh rows, the fully connected layer is connected with 4096 neurons. It can be seen that the K-Nearest Neighbor (KNN) classifier is used to classify the obtained features. Younis et al. classify skin cancer using a MobileNet-based neural network [4].

Shoieb et al. proposed a CNN structure to extract superficial features of skin cancers [19]. It classifies the data obtained from the proposed structure using the Support Vector Machine (SVM) algorithm. When we look at the literature, in deep learning, which is a sub-field of machine learning, original studies can be carried out in very different categorical areas such as natural language processing, text analysis, emotion analysis, speaker recognition, computer vision applications and artificial learning in health [20], [21]. In previous years, the high hardware requirements of deep learning algorithms prevented progress from being made. In today's conditions, interest in deep learning algorithms has increased due to the widespread use of high-powered computers and the increase in current dataset environments. CNN-based algorithms are defined as a subfield of deep learning. Natural language processing has achieved significant success in areas such as text and sentiment analysis, which are sub-topics of natural language processing. These achievements were crowned with the classification of the ImageNet dataset, a large dataset of 1.2 million images. A new method using CNN is presented to classify this dataset [22]. Since then, CNN methods have been used in various fields, especially in biomedical image analysis [12]. There are pre-trained deep neural networks based on CNN methods and models that do not use pre-trained networks.

In general, it is possible to classify skin cancers using transfer learning-based or non-transfer learning-based methods. Non-transfer learning methods generally use fewer layers than transfer learning methods. It is lighter than other models because of the small number of layers. Due to its light weight, it can perform faster training and classification processes. For this reason, a new CNN model that automatically classifies skin cancer types is presented in this study. This CNN model was used to attempt to classify seven different types of skin cancer that are commonly encountered.

One of the objectives of this study is to measure the effect of CNN models without using any weight values on the classification of skin cancers compared to transfer learning-based models.

Convolution layers, which are used to extract discriminative features that can be used in CNN models, are used successively in the first layers to reduce the noise in the images. In addition, the discriminative power of the model was increased by obtaining detailed features.

The contributions of the study carried out in this context to the literature are presented in articles.

- The SkinCNN, on the other hand, has achieved a 97% success rate by performing the training process 30 times faster than the proposed MobileNet V3 model.
- The SkinCNN is faster than existing transfer learning-based work in the literature, since it is built with basic convolution layers without using any weights.
- The reliability of the model was ensured by obtaining similar results in experimental studies using data separated by cross validation 5 techniques. It is proved that similar results are obtained instead of obtaining different results in each run of the SkinCNN.
- The SkinCNN model has 5% difference from the articles compared to the literature.
- A new deep learning-based CNN model has been proposed to assist healthcare professionals.

The following sections of the paper consist of three parts. In the first section following this chapter, we describe the theoretical background of the dataset experimentally studied and the models developed in this paper. The second section compares the performance measures of the proposed models. The third section concludes the paper with future work.

2. Material and Method

2.1. Materials

As a result of the experimental studies, it can be stated that the size and diversity of the dataset is effective in training the deep learning model. For this reason, a dataset with high data diversity was used in this article. The dataset [23] used was prepared by skin specialists in the Dermatology department of Austria. This dataset consists of labeled images obtained by experts in 2 different dermatology departments. The number of labelled images is 10.015 [23].

Seven different classes were examined in the dataset used. These seven different classes consist of the class labelled akiec, nv, bcc, bkl, df, mel, and vasc. The numbers of data belonging to the classes akiec, bkl, nv, bcc, df, mel, vasc are 327, 1.099, 6.705, 514, 115, 1.113, 142, respectively. It is seen that there is data imbalance between cancer classes in the dataset. In order to improve the classification results, horizontal and vertical rotation of the images from data augmentation techniques were applied to the images on a class basis to eliminate the data imbalance. These operations were applied to other classes other than the nv class, and the number of images belonging to each class was equalized to the nv class.

In Figure 1, each of akiec, nv, bcc, mel, bkl, df, vasc skin cancer types are seen in two. If fatal skin cancers are not detected early, the chance of survival drops to 15% [14]. In this case, the disease metastasizes as a result of the spread of disease lesions to neighboring organs. Among the types of skin cancer akiec, nv, bkl, mel, df, bcc, and vasc shown in Figure 1, the types of bcc and akiec are known to be more lethal than other types. These more lethal types can be completely cured if treated early. Bcc and akiec are the most common of the seven types listed. [19]. It is reported that there is a 5 percent increase in these species in the Americas region in 2021 [24].

The ozone layer is thinning due to environmental pollution caused by various reasons such as not recycling waste materials, polluting the soil with plastic materials, increasing harmful vehicle emission rates, unfiltered factory operation or filter renewal. As a result of the thinning of the ozone layer, which creates UV-B radiation, the skin is more exposed to harmful rays.

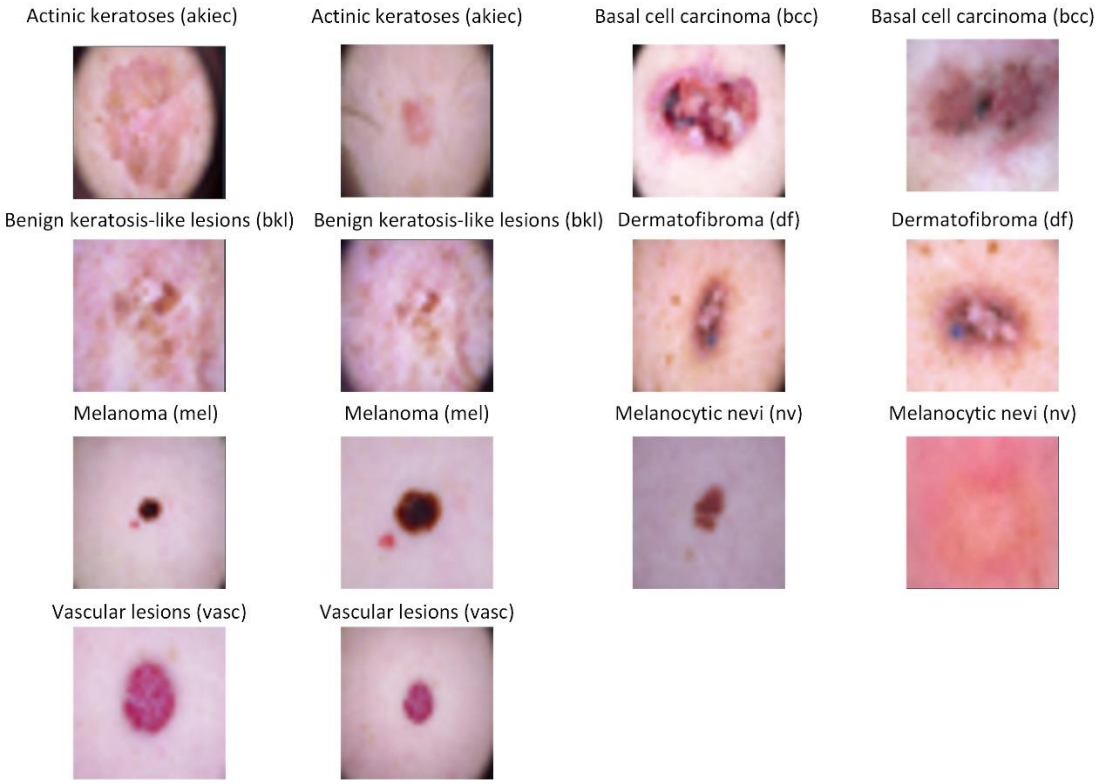

Figure 1. Skin lesion classes in the used dataset

In order to intervene in time on the increasing number of skin diseases due to the above-mentioned problems, it is imperative to develop decision support systems for medical professionals. For this purpose, two different deep learning models based on MobileNet V3 and CNN have been defined. While the MobileNet V3 model is based on pre-trained transfer learning, the CNN model is a model consisting of convolutional layers with different recommended filters. In this study, both models were compared according to the metrics F1 score, recall, precision, accuracy on the same dataset.

2.2. Materials

CNN networks for mobile devices have developed rapidly in recent years. There are three different versions of MobileNet networks [25]. One of them, the MobileNet V1 architecture, was developed on the basis of the VGG architecture [26]. Based on the MobileNet V1 architecture, a new architecture with a linear bottle beaker structure has been proposed [27]. The latest version of MobileNet networks is a model called MobileNet V3, which is created with the help of search optimization algorithms of the NAS and NetAdapt networks, leaving layers with high computational costs to increase efficiency and accuracy. In this model, the h-swish activation function is generally used instead of the ReLU activation function [28]. NetAdapt networks have the feature of working integrated with an algorithm that investigates the architectural structure of mobile phones. In order to achieve high accuracy, the swish function, which is used instead of the ReLU activation function, is also a kind of activation function. This activation function is defined in Equation 1.

$$swish(x) = x\emptyset\sigma(x) \qquad (1)$$

Since the sigmoid function in Equation 1 causes the processing load on mobile devices, the hard swish function of the swish function has been created.

$$h - swish[x] = x\frac{ReLU6(x+3)}{6} \qquad (2)$$

This function uses the ReLU6 function instead of the sigmoid function in the swish function. The use of the ReLU6 function instead of the sigmoid function is shown in Equation 2.

2.3. Proposed CNN Model (SkinCNN)

To classify common skin cancer types, two different models are proposed, based on the MobileNet V3 architecture, the third version of the MobileNet series, and the CNN architecture. With these deep learning architecture models, a new decision support system for skin specialists is presented. With the presented system, the infrastructure for accelerating and facilitating transactions is created. The proposed model has been named as SkinCNN. The SkinCNN system is shown in Figure 2 in detail. In addition to the 2D convolutional, max pooling layers, a dropout layer core structure is used that applies a 0.2% dropout. This structure is connected three times in a row. The convolutional layer in this core structure consists of the kernel with a 3x3 window and 16, 32 and 64 filters, respectively. In the second layer of the model, a convolution layer with a ReLU activation function with 16 filters is defined.

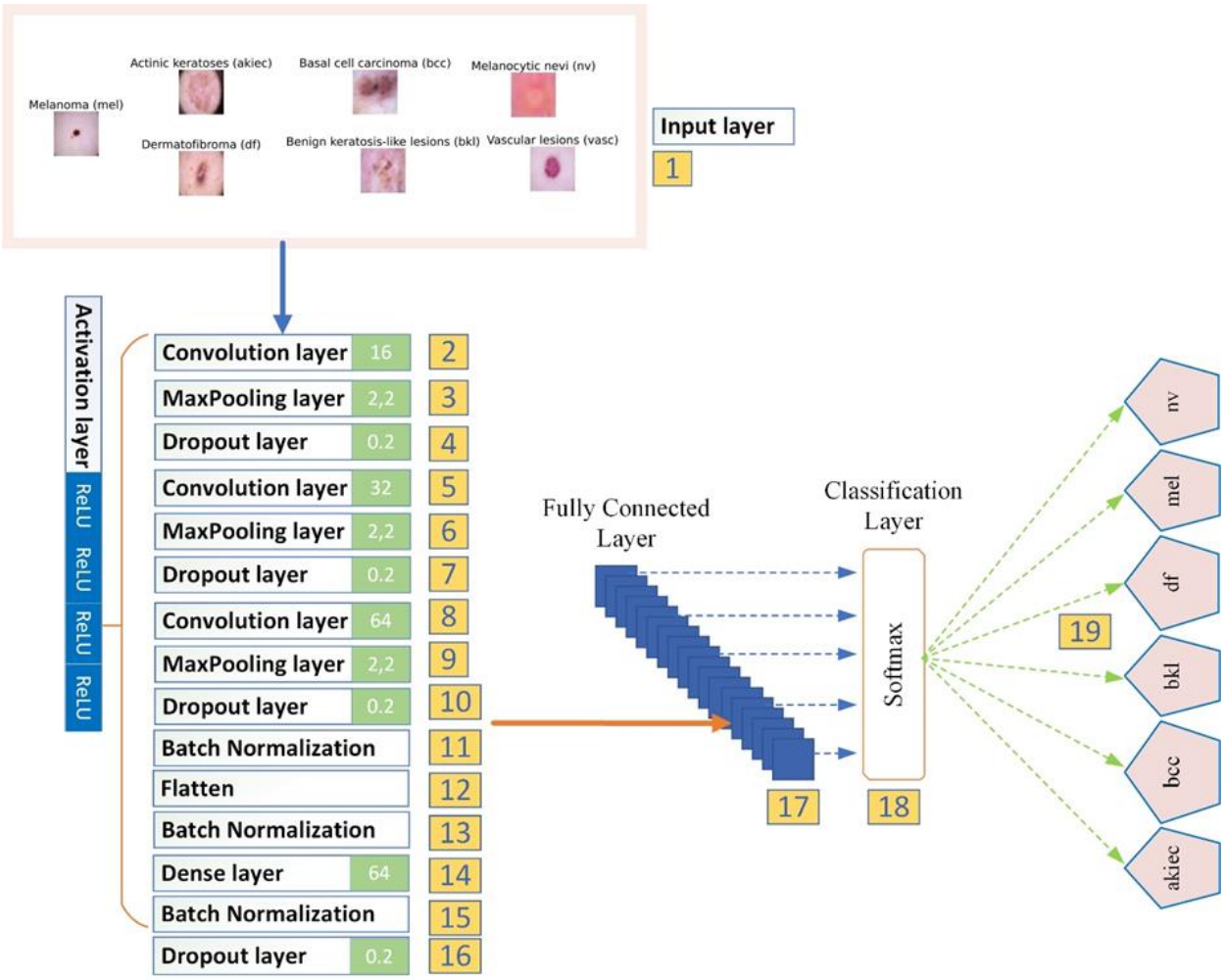

Figure 2. The SkinCNN for skin type classification

The third layer is a max pooling layer with 2x2 window sizes. The fourth layer is a dropout layer with a neuron dropout rate of 0.2%. The fifth layer is a convolution layer with a ReLU activation function with 32 filters. In the sixth layer, a max pooling layer was added, which performs feature selection in 2x2 window sizes. The seventh layer is a dropout layer with a neuron dropout rate of 0.2%.

The eighth layer is a convolution layer with a ReLU activation function with 64 filters. In the ninth layer, a new layer was added with maximum pooling in the third and sixth layers. The tenth layer is a dropout layer with a neuron dropout rate of 0.2%. In the eleventh step, shown in Figure 2, a batch normalization was performed to normalize the inputs between layers. In the on twelfth step, the flatten layer and the feature maps of the other

layers were transformed into a one-dimensional array. In the thirteenth step, the batch normalized layer was added again. In the fourteenth step, a dense layer of 64 neurons was added. In the fifteenth step, a third batch normalization layer was added to normalize the inputs between layers. In the sixteenth step, a 0.3% dropout layer was added. The purpose of this layer is to prevent the model from having an overfitting problem. In the seventeenth step, there is a fully connected layer which combines the attributes between the layers and gives input to the output. In the eighteenth step, there is a classification layer with a softmax activation function. This layer estimates the label of the target class according to the output obtained from the layers. In the nineteenth step, the target labels are displayed. The labels in the dataset containing the most common types of skin cancer are visualized.

In Figure 2, the entire flow diagram from input to output is shown with symbolic figures. The performance results of the model obtained as a result of the use of layers in this demonstration and the basic MobileNet V3 model are presented in Section 3. The performance comparison was made on a computer with the same graphics card and processor, with all operations turned off except for the training model. As a result of the comparison processes, both models proposed are light and fast.

3. Results and Discussion

A new method is presented to compare the performance of MobileNet V3 and SkinCNN models. Table 1 and Table 2 are given in order to test this presented method successfully. Table 1 gives the performance results of the basic MobileNet V3 model based on the cross validation 5 values. Table 2 presents the performance results of the SkinCNN according to the cross validation 5 values. Cross validation 5 was used to separate the training and test data of the dataset. By using this structure, training of models with the Adam optimization method is provided. The Adam optimization method was established with a learning rate of 0.001, with a delay value of 0. While Beta 1 value is 0.9, Beta 2 value is determined as 0.999.

The performance chart of the basic MobileNet V3 model is shown. The results obtained according to 5 different cross validation values are given separately. According to these results, loss and accuracy results are given. In addition to these, F1 score, recall, and precision measurement values are presented.

In Table 2, the performance results of the SkinCNN obtained according to 5 different cross validation values are given. As in Table 1, the accuracy and loss results are shown. In addition to these, F1 score, recall, and precision values are also presented. As shown in Table 2, the average accuracy rate of 95.47% was achieved from the SkinCNN. The accuracy and loss graphs of the results obtained from both models are presented together for convenience during comparison.

In the structure shown in Figure 3, the SkinCNN accuracy exceeds 92.5%. The accuracy of the basic MobileNet V3 model is about 77.5%. On average, the difference between the two models in training modelling is 15%. As the epoch value, the training process was carried out on 50 epoch iteration in both models. The SkinCNN has achieved a satisfactory result. The proposed abbreviation shown in the legend of the graphs represents the SkinCNN model.

Table 1. Performance results of the MobileNet V3 model according to cross validation 5 values

Cross validation	F1 Score	Recall	Precision	Accuracy	Loss
1	0.77	0.78	0.78	77.12	0.67
2	0.82	0.82	0.81	81.16	0.57
3	0.87	0.88	0.84	83.40	0.50
4	0.79	0.81	0.79	80,42	0.54
5	0.79	0.80	0.79	80,70	0.55
Average				80.56	0.56

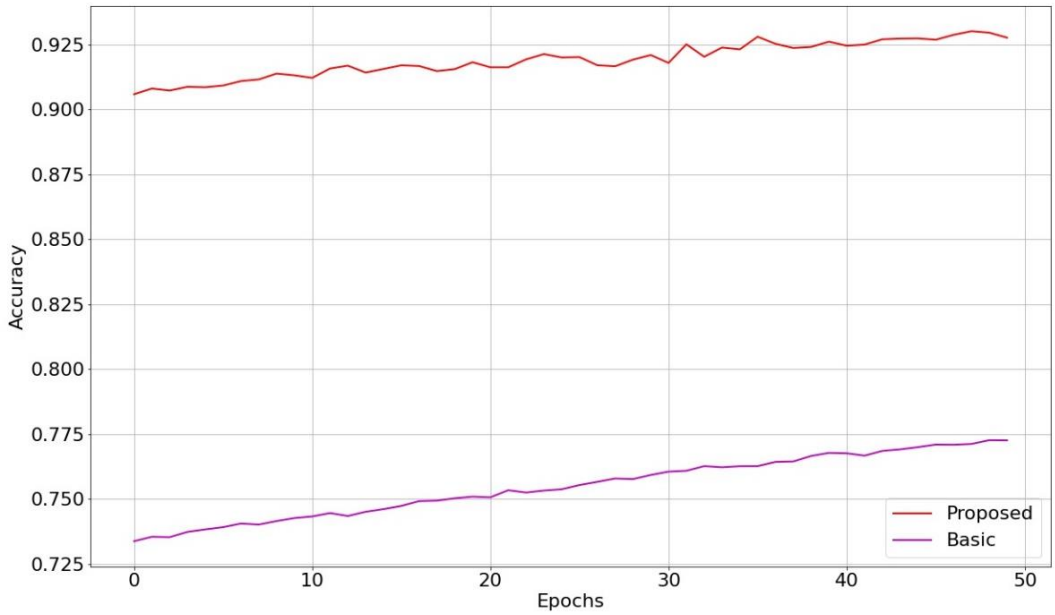

Figure 3. Training accuracy graph of MobileNet V3 and SkinCNN model

According to this result, the proposed system can be used on portable devices such as mobile devices. However, there will be a situation that we can say more clearly by looking at the test accuracy rates. Figure 4 shows the training loss graph for the basic MobileNet V3 and the SkinCNN. According to this average graph, the loss value of the SkinCNN is less than 0.2. The basic MobileNet V3 loss graph approaches 0.7. There is a loss value of 0.5 between the two models. The mean values of the SkinCNN are used in other given performance graphs, including the figures in Figure 3 and Figure 4. These mean values are shown in Table 2. However, in the compared MobileNet V3 model, the results of the highest cross validation value are reflected in the graph. However, the difference is quite large. When the structures of Figures 3 and 4 are examined, it can be said that both models can be used in the classification of skin cancer. However, to consolidate this decision, the test accuracy and loss graphs of both models should be presented. For this reason, the accuracy and loss graphs are presented in Figure 5 and Figure 6.

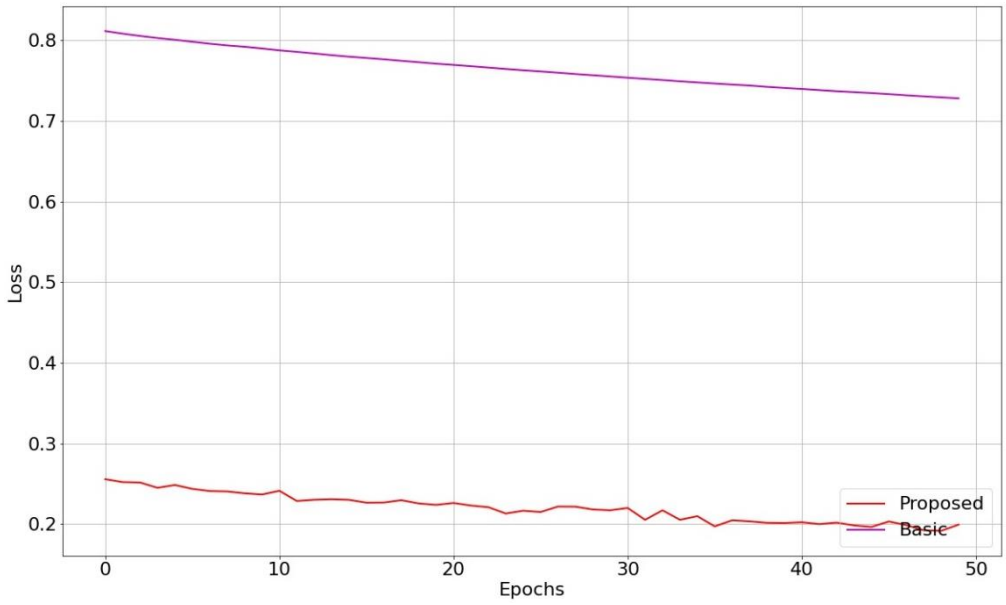

Figure 4. Training loss graph of MobileNet V3 and the SkinCNN model

After showing the loss values obtained as a result of the training modelling in Figure 4, the test accuracy and loss values can be checked. The average accuracy of the SkinCNN is over 0.95%. The accuracy of the basic MobileNet V3 model is close to 0.75%. There is a 20% difference between the accuracy rates of the two models.

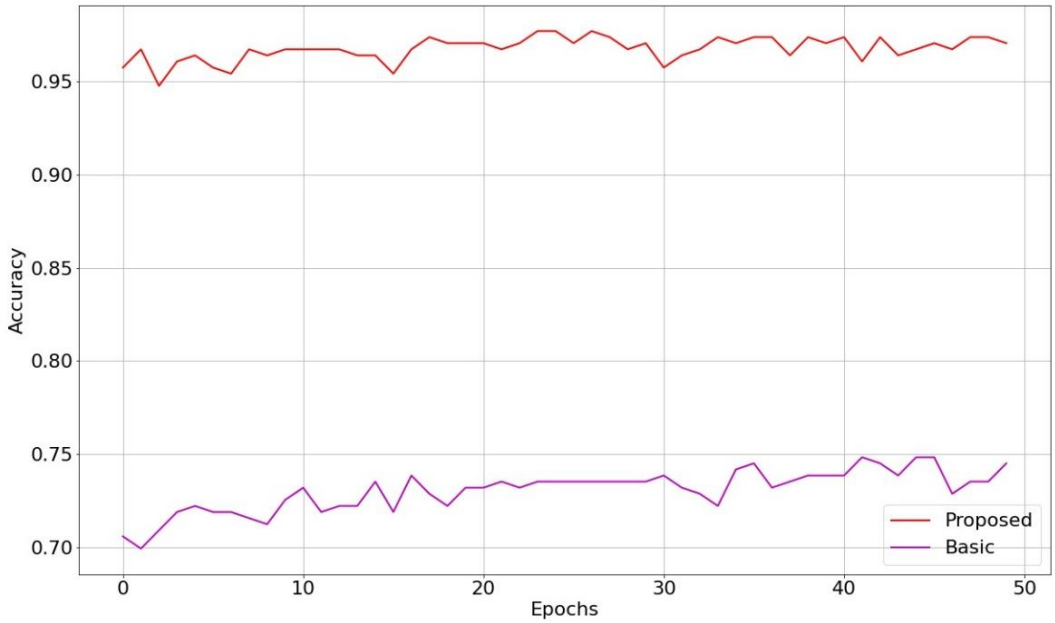

Figure 5. Test accuracy graph of MobileNet V3 and SkinCNN model

In Figure 6, the test loss graphs between the SkinCNN and the basic MobileNet V3 model are presented. Based on these values of the presented graph, the SkinCNN has a loss of less than 0.1%. The basic MobileNet V3 model has a loss of close to 0.8%.

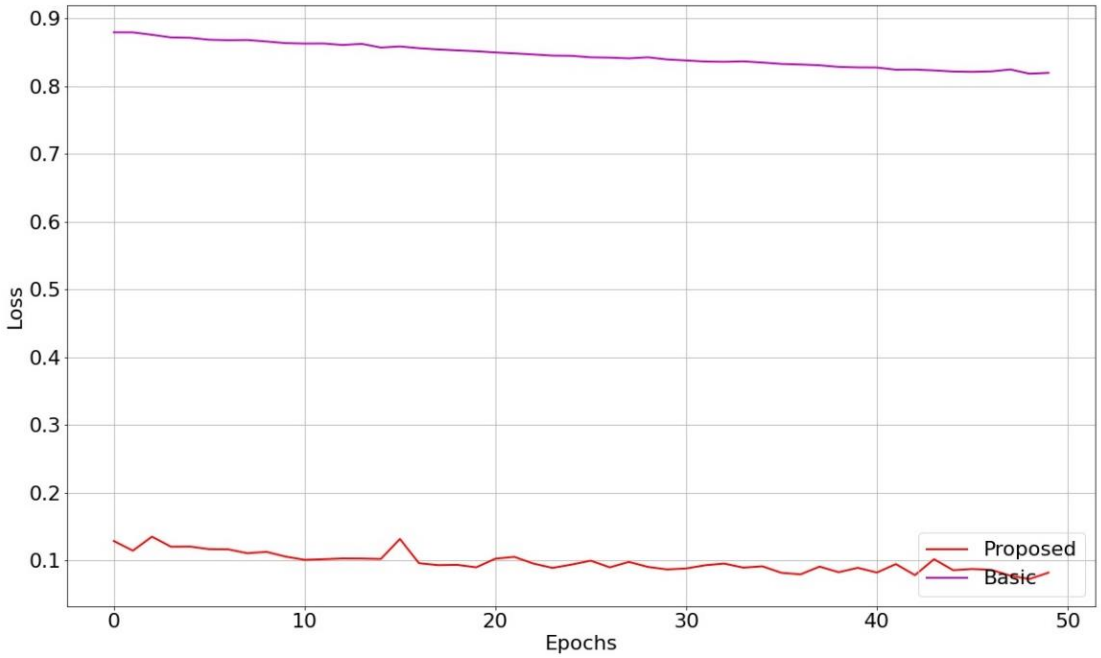

Figure 6. Test loss graph of MobileNet V3 and SkinCNN model

In Figure 7, the cross validation 5 accuracy result of the Fold option is shown, which has the highest accuracy value of the SkinCNN. According to the result shown, it goes above 97.5% towards the 50th epoch step.

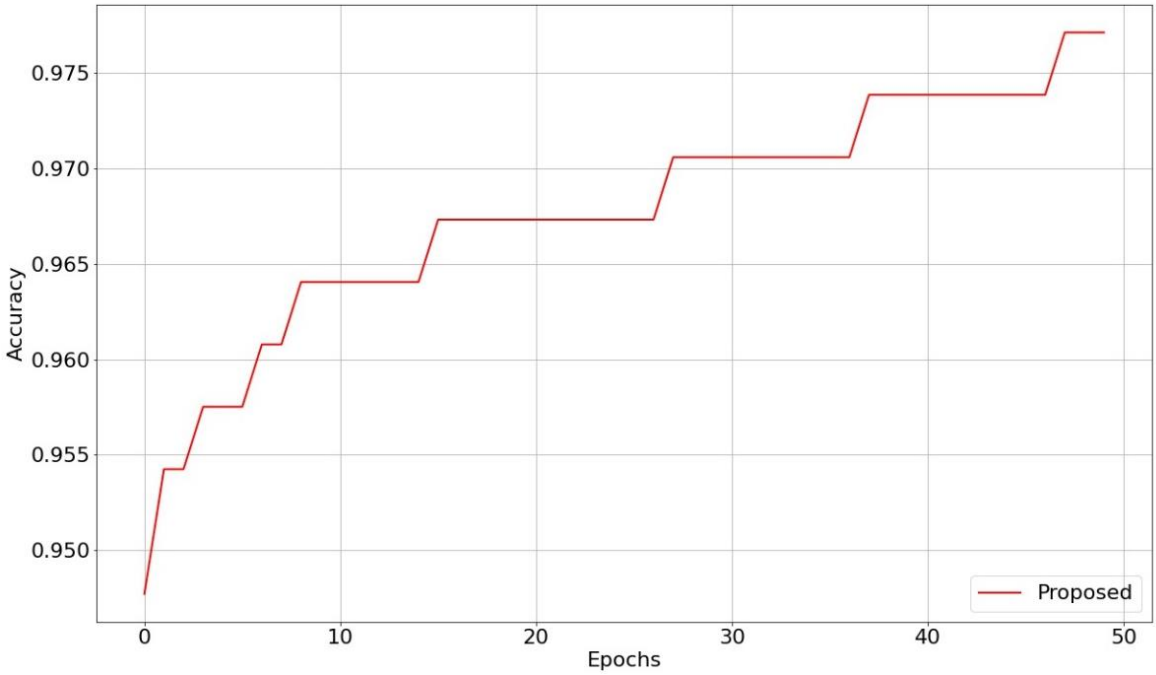

Figure 7. Test accuracy graph of the SkinCNN

Figure 8 shows the loss graph of the SkinCNN. According to this loss graph, it is seen that the loss value approaches 0.07% towards the 50th epoch step. As a result of the performance results obtained, it is possible to use the proposed structure actively in different biomedical problems. Due to its light weight, it can also be used on portable devices such as mobile devices.

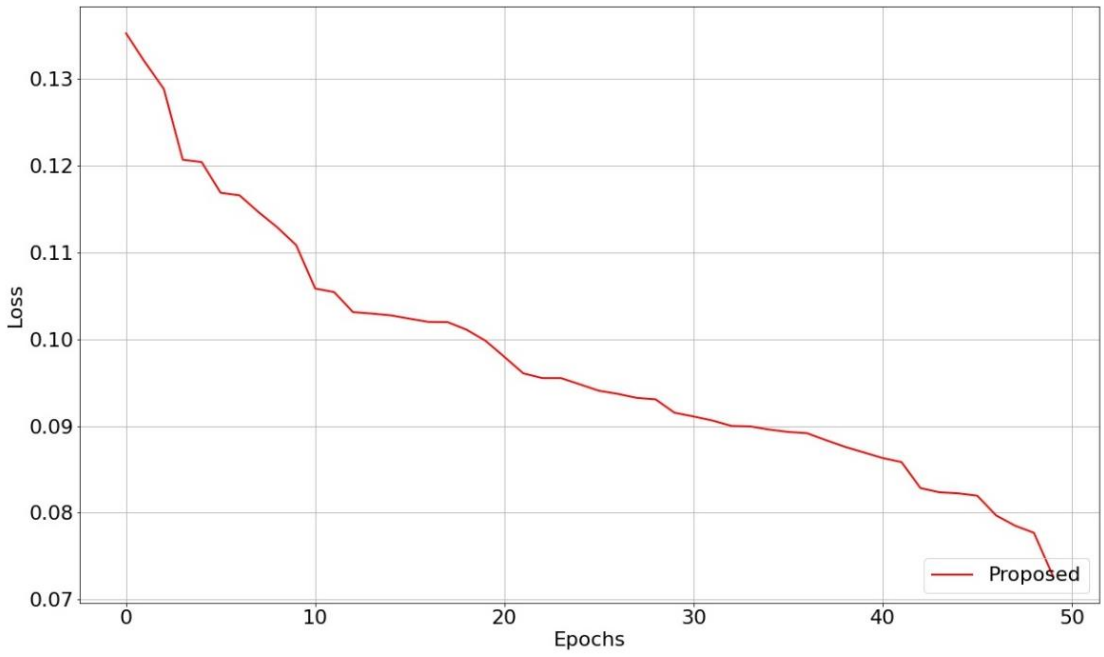

Figure 8. Test loss graph of the SkinCNN

In Table 3, the results obtained with the same or similar datasets are compared with the proposed study. Although the number of classes in the SkinCNN is 7, it can be seen that other studies compared use between 2 and 10 classes. There is only one exception. The exception is the study by Jianu et al. It was found that they classified melanoma, one of the types of skin cancer, as benign and malignant [29]. For this reason, the number of skin cancer types in this study was set to 1. The method, accuracy values and number of species for each of the other models compared are presented. The F1 score, recall and precision metrics were requested to be presented together to allow a detailed comparison with the proposed study in the specified table. However, as the metrics were not found in the compared articles, they are not included in Table 3.

Table 2. Comparison results on the same and similar skin datasets

References	Methods	Accuracy	Number of species
[29]	Feature and statistically based method	81%	1
[16]	Color and texture lesion descriptor method	81%	2
[30]	Regression based classifier, CNN deep learning	81.8%	10
[30]	Regression based classifier, CNN deep learning	85.5%	5
[30]	Regression based classifier, CNN deep learning	94.8%	2
[31]	Two deep learning	91.2%	3
[32]	Sparse coding, deep learning, SVM	93.1%	3
This study	SkinCNN	97.82%	7

According to Giotis et al. make the classification of melanoma and nevus types from skin cancer types by using color and texture features [16]. Kawahara et al. classified the features extracted by a pre-trained CNN method with the logistic regression classifier method [30]. There is a difference in the success rate depending on the number of classes. Li and Shen offered a deep learning framework that uses two fully connected layers [31]. Codella et al. used deep learning, sparse coding, and support vector machine methods to classify the types of species that emerged in the development of melanoma species [32].

4. Conclusion and Suggestions

Environmental pollution, which is increasing due to various reasons such as people's unconscious behavior, excessive consumption and non-compliance with regulations, is damaging the ozone layer. As a result of the damage to the ozone layer, the possibility of exposure to harmful solar radiation has also increased. For these reasons, a system that automatically classifies seven of the common types of skin cancer that can be seen in different age groups, young and old, has been proposed. The SkinCNN is compared in terms of performance with the MobileNet V3 model, a new architecture designed for use on mobile devices. From the results obtained, it is easy to say that the SkinCNN can be used in mobile devices together with the MobileNet V3 model.

The classification process using the SkinCNN and the MobileNet V3 model gave F1 score, recall, precision and accuracy values of 0.98, 0.97, 0.96, 0.97 and 0.87, 0.88, 0.84, 0.83 respectively. The performance results obtained show that the SkinCNN is as simple and stable as the MobileNet V3 model. To test the reliability of the results, cross-validation 5 data were disaggregated. If it is desired to develop models for which performance criteria are given by experimental studies, it would be appropriate to further develop the MobileNet V3 model. MobileNet is a model with three different structures with MobileNet V1, MobileNet V2 and MobileNet V3 models. It is possible to propose different models using this very successful model. It is possible to test these proposed structures on portable devices and equipment.

In further studies, this study can be developed into a system that can assist specialists in different locations, especially in areas where skin specialists or dermatologists are scarce. To

achieve this, the system can be transferred to different platforms and transformed into an environment where different user groups can upload and test skin images. In this way, different users, especially newly qualified dermatologists, can benefit.

Conflict of Interest Statement

There is no conflict of interest regarding the study.

Statement of Research and Publication Ethics

The study is complied with research and publication ethics.

References

[1] R. Perroy, "World population prospects," *United Nations*, vol. 1, no. 6042, pp. 587–592, 2015.

[2] D. Pimentel *et al.*, "Ecology of Increasing Diseases: Population Growth and Environmental Degradation," *Hum. Ecol. Interdiscip. J.*, vol. 35, no. 6, pp. 653–668, 2007, doi: 10.1007/s10745-007-9128-3.

[3] M. Plummer, C. de Martel, J. Vignat, J. Ferlay, F. Bray, and S. Franceschi, "Global burden of cancers attributable to infections in 2012: a synthetic analysis," *Lancet Glob. Heal.*, vol. 4, no. 9, pp. e609–e616, 2016.

[4] H. Younis, M. H. Bhatti, and M. Azeem, "Classification of Skin Cancer Dermoscopy Images using Transfer Learning," in *2019 15th International Conference on Emerging Technologies (ICET)*, Dec. 2019, pp. 1–4. doi: 10.1109/ICET48972.2019.8994508.

[5] U.-O. Dorj, K.-K. Lee, J.-Y. Choi, and M. Lee, "The skin cancer classification using deep convolutional neural network," *Multimed. Tools Appl.*, vol. 77, no. 8, pp. 9909–9924, 2018, doi: 10.1007/s11042-018-5714-1.

[6] A. J. McMichael and T. McMichael, *Planetary overload: global environmental change and the health of the human species*. Cambridge University Press, 1993.

[7] P. Martens and A. J. McMichael, *Environmental change, climate and health: issues and research methods*. Cambridge University Press, 2009.

[8] R. L. McKenzie, L. O. Björn, A. Bais, and M. Ilyasd, "Changes in biologically active ultraviolet radiation reaching the Earth's surface," *Photochem. Photobiol. Sci.*, vol. 2, no. 1, pp. 5–15, 2003.

[9] D. M. Parkin, D. Mesher, and P. Sasieni, "13. Cancers attributable to solar (ultraviolet) radiation exposure in the UK in 2010," *Br. J. Cancer*, vol. 105, no. 2, pp. S66–S69, 2011.

[10] R. J. Hay *et al.*, "The global burden of skin disease in 2010: an analysis of the prevalence and impact of skin conditions," *J. Invest. Dermatol.*, vol. 134, no. 6, pp. 1527–1534, 2014.

[11] D. R. Bickers *et al.*, "The burden of skin diseases: 2004: A joint project of the American Academy of Dermatology Association and the Society for Investigative Dermatology," *J. Am. Acad. Dermatol.*, vol. 55, no. 3, pp. 490–500, 2006.

[12] M. A. Morid, A. Borjali, and G. Del Fiol, "A scoping review of transfer learning research on medical image analysis using ImageNet," *Comput. Biol. Med.*, vol. 128, p. 104115, 2021, doi: https://doi.org/10.1016/j.compbiomed.2020.104115.

[13] F. Nachbar *et al.*, "The ABCD rule of dermatoscopy: high prospective value in the diagnosis of doubtful melanocytic skin lesions," *J. Am. Acad. Dermatol.*, vol. 30, no. 4, pp. 551–559, 1994.

[14] D. B. Mendes and N. C. da Silva, "Skin lesions classification using convolutional neural networks in clinical images," *arXiv Prepr. arXiv1812.02316*, 2018.

[15] C. Barata, M. Ruela, M. Francisco, T. Mendonça, and J. S. Marques, "Two systems for the detection of melanomas in dermoscopy images using texture and color features," *IEEE Syst. J.*, vol. 8, no. 3, pp. 965–979, 2013.

[16] I. Giotis, N. Molders, S. Land, M. Biehl, M. F. Jonkman, and N. Petkov, "MED-NODE: A computer-assisted melanoma diagnosis system using non-dermoscopic images," *Expert Syst. Appl.*, vol. 42, no. 19, pp. 6578–6585, 2015.

[17] D. Ruiz, V. Berenguer, A. Soriano, and B. Sánchez, "A decision support system for the diagnosis of melanoma: A comparative approach," *Expert Syst. Appl.*, vol. 38, no. 12, pp. 15217–15223, 2011.

[18] V. Pomponiu, H. Nejati, and N.-M. Cheung, "Deepmole: Deep neural networks for skin mole lesion classification," in *2016 IEEE International Conference on Image Processing (ICIP)*, 2016, pp. 2623–

2627. doi: 10.1109/ICIP.2016.7532834.
[19] D. A. Shoieb, S. M. Youssef, and W. M. Aly, "Computer-Aided Model for Skin Diagnosis Using Deep Learning," *J. Image Graph.*, vol. 4, no. 2, pp. 122–129, 2016, doi: 10.18178/joig.4.2.122-129.
[20] H. Çetiner, "Cataract disease classification from fundus images with transfer learning based deep learning model on two ocular disease datasets," *Gümüşhane Üniversitesi Fen Bilim. Enstitüsü Derg.*, vol. 13, no. 2, pp. 258–269, Jan. 2023, doi: 10.17714/gumusfenbil.1168842.
[21] H. Çetiner and B. Kara, "Recurrent Neural Network Based Model Development for Wheat Yield Forecasting," *J. Eng. Sci. Adiyaman Univ.*, vol. 9, no. 16, pp. 204–218, 2022, doi: 10.54365/adyumbd.1075265.
[22] A. Krizhevsky, I. Sutskever, and G. E. Hinton, "Imagenet classification with deep convolutional neural networks," *Adv. Neural Inf. Process. Syst.*, vol. 25, 2012.
[23] P. Tschandl, C. Rosendahl, and H. Kittler, "The HAM10000 dataset, a large collection of multi-source dermatoscopic images of common pigmented skin lesions," *Sci. data*, vol. 5, no. 1, pp. 1–9, 2018.
[24] K. M. Hosny, M. A. Kassem, and M. M. Fouad, "Classification of Skin Lesions into Seven Classes Using Transfer Learning with AlexNet," *J. Digit. Imaging*, vol. 33, no. 5, pp. 1325–1334, 2020, doi: 10.1007/s10278-020-00371-9.
[25] W. Bao, X. Yang, D. Liang, G. Hu, and X. Yang, "Lightweight convolutional neural network model for field wheat ear disease identification," *Comput. Electron. Agric.*, vol. 189, p. 106367, 2021, doi: https://doi.org/10.1016/j.compag.2021.106367.
[26] A. G. Howard *et al.*, "Mobilenets: Efficient convolutional neural networks for mobile vision applications," *arXiv Prepr. arXiv1704.04861*, 2017.
[27] M. Sandler, A. Howard, M. Zhu, A. Zhmoginov, and L.-C. Chen, "Mobilenetv2: Inverted residuals and linear bottlenecks," in *Proceedings of the IEEE conference on computer vision and pattern recognition*, 2018, pp. 4510–4520.
[28] S. Qian, C. Ning, and Y. Hu, "MobileNetV3 for Image Classification," in *2021 IEEE 2nd International Conference on Big Data, Artificial Intelligence and Internet of Things Engineering (ICBAIE)*, 2021, pp. 490–497. doi: 10.1109/ICBAIE52039.2021.9389905.
[29] S.-R.-S. Jianu, L. Ichim, D. Popescu, and O. Chenaru, "Advanced Processing Techniques for Detection and Classification of Skin Lesions," in *2018 22nd International Conference on System Theory, Control and Computing (ICSTCC)*, Oct. 2018, pp. 498–503. doi: 10.1109/ICSTCC.2018.8540732.
[30] J. Kawahara, A. BenTaieb, and G. Hamarneh, "Deep features to classify skin lesions," in *2016 IEEE 13th international symposium on biomedical imaging (ISBI)*, 2016, pp. 1397–1400. doi: 10.1109/ISBI.2016.7493528.
[31] Y. Li and L. Shen, "Skin lesion analysis towards melanoma detection using deep learning network," *Sensors*, vol. 18, no. 2, p. 556, 2018.
[32] N. Codella, J. Cai, M. Abedini, R. Garnavi, A. Halpern, and J. R. Smith, "Deep Learning, Sparse Coding, and SVM for Melanoma Recognition in Dermoscopy Images," in *International workshop on machine learning in medical imaging*, Springer, 2015, pp. 118–126. doi: 10.1007/978-3-319-24888-2_15.

Bitlis Eren Üniversitesi Fen Bilimleri Dergisi
BİTLİS EREN UNIVERSITY JOURNAL OF SCIENCE
ISSN: 2147-3129/e-ISSN: 2147-3188
VOLUME: 12 NO: 4 PAGE: 1117-1127 YEAR: 2023
DOI:10.17798/bitlisfen.1340121

The Selection of the Appropriate Conductive Yarn Using Analytical Hierarchy Process

Duygu ERDEM AKGÜN[1*], Münire Sibel ÇETİN[2]

[1]*Selcuk University, Faculty of Architecture and Design, Fashion Design Department, Konya, Turkey*
[2]*Istanbul Technical University, Faculty of Textile Technologies and Design, Textile Engineering Department, Istanbul, Turkey*
(ORCID: 0000-0002-8277-3589) (ORCID: 0000-0003-1875-3302)

Keywords: AHP, Conductive yarn, Electronic Textiles, Multi-criteria decision-making.

Abstract
Conductive yarns are one of the most preferred products that are used for electronic textile products. Although conductive yarns have a wide range of application areas, it is also important to choose the most appropriate yarn according to the intended use. In this study, it was aimed at selecting the most appropriate conductive yarn for a textile factory that makes production using conductive yarn. Within this scope, 8 criteria and 3 conductive yarn alternatives are determined, and a form that includes criteria was sent to 7 experts via e-mail and they were asked to evaluate the criteria for steel, graphene, and silver-plated yarns according to the AHP fundamental scale table. The matrices obtained from the forms filled out by the experts were evaluated with the help of the AHP method. As a result, it has been determined that graphene yarn is the most appropriate yarn for a textile factory among the alternatives according to the specified criteria.

1. Introduction

The rapid increase in technological developments after the Industrial Revolution and the fact that researchers turn to interdisciplinary studies enable innovative products to emerge. One of the most important technological developments that emerged as a result of interdisciplinary studies is wearable technologies [1]. "Wearable technology" concept is defined as the technology which is incorporated into the wearable accessories directly worn on the body [2].

Another concept developed from the concept of wearable technology is the concept of electronic textiles [3]. Electronic textiles are the technical and functional products that result from the combination of materials, design tools and production methods from the two major industries of textile and electronics industries that continue to develop [4].

Nowadays, the increasing importance of studies on electronic textiles and wearable electronics and the increase in commercial products developed and released in this category have led to the production of conductive yarn from sample size to commercial size. Conductive yarns are one of the most preferred conductive textile products that are used both to produce textile surfaces or textures and connection paths. Wearable products manufactured with conductive yarns are frequently encountered in fields such as healthcare, sports, the military, home textiles, and leisure-time products. Although conductive yarns have such a wide range of application areas, it is also important to choose the most appropriate yarn according to the intended use and the process to be applied. Metal ratio, conductivity, flexibility, biocompatibility, mechanical strength, washability, usability in the machine for production, and price are the most important criteria for conductive yarns [5]. In addition

*Corresponding author: duygu.erdem@selcuk.edu.tr
Received: 09.08.2023, Accepted: 08.12.2023

to these criteria, there are many different types of conductive yarns, too. The situation becomes more difficult in systems where there are multiple criteria affecting decision-making. In cases where there is a single criterion in decision-making processes, the problem can be easily solved; however, this becomes more difficult as the criteria increase [6].

The decision-making actions of companies are much more complicated and important than people's decision-making actions in daily life. The main reason for this is that every decision taken affects all other units of the company and has a much greater impact on the profitability of the company than expected. Today, different Multi-Criteria Decision-Making Methods (MCDMM) are available for the solution of decision-making problems that contain multiple evaluation criteria, both for companies and our daily lives. Multi-criteria decision-making techniques frequently encountered in literature are DEMATEL (The Decision-Making Trial and Evaluation Laboratory), AHP (Analytical Hierarchy Process), ANP (Analytic Network Process), VIKOR (Vise Kriterijumska Optimizacija I Kompromisno Resenje), TOPSIS (Technique for Order Preference by Similarity to Ideal Solution), MOORA (Ratios Analysis and Reference Point Approach) and ELECTRE (Elimination and Choice Translating Reality English) [6]-[9].

The choice of multi-criteria decision-making method to be used in the evaluation varies according to the level of knowledge required for each factor, and each method works with a different solution logic. In this paper, the Analytical Hierarchy Process (AHP) method, which is one of the multi-criteria decision-making methods, was chosen and applied. The AHP method decomposes the problem into subcomponents, and the basis of the AHP method is based on both criteria and binary comparisons between alternatives. These binary comparisons include a comparison of the importance of criteria or alternatives according to each other. The calculations for selection or grading are then performed on these binary comparison matrices [6], [10], [11].

In this study, it was aimed at selecting the most appropriate conductive yarn for a textile factory that makes production using conductive yarn. To construct a hierarchical structure, the alternatives are first determined as steel, graphene, and silver-plated yarns. Then, 8 criteria (metal ratio, conductivity, flexibility, biocompatibility, mechanical strength, washability, usability of the machine for production, and price) are determined. After generating the hierarchical structure, binary comparison matrices were established, and the alternatives were listed from the best to the worst.

2. Material and Method

Within the scope of this study, firstly, 8 criteria that are effective in the purchase of conductive yarn were determined. These criteria are metal ratio (C1), conductivity (C2), flexibility (C3), biocompatibility (C4), mechanical strength (C5), washability (C6), usability of the machine for production (C7), and price (C8). Then, 3 conductive yarn alternatives were determined. These alternatives are steel (A1), graphene (A2), and silver-plated (A3) yarns (Table 1).

Table 1. The properties of conductive yarn alternatives

Steel yarn	Graphene yarn	Silver-plated yarn
Bekinox® stainless steel yarns	RESISTEX® GRAPHENE	Shieldex silver-plated yarns
		
These stainless steel yarns are flexible and durable electrically conductive yarns. These yarns are used in a wide range of applications related to Anti-static (ESD), intelligent textiles, signal and power transfer, heat-resistant sewing yarn, and thermal conductivity. The yarns can be easily knit, sewn, or woven to produce any type of textile.	It has a higher tenacity and abrasion resistance than normal polyester or polyamide yarns. The electrical conductivity of this yarn can range from 10^3 Ω to 10^6 Ω, placing it in the range of both antistatic and conductive yarns.	This yarn has <600 Ω/m electrical resistance. Due to its higher silver content, it is highly conductive. With their antistatic and antibacterial properties and high electrical and thermal conductivity, these conductive yarns can be used in a wide range of applications. The full silver-plated polyamide yarns can be twisted, knitted, embroidered, woven, and spun like uncoated yarns.

After the determination of the criteria and alternatives, two forms (Appendix 1 and Appendix 2), which include criteria, were sent to 7 experts who are actively working in the textile sector and effective in the decision to purchase conductive yarn, and they were asked to evaluate the criteria for steel, graphene, and silver-plated yarns according to the AHP fundamental scale table. The matrices obtained from the forms filled out by the experts were evaluated with the help of the AHP method, priority vectors were determined, and the alternatives were listed according to their importance weight. Therefore, it has been determined which yarn is the most appropriate for a textile factory to choose among the alternatives according to the specified criteria.

In the study, Adobe Acrobat Pro DC was used to create the fillable forms, and Microsoft® Excel version 16.16.14 was used to make the calculations.

2.1. Analytical Hierarchy Process

There are many methods known as Multi-Criteria Decision Analysis (MCDA) for solving problems [11].

The Analytical Hierarchy Process (AHP) is a decision-making technique that measures all objective and subjective criteria by pairwise comparison and allows them to be quantitatively evaluated by determining their order of importance. Analytical Hierarchy Process (AHP), one of the multi-criteria decision-making methods, was introduced by Myers and Alpert in 1968, and it was developed by Thomas L. Saaty as a model [13].

This method can be applied easily, even to very complex problems, because it takes into account both quantitative and qualitative factors, is applicable to individuals or groups, is easy to use, and does not require special expertise [13], [14].

In this study, the Analytical Hierarchy Process was chosen because it is a widely used tool that enables decision-makers to make decisions, allowing all important criteria to be taken into account and arranged in a hierarchy.

In the Analytical Hierarchy Process, calculations for the selection problems are made using the simple four arithmetical operations. Criteria (price, quality, distance, etc.) that are considered important for the decision-maker are determined in order to carry out the selection process among the alternatives in the selection problem. Decision-makers should express the importance of each criterion according to themselves. Hence, the fundamental scale, which is recommended by Thomas L. Saaty and contains the determined values for importance, is used (Table 2) [15].

Table 2. The fundamental scale

The intensity of importance on an absolute scale	Definition	Explanation
1	Equal importance	Two activities contribute equally to the objective
3	Moderate importance of one over another	Experience and judgment strongly favor one activity over another
5	Essential or strong importance	Experience and judgment strongly favor one activity over another
7	Very strong importance	An activity is strongly favored and its dominance demonstrated in practice
9	Extreme importance	The evidence favoring one activity over another is of the highest possible order of affirmation
2, 4, 6, 8	Intermediate values between the two adjacent judgments	When comprimise is needed
Reciprocals	If activity i has one of the above numbers assigned to it when compared with activity j, then j has the reciprocal value when compared with i	
Rationals	Ratios arising from the scale	If consistency were to be forced by obtaining n numerical values to span the matrix

The Analytical Hierarchy Process has four different axioms. These are named reciprocal, homogeneity, independence, and expectation axioms. The AHP axioms allow for the derivation of ratio scales of absolute numbers through decision-makers' responses to pairwise comparisons [16].

1. Reciprocal Axiom: According to the decision-maker in this axiom, if criterion A is m times more important than criterion B, criterion B is 1/m times more important than criterion [12]. To give an example, if one stone is judged to be five times heavier than another, then the other is automatically one fifth as heavy as the first because it participated in making the first judgement [16]. This axiom is used to form the comparison matrices. By means of this axiom, the number of questions to be asked to the decision-maker in order to determine the importance of the criteria has fallen in half.

2. Homogeneity Axiom: This axiom is based on the fact that there is no significant difference between the elements to be compared. If the differences between the elements are high, significant measurement errors will occur. Therefore, homogeneity is important to make meaningful comparisons. Since the elements can't be compared to being infinitely significant (aij $\neq \infty$), a scale in the range 1-9 from the fundamental scale is used.

3. Independence Axiom: This axiom is also named the synthesis axiom. In this axiom, when binary comparisons are made between the alternatives in the selection problem and the criteria used to solve the problem, each alternative and criterion is assumed to be independent of each other. This means that the priorities of the higher-level criteria will not change when a new alternative is added or removed [14], [18], [19]. This axiom plays an active role in the generation of the hierarchical structure.

4. Expectation Axiom: This axiom states that all criteria and alternatives affecting the decision should be included in the hierarchical structure. Decision-makers want to make certain that all their ideas are adequately represented in a hierarchical structure, as they have reasons for their decisions. The hierarchical structure established should meet the expectations of the decision-makers and should include all the elements (objective/target, criteria, sub-criteria, and alternatives) related to the decision problem. Otherwise, the decision-maker will not use all criteria or alternatives, and the decision will be inadequate [19], [20].

2.1.1. Application Steps of Analytical Hierarchy Process

The Analytical Hierarchy Process consists of 7 steps in total.

Step 1: Defining the Problem and Constructing the Appropriate Hierarchical Structure

The first step of the AHP method is to identify the problem clearly after it is determined. After defining the problem, all the criteria required in the solution process and all the alternatives to be evaluated should be determined completely. Thereafter, the hierarchical structure is generated with the aim or target at the top, the criteria sets (criteria and sub-criteria) of the problem at the second level, and the alternatives to be evaluated in the problem at the bottom, as seen in Figure 1 [6].

The purpose of the hierarchical structure is to determine the effect of upper-level elements on lower-level elements or the contribution of lower-level elements to the importance or completion of upper-level elements [14].

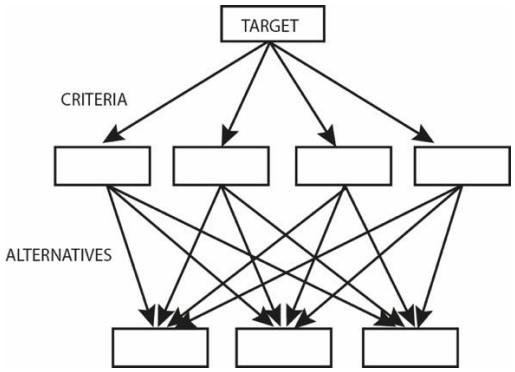

Figure 1. Analytical hierarchy structure

Step 2: Defining Priorities/Importance and Generating the Binary Comparison Matrices

After the problem is expressed in a hierarchical structure, it is necessary to calculate its importance relative to each other by comparing the elements that compose that level. For this purpose, binary comparison matrices are generated. The values in the fundamental scale proposed by Saaty are used to generate these matrices.

$$A = [a_{11}a_{12} \dots a_{1n}a_{21}a_{22} \dots a_{2n} \vdots \cdots \vdots a_{n2} \cdots a_{nn}]$$

A: Binary comparison matrix, a_{ij}: the importance of element "i" when compared to element "j" (i, j= 1, 2, 3, …., n)

Binary comparisons are performed for only one side of the principal diagonal of the comparison matrix based on the reciprocal axiom. The values at the bottom of the diagonal are determined according to the reciprocal axiom, and the values at the top of

the diagonal are inverted according to the multiplication, and filled into the cells in the symmetry of the principal diagonal. In other words, when the weight of property i is expressed as wi and the weight of property j is expressed as wj; it can be said that $a_{ij} = w_i / w_j$ [14].

$$A = \left[\frac{W_1}{W_1}\frac{W_1}{W_2}\cdots\frac{W_1}{W_n}\frac{W_2}{W_1}\frac{W_2}{W_2}\cdots\frac{W_2}{W_n}\vdots\cdots\vdots\frac{W_n}{W_1}\frac{W_n}{W_2}\cdots\frac{W_n}{W_n}\right]$$
$$= [1a_{12}\cdots a_{1n}\frac{1}{a_{12}}1\cdots a_{2n}\vdots\cdots$$
$$\vdots\frac{1}{a_{n1}}\frac{1}{a_{n2}}\cdots 1]$$

Since each criterion does not dominate over itself, the values on the principal diagonal are filled to be equally important (to take the value of 1) [6].

The binary comparison matrix is a n x n-sized square matrix. The values in the cells of this matrix indicate how much more important the element in each row is than the element in each column. The equation in which the number of comparisons to be used to form the binary comparison matrix can be calculated is as follows:

$$Number\ of\ comparison = \frac{(n)x(n-1)}{2} \quad (1)$$

n= Number of criteria to be evaluated

If the decision given for the solution of the problem will affect many people, binary comparison matrices form by combining the judgements of different individuals. In this combining process, geometric averages of the judgements of different individuals are generally taken to obtain consistent binary comparison matrices [14].

Step 3: Normalization Process and Generating of Priority Vector of Criteria

Once the binary comparison matrix is generated, the comparison matrix is first normalized to calculate the priority of weight vectors. The value in each cell of the binary comparison matrix is divided by the sum of the values in the column individually for the normalization process. The matrix obtained as a result of this process will be the normalization matrix (C). If this process is formulated, first of all, a B column vector is generated with n size and n components using the following formula:

$$b_{ij} = \frac{a_{ij}}{\sum_{i=1}^{n} a_{ij}} \quad (2)$$

$$B_i = [b_{11}b_{21}\vdots b_{n1}]$$

These matrix vectors are collocated and C matrix is obtained.

$$C = \begin{bmatrix} c_{11} & c_{12} & \cdots & c_{1n} \\ c_{21} & c_{22} & \cdots & c_{2n} \\ \cdot & & & \cdot \\ B_1 & & & \cdot \\ \cdot & & & \cdot \\ c_{n1} & c_{n2} & \cdots & c_{nn} \end{bmatrix}$$

Then, priority/weight vector (W) or percentage importance distributions that show the importance of the factors relative to each other can be obtained using the normalized matrix (C). The elements of the column vector, called the priority vector, are obtained by calculating arithmetic mean of the row elements of the matrix C using the following formula wi.

$$w_i = \frac{\sum_{j=1}^{n} c_{ij}}{n} \quad (3)$$

$$W = [w_1 w_2 \vdots w_n]$$

The results obtained from this formula represent the importance weights of the criteria if they were performed for the criteria and the weight vector of the alternatives for that criterion if they were performed for the alternatives [13], [14].

Step 4: Calculation of Consistency Ratio

It should be tested whether the decision-maker is consistent when performing binary comparisons between criteria. A consistency ratio (CR) must be found for each matrix to test its consistency. The consistency ratio is a ratio recommended by Saaty and used to determine the level of human error that can be made in binary comparison matrices. It is calculated by dividing the consistency index (CI) by the random consistency index (RI).

$$CR = \frac{CI}{RI} \quad (4)$$

Random consistency index (RI) is a predetermined index by Saaty based on the number of criteria, ie matrix size. RI values corresponding to the matrix size are shown in Table 3 [10].

Table 3. Random consistency index

n (matrix size)	1	2	3	4	5	6	7	8	9	10
Random consistency index (RI)	0	0	0.58	0.9	1.12	1.24	1.32	1.41	1.45	1.49

Consistency index is calculated using the following formula:

$$CI = \frac{\lambda_{max} - n}{n-1} \quad (5)$$

In this formula, λ_{max} represents the greatest eigenvalue. In order to calculate this value, firstly the column vector D is obtained by multiplying the binary comparison matrix (A) with the priority vector (W).

$$D = AxW = [a_{11}a_{12} \cdots a_{1n}a_{21}a_{22} \cdots a_{2n} \vdots \cdots \vdots a_{n1}a_{n2} \cdots a_{nn}]x[w_1w_2 \vdots w_n] \quad (6)$$

Then, a new column vector is obtained from the division of the reciprocal elements of column vector D and column vector W, which contains the fundamental values (E) for each evaluation factor. The largest eigenvalue (λmax) of the matrix is found by taking the arithmetic mean of the fundamental values in this vector [14], [21], [22].

$$E_i = \frac{d_i}{w_i} (i = 1,2,\cdots,n) \quad (7)$$

$$\lambda\max = \frac{\sum_{i=1}^{n} E_i}{n} \quad (8)$$

For a matrix obtained as a result of binary comparisons to be consistent, the largest eigenvalue (λmax) of the matrix must be equal to the size (n) of the matrix [24]. The largest eigenvalue obtained from these processes is placed in the formulas CI and CR, and CI and CR are calculated using the formulas, respectively. The consistency ratio is expected to be less than 0.1 at the end of the test. Results can be used if the test result is consistent. However, if it is inconsistent, comparisons should be repeated, or subjects that may be wrong should be reviewed.

Step 5: Calculation of Priority Vectors of Alternatives for Each Criteria

This step consists of 4 steps in itself.
Step 1: Binary comparison matrices are obtained by comparing alternatives for each criterion.
Step 2: The normalization of the binary comparison matrices is performed.
Step 3: From the normalization matrices obtained for each criterion, the process of generating priority vectors (column vectors of size mx1) is performed using formula (3).

$$S_i = [S_{11}S_{21} \vdots S_{m1}]$$

Step 4: λ_{max}, CI and CR values are calculated for each criterion separately, and consistency control is performed. If the matrices created for each criterion as a result of step 4 are consistent, it means that the results obtained through these matrices are usable. In other words, priority vectors obtained by binary comparison of alternatives for each criterion can be used in problem-solving when constructing a decision matrix [6].

Step 6: Generating the Decision Matrix with Aggregation Procedure

At this stage, the decision matrix (K) is generated by combining the priority vectors (Si, column vectors) obtained in the 5th step of the AHP application.

$$K = [S_{11}S_{12} \cdots S_{1n}S_{21}S_{22} \cdots S_{2n} \vdots \cdots \cdots \vdots S_{m1}S_{m2} \cdots S_{mn}]$$

The values in the obtained decision matrix represent the priority weights of the alternatives for each criterion [6].

Step 7: Sensitivity Analysis by Calculating Ultimate Priority Vectors

It should be determined that the model established depends on which criteria or criterion to what extent by sensitivity analysis [18]. For that purpose, column vector L with m elements is obtained by multiplying the priority vector (W, column vector) and the decision matrix (K) obtained in the 6th step.

$$L = KxW = [S_{11}S_{12} \cdots S_{1n}S_{21}S_{22} \cdots S_{2n} \vdots \cdots \cdots \vdots S_{m1}S_{m2} \cdots S_{mn}]x[w_1w_2 \vdots w_n] = [l_{11}l_{21} \vdots l_{m1}] \quad (9)$$

Each element of the obtained column vector (L) shows the percentage distribution/importance order of the decision alternatives. Consequently, the

sum of these elements will be 1. The alternative with the largest value/importance in the column vector L is the most suitable alternative [13], [23], [24].

3. Results and Discussion

The problem of this study is "the selection of the most appropriate conductive yarn for a textile factory that uses conductive yarn in its production line." To construct a hierarchical structure, first of all, the alternatives should be determined in this selection problem. For this purpose, three commonly used conductive yarn types have been identified. Secondly, in order to solve this problem with the analytical hierarchy process and construct a hierarchical structure, the criteria should be determined for the evaluation of conductive yarn selection. Therefore, studies in the literature have been examined, and it has been found that 8 of the criteria affecting the selection of conductive yarn have come into prominence.

The results obtained should be included in this section and supported by figures and tables if necessary. The findings can be compared with the relevant literature if required. Results should be clear and concise. In the discussion section, the important results of the study should be highlighted, and excessive citation and literature discussion should be avoided.

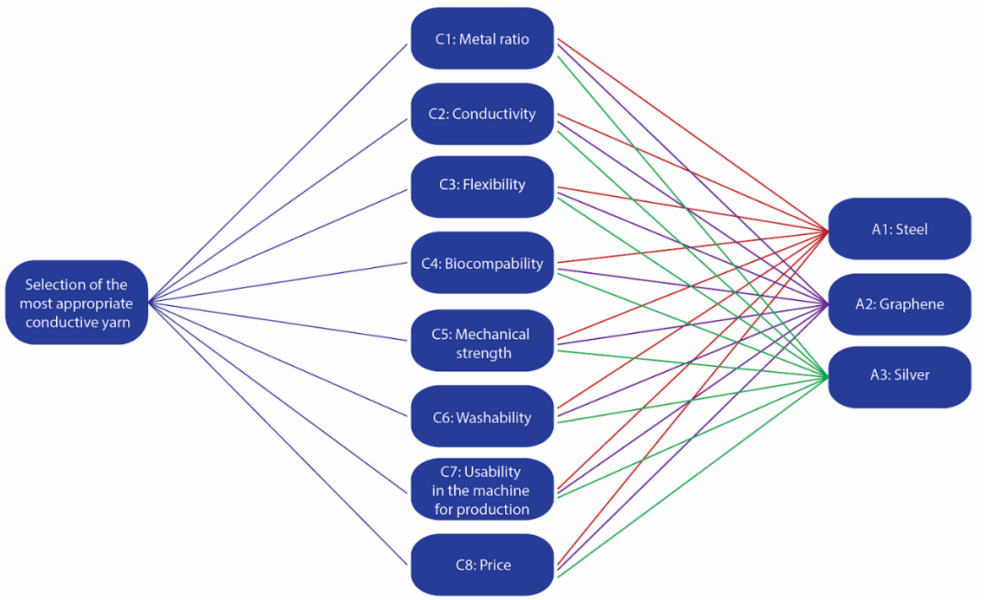

Figure 2. Hierarchical structure of appropriate conductive yarn selection problem

After constructing the hierarchical structure (Figure 2), a questionnaire was conducted to evaluate the alternatives according to the criteria. The questionnaire was applied online to 7 experts who were effective in their conductive yarn purchasing decisions. Using the data collected through questionnaires, a binary comparison matrix (A) containing the geometric mean of the judgments of 7 people was formed (Table 4).

Table 4. Binary comparison matrix (A)

	C1	C2	C3	C4	C5	C6	C7	C8
C1	1	0.11	0.8	0.47	1	2.05	0.12	0.98
C2	9	1	3.63	2.42	1.25	6.71	0.53	4.61
C3	1.25	0.28	1	0.3	1.26	3.39	0.6	2.62
C4	2.12	0.41	3.32	1	1.07	2.82	0.49	4
C5	1	0.8	0.79	0.93	1	4.11	0.75	2.12
C6	0.49	0.15	0.3	0.35	0.24	1	0.13	0.28
C7	8.16	1.89	1.67	2.04	1.33	7.5	1	3.42
C8	1.02	0.22	0.38	0.25	0.47	3.63	0.29	1
Total	24.04	4.86	11.89	7.76	7.62	31.21	3.91	19.03

The values in the binary comparison matrix indicate the importance of row elements relative to column elements. Using the formula (2), B column vectors were obtained. Then, these column vectors were placed side by side to form a normalization matrix (C) (Table 5).

Table 5. Binary comparison matrix (A)

	C1	C2	C3	C4	C5	C6	C7	C8	W
C1	0.0416	0.0226	0.0673	0.0606	0.1312	0.0657	0.0307	0.0515	0.0589
C2	0.3744	0.2058	0.3053	0.3119	0.1640	0.2150	0.1355	0.2422	0.2443
C3	0.0520	0.0576	0.0841	0.0387	0.1654	0.1086	0.1535	0.1377	0.0997
C4	0.0882	0.0844	0.2792	0.1289	0.1404	0.0904	0.1253	0.2102	0.1434
C5	0.0416	0.1646	0.0664	0.1198	0.1312	0.1317	0.1918	0.1114	0.1198
C6	0.0204	0.0309	0.0252	0.0451	0.0315	0.0320	0.0332	0.0147	0.0291
C7	0.3394	0.3889	0.1405	0.2629	0.1745	0.2403	0.2558	0.1797	0.2477
C8	0.0424	0.0453	0.0320	0.0322	0.0617	0.1163	0.0742	0.0525	0.0571
Column vectors	B_1	B_2	B_3	B_4	B_5	B_6	B_7	B_8	

The priority vector (W), which is seen in Table 5, was generated by calculating the arithmetic mean of the row elements of the normalization matrix (C). The priority vector (W) shows the importance weights of the criteria.

After this stage, it is necessary to test the consistency. For this purpose, firstly, the column vector D was generated using formula (6). A new column vector containing the fundamental values (E) for each evaluation factor was obtained by the formula (7). Afterwards, λmax was calculated using formula (8). The consistency index (CI) was calculated by substituting λmax in formula (5). Finally, the consistency ratio (CR) was calculated using the random consistency index (RI)=1.41, which corresponds to n=8 in the random consistency table, and the consistency index (CI) was calculated by means of formula (4) (Table 6).

Table 6. Consistency calculations

D	W	E
0.4981	0.0589	8.4562
2.2229	0.2443	9.0989
0.8326	0.0997	8.3507
1.2595	0.1434	8.7828
1.0127	0.1198	8.4532
0.2516	0.0291	8.6477
2.222	0.2477	8.9703
0.4784	0.0571	8.3788
	λ_{max}	8.6423
	CI	0.0918
	CR	0.0651

The consistency ratio (CR) should be less than 0.1 for the test result to be consistent. In this study, the consistency ratio (CR) is calculated as 0.0651, and it can be said that our test result is consistent. As the test result is consistent, the priority vector W, which shows the importance weights of the appropriate conductive yarn selection problem criteria given in Table 5, can be used to solve the problem. Binary comparison matrices were established by comparing alternatives for each criterion. The 8 matrices obtained were normalized. Then, their consistency was tested by calculating the priority vectors (Si), λmax, CI, and CR values of these matrices. The results of these calculations can be seen in Table 7.

Table 7. Priority vectors and consistency ratios of alternatives for each criteria

C1	S1	D	E	λ_{max}	CI	CR
	0.1062	0.3197	3.0112	3.0387	0.0194	0.0334
	0.6333	1.9456	3.072			
	0.2605	0.7901	3.033			
C2	S2	D	E	λ_{max}	CI	CR
	0.0567	0.1709	3.0119	3.0813	0.0407	0.0701
	0.6486	2.0432	3.1501			
	0.2946	0.908	3.0819			
C3	S3	D	E	λ_{max}	CI	CR
	0.0567	0.1709	3.0119	3.0813	0.0407	0.0701
	0.6486	2.0432	3.1501			
	0.2946	0.908	3.0819			
C4	S4	D	E	λ_{max}	CI	CR
	0.0667	0.2001	3.0002	3.0002	0.0001	0.0002
	0.4667	1.4001	3.0002			
	0.4667	1.4001	3.0002			
C5	S5	D	E	λ_{max}	CI	CR
	0.1062	0.3196	3.0111	3.0387	0.0193	0.0333
	0.6334	1.9456	3.0719			
	0.2605	0.7901	3.0329			
C6	S6	D	E	λ_{max}	CI	CR
	0.0664	0.1998	3.0101	3.0542	0.0271	0.0467
	0.5706	1.7613	3.0869			
	0.3631	1.1129	3.0654			
C7	S7	D	E	λ_{max}	CI	CR
	0.0567	0.1709	3.0119	3.0813	0.0407	0.0701
	0.6486	2.0432	3.1501			
	0.2946	0.908	3.0819			
C8	S8	D	E	λ_{max}	CI	CR
	0.6334	1.9456	3.0719	3.0387	0.0193	0.0333
	0.2605	0.7901	3.0329			
	0.1062	0.3196	3.0111			

As seen in the table above, all matrices are consistent (CR < 0.1). As the AHP analysis results are consistent, Si priority vectors showing the importance weights of the appropriate conductive yarn selection problem criteria given in Table 6 can be used to solve the problem.

Priority vectors in Table 6 were combined side by side to form a decision matrix (K) which

shows the priority weights of alternatives for each criterion (Table 8).

Table 8. Decision matrix (K)

Criteria weights (Wi)	0.0589	0.2443	0.0997	0.1434	0.1198	0.0291	0.2477	0.0571
	C1	**C2**	**C3**	**C4**	**C5**	**C6**	**C7**	**C8**
A1	0.1062	0.0567	0.0567	0.0667	0.1062	0.0664	0.0567	0.6334
A2	0.6333	0.6486	0.6486	0.4667	0.6334	0.5706	0.6486	0.2605
A3	0.2605	0.2946	0.2946	0.4667	0.2605	0.3631	0.2946	0.1062

Finally, the ultimate priority vectors were calculated. The formula (9) is used in this calculation.

Table 9. Ultimate priority vector (L) of the alternatives and ranking results

	Ultimate Priority Vector of the Alternatives	**Ranking**
A1	0.1002	3
A2	0.5954	1
A3	0.3044	2

The results in the ultimate priority vector (L) in Table 9 are listed in descending order. As a result of the ranking, the alternative with the biggest value, A2 (Graphene), is the best alternative.

4. Conclusion and Suggestions

In this study, a questionnaire consisting of two parts, which collect general information online and evaluate the conductive yarns they received, was conducted to the experts who are effective in purchasing the conductive yarns of the factories producing textile products.

The matrices obtained from the forms filled out by the experts were evaluated with the help of the AHP method, priority vectors were determined, and the alternatives were listed according to their importance weight. Therefore, it has been determined that graphene yarn is the most appropriate yarn for a textile factory among the alternatives according to the specified criteria.

Graphene is a material that stands out with its high conductivity and flexibility. Graphene yarns can be produced in large quantities, and they are washable, inexpensive, and soluble in nature. Also, graphene is a material that is highly sensitive to changes in the environment, as each atom is in contact with its environment. When the AHP analysis results are taken into consideration in light of this information, it is concluded that graphene is a good choice in many aspects of the production of electronic textiles and wearable products.

Contributions of the authors

All authors have contributed equally.

Conflict of Interest Statement

There is no conflict of interest between the authors.

Statement of Research and Publication Ethics

The study is complied with research and publication ethics.

References

[1] G. Yetmen, Giyilebilir teknoloji, *Ulakbilge*.Vol.5, no.9, pp.275-289, 2017.

[2] Y. Gao, H. Li, and Y. Luo, An empirical study of wearable technology acceptance in healthcare, *Industrial Management & Data Systems*, Vol.115, pp.1074-1723, 2015.

[3] S. Wagner, E. Bonderover, W. B. Jordan, and J. C. Sturm, Electrotextiles: concepts and challenges, *International Journal of High Speed Electronic Systems*, Vol.12, pp. 391-399, 2002.

[4] E. Ethridge, *Electrotextiles-technology to applications, Proc. of the Materials Research Society Conference Symposium, Boston, ABD*, 2002, pp. 1-10.

[5] M. S. Çetin, and D. Erdem, İletken iplik alımında etkili kriterler arasındaki ilişkilerin DEMATEL yöntemi ile belirlenmesi, *Avrupa Bilim ve Teknoloji Dergisi*, Vol.17, pp.152-160, 2019.

[6] Y. Çelikbilek, *Çok Kriterli Karar Verme Yöntemleri-Açıklamalı ve Karşılaştırmalı Sağlık Bilimleri Uygulamaları ile*, Nobel Akademik Yayıncılık Eğitim Danışmanlık Tic. Ltd. Şti., Ankara, 2018, pp. 43-51.

[7] M. Velasquez, and P. T. Hester, An analysis of multi-criteria decision making methods, *International Journal of Operations Research*, Vol.10, pp. 56-66, 2013.

[8] N. G. Akın, İşletme Bölümü Öğrencilerinin Meslek Seçimini Etkileyen Faktörlerin Bulanık Dematel yöntemi ile Değerlendirilmesi. *Uluslararası Yönetim İktisat ve İşletme Dergisi,* Vol. 13(4), pp. 873-890, 2017.

[9] B. Paçacı, S. Erol ve K. Çubuk , AHP Application for Logistics Center Location Selection According to Criteria, *Bitlis Eren Üniversitesi Fen Bilimleri Dergisi*, Vol. 11, no. 4, pp. 943-952, 2022.

[10] R. W. Saaty, The analytic hierarchy process—what it is and how it is used, *Mathematical Modelling*, Vol. 9, pp. 161-176, 1987.

[11]. B. L. Golden, E. A. Wasil, and P. T. Harker, *The Analytic Hierarchy Process. Applications and Studies*, Springer, Berlin, 1989, pp. 37-58.

[12] A. Ishizaka, and P. Nemery, *Multi-Criteria Decision Analysis Methods and Software*, Wiley & Sons, Ltd., West Sussex, 2013, pp. 13-50.

[13] A. Abdulvahitoğlu, *Yeni ürün tasarımında Triz ve Ahp ile en uygun kararın verilmesi*, Master Thesis (Çukurova University, Adana, 2012).

[14] E. G. Türkmen, İ. Güngör, and F. Erinci, Öğretmenlerin tayin yeri seçiminde analitik hiyerarşi proses uygulaması, *Uluslararası Alanya İşletme Fakültesi Dergisi*, Vol.7, pp. 35-49, 2015.

[15] T. L. Saaty, How to make a decision: the analytic hierarchy process, *European Journal of Operational Research*, Vol. 48, pp. 9-26, 1990.

[16] D. A. Regier, and S. Peacock, *Multi-Criteria Decision Analysis to Support Healthcare Decisions*, eds. K. Marsh, M. Goetghbeur, P. Thokala, and R. Baltussen, Springer, Berlin, 2017, pp.19-21.

[17] T. L. Saaty, Axiomatic foundation of the analytic hierarchy process, *Management Science*, Vol. 32, pp. 841-855, 1986.

[18] Ö. F. Ünal, Performans değerlemede analitik hiyerarşi prosesi (AHP) uygulamaları, *Sosyal Bilimler Araştırmaları Dergisi,* Vol. 7, pp. 37-55, 2012.

[19] E. İmren, *Mobilya endüstrisinde analitik hiyerarşi prosesi (AHP) yöntemi ile kuruluş yeri seçimi*, Master Thesis (Bartın University, Bartın, 2011).

[20] G. Kecek, and A. G. E. Yıldırım, Kurumsal kaynak planlama (ERP) sisteminin analitik hiyerarşi süreci (AHP) ile seçimi: otomotiv sektöründe bir uygulama, *Suleyman Demirel University Journal of Faculty of Economics & Administrative Sciences*, Vol. 15, pp. 193-211, 2010.

[21] E. G. Kadak, *Türkiye'de AHP tekniğinin performans değerlendirmedeki yeri ve ilaç dağıtım sektöründe uygulanması*, Master Thesis (Çukurova University, Adana, 2006).

[22] E. Ç. Turgut, *Tedarik zinciri yönetiminde AHP ve bulanık AHP yöntemi kullanılarak tedarikçilerin performansının ölçülmesi, yeni yöntem önerileri ve uygulamaları*, Ph.D. Thesis (Dokuz Eylül University, İzmir, 2015).

[23] T. Eren, M. Hamurcu, and N. İ. Süt, Analitik hiyerarşi süreci kullanılarak ankara-sivas yüksek hızlı tren hat güzergahının değerlendirilmesi, *Harran Üniversitesi Mühendislik Dergisi*, Vol.3, pp. 22-30, 2018.

[24] N. Karakaşoğlu, *Bulanık çok kriterli karar verme yöntemleri ve uygulama*, Master Thesis (Pamukkale University, Denizli, 2008).

Bitlis Eren Üniversitesi Fen Bilimleri Dergisi
BİTLİS EREN UNIVERSITY JOURNAL OF SCIENCE
ISSN: 2147-3129/e-ISSN: 2147-3188
VOLUME: 12 NO: 4 PAGE: 1128-1138 YEAR: 2023
DOI:10.17798/bitlisfen.1343747

Digital Certificate Security: A Blockchain-based Approach for Fraud Prevention and Verification

Nihat ZAMAN[1], Işıl KARABEY AKSAKALLI[1], Nursena BAYĞIN[1*]

[1]*Department of Computer Engineering, Erzurum Technical University, 25000 Erzurum, Türkiye (ORCID: 0009-0001-6061-1482) (ORCID: 0000-0002-4156-9098) (ORCID: 0000-0003-4457-5503)*

Keywords: Blockchain, Digital Certificate, NFT, Smart Contract.

Abstract

With the rise of digitalization and increased internet usage, digital certificates' security issues have gained significant importance. The utilization of counterfeit certificates can lead to deceptive identity and capability verifications, allowing untrustworthy individuals to assume misleading positions. Simultaneously, factors such as data leaks and technical glitches can jeopardize the security of certificates. These challenges can complicate talent verification processes and result in unsuitable individuals being placed in incorrect roles. The proposed work aims to thwart forged certificates and ensure their verifiability within this context. The methodology employed in the study strives to mitigate potential data loss or accessibility problems by adopting a decentralized storage structure. The primary objective is to establish certificates that are reliable, traceable, and capable of being verified. A rapid and efficient user interface was developed using React.js to achieve this aim. Smart contracts were scripted on the Ethereum blockchain using Solidity, and data, including user information and certificate details, were stored within components like MongoDB. In the phase of practical implementation, diverse scenarios have been designed to facilitate the generation, verification, and monitoring of certificates. The proposed approach is geared towards deterring forgery and enhancing the credibility of certificates. Through this system, users and organizations can authenticate certificates and prevent the proliferation of counterfeit ones. Furthermore, the enhanced security and ease of sharing certificates on digital platforms offer substantial advantages to certificate holders. In summary, this study strives to enhance the safeguarding and dependability of certificates by addressing the security concerns posed by the era of digitalization.

1. Introduction

The initial utilization of blockchain technology commenced with Bitcoin. Bitcoin, the pioneering blockchain, was introduced in 2008 by an anonymous individual or group using the pseudonym Satoshi Nakamoto [1]. Nakamoto delineated Bitcoin as a "P2P electronic cash system." The published paper on Bitcoin highlights four fundamental attributes: traceability of transactions accessible to all, execution of immutable and secure transactions, peer-to-peer (P2P) transactions, and decentralized management [2].

With the emergence of Bitcoin and the acknowledgment of cryptocurrency, the concept of blockchain has garnered broader recognition. Subsequent to Bitcoin, another blockchain known as Ethereum was developed. Ethereum is conceived as a platform that fosters applications and smart contracts on the blockchain, alongside its own native cryptocurrency. This expansion has led to the utilization of blockchain in various domains beyond cryptocurrencies. Presently, blockchain finds extensive application, particularly in systems necessitating enhanced security. Furthermore, blockchain technology is intricately linked with

*Corresponding author: nursena.baygin@erzurum.edu.tr
Received: 15.08.2023, Accepted: 31.10.2023

various domains, including but not limited to personal asset registration, document archival, survey or election processes, the financial industry, payment transactions, fund transfers, trading platforms, exchange administration, authorization, validation, digital identity oversight, and document control [3-5]. In recent years, alongside established blockchains like Ethereum and Bitcoin, numerous novel blockchains and cryptocurrencies have emerged. Consequently, the number of individuals engaging with blockchains continues to grow. The user count, which stood at 106 million in 2020, surpassed 295 million in 2021. Based on projections, this figure is anticipated to exceed 1 billion by the conclusion of 2022 [6].

Web 2.0 is the collective term for a version of the internet that is familiar to many people today. The primary objective of Web 2.0 companies is to deliver services to users by converting the vast amount of user-generated big data into meaningful insights. On the contrary, Web 3.0 represents an evolution of Web 2.0 applications onto the blockchain, an architecture that places a significant emphasis on decentralized personal data and individual privacy, without any form of monopoly. Recent incidents of user data breaches have heightened interest in the features offered by Web 3.0. One of the Web 3.0 tools developed on the Ethereum platform is non-fungible tokens (NFT). NFTs play a crucial role in decentralizing the network, with a primary focus on establishing ownership rights. For instance, early adopters of an emerging network may be granted an NFT that serves as evidence of their initial use of the network. However, since NFTs are transferable, the holder has the option to transfer it even to individuals who have never used it. The introduction of NFTs enables a reliable determination of ownership and affiliation on the blockchain [7-9]. In this context, some studies in the literature are summarized in Table 1.

Table 1. NFT based certification studies in literature

Author(s)	Year	Objective	Contributions	Limitations
Alnuaimi et al. [10]	2022	Securing precious stones digitally	Digital certification of NFT-based jewelry and precious stones provides proof of information such as proof of ownership, sales history, bidding and quality	Since the proposed system is a decentralized application, it creates additional overhead. Latency, which is a general characteristic of the Ethereum network, was encountered
Murugavel et al. [11]	2023	Reducing the use of forged certificates using Polygon blockchain and NFT	Certificate printing is provided on a single platform. Additionally, the costs of transactions have been reduced by using Polygon	The application requires a central administration to obtain certificates from all organizations. This is against the logic of blockchain
Tahlil et al. [12]	2022	Developing an attack-resistant certificate application by preventing identity fraud in education	An NFT-based certificate security, transcript verification, self-sovereign (SSI) prototype has been developed	NFT may cause undesirable consequences as a result of its ability to transfer ownership to those who do not have a certificate
Nikolic et al. [13]	2022	Creating a blockchain-based digital certificate school management system and keeping information about certificates and participants and events	The certificates were stored in the Polygon Supernets blockchain and given to students in the form of NFT	NFT transfer is an important problem and it has been emphasized that it will be overcome with Soulbound tokens
Allwinnaldo et al. [14]	2023	Ensuring the security of digital certificates indicating the authenticity of exotic fish	It is aimed to prevent fraud in the exotic fish industry by producing NFT-based certificates. A cost-effective and efficient system is offered to users.	While blockchain provides security, it has given additional system costs to all nodes.

In this proposed study, our goal is to develop a system that integrates blockchain technology and NFTs to monitor and validate certificate ownership within a digital setting, all the while maintaining the security of these certificates. The system addresses the need for transparency and security by harnessing the advantages of blockchain technology. This approach aims to tackle the challenge of ensuring global certificate security and verifiability through the utilization of blockchain's transferable intellectual property capabilities. The research gaps observed as a result of the literature reviews are as follows:

- Certificate issuance and control mechanisms at the global level are inadequate. In addition, the security of existing certificates is uncertain.
- There are significant problems in certificate verification and recognition across countries and regions. The establishment of a blockchain-based certificate verification mechanism has the potential to contribute to the development of international cooperation and standards.
- One of the most important problems globally is the issuance and dissemination of counterfeit certificates. With certificates that can be verified from a single point, it is quite possible to prevent these situations.

In this context the following provides a concise overview of the key contributions and motivations behind our proposed approach.

- The aim is to utilize the blockchain to store certificates containing non-transferable qualified intellectual property.
- The objective is to authenticate users' and institutions' identities and link the resulting certificates to users' blockchain wallets.
- By creating a unified system, institutions can securely access individuals' NFT certificates and diplomas, effectively preventing the circulation of counterfeit credentials.
- The goal is to evaluate the existing paper diploma storage and verification methods and improve their effectiveness by transitioning to a blockchain-based environment.
- The systems and tools utilized by counterfeit certificate producers should be analyzed, necessary precautions should be implemented, and these vulnerabilities should be eradicated.
- The aim is to amass user certificates within a decentralized framework and integrate institutions, organizations, and users worldwide into this system.

The rest of this manuscript is organized in a subsequent manner: Section 2 delves into an exhaustive examination of the scholarly literature concerning blockchain and NFT, the pivotal technological components underpinning the scope of this pertinent study. Section 3 outlines the proposed methodology and includes visual depictions of the implementation. Section 4 furnishes the outcomes attained through the proposed approach.

2. Technical Component

With the integration of blockchain technology into our daily lives, numerous distinct and novel terms have arisen. This section elucidates the definitions of blockchain terminology and qualified intellectual property terms to enhance comprehension of the study.

2.1. Terminology of Blockchain

The notion of blockchain surfaced subsequent to the release of the Bitcoin paper. In Bitcoin [2], Satoshi Nakamoto opted for the term "proof-of-work chain" instead of blockchain. The terminologies associated with blockchain, including many others, were initially explored in the Ethereum White Paper. This section offers a comprehensive outline of blockchain terminology.

2.1.1. Block Description and Transaction Approval

A block is a segment that contains portions of data from valid transactions conducted on the chain. Within a block:

- Once the block is mined
- The blockchain's length in blocks
- Minimum gas fee needed to include the transaction in the block
- Effort needed to remove the block
- Distinct identifier for the block
- Distinct identifier of the preceding block
- Transactions encompassed within the block
- A password demonstrating the block's successful completion of the proof of stake [3, 15, 16].

Blockchain technology derives its name from its function of storing verified transaction records in blocks. A blockchain is basically composed of two key elements: validators and users. As shown in Figure 1, a user requests a transaction to the blockchain. The transaction is

broadcast and, if verified, is added to the ledger by validation nodes. Once validated, the block is sent to validators for authorization. The first validator to authorize the transaction gets the right to create the corresponding block. When the block is subsequently validated by other validators, the transaction is recorded in a block within the blockchain and added to the chain.

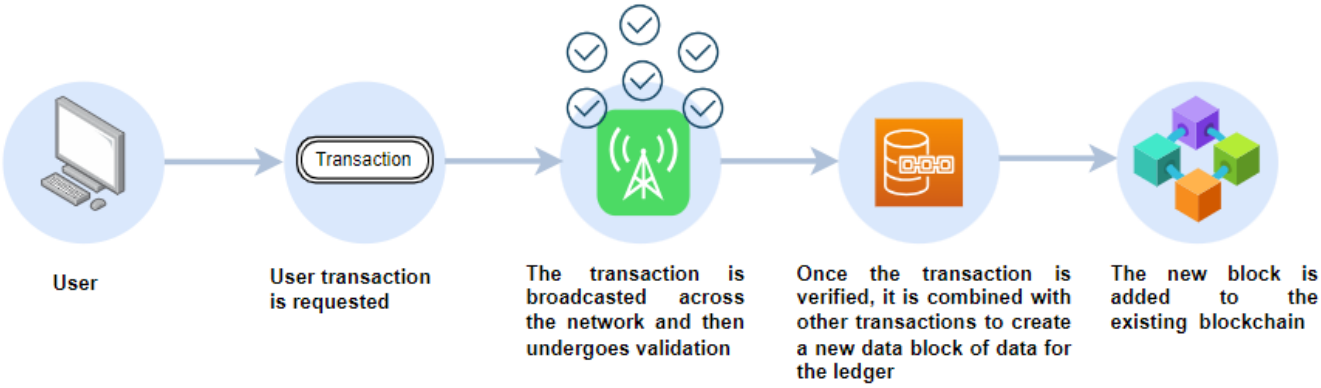

Figure 1. The working principle of blockchain

2.1.2. Address and Transaction

An "address" is a publicly accessible combination of alphanumeric characters enabling communication between blockchain users and smart contracts [17]. A "transaction" constitutes a fundamental element within the blockchain framework, denoting transfers or actions occurring within the chain [18].

2.1.3. Ledger

A ledger represents a heightened level of secure transfer, transitioning traditional accounting ledgers into the blockchain realm. This ledger serves as the repository for recording network transactions, rendering any alteration or deletion of ledger transactions impossible; a pivotal facet emblematic of blockchain technology [17, 19].

2.1.3. Smart Contract

Smart contracts are decentralized applications that execute automated transactions based on data and functions within the blockchain, following regulations defined by the contract's creators [17, 20].

2.2. Key Features of Blockchain

In the Bitcoin article authored by Satoshi Nakamoto, the foundational principles of the blockchain on which Bitcoin is constructed were elucidated [2]. These principles are outlined as follows:

2.2.1. Decentralized

In contrast to the conventional monetary system, where transactions frequently require endorsement from regulatory entities such as governments and financial institutions, blockchain technology introduces a distinct paradigm. Transactions executed on the blockchain solely necessitate validation from the involved users. This approach guarantees the security and resilience of blockchain transactions against external interventions [21]. Unlike conventional systems, blockchain operates without centralized authority, upholding data across a distributed network.

2.2.2. Transparency and Traceability

In conventional systems, authorities and diverse institutions exclusively retain the ability to audit all transactions, yet blockchain diverges from this norm. Each transaction conducted within the blockchain framework is archived in a ledger that remains both traceable and immutable to all [21]. This fosters an environment wherein all participants gain visibility into and real-time monitoring of their transaction history.

2.2.3. Immutability

Each transaction executed within the blockchain is meticulously documented through a mechanism known as a ledger. Subsequently, this ledger is employed to incorporate these transactions into blocks. The incorporated transactions become indelibly ensconced within the blockchain, impervious to any form of alteration or reversal.

This characteristic not only substantiates the dependability of blockchain transactions but also safeguards an incontrovertible chronicle of the conducted transactions [21, 22].

2.2.4. Anonymity

In centralized systems, individuals are required to divulge their personal data for the execution of transactions. In contrast, blockchain technology operates differently, as transactions within the network do not necessitate authentication [21, 23].

2.3. NFT

NFTs (Non-Fungible Tokens) are a category of cryptocurrencies that originate from Ethereum smart contracts. They were initially introduced in Ethereum Improvement Proposals (EIP)-721 and subsequently refined in EIP-1155. NFTs distinguish themselves from conventional cryptocurrencies like Bitcoin, which are considered fungible, with all units being identical. In contrast, NFTs possess unique characteristics and are immutable, enabling them to represent distinct digital assets [24]. Due to their creation on a decentralized blockchain, NFT authenticity can only be reliably verified within decentralized applications. This circumstance has led to the emergence of counterfeit NFTs sharing the same name and image, potentially deceiving individuals. NFTs are generated through smart contracts, which are integrated into the blockchain for public interaction. However, security vulnerabilities within the code of a smart contract can jeopardize the integrity of NFTs and the wallets of their holders. A viable solution to mitigate this risk is to subject the smart contract to cybersecurity assessments. Regrettably, this solution incurs substantial costs that many NFT projects and creators choose to evade, thereby compromising user security.

3. Proposed Method

This paper presents the development of a certification and verification system utilizing non-transferable tokens (NTT) on the blockchain. The previously introduced theoretical concept is realized through real-time implementation in this study [25]. Within the framework of this research, an examination of trends in the realm of NFT (Non-Fungible Token) and NTT is conducted, accompanied by a comprehensive review of related technological efforts. Analyses are conducted to comprehend the challenges associated with counterfeit certificate creation and the predicaments faced by victims of such fraudulent certificates. Concurrently, the foundational principles for our decentralized system are established.

The purpose of this system is to safeguard stored data, counteract counterfeit diplomas and certificates, and ensure the security of companies and institutions involved in the certification process. Operating on the Ethereum platform, this system employs the ERC-721 [5] non-fungible token standard for the creation of certificates. Both certificate issuers and recipients are mandated to verify their personal or organizational identities in adherence to legal obligations. This proposed methodology effectively curbs the proliferation of fake certificates and diplomas, as individuals and entities undergo the authentication process.

As can be seen in Figure 2, within the proposed methodology, a smart contract is generated by the organization, laying out the requisite conditions. Subsequently, users slated to obtain certificates are attributed with unique identities. Upon successful completion of their respective examinations, certificates are formulated and endorsed by the organization. Ultimately, certificates are dispensed to duly eligible users.

The following steps were performed in the proposed study:

- A comprehensive analysis of fundamental state functions and ongoing trends within the blockchain domain has been conducted.
- The advantages exploited by malevolent actors engaged in the production of counterfeit certificates/diplomas, as well as the challenges confronted by individuals and organizations falling victim to fraudulent credentials, have been thoroughly examined.
- The architecture, design concepts, and algorithmic structure intended for the creation of the decentralized website within this study have been determined.
- Appropriate methodologies have been formulated to facilitate the effective utilization of the blockchain environment by institutions/organizations and individuals.
- Strategic measures to ensure the global availability and accessibility of the developed system have been meticulously calculated.

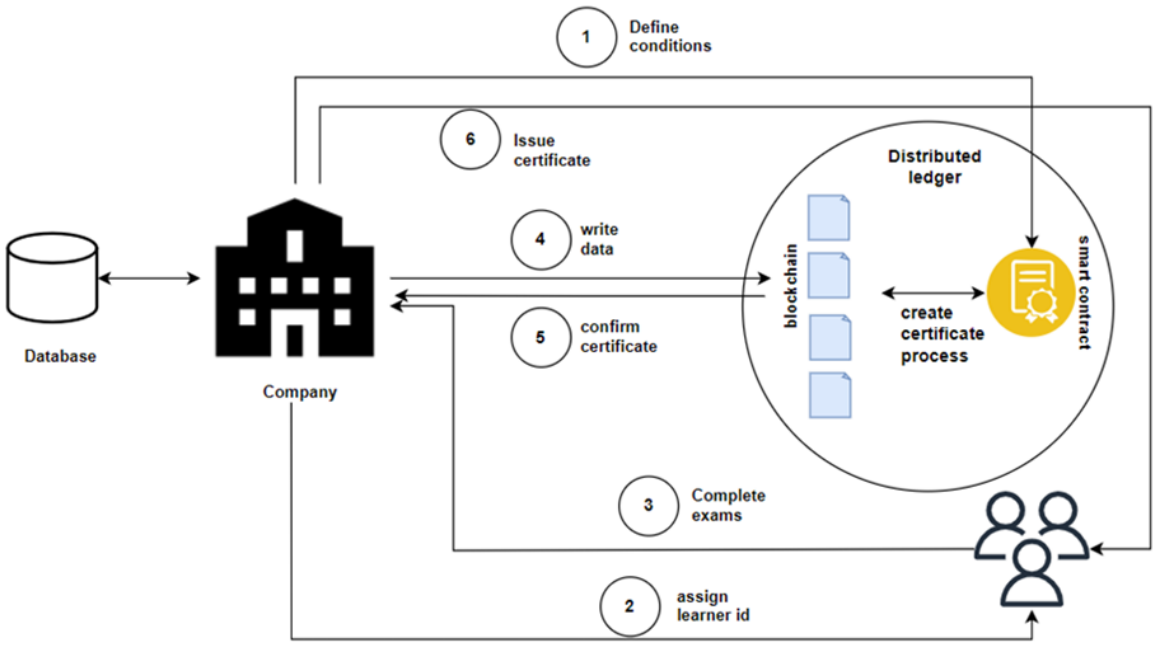

Figure 2. Diagram of the proposed method

The details of the proposed method are given below under subheadings.

3.1. Back-end of the Application

In this research, a novel blockchain-based solution is presented for digital certificate security. The main objective of the proposed model is fraud prevention and certificate verification processes for this purpose. The first phase of this blockchain-based model is the realization of the back-end component. The back-end component of the model developed to ensure digital certificate security basically consists of 4 main parts. These are certificate generation, certificate verification, certificate monitoring and main program respectively. At this point, a pseudocode for the certificate generation phase is given in Algorithm 1.

Algorithm 1. Create Certificate Function

Input: User Information and Certificate Details. **Output:** Blockchain Transaction ID.
1: COMBINE the user information and certificate details into a single certificate structure. 2: ADD a timestamp to the certificate to mark the current time. 3: SAVE the certificate onto the blockchain. 4: RECORD the transaction made on the blockchain when saving the certificate. 5: RETURN the recorded transaction ID.

As can be seen from Algorithm 1, the system takes user information and certificate details as input parameters. After that, the certificate is created using the user information, certificate details (content, etc.) and the current time stamp information. The generated certificate is registered to the blockchain and the transaction id information received after the registration process is completed is returned. The second phase of the model is certificate verification. This process is given in Algorithm 2.

Algorithm 2. Certificate Verification

Input: Certificate and Issuer Public Key. **Output:** Valid or Non-Valid.
1: // Verify the authenticity of the certificate using the issuer's public key. 2: IF Blockchain.VerifySignature(certificate, issuerPublicKey) is true 3: RETURN "Certificate is valid" 4: ELSE 5: RETURN "Certificate is not valid" 6: END IF

As given in Algorithm-2, the certificate verification function takes the certificate information and the issuer's public key as input parameters. Afterwards, the signature verification process is performed and the result of this process returns the certificate's validation/non-validation status. The third phase of the application is certificate monitoring, the pseudocode for which is given in Algorithm 3.

Algorithm 3. Certificate Monitoring

Input: All Certificate. **Output:** Monitoring Action.
1: // Retrieve and monitor certificates stored on the blockchain. 2: certificates = Blockchain.GetCertificates() 3: // Iterate through the list of certificates 4: FOR EACH certificate IN certificates 5: // Perform monitoring actions, if needed 6: END FOR

As shown in Algorithm 3, certificate monitoring involves reading all certificates in the network and traversing them through a loop. During the traversal, if necessary, the required operations are performed on the certificate. The section where the model is tested is the main function. A sample pseudocode covering a sample certificate generation and submission/verification to the network is given in Algorithm 4.

Algorithm 4. Main Function

Input: User Information, Certificate Detail and Issuer Public Key. **Output:** Storage Approval.
1: userInformation = {name: "Test Test", email: "testtest@test.com"}. 2: certificateDetails = {type: "Professional Certification", issuer: "Organization Test"} 3: issuerPublicKey = "0xissuerPublicKey1234" 4: // Create a certificate using user information and certificate details 5:certificateTransaction= CreateCertificate(userInformation, certificateDetails) 6: // Verify the certificate's authenticity using the issuer's public key 7:verificationResult= VerifyCertificate(certificateTransaction, issuerPublicKey) 8: // Check the verification result and print a corresponding message 9: IF verificationResult equals "Certificate is valid" 10: THEN 11: PRINT "Certificate is valid and has been stored on the blockchain." 12: ELSE 13: PRINT "Certificate is not valid or has not been stored correctly." 14: END IF

Algorithm 4 basically illustrates a certificate generation and verification activity. As mentioned at the beginning of this section, the back-end of the blockchain application consists of four phases. These phases are given in Algorithms 1, 2, 3 and 4 respectively.

3.2. Front- end of the Application

In this section, we detail the technologies used for the front end of the proposed method, its components, and the implemented design.

3.2.1. Front-end Components

The proposed method requires a powerful front end to facilitate user interaction and visualize data effectively. For this purpose, the React.js library was utilized for front-end development. React.js offers a component-based approach to building user interfaces (UI). This makes the code reusable and easier to manage. Each component has its own state and logic, and when the state of a component in the UI changes, React.js automatically redraws that component.

The front end is structured using a component hierarchy, which follows a modular arrangement. This approach enables primary components to be composed of various sub-components. This hierarchical structure facilitates the independent and isolated functioning of components, contributing to better code manageability and reduced potential for errors. The design and styling aspects are handled using the Tailwind CSS library, which offers extensive design customization and rapid prototyping capabilities. Additionally, the Axios library is employed for facilitating data exchange between the front end and back end. Axios serves as a tool for managing HTTP requests and establishing effective communication with the server side. API requests are utilized for data retrieval, creation, updating, and deletion purposes. Through this integrated framework, the proposed methodology operates efficiently and in an organized manner.

3.2.2. User Interface

The user interface has been meticulously crafted to facilitate the seamless creation and validation of certificates by users. The entire spectrum of user transactions is planned to be overseen through a user-friendly and intuitive interface, ensuring a smooth experience. The interface shown in Figure

3 has been tailored for companies seeking to establish project pages and distribute certificates to applicants. Upon inputting the necessary project details, the application undergoes submission to the administrator for evaluation. Upon successful completion of the application process, the company becomes eligible to dispense certificates. This design approach ensures a comprehensive and user-centric experience within the proposed system.

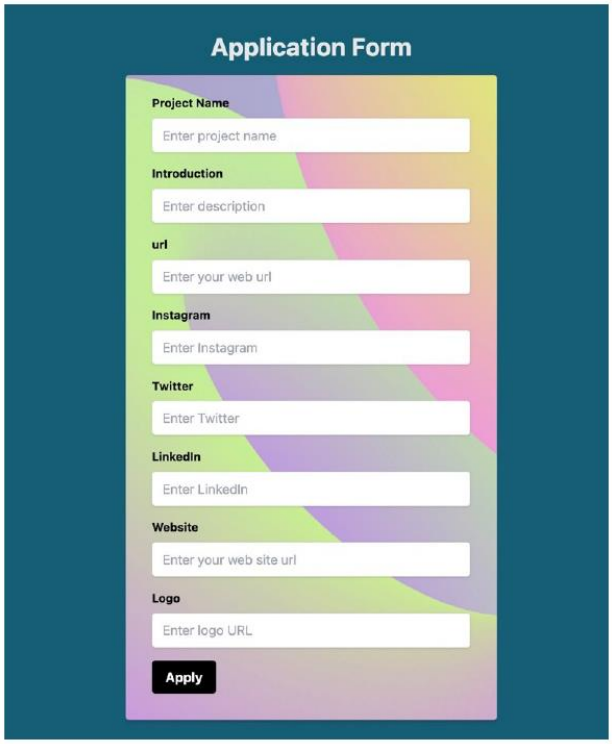

Figure 3. Project creation form

The interface depicted in Figure 4 showcases the roster of active certificate-issuing companies within the platform established in alignment with the proposed methodology. This designated page empowers users to peruse certificates by navigating to the respective project page from which they intend to acquire a certificate. As illustrated in Figure 5, the company page interface provides comprehensive insights into a company's particulars and the array of certificates it has issued. This dynamic interface design augments user accessibility and engagement, bolstering the efficacy of the proposed approach. Figure 6 shows an image of the certificate acquisition page. On this page, users are able to take ownership of the certificate reserved for them.

Figure 4. Active certificate page

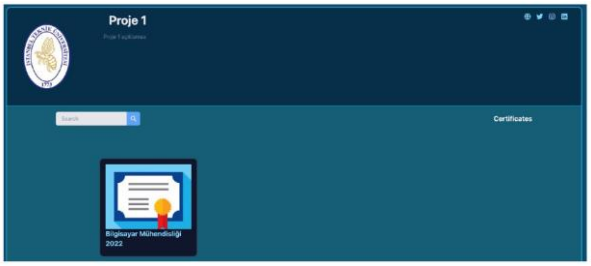

Figure 5. Company page interface design

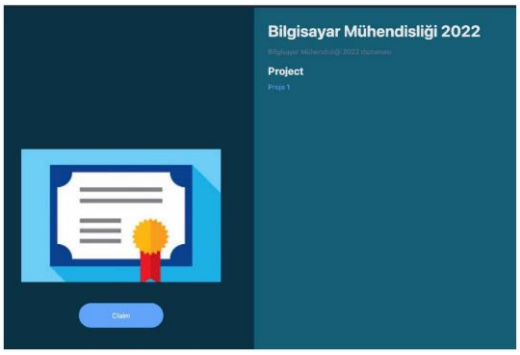

Figure 6. Certification page

3.2.3. Database and Data Management

This section furnishes details concerning the server-side components employed in the suggested approach and the underlying technologies utilized. The server side constitutes a pivotal facet of the proposed methodology, encompassing data processing and the implementation of business logic. Throughout this process, technologies such as Node.js and the Express library are harnessed. Node.js serves as a JavaScript-based environment that facilitates server-side processing, while the Express library functions as a conduit bridging the gap between the front-end and server-side for web applications. Moreover, the API (Application Programming Interface) architecture facilitates seamless data communication between the server and the client.

Database management is one of the most important components of the proposed work. The data needs of the project were met using the MongoDB database. MongoDB is a document-based NoSQL database and offers a flexible data model that suits the requirements of the project. In our data model, separate collections were created

for users, projects, certificates and other related data. Figure 7 shows the tables in the database. These tables contain the assets necessary for the website to fulfill its function.

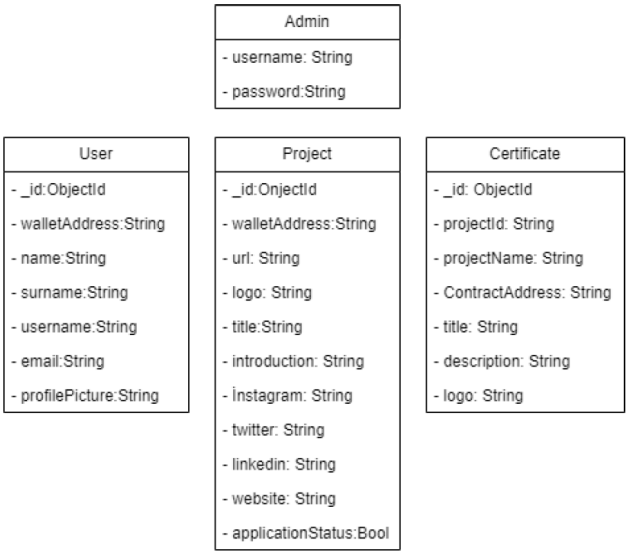

Figure 7. Database table of the proposed method

In this application, a decentralized storage structure is adopted. The reasons for choosing decentralized storage structure instead of centralized storage are given below:

- *Reliability:* In distributed storage systems, data is replicated across multiple nodes. This minimizes the risk of data loss.
- *High Security:* Data is encrypted in the distributed storage structure. In this way, unauthorized access to data is restricted and data integrity is ensured.
- *Scalability:* Distributed storage structure allows more data to be easily added to the system. With this structure, growth requirements can be realized.
- *Compatibility:* The distributed storage approach is compatible with blockchain technologies. This solution increases the security and verifiability of certificates.
- *Low Cost:* Unlike centralized server infrastructures, distributed storage enables effective use of available resources.
- *Continuity:* A problem that may occur in centralized servers can affect the entire system. In the distributed storage approach, independence is provided against possible problems. Because data is copied to many nodes.

3.2.4. Used Packages and Development Tools

Several libraries and packages were employed in the development of the proposed methodology. These libraries played a pivotal role in ensuring an efficient and user-friendly implementation of the proposed approach. Additionally, various development tools were utilized to test and effectively utilize the aforementioned packages and libraries.

Libraries and Packages

ThirdWeb: This package is used to realize the blockchain connection on the website. This package includes structures that facilitate the use of blockchain actions on the website.

Axios: Axios package was used to realize the data communication between the server side and the front end. Axios provides the communication of the tables created on the server side with the front-end thanks to the functions it contains.

React DataTable: React DataTable library is used to create tables and organize data.

React Carousel: React Carousel library was used to create the component with informative visuals on the home page.

4. Conclusion

The proposed methodology aims to mitigate the proliferation of counterfeit certificates and establish a robust verification system. The existence of fraudulent certificates complicates talent verification processes and may lead to the appointment of ill-suited individuals to deceptive positions. The primary objective of this methodology is to address this issue and ensure the trustworthiness, traceability, and verifiability of certificates. To achieve this goal, the methodology is crafted using three core components: React.js for the user interface, Solidity for crafting smart contracts on the Ethereum blockchain, and MongoDB for the storage and management of user data, certificate particulars, and organizational details. Throughout the implementation phase of the approach, diverse usage scenarios were identified for certificate generation, verification, and monitoring. System administrator users possess the ability to assess applications and conduct Know Your Customer (KYC) procedures. Project participants have the capability to create certificates by linking their blockchain wallets to the web platform. Meanwhile, regular users can connect their blockchain wallets to input their

profile data and generate their certificates. The primary aim of the proposed method is to elevate the reliability of certificates and furnish safeguards against fraudulent activities. Thanks to the integration of blockchain technology, every facet of the certificate lifecycle becomes traceable, and smart contracts facilitate the secure creation and verification of certificates. Through this system, both users and organizations can validate certificates, thwarting the proliferation of counterfeit documentation. One potential repercussion of this method is a reduction in the risk of forgery during job applications and talent verification procedures, streamlining the process of recruiting individuals with the requisite skills. Moreover, certificates can be shared and authenticated more seamlessly in digital realms, engendering greater confidence and assurance among certificate holders.

Funding: This research is supported by the 1919B012223104 project fund provided by the Scientific and Technological Research Council of Turkey (TUBITAK).

Ethics: There are no ethical issues after the publication of this manuscript.

References

[1] S. Ghimire and H. Selvaraj, "A survey on bitcoin cryptocurrency and its mining," 2018: *IEEE*, pp. 1-6.
[2] S. Nakamoto, "Bitcoin: A peer-to-peer electronic cash system," *Decentralized business review*, 2008.
[3] A. Gorkhali, L. Li, and A. Shrestha, "Blockchain: A literature review," *Journal of Management Analytics*, vol. 7, no. 3, pp. 321-343, 2020.
[4] A. Kurnaz, "A Review on Usage Areas of Blockchain Technology in Architecture," *International Journal of Scientific and Technological Research*, no, 2021.
[5] M. K. Shrivas and T. Yeboah, "The disruptive blockchain: types, platforms and applications," *Texila International Journal of Academic Research*, vol. 3, pp. 17-39, 2019.
[6] crypto.com. "Crypto Market Sizing Report 2021 and 2022 Forecast." crypto.com. https://crypto.com/research/2021-crypto-market-sizing-report-2022-forecast (accessed 2023).
[7] S. Osivand, "Smart collectibles; use case of NFT tokens," *Open Access Research Journal of Engineering and Technology*, vol. 1, no. 2, pp. 024-031, 2021.
[8] S. M. H. Bamakan, N. Nezhadsistani, O. Bodaghi, and Q. Qu, "A decentralized framework for patents and intellectual property as nft in blockchain networks," 2021.
[9] D. Ghelani, "What is Non-fungible token (NFT)? A short discussion about NFT Terms used in NFT," Authorea Preprints, 2022.
[10] N. Alnuaimi, A. Almemari, M. Madine, K. Salah, H. Al Breiki, and R. Jayaraman, "NFT Certificates and Proof of Delivery for Fine Jewelry and Gemstones," *IEEE Access*, vol. 10, pp. 101263-101275, 2022.
[11] B. Kamaleshwaran, M. Sneha, and S. Kavitha, "Digital Certification–Certification Credential as Non Fungible Token (NFT)," 2023: *IEEE*, pp. 1-7.
[12] T. Tahlil, S. S. Gomasta, and A. B. M. S. Ali, "AlgoCert: Adopt Non-transferable NFT for the Issuance and Verification of Educational Certificates using Algorand Blockchain," 2022: IEEE, pp. 1-8.
[13] S. Nikolić, S. Matić, D. Čapko, S. Vukmirović, and N. Nedić, "Development of a blockchain-based application for digital certificates in education," 2022: *IEEE*, pp. 1-4.
[14] M. R. R. A. Allwinnaldo, R. N. Alief, I. S. Igboanusi, J. M. Lee, and D.-S. Kim, "Advance NFT-Based Digital Certificate for Efficient Exotic Fish Ownership."
[15] W. Gao, W. G. Hatcher, and W. Yu, "A survey of blockchain: Techniques, applications, and challenges," 2018: *IEEE*, pp. 1-11.
[16] J. Zhang, S. Zhong, T. Wang, H.-C. Chao, and J. Wang, "Blockchain-based systems and applications: a survey," *Journal of Internet Technology*, vol. 21, no. 1, pp. 1-14, 2020.
[17] Ö. Özkan, *Kişisel Verilerin Korunması Hukuku Ve Blokzinciri Teknolojisi Raporu*, Türkiye Bilişim Vakfı. İstanbul: Blockcahin Türkiye, 2019.
[18] S. Gupta and M. Sadoghi, "Blockchain transaction processing," arXiv preprint arXiv:2107.11592, 2021.
[19] L. Ismail and H. Materwala, "A review of blockchain architecture and consensus protocols: Use cases, challenges, and solutions," *Symmetry*, vol. 11, no. 10, p. 1198, 2019.

[20] S. Singh, A. S. M. S. Hosen, and B. Yoon, "Blockchain security attacks, challenges, and solutions for the future distributed iot network," *IEEE Access*, vol. 9, pp. 13938-13959, 2021.

[21] Ü. Gökhan and Ç. Uluyol, "Blok zinciri teknolojisi," *Bilişim Teknolojileri Dergisi*, vol. 13, no. 2, pp. 167-175, 2020.

[22] F. Hofmann, S. Wurster, E. Ron, and M. Böhmecke-Schwafert, "The immutability concept of blockchains and benefits of early standardization," in *2017 Kaleidoscope: Challenges for a Data-Driven Society (ITU K)* 2017.

[23] N. Andola, V. K. Yadav, S. Venkatesan, and S. Verma, "Anonymity on blockchain based e-cash protocols—A survey," *Computer Science Review*, vol. 40, p. 100394, 2021.

[24] Q. Wang, R. Li, Q. Wang, and S. Chen, "Non-fungible token (NFT): Overview, evaluation, opportunities and challenges," arXiv preprint arXiv:2105.07447, 2021.

[25] N. Zaman and N. BayĞIn, "Digital Assurance and Traceability of NFT-based Certificates," *İleri Teknolojilerde Çalışmalar Dergisi*, vol. 1, no. 1, pp. 17-25, 2023.

Bitlis Eren Üniversitesi Fen Bilimleri Dergisi
BİTLİS EREN UNIVERSITY JOURNAL OF SCIENCE
ISSN: 2147-3129/e-ISSN: 2147-3188
VOLUME: 12 NO: 4 PAGE: 1139-1149 YEAR: 2023
DOI:10.17798/bitlisfen.1347396

Autonomous Cargo Carrier Robot in GPS Denied Indoor Environment

Hakan ÜÇGÜN[1*], Fatmanur KIRBOĞA[1]

[1]*Bilecik Şeyh Edebali Üniversitesi Mühendislik Fakültesi Bilgisayar Mühendisliği Bölümü, Bilecik, Türkiye*
(ORCID: 0000-0002-9448-0679) (ORCID: 0009-0007-9715-0898)

Keywords: Mobile Robot, Indoor Navigation, Cargo Robot, Compass Sensor, Arduino.

Abstract

The mobile robot industry, which has become a rapidly growing sector, can easily perform many activities or tasks that can be dangerous, laborious or tiring for humans. A mobile robot helps people by performing the desired tasks in areas such as medical, military, household and cargo. Robots, which perform their duties indoor or outdoor environments, use navigation systems to reach the desired destination. While the global positioning system is generally used in the external environment, different navigation methods are used in the indoor environment. The accuracy of navigation is of great importance when passing through complex, narrow and obstructed roads while going to the relevant target location in the indoor environment. In this study, a cargo carrier robot that can autonomously travel to a location determined by the user in indoor conditions has been developed. After the target point is determined, the cargo vehicle takes action automatically from the starting point, and continuously detects location in order to reach the target with the compass sensor on it. Ultrasonic sensors have been used so that the cargo vehicle can continue to move without hitting any object that may come in front of it while it is going to the target location. A mobile application has been developed to give the destination location of the cargo vehicle and to follow the vehicle. The movements of the autonomous vehicle are controlled by the commands sent via Bluetooth.

1. Introduction

Today's technology is renewing itself day by day and making people's lives easier. Robot technology, which has accelerated the development process with the support of Industry 4.0 in recent years, serves people in many areas such as industry, household, cargo transportation, transportation, shopping [1]. Mobile robots that can move autonomously with the support of smart systems and sensor technologies are among the robot technologies used in indoor and outdoor environments and controlled by various navigation methods. Mobile robots, which have the ability to move autonomously by processing the data received from the sensors on them [2], can perform complex tasks such as transporting products within the factory, performing operations that are dangerous for human health, patrolling indoors, and performing repetitive processing processes [3].

Due to the increase in smart production and e-commerce activities carried out around the world and their inability to meet industrial requirements, traditional sorting and transportation processes have been replaced by contemporary logistics and smart storage methods. Intelligent robots used in operations carried out indoors can replace humans by making delivery and working processes smart. With autonomous transport systems, operations can be performed more efficiently and reliably [4]. In this progress, intelligent robots can make inferences similar to humans by observing the working environment. In the navigation studies carried out in a dynamic environment, it can direct the movement by improving the training process by making inferences from the objects or obstacles seen [5].

*Corresponding author: hakan.ucgun@bilecik.edu.tr
Received: 21.08.2023, Accepted: 16.10.2023

Sensor technologies and smart algorithms are used to overcome such questions affecting navigation processes.

In this study, a cargo carrier robot that operates in the indoor environment and can autonomously travel from the starting location to the target location determined by the user has been realized. In the implemented system, the cargo carrier robot is guided towards the target location by using the compass sensor in indoor navigation processes. Servo motor and ultrasonic sensor were used to prevent the vehicle from being hit by any obstacle during the process of going towards the target location. In order to give the target location, a mobile application was developed and data transmission was ensured by communicating via Bluetooth. The cargo carrier robot that goes to the target location then returns to the starting location and ends its movement.

2. Related Work

With the advancement of artificial intelligence technologies in every field today, significant progress has been experienced in the robot industry. Technologies such as domestic service robots, food delivery robots, and cleaning robots that are offered to people can perform many tasks with their artificial intelligence-based interactions. Robots with artificial intelligence-based speech recognition systems handle some semantic symbols and extract information about their environment by basing these symbols on real reference points. As a result, robots try to recognize their internal environment and fulfill their duties [6]. While the robots used for service or service can easily move to target points with the support of GPS technology in outdoor environments, this process is more difficult in indoor environments. For this reason, the service robots can successfully move to the service robots during the trips to be made in indoor environments where GPS is not available [7]. In this section, some studies developed to fulfil various tasks in indoor environments and which have a place in the literature are given. A comparison table of the studies conducted in the literature is given in Table 1.

Nafais et al. [8], developed an IoT-based cargo carrier robot that can be used to transport products in cargo companies. For the control and sustainability of the system, Arduino Uno board, infrared sensor for tracking the lines on the route, pressure sensor for determining the weight of the object to be transported, position sensor for determining the position of the line, temperature sensor for detecting temperature, vibration sensor for controlling vibrations on the robot are used. The control of the robot was sent through the computer connected via the serial port. The performance of the robot in different conditions was discussed in the test operations carried out with straight, curved and intersection lines on the road. In the test results, it was seen that the robot follows the specified lines with an error margin of less than 1 cm. Chandra et al. [9], developed a vehicle prototype that can be used to transport products in a factory environment, reduce cargo handling accidents, and alleviate high-risk tasks for people to transport. The cargo robot, created with Arduino Uno controller card and Motor Shield card, is controlled via Bluetooth over mobile program. With the various commands sent over Bluetooth, the movements of the vehicle such as stop, forward, right, left and back were carried out. Kang et al. [10], developed a manipulation robot to autonomously perform product service operations indoors. The robot, which offers general-purpose use, has the ability to move in multiple directions and pass through narrow spaces. The robot, which can place and carry more than one object at the same time with the help of its arm during the product transport process, senses the objects around it thanks to its modular software and has the ability to navigate without hitting these objects. In test processes, it has demonstrated capabilities such as taking more than one product autonomously and transmitting it to the relevant areas during product service. Zeng et al. [11], developed a low-cost robot that can autonomously deliver food according to given commands. For the service robot, which will operate in indoor conditions, target detection has been made by means of infrared navigation method. The vehicle includes hardware MSP430 microprocessor, infrared sensor, ultrasonic sensor, Wi-Fi module, navigation module. Based on the information obtained from the sensors, PWM signals were given to the vehicle's motors and the movement of the vehicle was controlled. By combining the components inside the vehicle in a modular manner, the task of food delivery has been successfully accomplished. Tan et al. [12], developed a robot consisting of 3 different parts and working in the indoor environment. At the top of the robot are the IMU, camera, Ultra wide-band and laser radar used for navigation and location detection. In the middle section, there is the mechanism necessary for the robot to work. At the bottom, there are the STM32F103 microcontroller and DC motors used for the movement of the frame. The data received from the sensors at the top are processed with the Raspberry Pi 4 card and location information is obtained. The obtained location information is sent to the STM32F103 card in the lower section via serial communication protocol. The data coming to the lower section is processed and the vehicle is ensured

to move towards the destination. In the test studies, it has been seen that the location detection and navigation process in the interior is done correctly with the system based on multiple sensors. Wu et al. [13], performed a precise positioning process in order to remotely monitor and control the robot, which will serve for food delivery indoors. Ultra wide band wireless transmitter module DWM1000 and ESP8266 microcontroller were used for indoor positioning. During the food delivery task of the robot, real-time location information is sent to the remote server in order to receive real-time location information and to remotely control the movements. This information is processed with various algorithms to control the indoor food delivery robot. Sun et al. [14], developed a food delivery robot that performs positioning and navigation by using sources such as ultra wide-band and sensor technologies (gyroscope, compass, and odometer). The kinematic equations for the accuracy and stability of the position are generated using an extended Kalman filter. In this way, it has been tried to provide more secure coordinate data. Thanks to this method, the food delivery robot has a wide usage area, low cost installation opportunity and high position accuracy. Cao et al. [15], developed a robot powered by Cloud and IoT technology that will serve for drug delivery in the indoor environment. When the robot starts to move, the relevant node information is received via the STM32F103RC microcontroller and sent to the data processing center with the Wi-Fi module. Depending on the processing of the received data, the direction of movement is determined. In the test processes in the laboratory environment, the performance analysis of the vehicle were made and the drug delivery times between the nodes were discussed. Mobile and PC terminals are designed for remote control of the robot.

3. System Overview

The working principle of the autonomous cargo carrier vehicle developed within the scope of the study is given in Figure 1. Arduino Uno microcontroller, compass sensor, ultrasonic sensor, Bluetooth module and motor driver circuit are used as hardware in the cargo carrier robot. Looking at the working process of the system, firstly it is expected that the data of the target location will arrive via the Bluetooth module. The cargo carrier robot, which takes action after the target location information is received, performs direction determination processes by detecting location and obstacles based on instant data from compass and ultrasonic sensors. With the developed direction detection algorithm, direction determination is made over the sensor data and the movement process is carried out by adjusting the motor directions towards the determined direction. In this section describes system overview inclusive of controller card, sensor configuration, software architecture, and mobile application platform.

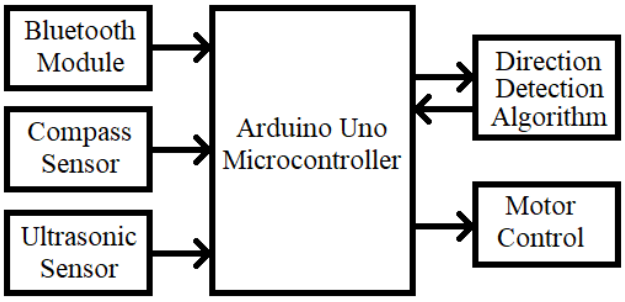

Figure 1. Working Principle of the Cargo Carrier Robot

Table 1. Literature Comparison

Ref.	Controller	Work Area	Environment	Movement Mode	Low Cost	Position Detection
8	Arduino Uno	Cargo	Indoor	Computer Control	Yes	Sensor System
9	Arduino Uno	Cargo	Indoor	Mobile Application	Yes	Manuel
10	Nvidia Jetson Xavier NX	Service	Indoor	Autonomous	No	SLAM
11	MSP430	Food Service	Indoor	Wi-Fi Communication	Yes	Infrared Tracking Navigation
12	Raspberry Pi 4 / STM32F103	Service	Indoor	Remotely Control	No	Laser Radar, UWB, Camera
13	ESP8266	Food Service	Indoor	Remotely Control	Yes	Ultra-wideband Navigation
14	STM32	Food Delivery	Indoor	Remotely Control	Yes	Ultra-wideband, Sensor System
15	STM32F103RC	Medicine Delivery	Indoor	Remotely Control	No	GPS
This Study	**Arduino Uno**	**Cargo**	**Indoor**	**Autonomous**	**Yes**	**Sensor System**

3.1. Arduino Uno Microcontroller

The Arduino platform is a technology that provides common use in the electronic and hardware information processing process and is becoming widespread with its open source applications. The microcontrollers used in this platform have a structure that can perform operations similar to a traditional computer structure and give outputs according to various data types. While there are many Arduino models available today, one of the most frequently used models is the Arduino Uno R3 model. This model, which contains the Atmega328 processor, has various input and output pins, both digital and analog. With the Arduino Uno card used in embedded systems, communication and data transfer operations are carried out between different systems via PWM, ADC, Timer, Interrupt and Serial communication modules [16]. Arduino Uno microcontroller is shown in Figure 2.

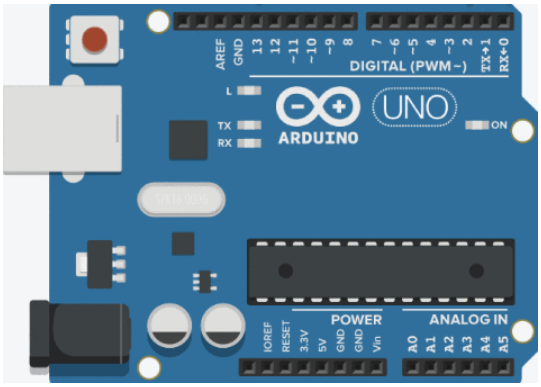

Figure 2. Arduino Uno R3 Microcontroller [16]

3.2. Sensor Units

The detection unit created to control the position, obstacle avoidance and movement processes in the cargo carrier robot consists of 3 sensors (compass sensor, ultrasonic sensor, Bluetooth sensor). The HMC5883L compass sensor is a digital sensor used to measure movements in the X, Y and Z axes. The 3-axis sensor, manufactured by Honeywell Company, communicates with the I2C serial communication protocol. The HMC5883L compass sensor is shown in Figure 3.a. The HC-SR04 distance sensor is one of the popular ultrasonic sensors used to measure distances between 2-400 mm, with a receiver and transmitter eye on it. In order to measure the distance of an object around, the ultrasonic sensor detects the distance with the signal during the return of the sound wave sent from the output unit after hitting the object. The HC-SR04 distance sensor is shown in Figure 3.b.

The HC-05 Bluetooth sensor is a sensor used for wireless communication and supports the Bluetooth 2.0 protocol. With the sensor, which has a range of about 10 meters in the open area, Arduino-based systems can be easily controlled remotely. The HC-05 Bluetooth sensor is shown in Figure 3.c.

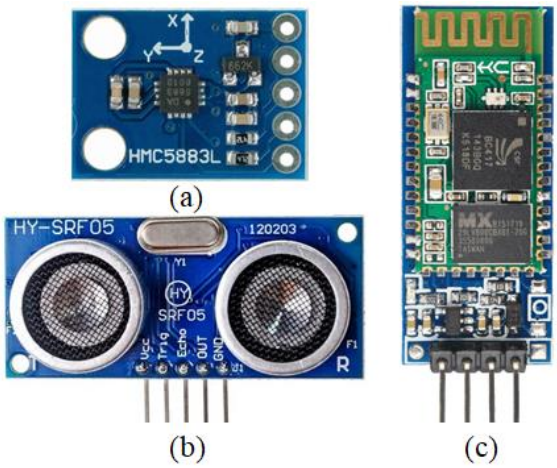

Figure 3. Cargo Carrier Robot Sensing Unit

3.3. Software Architecture

Two different software processes are discussed for the autonomous cargo carrier robot. In the first stage, controlling the data coming from the Bluetooth sensor is discussed. The target point sent via Bluetooth via the mobile application is detected and the movement of the vehicle is started. In the second step, the process from the beginning to the end of the movement is discussed. In this process, operations are carried out to ensure that the cargo vehicle can avoid obstacles that may come in its way, and to constantly control the status of arriving at the determined target point. The flow diagram of the working structure of the cargo transport vehicle is given in Figure 4. When the working structure is examined through the flow chart;

1. Firstly, a connection is expected between the mobile application and the Bluetooth sensor. After the Bluetooth connection, information about the target location is sent via the mobile application.
2. If the incoming location information is “B”, “C” or “D”, while operations are being performed to go to the relevant location, if “A” or a different command is sent, a warning is given and a command is expected to be sent again.
3. When one of the "B", "C" or "D" positions comes, the distance information is calculated in

meters according to the target location sent in the Arduino Uno microcontroller.

4. After the distance of the current location is determined, the compass sensor is expected to find its direction. Then the movement process is started.
5. Whether the robot should turn left or right is determined by the distance measured by the ultrasonic sensor. The distance is detected 10 cm before the obstacle and the motor rotation directions are determined according to the position of the obstacle.
6. The movement of the carrier robot continues along the route determined based on the obstacles encountered during the movement.
7. Whether the robot reaches its target point is determined by the threshold level value (Threshold Level, 15 cm selected).
8. If the threshold level is not reached, the robot tries to reach the target by recalculating the target direction, the current direction angle and the angle to the target. This process continues until the goal is reached.
9. The cargo carrier robot waits for 10 seconds after reaching the target point. This hold was chosen to represent the release of cargo.
10. After the waiting period, the cargo carrier robot returns to its starting point “A” and ends its movement.

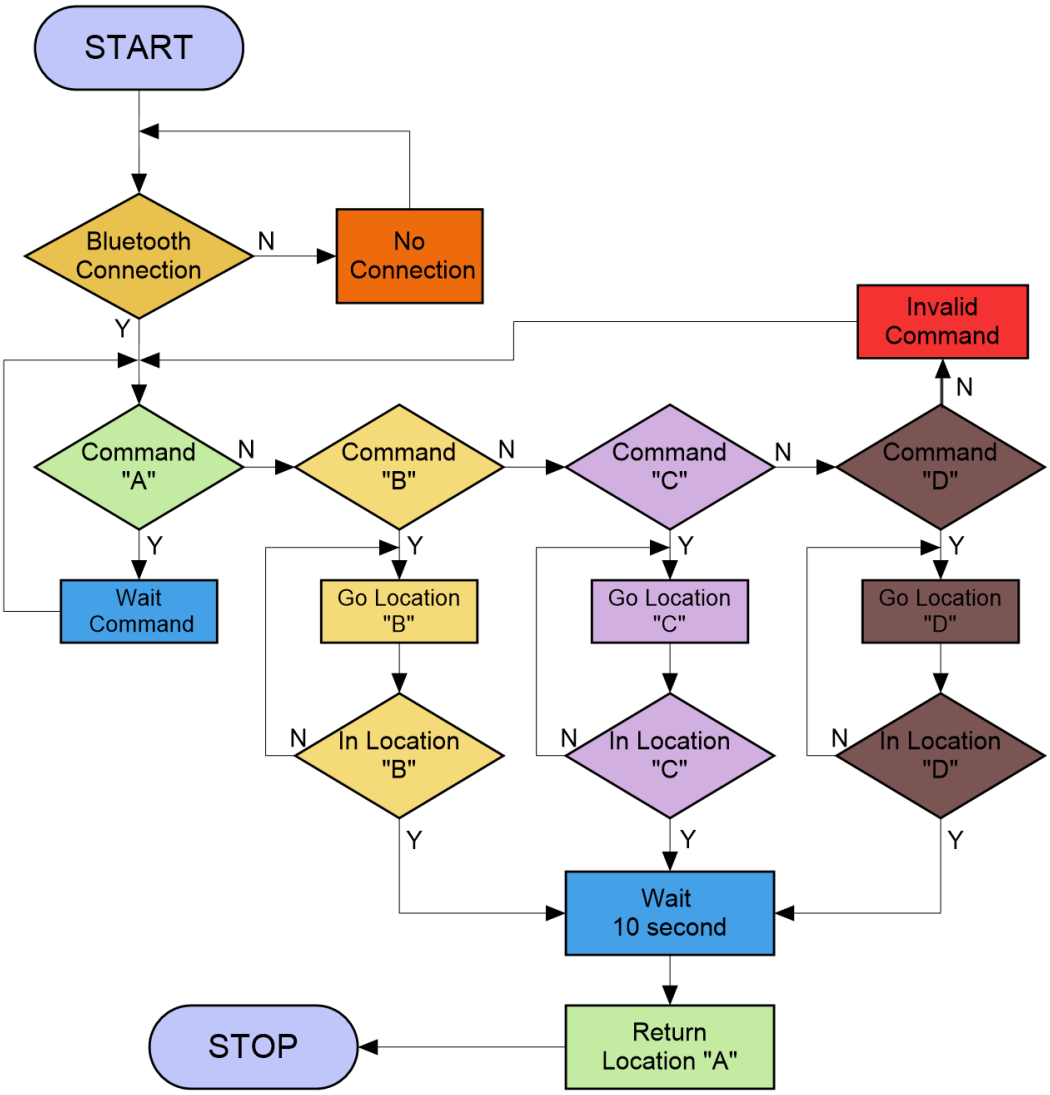

Figure 4. Flow Diagram of the Working Structure

3.4. Software Architecture

Cargo robots are used to perform delivery tasks, an important example of automation systems. In terms of working area, these robots can generally work in indoor environments or complex areas where GPS cannot be used. The cargo vehicle developed within the scope of the study was designed to operate in such an indoor environment. In the developed direction detection algorithm, map-based guidance and obstacle avoidance operations were performed for the cargo robot. The flow diagram of the working structure of the direction detection algorithm is given in Figure 5.

Since the cargo robot will be operated in an environment where GPS is not used, a data set containing map information of the task area has been prepared. In the created map structure, location information is determined for each corner point (A, B, C, and D). The task area used in the studies carried out in the test environment was prepared as 1.5 * 1.5 meters in size and the coordinates of the corner points were determined. The coordinates were set as point A (0, 0), point B (1.5, 0), point C (1.5, 1.5) and point D (0, 1.5). During the movement from the starting point to the target point, the direction information on the x and y coordinate axis is checked with the compass sensor and the direction of the cargo robot is determined in this way. Whether the cargo robot reaches the target point or not is checked by comparing the instantaneous x and y coordinates of the robot in motion with the x and y coordinates of the target point.

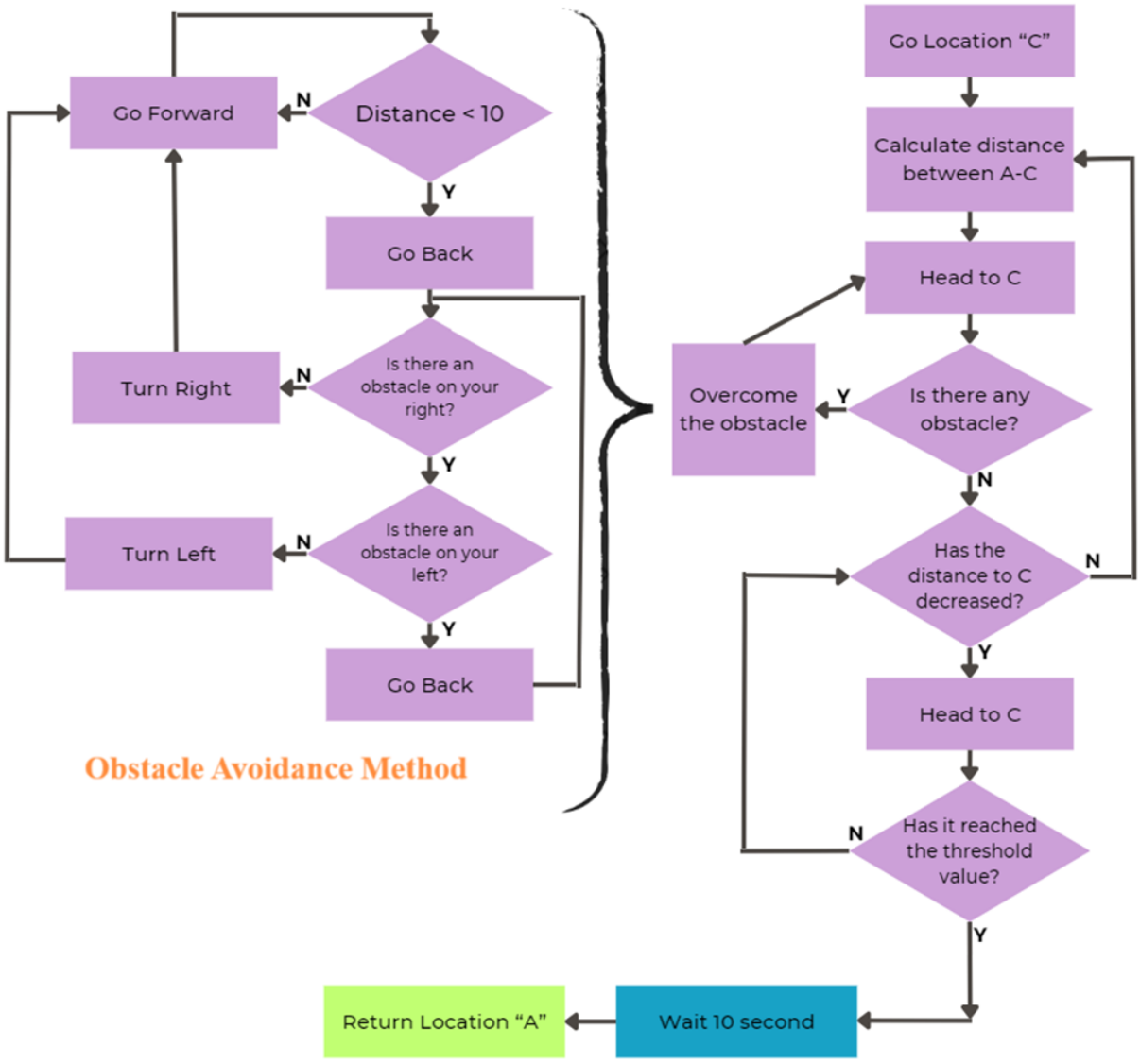

Figure 5. Flow Diagram of the Direction Detection Algorithm

When the cargo vehicle starts its movement, first the coordinate information between the starting point and the target point is taken into account and the distance between these two points is calculated. After this process, movement towards the target point is carried out. An ultrasonic sensor has used to detect obstacles and avoid these obstacles that may appear in front of the cargo robot during its movement. If there is an obstacle in front of the cargo vehicle, the ultrasonic sensor connected to the servo motor controls the right side of the robot, and if there is no obstacle, the robot turns to the right side. If there is any obstacle on the right side, the robot turns to the left side. If there is an obstacle on both the right and left sides at the same time, the robot goes back and continues on its way by making the same checks again. After overcoming the obstacles, distance checks based on coordinate information are made again while moving towards the target location. The decision as to whether the target point has been reached or not is made based on the threshold level value of the relevant target point. In making this decision, the proximity of the x and y coordinates of the target point and the instantaneous x and y coordinates of the robot (threshold 15 cm) is taken into consideration. After the cargo robot reaches the target point, it moves towards the starting point by repeating the same steps algorithmically. As a result, the direction detection algorithm developed enables the cargo robot that will operate in indoor environments to operate via a map-based guidance system, independent of GPS

3.5. Mobile Application Platform

A mobile application has been developed to remotely control the cargo carrier robot and send information about the destination point. The interface of the developed mobile application is shown in Figure 6. In the mobile application developed with the MIT App Inventor interface, Bluetooth connection is first performed. The information of the relevant Bluetooth sensor is selected via the mobile application and the wireless connection process is performed. After the connection process, one of the 3 destination points (“B”, “C”, “D”) determined to carry cargo through the application is selected, and the cargo carrier robot is activated. Information about the relevant target location is sent to the Arduino Uno microcontroller board via the Bluetooth sensor. The robot starts its movement by making calculations about the received target information.

During the cargo transportation process, informational messages are also sent through the application depending on the destination points. After reaching the target, a return to the starting point is performed after a certain period of time, and the movement of the vehicle is terminated until the next command is received. If a different command is received via Bluetooth while the cargo carrier robot is going to the destination, it is not allowed to make any changes in the robot's movement route. In this way, it is aimed to prevent erroneous location detections that may occur.

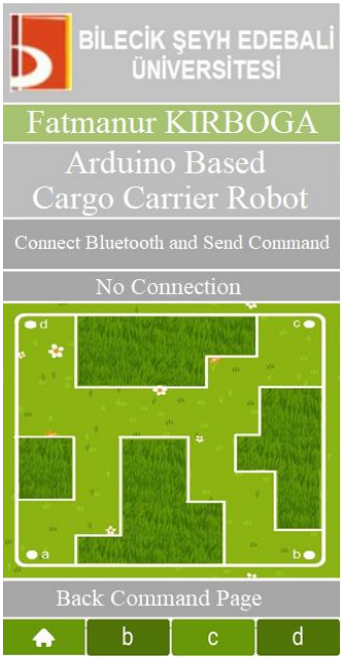

Figure 6. Mobile Application Interface

4. Indoor Environment Experimental Tests

During the development process of the autonomous cargo carrier robot, various tests were carried out. Firstly, test procedures were made for the individual operation of electronic components (Servo motor, DC motor driver, Bluetooth Sensor, Compass Sensor, Ultrasonic Sensor) with the Arduino Uno board, and each component was controlled. After the control of the electronic components, the tests related to the communication of the mobile application and the Arduino Uno board were started. In these test processes, test operations such as sending and receiving data to Arduino Uno via the mobile application were carried out. After controlling the carrier robot manually via the mobile interface, autonomous driving tests were started.

In autonomous driving tests, individually tests were performed such as for detecting objects around the vehicle and moving without hitting these objects, direction determination accurately moving to a given target point, and returning to the starting position. Finally, in the integrated system tests, tests were carried out to reach the target point and return to the starting point again without hitting the obstacles in front of the cargo carrier robot, which moves autonomously towards the target received via the mobile interface. The block diagram showing the hardware connection of the Arduino Uno board and electronic components is given in Figure 7.

The pin connections between the hardware components used in the cargo carrier robot and the Arduino Uno microcontroller are given in Table 2. A 4WD model car frame was used for the robot to carry the hardware components. Three pieces 1S LiPo batteries were used to meet the energy need of the system. Before moving to the integrated system, test work was carried out on each hardware. After the related hardware studies were successful, we were passed to the next hardware. In this way, hardware connection problems that may occur in the integrated system of the cargo carrier robot are prevented.

Table 2. Pin Connections

Arduino Uno	Hardware Component
D0	RX (Bluetooth)
D1	TX (Bluetooth)
D5	ENB (L298N)
D6	IN4 (L298N)
D7	IN3 (L298N)
D8	IN2 (L298N)
D9	IN1 (L298N)
D10	ENA (L298N)
D11	Servo Motor
D12	Echo Pin (Ultrasonic)
D13	Trig Pin (Ultrasonic)
A4	SDA (Compass)
A5	SCL (Compass)
VCC	Common +5V
GND	Common Ground

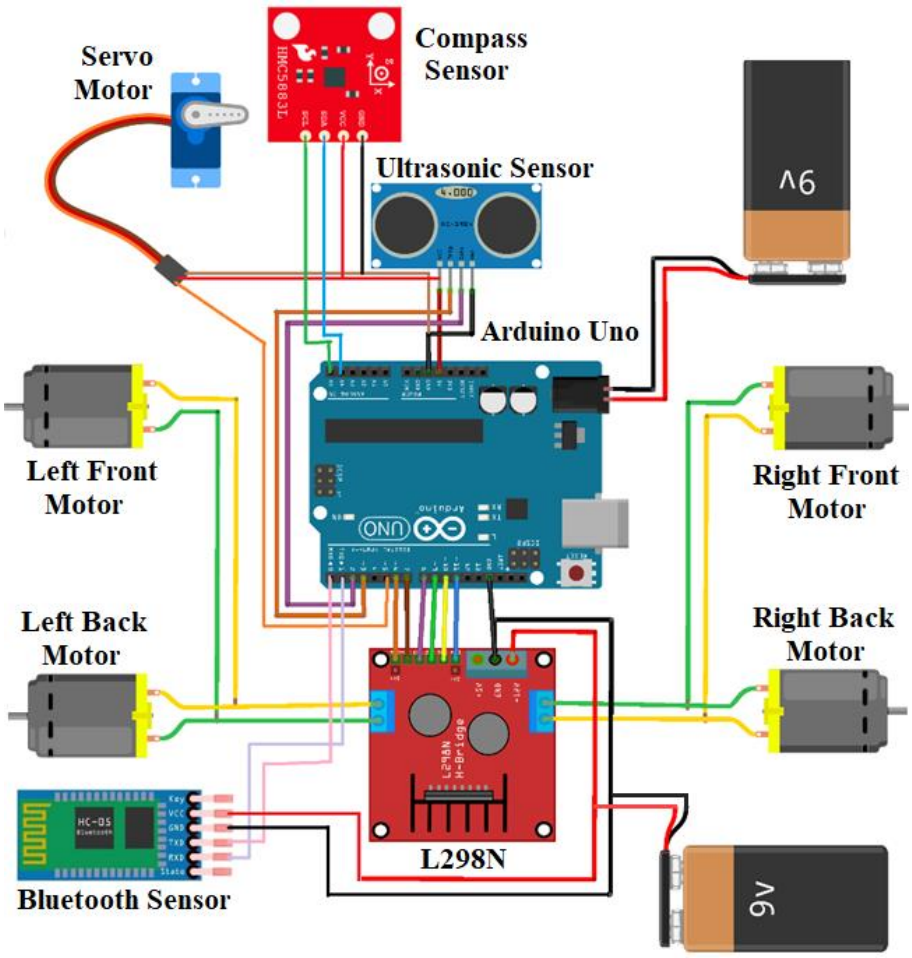

Figure 7. Block Diagram of Cargo Carrier Robot

A test environment has been prepared in order to conduct driving tests of the cargo carrier robot developed within the scope of the study and to control the status of going to the determined destination points. With the environment developed similar to the interface controlled via the mobile application, tests were carried out for the cargo transport vehicle to go to the given destination points. In Figure 8, the visuals of the test environment created and the visuals of the test process are given. During the test operations, it was observed that the robot went to all 3 determined locations and did not hit the obstacles that it encountered during its movement. With the test processes, navigation was carried out independently of GPS, which is one of the cargo transportation processes that can be done indoor environment.

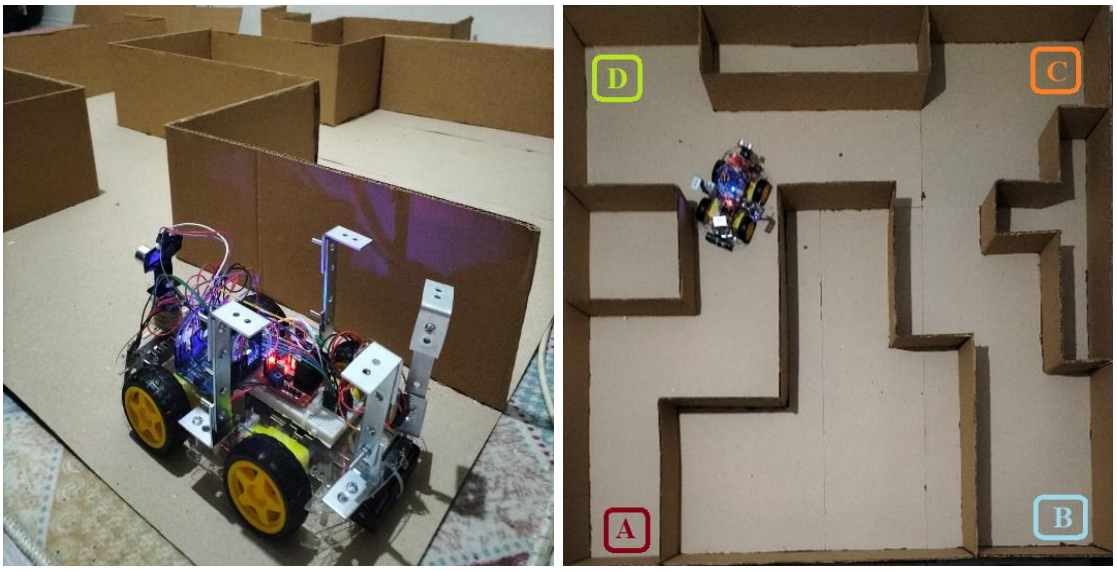

Figure 8. Test Environment

In the test processes, the cargo robot was enabled to change its direction of movement depending on the obstacles it encountered and to continue its movement in this way and move towards the target point. The angle-time graph of the servo motor is given in Figure 9 in order to observe the rotation movements of the robot as it moves from the starting position to the target position. In the given graph, the movement time to destination points B, C and D and the return time from these points to the starting point are shown separately. For example; During the cargo robot's movement towards point C, it took approximately 2 minutes to reach the target point, approximately 2 minutes to return to the starting point, and the total time was 4 minutes (B => ~3.20 min - ~3.30 min, D => ~1 min - ~1 min).

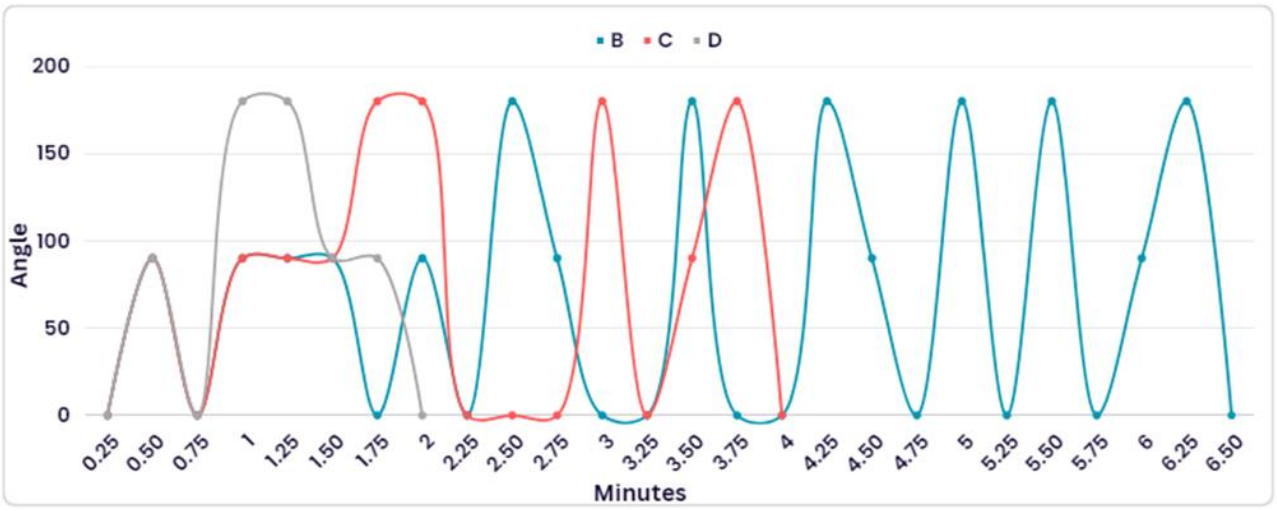

Figure 9. Angle-Time Graph of the Servo Motor

In the angle time graph for the servo motor, there are angles of 0º, 90º and 180º. At the beginning of the movement, the angle value of the servo motor was initially taken as 0o. When an obstacle appears in front of the robot, the servo motor first turns to the right and the angle value is recorded as 90º. If there is an obstacle on the right side, the servo motor rotates to the left and the angle is recorded as 180º (-90º). In this way, the movement process of the cargo robot was discussed by taking samples step by step while moving from the starting point to the target point.

5. Conclusion

Robot technologies, which are in their golden age with the Industry 4.0 revolution, are increasing their popularity in the service industry day by day, thanks to their high efficiency, reliability and low cost. Robots, whose assigned tasks are performed quickly and independently, provide many conveniences to their users in areas such as the service sector, transportation, delivery, food service, laboratory work, and household cleaning. Robots working indoors may encounter problems such as poor navigation, narrow spaces and obstacles in general. Intelligent algorithms and sensor systems are used to eliminate such problems.

In this study, a cargo carrier robot has been developed to move products between different locations in indoor environments. The specially designed cargo robot carries out its transportation operations autonomously. The developed robot can move easily indoors, thanks to its small size and ability to quickly turn in different directions. In this way, it can easily continue its movement on narrow and disabled roads.

The cargo carrier robot starts to move depending on the information about the target location coming from the mobile application prepared within the scope of the study. A navigation process independent of GPS signals was carried out in the path detection process of the cargo robot used in the indoor environment. For this process, axis informations was obtained from the compass sensor and the cargo robot was allowed to move towards the target location. During the movement of the cargo robot, obstacles were detected with the ultrasonic sensor integrated into the servo motor in front the robot and the movement continued without hitting these obstacles. After reaching the target point, the cargo robot waits for a certain time and then moves towards the starting point again. A test environment has been prepared to test the developed system. In the test environment, it was checked whether the vehicle autonomously went to the given target point. In addition to being more cost-effective compared to other studies, the application has advantages in terms of features such as being able to move autonomously and having a return to home feature.

Contributions of the authors

All authors contributed equally to the study.

Conflict of Interest Statement

There is no conflict of interest between the authors.

Statement of Research and Publication Ethics

The study is complied with research and publication ethics.

References

[1] S. I. A. P. Diddeniya, A. M. S. B. Adikari, H. N. Gunasinghe, P. R. S. De Silva, N. C. Ganegoda and W. K. I. L. Wanniarachchi, "Vision Based Office Assistant Robot System for Indoor Office Environment," *in 2018 3rd International Conference on Information Technology Research (ICITR)*, Moratuwa, Sri Lanka, 2018, pp. 1-6. doi: 10.1109/ICITR.2018.8736141.

[2] S. Noh, J. Park and J. Park, "Autonomous Mobile Robot Navigation in Indoor Environments: Mapping, Localization, and Planning," *in 2020 International Conference on Information and Communication Technology Convergence (ICTC)*, Jeju, Korea (South), 2020, pp. 908-913. doi: 10.1109/ICTC49870.2020.9289333.

[3] J. Huang, S. Junginger, H. Liu, and K. Thurow, "Indoor Positioning Systems of Mobile Robots: A Review" *Robotics*, vol. 12, no. 2, p. 47, 2023. https://doi.org/10.3390/robotics12020047.

[4] X. He, Y. Kuang, N. Song and F. Liu, "Intelligent Navigation of Indoor Robot Based on Improved DDPG Algorithm", *Mathematical Problems in Engineering*, vol. 2023, pp. 1-11, 2023. https://doi.org/10.1155/2023/6544029.

[5] A. Loganathan and N. S. Ahmad, "A systematic review on recent advances in autonomous mobile robot navigation", *Engineering Science and Technology, an International Journal*, vol. 40, no. 101343, p. 101343, 2023. https://doi.org/10.1016/j.jestch.2023.101343.

[6] X. Song, X. Liang, Z. Zhijiang and Z. Huaidong, "A Object-augmented Semantic Mapping System for Indoor Mobile Robots," in *2022 IEEE 2nd International Conference on Software Engineering and Artificial Intelligence (SEAI)*, Xiamen, China, 2022, pp. 225-229. doi: 10.1109/SEAI55746.2022.9832075.

[7] R. A. Deshmukh and M. A. Hasamnis, "A navigation scheme for autonomous mobile service robots working in GPS denied commercial indoor spaces," *in 2023 International Conference on Communication, Circuits, and Systems (IC3S)*, BHUBANESWAR, India, 2023, pp. 1-5. doi: 10.1109/IC3S57698.2023.10169514.

[8] A. Suhana Nafais, S. L. Cibi, A. Harish Kumar, M. Tharani and S. P. Viswak Avinash, "An IoT based Intelligent Cargo Carrier," *in 2023 7th International Conference on Intelligent Computing and Control Systems (ICICCS)*, Madurai, India, 2023, pp. 1569-1574. doi: 10.1109/ICICCS56967.2023.10142786.

[9] Y. I. Chandra, Irfan and A. S. R. Putro, "Cargo Simulation Robot Prototype with Bluetooth Based Motor Driver Shield Using Arduino Uno Microcontroller", *International Journal of Artificial Intelligence & Robotics (IJAIR)*, vol. 4, no. 1, pp. 1-8, 2022. https://doi.org/10.25139/ijair.v4i1.4326.

[10] T. Kang, J. Kim, D. Song, T. Kim and S. -J. Yi, "Design and Control of a Service Robot with Modular Cargo Spaces," *in 2021 18th International Conference on Ubiquitous Robots (UR)*, Gangneung, Korea (South), 2021, pp. 595-600. doi: 10.1109/UR52253.2021.9494635.

[11] H. Zeng, Z. Zhang, and Y. Hong, "Control system design of an intelligent food delivery robot," *E3S Web Conf.*, vol. 267, p. 01059, 2021. https://doi.org/10.1051/e3sconf/202126701059.

[12] X. Tan, S. Zhang and Q. Wu, "Research on Omnidirectional Indoor Mobile Robot System Based on Multi-sensor Fusion," *in 2021 5th International Conference on Vision, Image and Signal Processing (ICVISP)*, Kuala Lumpur, Malaysia, 2021, pp. 111-117. doi: 10.1109/ICVISP54630.2021.00028.

[13] P. Wu and D. Wen, "Positioning Information System of Indoor Food Delivery Robot Based on UWB", J. Phys. Conf. Ser., vol. 1732, no. 1, p. 012129, 2021. doi: 10.1088/1742-6596/1732/1/012129.

[14] Y. Sun, L. Guan, Z. Chang, C. Li and Y. Gao, "Design of a Low-Cost Indoor Navigation System for Food Delivery Robot Based on Multi-Sensor Information Fusion", *Sensors*, vol. 19, no. 22, pp. 1-26, 2019. https://doi.org/10.3390/s19224980.

[15] H. Cao, X. Huang, J. Zhuang, J. Xu and Z. Shao, "CIoT-Robot: Cloud and IoT Assisted Indoor Robot for Medicine Delivery", *in Procedings 2018 Joint International Advanced Engineering and Technology Research Conference (JIAET 2018)*, Xi'an, China, 2018, pp. 1-5. doi: 10.2991/jiaet-18.2018.14.

[16] M. Tupac-Yupanqui, C. Vidal-Silva, L. Pavesi-Farriol, A. Sánchez Ortiz, J. Cardenas-Cobo and F. Pereira, "Exploiting Arduino Features to Develop Programming Competencies," *IEEE Access*, vol. 10, pp. 20602-20615, 2022. doi: 10.1109/ACCESS.2022.3150101.

Bitlis Eren Üniversitesi Fen Bilimleri Dergisi
BİTLİS EREN UNIVERSITY JOURNAL OF SCIENCE
ISSN: 2147-3129/e-ISSN: 2147-3188
VOLUME: 12 NO: 4 PAGE: 1150-1159 YEAR: 2023
DOI:10.17798/bitlisfen.1348351

Aerogel Production and Determination of Its Thermophysical and Characteristic Properties

Mehmet Zerrakki IŞIK[1*], Hasan OKTAY[1], Mehmet KAYIR[2], Hasan SAYĞILI[3]

[1]*Batman University, Department of Mechanical Engineering*
[2]*Turkish Air Force, Ministry of National Defence*
[3]*Batman University, Vocational School of Technical Sciences*
(ORCID: 0000-0001-9753-6458) (ORCID: 0000-0002-0917-7844) (ORCID: 0000-0001-6217-0492) (ORCID: 0000-0003-4900-8268)

Keywords: Aerogel 1, Porous materials 2, TEOS 3, TMOS 4, Insulation 5

Abstract
Porous materials are at the forefront of research in terms of providing superior insulation properties and energy efficiency. The most important point that makes porous materials different and unique is the space inside the pore. Aerogel has become the insulation material that stands out as the most interesting alternative in this context. In this study, the production of aerogel insulation materials with high insulation properties, suitable mechanical properties, and different contents was aimed at. Silica aerogels are synthesized using the sol-gel technique with Hydrolysis, Condensation, Aging, Solvent change, and Surface modification, Drying main steps in general. According to the results obtained, it was determined that the densities of the aerogels produced were in the range of 0.66 to 1.053 g/mL, and the thermal conductivity values were in the range of 0.067 to 0.097 W/mK. The results show that many opportunities are available to improve the insulation property of aerogel, which is considered an important insulation material of the future.

1. Introduction

The need for energy, which is the most important indicator of economic and social development, continues to increase today due to population growth and technological developments. In order to ensure the continuity of the existing system, it is of great importance to ensure the maximum benefit from data sources. In this direction, focusing on insulation applications for thermal interactions in systems will contribute more to getting results. The purpose of insulation is to approach the theoretical cycle calculations by keeping the system as far away from the influence of the external environment as possible. This use may be an industrial process cycle, or it may also occur as a requirement for the conditioning of a living space.

Porous materials are at the forefront of research in terms of providing superior insulation properties and energy efficiency. Porous materials are used in many different fields, such as adsorbents, catalysts, and support materials, due to their large surface areas. The presence of nanometer-sized voids in their structure and their controllability have brought porous materials to an important place in terms of science and technology. The most important point that makes porous materials different and unique is the space inside the pore. The pore sizes of porous materials are classified into three different categories according to the international standard IUPAC (International Union of Pure and Applied Chemistry) definition. If their diameter is less than 2 nm, it is called a micropore; if it is between 2 and 50 nm, it is called a mesopore; and if it is larger than 50 nm, it is called a macropore [1].

Aerogel has become the insulation material that stands out as the most interesting alternative in this context. Aerogels are silica-based solid substances obtained by replacing the liquid component in their structure with air. It was first

*Corresponding author: mehmetzerrakki.isik@batman.edu.tr
Received: 22.08.2023, Accepted: 15.12.2023

produced by Stefan Kistler in early 1931. The surface of aerogels, which consists of very small pores, is reminiscent of a sponge. Since there is 99.8% air in their structure, they are insulating, lightweight, and low-density materials. Aerogels are known as the lightest and lowest-density solids in the world [2]. For this reason, it is used in many different fields, such as isolation, storage and transportation media, sensors, catalysts, and separation processes. Silica-based aerogels are produced by the sol-gel method using silicon sources in an acidic or basic environment. The sources of silica used in the production of silica-based aerogels are usually Tetraethyl orthosilicate (TEOS), Tetramethyl orthosilicate (TMOS), sodium silicate, and water glass. The production cost can be reduced by using various industrial wastes while aerogel is synthesized. Considering this feature, there is a need to develop environmentally friendly methods [3].

There are various types of aerogels, such as carbon, silica, alumina, metal, and nanotube aerogels. It is the most widely used because it is synthesized from natural raw materials and is environmentally friendly; silica is an aerogel. Silica aerogels have superior properties such as high surface area, high porosity, low density, low dielectric constant, and high porosity. Aerogels are synthesized by the sol-gel method, which consists of gel preparation, aging, and drying stages [4].

In their study, Li and his colleagues produced silica aerogel at an atmospheric pressure of 40 ºC using the sol-gel process. In the analyses of the obtained silica aerogels, the bulk density of the silica aerogel was found to be 0.33 g/cm3, its porosity was 87%, the total pore volume was 3.31 cm3/g, the average pore diameter was 26.5 nm, and the specific surface area was 500 m2/g [5], [6]. In a study, it was found that silica aerogel, which was supercritically dried, contained fewer fire hazards and had lower smoke toxicity. However, in general, it has been found that hydrophobic silica aerogel is risky in terms of fire hazards [7]. In another study, Jones and colleagues evaluated the aerogel's low density, high porous structure, and ability to form a thermal barrier. It has been reported that composite materials consisting of silica aerogel and oxide will offer new possibilities for the design of thermoelectric devices and space studies [8].

In this study, different aerogel materials with high thermal resistance, insulation properties, and suitable mechanical properties were produced. In this regard, silica aerogels were synthesized using ethanol and methanol as TMOS and TEOS hydrolysis catalysts and NH4OH and NH4F as condensation catalysts. Then TMOS and TEOS were diluted with different concentrations of ethanol and methanol.

2. Material and Method

Silica aerogels are nanostructured materials that are of great interest due to their effective properties such as low density, transparency, high surface area and high porosity, and low thermal conductivity. Silica aerogels are three-dimensional nanostructured materials containing a cross-linked SiO2 network [9]. The properties of silica aerogels are also indicated in Table 1.

Table 1. General Properties of Silica Aerogels [9, 10].

Property	Value
Intensity	0.003 g/cm^3
Surface area	500-1000 m^2/g
Porosity	% 80-99.8
Pore diameter	20-150 nm
Primary connection diameter	2-5 nm
Thermal conductivity	0.017-0.021 W/mK
Sound speed	100 m/s
Dielectric constant	1.1
Refractive index	1-1.05

Silica aerogels are synthesized using the sol-gel technique with Hydrolysis, Condensation, Aging, Solvent change and Surface modification, Drying main steps in general. Aerogel synthesis begins with the creation of a gel with a porous structure, the pores of which are filled with liquid. Aerogel is obtained by replacing the liquid in the pores with air without changing the network structure of the gel. A two-stage sol-gel method was chosen to control the microstructure of aerogels.

2.1. Content of Silica Aerogel

In the synthesis of Silica Aerogel; Tetramethyl orthosilicate (TMOS-$Si(OCH_3)_4$) and Tetra-ethoxysilane (TEOS-$Si(OC_2H_5)_4$) were used as the source materials of silica; Ammonium Hydroxide (NH_4OH) and Ammonium Fluoride (NH_4F) as base catalysts; and Methanol (CH_3OH) and Ethanol (C_2H_5OH) as structural water removers. Within the scope of the experimental researche, the parameters affecting aerogel synthesis were examined. The properties of the materials used in the production of silica aerogel are given in Table 2.

Table 2. Properties of materials used in making aerogels [9], [10].

Material	Formula	Density kg/m³	Molar mass g/mol	Melting point °C	Boiling point °C
TMOS	$SiC_4H_{12}O_4$	1003	152.22	5	122
TEOS	$SiC_8H_{20}O_4$	940	208.33	-77	168
Ammonium hydroxide	NH_4OH	880	35.04	91.5	24.7
Ammonium fluoride	NH_4F	1001	37.037	100	260
Methanol	CH_3OH	792	32.04	-97.6	64.7
Ethanol	C_2H_5OH	789	46.07	-114.1	78.37

In the catalyst addition steps, the other steps are the same except that the catalysts are changed. The experiment consists of five stages. First of all, TMOS and TEOS were diluted with ethanol and methanol in different concentrations. Then, water and alcohol were added under continuous stirring to initiate hydrolysis. Condensation was initiated by the addition of the base catalyst, and the solution was filled into pre-prepared molds (5 mL).

2.2. Synthesis of TMOS and TEOS Solutions

The experimental procedure for the production of silica aerogel is as follows: Ammonium hydroxide solution is prepared by adding 5.4 mL of concentrated ammonium hydroxide to 1000 mL of water. During the hydrolysis stage, 10 mL of TMOS and 10 mL of methanol are filled into a beaker to form an alkoxide solution and mixed in a magnetic mixer until a homogeneous solution is formed. During the condensation stage, it is mixed with 5 mL of ammonium hydroxide stock solution and 10.0 mL of methanol in another beaker and mixed in a magnetic mixer until a homogeneous solution is formed. This mixture is the catalyst solution. Then, the solution formed by combining the alkoxide solution with the catalyst solution is mixed in a magnetic mixer at 25 °C for 3-5 minutes, and filling is performed into previously prepared molds. The gelling process is completed in an average of 8 to 15 minutes. After the gel hardens, the gel is allowed to age for at least 24 hours with methanol. The aging process is done by replacing the gel with methanol at least four times between a few days and a week. If liquid is observed in the gel, it is decided that it should wait for gelification.

It is the same as the TMOS stages, but the prescription is different. Ammonium fluoride/ammonium hydroxide solution is prepared by adding 1.852 g of NH4F and 22.78 mL of ammonium hydroxide solution to 100 mL of water. In the hydrolysis stage, 5 mL of TEOS and 11 mL of ethanol are filled into a beaker to form an alkoxide solution and mixed on a magnetic stirrer until a homogeneous solution is formed. In the condensation phase, 7.0 mL of distilled water and 11.0 mL of ethanol are mixed in another beaker, and 0.371 mL of ammonium fluoride/ammonium hydroxide stock solution is added. The aging process involves the addition of new monomers to the silica network and an increase in the degree of crosslinking of siloxane. The stiffness and strength value of the aerogel formed during aging increases and gel bonds strengthen. Gels prepared from the same solutions and having the same concentration by weight are placed in different aging solutions at the same time, while the control sample is transferred directly to ethanol or methanol. The contents of the different samples prepared according to the solution changes are given in Table 3. The realization stages of the synthesis of TMOS and TEOS silica aerogels are given in Figure 1.

Table 3. The content of produced Silica Aerogel samples.

No	TMOS g	TEOS g	Ethanol g	Methanol g	Pure water g	NH_4OH g	NH_4F g
1	-	5.26	19.56	-	8.21	0.06	0.006
2	-	5.52	20.54	-	8.63	0.07	0.007
3	11.66	-	-	18.1	5.55	0.027	-
4	12.24	-	-	19.0	5.97	0.029	-
5	10.35	-	8.03	-	5.04	0.025	-

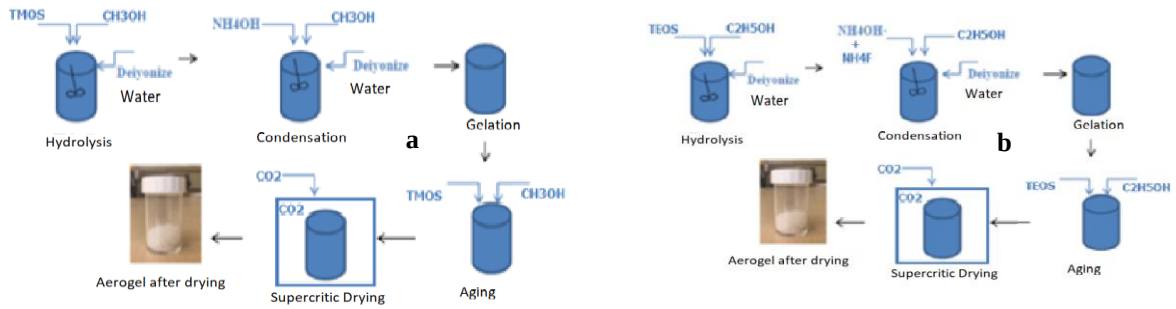

Figure 1. The synthesis of silica aerogels: a) TMOS b) TEOS.

The gelation time changes with the change in TEOS and TMOS concentrations in the solutions. This time may be as short as a few minutes, starting with the addition of the catalyst solution, and sometimes there may not be enough time for the solution to be molded. Since the gel adheres to the test tube after the gelation point is reached, drying was achieved without removing the molds in which gelation took place, thus producing aerogels with a monolithic structure. In addition, the use of round-shaped Teflon molds to reduce the adhesion forces in the gel pores and prevent adhesion has contributed to the formation of a crack-free monolith structure.

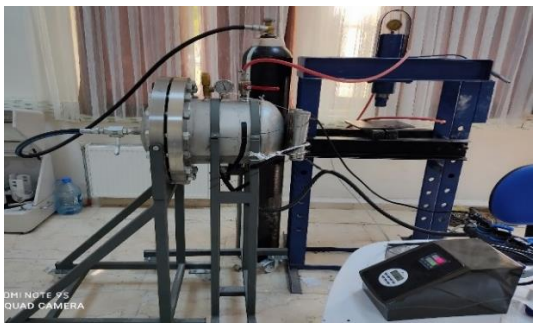

Figure 2. Supercritical drying experimental set.

The entire aerogel production process, including supercritical drying, takes about 3 days (Figure 2). Before the drying process is started, the wet gel-filled molds are placed in the reactor and filled with a sufficient level of alcohol to prevent initial evaporation. Then the lid is closed, and sealing is ensured with nuts and bolts on the reactor. The loading process is started by opening the valve for the liquid carbon dioxide. In order to prevent the pore structures of the gels contained in the reactor from deteriorating, the loading process is performed for 1 hour. Until the reactor reaches full filling, when the pressure inside the reactor is equal to the carbon dioxide tube pressure (55 bar), the reactor inlet valve is closed to ensure tightness control. After the impermeability is achieved, the solvent alcohol in the reactor is expected to be replaced with liquid carbon dioxide for 2 days. In this case, the speed of the drying process is mainly controlled by the diffusion of ethanol through the pores. In the next step, the supercritical drying state is passed.

In the supercritical process, first of all, heating is performed until the pressure inside the reactor reaches 82.7 kPa and the temperature reaches 40 °C. As the reactor is heated, the pressure will rise quite rapidly. The pressure control valve on the reactor switches to unloading if high pressures are reached and ensures that the pressure remains within safety limits. Thus, the pressure was reduced to 73.9 kPa (preferably higher pressure) by using the discharge valve on the reactor, as shown in Figure 3.

Figure 3. CO_2 reaching supercritical state in the reactor.

In this case, the temperature inside the reactor was kept constant at around 31.1 °C, allowing the carbon dioxide gas to reach the critical state. This critical situation has been ensured to last for at least 3 hours. After completely replacing the ethanol contained in the pores of the gel with supercritical carbon dioxide, the carbon dioxide gas was completely discharged from the reactor by reducing the pressure by 7 kPa per hour. The aerogels obtained after the supercritical drying stage were brought to room temperature, and it was ensured that they took their final form. After all the stages of the drying process have been completed, the condition of the gels is given in Figure 4.

Figure 4. TEOS-TMOS aerogels after drying.

2.3. Test Methods Applied to Aerogel Samples

Several test methods applied to aerogel samples were carried out as follows: Thermal, physical, and material characterization tests. The thermal and physical tests consist of density and mass loss determination and thermal conductivity tests, and the characterization consists of porosity, specific surface (bet surface) determination, XRD, and SEM tests.

Sol-gel and Air-gel samples prepared in certain volumes (V) in accordance with the known recipe are weighed with an accuracy of 0.01 grams, and the density values are calculated by taking the average of the three samples.

$$\rho_k = \frac{M_k}{V} \quad (1)$$

The thermal conductivity test was determined by using a Thermtest portable device, as indicated in Figure 5. The Thermtest device uses the Transient line source (TLS) method for thermal conductivity measurement. After the heating period is complete, temperature readings are taken at the same intervals throughout the cooling period. The thermal conductivity is then calculated from this temperature information using the following equation:

$$k = \frac{q}{4\pi a} \quad (2)$$

where k is the thermal conductivity (W/mK), q is the heating power of the needle, and a is the slope of the line for temperature rise over the log of time.

Figure 5. Thermal conductivity tests applied to aerogels.

Scanning electron microscope (JEOL JSM 7001F) device for the acquisition of SEM images for the examination of the surface morphological changes of the produced aerogel materials. The surface area and pore analysis (Micromeritics-TriStar II Plus 3030) device was used for pore characterization, and the X-ray diffractometer (Bruker D8 Advance) device was used for crystal structure analysis.

3. Results and Discussion

In this study, different aerogel samples were produced with the synthesis of TMOS and TEOS alkaline solutions. The thermophysical and microstructure properties of the aerogel samples were determined by applied tests, and the results are shown in Table 4. It was determined from the results that the densities of the produced aerogels were in the range of 0.66 to 1.053 g/mL, and the thermal conductivity values were in the range of 0.067 to 0.097 W/mK.

Table 4. The content of produced Silica Aerogel samples.

No	Density of Sol-gel g/mL	Density of Aero-gel g/mL	Thermal conductivity W/mK
1	0.946	0.589	0.087
2	0.990	0.620	0.091
3	1.002	0.636	0.092
4	1.053	0.670	0.097
5	0.660	0.420	0.067

When the results obtained were examined, it was seen that samples with higher values of density and thermal conductivity were obtained compared to the literature. The expected thermophysical targets have not been fully achieved; however, the thermal conductivity values of the samples are below 0.1 W/mK, which shows that they can be used as an insulating material. In addition, it was determined that an increase in the concentrations of TEOS and TMOS sol-gels during the production phase caused an increasing trend in density and indirectly in thermal conductivity values for those aerogels.

Pore size distribution (BET), surface morphology (SEM), and crystal structure (XRD) analyzes play an important role in the characterization of the produced materials. Thanks to these analyses, the properties of materials produced under different conditions and contents can be compared, and performance evaluations can be performed.

SEM images of silica aerogels at different magnification ratios (x500, x1000) are given in Figure 6. When the morphology of all silica aerogels was investigated, it was generally seen that spherical particles with nanometer sizes form agromel (combined) structures. These combined structures vary in the range of 2-20 µm. Although the surface morphologies of aerogels produced by three different methods are very close to each other, it can be clearly detected from SEM photographs that they exhibit regional differences.

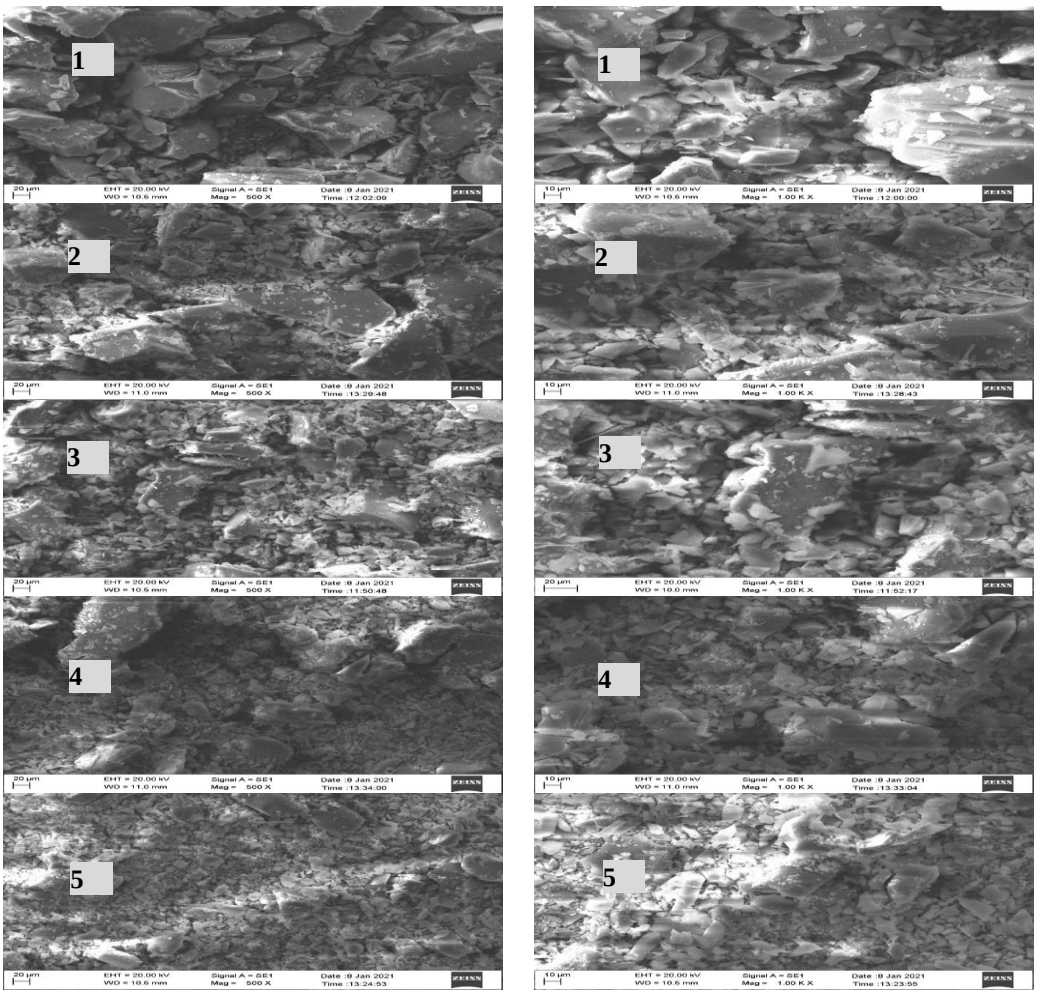

Figure 6. SEM images of synthesized silica aerogels at different magnifications (x500, x1000).

The results obtained from the Sem analysis show that aerogels have advanced micro and primary mesopores. The XRD patterns of the synthesized silica aerogels are shown in Figure 7. The broad bands seen around 2θ=22° in the diffractograms proved that silica materials in an amorphous structure were obtained.

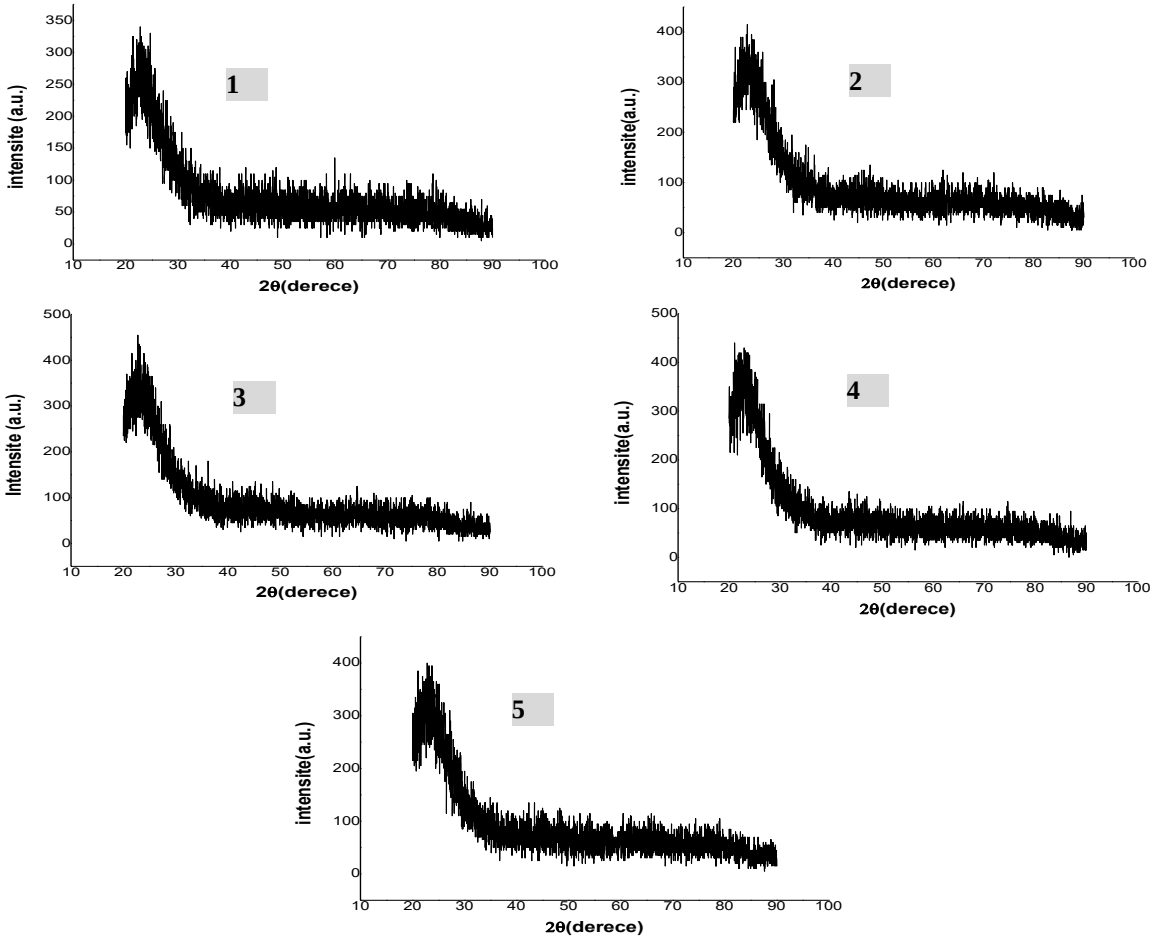

Figure 7. XRD patterns of synthesized silica aerogels.

The surface area (m^2/g), pore size (nm), and porosity (%) of the silica aerogels synthesized in the study are given in Table 5. When the table is examined, it is seen that the highest surface area belongs to TMOS + Ethanol aerogel. In Figure 8, adsorption-desorption isotherm curves in the bet analysis were performed. The fact that the values and changes are very close to each other shows that the materials produced are structurally very close to each other.

Table 5. The porosity values of the silica aerogels.

No	Average pore diameter nm	Porosity %	Specific surface m^2/g
1	2.84	88.85	662.08
2	3.50	86.45	653.15
3	3.41	84.89	646.08
4	3.19	78.76	608.88
5	3.09	96.36	715.53

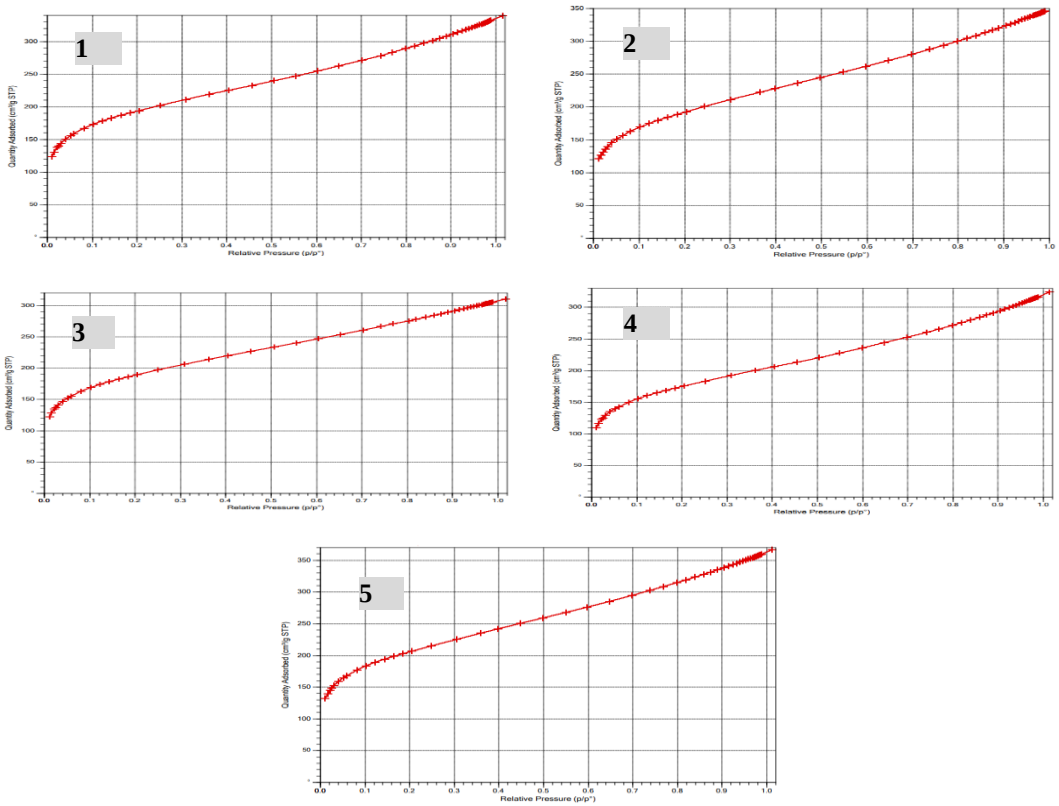

Figure 8. Adsorption-desorption isotherm curves of aerogel samples.

It can be said from Figure 9 that the N_2 adsorption isotherms of the produced aerogels comply with the combination of Type II and Type IV isotherms in the B.D.D.T. (Brunauer, Deming, Deming and Teller) classification defined according to IUPAC (International Union of Pure and Applied Chemistry, 1985). This indicates that aerogels have advanced micro and primary mesopores whose radii are between 2nm and 50 nm.

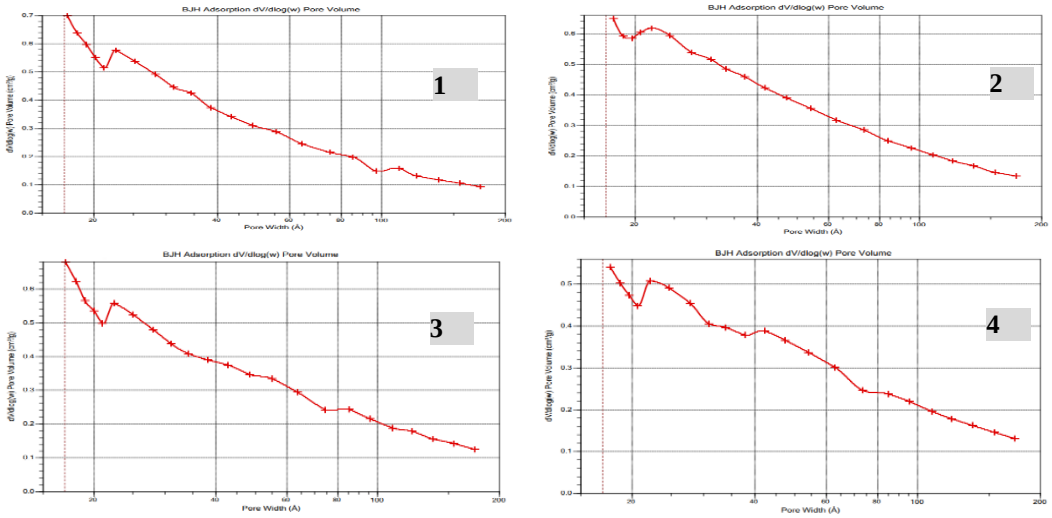

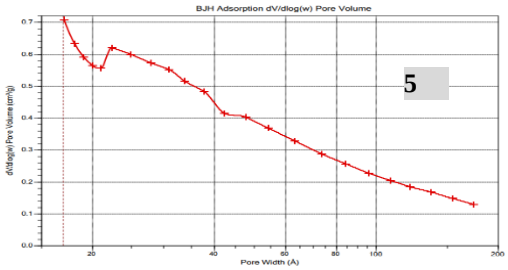

Figure 9. Space distribution curves of synthesized aerogel samples.

4. Conclusion and Suggestions

In this study, five different syntheses were applied for the production of aerogels; the necessary tests were performed, and the determined data were analyzed. According to the results obtained, it was determined that the densities of the aerogels produced were in the range of 0.66 to 1.053 g/mL, and the thermal conductivity values were in the range of 0.067 to 0.097 W/mK. Due to the thermal conductivity values of the samples formed being below 0.1 W/mK, they can be used as an insulating material. In addition, the increase in TEOS and TMOS concentrations during the production phase has led to an increase in the density and thermal conductivity of aerogel samples. To solve the problem, the integration of a carbon dioxide drainage line for solvent removal provided partial improvements. Due to the large internal volume of the reactor and, in particular, the inability to control the temperature stages precisely, the structural effects of different pressure-temperature transition processes have affected the approach to the targeted thermophysical properties. Factors such as the fact that the drying process is carried out under high-pressure conditions such as 100 bar, the long and arduous preparation process, and the high cost of the chemicals used have limited the number of solution trials. As a result of this study conducted with limited facilities, it is thought that if the necessary supports are provided, many opportunities are available to improve the insulation property of aerogel, which is considered an important insulation material of the future.

Contributions of the authors

M.Z. IŞIK and M. KAYIR conceived of the presented idea. H. OKTAY developed the theory and H. SAYĞILI performed the test. M.Z. IŞIK and H. OKTAY verified the analytical methods. M.Z. IŞIK encouraged M. KAYIR to investigate [a specific aspect] and supervised the findings of this work. All authors discussed the results and contributed to the final manuscript.

Conflict of Interest Statement

There is no conflict of interest between the authors.

Statement of Research and Publication Ethics

The study is complied with research and publication ethics

References

[1] A. Enes, "Silika Aerojel Sentezinde Farklı Katalizör Kullanımının Etkisi ve Adsorpsiyon Kapasitesinin Belirlenmesi," Gazi Üniversitesi, Ankara, 2019.

[2] R. Baetens, B. P. Jelle, and A. Gustavsen, "Aerogel insulation for building applications: A state-of-the-art review," *Energy Build.*, vol. 43, no. 4, pp. 761–769, 2011.

[3] N. K. Mermer, "Silika Temelli Aerojellerin Sol-Jel Yöntemi ile Sentezi ve Yapısal Özelliklerin İncelenmesi," Yıldız Teknik Üniversitesi, Istanbul, 2018.

[4] N. Saraç, "Silika esaslı doğal hammadde ve atıklardan aerojel tozu üretimi ve karakterizasyonu," Sakarya Üniversitesi, Sakarya, 2018.

[5] T. Li and T. Wang, "Preparation of silica aerogel from rice hull ash by drying at atmospheric pressure," *Mater. Chem. Phys.*, vol. 112, no. 2, pp. 398–401, 2008.

[6] Y. Yilmaz, "Farklı başlangıç maddeleri kullanılarak sol-jel yöntemiyle monolitik silika aerojel ve silika aerojel sentezi ve karakterizasyonu," Gazi Üniversitesi, Ankara, 2013.

[7] Z. Li, X. Cheng, L. Gong, Q. Liu, and S. Li, "Enhanced flame retardancy of hydrophobic silica aerogels by using sodium silicate as precursor and phosphoric acid as catalyst," *J. Non Cryst. Solids*, vol. 481, pp. 267–275, 2018.

[8] S. M. Jones, "Aerogel: Space exploration applications," *J. Solgel Sci. Technol*., vol. 40, no. 2–3, pp. 351–357, 2006.

[9] N. Siyin, "Yüksek Sıcaklık Isı Yalıtım Uygulamalarına Yönelik Üstün Performanslı Aerojel Şilte Sentezi ve Karakterizasyonu," İstanbul Teknik Üniversitesi, İSTANBUL, 2016.

[10] S.-W. Hwang and S.-H. Hyun, "Capacitance control of carbon aerogel electrodes," *J. Non Cryst. Solids*, vol. 347, no. 1–3, pp. 238–245, 2004.

Bitlis Eren Üniversitesi Fen Bilimleri Dergisi
BİTLİS EREN UNIVERSITY JOURNAL OF SCIENCE
ISSN: 2147-3129/e-ISSN: 2147-3188
VOLUME: 12 NO: 4 PAGE: 1160-1170 YEAR: 2023
DOI:10.17798/bitlisfen.1349138

Comparison of Antioxidant Activity, Metal Chelating Power and Antibacterial Activity in Different Tissues of Alcea calvertii (Boiss.) Boiss

Ayse Gozde BICEK[1], Deniz IRTEM KARTAL[2], Fevzi OZGOKCE[3], Tugba OZAKTAS[4*]

[1]*Institute of Natural and Applied Sciences, Van Yüzüncü Yil University, Van, Türkiye*

[2]*Department of Molecular Biology and Genetics, Division of Molecular Biochemistry, Faculty of Science, Van Yüzüncü Yil University, Van, Türkiye*

[3]*Department of Molecular Biology and Genetics, Division of Bioinformatics, Faculty of Science, Van Yüzüncü Yil University, Van, Türkiye*

[4]*Department of Molecular Biology and Genetics, Division of Microbiology, Faculty of Science, Van Yüzüncü Yil University, Van, Türkiye*

(ORCID: 0000-0003-4358-9962) (ORCID: 0000-0001-9669-5828)
(ORCID: 0000-0002-3119-8561) (ORCID: 0000-0001-8091-0909)

Keywords: *Alcea calvertii*, Total Phenolic Content, Total Flavonoid Content, Metal Chelating Power, Antibacterial Activity, Traditional Medicine.

Abstract

The traditionally used plant *Alcea calvertii* (Boiss.) Boiss. (Malvaceae) was extracted by two more methods in addition to those used by the locals, in this study. It was found that ethanol extraction significantly improved the release of total phenolic content of all plant parts compared to extraction by infusion and traditional use. In addition, ethanol appears to be a good solvent for the extracting flavonoids and phenolic contents from *A. calvertii*. However, metal chelating power was found to be higher in the infusion extracts than in the ethanolic extracts. The antibacterial activities of all extracts from the plant parts were also tested. As a result, it has been confirmed in this study that *A. calvertii* is rich in phenolic compounds and flavonoids and has high antioxidant activity with strong metal chelating power, however, the right plant parts must come together with the right extraction method for this effect to occur.

1. Introduction

Plants have an antioxidant effect that neutralizes free radicals because they contain phytochemicals and secondary metabolites. This fact makes plants a potential natural source for the production of new drugs [1]. Flavonoids and phenols are included the most important bioactive compounds in addition to alkaloids, saponins, and tannins in plants [2], [3]. Polyphenols are multiple phenol groups (i.e., aromatic rings with hydroxyl groups) derived from L-phenylalanine [4], and the most important are phenolic acids, containing polymeric structures, such as hydrolyzing tannins, lignans, stilbenes, and flavonoids. The vast number of flavonoids, including flavonols, flavones, isoflavones, flavanones, and anthocyanidins, are also important for their antioxidant and antimicrobial activities [5], [6].

Alcea calvertii (Boiss.) Boiss. (Malvaceae), locally known as hatmi and hiro, has been used in traditional medicine to treat or alleviate various diseases or ailments [7] - [9]. Especially the flowers are boiled with water and used in various ways in Anatolia. Malvaceae family is known for its high antioxidant potential [10], [11]. It is known that many of the plants belonging to the genus *Alcea* L. have ethnomedicinal and biological properties associated

* Corresponding author: tugbaozaktas@yyu.edu.tr
Received:24.08.2023, Accepted:30.10.2023

with antiviral [12], [13], anti-inflammatory, diuretic, astringent, demulcent, febrifugal, circulatory [14], antidiarrheal [15], and antimicrobial activity [16]. Recent studies have shown that *A. calvertii* the flower part or the aerial part of the plant has antioxidant activity [17], [18]. However, the antioxidant properties of four different tissues of *A. calvertii* have not been studied separately. The present study, therefore, aimed to (I) determine the antioxidant capacity of different tissues of *A. calvertii* (Boiss.) Boiss; (II) evaluate the effects of different extraction methods on total phenolic content, total flavonoid content, metal chelation and antibacterial activity in these plant tissues.

2. Material and Method

2.1. Extraction of Plant Sample

Plants used in the study were collected in Catak, Van, Türkiye (38°08'29.3"N 43°10'24.4"E), in July 2020. The GPS location of *A. calvertii* is shown in Figure 1. The specimen was assigned a reference number (F15268) and stored in the VANF Herbarium unit (VANF-20298) of Van Yüzüncü Yil University (Van YYU). The identification of the species was confirmed as *Alcea calvertii* (Boiss.) Boiss. by Van YYU botanist Prof. Dr. Fevzi Ozgokce. Plant specimens were purified from soil and other substances and dried for 6 days at room temperature (RT) at shade. Flowers, seeds, roots, and leaves were separated and cut into small pieces. The plant extract was obtained by three different methods: (I) In the method using ethanol as solvent: 10 g of each plant part was mixed separately with 75 mL of hexane and stirred at 40 °C for 18 hours. After the hexane was filtered, 75 mL of ethanol was added to the extract remaining in the tube and incubated for 48 hours at 4 °C in the dark. The ethanol was removed by evaporation. Then, 75 mL of dH_2O was added to the extract and incubated at 40 °C for 48 hours. After the dH_2O of the mixture was filtered, it was stored horizontally overnight at -80 °C. In order to remove the water from the samples, they were kept in a lyophilizer for 72 hours. The dried samples were stored at -20°C for the subsequent experimental steps. (II) In the infusion method, the prepared plant parts were boiled separately in a closed system. After the obtained extract was kept at -80 °C for at least 48 hours, the water was removed from the samples using the lyophilizer. The extract was stored at -20 °C for further experiments.

The efficiency of the samples in both extraction methods was calculated using the following equation:

Percentage of Plant Extract (w/w) = (Mass of Dried Extract) / (Total Mass of Sample) x 100 (1)

(III) In the traditional method, the prepared plant parts were boiled separately in a closed system and passed through a filter paper. The resulting liquid fraction was used for the experimental steps.

2.2. Measurement of Total Phenolic Content

Total phenolic content (TPC) in the extracts of plant tissues was determined using the Folin-Ciocalteu method [19]. For each plant part, 20 µL of the extract was mixed with 20 µL of the 25% Folin-Ciocalteu reagent. Then 80 µL of 10% Na_2CO_3 was added and left in the dark at RT for 30 minutes. The absorbance of the samples was measured at 750 nm using a microplate reader. TPC was expressed as mg GAE/ g plant part using the equation derived from a calibration curve of gallic acid (GA). All samples were measured in triplicate.

2.3. Measurement of Total Flavonoid Content

The method to determine the Total flavonoid content (TFC) of tissue extracts was adapted from Zhishen *et al.* [20]. For each plant part, 20 µL of the plant extract was mixed with 80 µl dH_2O and 6 µl of 5% $NaNO_2$. This mixture was incubated for 5 minutes at RT. Then 6 µL $AlCl_3$ was added and incubated for another 6 minutes 40 µL 1M NaOH was added and the total volume was made up to 200 µl with dH_2O. Measurements were made at 415 nm for quercetin and 510 nm for catechin using a microplate reader. TFC was expressed as mg quercetin equivalent (QE)/ g plant part and mg catechin equivalent (CE)/ g plant part using the equation derived from a calibration curve of quercetin and catechin, respectively. All samples were measured in triplicate.

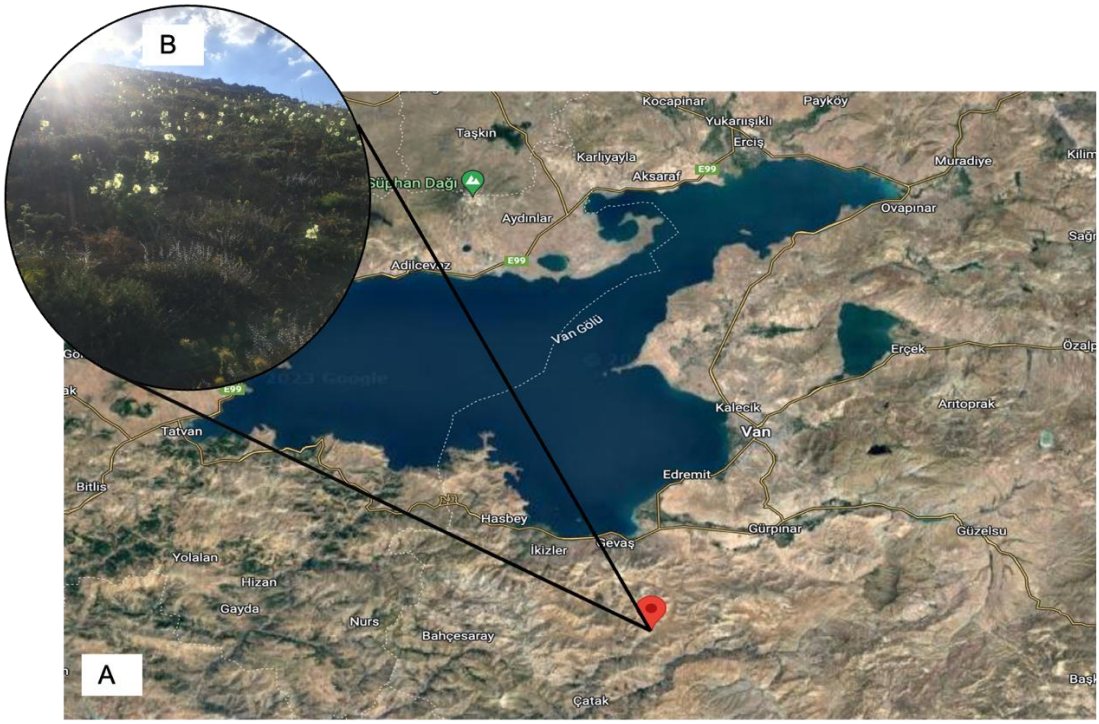

Figure 1. The location where the plant was collected (A) and the natural distribution of *A. calvertii* (Boiss.) Boiss. in the area (B)

2.4. Measurement of Metal Chelating Activity

The metal chelating activity of the plant parts was determined according to a modified method of Dinis *et al.* [21]. For each plant part, 40 µL of the plant extract was mixed with 8 µL of 5 mM ferrozine and 4 µL of 2 mM $FeCl_2$. The total volume was then made up with absolute methanol and incubated for 10 minutes at RT. The absorbance was measured at 562 nm in a microplate reader after 200 µL of the mixture was added in triplicate to 96-well plates.

Percentage inhibition of the EDTA chelating agent and samples was calculated as follows:

$$\% \text{ Inhibition} = (Abs_{blank}-Abs_{sample})/ (Abs_{blank}) \times 100 \quad (2)$$

where Abs_{blank} is the absorbance of the negative control and Abs_{sample} is the absorbance of the sample or reference.

2.5. Determination of Antibacterial Activity

Determination of antibacterial activity of the plant extracts different reference bacterial strains (*Escherichia coli* ATCC 35213, *E. coli* ATCC 35218, *Staphylococcus epidermidis* ATCC 12228, *Bacillus cereus* DSM 22648) were studied. Bacterial cell densities were adjusted with an optical density of 0.5 according to the McFarland standard. Bacterial suspensions were inoculated on Mueller-Hinton agar (MHA). Sterile filter paper disks were impregnated with different concentrations of each tissue. Discs impregnated with dH_2O were used as negative control and Ampicillin (5 µg/ mL) and Kanamycin (5 µg/ mL) were used as positive control. MHA plates were incubated for 24 hours at 37°C. The diameters of inhibition zones were measured in mm. The experiments included three replicates.

2.6. Statistical Analysis

Statistical analyses were performed using GraphPad Prism (v.9.0) software. One-way ANOVA was used to compare more than two groups in the analyses. T-test was used for pairwise comparison of the plant parts. *p* values <.05 were considered significant.

3. Results and Discussion

3.1. Yield of the Ethanolic Extracts and the Infusion Extracts

The mass and percent yield of the ethanolic and the infusion extracts from seed, flower, leaf, and root parts of *A. calvertii* are given in Table 1. In the traditional method, no dry extract was used, but only a liquid extract, as this is the form used by the locals. For this reason, the mass and percentage yield were not calculated in the traditional extraction method used in the study. The dried plant extract in the plant tissues obtained by ethanol extraction ranged from 8.93% to 40.76%; the same value was found between 0.62% and 47.37% for the extracts obtained by infusion method. The highest yields of both extractions were obtained from the seed part of the plant. The yields of leaves in ethanol extraction and infusion method were 13.50% and 22.32%, respectively. The lowest yield was found in the flower part (8.93%) in the ethanolic extracts, while the lowest yield was found in the root (0.62%) in the infusion extracts. However, since the mucosity was too high in the flowers in the infusion method, the yield of the flowers could only be calculated for the ethanol extraction.

Table 1. Mass and percentage yield of dried extract of different tissues of *A. calvertii*

Extract	Plant parts	Mass of dried extract (g)	Percentage yield (%)
Ethanol	Seed	0.92	40.76
	Flower	0.89	8.93
	Leaf	1.35	13.50
	Root	1.27	12.73
Infusion	Seed	0.73	47.37
	Leaf	1.12	22.32
	Root	0.03	0.62

According to Wong and Chye [22], compounds with structures containing hydroxyl and carboxyl groups, such as phenolic acids, lignans, flavonoids, are easily extracted by polar solvents. It is also known that reducing the particle size facilitates solvent extraction [23] and significantly increases the yield due to better extractability [22]. However, Amin *et al.* [24] reported that the extracts were affected by the polarity of the extraction medium, which could selectively determine the type of phenolic groups extracted, whether in the form of glycosides or bound to the cell wall. In this study, yield was calculated for the first time for *A. calvertii* and even for the genus *Alcea*; therefore, no comparative data are available. As a result, there were differences in yield by extraction methods for all plant parts except seed. Ghisalberti [25] interpreted that an alcoholic medium allows a greater amount of endocellular material to be extracted because it damages cell membranes. However, in this study, the yield was higher for the infusion method, which does not contain alcoholic medium, than for the ethanolic extracts for all tissues.

3.2. The Effect of Different Extraction Methods on the Total Phenolic Content

The TPC of different tissues of *A. calvertii* extracted by three methods, as determined by the Folin–Ciocalteu colorimetric method, is shown in Tables 2 and 3. The TPC in the extracts was calculated using the regression equation (y=9.923x; R^2=0.9988) of the calibration curve. The highest amount was found in the ethanol extract of flowers (674.55 mg gallic acid equivalent (GAE)/ g), the lowest amount was found in the traditionally extracted root (4.50 mg GAE/ g) in all measurements (Table 2). Table 3 also shows the comparisons of each plant tissue according to the extraction method. Thus, the TPC of ethanol extraction for leaves (519.55 mg GAE/ g) and roots (190.27 mg GAE/ g) was significantly higher than for other extraction methods. In terms of seeds, both ethanol (260.89 mg GAE/ g) and infusion (296.16 mg GAE/ g) were found to be significantly higher than the traditional method (8.02 mg GAE/ g). Also, the flowers extracted with ethanol (674.55 mg GAE/ g) had a significantly higher TPC than the traditionally extracted flowers (55.75 mg GAE/ g).

It is known that the biologically active compounds in plants are responsible for their antioxidant activity. Phenols are important constituents that acts as radical scavengers due to their hydroxyl groups and thus can directly contribute to the antioxidant activity [22]. In this study, the highest amount of TPC was found in the ethanol extract of flowers (674.55 mg GAE/ g) and the second highest value in the ethanol extraction of leaves (519.55 mg GAE/ g). Based on the extraction methods, the leaves extracted by infusion and traditional methods had higher TPC values than other parts of the plant, with values of 407.08 and 232.98 mg GAE/ g, respectively.

Previous research related to *A. calvertii* found the highest TPC value in all extractions for the water extract of flowers (65.06 mg GAE/ g) [17]; this value is similar to our result of traditional extraction of flowers (55.75 mg GAE/ g). However, our results of ethanol extraction of flowers were much higher (674.55 mg GAE/ g) compared to their ethanolic extract of flowers, which contained only 31.79 mg GAE/ g, because the two ethanol extraction methods differed from each other. According to another study with *A. calvertii* [18], water extraction of the whole upper parts of plant contained lower TPC than methanol extraction, which is similar to our extraction classification; however, their value was very low (64.17 µg GAE/ g).

The seed and root parts of all three extractions had lower TPC compared to the flowers and leaves. On the other hand, opposite results were found for the TPC of seeds in other species of the genus *Alcea*. For example, although methanol extraction showed the highest value for seed extracts compared to flower and leaf extracts of *A. hyrcana* Grossh [26], the values were lower than the result of this study. Moreover, the amount of total phenolics in all our seed extracts varied from 8.02 to 296.16 mg GAE/ g, while the other study [10] found higher values of as 149.01 and 412.23 mg GAE/ g in both water and methanol extracts, respectively. The discrepancy in the values of the same plant parts might be due to the different origin of the samples, harvest period, storage time, the difference in species and different extraction methods. Polar components such as phenolic compounds in plants can be easily extracted with a polar solvent such as water [22], [27]. Moreover, according to Guler [28], these molecules have strong antioxidant capacities as they can stop the formation of free radical chain reactions in the presence of hydroxyl groups that act as reducing agents.

3.3. The Effect of Different Extraction Methods on the Total Flavonoid Content

Two flavonoids, catechin and quercetin, were used as standards to determine the TFC in different tissues of *A. calvertii*. The TFC in the plant extracts was calculated from the regression equations (y= 0.0013x; R^2= 0.9996 for quercetin, y=0,0011x; R^2= 0.9995 for catechin) of the calibration curves. TFC values differed significantly for almost all plant parts studied (Table 2) and for each extraction method (Table 3). When considering QE, the highest values in TFC were found for the flowers (1784.52 mg QE/ g) of ethanolic extract, and the lowest in the traditionally extracted roots (26.50 mg QE/ g). Considering the values of CE, the TFC value was highest in the roots extracted with ethanol (1237.78 mg CE/ g), followed by the flowers extracted with ethanol (1061.10 CE/ g). The lowest TFC value was found in the traditionally extracted roots (16.14 mg CE/ g). In addition, significant differences were found in the TFC values of the different parts of the plant. Thus, the ethanolic extracts showed the highest values for leaf and root parts, while the traditional method gave the lowest values. The TFC content of flower was significantly higher in ethanol extraction (1784.52 mg QE/ g; 1061.10 mg CE/ g) than in traditional extraction (446.36 mg QE/ g; 187.22 mg CE/ g).

Flavonoids have radical-scavenging activity due to their hydroxyl group acting as proton donor [29]. The TFC values in *A. calvertii* differ depending on the extraction method. This could be because the flavonoids have different structural types. In addition, there are numerous bioactive compounds with different activities in the extracts [29]. In accordance with the previous study with *A. calvertii* [17], the highest TFC value for CE among the different extractions was found for the methanol extraction of the flowers while in our study, the highest value was obtained from the ethanol extraction of flowers. Moreover, this value was about 1000 times higher than the value obtained in their study. Zakizadeh *et al.* [26] reported that methanol extraction of leaves of *A. hyrcana* had a higher TFC value than extraction of seeds and flowers; these results were similar for hot water-based extractions (infusion and traditional extraction methods) in this study, whereas, in contrast, flowers had the highest TFC values in ethanolic extracts. Previous studies have shown that there is a linear relationship between antioxidant activity and phenolic and flavonoid content [30], [31], and the results of this study confirm this statement. The antioxidant activity of the extracts is affected by the variety of phytochemical content [32]. In the present study, the extracts from the different parts of *A. calvertii* exhibited high antioxidant activity. In particular, the ethanolic extracts were the most active fraction in almost all tissues (Table 3). The literature also reports that the polarity of ethanol is lower than that of water [33]. Furthermore, some flavonoids, such as O-methylated flavonoids, are considered to be less polar compounds compared to unmethylated flavonoids [34]. Moreover, some tissues in this study had comparatively low TPC but comparatively high TFC, for example the ethanolic extract of the root as 190.27 mg GAE/ g versus the ethanolic extract of the root as 871.43 mg QE/ g and 1237.78 mg CE/ g. These

results suggest that the main antioxidant components could be flavonoids in some tissues, while other phenolic compounds are in other tissues. Moreover, synergistic effects among bioactive compounds could influence the high level of antioxidant activity [35]. Our results were also confirmed by previous studies with other species of the genus *Alcea* [36] and some medicinal plants which that exhibited antioxidant activities with different levels of phenolic and flavonoid compounds [37], [38].

Table 2. TPC and TFC of three different extracts from the seeds, flowers, roots, and leaves of *A. calvertii*

Extract	Plant parts	TPC (mg GAE/g)	TFC (mg QE/ g)	TFC (mg CE/ g)
Ethanol	Seed	260.89 ^{a} ± 3.32	333.33 ^{a} ± 26.94	677.77 ^{a,b} ± 141.42
	Flower	674.55 ^{b} ± 6.36	1784.52 ^{b} ± 5.05	1061.10 ^{b} ± 7.86
	Leaf	519.55 ^{c} ± 12.84	1000.00 ^{c} ± 26.93	725.00 ^{a} ± 35.36
	Root	190.27 ^{d} ± 1.06	871.43 ^{c} ± 60.61	1237.78 ^{b} ± 144.57
Infusion	Seed	296.16 ^{a} ± 18.80	517.86 ^{a} ± 21.88	336.11 ^{a} ± 3.92
	Flower	-	-	-
	Leaf	407.08 ^{b} ± 12.40	895.24 ^{b} ± 26.93	416.66 ^{a} ± 39.29
	Root	38.78 ^{c} ± 0.05	160.71 ^{c} ± 1.68	161.11 ^{b} ± 0
Traditional	Seed	8.02 ^{a} ± 0.02	-	834.37 ^{a} ± 35.95
	Flower	55.75 ^{b} ± 2.01	446.36 ^{a} ± 1.51	187.22 ^{b} ± 9.42
	Leaf	232.98 ^{c} ± 23.70	845.56 ^{b} ± 1.04	366.83 ^{c} ± 5.56
	Root	4.50 ^{d} ± 0.05	26.50 ^{c} ± 6.07	16.14 ^{d} ± 0.21

All values are expressed as mean ± standard error of the mean (SEM) (n=3). Means with different superscripts indicate a significantly difference ($p < .05$) among different plant tissues extracted with the same method

Table 3. TPC and TFC of seed, flower, root, and leaf of *A. calvertii* for each extraction method

Plant parts	Extract	TPC (mg GAE/g)	TFC (mg QE/g)	TFC (mg CE/g)
Seed	Ethanol	260.89 ^{a} ± 3.32	333.33 ^{a} ± 26.94	677.77 ^{a,b} ± 141.42
	Infusion	296.16 ^{a} ± 18.80	517.86 ^{b} ± 21.88	336.11 ^{b} ± 3.92
	Traditional	8.02 ^{b} ± 0.02	-	834.37 ^{a} ± 35.95
Flower	Ethanol	674.55 ^{a} ± 6.36	1784.52 ^{a} ± 5.05	1061.10 ^{a} ± 7.86
	Traditional	55.75 ^{b} ± 2.01	446.36 ^{b} ± 1.51	187.22 ^{b} ± 9.42
Leaf	Ethanol	519.55 ^{a} ± 12.84	1000.00 ^{a} ± 26.93	725.00 ^{a} ± 35.36

	Infusion	407.08 ^{b} ± 12.40	895.24 ^{a,b} ± 26.93	416.66 ^{b} ± 39.29
	Traditional	232.98 ^{c} ± 23.70	845.56 ^{b} ± 1.04	366.83 ^{b} ± 5.56
	Ethanol	190.27 ^{a} ± 1.06	871.43 ^{a} ± 60.61	1237.78 ^{a} ± 144.57
Root	Infusion	38.78 ^{b} ± 0.05	160.71 ^{b} ± 1.68	161.11 ^{b} ± 0
	Traditional	4.50 ^{c} ± 0.05	26.50 ^{c} ± 6.07	16.14 ^{c} ± 0.21

All values are expressed as mean ± SEM (n=3). Means with different superscripts indicate a significant difference (p < .05) in the same plant tissue extracted by different methods

3.4. The Effect of Different Extraction Methods on Metal Chelating Power

The experiment was designed to determine whether the chelating activity of iron (II) (Fe^{2+}) is due to the chelation of this metal ion with ferrozine to form a red coloured complex. In the presence of other chelating agents, the formation of the iron (II)-ferrozine complex was impaired and the red colour of the complexes was reduced. Therefore, measuring the percent inhibition allows us to estimate the chelating power of iron [39]. Figure 2 shows the metal chelating power of the two extraction methods for tissues of *A. calvertii*. When comparing the ethanol extracts of the plant tissues, the leaves extract had the best chelating effect (52.20% at 0.5 mg/mL and 42.82% at 1 mg/mL), followed by the seed extract (44.57% at 0.5 mg/mL and 41.93% at 1 mg/mL), the root extract (39.39% at 0.5 mg/mL and 40.90% at 1 mg/mL), and finally, the flower extract (38.79% at 0.5 mg/mL). Similar results were obtained for the infusion extracts of the three parts studied. The leaf extract (57.27% at 0.5 mg/mL and 54.55% at 1 mg/mL) had the highest antioxidant activity, followed by the root extract (55.15% at 0.5 mg/mL and 53.03% at 1 mg/mL), and the seed extract (45.45% at 0.5 mg/mL and 43.64% at 1 mg/mL). However, at the same concentrations, the chelating effect of the synthetic metal chelator EDTA were recorded as 90.1% iron chelation percentage at 0.5 mg/mL and 91.46% at 1 mg/mL.

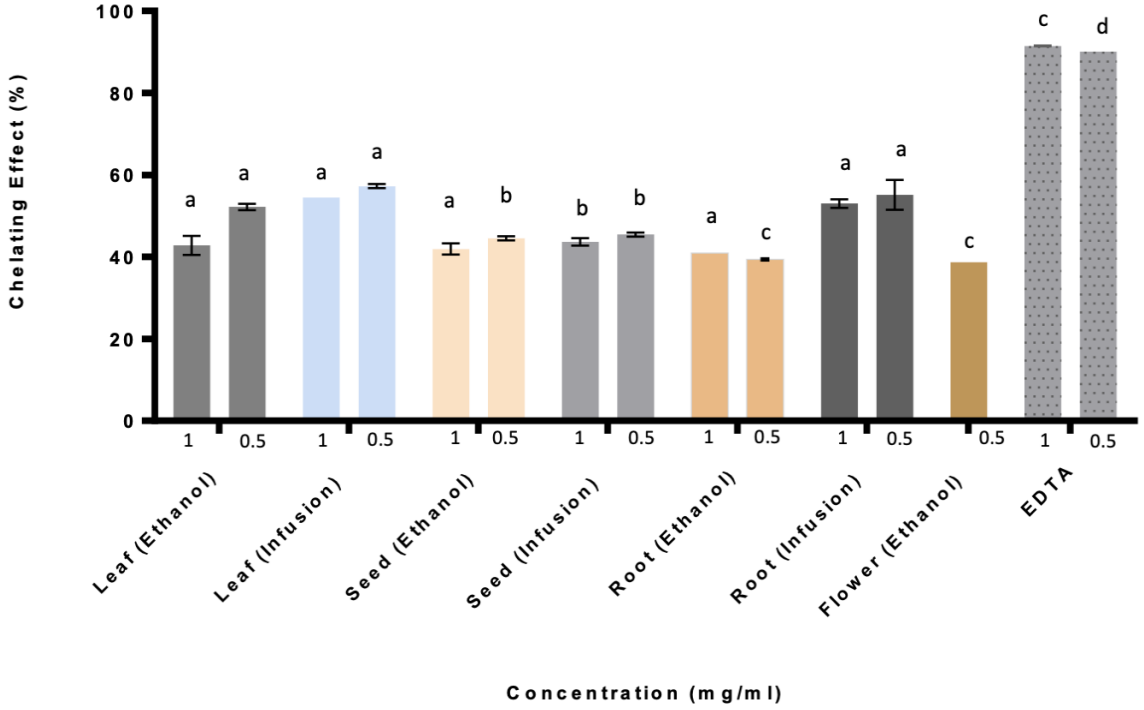

Figure 2. Metal chelating effect of ethanolic extracts and infusion extracts of the leaves, seeds, roots and flowers of *A. calvertii*. Each value is the mean ± SEM (n=3). Different letters indicate a significantly difference (p< .05) among different plant tissues extracted by the same method at the same concentration.

Halliwell [40] had explained that iron stimulates lipid peroxidation through the Fenton reaction and accelerates peroxidation by decomposing lipid hydroperoxides into peroxyl and alkoxyl radicals, which can abstract hydrogen and maintain the chain reaction of lipid peroxidation. According to the results, the chelating capacity of Fe^{2+} varied significantly among different plant parts. In addition, it was determined that infusion extraction was more effective than ethanol extraction for iron chelating capacities, especially in the leaf and root parts. However, Figure 2 shows that both extracts from all parts of *A. calvertii* exhibited pronounced iron binding capacity, suggesting that their effect as peroxidation protectants might be related to their iron binding capacity. It was also observed the increase in activity was proportional to the respective concentration in all extracts and all tissues. In a previous study with the whole upper parts of *A. calvertii*, in contrast to this study, a higher metal chelating activity was observed in the methanolic extract than in the water extract [18]. Moreover, methanolic extracts of leaves and flowers of *A. hyrcana* have been shown to have higher reducing power than the seeds [26]; however, in this study the ethanolic extracts of leaves were found to be higher than those of seeds and flowers. This may be due to the fact that the content of biologically active compounds differs even among species within the same genus, and that climatic and geographic structural characteristics of the soil affect these contents. Yuan *et al.* [41] reported that compounds with structures containing two or more of the functional groups -OH, -SH, -COOH, $-PO_3H_2$, C=O, $-NR_2$, -S and –O are suitable for metal chelation. Thus according to Bhandari and Kawabata [42], molecules containing organic acids and polyphenols can increase the chelating ability of the plant. Moreover, they prevent the formation of free radicals by chelating pro-oxidant metal ions such as iron and copper.

3.5. The Effect of Different Extraction Methods on the Antibacterial Activity

The antibacterial activity of seed, flower, leaf, and root parts of three different extracts obtained at different concentrations was tested by the disc diffusion method. However, no inhibitory activity was detected against the four tested bacteria (*E. coli* ATCC 35213, *E. coli* ATCC 35218, *S. epidermidis* ATCC 12228, *B. cereus* DSM 22648). Although the antibacterial effect has been described as weak or moderate in the literature in *A. calvertii* [16], [17] and other studies with other species of the genus *Alcea* [31], [43], there was no evidence of antibacterial effect in this study. The reason for the lack of effect may be due to the differences in the strains and species tested.

4. Conclusion and Suggestions

This study showed interesting results and indicated that the traditional use of *A. calvertii* has antioxidant potential. However, it was also emphasized that the extraction methods are important to fully determine the exact antioxidant capacity of the plant. In view of these experiments, it was concluded that the different tissues of the plant have different potential for TPC, TFC, and metal chelating power. The results showed that the ethanol extraction had higher efficacy on TPC and TFC in almost all parts of the plant compared to hot water-based extractions, while hot-water based extractions had higher efficacy only in the seeds. The infusion extraction was also found to be more effective than the ethanol extraction in terms of yield and metal chelating ability in the plant parts studied. Therefore, *A. calvertii* is considered as a potential source of natural antioxidants. However, it is important to choose an appropriate solvent and methodology variables to obtain the valuable result. In addition, the purified constituents could be even more effective in terms of their pharmacological abilities.

Acknowledgment

This work was supported by the [Scientific and Technological Research Council of Türkiye (TUBİTAK), 2209-A-2020-Research Project Support Program for Undergraduate Students] under Grant [number 1919B011903423]; the [Research Fund of the Van YYU] under Grant [number FHD-2022-10148]; and the [Research Fund of the Van YYU] under Grant [number FBG-2019-8381].

Contributions of the authors

Fevzi Ozgokce and Ayse Gozde Bicek collected plant materials and identified, Deniz Irtem Kartal and Ayse

Gozde Bicek designed extraction and antioxidant experiments. Tugba Ozaktas and Ayse Gozde Bicek conducted antibacterial experiments and wrote the manuscript. Tugba Ozaktas proofread the manuscript. Finally, all authors read and approved the manuscript.

Conflict of Interest Statement

There is no conflict of interest between the authors.

Statement of Research and Publication Ethics

The study is complied with research and publication ethics.

References

[1] N. Ibrahim, I. Mat, V. Lim, and R. Ahmad, "Antioxidant activity and phenolic content of Streblus asper leaves from various drying methods," *Antioxidants*, vol. 2, no. 3, pp. 156–166, 2013.

[2] M. Dash, J. K. Patra, and P. P. Panda, "Phytochemical and antimicrobial screening of extracts of Aquilaria agallocha Roxb," *Afr. J. Biotechnol.*, vol. 7, no. 20, pp. 3531–3534, 2008.

[3] H. Jemai, A. El Feki, and S. Sayadi, "Antidiabetic and antioxidant effects of hydroxytyrosol and oleuropein from Olive leaves in alloxan-diabetic rats," *J. Agric. Food Chem.*, vol. 57, no. 19, pp. 8798–8804, 2009.

[4] A.-M. Boudet, "Evolution and current status of research in phenolic compounds," *Phytochemistry*, vol. 68, no. 22–24, pp. 2722–2735, 2007.

[5] C. Manach, A. Scalbert, C. Morand, C. Rémésy, and L. Jiménez, "Polyphenols: food sources and bioavailability," *Am. J. Clin. Nutr.*, vol. 79, no. 5, pp. 727–747, 2004.

[6] A. Scalbert and G. Williamson, "Chocolate: Modern science investigates an ancient medicine. foreword," *J. Nutr*, vol. 130, no. 8, pp. 2073–2085, 2000.

[7] E. Altundag and M. Ozturk, "Ethnomedicinal studies on the plant resources of east Anatolia, Turkey," *Procedia. Soc. Behav. Sci.*, vol. 19, pp. 756–777, 2011.

[8] F. Naghibi, S. Esmaeili, M. Hassanpour, and A. Mosaddegh, "Ethnobotanical survey of medicinal plants used traditionally in two villages of Hamedan, Iran," *Iran. Res. J. Pharm.*, vol. 1, no. 3, pp. 7–14, 2014.

[9] M. Mosaddegh, S. Esmaeili, A. Hassanpour, M. Malekmohammadi, and F. Naghibi, "Ethnobotanical study in the highland of Alvand and Tuyserkan, Iran," *Iran Res. J. Pharm.*, vol. 3, no. 1, pp. 7–17, 2016.

[10] P. A. Dar, F. Ali, I. A. Sheikh, S. A. Ganie, and T. A. Dar, "Amelioration of hyperglycaemia and modulation of antioxidant status by *Alcea rosea* seeds in alloxan-induced diabetic rats," *Pharm. Biol.*, vol. 55, no. 1, pp. 1849–1855, 2017.

[11] N. A. Abdel-salam *et al.*, "Flavonoids of *Alcea rosea* L. and their immune stimulant, antioxidant and cytotoxic activities on hepatocellular carcinoma HepG-2 cell line," *Nat. Prod. Res.*, vol. 32, no. 6, pp. 702–706, 2018.

[12] K. Asres, F. Bucar, T. Kartnig, M. Witvrouw, C. Pannecouque, and E. De Clercq, "Antiviral activity against human immunodeficiency virus type 1 (HIV-1) and type 2 (HIV-2) of ethnobotanically selected Ethiopian medicinal plants," *Phytother. Res.*, vol. 15, no. 1, pp. 62–69, 2001.

[13] S. M. Seyyednejad, H. Koochak, E. Darabpour, and H. Motamedi, "A survey on Hibiscus rosa—sinensis, Alcea rosea L. and Malva neglecta Wallr as antibacterial agents," *Asian Pac. J. Trop. Med.*, vol. 3, no. 5, pp. 351–355, 2010.

[14] V. Tene, O. Malagón, P. V. Finzi, G. Vidari, C. Armijos, and T. Zaragoza, "An ethnobotanical survey of medicinal plants used in Loja and Zamora-Chinchipe, Ecuador," *J. Ethnopharmacol.*, vol. 111, no. 1, pp. 63–81, 2007.

[15] D. Hamdy and A. Hassabo, "Various natural dyes using plant palette in coloration of natural fabrics," *J.Text. Color. Pol. Sci.*, vol. 0, no. 0, pp. 0–0, 2021.

[16] B. K. G. N. Mehlika, B. l. Uuml mit, G. Fatmaguuml l, and Y. Nazife, "Antimicrobial activity of some endemic plant species from Turkey," *Afr. J. Biotechnol.*, vol. 6, no. 15, pp. 1774–1778, 2007.

[17] S. Keser *et al.*, "In vitro Antiradical, Antimicrobial and Antiproliferative Activities and Phytochemical Compositions of Endemic Alcea calvertii (Boiss) Boiss. Flowers," *Düzce Üniv. Bil. Teknol. Derg.*, vol. 8, no. 1, pp. 693–701, 2020.

[18] M. Abudayyak, Ş. Kanbolat, R. Ergene, Ş. Batur, and R. Aliyazicioğlu, "Investigation of the Biological

Activities of Alcea calvertii," *KSU J. Agric. Nat.*, vol. 25, no. 5, pp. 955–964, 2022.

[19] V. L. Singleton, R. Orthofer, and R. M. Lamuela-Raventós, "[14] Analysis of total phenols and other oxidation substrates and antioxidants by means of folin-ciocalteu reagent," *Meth. Enzymol.*, vol. 299, pp. 152–178, 1999.

[20] J. Zhishen, T. Mengcheng, and W. Jianming, "The determination of flavonoid contents in mulberry and their scavenging effects on superoxide radicals," *Food Chem.*, vol. 64, no. 4, pp. 555–559, 1999.

[21] T. C. Dinis, V. M. Maderia, and L. M. Almeida, "Action of phenolic derivatives (acetaminophen, salicylate, and 5-aminosalicylate) as inhibitors of membrane lipid peroxidation and as peroxyl radical scavengers," *Arch. Biochem. Biophys.*, vol. 315, no. 1, pp. 161–169, 1994.

[22] J. Y. Wong and F. Y. Chye, "Antioxidant properties of selected tropical wild edible mushrooms," *J. Food Compost. Anal.*, vol. 22, no. 4, pp. 269–277, 2009.

[23] F. Bonilla, M. Mayen, J. Merida, and M. Medina, "Extraction of phenolic compounds from red grape marc for use as food lipid antioxidants," *Food Chem.*, vol. 66, no. 2, pp. 209–215, 1999.

[24] I. Amin, Y. Norazaidah, and K. I. E. Hainida, "Antioxidant activity and phenolic content of raw and blanched Amaranthus species," *Food Chem.*, vol. 94, no. 1, pp. 47–52, 2006.

[25] E. L. Ghisalberti, "Detection and isolation of bioactive natural products," *Bioact. Nat. Prod.*, 25-90, CRC Press, 1993.

[26] M. Zakizadeh, S. F. Nabavi, S. M. Nabavi, and M. A. Ebrahimzadeh, "In vitro antioxidant activity of flower, seed and leaves of Alcea hyrcana Grossh," *Eur. Rev. Med. Pharmacol. Sci.*, vol. 15, no. 4, pp. 406–412, 2011.

[27] M. S. M. Sopee, A. Azlan, and H. E. Khoo, "Comparison of antioxidants content and activity of Nephelium mutabile rind extracted using ethanol and water," *J. Food Meas. Charact.*, vol. 13, no. 3, pp. 1958–1963, 2019.

[28] G. O. Guler, "Studies on antioxidant properties of the different solvent extracts and fatty acid composition of Hyoscyamus reticulatus L," *J. Food Biochem.*, vol. 36, no. 5, pp. 532–538, 2012.

[29] K. Ghasemi, Y. Ghasemi, and M. A. Ebrahimzadeh, "Antioxidant activity, phenol and flavonoid contents of 13 citrus species peels and tissues," *Pak. J. Pharm. Sci.*, vol. 22, no. 3, pp. 277–281, 2009.

[30] S. Silva, L. Gomes, F. Leitão, A. V. Coelho, and L. V. Boas, "Phenolic compounds and antioxidant activity of *Olea europaea* L. fruits and leaves," *Food Sci. Technol. Int.*, vol. 12, no. 5, pp. 385–395, 2006.

[31] A. Ertas *et al.*, "Fatty acid, essential oil and phenolic compositions of Alcea pallida and Alcea apterocarpa with antioxidant, anticholinesterase and antimicrobial activities," *Chiang Mai J. Sci.*, vol. 43, no. 1, pp. 89–99, 2016.

[32] M. Ong, S. Mat Yusuf, and V. Lim, "Pharmacognostic and Antioxidant Properties of Dracaena sanderiana Leaves," *Antioxidants*, vol. 5, no. 3, p. 28, 2016.

[33] M. Rosas, C. Rafols, J. Ortega, and E. Bosch, "Solute- solvent and solvent-solvent interactions in binary solvent mixtures. Part 1. A comparison of several preferential solvation models for describing ET (30) polarity of bipolar hydrogen bond acceptor-cosolvent mixtures," *J. Chem. Soc. Perkin Trans.*, vol. 2, no. 8, pp. 1607–1615, 1995.

[34] Ö. V. Rúnarsson *et al.*, "Antibacterial activity of methylated chitosan and chitooligomer derivatives: Synthesis and structure activity relationships," *Eur. Polym. J.*, vol. 43, no. 6, pp. 2660–2671, 2007.

[35] L. R. Saikia and S. Upadhyaya, "Antioxidant activity, phenol and flavonoid content of some less known medicinal plants of assam," *Int. J. of Pharma Bio Sci.*, vol. 2, no. 2, pp. 383–388, 2011.

[36] Y. Pirmohammadi, S. Asnaashari, H. Nazemiyeh, and S. Hamedeyazdan, "Bioactivity assays and phytochemical analysis upon Alcea glabrata; focusing on xanthine oxidase inhibitory and antimalarial properties," *Toxicon*, vol. 229, no. 107140, p. 107140, 2023.

[37] E. Karimi, H. Z. E. Jaafar, and S. Ahmad, "Phytochemical analysis and antimicrobial activities of methanolic extracts of leaf, stem and root from different varieties of labisa pumila Benth," *Molecules*, vol. 16, no. 6, pp. 4438–4450, 2011.

[38] M. Krishnaveni, P. Madhaiyan, S. Durairaj, L. Amsavalli, and R. Chandrasekar, "Antioxidant activity of plants at Chinnatirupathi, Salem, Tamil Nadu, India," *Int. J. Pharma. Sci. Res.*, vol. 4, no. 10, 2013.

[39] S. Ouahhoud *et al.*, "Antioxidant activity, metal chelating ability and DNA protective effect of the hydroethanolic extracts of Crocus sativus stigmas, tepals and leaves," *Antioxidants*, vol. 11, no. 5, pp. 932, 2022.

[40] B. Halliwell, "Reactive oxygen species in living systems: Source, biochemistry, and role in human disease," *Am. J. Med.*, vol. 91, no. 3, pp. S14–S22, 1991.

[41] Y. V. Yuan, D. E. Bone, and M. F. Carrington, "Antioxidant activity of dulse (Palmaria palmata) extract evaluated in vitro," *Food Chem.*, vol. 91, no. 3, pp. 485–494, 2005.

[42] M. R. Bhandari and J. Kawabata, "Organic acid, phenolic content and antioxidant activity of wild yam (Dioscorea spp.) tubers of Nepal," *Food Chem.*, vol. 88, no. 2, pp. 163–168, 2004.

[43] A. Azab, "Alcea: Traditional medicine," *Cur. Res. Fut. Op.*, vol. 5, pp. 505–514, 2016.

Bitlis Eren Üniversitesi Fen Bilimleri Dergisi
BİTLİS EREN UNIVERSITY JOURNAL OF SCIENCE
ISSN: 2147-3129/e-ISSN: 2147-3188
VOLUME: 12 NO: 4 PAGE: 1171-1184 YEAR: 2023
DOI:10.17798/bitlisfen.1358965

Evaluation of Road Roughness and Vehicle Speed Effects on Vibration Comfort of School Bus Driver Seats following the ISO 2631-1 Standard and Occupational Health and Safety Legislation

Akif YAVUZ[1], Suleyman Enes HACIBEKTASOGLU[2*]

[1]*Istanbul Technical University Department of Mechanical Engineering, Istanbul, Türkiye*
[2]*Sinop University Department of Occupational Health and Safety, Sinop, Türkiye*
(ORCID: 0000-0002-9447-7306) (ORCID: 0000-0002-8997-8480)

Keywords: School bus driver, Vehicle seat comfort, Road roughness, Seat vibrations, Occupational health and safety

Abstract
Human perception in terms of vehicle comfort problems is a significant issue for automotive manufacturers and academic researchers, as evident from the scientific papers available in the literature. In this study, the maximum vehicle speed is predicted for the comfortable driving of school bus drivers under certain working conditions. First, a full-vehicle school bus model, which consists of a seat, vehicle body, wheels, and suspension systems, is developed to evaluate vehicle seat comfort following ISO 2631-1 and Occupational Health and Safety (OHS) legislation. Second, the experimentally collected power spectrum densities of road roughness are converted to amplitude form in order to be an input to the developed full-vehicle model. Third, the frequency weighting factor, which is determined by ISO 2631-1, is applied to the calculated RMS acceleration of the seat. Finally, frequency-weighted RMS accelerations of the seat for various conditions of road roughness and vehicle speeds are obtained, and they are used to evaluate the bus driver seat comfort by ISO 2631-1. In addition, RMS accelerations of the bus driver seat are used to evaluate vehicle seat comfort by OHS legislation. It is concluded that the effects of vehicle speed and road roughness on comfortable driving are observed, and maximum vehicle speed for comfortable driving decreases as the power spectrum density of road roughness increases. According to the results, measures to be taken following the OHS legislation are suggested.

1. Introduction

Vibration-induced vehicle problems are a considerably significant issue regarding human health and comfort. Nowadays, many automotive companies aim to minimize tiredness and discomfort during long journeys due to vehicle seat vibrations. Therefore, studies in the literature about vehicle comfort problems have investigated that vehicle seat vibrations in the normal direction cause health problems for drivers and passengers. Long-duration and high-amplitude vibrations have physiological and psychological problems for humans, such as motion sickness and discomfort. Many automotive manufacturers and academic researchers have been working for a long time to reduce the amplitude of seat vibrations [1]-[3].

With the OHS activities carried out in the workplace, employers aim to ensure that the employees are in a state of complete physical and mental well-being. In this context, it is necessary to determine the hazards in the working environment and the risks arising from these hazards. Employers are obliged to take measures to eliminate these determined risks or to bring them to an acceptable level in accordance with the OHS regulations. For this purpose, the risk assessment studies to be carried out in the workplaces should be applied in detail with a risk analysis method that is suitable for the workplace, and the precautions to be taken should be determined [4]-[7].

*Corresponding author: shacibektasoglu@sinop.edu.tr
Received: 12.09.2023, Accepted: 11.12.2023

Vibration is one of the physical risk factors that employees are exposed to due to the machinery and equipment they use in the workplace. Based on the type of work, they are exposed to hand-arm or whole-body vibration. As a result of this exposure, employees experience various health problems, especially in the musculoskeletal system. In Türkiye, in accordance with the Occupational Health and Safety Law No. 6331, which was enacted in 2012, employers are obliged to carry out risk assessments to ensure the safety and health of employees at workplaces. In addition, according to the regulation of vibration enacted in accordance with this law, the limit values to which employees can be exposed to different types of vibration are given in Table 1. Vibration exposure values should be determined with the measurements, and these values should be reduced to an acceptable level with the precautions for inappropriate values [8]-[12].

Table 1. Exposure values for exposure types in accordance with OHS regulations [8]

Types of Exposure	**Exposure Action Value (m/s^2)**	**Exposure Limit Value (m/s^2)**
Hand-Arm Vibration	2,5	5
Whole Body Vibration	0,5	1,15

The oscillations on the vehicle body due to road excitations are generally between the frequencies of 0 Hz and 25 Hz [13]. The road roughness, which is an input of vehicle system dynamics, is transferred to the wheel, and then it is transmitted to the axle body with the elastic parts of the vehicle [14]. Synthetic road profiles, depending on ISO 8608 classifications, are commonly used for simulating various tasks in vibration analysis. Múčka's study compared these synthetic road classes with real road spectra and found significant differences [15]. There are also many studies in the field of road surface [16]-[18]. In addition to the road roughness, driving characteristics and the transmission path of vibration, which is a characteristic for transferring vibration signals from road excitation to the seat, cause discomfort while driving. Vehicle comfort, corresponding to seat vibrations in the vertical direction, is a significant parameter that affects the driver's health. In order to evaluate the vehicle's comfort related to the driver seat, rms vertical acceleration data in the time domain of the driver seat is used as an identification parameter of comfort [19]. The effects of vertical seat acceleration amplitudes on comfortable driving were investigated by an analytical model of the selected vehicle [20]. To evaluate the vehicle comfort, in addition to the acceleration data from the seat, International Standardization Organization (ISO) 2631-1 is also implemented. ISO 2631-1 was developed under the purview of the Technical Committee ISO/TC 108, which is responsible for matters related to mechanical vibration and shock. The principal objective of ISO 2631-1 is to delineate quantitative methodologies pertaining to whole-body vibration, encompassing aspects related to human health, comfort, the discernibility of vibration, as well as the potential effects of vibration on the occurrence of health-related issues, as referenced in [21]. Using ISO 2631-1 to evaluate the comfort of a vehicle seat in the vertical direction is a widely performed method in terms of vibration data. The criteria of rms acceleration and frequency-weighted transformations in ISO 2631-1 are considered a method of vehicle comfort evaluation.

In this study, a full vehicle vibration model, which has eight degrees of freedom, is developed to investigate the effect of vehicle speed and road roughness on comfortable driving in accordance with ISO 2631-1 and OHS legislation. The eight-degrees–of-freedom model consists of a linear elastic spring and damping elements. Note that the input of the mathematical model is the road excitations, which are obtained experimentally for different types of roads. The linear equations of motion are solved with the Runge-Kutta time step integration to obtain time-series responses such as the RMS acceleration data of the bus driver seat. Thus, the frequency-weighted RMS acceleration data of the bus driver seat is determined by the frequency-weighted curve in ISO 2631-1 to evaluate vehicle comfort. Consequently, the main objectives of this study are listed as follows: 1) Evaluation of road roughness and vehicle speed effects on the vibration comfort of the school bus driver seat using frequency-weighted RMS accelerations of the seat in conjunction with ISO 2631-1 2) Determine the maximum vehicle speed for comfortable driving of different types of roads, which are concrete, asphalt, cobblestone, and dirt, in accordance with ISO 2631-1 3) Evaluation of road roughness and vehicle speed effects on the vibration comfort of the school bus driver seat using RMS accelerations of the seat in accordance with OHS legislation 4) Comparison of ISO 2631-1 evaluations and OHS legislation evaluations in terms of school bus driver seat comfort. The main purpose of the study is to compare the OHS regulations in Türkiye with ISO 2631 in terms of whole-body vibrations. When both regulations are compared, it is observed that ISO 2631-1 is more comprehensive and

categorizes exposure. The novelty of this study is to detect the performance of whole-body vibration assessments with OHS legislation from Türkiye compared to ISO 2631-1.

2. Mathematical Model School Bus

The full-vehicle model, which consists of mass-spring-damping elements, is developed to mimic a real vehicle in terms of the dynamic behaviors of a vehicle. The comprehensive full-vehicle analytical model is visually represented in Figure 1, while the corresponding definitions and symbols employed in the model can be found in Table 2. The developed full-vehicle model with a passive suspension system has pitch and roll motion at the body. The eight degrees of freedom model has a vertical motion of the seat, body, and four wheels, and two rotational motions of the body. The rolling and pitch angles of the body are assumed to be very small to simplify the system in accordance with real vehicle dynamics. Vehicle suspension systems in the model are assumed to be linear and passive. The tires within the vehicle system are conceptualized as linear springs devoid of dampening mechanisms. The formulation of the differential equations governing motion is dependent on Newton's second law, which is facilitated through the utilization of the free-body diagram framework. These equations are represented as Equations 1-8.

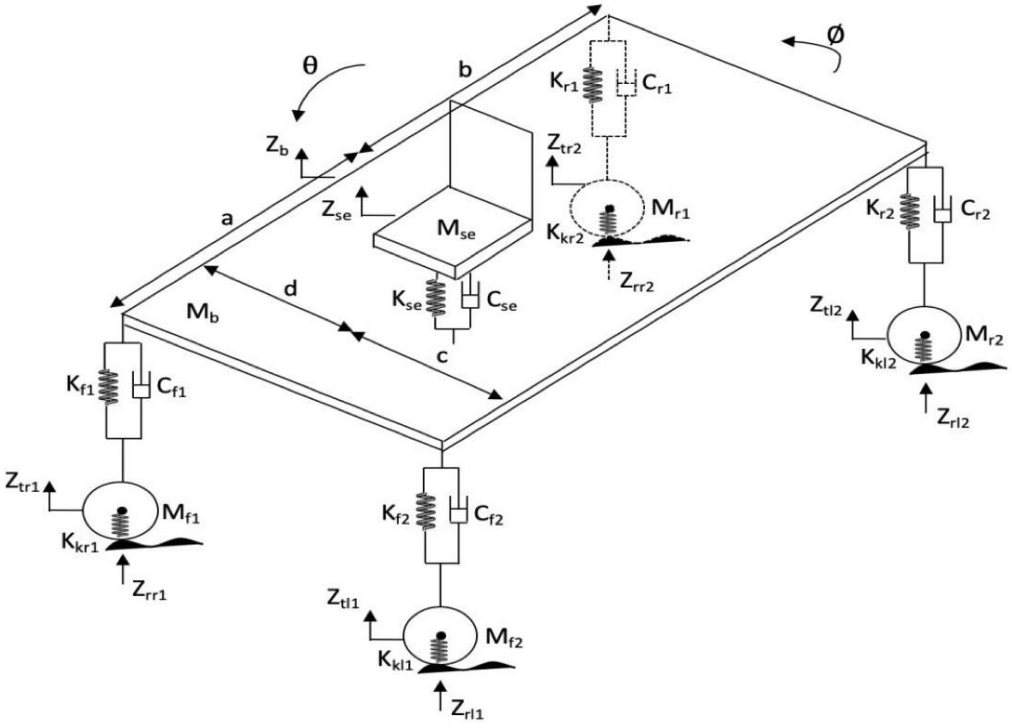

Figure 1. Full vehicle model of school bus.

Table 2. Definitions and symbols of the full-vehicle model.

C_{se}	seat damping coefficient	M_{f1}	front right wheel unsprung mass
C_{f1}	front right suspension damping	M_{f2}	front left unsprung wheel mass
C_{f2}	front left suspension damping	M_{r1}	rear right wheel unsprung mass
C_{r1}	rear right suspension damping	M_{r2}	rear left wheel unsprung mass
C_{r2}	rear left suspension damping	Z_{rr1}	front right road roughness
K_{se}	seat stiffness	Z_{rl1}	front left road roughness
K_{f1}	front right suspension stiffness	Z_{rr2}	rear right road roughness
K_{f2}	front left suspension stiffness	Z_{rl2}	rear left road roughness

K_{r1}	rear right suspension stiffness	Z_b	vehicle body vertical displacement
K_{r2}	rear left suspension stiffness	Z_{se}	seat vertical displacement
K_{kr1}	front right tire stiffness	Z_{tr1}	front right wheel vertical displacement
K_{kl1}	front left tire stiffness	Z_{tl1}	front left wheel vertical displacement
K_{kr2}	rear right tire stiffness	Z_{rr2}	rear right wheel vertical displacement
K_{kl2}	rear left tire stiffness	Z_{rl2}	rear left wheel vertical displacement
M_b	vehicle body mass	θ	pitch angle of vehicle body
M_{se}	seat mass	$\emptyset$	roll angle of vehicle body
a	distance from the sprung vehicle body mass CG to the front axle	b	distance from the sprung vehicle mass CG to the rear axle
c	distance from the sprung vehicle body mass CG to the vehicle left side	d	distance from the sprung vehicle mass CG to the vehicle right side

$$M_b\ddot{Z}_b + Z_b\left(K_{f1} + K_{f2} + K_{r1} + K_{r2}\right) + \left(C_{f1} + C_{f2} + C_{r1} + C_{r2}\right)\dot{Z}_b - \left(K_{f1}a + K_{f2}a - K_{r1}b - K_{r2}b\right)\theta - \left(C_{f1}a + C_{f2}a - C_{r1}b + C_{sl2}b\right)\dot{\theta} - \left(K_{f1}c - K_{f2}d - K_{r1}c + K_{r2}d\right)\emptyset - \left(C_{f1}c - C_{f2}d + C_{r1}c - C_{r2}d\right)\dot{\emptyset} + K_{se}(Z_b - Z_{se} + \theta c - \emptyset a) + C_{se}\left(\dot{Z}_b - \dot{Z_{se}} + \dot{\theta}c - \dot{\emptyset}a\right) - K_{f1}Z_{wr1} - K_{f2}Z_{tl1} - K_{r1}Z_{tr2} - K_{r2}Z_{tl2} - C_{f1}\dot{Z_{tr1}} - C_{f2}\dot{Z_{tl1}} - C_{r1}\dot{Z_{tr2}} - C_{r2}\dot{Z_{tl2}} = 0 \quad (1)$$

$$I_{yy}\ddot{\theta} - K_{f1}(Z_b - \theta a - \emptyset c + Z_{tr1})a - K_{f2}(Z_b - \theta a + \emptyset d - Z_{tl1})a + K_{r1}(Z_b + \theta b - \emptyset c - Z_{tr2})b + K_{r2}(Z_b + \theta b + \emptyset d - Z_{tl2})b + C_{f1}\left(\dot{Z}_b - \dot{\theta}a - \dot{\emptyset}c - \dot{Z_{tr1}}\right)a - C_{f2}\left(\dot{Z}_b - \dot{\theta}a + \dot{\emptyset}d - \dot{Z_{tl1}}\right)a + C_{r1}\left(\dot{Z}_b + \dot{\theta}b - \dot{\emptyset}c - \dot{Z_{tr2}}\right) + C_{r2}\left(\dot{Z}_b + \dot{\theta}b + \dot{\emptyset}d - \dot{Z_{tl2}}\right)b + K_{se}(Z_b - Z_{se} + \theta c - \emptyset a) + C_{se}\left(\dot{Z}_b - \dot{Z_{se}} + \dot{\theta}c - \dot{\emptyset}a\right) = 0 \quad (2)$$

$$I_{xx}\ddot{\emptyset} - -K_{f1}(Z_b - \theta a - \emptyset c + Z_{tr1})c + K_{f2}(Z_b - \theta a + \emptyset d - Z_{tl1})d - K_{r1}(Z_b + \theta b - \emptyset c - Z_{tr2})c + K_{r2}(Z_b + \theta b + \emptyset d - Z_{tl2})d - C_{f1}\left(\dot{Z}_b - \dot{\theta}a - \dot{\emptyset}c - \dot{Z_{tr1}}\right)c + C_{f2}\left(\dot{Z}_b - \dot{\theta}a + \dot{\emptyset}d - \dot{Z_{tl1}}\right)d - C_{r1}\left(\dot{Z}_b + \dot{\theta}b - \dot{\emptyset}c - Z_{tr2}\right)c + C_{r2}\left(\dot{Z}_b + \dot{\theta}b + \dot{\emptyset}d - \dot{Z_{tl2}}\right)d - K_{se}(Z_b - Z_{se} + \theta c - \emptyset a) - C_{se}\left(\dot{Z}_b - \dot{Z_{se}} + \dot{\theta}c - \dot{\emptyset}a\right) = 0 \quad (3)$$

$$M_{f1}\ddot{Z_{wr1}} - K_{f1}(Z_b - \theta a - \emptyset c - Z_{tr1}) + K_{kr1}(Z_{tr1} - Z_{rr1}) - C_{f1}\left(\dot{Z}_b - \dot{\theta}a - \dot{\emptyset}c - \dot{Z_{wr1}}\right) = 0 \quad (4)$$

$$M_{f2}\ddot{\mathrm{Z}_{\mathrm{wl1}}} - \mathrm{K_{f2}}(\mathrm{Z_b} - \theta\mathrm{a} - \emptyset\mathrm{c} - \mathrm{Z_{tl1}}) + \mathrm{K_{kl1}}(\mathrm{Z_{tl1}} - \mathrm{Z_{rl1}}) - \mathrm{C_{f2}}\left(\dot{\mathrm{Z}}_{\mathrm{b}} - \dot{\mathrm{Z}_{\mathrm{tl1}}} - \dot{\theta}\mathrm{a} - \dot{\emptyset}\mathrm{c}\right) = 0 \quad (5)$$

$$M_{r1}\ddot{\mathrm{Z}_{\mathrm{wr2}}} - \mathrm{K_{r1}}(\mathrm{Z_b} - \emptyset\mathrm{c} - \mathrm{Z_{tr2}} - \theta\mathrm{a}) + \mathrm{K_{kr2}}(\mathrm{Z_{tr2}} - \mathrm{Z_{rr2}}) - \mathrm{C_{r1}}\left(\dot{\mathrm{Z}}_{\mathrm{b}} - -\dot{\mathrm{Z}_{\mathrm{tr2}}} - \dot{\theta}\mathrm{a} - \dot{\emptyset}\mathrm{c}\right) = 0 \quad (6)$$

$$M_{r2}\ddot{\mathrm{Z}_{\mathrm{wl2}}} - \mathrm{K_{r2}}(\mathrm{Z_b} - \mathrm{Z_{tl2}} - \theta\mathrm{a} - \emptyset\mathrm{c}) + \mathrm{K_{kl2}}(\mathrm{Z_{tl2}} - \mathrm{Z_{rl2}}) - \mathrm{C_{r2}}\left(\dot{\mathrm{Z}}_{\mathrm{b}} - \dot{\emptyset}\mathrm{c} - \dot{\theta}\mathrm{a} - \dot{\mathrm{Z}_{\mathrm{tl2}}}\right) = 0 \quad (7)$$

$$M_{se}\ddot{\mathrm{Z}_{\mathrm{se}}} - \mathrm{K_{se}}(\theta\mathrm{c} + \mathrm{Z_b} - \mathrm{Z_{se}} - \emptyset\mathrm{a}) - \mathrm{C_{se}}\left(\dot{\theta}\mathrm{c} + \dot{\mathrm{Z}}_{\mathrm{b}} - \dot{\mathrm{Z}_{\mathrm{se}}} - \dot{\emptyset}a\right) = 0 \quad (8)$$

Road roughness for the different classes of roads, which are concrete, asphalt, cobblestone, and dirt, is collected experimentally in terms of displacement power spectrum density ($\Phi_{\mathrm{h}}(\Omega_0)[\mathrm{cm}^3]$). In order to be the input parameter for road excitation in the developed full-vehicle model, the obtained road roughness should be determined as an amplitude instead of $\Phi_{\mathrm{h}}(\Omega_0)$. Hence, experimentally measured power spectrum densities (PSD) based on reference angular spatial frequency ($\Omega_0 = 1\,rad/m$) are converted to amplitude. Therefore, the full vehicle model can be excited by the amplitude as an input, which depends on the wavelength of road roughness. The full-vehicle car model is stimulated by road amplitudes with the same signal on the left and right sides of the school bus ($Z_{rr1} = Z_{rl1} = Z_{rr2} = Z_{rl2}$).

The RMS of the excitation function (Δh) is established within the framework of a defined wavelength range (ΔL), resulting in the derivation of a singular harmonic function denoted as $\hat{b}_{abs}$ amplitude, representative of the average wavelength (L). The inclusion of a √2 factor is assumed for the purpose of converting the harmonic function, as indicated by previous references [22], [23].

$$\widetilde{\Delta h} = \sqrt{\int_{\bar{L}-\Delta L/2}^{\bar{L}+\Delta L/2} \Phi_h(L)dL} = \sqrt{\Phi_h(\bar{L})\Delta L} = \frac{\hat{b}_{abs}}{\sqrt{2}} \quad (9)$$

$$\hat{b}_{abs} = \sqrt{\frac{\Omega^2}{\pi}\Phi_h(\Omega_0)\Delta L} \quad (10)$$

According to the experimental results, the concrete, asphalt, cobblestone, and dirt classes of roads are categorized as 4, 3, 4, and 4 road types, respectively. The road classes and their road types are given in Table 3. The transformation of the obtained displacement power spectrum density ($\Phi_h(\Omega_0)[cm^3]$) to amplitude calculations is performed for concrete, asphalt, cobblestone, and dirt roads, as given in Table 3. Note that the classes of A, B, C, and D roads, which are used in this study as road excitations, are good concrete ($\Phi_h(\Omega_0) = 3\ cm^3$), very good asphalt ($\Phi_h(\Omega_0) = 8\ cm^3$), medium cobblestone ($\Phi_h(\Omega_0) = 27\ cm^3$) and bad dirt ($\Phi_h(\Omega_0) = 60\ cm^3$), respectively. These four classes of road types are assumed to be input for the full-vehicle model. The simulated road profile is depicted for only good concrete roads ($\Phi_h(\Omega_0) = 3\ cm^3$) in Figure 2.

The sensitivity of people to whole-body vibrations varies with frequency. Frequency weighting factors evaluate the effects of frequencies on people [22]. The frequency weighting factors are determined in ISO 2631-1. In this study, W_k frequency weighting curve for vertical whole-body vibrations is used. It is given in Figure 2. The mathematical representation of the RMS acceleration of the seat (a_{rms}) is given in the Equation 11:

$$a_{rms} = \left\{\frac{1}{T}\int_0^T [a(t)]^2 dt\right\}^{\frac{1}{2}} \quad (11)$$

a(t) - seat acceleration (m/s^2)
T - duration of the measurement in seconds (s).

Table 3. Measured PSD for different types of roads [21].

Road Class	Road Type	w	$\Phi_h(\Omega_0)cm^3$
Concrete	Very good	2.29	0.6
	Good (A)	1.97	3
	Medium	1.97	8.7
	Bad	1.72	56
Asphalt	Very good (B)	2.20	8
	Good	2.18	11
	Medium	2.18	22
Cobblestone	Good	1.75	14
	Medium (C)	1.75	27
	Bad	1.81	36
	Very bad	1.81	323
Dirt	Good	2.25	32
	Medium	2.25	44
	Bad (D)	2.14	60
	Very bad	2.14	16300

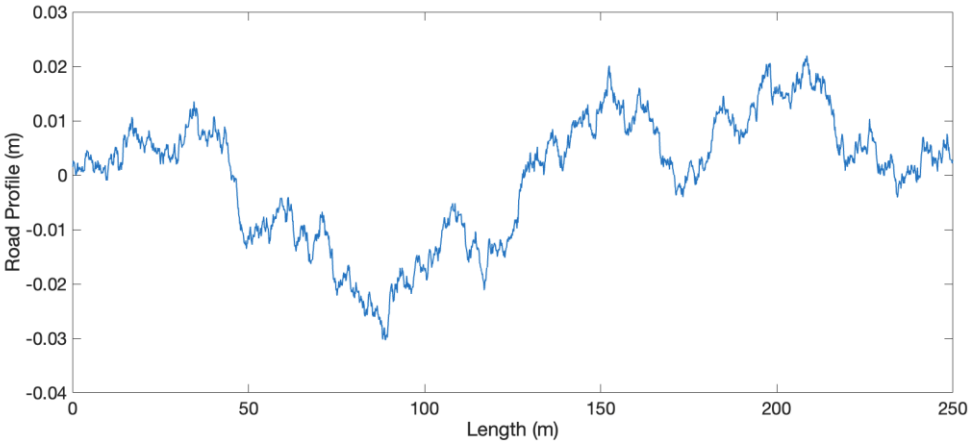

Figure 2. Road profile for good concrete.

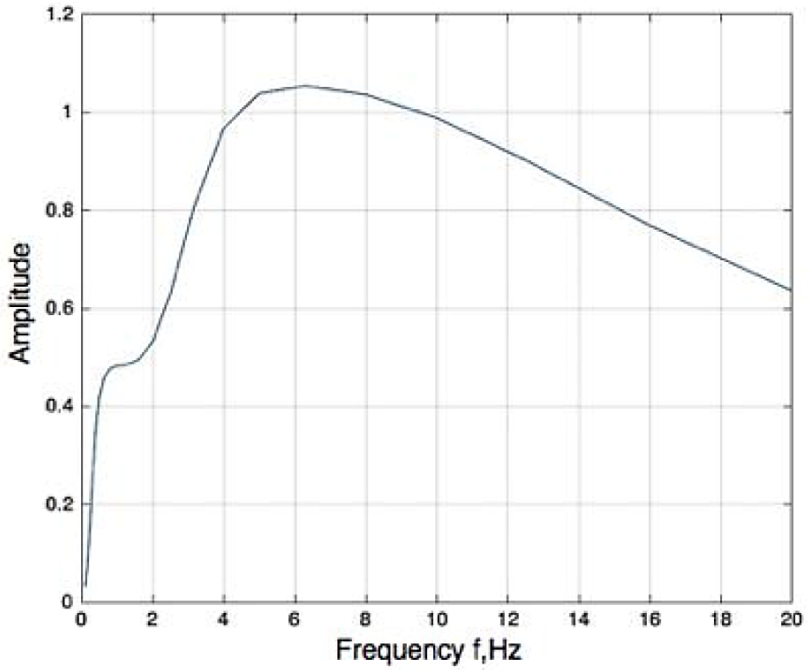

Figure 3. The converted $\mathbf{W_k}$ frequency weighting curve in ISO 2631-1 in terms of amplitude.

W_k frequency weighting curve is used to determine the frequency-weighted RMS accelerations of the seat in the vertical direction. The frequency-weighted acceleration (RMS) of the seat ($a_{w,rms}$) is obtained with the Equation 12:

$$a_{w,rms} = \left[\sum_i (W_i a_{rms})^2\right]^{\frac{1}{2}} \qquad (12)$$

where $a_{w,rms}$ is the frequency-weighted RMS accelerations of the seat and W_i is the weighting factor.

3. Results

3.1. Evaluation with ISO 2631-1

To ascertain the RMS acceleration of the seat in the vertical direction, the governing linear equations are subject to numerical resolution through the utilization of the 4th-order explicit Runge-Kutta technique, thereby yielding temporal domain responses [24]. Furthermore, the calculated RMS acceleration of the seat from time series responses is converted to the frequency-weighted RMS accelerations of the seat in order to assess comfortable driving in accordance with ISO 2631-1. According to 2631-1, the seat

frequency-weighted RMS acceleration of $\mathbf{0.315}\boldsymbol{m/s^2}$ value is the upper threshold for comfortable driving [22]. This threshold value of acceleration for comfortable driving is an assumed comfort criterion. Although this frequency-weighted RMS acceleration ($\mathbf{0.315}\boldsymbol{m/s^2}$) is the comfort limit value, the comfort zones corresponding to different frequency-weighted RMS acceleration values are classified in ISO 2631-1 (Table 4). When looking at the comfort zones, there are no exact sharp ranges; there are blurred ranges. However, the acceleration value evaluated in the study is assumed to be in the comfort range, where it is closer to the upper value. For example, the value of $\mathbf{0.55}\ \boldsymbol{m/s^2}$ is considered to be in the fairly uncomfortable zone, not a little uncomfortable zone. Because the lower initial value of the fairly uncomfortable zone ($\mathbf{0.5}\ \boldsymbol{m/s^2}$) is closer to $\mathbf{0.55}$.

Table 4. Comfort zones from ISO 2631-1.

Frequency-weighted RMS acceleration (m/s^2)	Comfort Index
$< \mathbf{0.315}$	Not uncomfortable
$\mathbf{0.315 - 0.63}$	A little uncomfortable
$\mathbf{0.5 - 1}$	Fairly uncomfortable
$\mathbf{0.8 - 1.6}$	Uncomfortable
$\mathbf{1.25 - 2.5}$	Very uncomfortable
$> \mathbf{2}$	Extremely uncomfortable

In order to understand the effects of road roughness and vehicle speed on comfortable driving, the full-vehicle model is analyzed at four different PSDs of road roughness. Frequency-weighted RMS accelerations of the bus seat in the vertical direction are determined for different road roughnesses, which are $\boldsymbol{\Phi_h(\Omega_0) = 3\ cm^3}$, $\boldsymbol{\Phi_h(\Omega_0) = 8\ cm^3}$, $\boldsymbol{\Phi_h(\Omega_0) = 27\ cm^3}$, and $\boldsymbol{\Phi_h(\Omega_0) = 60\ cm^3}$. Note that the applied road roughnesses to the full-vehicle model are given in Table 3. Comfortable driving is proven with a value of $\mathbf{a_{w,rms}}$ less than 0.315 $\boldsymbol{m/s^2}$. When the value of $\mathbf{a_{w,rms}}$ exceeds $\mathbf{0.315}\ \boldsymbol{m/s^2}$, uncomfortable driving can be observed. For comfortable driving at selected road roughness, maximum school bus speeds are given in Table 5. The area above the region expressed by the dashed lines is an uncomfortable driving zone in Figure 3. To maintain comfortable driving, the vehicle speed should not exceed the values of $\mathbf{22.4}\ \boldsymbol{m/s}$, $\mathbf{12.8}\ \boldsymbol{m/s}$, $\mathbf{5.5}\ \boldsymbol{m/s}$ and $\mathbf{3.1}\ \boldsymbol{m/s}$ for $\boldsymbol{\Phi_h(\Omega_0) = 3\ cm^3}$, $\boldsymbol{\Phi_h(\Omega_0) = 8\ cm^3}$, $\boldsymbol{\Phi_h(\Omega_0) = 27\ cm^3}$ and $\boldsymbol{\Phi_h(\Omega_0) = 60\ cm^3}$ road roughnesses, respectively. For higher vehicle speeds than the calculated maximum speeds, uncomfortable driving will be inevitable, according to ISO 21631-1. The tolerance of the vehicle with $\boldsymbol{\Phi_h(\Omega_0) = 3\ cm^3}$ is higher than that of others. It can be comfortable driving up to the PSD level of $\mathbf{22.4}\ \boldsymbol{m/s}$. As seen in Figure 3, driving on bad roads at high speeds causes uncomfortable driving. The selected PSDs of road roughness (A, B, C and D) are used as input for the full-vehicle model, and then maximum vehicle speeds are determined in terms of comfortable driving in Table 5. The driver should drive at very low speeds on D-class roads, otherwise, drivers may experience a high level of discomfort. If the maximum vehicle speed limit is exceeded, discomfort occurs, according to the 2631-1 Standard. Hence, if the limit is exceeded for a long time, health problems occur for the driver.

A general overview of the school bus model for road roughness and vehicle speed in terms of ISO 2631-1 is shown in Table 6 with color coding. If the frequency-weighted RMS accelerations of the bus seat vibrations that the driver is exposed to are higher than 0.315 $\boldsymbol{m/s^2}$, it is defined as uncomfortable driving. However, there are degrees of discomfort in this driving, depending on the acceleration values as given in Table 4. While the area below 0.315 $\boldsymbol{m/s^2}$ represents comfortable driving, exposure above 2 $\boldsymbol{m/s^2}$ represents an extremely uncomfortable driving zone. The frequency-weighted RMS acceleration values from the vehicle driver seat are evaluated in terms of driving comfort according to Table 4.

The cells of the table, which are filled in black, denote the cases where extremely uncomfortable driving is observed ($\mathbf{a_{w,rms} > 2}\ \boldsymbol{m/s^2}$). The grey, red, yellow, and blue cells in Table 6 represent very uncomfortable, uncomfortable, fairly uncomfortable, and a little uncomfortable driving, respectively. In addition, green areas represent comfortable driving. As seen in Table 6, uncomfortable driving conditions begin to appear as vehicle speed and the PSD of road roughness increase. Unhealthy driving zones are observed clearly in cases where PSDs of road roughness are very high ($\boldsymbol{\Phi_h(\Omega_0) = 323\ cm^3}$ and $\boldsymbol{\Phi_h(\Omega_0) = 16300\ cm^3}$). However, the condition of very low PSD of road roughness ($\boldsymbol{\Phi_h(\Omega_0) = 0.6\ cm^3}$) is suitable for comfortable driving at all vehicle speeds. Thus, the effects of vehicle speed and road roughness on driving comfort are analyzed in detail.

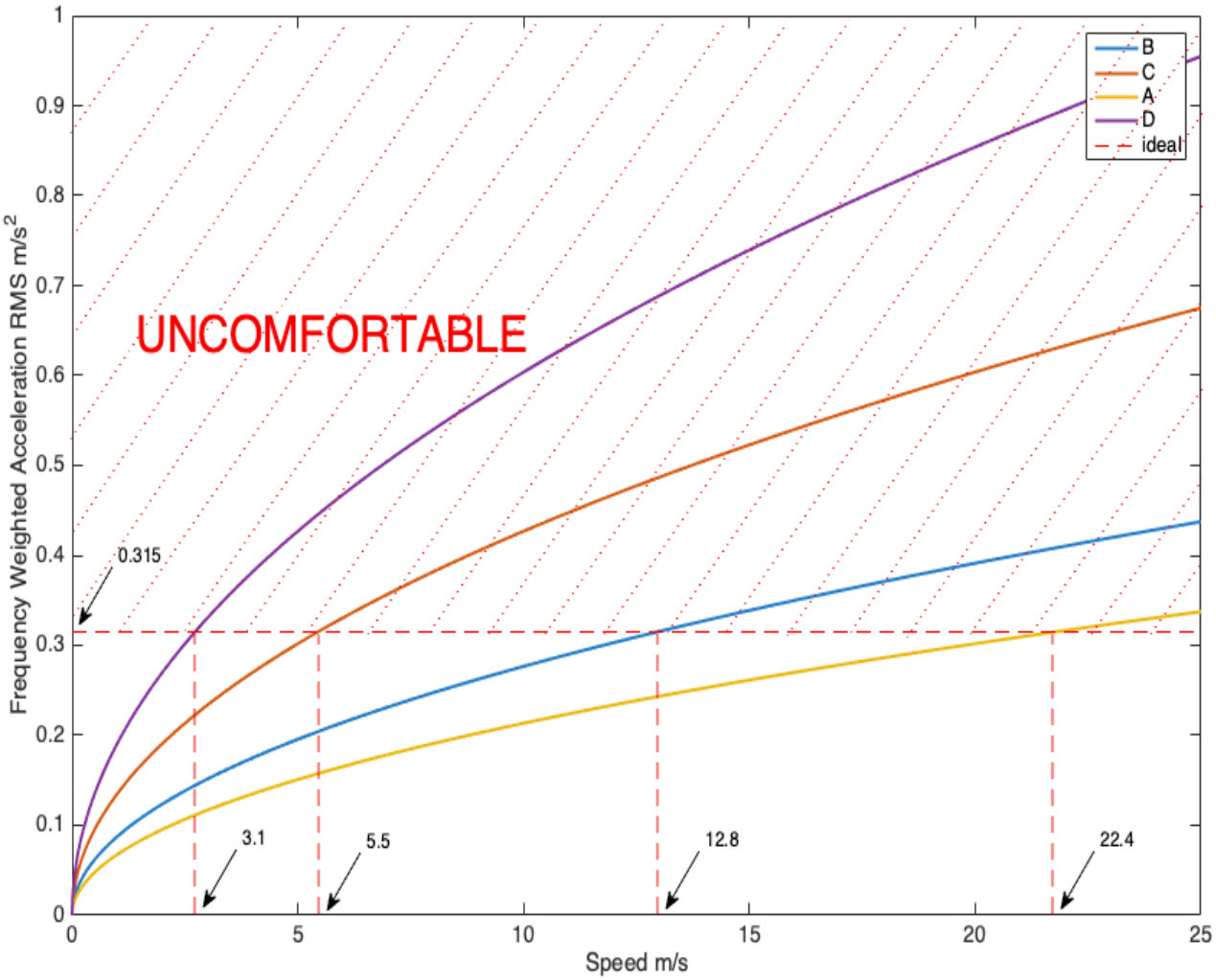

Figure 4. RMS acceleration vs vehicle speed for different road class.

Table 5. Maximum vehicle speeds based on different road types for comfortable driving.

Types of Roads	**PSD of Road Roughness** $(\Phi_h(\Omega_0)cm^3)$	**Maximum Vehicle Speeds** (m/s)
A	3	22.4
B	8	12.8
C	27	5.5
D	60	3.1

Table 6. The effects of road classes and vehicle speeds on driving comfort according to ISO 2631-1. not uncomfortable driving, a little uncomfortable driving, fairly uncomfortable driving, uncomfortable driving, very uncomfortable driving, extremely uncomfortable driving.

Road Class	Road Type	$\Phi_h(\Omega_0) cm^3$	Vehicle Speed (m/s) 1 3 5 7 9 11 13 15 17 19 21 23 25
Concrete	Very good	0.6	
	Good (A)	3	
	Medium	8.7	
	Bad	56	
Asphalt	Very good(B)	8	
	Good	11	
	Medium	22	
Cobblestone	Good	14	
	Medium (C)	27	
	Bad	36	
	Very bad	323	
Dirt	Good	32	
	Medium	44	
	Bad (D)	60	
	Very bad	16300	

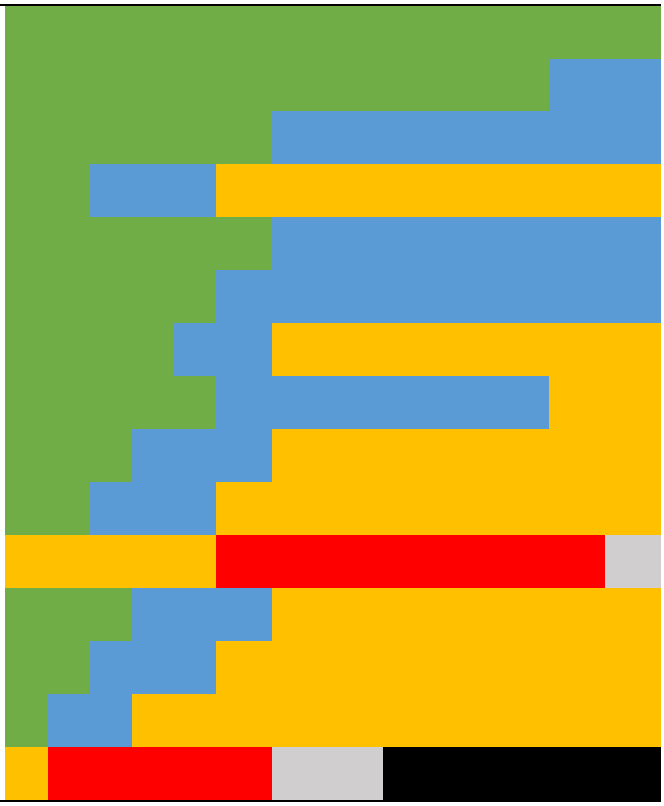

3.2 Evaluation with Occupational Health and Safety Legislation

According to OHS regulations in Turkey, the evaluation of the vehicle speed and road roughness effects on bus driver health is observed in terms of bus seat vibrations in Table 7. Depending on this regulation, if the RMS accelerations of the bus seat vibrations that the driver is exposed to are higher than 0.5 m/s^2, it is defined as uncomfortable driving. Although frequency-weighted RMS accelerations of the bus seat vibrations are used as a comfort evaluation parameter for ISO 2631-1 evaluation, RMS accelerations of the bus seat vibrationsare used as an evaluation parameter in terms of bus driver health for OHS legislation evaluation. As seen in Table 7, the results evaluated with OHS regulations are different from the results evaluated with ISO 2631-1, especially at low PDS of road roughness. Healthy driving without precautions in terms of OHS regulations is observed in cases where PSDs of road roughness are low levels ($\Phi_h(\Omega_0) = 0.6\ cm^3$ and $\Phi_h(\Omega_0) = 3\ cm^3$, $\Phi_h(\Omega_0) = 8.7\ cm^3$ and $\Phi_h(\Omega_0) = 8\ cm^3$) for all vehicle speeds. However, the working conditions where measures should be taken by the employers arise in high road roughness ($\Phi_h(\Omega_0) = 323\ cm^3$ and $\Phi_h(\Omega_0) = 16300\ cm^3$) in accordance with OHS regulations.

Table 7. The effects of road classes and vehicle speeds on comfortable driving in accordance with OHS regulations. comfortable driving, uncomfortable driving.

Road Class	Road Type	$\Phi_h(\Omega_0)cm^3$	Vehicle Speed (m/s) 1 3 5 7 9 11 13 15 17 19 21 23 25
Concrete	Very good	0.6	
	Good (A)	3	
	Medium	8.7	
	Bad	56	
Asphalt	Very good(B)	8	
	Good	11	
	Medium	22	
Cobblestone	Good	14	
	Medium (C)	27	
	Bad	36	
	Very bad	323	
Dirt	Good	32	
	Medium	44	
	Bad (D)	60	
	Very bad	16300	

4. Discussions

ISO 2631-1:1997 is an important standard for assessing the influences of whole-body vibration on driving comfort and human health. In this standard, procedures are proposed for assessing the influences of whole-body vibrations upon human health and driving comfort [25]. Standards are periodically revised to reflect advances in research and technology. Therefore, the specific requirements and criteria in each standard may change over time. BS 6841 is a British Standard with a focus on vertical whole-body vibrations and is primarily applicable in the UK, while ISO 2631-1 is an international standard that considers both vertical and horizontal vibrations and is widely recognized globally [26]. The choice of which standard to use may depend on regional regulations, industry practices, and the specific requirements of the assessment. The primary disparity discerned between BS 6841 and ISO 2631-1 lies in the distinct nature of the frequency weighting filters applied to vertical accelerations experienced on the seat cushion. Furthermore, in accordance with BS 6841:1987, it is suggested that the assessment of the impact of whole-body vibration on human health involves the consideration of the cumulative vibration resulting from three translational accelerations experienced on the seat cushion in conjunction with longitudinal accelerations experienced on the seat back. However, in ISO 2631-1:1997, it is recommended to take the highest value of the three translational accelerations on the seat cushion, or the vibration total value. The limits of the health guidance warning zone (HGCZ) in ISO 2631-1 are different from the EU Directive limits. The lower and upper limit values in ISO 2631-1, the EU 2002/44/EC directive, and the BS 6841 standard used in the assessment of whole-body vibration exposure differ in terms of vibration dose and vibration acceleration [27], [28]. When local regulations related to OHS are compared to all these standards, it is concluded that the regulations related to vibration are inadequate and limited in Turkey. While technical details, vibration dose calculations, and the effects of vibration on comfort are given in detail in other standards (ISO 2631-1, BS 6841, and EU), a general solution to

vibration exposure is provided in the OHS local regulation in Turkey. This solution is quite inadequate in terms of the direction of vibration motion and calculations. While the classification of comfort criteria is detailed in the others, in the local OHS vibration regulation, which represents the local regulations, it is recommended to take the measures above $\mathbf{0.5}\ \boldsymbol{m/s^2}$ and not exceed $\mathbf{1.15}\ \boldsymbol{m/s^2}$ under any circumstances. This makes the regulation simple and less sensitive.

One of the innovative aspects of this study is the evaluation of vehicle seat vibrations using the local OHS vibration regulation and the comparison of these evaluations with ISO 2631-1. Also, the differences between the OHS regulation and other standards, as mentioned above, are discussed. The vibration exposures of school bus drivers at different road roughnesses and speeds are analyzed in terms of both ISO 2631-1 and OHS local regulations. As a result, it has been observed that ISO 2631-1 is more detailed and comprehensive in assessing the comfort status of school bus drivers.

The results from this study are compared with the seat vibration levels ($\mathbf{a_{w,rms}}$) reported in the literature for various road types and vehicle speeds in Table 8. The road types in our study were selected by estimating their correspondence to the road types in the literature. Subsequently, comparisons were made with the literature at equivalent speeds. This approach involved a thoughtful matching of road types from our study to those existing in the literature, followed by a thorough analysis and comparison of performance indicators, particularly at comparable speeds. This method ensured a systematic and meaningful alignment between our chosen road types and those identified in the literature, facilitating a comprehensive evaluation of the results within the established research context. It's observed that there are few differences between the study results and the findings of Lewis and Johnson, Blood et al., and Thamsuwan et al. [29]-[31]. The percentage error values highlight the extent of these differences. When this study is compared with the experimental studies in the literature, it is observed that the success of predicting $\mathbf{a_{w,rms}}$ values is high. It's important to note that variations may arise due to factors such as road conditions, asphalt quality, and the specific methodologies employed in different studies. The comparison provides valuable insights into the consistency and reliability of the study's vibration measurements across diverse road types and speeds.

Table 8. Comparison of the results of the study with the results of experimental studies in the literature.

Vehicle Speed (m/s)	Road types in literature	Road types in this study	This study results ($\mathbf{a_{w,rms}}$)	Lewis and Johnson results [29] ($\mathbf{a_{w,rms}}$)	Blood et. al. results [30] ($\mathbf{a_{w,rms}}$)	Thamsuwan et. al. results [31] ($\mathbf{a_{w,rms}}$)	Error (%)
23	Freeway	Medium Concrete	0.53	0.51	-	-	3.92
9	City Street	Medium Asphalt	0.42	0.47	-	-	10.63
8	City Street	Medium Asphalt	0.39	-	0.36	-	8.33
23	New freeway	Good Concrete	0.46	-	0.43	-	6.97
23	Old freeway	Bad Concrete	0.55	-	0.51	-	7.84
23.5	Smooth freeway	Good Concrete	0.47	-	-	0.42	11.89
26	Rough freeway	Bad Concrete	0.57	-	-	0.53	7.54
8.5	City street	Medium Asphalt	0.40	-	-	0.39	2.56

5. Conclusion and Suggestions

The eight-degrees-of-freedom vehicle model is developed to predict the maximum road roughness and vehicle speed for comfortable driving in terms of ISO 2631-1. This study is not performed with a real vehicle because the effect of changes in parameters cannot be clearly observed. Instead, the investigations are observed on the full-vehicle mathematical model. The analysis results in this study enabled us to consider the effects of different road roughness and vehicle speeds on frequency-weighted RMS accelerations of the seat, which are determined using weighted curves in the ISO 2631-1 Standard. Based on the observations from the study, the following conclusions in accordance with 2631-1 are reached:

- In order to be comfortable driving, it is concluded that the maximum vehicle speed increases as the PSD of road roughness decreases.
- The vehicle comfort problem can begin to feel as vehicle speed and PSD of road roughness rise.
- The vehicle speed range at which the vehicle can be driven comfortably is high at low PSDs.
- The maximum vehicle speed for comfortable driving increases as the value of PDS decreases.

The maximum vehicle speeds as a function of different road classes are determined in accordance with ISO 2631-1 and OHS legislation for comfortable driving. The comparison of OHS legislation and ISO 2631-1 evaluations is given in Table 8. Based on the comparisons, the following conclusions are reached:

- The driver's comfort is changed by the PSD of road roughness, regardless of evaluation methods.
- Safe and comfortable driving can be achieved with concrete roads. In order to feel comfortable driving on cobblestone roads, it is necessary to drive at low speeds.
- The maximum vehicle speed for comfortable driving decreases as road conditions worsen in both OHS legislation and ISO 2631-1 evaluations.
- For all road classes, OHS legislation offers a wider range of comfortable driving in terms of vehicle speed. For example, while uncomfortable driving begins to appear at $\mathbf{22.3}\ \boldsymbol{m/s}$ vehicle speed on a good asphalt road in accordance with OHS legislation, it occurs at $\mathbf{11.7}\ \boldsymbol{m/s}$ in accordance with ISO 2631-1.
- The health hazard is not observed on a very good concrete road in both OHS legislation and ISO 2631-1 evaluations.
- For all vehicle speeds, uncomfortable driving is inevitable on very bad dirt roads in both evaluation methods.
- Comfortable driving is suitable for all vehicle speeds on good concrete and medium concrete roads in accordance with OHS legislation. However, according to ISO 2631-1, uncomfortable driving occurs at higher speeds than 22.4 m/s and 11.7 m/s speeds ongood concrete and medium concrete roads, respectively.

The following precautions can be taken to reduce the effects of vibration on bus drivers in accordance with occupational health and safety:

- Minimizing travel distance
- Limiting vehicle speed
- Removing obstacles, filling potholes, and smoothing driving surfaces
- Providing a suitable suspension seat correctly adjusted for the driver's weight
- Equipping the driver seat with suspension
- Use of ergonomically designed seats and backrests that provide adequate padding
- Training school bus drivers for correct seat adjustment
- The school bus driver seat can be adjusted in various directions (up-down, front-back, right-left)

Contributions of the authors

Conceptualization, A.Y. and S.E.H.; methodology, A.Y.; validation, A.Y. and S.E.H.; formal analysis, A.Y.; investigation, A.Y. and S.E.H.; resources, A.Y.; data curation, A.Y. and S.E.H.; writing-original draft preparation, A.Y. and S.E.H.; writing-review and editing, A.Y. and S.E.H.; visualization, A.Y. and S.E.H. All authors have read and agreed to the published version of the manuscript.

Conflict of Interest Statement

There is no conflict of interest between the authors.

Table 9. Comparison of OHS legislation and ISO 2631-1 evaluations.

Road Class	Road Type	Maximum Vehicle Speed for Comfortable Driving (m/s)	
		OHS Legislation	**ISO 2631-1**
Concrete	Very good	-	-
	Good (A)	-	22.4
	Medium	-	11.7
	Bad	5.6	3.7
Asphalt	Very good (B)	-	12.8
	Good	22.3	11.7
	Medium	15.3	7.4
Cobblestone	Good	20.2	10.1
	Medium (C)	13.1	5.5
	Bad	9.7	3.7
	Very bad	0.2	0
Dirt	Good	11.7	5.2
	Medium	7.8	3.8
	Bad (D)	5.4	3.1
	Very bad	0	0

References

[1] M. Kolich and S. M. Taboun, "Ergonomics modelling and evaluation of automobile seat comfort," *Ergonomics*, vol. 47, no. 8, pp. 841-863, 2004.

[2] A. Yavuz and A. Guney, "Optimization of Suspension Characteristics for Increasing Expected Daily Exposure Durations in Vehicles According to ISO 2631-1 Standard using Genetic Algorithms," *INTER-NOISE and NOISE-CON Congress and Conference Proceedings*, vol. 259, pp. 6225–6234, 2019.

[3] N. Gültekin, M. Mayda, and M. Kilit, "Benzin ve Dizel Motorlarda Devir Sayısının Titreşime Olan Etkisinin İncelenmesi/Investigation of the Effect of Revolution of Diesel and Gasoline Engines on Their Vibration," *Bitlis Eren Üniversitesi Fen Bilimleri Dergisi*, vol. 6, no. 2, pp. 39–43, 2017.

[4] S. E. Hacibektasoglu, B. Mertoglu, and H. Tozan, "Application of a novel hybrid f-SC risk analysis method in the paint industry," *Sustainability*, vol. 13, no. 24, p. 13605, 2021.

[5] I. Morag and G. Luria, "A framework for performing workplace hazard and risk analysis: a participative ergonomics approach," *Ergonomics*, vol. 56, no. 7, pp. 1086–1100, 2013.

[6] J. Wang, S. Han, and X. Li, "3D fuzzy ergonomic analysis for rapid workplace design and modification in construction," *Autom. Constr.*, vol. 123, no. 103521, p. 103521, 2021.

[7] P. K. Marhavilas, D. Koulouriotis, and V. Gemeni, "Risk analysis and assessment methodologies in the work sites: On a review, classification and comparative study of the scientific literature of the period 2000–2009," *J. Loss Prev. Process Ind.*, vol. 24, no. 5, pp. 477–523, 2011.

[8] *Çalışanların Titreşimle İlgili Risklerden Korunmalarına Dair Yönetmelik, Official Gazette 28743*. 2013.

[9] R. M. Lorente-Pedreille, F. Brocal, M. A. Saenz-Nuño, and M. A. Sebastián, "Analysis of metrological requirements in occupational health and safety regulations related to the emerging risk of exposure to vibrations," *Appl. Sci. (Basel)*, vol. 10, no. 21, p. 7765, 2020.

[10] M. Bovenzi, "Low back pain disorders and exposure to whole-body vibration in the workplace," *Semin. Perinatol.*, vol. 20, no. 1, pp. 38–53, 1996.
[11] M. Milosevic and K. M. V. McConville, "Evaluation of protective gloves and working techniques for reducing hand-arm vibration exposure in the workplace," *J. Occup. Health*, vol. 54, no. 3, pp. 250–253, 2012.
[12] I. J. Tiemessen, C. T. J. Hulshof, and M. H. W. Frings-Dresen, "An overview of strategies to reduce whole-body vibration exposure on drivers: A systematic review," *Int. J. Ind. Ergon.*, vol. 37, no. 3, pp. 245–256, 2007.
[13] A. Guney, "Taşıtlarda Titreşim ve Gürültü," Lecture Notes, İTÜ, İstanbul, pp. 3-10, 1992.
[14] T. D. Gillespie, "Heavy Truck Ride," *in SAE Technical Paper Series*, 1985.
[15] P. Múčka, "Simulated road profiles according to ISO 8608 in vibration analysis". *Journal of Testing and Evaluation, vol.* 46, no. 1, pp. 405-418, 2017.
[16] P. Múčka, "Relation Between Seated Person Vibrations and the International Roughness Index" *Transportation Research Record*, vol. 2677, no. 6, pp. 351-364, 2023.
[17] P. Múčka, "New Transverse Unevenness Indexes of the Road Profile" *Journal of Transportation Engineering, Part B: Pavements*, vol. 148, no. 3, pp. 04022046, 2022.
[18] P. Múčka, G. J. Stein, P. Tobolka, "Whole-body vibration and vertical road profile displacement power spectral density" *Vehicle System Dynamics*, vol. 58, no. 4, pp. 630-656, 2020.
[19] İ. Karen, N. Kaya, F. Öztürk, İ. Korkmaz, M. Yıldızhan, and A. Yurttaş, "A design tool to evaluate the vehicle ride comfort characteristics: modeling, physical testing, and analysis," *Int. J. Adv. Manuf. Technol.*, vol. 60, no. 5–8, pp. 755–763, 2012.
[20] D. Sekulic, V. Dedovic, "The Effect of Stiffness and Damping of the Suspension System Elements on the Optimızation of the Vibratıonal Behaviour of a Bus," *International Journal for Traffic and Transport Engineering*, vol. 1, no. 4, pp. 231–244, 2011.
[21] H. Braun, T. Hellenbroich, "Messergebnisse von Straßenunebenheiten", VDI- Berichte Nr. 877, Düsseldorf: VDI-Verlag, 47-80, 1991.
[22] Mechanical Vibration and Shock-Evaluation of Human Exposure to Whole Body Vibration Part 1: General Requirements, International Organization for Standardization. Switzerland, 1997.
[23] M. Mitschke, Dynamik der Kraftfahrzeuge. Berlin: Springer-Verlag, 1984.
[24] MathWorks, Inc., *Student Edition of MATLAB Version 4: Student User Guide*. London, England: Prentice-Hall, 1995.
[25] P. Múčka, "Road roughness limit values based on measured vehicle vibration" *Journal of Infrastructure Systems*, vol. 23, no. 2, pp. 04016029, 2017.
[26] *Measurement and Evaluation of Human Exposure to Whole-Body Mechanical Vibration and Repeated Shock.* British Standards Institution, BS 6841, 1987.
[27] *Directive 2002/24/EC of the European Parliament and of the Council.* Official Journal of the European Communities, 2002.
[28] *T. Doğan, B. Erdem, Z. Duran, "Oturma Pozisyonunda Çalışanların Tüm Vücut Titreşimi Maruziyetlerinin Belirlenmesinde Kullanılan ISO2631-1, ISO2631-5, BS6841 ve Avrupa Birliği Direktifi (EU) 2002/44/EC'nin Karşılaştırılması" Ergonomi*, vol. 3, no. 2, pp. 108-117, 2020.
[29] *C.A. Le*wis, P.W. Johnson, "Whole-body vibration exposure in metropolitan bus drivers" *Occupational medicine*, vol. 62, no. 7, pp. 519-524, 2012.
[30] R.P. Blood, J.D. Ploger, M.G. Yost, R.P. Ching, P.W. Johnson, "Whole body vibration exposures in metropolitan bus drivers: A comparison of three seats" *Journal of Sound and Vibration*, vol. 329, no. 1, pp. 109-120, 2010.
[31] O. Thamsuwan, R.P. Blood, R.P. Ching, L. Boyle, P.W. Johnson, "Whole body vibration exposures in bus drivers: A comparison between a high-floor coach and a low-floor city bus" *International Journal of Industrial Ergonomics*, vol. 43, no. 1, pp. 9-17, 2013.

Bitlis Eren Üniversitesi Fen Bilimleri Dergisi
BİTLİS EREN UNIVERSITY JOURNAL OF SCIENCE
ISSN: 2147-3129/e-ISSN: 2147-3188
VOLUME: 12 NO: 4 PAGE: 1185-1194 YEAR: 2023
DOI:10.17798/bitlisfen.1360049

Urinary Bladder Inflammation Prediction with the Gray Wolf Optimization Algorithm and Multi-Layer Perceptron-Based Hybrid Architecture

Mehmet Akif BÜLBÜL[1*]

[1]*Nevşehir Hacı Bektaş Veli University, Faculty of Engineering-Architecture, Computer Engineering, Nevşehir, Turkey*
(ORCID: 0000-0003-4165-0512)

Keywords: Gray Wolf Optimization Algorithm, Multi-Layer Perceptron, Decision Support Systems.

Abstract
This study presents a decision-support system for predicting bladder inflammation. The proposed decision support system is built by establishing a hybrid architecture with the Gray Wolf Optimization algorithm (GWO) and Multi-Layer Perceptron (MLP). In addition to optimizing the hyperparameters in the MLP structure with GWO, the hybrid architecture also optimizes the order of input values to be presented to the MLP structure. The Acute Inflammations data set in the UCI Machine Learning repository was used as the data set in the study. Classification operations were carried out on this data set with the models obtained with hybrid architecture, Decision trees, k-Nearest Neighbors, and Support Vector Machines methods. The controversial findings from experimental studies have shown that the proposed hybrid architecture produces more successful results than other machine learning methods used in the study. In addition, the MLP structure optimized with the hybrid architecture offers a new diagnostic method for patient decision support systems.

1. Introduction

Inflammation is a defense mechanism that recognizes cell damage and aims to repair it. It also acts to clear damaged cells. There are two basic types: Acute inflammation is generally characterized by dilation of blood vessels, accumulation of fluid between cells, movement of neutrophils, and sometimes activation of the coagulation process [1]. One of the acute inflammations seen in the human body is urinary bladder inflammation. In later stages, the inflammation in the body damages organs and tissues. Early diagnosis and treatment are extremely important to minimize this damage.

Decision support systems developed in the field of health in recent years play an important role in the early prediction and diagnosis of many diseases [2], [3]. Adem et al. [4] used a stacked autoencoder and softmax classification for the classification and diagnosis of cervical cancer. In the study, machine learning methods such as Rotation Forest (RF), Support Vector Machines (SVM), Feed Forward Neural Network, and k-Nearest Neighbors (kNN) were also used. All machine learning methods used in the study were tested on data taken from the UCI database. The findings show that the presented model performs classification more successfully than other machine learning methods.

Giorgio et al. [5] implemented the ECG signal processing chain for arrhythmia detection, QT segment prolongation assessment, and pulmonary embolism risk assessment. The decision support system developed using programmable logic devices (PLDs) and field programmable gate arrays (FPGAs) is also wearable. As a result of the studies, successful results were obtained in ECG signal processing.

Kim et al. [6] have developed a rules-based speech analysis diagnostic system to evaluate the risk of stroke due to neurogenic bladder disease in elderly individuals. The created model was evaluated in real-time on 30 abnormal data points and 30 normal data points. The findings demonstrated a high test

*Corresponding author: makifbulbul@nevsehir.edu.tr
Received: 14.09.2023, Accepted: 21.11.2023

accuracy of 98.7% for normal data and 99.6% for abnormal data.

Casal-Guisande et al. [7] developed a decision support system using the Synthetic Minority Oversampling Technique for Nominal and Continuous (SMOTE-NC) and Fuzzy logic methods for the diagnosis of sleep apnea. The proposed decision support system has achieved successful results in experimental studies on a dataset of 4400 patients.

Javed et al. [8] used RF and SMOTE to predict heart failure. In the study, techniques such as Navian Bayes (NB), Logistic Regression (LR), Decision Trees (DT), and SVM, which are frequently used in the literature, were used, and more successful results were produced with the proposed method.

For the developed systems to produce better results, many machine learning methods are used in studies. These methods are part of a continuous improvement effort. One of the most prominent techniques in this continuous improvement effort is optimization algorithms [9], [10]. One of the optimization algorithms frequently used in the literature is the Gray Wolf Optimization (GWO) algorithm. When we look at the studies using GWO, Jeyafzam et al. [11] used the Grey Wolf Optimization algorithm to optimize the hyperparameters in the SVM model they used for the prediction of diabetes. Classification methods such as DT, Multilayer Perceptron Neural Network, Simple Bayes, and Temporal Fuzzy Min-Max Neural Network were also used in the study. The model optimized with GWO produced more successful results than other ML methods.

Magdy et al. [12] used various machine-learning methods for skin cancer classification in their study. They used the gray wolf optimization algorithm to optimize AlexNet hyperparameters and achieved successful results in skin cancer classification.

The ML methods used in the studies in the literature contain many hyperparameters. The success of the methods depends on these hyperparameters [13]. It is almost impossible to adjust these parameters using trial-and-error methods to produce successful results. Problem-specific tuning of these hyperparameters will only be possible with the development of hybrid models [14], [15].

In this study, a hybrid architecture using the GWO algorithm and Multi-Layer Perceptron (MLP) Networks is proposed for the prediction of urinary bladder inflammation. The hyperparameters in the MLP structure in the proposed architecture are optimized with GWO. In the study, DT, KNN, and SVM methods, which are frequently used in classification problems in the literature, are also used. All the methods are tested on the Acute Inflammation dataset in the UCI database, and the findings are presented comparatively.

2. Material and Method

In this part of the study, GWO, MLP, and other ML methods used to predict urinary bladder inflammation are mentioned in detail.

2.1. Multi-Layer Perceptron (MLP)

MLP is a kind of artificial neural network [16], which has several advantages such as simple structure, intuitive model parameters, and fast model training speed. In the MLP structure, there are an input layer, hidden layers, and an output layer. A simple MLP structure is shown in Figure 1.

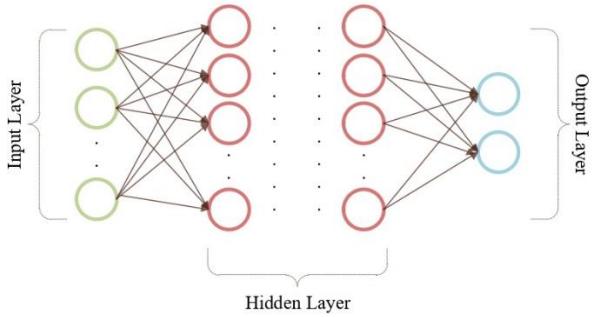

Figure 1. MLP structure.

In the MLP structure presented in Figure 1, information flow is transmitted from the input layer to the output layer. Each layer consists of neuron cells. The incoming data in the neuron cells is multiplied by the weights determined by the network and sent to an aggregation function. A bias value determined by the network is added to the data coming out of the aggregation function [14]. The data is translated by passing it through the activation function within the neuron cell, and the net output for that neuron cell is produced. In MLP structures, the output of one neuron cell is used as input for the neuron cell in the next layer. At the end of the network, the error rate between the generated output and the target output is calculated, and this error rate is reflected to the network by back propagation [15].

2.2. Gray Wolf Optimization Algorithm (GWO)

Proposed in 2014 by Faris et al., GWO is a metaheuristic algorithm and has been used in different optimization domains [17]. Gray wolves live in packs

in nature. There is a hierarchy in gray wolf packs. This hierarchy is shown in Figure 2.

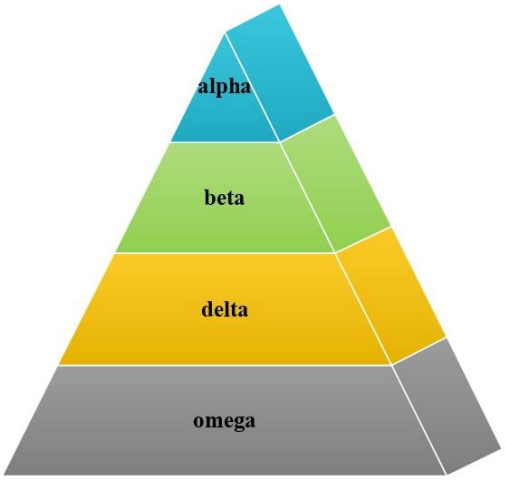

Figure 2. Gray wolf pack hierarchy.

As shown in Figure 2, there are 4 different groups in the hierarchy: α (apha) wolves, β (beta) wolves, δ (delta) wolves, and ω (omega) wolves. The alpha wolves in the pack are responsible for hunting, resting, and other group movements and the other gray wolves follow the alpha. Therefore, alpha gray wolves are seen as leaders in the pack [18].

When gray wolves hunt, they first calculate the distance between their current position and the prey to encircle it. They then update their position according to this distance. This is how gray wolves' hunting behavior is described. The mathematical representation of gray wolves surrounding their prey is shown in Equation 1 [19].

$$X(t+1) = X_p(t) - A * D \qquad (1)$$

In Equation 1, the position of the gray wolf is updated. Where t is the current iteration number, $X_p(t)$ and $X(t)$ are the current position vectors of the prey and gray wolf at iteration *t*, respectively. D represents the distance between the gray wolf and the prey and is calculated as shown in Equation 2 [20].

$$D = |C * X_p(t) - X(t)| \qquad (2)$$

A and C are the coefficient vectors presented in Equation 1 and Equation 2. These coefficient vectors are calculated as presented in Equations 3 and 4 [21].

$$A = 2 * a * r_1 - a \qquad (3)$$

$$C = 2 * r_2 \qquad (4)$$

The values r_1 and r_2 in the equations are random vectors. In Equation 3, a represents the convergence factor. The value of a converges linearly from two to zero as the iteration increases. The value of a is calculated as shown in Equation 5.

$$A = 2 - 2 * \frac{t}{t_{max}'} \qquad (5)$$

In the gray wolf model of hunting behavior, α (alpha), β (beta), and δ (delta) wolves are considered to have a better understanding of the potential location of prey. In this hierarchy, the α wolf represents the most optimal solution, the β wolf represents a suboptimal solution, and the δ wolf represents the third-best solution. The other gray wolves use computational formulas to update their position relative to the α, β, and δ wolves, which are shown in Equations 6-8 [22].

$$\begin{aligned} D_\alpha &= |C_1 * X_\alpha - X(t)| \\ D_\beta &= |C_2 * X_\beta - X(t)| \\ D_\delta &= |C_3 * X_\delta - X(t)| \end{aligned} \qquad (6)$$

$$\begin{aligned} X_1 &= |X_\alpha * A_1 * D_a| \\ X_2 &= |X_\beta * A_1 * D_\beta| \\ X_3 &= |X_\delta * A_1 * D_\delta| \end{aligned} \qquad (7)$$

$$X(t+1) = (X_1 + X_2 + X_3)/3 \qquad (8)$$

In the equations, D_α represents the distance between the current gray wolf and α gray wolf. D_β represents the distance between the current gray wolf and the β gray wolf. D_δ represents the distance between the current gray wolf and the δ gray wolf. X_α represents the α gray wolf position vector. X_β represents the β gray wolf location vector. X_δ, δ represents the gray wolf position vector. *X(t)* represents the position of the gray wolf at iteration *t*. C_1, C_2, and C_3 are random vectors and are calculated as presented in Equation 4. The position of the gray wolves is updated with Equation 8.

The flow diagram of the gray wolf optimization algorithm is shown in Figure 3.

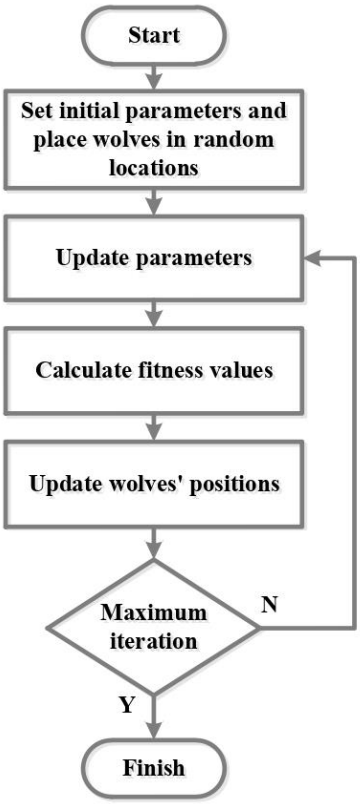

Figure 3. GWO flowchart.

What is remarkable about GWO is its ability to strike a simple balance between global search and local exploration, even though several parameters need to be tuned to achieve efficient convergence [17]. For this reason, it has been widely used in the literature in recent years [23].

2.3. Other Machine Learning Methods Used in This Study

In this study, ML methods, which are commonly used in classification problems in the literature, were also used for bladder inflammation prediction. The methods used are shown in Table 1.

ML methods presented in Table 1 produce successful results in classification problems [28]–[30].

Table 1. Other machine learning methods used in this study

ML Methods	Description
DT	Decision trees consisting of a root node, sub-branches, and nodes use multiple features and labels. A node with no sub-branches belongs to a class [24].
KNN	When classifying, KNN determines which class a new data point belongs to based on its distance from other data points [25].
SVM	SVM is a classifier that separates data placed in a given coordinate plane by drawing the best-discriminating hyperplane [26], [27].

2.4. Dataset

In this study, we used the Acute Inflammations dataset from the UCI Machine Learning repository for urinary bladder inflammation prediction [31]. This dataset was created by Dr. Jacek Czerniak at the Laboratory of Intelligent Systems of the Polish Academy of Sciences, Systems Research Institute in Warszawa, Poland [32]. The attributes in the dataset and the types of values they receive are shown in Table 2 [32].

Table 2. Data set description

No	Parameters	Data Type	Values
1	Temperature of patient	Input	35C-42C
2	Occurrence of nausea	Input	No, Yes
3	Lumbar pain	Input	No, Yes
4	Urine pushing (continuous need for urination)	Input	No, Yes
5	Micturition pains	Input	No, Yes
6	Burning of urethra, itch, swelling of urethra outlet	Input	No, Yes
7	Inflammation of uthe rinary bladder	Output	No, Yes

There are a total of 120 people in the dataset whose attributes are presented in Table 2. The dataset is randomly divided into two parts; 70% for training and 30% for testing.

2.4. Evaluation Metrics

In this study, we will calculate the recall, precision, f-score, and accuracy values used in the literature to measure the performance of urinary bladder

inflammation classifiers [33]. There are two classes in the dataset for bladder inflammation prediction. In order to calculate these evaluation criteria for the two classes, the results obtained from the classifiers must first be placed in the complexity matrix [34]. The complexity matrix for the two classes is shown in Figure 4.

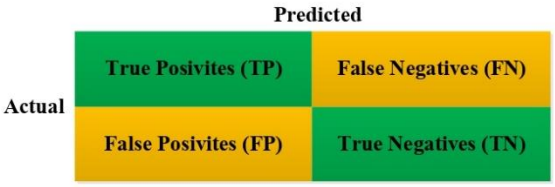

Figure 4. Confusion matrix

In the complexity matrix given in Figure 4, TP (True Positive) represents the number of people who are not actually sick and are classified as not sick. FN (False Negative) represents the number of people who are not actually sick and are classified as sick. FP (False Positive) represents the number of people who are actually sick and healthy. TN (True Negative) represents the number of people who are actually sick and classified as sick [35]. Based on these values in the complexity matrix, recall, precision, F-score, and accuracy values are calculated as presented in Equations 9-12 [36].

$$\text{Recall}(R) = \frac{TP}{TP\ +\ FN} \tag{9}$$

$$\text{Precision(P)} = \frac{TP}{TP + FP} \tag{10}$$

$$\text{F-score} = \frac{2 * P * R}{P + R} \tag{11}$$

$$\text{Accuracy(A)} = \frac{TP + TN}{TP\ + TN + FN + \ FP} \tag{12}$$

2.4. Hybrid GWO-MLP Model

In this part of the study, a hybrid architecture was created using the GWO algorithm and MLP for the prediction of urinary bladder inflammation. With this architecture, is aimed at optimizing the ranking of MLP parameters that will make the best classification and the parameters to be given as input to the MLP structure. The GWO-MLP architecture is shown in Figure 5.

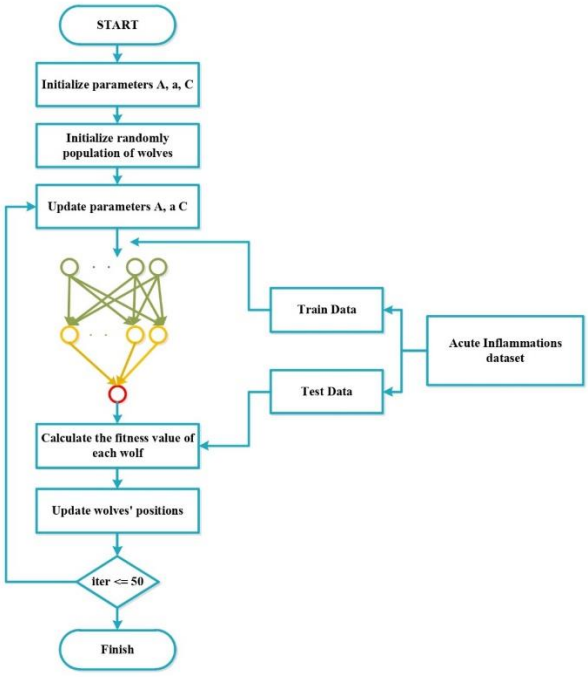

Figure 5. GWO-MLP architecture

As a first step in the hybrid architecture presented in Figure 5, GWO initial parameters were determined as a result of experimental studies. These values are shown in Table 3.

Table 3. GWO parameters

Parameters	Values
Number of Gray Wolves (n)	20
İteration Number (t)	50

In the proposed hybrid architecture, gray wolves will hunt in 6 dimensions: the input data sequence, the number of hidden layers in the MLP structure, the number of neurons in these hidden layers, the activation functions in the structure of neuron cells, the activation function in the output layer, and the learning function of the MLP. While creating a random population in these 6 dimensions, the representation and boundary values of these dimensions were determined as presented in Table 4.

The activation functions corresponding to each AFN and OLAF value in Table 4 are shown in Table.

The learning function corresponding to each LFMLP value in Table 4 is shown in Table 6.

Table 4. Solution space and boundary values

Representation	Description	Minimum Value	Maximum Value
IS	Input data sequence	6	6
NH	Number of hidden layers in the MLP structure	2	8
NN	Number of neurons in hidden layers	2	8
AFN	Activation functions used in neurons	1	6
OLAF	Output layer activation function	1	6
LFMLP	Learning function of MLP structure	6	6

Table 5. AFN and OLAF values

Representation	Corresponding Activation Function
1	radbas
2	purelin
3	logsig
4	hardlim
5	tansig
6	hardlims

Table 6. LFMLP values

Representation	Corresponding Activation Function
1	traingda
2	trainrp
3	trainbr
4	trainscg
5	traincgp
6	traingd
7	trainc
8	traingdm
9	traingdx
10	trainoss
11	traincgb
12	traincgf
13	trainb
14	trainbfg
15	trainr

The fitness function presented in Equation 13 was used to identify alpha, beta, and delta wolves in the gray wolf pack randomly generated by the number of populations given in Table 3.

$$FitF(W_i) = Test - Accuracy(MLP_i) \quad (13)$$

In Equation 13, $FitF(W_i)$ represents the fitness value of the i. gray wolf. MLP_i i. represents the MLP structure generated with the parameters of the gray wolf positions. The MLP structure obtained with the parameters of each gray wolf location performs classification on the test data.

In the presented hybrid architecture, in the next step, the positions of the gray wolves are updated according to Equation 8.

As presented in Table 3, the hybrid architecture was run for 50 iterations. After 50 iterations, the parameters and corresponding values of the location of the alpha gray wolf are shown in Table 7.

Table 7. Alpha gray wolf location and values

Parameters	Values
IS	2-1-3-6-4-5 (Table 4 indices)
NH	1
NN	6
AFN	hardlims
OLAF	tansig
LFMLP	trainoss

The MLP classifier structure obtained with the alpha wolf position information presented in Table 7 is shown in Figure 6.

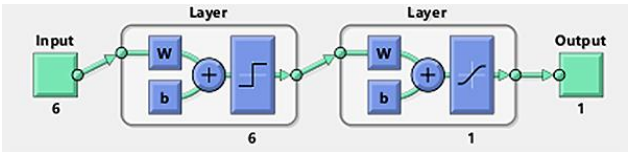

Figure 6. MLP structure formed by the alpha wolf position

3. Results and Discussion

In the experimental studies for bladder inflammation prediction, different machine-learning methods were used along with the presented hybrid architecture. The complexity matrices created by the classification processes in light of the experimental studies using DT, KNN, and SVM methods and the findings obtained as a result of the hybrid architecture are shown in Figure 7.

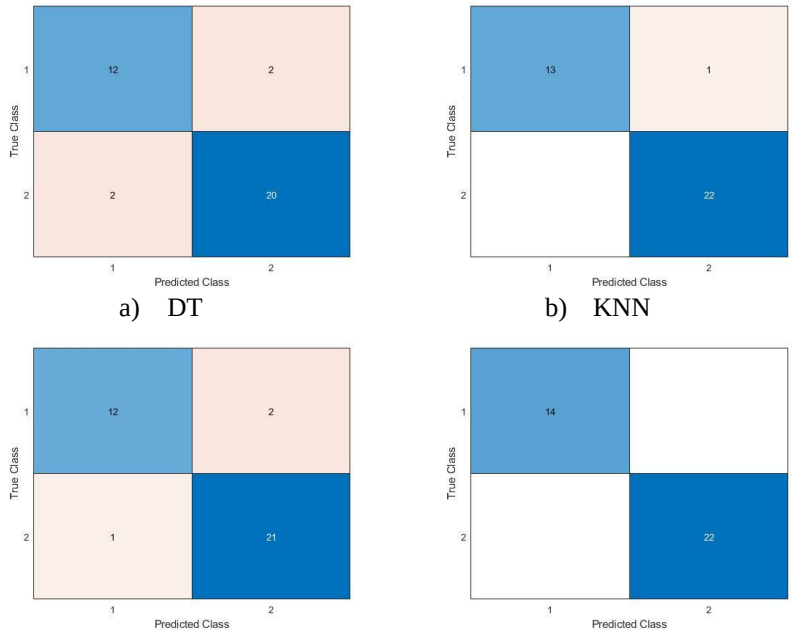

a) DT b) KNN

c) SVM d) Proposed Hybrid architecture

Figure 7. Confusion matrices of the classifiers used

According to the confusion matrices shown in Figure 7, the most successful classifier is the hybrid architecture that correctly predicts all test data.

A prominent criterion for evaluating the performance of ML models is the Receiver Operating Characteristic (ROC) curve [33]. ROC curves for each classifier are presented in Figure 8.

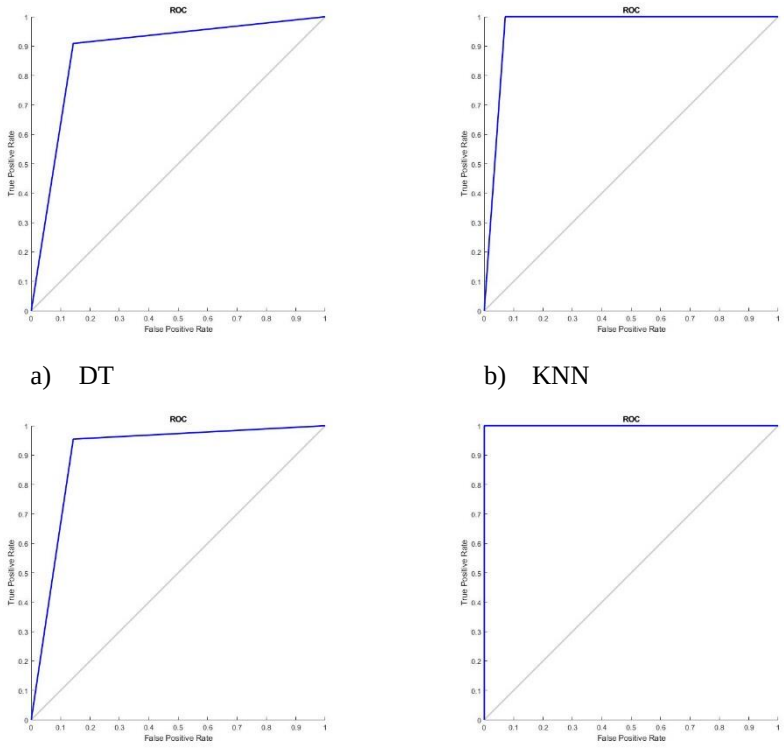

a) DT b) KNN

c) SVM d) Proposed Hybrid architecture

Figure 8. ROC curves of the classifiers

The ROC curve represents the false positive rate (FPR) on the x-axis and the true positive rate (TPR) on the y-axis. We refer to the area under the ROC curve as the AUC (Area Under the Curve). The AUC measures the classification ability of a model; the larger it is, the higher the success of the model. The most desirable value for AUC is 1, indicating that the area under the ROC curve of a perfect model is 1. Looking at the ROC curves given in Figure 8, the classification with the presented hybrid architecture produced more successful results than other ML methods.

The performance of the ML methods used in the classifications for bladder inflammation prediction is calculated according to Equations 9-12 and shown in Table 8.

Table 8. Experimental results for bladder inflammation classification

Models	Precision	Recall	F-scor	Accuracy
DT	0,86	0,86	0,86	0,89
KNN	**1**	0,93	0,96	0,97
SVM	0,92	0,86	0,89	0,92
Proposed model	**1**	**1**	**1**	**1**

According to the evaluation criteria shown in Table 8, the proposed hybrid architecture achieved high success compared to other classifiers.

4. Conclusion and Suggestions

Patient decision support systems designed with new-generation technologies realize early prediction and diagnosis of many health problems. Early diagnosis and treatment of diseases are of great importance for the protection of human health and to reduce or eliminate the negative effects caused by diseases. In this study, a GWO-MLP-based hybrid architecture is proposed to predict urinary bladder inflammation. With the proposed hybrid architecture, all hyperparameters that make up the MLP structure are optimized. In addition, the order of input information to be used as inputs in the MLP structure is also optimized by determining the order of input information within the architecture. The Acute Inflammation dataset in the UCI Machine Learning repository was used to measure the performance of the MLP structure established with the optimized parameters thanks to the hybrid architecture presented. Machine learning techniques commonly used in the literature were also used in the experimental studies on the dataset. The results of the studies showed that the hybrid GWO-MLP architecture provided accurate classification with 100% success on the test dataset for the prediction of urinary bladder inflammation. With the presented hybrid architecture, the parameters of an MLP architecture that should be created for bladder inflammation were determined, and the input data was sequenced.

The presented architecture can be easily used as an alternative method in health decision support systems. In future studies, mobile or web-based applications can be developed with these parameters.

Conflict of Interest Statement

There is no conflict of interest regarding the study.

Statement of Research and Publication Ethics

The study complies with research and publication ethics

References

[1] G. Salanturoğlu, "The Effect of Agmatine on Experimentally Generated Acute Inflammation Models," M.S. thesis, Health Sciences Institute, Marmara University, İstanbul, Turkey, 2005.

[2] L. Heuft, J. Voigt, L. Selig, M. Stumvoll, H. Schlögl, and T. Kaiser, "Refeeding syndrome—diagnostic challenges and the potential of clinical decision support systems," *Dtsch. Arztebl. Int.*, 2023, doi: 10.3238/arztebl.m2022.0381.

[3] M. A. Bülbül, "Performance of different membership functions in stress classification with fuzzy logic," *Bitlis Eren Univ. J. Sci. Technol.*, vol. 12, no. 2, pp. 60–63, 2022, doi: 10.17678/beuscitech.1190436.

[4] K. Adem, S. Kiliçarslan, and O. Cömert, "Classification and diagnosis of cervical cancer with stacked autoencoder and softmax classification," *Expert Syst. Appl.*, vol. 115, pp. 557–564, 2019, doi: 10.1016/j.eswa.2018.08.050.

[5] A. Giorgio, C. Guaragnella, and M. Rizzi, "FPGA-Based Decision Support System for ECG Analysis," *J. Low Power Electron. Appl.*, vol. 13, no. 1, p. 6, 2023, doi: 10.3390/jlpea13010006.

[6] E. S. Kim, D. J. Shin, S. T. Cho, and K. J. Chung, "Artificial Intelligence-Based Speech Analysis

System for Medical Support," *Int. Neurourol. J.*, vol. 27, no. 2, pp. 99-105, 2023, doi: 10.5213/inj.2346136.068.

[7] M. Casal-Guisande, L. Ceide-Sandoval, M. Mosteiro-Añón, M. Torres-Durán, J. Cerqueiro-Pequeño, J. Bouza-Rodríguez, A. Fernández-Villar and A, Comesaña-Campos, "Design of an Intelligent Decision Support System Applied to the Diagnosis of Obstructive Sleep Apnea," *Diagnostics,* vol. 13, no. 11, p.1854, 2023, doi: 10.3390/diagnostics13111854.

[8] A. Javeed, M. A. Saleem, A. L. Dallora, L. Ali, J. S. Berglund, and P. Anderberg, "Decision Support System for Predicting Mortality in Cardiac Patients Based on Machine Learning," *Appl. Sci.*, vol. 13, no. 8, p. 5188, 2023, doi: 10.3390/app13085188.

[9] M. A. Bülbül, C. Öztürk, and M. F. Işık, "Optimization of Climatic Conditions Affecting Determination of the Amount of Water Needed by Plants in Relation to Their Life Cycle with Particle Swarm Optimization, and Determining the Optimum Irrigation Schedule," *Comput. J.*, 2021, doi: 10.1093/comjnl/bxab097.

[10] M. F. Işık, F. Avcil, E. Harirchian, M. A. Bülbül, M. Hadzima-Nyarko, E. Işık, R. İzol, D. Radu, "A Hybrid Artificial Neural Network-Particle Swarm Optimization Algorithm Model for the Determination of Target Displacements in Mid-Rise Regular Reinforced-Concrete Buildings," *Sustainability*, vol. 15, no. 12, p.1975, 2023, doi: 10.3390/su15129715.

[11] F. Jeyafzam, B. Vaziri, M. Y. Suraki, A. A. R. Hosseinabadi, and A. Slowik, "Improvement of grey wolf optimizer with adaptive middle filter to adjust support vector machine parameters to predict diabetes complications," *Neural Comput. Appl.*, vol. 33, no. 22, pp. 15205-15228, 2021, doi: 10.1007/s00521-021-06143-y.

[12] A. Magdy, H. Hussein, R. F. Abdel-Kader, and K. A. El Salam, "Performance Enhancement of Skin Cancer Classification using Computer Vision," *IEEE Access*, vol. 11, pp.72120-72133, 2023, doi: 10.1109/ACCESS.2023.3294974.

[13] E. Işık, N. Ademović, E. Harirchian, F. Avcil, A. Büyüksaraç, M. Hadzima-Nyarko, M. A. Bülbül, M. F. Işık and B. Antep, "Determination of Natural Fundamental Period of Minarets by Using Artificial Neural Network and Assess the Impact of Different Materials on Their Seismic Vulnerability," *Appl. Sci.*, vol. 13, no. 2, p. 809, 2023, doi: 10.3390/app13020809.

[14] M. A. Bülbül and C. Öztürk, "Optimization, Modeling and Implementation of Plant Water Consumption Control Using Genetic Algorithm and Artificial Neural Network in a Hybrid Structure," *Arab. J. Sci. Eng.*, vol. 47, no. 2, pp. 2329-2343, 2022, doi: 10.1007/s13369-021-06168-4.

[15] M. A. Bülbül, E. Harirchian, M. F. Işık, S. E. Aghakouchaki Hosseini, and E. Işık, "A Hybrid ANN-GA Model for an Automated Rapid Vulnerability Assessment of Existing RC Buildings," *Appl. Sci.*, vol. 12, no. 10, 2022, doi: 10.3390/app12105138.

[16] M. Zhu, G. Zhang, L. Zhang, W. Han, Z. Shi, and X. Lv, "Object Segmentation by Spraying Robot Based on Multi-Layer Perceptron," *Energies*, vol. 16, no. 1, p. 232, 2023, doi: 10.3390/en16010232.

[17] H. Faris, I. Aljarah, M. A. Al-Betar, and S. Mirjalili, "Grey wolf optimizer: a review of recent variants and applications," *Neural Computing and Applications*., vol. 30, no. 2, pp. 413-435, 2018. doi: 10.1007/s00521-017-3272-5.

[18] D. S. Khafaga, E. S. M. El-kenawy, F.K. Karim, M. Abotaleb, A. Ibrahim, A. A. Abdelhamid, and D. L. Elsheweikh, "Hybrid Dipper Throated and Grey Wolf Optimization for Feature Selection Applied to Life Benchmark Datasets," *Comput. Mater. Contin.*, vol. 74, no. 2, pp. 4531-4545, 2023, doi: 10.32604/cmc.2023.033042.

[19] Y. Ou, P. Yin, and L. Mo, "An Improved Grey Wolf Optimizer and Its Application in Robot Path Planning," *Biomimetics*, vol. 8, no. 1, p.84, 2023, doi: 10.3390/biomimetics8010084.

[20] T. C. Tai, C. C. Lee, and C. C. Kuo, "A Hybrid Grey Wolf Optimization Algorithm Using Robust Learning Mechanism for Large Scale Economic Load Dispatch with Vale-Point Effect," *Appl. Sci.,* vol. 13, no. 4. p.2727, 2023, doi: 10.3390/app13042727.

[21] P. He and W. Wu, "Levy flight-improved grey wolf optimizer algorithm-based support vector regression model for dam deformation prediction," *Front. Earth Sci.*, vol. 11, 2023, doi: 10.3389/feart.2023.1122937.

[22] A. I. Lawah, A. A. Ibrahim, S. Q. Salih, H. S. Alhadawi, and P. S. Josephng, "Grey Wolf Optimizer and Discrete Chaotic Map for Substitution Boxes Design and Optimization," *IEEE Access*, vol. 11, pp. 42416-42430, 2023, doi: 10.1109/ACCESS.2023.3266290.

[23] K. Mehmood, N. I. Chaudhary, Z. A. Khan, K. M. Cheema, and M. A. Z. Raja, "Variants of Chaotic Grey Wolf Heuristic for Robust Identification of Control Autoregressive Model," *Biomimetics*, vol. 8, no. 2, p.141, 2023, doi: 10.3390/biomimetics8020141.

[24] N. Ji, R. Bao, X. Mu, Z. Chen, X. Yang, and S. Wang, "Cost-sensitive classification algorithm combining the Bayesian algorithm and quantum decision tree," *Front. Phys.*, vol. 11, 2023, doi: 10.3389/fphy.2023.1179868.

[25] G. Vinayakumar, A. P. Alex, and V. S. Manju, "A Comparison of KNN Algorithm and MNL Model for Mode Choice Modelling," *Eur. Transp. - Trasp. Eur.*, no. 92, pp. 1-14, 2023, doi: 10.48295/ET.2023.92.3.

[26] N. Vanitha, C. R. Rene Robin, and D. Doreen Hephzibah Miriam, "An Ontology Based Cyclone Tracks Classification Using SWRL Reasoning and SVM," *Comput. Syst. Sci. Eng.*, vol. 44, no. 3, pp. 2323-2336, 2023, doi: 10.32604/csse.2023.028309.

[27] M. F. Akay, F. Abut, M. Özçiloğlu, and D. Heil, "Identifying the discriminative predictors of upper body power of cross-country skiers using support vector machines combined with feature selection," *Neural Comput. Appl.*, vol. 27, no. 6, pp. 1785-1796, 2016, doi: 10.1007/s00521-015-1986-9.

[28] D. Chrimes, "Using Decision Trees as an Expert System for Clinical Decision Support for COVID-19," *Interact. J. Med. Res.*, vol. 12, p.e42540, 2023, doi: 10.2196/42540.

[29] C. Wang, J. Xu, J. Li, Y. Dong, and N. Naik, "Outsourced Privacy-Preserving kNN Classifier Model Based on Multi-Key Homomorphic Encryption," *Intell. Autom. Soft Comput.*, vol. 37, no.2, pp. 1421-1436, 2023, doi: 10.32604/iasc.2023.034123.

[30] H. Nakao, M. Imaoka, M. Hida, R. Imai, M. Nakamura, K. Matsumoto, and K. Kita, "Determination of individual factors associated with hallux valgus using SVM-RFE," *BMC Musculoskelet. Disord.*, vol. 24, no. 1, 2023, doi: 10.1186/s12891-023-06303-2.

[31] M. Lichman, "UCI Machine Learning Repositor," *Irvine, CA: University of California, School of Information and Computer Science*, 2013.

[32] H. Kahramanlı, "Determining the Acute Inflammations using Back Propagation Algorithm with Adaptive Learning Coefficients," 2016. doi: 10.15242/dirpub.dir1216009.

[33] M. A. Bülbül, "Optimization of artificial neural network structure and hyperparameters in hybrid model by genetic algorithm: iOS–android application for breast cancer diagnosis/prediction," *J. Supercomput.*, 2023, doi: 10.1007/s11227-023-05635-z.

[34] C. Öztürk, M. Taşyürek, and M. U. Türkdamar, "Transfer learning and fine-tuned transfer learning methods' effectiveness analyse in the CNN-based deep learning models," *Concurr. Comput. Pract. Exp.*, vol. 35, no. 4, 2023, doi: 10.1002/cpe.7542.

[35] M. A. Bülbül, "A Hybrid Approach for Multiclass Classification of Dry Bean Seeds," *Journal of the Institute of Science and Technology.*, vol. 13, no. 1, pp. 33-43, 2023, doi: 10.21597/jist.1185949.

[36] M. Taşyürek, "ODRP: a new approach for spatial street sign detection from EXIF using deep learning-based object detection, distance estimation, rotation and projection system," *Vis. Comput.*, 2023, doi: 10.1007/s00371-023-02827-9.

Bitlis Eren Üniversitesi Fen Bilimleri Dergisi
BİTLİS EREN UNIVERSITY JOURNAL OF SCIENCE
ISSN: 2147-3129/e-ISSN: 2147-3188
VOLUME: 12 NO: 4 PAGE: 1195-1211 YEAR: 2023
DOI:10.17798/bitlisfen.1362136

Theoretical Models Constructed by Artificial Intelligence Algorithms for Enhanced Lipid Production: Decision Support Tools

Aytun ONAY[1*]

[1]*Turkish Aeronautical Assocation University Engineering Faculty, Software Engineering, Ankara, 06790, Turkey*

(ORCID: 0000-0001-5104-0668)

Keywords: Artificial intelligence algorithms, Biodiesel, Chlorella minutissima, Ensemble learning algorithms, Microalgal lipid content, Response surface methodology.

Abstract

Theoretical models that predict the lipid content of microalgae are an important tool for increasing lipid productivity. In this study, response surface methodology (RSM), RSM combined with artificial neural network (ANN), and RSM combined with ensemble learning algorithms (ELA) for regression were used to calculate the maximum lipid percentage (%) from Chlorella minutissima (C. minutissima). We defined one set of rules to achieve the highest lipid content and used trees.RandomTree (tRT) to simulate the process parameters under various conditions. Among the various models, results showed the optimum values of the root mean squared error (0.2156), mean absolute error (0.1167), and correlation coefficient (0.9961) in the tRT model. RSM combined with tRT estimated that the lipid percentage was 30.3% in wastewater (< 35%), lysozyme (≥ 3.5 U/mL), and chitinase (< 15 U/mL) concentrations, achieving the best model based on experimental data. The optimal values of wastewater concentration, chitinase, and lysozyme were 20% (v/v), 5 U/mL, and 10 U/mL, respectively. Also, the if-then rules obtained from tRT were also used to test the process parameters. The tRT model served as a powerful tool to obtain maximum lipid content. The final rankings of the performance of various algorithms were determined. Furthermore, the models developed can be used by the fuel industry to achieve cost-effective, large-scale production of lipid content and biodiesel.

1. Introduction

The demand for renewable energy has increased in emerging nations. The majority of countries are trying to find renewable energy alternatives to replace fossil fuels [1], [2]. Biodiesel production has become very important for the global fuel market due to the consumption of fossil fuels, growing energy consumption, climate change, and environmental pollution, but it needs highly innovative research and development [3], [4]. Biodiesel obtained from microalgal biomass is an encouraging source of renewable energy; however, there are some difficulties in producing algae-derived biodiesel [5]-[7]. Therefore, researchers are looking into new economical production techniques [8]-[10]. Biomass features intracellular lipids and rigid cell walls thus an appropriately selected solvent is needed to extract the lipids [11], [12]. Many studies have been conducted to investigate cell wall destruction and optimal solvent selection to improve microalgal lipid yields. Water in biomass also acts as a barrier to achieving lipid extraction. The biodiesel efficiency of microalgae is based on dry biomass [13], [14]. The industry has struggled to decrease the cost of not only wet but also high-water-content algal biomass. Microalgae are used as health foods and in cosmetics by different industries. They have produced some impressive products, like lipids, carbohydrates, pigments, and proteins [15]. The high-volume

*Corresponding author: aonay@thk.edu.tr
Received: 18.09.2023, Accepted: 02.12.2023

production of various metabolic products looks quite promising for obtaining lipids, biomass, green energy products, enzymes, polymers, toxins, and pigments. Microalgae use solar energy and consume carbon dioxide for photosynthesis [16], [17]. The cultivation conditions are important for microalgae, affecting their growth characteristics and cellular composition [18], [19]. The most-used culture media include photoautotrophic, heterotrophic, and mixotrophic media. The major drawback is the cultivation cost to obtain biomass. Nitrogen (80 kg) and phosphorous (5 kg) are needed to get about one ton of biomass [20]. Therefore, optimizing the process parameters is important to obtain high amounts of lipids in a cost-effective way. Researchers have searched for different theoretical methods and developed software tools to predict the maximum lipid content and biomass productivity based on cultivation conditions and medium compositions. Among them, RSM is the major optimization technique [21]–[24]. RSM combined with ANN has also been performed to determine the optimal medium components and cultivation conditions [25], [26]. Furthermore, based on optimization studies in the literature, the genetic algorithm with support vector machines (SVM) and fuzzy logic methods (FLM) were implemented. Mondal et al. [27] performed the central composite design (CCD) to optimize three main process parameters: temperature, light intensity, and CO2. Chlorella sp. BTA 9031 was used in the cultivation medium for biomass and lipid formation. The optimum levels of 28.26 °C, 76.64 μmol m−2s−1, and 4.00% CO2 were determined for temperature, light intensity, and CO2, respectively. The results show that the model achieved reliable results. Alam et al. [28] searched for the effects of process parameters on three-phase partitioning performance (TPP). The temperature, incubation duration, and extraction time were optimized by using RSM. C. vulgaris, which has a high water content, was used for the extraction of lipids. At a ratio of 1:1 solvent to DKP, the optimum results for the temperature, incubation duration, and extraction time were 60 °C, 120 min, and 60 min, respectively. The results revealed that the lipid extraction procedure can be performed to form biodiesel. Ishola et al. [29] focused on developing a model. The transformation of sorrel (Hibiscus sabdariffa) oil to H. sabdariffa methyl esters (HSME) was modeled using RSM, ANN, and a neuro-fuzzy inference system (ANFIS). According to the statistical tests, the models developed to describe the transesterification process were very precise and reliable. The ANFIS model achieved the highest R2 value (0.9944). The ANFIS model optimized with genetic algorithm (GA) predicted the optimum conditions for maximum HSME product yield (99.71 wt%) at the methanol/oil molar ratio of 8:1. Catalyst weight, reaction time, and temperature were found to be 1.23 wt%, 43 min, and 65 °C, respectively. The results show that the HSME can be used as an alternative to petro-diesel.

In this study, RSM, RSM combined with ANN, and RSM combined with ELA [random forest (RF), random tree (RT), and bagging (BA)] were used to calculate the maximum lipid percentage (%) from C. minutissima using the MATLAB, SIMULINK and Weka software [30]-[34]. Different concentrations of wastewater, chitinase, and lysozyme were tested using Box-Wilson design to observe the process parameters that cause changes in the lipid content.

Wastewater can be used to produce biofuels from microalgae. High levels of carbon, nitrogen, and phosphorus in wastewater can act as nutrients for microalgae and enable them to grow. The microalgal mass obtained in large amounts can also be used in biofuel production. Thus, economically advantageous biofuel can be obtained without providing carbon, nitrogen, and phosphorus input to the system from the outside [35]. Chitinase and lysozyme are two important enzymes that can take part in the degradation of the outer surface of microalgae cells. With this pre-treatment technique, the outer membranes of microalgae can be further broken down, and quickly, enabling greater access to their metabolic contents. In this case, it means producing more lipids [36]. Since the optimization of variables such as carbon source, temperature, pH, and light in biodiesel production is well known, the parameters used in this study can increase the lipid amount and generate more metabolic content. The synergistic effects of the parameters on lipid content were also examined by performing a circumscribed central composite design (CCCD) of RSM. In this study, AI algorithms were run together with RSM in a combined structure. The literature describes the ANN and RSM models on biofuel production as “black boxes.” By developing explainable platforms and simplifying the models for the researcher’s understanding, we make the models more robust and transparent. Also, there are few reported models and articles on biofuel research using combined RSM-ELA models. The trees.RandomTree (tRT) model is an explainable machine-learning model that lays out one set of rules to achieve the optimal parameters and serves as a decision-support tool to achieve maximum lipid content. This theoretically obtained decision mechanism is of great importance to researchers. Interactive response surface modeling

(rstool) and prediction plots were also developed and drawn for the three process parameters of wastewater concentration (v/v %), chitinase (U/mL), and lysozyme (U/mL). The novelty of this study is the production of lipids, which are biodiesel raw materials, theoretically in high amounts by using wastewater-containing nutrients for microalgae and enzyme technologies such as chitinase and lysozyme. This theoretical study can be achieved by using the parameters without the need for repeated experiments in the production of biodiesel. Thus, the cost will be reduced, as no experimental repetitions are made. The paper also overviews AI algorithms that can be used in other projects with similar conditions and practical applications.

2. Material and Method

ANN is ideal for building regression models and conditions, and it has the ability to learn and model nonlinear and complicated interactions, which is crucial because the parameter relationships (wastewater concentration, chitinase, and lysozyme) between inputs and outputs are nonlinear and complex. As the number of parameters used in biofuel studies increases, using a decision tree structure in optimization studies is very important in terms of simulating parameter values under various environmental conditions. In this regard, our research is important. Bagging of regression trees helps to make machine-learning algorithms work better and more accurately. They are used to deal with trade-offs between bias and variance and to lower the variance of a prediction model. Therefore, RSM combined with ELA models were used for regression. The performance results of all the algorithms were given to the researchers for comparison.

2.1. Cultivation of Microalgae and Lipid Extraction

The experimental data related to C. minutissima CCALA 723 were obtained from Van YYU, Department of Environmental Engineering, Turkey. Microalgae were grown in BG-11 medium and municipal wastewater. Wastewater was prepared according to Khan's method with a few modifications [37]. The medium includes glucose (540 mg/L), ammonium chloride (180 mg/L), sodium bicarbonate (140 mg/L), and potassium dihydrogen phosphate (55 mg/L). The medium was mixed with distilled water in a ratio of 1:50. Wastewater (0–100%) was mixed with BG-11 medium proportionally. Chitinase (0–50 U/mL) and lysozyme (0–20 U/mL) were combined for the disruption of microalgae. Microalgae were harvested by centrifugation at 3000g for 10 min, and lipid extraction was performed according to the Folch method [38]. The final ratio of methanol, chloroform, and water was 1:1:0.9. Lipid samples were weighed gravimetrically.

2.2. Design of Experiments

2.2.1. Quadratic Response Surfaces for Modeling

The synergistic and individual effects of the parameters were examined with CCCD to calibrate the quadratic models and construct a five-level three-factor model. This model generated 24 theoretical runs. The theoretical design contained 8 factorials, 6 axial points, and 10 replicate results at the center points, maintaining knowledge of the interior of the experimental region. To determine the repeatability of the method, the center point was repeated ten times. Using a Box-Wilson model, the ideal levels of three process variables were determined: wastewater concentration (% v/v) (X_1), chitinase (U/mL) (X_2), and lysozyme (U/mL) (X_3). Factors X_1, X_2, and X_3 were figured out on -2 (the axial points), -1, 0 (central point), +1 and +2 (the axial points) theoretical levels, as given in Table 1. Each test was implemented on the data to determine the average of the duplicates. The relationship between the independent factors and the dependent value Y was modeled as the second-degree polynomial in X_1, X_2, and X_3. The second-order polynomial coefficients were solved by MATLAB to obtain high amounts of lipids. The results were also used to generate the response surface graphs. The quadratic equation was solved to determine the response Y value of the model given as follows:

$$\mathbf{Y}_{\text{lipidpercentage}}=\boldsymbol{\beta_0}+\boldsymbol{\beta_1}X_1+\boldsymbol{\beta_2}X_2+\boldsymbol{\beta_3}X_3+\boldsymbol{\beta_{12}}X_1X_2+\boldsymbol{\beta_{13}}X_1X_3+\boldsymbol{\beta_{23}}X_2X_3+\boldsymbol{\beta_{11}}X_1X_1+\boldsymbol{\beta_{22}}X_2X_2+\boldsymbol{\beta_{33}}X_3X_3 \quad (1)$$

where Y was the predicted lipid percentage (%). $\boldsymbol{\beta_0}$ represents the intercept; $\boldsymbol{\beta_1}, \boldsymbol{\beta_2}, \boldsymbol{\beta_3}$ the linear effect, $\boldsymbol{\beta_{11}}, \boldsymbol{\beta_{22}}, \boldsymbol{\beta_{33}}$ the quadratic coefficients, and

Table 1. The axial and central points for the model

Factors	Variables codes	Coded factor levels*				
		-2 (-∝)	-1	0	+1	+2 (+∝)
Wastewater concentration (% v/v)	X_1	0	20	50	80	100
Chitinase (U/mL)	X_2	0	5	10	25	50
Lysozyme (U/mL)	X_3	0	2	5	10	20

*+∝ and - ∝ indicate the axial points

$\boldsymbol{\beta_{12}\beta_{13}\beta_{23}}$ the interaction effect. The theoretical data obtained from CCCD were adjusted for the quadratic equation.

2.2.2. ANOVA Statistics

The analysis of variance (ANOVA) was calculated to determine the accuracy of the RSM model with the degree of freedom (DF) values for each term, sum of squares (SS) for the regression model, mean squared error (MSE) for each term, F-statistic value, and P-value for the F-test. The coefficient of determination (R^2) and the adjusted R^2 were used to denote the validity of the model. The R^2 value is advanced by approximately 1. When p has a very small value ($p < 0.05$), the involved term in the model achieves an important action on the response. The best model is constructed by getting a very good agreement between predicted and experimental results. MATLAB was run to perform the ANOVA calculation.

2.3. Application of the ANN Model

ANN closely mimics the human brain and has several advantages over the traditional theoretical model. It can be implemented quickly into rigorous phenomenological models. The network design was constructed with MATLAB to model the optimization process of lipid extraction. A two-layer feed-forward network with sigmoid hidden neurons and linear output neurons was defined for the network architecture. The Levenberg-Marquardt algorithm was used to train the neural network. The experimental data were arbitrarily split into three groups: 70% for the training set, 15% for the validation set, and 15% for the test set. The model was based on this dataset. After training the network, MSE, and regression analysis were used to evaluate its performance. MSE measures the average squared difference between the output and targets. The lower the MSE value, the stronger the model is. In addition, regression (R) predicts the relationships between the response variable and predictors or features. An R is expected to be close to 1. In this study, the network was formed from an input layer, a hidden layer, and an output layer. An input layer had three neurons, such as wastewater concentration, chitinase, and lysozyme. The number of hidden neurons (20) was optimized to get the minimum value of MSE. Also, an output layer had one neuron.

2.4. Interactive Response Surface Modeling and Prediction Plots

The maximum values of y were searched by using rstool. Rstool displays a graphical user interface for exploring one-dimensional contours of multidimensional response surface models interactively using MATLAB. Syntax was determined as rstool (x, y, quadratic, alpha, xname, yname). X defines the input values, y defines the response values, and alpha is 0.01. The y values were theoretically found for the ANN and ELA models, and the y values for the RSM model were experimentally determined. For the fitted response surface, rstool plots two red curves, representing a 95% confidence band. Input values were given in the text boxes on the horizontal axis and marked by vertical dashed blue lines in the plots. In this study, interactions and full quadratic models were used. The interaction model contains constant, linear, and interaction terms. The full quadratic model also contains squared terms. These terms take place in the quadratic response surface equation as given in Eq. 1. By interacting with the rstool interface, the RSM, ANN, and ELA demos are able to display the outcomes of simulated experiments involving data or pre-specify combinations of predictors. The maximum lipid percentages for each model were predicted. Root mean squared error (RMSE) and beta/constant (intercept) values were used to evaluate the model performance.

2.5. Ensemble Learning Algorithms

RF, RT, and BA were used for building regression models. Weka software was used to execute algorithms to obtain the maximum lipid content. The experiments were done in 24 sets, as mentioned above.

To improve the accuracy of the model, runs 15 to 24 were set at the same input conditions. After

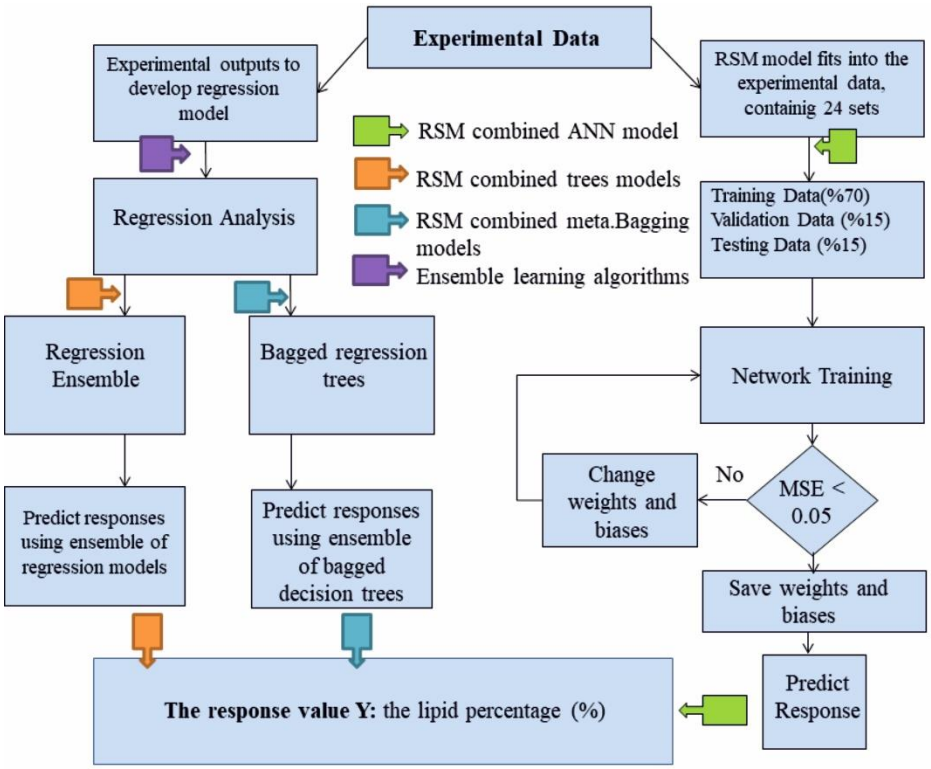

Figure 1. Graphical representation of the various models.

performing the experiments, the outputs were collected. Then, the RSM model was obtained to fit the data. The experimental outputs were used to develop regression models. Predictor variables (X_1, X_2, X_3) and response variables (Y) built the model. The correlation coefficient, mean absolute error, and RMSE were calculated to prove the accuracy of the regression model parameters. Figure 1 shows the different models in a simplified diagram.

AI algorithms are used to perform various tasks such as classification, clustering, and regression. In this study, RF and RT were used to determine the most effective parameters for lipid production. The model developed with RF or RT can be used as a decision-support tool. RF was extended by Leo Breiman and Adele Cutler, who obtained a trademark for the tool [39], [40]. Both RF and RT achieved good results to estimate the lipid percentage (%). The if-then rules obtained from tree algorithms are provided in the results section.

The learning models used by Random Forest consist of numerous decision trees. For each model, we create a sample dataset by randomly selecting rows and features from the dataset. This section is known as Bootstrap.

BA has three stages. Firstly, it creates several samples from the main training set by assigning each combination the same probability. Then, it performs a base learner (regression tree in our case) model for the samples. Finally, it averages the values calculated for the test sets over the models. Weka builds this process using "meta-learning" under the name bagging. The dataset was in .csv format and contained 24 experimental run results with regard to the three attributes (inputs) and response values (outputs; see Table 2). Our data matrix was composed of three parameters. The training set in .csv format was used to obtain developed regression models in this study. After the file in .csv format is converted to .arff, this model can be loaded into the Weka software and used to make predictions on new data. All models obtained in the study can be run by researchers to perform the prediction procedure on the lipid percentage (%).

Because of the little available data (Table 2), cross-validation was performed to improve the model's predictive performance. K-fold (a cross-validation technique) was used in this part of the study, and 10-fold validation (k = 10) was chosen. This technique is done k times such that each subset is validated exactly once. For smaller datasets, k-fold technique is recommended. Because training and validation are performed multiple times, cross-

validation can be a computationally costly procedure. It is, nonetheless, an important stage in the model building since it reduces the risk of overfitting or underfitting a model. The average errors across all k = 10 partitions are reported in this study. After loading the models to Weka software, the results of the new test sets for which the option "Re-evaluate model on current test set" is worked can be obtained using the algorithms above. The predictions for each new test are given in the "Classifier Output" pane in the program.

3. Result and Discussion

In this section, the interactions of wastewater concentration, chitinase, and lysozyme and their impacts, positive or negative, on the lipid percentage (%) are discussed.

3.1. Comparison of The Quadratic RSM and ANN Model

RSM is a practical technique for searching for the effects of several factors affecting the process of calling the optimal terms. This method provides a way to reduce the number of experiments, evolve statistical interpretation possibilities, and specify the interaction among various variables. The equation was improved to correlate Y with the functions of X_1, X_2, and X_3. The empirical model developed by RSM is given by the equation below:

$$Y = 20.879 + 0.0897\ X_1 - 0.0927\ X_2 + 1.446\ X_3 + 0.0018\ X_1X_2 + 0.0016\ X_1X_3 - 0.0031\ X_2X_3 - 0.0014\ X_1X_1 - 0.0011\ X_2X_2 - 0.0604\ X_3X_3 \quad (2)$$

RSM results showed that the MSE, R^2, and adjusted R^2 values are 0.2414, 0.9765, and 0.9614, respectively. The MSE of a model relative to a test set is the mean of the squared prediction errors in all instances in the test set. When there are no errors in a model, the MSE equals 0. The proportion of the variance in the dependent variable that can be defined by the independent variable is evaluated by R^2. R^2 indicates how well the data fit the regression model (the goodness of fit). The greater the R^2 value, the smaller the MSE. If the value of R^2 reaches 1 (ideal-world scenario), the model fully fits the data with an MSE of 0. Adjusted R^2 is a modified form of R^2 that adjusts for nonsignificant factors in a regression model. The modified R^2 indicates whether the addition of more predictors improves a regression model. Adjusted R^2 will never exceed R^2. R^2 states that every variable explains the variation in the dependent variable. Adjusted R^2 signifies how much variation is explained by independent variables that affect the dependent variable. A higher adjusted R^2 in a model with additional input variables implies that the additional input variables provide value to the model. Table 2 shows both the experimental design and the results.

Lipid content ranges from 21.4% to 30.3% for experimental data (Table 2). Interdependent effects are denoted by a positive sign in front of the variables, whereas opposite effects are denoted as a negative sign in equation Y, which included linear, interaction, and squared terms with the three factors. P-value (probability value) is expected to be less than 0.05, and F-value is expected to be high (~1) in the models. MATLAB was used to construct the models. The maximum lipid percentage of 30.4% was obtained by using RSM, in which wastewater concentration, chitinase, and lysozyme were 20% (v/v), 5 U/mL, and 10 U/mL, respectively. The highest lipid percentage determined by the experiments was 30.3%. ANOVA was used to calculate degrees of freedom (DF), sum of square (SS), MSE, F-statistic value, and P-value for the model. It measures the model effectiveness and the fitness of the regression model. ANOVA results for the RSM are presented in Table 3. As shown in Table 3, the P-value and F-value were found to be 0.00001 and 64.7132, respectively. The results show that the quadratic model is highly important to predict lipid content based on the experimental data.

The regression equations (Eq. 2) that describe the impacts of independent process factors on lipid production are graphically represented in the 3D and 2D plots. The elliptical shape in the contours defines important impacts among parameters. The spherical form of the contour plot indicates that the interaction effect of parameters is insignificant. The maximum value for the lipid content is indicated by the center ellipse in the contour plot. This value is found within the intervals of parameters that have been specified. The 3D and 2D plots that are obtained depend on two parameters, while the third parameter stays the same at the origin. In Figure 2a, a surface plot (3D) displays both mutual and interaction effects between X_1 and X_2. The increase in X_2 from low to high levels decreased the lipid content. The maximum lipid content occurred when X_1 (50 %) was at the middle level and X_2 was at the minimum level. Lipid content was thus significantly affected by the interaction between X_1 and X_2. P-value (0.0048333) is an indicator of this. The form of the contours in Figure 2b clearly reveals significant interactions between factors. As shown in Figure 2c, the 3D surface plot displays the mutual and interaction effects of X_1 and X_3 on the lipid content. Increasing X_1 and X_3 caused an increase in the lipid content to some extent, but then it had an adverse effect on the

Table 2. RSM and ANN model-based design for optimization of lipid content

Exp. order	Process parameters			Lipid percentage (%)		
	Wastewater concentration (% v/v)	Chitinase (U/mL)	Lysozyme (U/mL)	Experimental	RSM predicted	ANN predicted
1	20	5	2	24.4	24.5	24.4
2	20	5	10	30.3	30.4	30.3
3	20	25	2	22.0	22.6	22.0
4	20	25	10	28.1	28.0	28.1
5	80	5	2	21.4	22.1	22.8
6	80	5	10	29.0	28.7	29.0
7	80	25	2	22.2	22.4	22.2
8	80	25	10	28.2	28.6	28.2
9	0	10	5	25.6	25.4	24.5
10	100	10	5	23.2	22.8	23.2
11	50	0	5	27.4	27.9	27.4
12	50	50	5	24.6	24.4	20.2
13	50	10	0	22.5	21.7	22.5
14	50	10	20	27.4	27.4	27.4
15	50	10	5	28.1	27.7	27.7
16	50	10	5	27.3	27.7	27.7
17	50	10	5	27.9	27.7	27.7
18	50	10	5	27.3	27.7	27.7
19	50	10	5	27.8	27.7	27.7
20	50	10	5	28.4	27.7	27.7
21	50	10	5	27.5	27.7	27.7
22	50	10	5	27.8	27.7	27.7
23	50	10	5	27.6	27.7	27.7
24	50	10	5	27.5	27.7	27.7

Table 3. ANOVA Results for the RSM

Source	Lipid percentage (%)					
	DF [a]	SS[b]	MS[c]	*F*-value	*P*-value	Significance
Model	9.0000	140.5901	15.6211	64.7132	0.0000	Significant
Residual	14.0000	3.3795	0.2414			
Total	23.0000	143.9696				

[a]Degrees of freedom for each term
[b]Sum of square for the regression model
[c]Mean squared error for each term

the lipid content. Figure 2d shows that there is no significant interaction effect between X_1 and X_3 to contribute to lipid content. This can be also observed from the P-value (0.28883).

Figure 2a and Figure 3a show that the interaction of X_1 and X_2 was more significant than that of X_2 and X_3 on lipid content. Lipid content also shows a nonlinear effect with the increase of X_3 from 0 to 20, and with the increase of X_2 from 0 to 50 under constant X1. The irregular contour plot in Figure 3b shows that both X_2 and X_3 had an interaction effect, but it was not enough to change the lipid content (P-value, 0.4727). According to the ANOVA results, the overall model is important (P-value < 0.00001). ANN, based on feed-forward neural networks with TANSIG transfer function, was used to optimize the process variables on lipid content. The model predicted lipid percentage (%) at the times (t = 0, t + n), presented in Table 2. ANN was iterated with varying numbers of hidden neurons with transfer functions in the layer to optimize the training and validation data set to achieve a coefficient of determination. Figure 4 shows all input and output variables that compare the R^2 value of the training, the validation and test data, and all prediction networks, with the values 0.99548, 0.96336, 0.98257, and 0.92838, respectively.

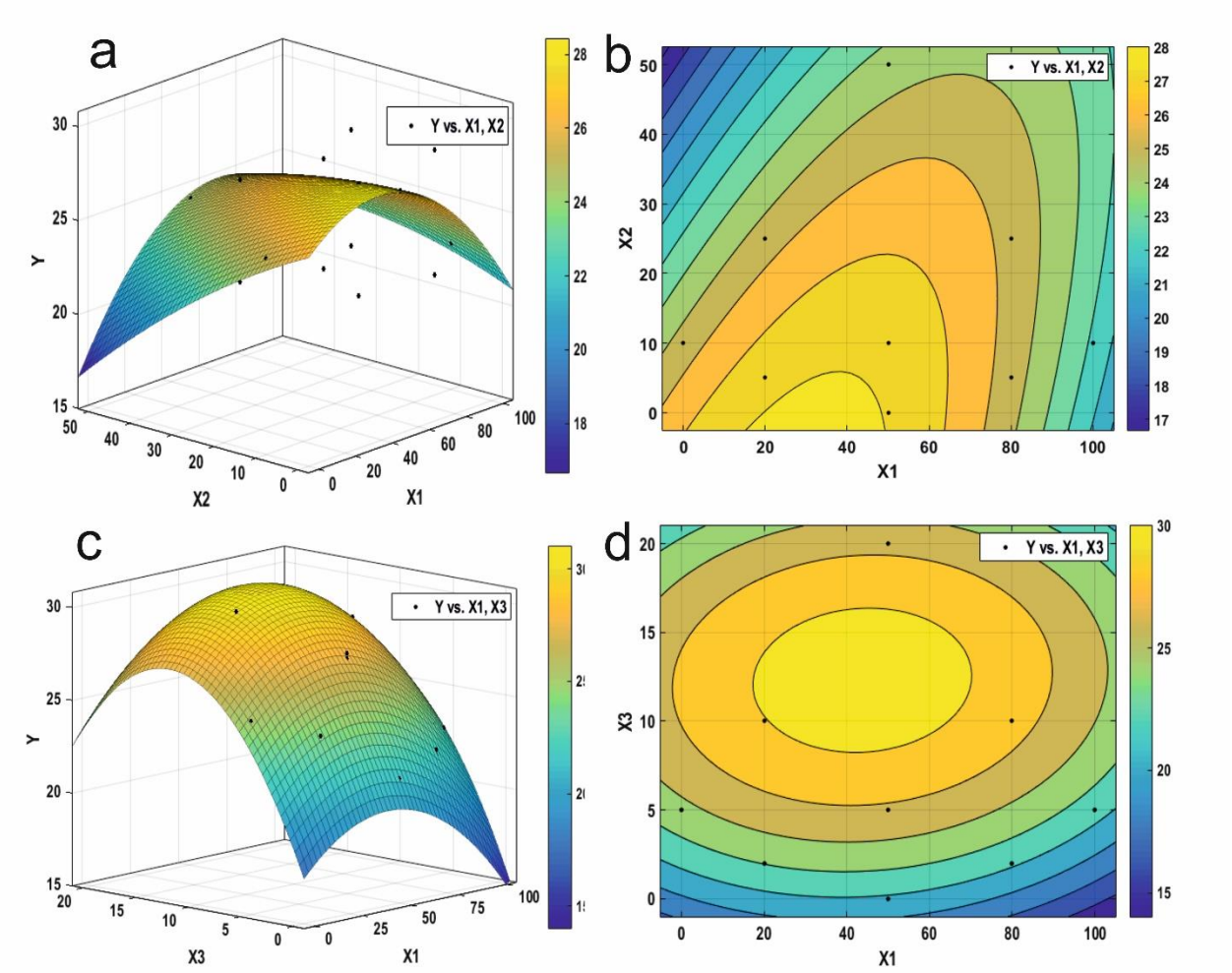

Figure 2. 3D and related 2D plots for the various effects of (a-b) wastewater concentration (X_1) and chitinase (X_2); (c-d) wastewater concentration (X_1) and lysozyme (X_3) on the lipid percentage (%).

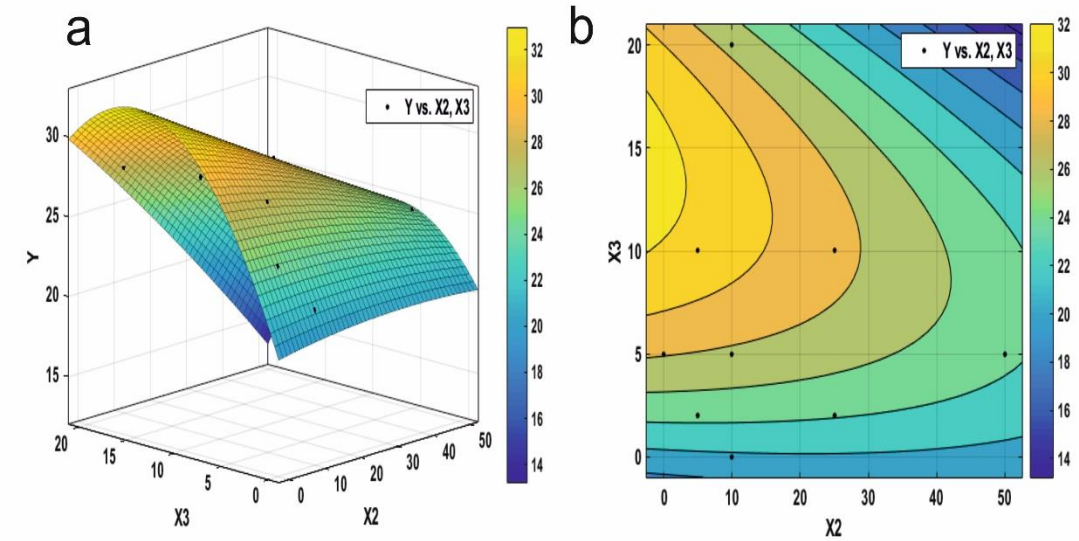

Figure 3. (a) 3D and (b) related 2D contour plots for the various effects of chitinase (X_2) and lysozyme (X_3) on the lipid percentage (%).

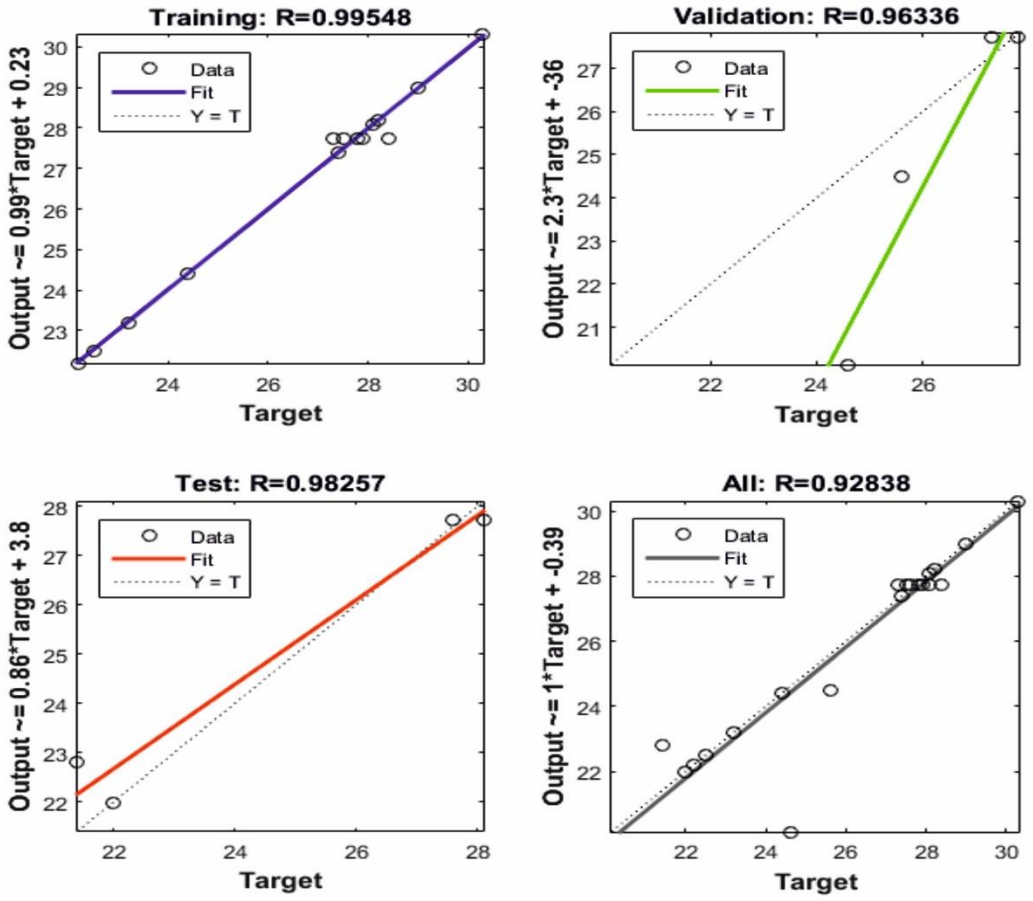

Figure 4. Fitness of the different datasets and all prediction networks in the ANN model.

ANN model reached an R^2 value close to 1 for the data sets in Figure 4 and had high-accuracy results in modeling to the output parameters estimating lipid content. The MSEs of the ANN model for the training and test data were 0.0484 and 0.5221, respectively. The model estimated the optimum conditions for maximum lipid content as X_1 = 20% (v/v), X_2 = 5 U/mL, and X_3 = 10 U/mL, with a maximum lipid percentage of 30.3%. These results indicate that the ANN outperformed RSM in predicting lipid content.

In this section, literature-based studies on experimental designs and theoretical models are presented. Mäkelä [22] presented a review of the energy field, which provides many aspects of experimental design and RSM with applications. Mäkelä (2017) reported many solutions for the modeling studies. Tourang et al. [20] studied the optimization of macronutrient concentrations for *Spirulina* microalgae, and CCD was used to optimize the culture medium. Muthuraj et al. [41] studied lipid-rich biomass with a high density of *Chlorella sp*. FC2 IITG under photoautotrophic conditions using a process engineering strategy. They used ANN or RSM with a genetic algorithm (GA) for medium optimization, and the results showed that ANN-GA achieved an increase in biomass titer of 157% (0.95 g L^{-1}) in a shake flask. Thanaa et al. [42] researched 13 filamentous fungi for their lipid production. CCD was performed to obtain the optimum concentrations to increase lipid productivity, and they concluded *P. brevicompactum* NRC 829 may be used for commercial development. Dammak et al. [43] optimized the V2-strain to maximize the cell growth and lipid content of the oleaginous microalgae by using RSM. The results indicated that strain V2 was convenient for food and nutraceutical applications. By using RSM, Onay (2020) studied increasing the lipid content of *N. gaditana* using several assisted lipid extraction methods. The greatest lipid content was achieved in 10 KCI% osmotic shock, 30 kHz ultrasound, and 10 U/mL lysozyme with a lipid percentage of 37% [44]. Khaouane et al. [45] used a hybrid method with CDD, ANN, and the particle swarm optimization algorithm (PSO) to optimize the culture conditions of pleuromutilin production. The hybrid technique determined the optimum levels of culture conditions at 242 rpm agitation speed,

temperature of 26.88 °C, and pH of 6.06 with a pleuromutilin yield of 10.074 ± 500 µg/g. Sohedein et al. (2020) used RSM to construct an optimization model to extract the maximum biomass (6.25 g L^{-1}) and lipid content (14.88% DW) from *Aurantiochytrium sp*. They concluded that biomass concentration in the bioreactor increased 2.12-fold compared to the shake flask culture. The optimized model could provide large-scale biodiesel production [46]. Chakravarty et al. (2019) performed three sets of optimization with a central composite rotary design. Using the effects of nitrate, phosphate, and NaCl, they considered the fourth factor, incubation period, to achieve optimum lipid content in a minimum of days. *Selenastrum sp.* GA66 was subjected to stress factors. Researchers observed that the optimized process parameters required less nitrate. The improved model can be used to obtain biodiesel economically [47]. Zhang et al. [48] improved lipid extraction yield from *Scenedesmus sp.* This study involved cell-wall disruption. The RSM method was used to optimize enzyme-assisted lipid extraction methods. The analysis showed that the optimal conditions produced twice as much lipid content as not using enzymes. Ayoola et al. [26] performed RSM and ANN to determine the effects of KOH and NaOH catalysts on waste groundnut oil (WGO) biodiesel production. They reported that the maximum yield of biodiesel was obtained from KOH catalyst. The results show that ANN and RSM can be used to solve complex problems in biodiesel production. To maximize the lipid content of various microalgae, RSM or RSM combined with ANN methods are the most studied in literature. RSM combined with ELA was also performed in our study for lipid-rich biomass.

3.2. Interactive Response Surface Method

Interactive response surfaces with full quadratic and interaction models were improved to calculate the maximum lipid content. Fitted coefficients were determined for RSM, ANN, and ELA-based designs. The RMSE values for the full quadratic models were 0.4913, 0.2500, and 0.6104 for RSM, ANN, and tRF, respectively. When modifying the value of a predictor, all plots are automatically updated to reflect the new data point within the predictor space. Therefore, when the value of a predictor changes, we can simultaneously observe it graphically. The models predicted the maximum lipid percentage at 50% v/v of X_1, 12.9167 U/mL of X_2, and 5.75 U/mL of X_3. The fitted coefficients are displayed in Table 4.

Beta terms were also given to all developed models. From the beta terms, the effects of contributions from linear, interaction, and squared terms on the lipid content (Y), as functions of process variables, were found separately. Rstool models are displayed in Figure 5 for RSM.

The RMSE value of 0.4021 was observed with a lipid percentage of 28.1678 ± 0.85206 % for tRT. In terms of making reliable predictions, a smaller RMSE is better. The experimental results were quite consistent with the predicted results. According to the tRT model, the contribution of linear and interaction terms to equation Y is mostly positive, whereas the contribution of squared terms to equation Y is negative. The lowest RMSE of 0.2500 was obtained from the ANN model. The tRT model also achieved a lower RMSE of 0.4021 than the other decision tree ensemble models.

3.3. Ensemble Learning Algorithms for Regression

In the Weka software, optimization of factor levels that satisfy the conditions was performed on the process parameters and responses. Table 5 shows the decision tree ensemble models used for the regression to predict the percentage of lipid content.

According to the tRT model, the optimal values of X_1, X_2, and X_3 were determined at 20 % (v/v), 5 U/mL, and 10 U/mL, respectively. The model estimated a maximum lipid percentage of 30.3%, which is the same as the experimental result. In addition, the highest lipid percentages obtained for tRF and meta.Bagging.Classifier:RandomForest were 29.1% and 29.0%, respectively. RMSE is used to determine the data that is closest to the line of best fit. In this study, RMSE was used in regression analysis to validate experimental data. The predictive accuracy for ensemble algorithms is given in Table 6.

Table 4. Fitted coefficients of developed RSM, ANN, and tRF models

Fitted coefficients	RSM		ANN		tRF	
	Full quadratic	Interactions	Full quadratic	Interactions	Full quadratic	Interactions
RMSE	0.4913	2.1402	0.2500	2.0694	0.6104	1.8028
Lipid percentage (%)	28.1678 +/- 1.0411	26.4028 +/- 2.2909	28.2956 +/- 0.5298	26.2335 +/- 2.2152	27.8616 +/- 1.2935	26.5171 +/- 1.9298
beta						
Constant	20.8791	28.6302	19.7759	28.5802	21.4511	27.4311
X_1	0.0897	-0.0523	0.1201	-0.0284	0.0797	-0.0292
X_2	-0.0927	-0.2249	-0.0138	-0.2987	-0.0710	-0.1450
X_3	1.4460	0.1138	1.4012	0.1118	1.2457	0.1488
X_1X_2	0.0018	0.0018	0.0013	0.0013	0.0009	0.0009
X_1X_3	0.0016	0.0015	7.6747	7.6747	0.0004	0.0004
X_2X_3	-0.0031	0.0134	0.0012	0.0196	-0.0014	0.0116
X_1X_1	-0.0014		-0.0015		-0.0011	
X_2X_2	-0.0011		-0.0041		-0.0002	
X_3X_3	-0.0604		-0.0573		-0.0499	

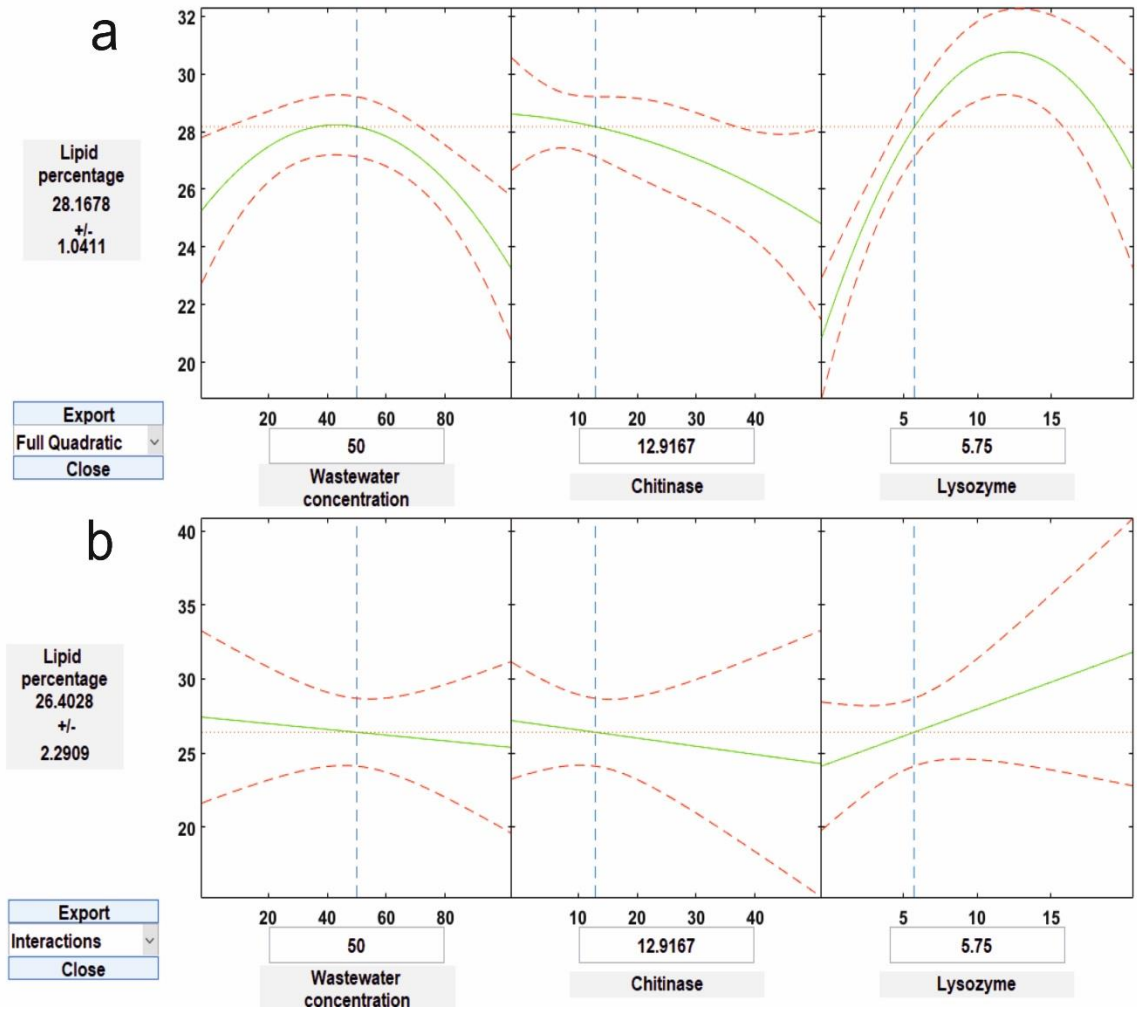

Figure 5. Rstool modeling for RSM

Table 5. ELA for regression to predict the percentage of lipid content

Exp. order	Process P[a]			Lipid P (%)[b]				
					trees.		meta.Bagging	
	WC (% v/v) [c]	C (U/mL)[d]	L (U/mL)[e]	Exp[f]	RandomForest predicted	RandomTree predicted	Classifier: RandomForest predicted	Classifier: RandomTree predicted
1	20	5	2	24.4	24.0	24.4	24.4	23.9
2	20	5	10	30.3	29.1	30.3	29.0	30.0
3	20	25	2	22.0	22.7	22.0	23.1	22.6
4	20	25	10	28.1	28.0	28.1	27.4	28.3
5	80	5	2	21.4	22.5	21.4	23.5	22.6
6	80	5	10	29.0	28.0	29.0	28.0	28.8
7	80	25	2	22.2	22.6	22.2	22.8	22.3
8	80	25	10	28.2	27.7	28.2	27.0	28.4
9	0	10	5	25.6	26.5	25.6	26.8	26.6
10	100	10	5	23.2	24.6	23.2	24.8	23.0
11	50	0	5	27.4	27.6	27.4	27.7	27.9
12	50	50	5	24.6	25.9	24.6	26.0	26.0
13	50	10	0	22.5	22.7	22.5	23.9	23.2
14	50	10	20	27.4	27.8	27.4	28.0	28.0
15	50	10	5	28.1	27.7	27.7	27.7	27.7
16	50	10	5	27.3	27.7	27.7	27.7	27.7
17	50	10	5	27.9	27.7	27.7	27.7	27.7
18	50	10	5	27.3	27.7	27.7	27.7	27.7
19	50	10	5	27.8	27.7	27.7	27.7	27.7
20	50	10	5	28.4	27.7	27.7	27.7	27.7
21	50	10	5	27.5	27.7	27.7	27.7	27.7
22	50	10	5	27.8	27.7	27.7	27.7	27.7
23	50	10	5	27.6	27.7	27.7	27.7	27.7
24	50	10	5	27.5	27.7	27.7	27.7	27.7

[a]Process parameters [b]Lipid percentage (%) [c]Wastewater concentration (% v/v) [d]Chitinase (U/mL) [e]Lysozyme (U/mL) [f]Experimental

Table 6. Comparison of the predictive accuracy for ELA models

Lipid percentage (%) predicted (10-fold validation (k = 10), Total number of instances 24)					
Ensemble algorithms	Correlation coefficient	Mean absolute error	Root mean squared error	Relative absolute error (%)	Root relative squared error (%)
trees. RandomForest	0.9731	0.5290	0.6723	25.1221	27.4493
trees. RandomTree	0.9961	0.1167	0.2156	5.5409	8.8043
meta.Bagging Classifier: RandomForest	0.9641	0.7202	0.9132	34.2064	37.2844
meta.Bagging Classifier: RandomTree	0.9795	0.4393	0.5620	20.8628	22.9469

The statistical analysis showed that the tRT model produced the lowest RMSE value. Additionally, the meta.Bagging.Classifier:RandomTree model has a very low RMSE value. Correlation analysis is performed to evaluate the linear association between two variables, and it takes a value between -1 and +1. In Table 6, tRT achieved the highest correlation coefficient of 0.9961 and the lowest MAE, another loss function performed for regression models. MAE was calculated to prove the sum of the absolute differences between our target and predicted parameters. Therefore, the tRT model was more successful than others. All models can be used to evaluate estimation procedures for the lipid percentage (%). Figure 6 shows the performance of

the RSM, ANN, and tRT models against the experimental data.

Different methods and algorithms have been used in the literature to perform optimization. Zhang et al. [49] developed models for microbial lipid production. The genetic algorithm with SVM was performed to obtain the optimum parameters, including biomass, lipid content, and chemical oxygen demand removal rate. SVM was the best-fitting model to optimize fermentation conditions. The optimum biomass and lipid content were 11.87 g/L and 2.18 g/L, respectively. Nassef et al. [50] focused on enhancing lipid extraction from *S. quadricauda* by using fuzzy modeling and particle swarm optimization. The effect of the process parameters, including power (W), heating time (min), and extraction time (h), on the lipid content was investigated. They reported that the fuzzy model outperformed experimental studies in terms of lipid extraction by 22%.

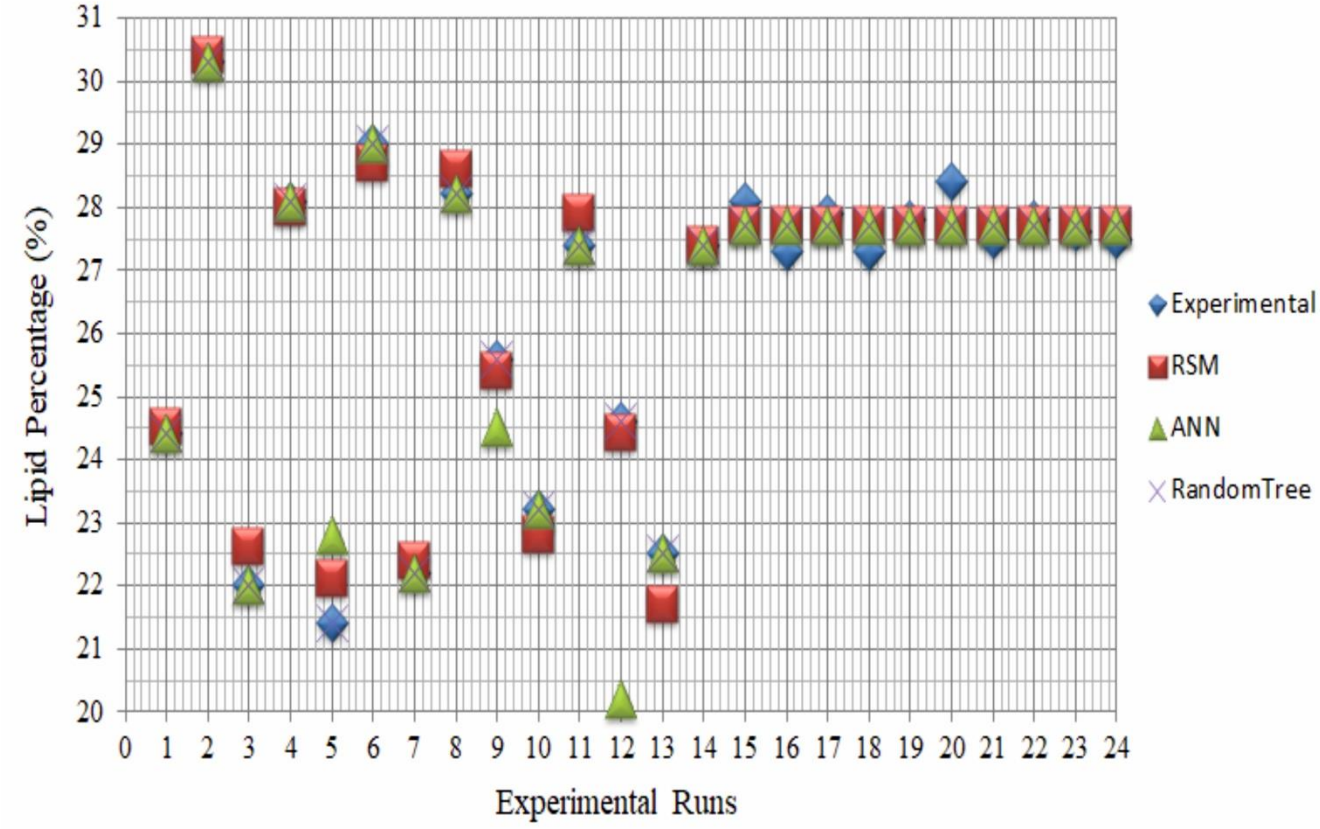

Figure 6. Performance of RSM, ANN, and tRT models against experimental data.

3.4. Explainable Machine Learning Model: tRT

Large-scale biofuel production from microalgae has not yet been realized. Major research gaps, such as the reduction of energy input, maximization of yield, and those related to the effective use of materials and energy, remain unresolved. In microalgae cultivation, the nutrient supply has a considerable effect on cost, sustainability, and yield [51]. The aim is to research and create simulation tools in order to address these problems. Figure 7 shows the tRT model and the size of the tree.

The ruleset given below was obtained from the tRT model for the dataset (Table 2). It was simulated under various parameters affecting lipid content.

- **if** wastewater concentration < 65
- **and** lysozyme ≥ 3.5
- **and** chitinase < 37.5
- **and** wastewater concentration ≥ 10
- **and** wastewater concentration < 35
- **and** chitinase < 15
- **then** lipid percentage = 30.3

The explainable system [52] can be turned into an application program for different laboratories to use. The user can enter input values into the program and calculate the maximum biodiesel production for each AI model. The biggest advantage of this model is that when human-computer interaction is considered, the structure of the system can be observed in the decision tree. In this way, researchers understand how the decision stage is reached. The decision support tool can be easily used for the following purposes:

- Model validation in labs
- Validation of the lipid-production process in small-scale facilities
- There is no need for repeated experiments on biodiesel production.

In addition, there are many large and small-scale algal biofuel companies producing algae biomass and biofuel throughout the world. Some of the companies throughout the world are Albemarle Corporation (USA), Algenol Biofuels (USA), Aquaflow Bionomics (New Zealand), and Malaysian Rubber (Australia). In the near future, various models and tools can be collected and then presented to these companies as a service (i.e., the AI-Library) to upscale the production volumes.

```
WASTEWATER < 65
|   LYSOZYME < 3.5
|   |   WASTEWATER < 35
|   |   |   CHITINASE < 15 : 24.4 (1/0)
|   |   |   CHITINASE >= 15 : 22 (1/0)
|   |   WASTEWATER >= 35 : 22.5 (1/0)
|   LYSOZYME >= 3.5
|   |   CHITINASE < 37.5
|   |   |   WASTEWATER < 10 : 25.6 (1/0)
|   |   |   WASTEWATER >= 10
|   |   |   |   WASTEWATER < 35
|   |   |   |   |   CHITINASE < 15 : 30.3 (1/0)
|   |   |   |   |   CHITINASE >= 15 : 28.1 (1/0)
|   |   |   |   WASTEWATER >= 35
|   |   |   |   |   LYSOZYME < 12.5
|   |   |   |   |   |   CHITINASE < 5 : 27.4 (1/0)
|   |   |   |   |   |   CHITINASE >= 5 : 27.72 (10/0.11)
|   |   |   |   |   LYSOZYME >= 12.5 : 27.4 (1/0)
|   |   CHITINASE >= 37.5 : 24.6 (1/0)
WASTEWATER >= 65
|   LYSOZYME < 7.5
|   |   LYSOZYME < 3.5
|   |   |   CHITINASE < 15 : 21.4 (1/0)
|   |   |   CHITINASE >= 15 : 22.2 (1/0)
|   |   LYSOZYME >= 3.5 : 23.2 (1/0)
|   LYSOZYME >= 7.5
|   |   CHITINASE < 15 : 29 (1/0)
|   |   CHITINASE >= 15 : 28.2 (1/0)

Size of the tree : 29
```

Figure 7. The trees.RandomTree model.

4. Conclusion and Suggestions

For the maximum lipid content from *C. minutissima*, the RSM model predicted process parameters of 20% (v/v) wastewater concentration, 5 U/mL chitinase, and 10 U/mL lysozyme. Under these conditions, the lipid percentage was 30.4% with a very low MSE (0.2414) and a very high R^2 value (0.9765). According to the ANOVA results, *P*-values (0.00021134 and 1.5141e^{-08}) indicated that wastewater concentration and lysozyme had a positive effect on lipid production at a 95% confidence level, but chitinase had a negative effect. The ANN model, with a minimal experimental setup, can reduce chemical usage and provide low-cost lipid production. Under the conditions of 20% (v/v) wastewater concentration, 5 U/mL chitinase, and 10 U/mL lysozyme, the lipid concentration was 30.3%. The R^2 values of the training, validation and test data were 0.99548, 0.96336, and 0.98257, respectively. The effects of parameters were also examined by decision tree ensemble models.

The tRT model had the lowest RMSE of 0.2156 and MAE of 0.1167, with the highest correlation

coefficient of 0.9961. Also, the lipid percentage was 30.3% for the combined RSM-tRT model. The optimal values of wastewater concentration, chitinase, and lysozyme were 20% (v/v), 5 U/mL and 10 U/mL, respectively. Compared to the RSM and ANN models, the tRT model was better at fitting experimental data and generalizing from it. It was also a powerful tool to help make decisions and optimize parameters. The if-then rules extracted from tRT are also given to researchers to test the new parameters in the model. The fuel industry can benefit from the developed models. This work further demonstrates that the combined RSM-tRT model is very close to experimental results and can also be used to obtain biodiesel in a more economical way.

Acknowledgment

I would like to thank Van Yuzuncu Yıl University, Department of Environmental Engineering, and Dr. Erdinç Aladağ for the experimental data.

Conflict of Interest Statement

The author has no conflicts of interest.

Statement of Research and Publication Ethics

The study is complied with research and publication ethics.

References

[1] S. Anto, S.S. Mukherjee, R. Muthappa, T. Mathimani, G. Deviram, S.S. Kumar, T.N. Verma, A. Pugazhendhi, "Algae as green energy reserve: Technological outlook on biofuel production," *Chemosphere*, vol. 242, 125079, 2020.

[2] A. Garg, S. Jain, "Process parameter optimization of biodiesel production from algal oil by response surface methodology and artificial neural networks," *Fuel*, vol. 277, 118254, 2020.

[3] G. Srivastava, A.K. Paul, V.V. Goud, "Optimization of non-catalytic transesterification of microalgae oil to biodiesel under supercritical methanol condition," *Energy Convers Manag*, vol. 156, pp. 269–278, 2018.

[4] M. Karimi, "Exergy-based optimization of direct conversion of microalgae biomass to biodiesel," *J Clean Prod*, vol. 141, pp. 50–55, 2017.

[5] S. Nagappan, S. Devendran, P.C. Tsai, H.U. Dahms, V.K. Ponnusamy, "Potential of two-stage cultivation in microalgae biofuel production," *Fuel*, vol. 252, pp. 339–349, 2019.

[6] M. Nayak, G. Dhanarajan, R. Dineshkumar, R. Sen, "Artificial intelligence driven process optimization for cleaner production of biomass with co-valorization of wastewater and flue gas in an algal biorefinery," *J Clean Prod*, vol. 201, pp. 1092–1100, 2018.

[7] S. Chakravarty, N. Mallick, "Optimization of lipid accumulation in an aboriginal green microalga Selenastrum sp. GA66 for biodiesel production," *Biomass and Bioenergy*, vol. 126, pp. 1–13, 2019.

[8] W.B. Kong, S.F. Hua, H. Cao, Y.W. Mu, H. Yang, H. Song, C.G. Xia, "Optimization of mixotrophic medium components for biomass production and biochemical composition biosynthesis by Chlorella vulgaris using response surface methodology," *J Taiwan Inst Chem Eng*, vol. 43, pp. 360–367, 2012.

[9] S. Singh, J.P. Chakraborty, M.K. Mondal, "Optimization of process parameters for torrefaction of Acacia nilotica using response surface methodology and characteristics of torrefied biomass as upgraded fuel," *Energy*, vol. 186, 115865, 2019.

[10] U. Suparmaniam, M.K. Lam, Y. Uemura, J.W. Lim, K.T. Lee, S.H. Shuit, "Insights into the microalgae cultivation technology and harvesting process for biofuel production: A review," *Renew Sustain Energy Rev*, vol. 115, 109361, 2019.

[11] S.O. Ajala, M.L. Alexander, "Multi-objective optimization studies of microalgae dewatering by utilizing bio-based alkali: a case study of response surface methodology (RSM) and genetic algorithm (GA)". *SN Appl Sci*, vol. 2, pp. 1–20, 2020.

[12] A. Kirrolia, N.R. Bishnoi, R. Singh, "Response surface methodology as a decision-making tool for optimization of culture conditions of green microalgae Chlorella spp. for biodiesel production," *Ann Microbiol*, vol. 64, pp. 1133–1147, 2014.

[13] G. Satpati, S.K. Mallick, R. Pal, "An alternative high-throughput staining method for detection of neutral lipids in green microalgae for biodiesel applications," *Biotechnol Bioprocess Eng.* vol. 20, pp. 1044–1055, 2015.

[14] F.J. Chu, T.J. Wan, T.Y. Pai, H.W. Lin, S.H. Liu, C.F. Huang, "Use of magnetic fields and nitrate concentration to optimize the growth and lipid yield of Nannochloropsis oculata," *J Environ Manage*, vol. 253, 109680, 2020.

[15] M.F. Kamaroddin, A. Rahaman, D.J.Gilmour, W.B. Zimmerman, "Optimization and cost estimation of microalgal lipid extraction using ozone-rich microbubbles for biodiesel production," *Biocatal Agric Biotechnol*, vol. 23, 101462, 2020.
[16] Supriyanto, R. Noguchi, T. Ahamed, D.S. Rani, K. Sakurai, M.A. Nasution, D.S. Wibawa, M. Demura, M.M. Watanabe, "Artificial neural networks model for estimating growth of polyculture microalgae in an open raceway pond," *Biosyst Eng*, vol. 177, pp. 122–129.
[17] E. Baldev, D. Mubarakali, K. Saravanakumar, C. Arutselvan, N.S. Alharbi, S.A. Alharbi, V. Sivasubramanian, N. Thajuddin, "Unveiling algal cultivation using raceway ponds for biodiesel production and its quality assessment," *Renew Energy*, vol. 123, pp. 486–498, 2018.
[18] C. Zhang, Y. Zhang, B. Zhuang, X. Zhou, "Strategic enhancement of algal biomass, nutrient uptake and lipid through statistical optimization of nutrient supplementation in coupling Scenedesmus obliquus-like microalgae cultivation and municipal wastewater treatment," *Bioresour Technol*, vol. 171, pp. 71–79, 2014.
[19] P. Polburee, S. Limtong, "Economical lipid production from crude glycerol using Rhodosporidiobolus fluvialis DMKU-RK253 in a two-stage cultivation under non-sterile conditions," *Biomass and Bioenergy*, vol. 138, 105597, 2020.
[20] M. Tourang, M. Baghdadi, A. Torang, S. Sarkhosh, "Optimization of carbohydrate productivity of Spirulina microalgae as a potential feedstock for bioethanol production," *Int J Environ Sci Technol*, vol. 16, pp. 1303-1318, 2017.
[21] C. Huang, H. Wu, R. feng Li, M. hua Zong, "Improving lipid production from bagasse hydrolysate with Trichosporon fermentans by response surface methodology," *N Biotechnol*, vol. 29, pp. 372–378, 2012.
[22] M. Mäkelä, "Experimental design and response surface methodology in energy applications: A tutorial review," *Energy Convers Manag*, vol. 151, pp. 630–640, 2017.
[23] S.K. Yellapu, J. Bezawada, R. Kaur, M. Kuttiraja, R.D. Tyagi, "Detergent assisted lipid extraction from wet yeast biomass for biodiesel: A response surface methodology approach," *Bioresour Technol*, vol. 218, pp. 667–673, 2016.
[24] A. Onay, "Investigation of biomass productivity from Nannochloropsis gaditana via response surface methodology using MATLAB," *Energy Reports*, vol. 6, pp. 44-49, 2020.
[25] S.M. Huang, C.H. Kuo, C.A. Chen, Y.C. Liu, C.J. Shieh, "RSM and ANN modeling-based optimization approach for the development of ultrasound-assisted liposome encapsulation of piceid," *Ultrason Sonochem*, vol. 36, pp. 112–122, 2017.
[26] A.A. Ayoola, F.K. Hymore, C.A. Omonhinmin, O.C. Olawole, O.S.I. Fayomi, D. Babatunde, O. Fagbiele, "Analysis of waste groundnut oil biodiesel production using response surface methodology and artificial neural network," *Chem Data Collect*, vol. 22, 100238, 2019.
[27] M. Mondal, A. Ghosh, K. Gayen, G. Halder, O.N. Tiwari, "Carbon dioxide bio-fixation by Chlorella sp. BTA 9031 towards biomass and lipid production: Optimization using Central Composite Design approach," *J CO2 Util*, vol. 22, pp. 317–329, 2017.
[28] M.A. Alam, J. Wu, J. Xu, Z. Wang, "Enhanced isolation of lipids from microalgal biomass with high water content for biodiesel production," *Bioresour Technol*, vol. 291, 121834, 2019.
[29] N.B. Ishola, A.A. Okeleye, A.S. Osunleke, E. Betiku, "Process modeling and optimization of sorrel biodiesel synthesis using barium hydroxide as a base heterogeneous catalyst: appraisal of response surface methodology, neural network and neuro-fuzzy system," *Neural Comput Appl*, vol. 31, pp. 4929–4943, 2019.
[30] S. González, S. García, J.D. Ser, L. Rokach, F. Herrera, "A practical tutorial on bagging and boosting based ensembles for machine learning: Algorithms, software tools, performance study, practical perspectives and opportunities," *Inf Fusion*, vol. 64, pp. 205–237, 2020.
[31] S. Das, R. Chakraborty, A. Maitra, "A random forest algorithm for nowcasting of intense precipitation events," *Adv Sp Res*, vol. 60, pp. 1271–1282, 2017.
[32] L. Wang, X. Zhou, X. Zhu, Z. Dong, W. Guo, "Estimation of biomass in wheat using random forest regression algorithm and remote sensing data," *Crop J*, vol. 4, pp. 212–219, 2016.
[33] L. Rokach, "Decision forest: Twenty years of research," *Inf Fusion*, vol. 27, pp. 111–125, 2016.
[34] A. Onay, M. Onay, "A Drug Decision Support System for Developing a Successful Drug Candidate Using Machine Learning Techniques," *Current Computer-Aided Drug Design*, vol. 16, pp. 407-419, 2020.
[35] Y. Song, L. Wang, X. Qiang, W. Gu, Z. Ma, G. Wang, "The promising way to treat wastewater by microalgae: Approaches, mechanisms, applications and challenges," *Journal of Water Process Engineering*, vol. 49, 103012, 2022.

[36] W.N.A. Kadir, M.K. Lam, Y. Uemura, J.W. Lim, K.T. Lee, "Harvesting and pre-treatment of microalgae cultivated in wastewater for biodiesel production: A review," *Energy Conversion and Management*, vol. 171, pp. 1416-1429, 2018.
[37] S. I. Khan, I. Hashmi, S.J. Khan, R. Henderson, "Performance and optimization of lab-scale membrane bioreactors for synthetic municipal wastewater," *Desalin Water Treat*, vol. 57, pp. 29193–29200, 2016.
[38] F. Jordi, M. Lees , G.M. Sloane-Stanley, "A simple method for the isolation and purification of total lipids from animal tissues," *J Biol Chem*, vol. 226, pp. 497-509, 1957.
[39] A. Cutler, D.R. Cutler, J.R. Stevens, "Ensemble Machine Learning," *Ensemble Mach Learn*, 2012.
[40] L. Breiman, "Random Forests," *Machine Learning*, vol. 45, pp. 5–32, 2001.
[41] M. Muthuraj, N. Chandra, B. Palabhanvi, V. Kumar, D. Das, "Process Engineering for High-Cell-Density Cultivation of Lipid Rich Microalgal Biomass of Chlorella sp. FC2 IITG," *Bioenergy Res*, vol. 8, pp. 726–739, 2015.
[42] H.A. Thanaa, S.E.G. Mamdouh, H.E.G. Dina, E.A. Ghada, E.T. Amir, "Improvement of lipid production from an oil-producing filamentous fungus, Penicillium brevicompactum NRC 829, through central composite statistical design," *Ann Microbiol*, vol. 67, pp. 601–613, 2017.
[43] M. Dammak, S.M. Haase, R. Miladi, F.B. Amor, M. Barkallah, D. Gosset, C. Pichon, B. Huchzermeyer, I. Fendri, M. Denis, S. Abdelkafi, "Enhanced lipid and biomass production by a newly isolated and identified marine microalga," *Lipids Health Dis*, vol. 15, pp. 1–13, 2016.
[44] A. Onay, "Optimization of lipid content of Nannochloropsis gaditana via quadratic models using Matlab Simulink," *Energy Reports*, vol. 6, pp. 128–133, 2020.
[45] L. Khaouane, C. Si-Moussa, S. Hanini, O. Benkortbi, "Optimization of culture conditions for the production of pleuromutilin from pleurotus mutilus using a hybrid method based on central composite design, neural network, and particle swarm optimization," *Biotechnol Bioprocess Eng*, vol. 17, pp. 1048–1054, 2012.
[46] M.N.A. Sohedein, W.A.A.Q.I. Wan-Mohtar, Y. Hui-Yin, Z. Ilham, J.S. Chang, S. Supramani, P. Siew-Moi, "Optimisation of biomass and lipid production of a tropical thraustochytrid Aurantiochytrium sp. UMACC-T023 in submerged-liquid fermentation for large-scale biodiesel production," *Biocatal Agric Biotechnol*, vol. 23, 101496, 2020.
[47] S. Chakravarty, N. Mallick, "Optimization of lipid accumulation in an aboriginal green microalga Selenastrum sp. GA66 for biodiesel production," *Biomass and Bioenergy*, vol. 126, pp. 1–13, 2019.
[48] Y. Zhang, X. Kong, Z. Wang, Y. Sun, S. Zhu, L. Li, P. Lv, "Optimization of enzymatic hydrolysis for effective lipid extraction from microalgae Scenedesmus sp.," *Renew Energy*, vol. 125, pp. 1049–1057, 2018.
[49] L. Zhang, B. Chao, X. Zhang, "Modeling and optimization of microbial lipid fermentation from cellulosic ethanol wastewater by Rhodotorula glutinis based on the support vector machine," *Bioresour Technol*, vol. 301, 122781, 2020.
[50] A.M. Nassef, H. Rezk, M.A. Abdelkareem, A. Alaswad, A. Olabi, "Application of fuzzy modelling and Particle Swarm Optimization to enhance lipid extraction from microalgae," *Sustain Energy Technol Assessments*, vol. 35, pp. 73–79, 2019.
[51] J. Ferrell and V. Sarisky-Reed, "National Algal Biofuels Technology Roadmap," U.S. Department of Energy, Office of Energy Efficiency and Renewable Energy, *Biomass Program*, 2010.
[52] S. Ali, T. Abuhmed, S. El-Sappagh, K. Muhammad, J. M. Alonso-Moral, R. Confalonieri, R. Guidotti, J. Del Ser, N. Díaz-Rodríguez, F. Herrera, "Explainable Artificial Intelligence (XAI): What we know and what is left to attain Trustworthy Artificial Intelligence," *Information Fusion*, vol. 99, 101805, 2023.

Bitlis Eren Üniversitesi Fen Bilimleri Dergisi
BİTLİS EREN UNIVERSITY JOURNAL OF SCIENCE
ISSN: 2147-3129/e-ISSN: 2147-3188
VOLUME: 12 NO: 4 PAGE: 1212-1225 YEAR: 2023
DOI:10.17798/bitlisfen.1364332

A Comparative Study of Breast Mass Detection Using YOLOv8 Deep Learning Model in Various Data Scenarios on Multi-View Digital Mammograms

Muhammet Üsame ÖZİÇ[1*], Ayşe Sidenur YILMAZ[1], Halil ibrahim SANDIRAZ[1] Baihaqi Hilmi ESTANTO[1]

[1]*Department of Biomedical Engineering, Faculty of Technology, Denizli, Türkiye (ORCID:0000-0002-3037-2687) (ORCID: 0009-0005-9014-1038) (ORCID: 0009-0002-0904-5806) (ORCID: 0009-0005-8468-2970)*

Keywords: Breast Cancer, Deep Learning, Mass,VinDr-Mammo, YOLOv8

Abstract

Breast cancer is one of the most common lethal cancer types in the female population globally. It typically begins with abnormal cell growth in the breast glands or milk ducts and can spread to other tissues. Many breast cancer cases start with the presence of a mass and should be carefully examined. Masses can be monitored using X-ray-based digital mammography images, including left mediolateral oblique, right craniocaudal, left craniocaudal, and right mediolateral oblique views. In this study, automatic mass detection and localization were performed on mammography images taken from the VinDr-Mammo full-field digital mammography dataset using the YOLOv8 deep learning model. Three different scenarios were tested: raw data, data with pre-processing to crop breast regions, and data with only mass regions cropped to a 1.2x ratio. The data were divided into 80% for training and 10% each for validation and testing. The performance results were calculated using metrics such as precision, recall, F1-score, mAP, and training graphs. At the end of the study, it is demonstrated that the YOLOv8 deep learning model provides successful results in mass detection and localization, indicating its potential use as a computer-based decision support system.

1. Introduction

Today, breast cancer is considered one of the most common cancers that threaten the lives of women. Breast cancer occurs as a result of uncontrolled growth of breast tissue. Approximately 685,000 women died due to breast cancer in 2020. These statistics account for 16% or 1 in every 6 cancer deaths in women. Therefore, research and development to detect breast cancer early with correct diagnosis and treatment is extremely important to enhance the survival rate. Many cases of breast cancer begin with the presence of a mass in the breast, and when a patient presents with suspicion of cancer, various methods are carefully employed to examine whether a mass exists. Masses can be benign, non-cancerous, or malignant, indicating a potential for cancer. Usually, breast cancer manifests itself with the formation of a mass or masses and can be detected in the early stages using different imaging methods [1-3]. Mammography is a commonly used X-ray-based imaging technique for screening and diagnosing breast masses. In general, images are taken from four different angles and views: Left Mediolateral Oblique (LMLO), Right Mediolateral Oblique (RMLO), Right Craniocaudal (RCC), and Left Craniocaudal (LCC) [4, 5]. Radiologists analyze these four views to analyze cancerous and suspicious masses. In recent years, the use of deep learning methods in breast cancer screening and diagnosis using mammography images has made great progress. Many studies have shown that artificial intelligence systems can reduce the workload of screening mammograms. In the literature, artificial intelligence-based mass detection and breast cancer classification studies are still hot topics on which applications are

*Corresponding author: muozic@pau.edu.tr
Received: 21.09.2023, Accepted: 01.12.2023

being carried out [6-19]. The data used in the studies are generally collected from international databases. They are extremely variable regarding image size, resolution, number of data, image views, labels, and breast density differences [20-23]. Therefore, comparisons across studies are entirely relative, but the studies performed show promising results for early-stage diagnosis of breast cancer. VinDr-Mammo dataset is a project with richer content than the current databases, with four-view mammography of each recently released case, high-resolution radiology images, different findings labels, different breast density values, data observed by several radiologists, and other features [24]. You Only Look Once (YOLO) deep learning model among object detection methods has been popularly used in medical and other fields [25, 26]. The algorithm, which is updated periodically with different versions, emerges with its powerful features compared to other object detection algorithms [27-30]. The n, s, m, l, and x models with different parameters and network sizes of the YOLOv8 model, which is one of the latest versions, are available to researchers [31]. In this study, the performance of the YOLOv8 algorithm on the automatic detection and localization of mass regions was investigated by creating datasets in three different scenarios from the mass-labeled RCC, LCC, RMLO, and LMLO views using the VinDr-Mammo [24]. Although the RCC, LCC, RMLO, and LMLO views have different directions and pixel density values, how the algorithm models perform has been investigated. Three different scenarios were prepared for this research. Four views were taken as raw data in the first scenario, and applications were carried out. In the second scenario, a dataset was created by removing the black pixel regions in the background as much as possible with a pre-processing method developed for this study. In the third scenario, a dataset was created by cropping the mass-labeled regions to a 1.2x ratio, resulting in only the mass regions and some surrounding tissues. These scenarios aim to investigate how algorithm performance will perform on raw and Region of Interest (ROI) data. Data were labeled and annotated according to the mass coordinate regions given from the VinDr-Mammo dataset. Performance criteria were calculated by training the data separated as 80% training, 10% validation, and 10% testing with the n model of YOLOv8. The most important contribution of this study, compared to other studies in the literature, is that it examines the breast mass detection performance in classes created in different scenarios in the rich data set mentioned above, without applying complex pre-processing methods to the images (filtering, adaptive histogram equalization, denoising flipping images right or left, histogram equalization, etc.). At the same time, it has been observed how the algorithm performance is affected as the examined region becomes smaller. At the end of the study, the advantages and disadvantages of the experiments of the proposed systems were discussed. The results demonstrate that the YOLOv8 model is suitable for computer-based clinical decision support processes as it can detect masses on mammography images regardless of views and densities.

2. Material and Method

2.1. Data

The VinDr-Mammo dataset used in this study is an open-source project developed by Vietnam National University and VinBrain AI [24]. Using this data, researchers have developed artificial intelligence-based computer-aided diagnostic systems [32-36]. This dataset contains 20,000 images, 5,000 of which are four-view (full-field) radiographs (LMLO, LCC, RMLO, RCC). Evaluations, findings, and annotation information of the images are also given. Images are labeled as laterality, view information, image size, Breast Imaging Reporting and Data System(BI-RADS) category, composition information and breast density (A, B, C, D), category of findings (skin retraction, suspicious lymph node, skin thickening, asymmetry, focal asymmetry, suspicious calcification, nipple retraction, architectural distortion, global asymmetry, mass). BI-RADS is a classification system developed by the American College of Radiology and used to standardize breast imaging results. BI-RADS 0 to 6 categorizes the severity of the findings. Generally classified as BI-RADS-0 additional imaging or further evaluation, BI-RADS-1 normal, BI-RADS-2 benign, BI-RADS-3 possibly benign, BI-RADS-4 suspicious malignant lesion (between 2% and 95% probability of malignancy), BI-RADS-5 high-grade suspicious malignant lesion, BI-RADS-6 lesion known to be malignant by biopsy [37, 38]. Breast density information is divided into four main categories, A, B, C, and D, which represent the ratio of fat, fibroglandular tissue, and dense tissue in the breast. The breast density, which is a relatively easy-to-detect anomaly and consists of mostly adipose tissue with low density, is classified as category A, and the breast with a balanced structure between adipose tissue and fibroglandular tissue, with medium density, is classified as category B. The increase in density, in which the detection of anomaly becomes relatively more difficult with the increase in the ratio of fibroglandular tissue, is classified as category C, and

the composition consisting of mostly fibroglandular tissue with high density and difficult-to-detect anomaly is classified as category D [39]. In this study, a dataset with different BI-RADS categories and breast density levels labeled with mass was created from the VinDr-Mammo dataset. The mass represents a lesion or abnormality. 1226 findings are labeled as "mass" and the coordinates (Xmin, Ymin, Xmax, Ymax) where the mass is located are given in the *.CSV file. These findings can be one or more in an image. Therefore, there are 1113 mammograms with 1226 mass findings. Mammograms are recorded in Digital Imaging and Communications in Medicine (DICOM) format. Therefore, the radiographs were converted to high-contrast Portable Network Graphics (PNG) format using a DICOM viewer. The coordinate information given by VinDr-Mammo was converted to YOLO format and checked in the browser-based "makesense" labeling program. These images have dimensions of 2800x3518 and a depth of 8 bits. Mass labeled dataset has different BI-RADS categories, different views, and breast density. In Figure 1, a patient's RCC, RMLO, LCC, and LMLO image is given. While the mass is seen in RCC and RMLO views, there is no finding in LCC and LMLO images. Table 1 shows the distribution label of the data used in the study regarding BI-RADS category, density, and view.

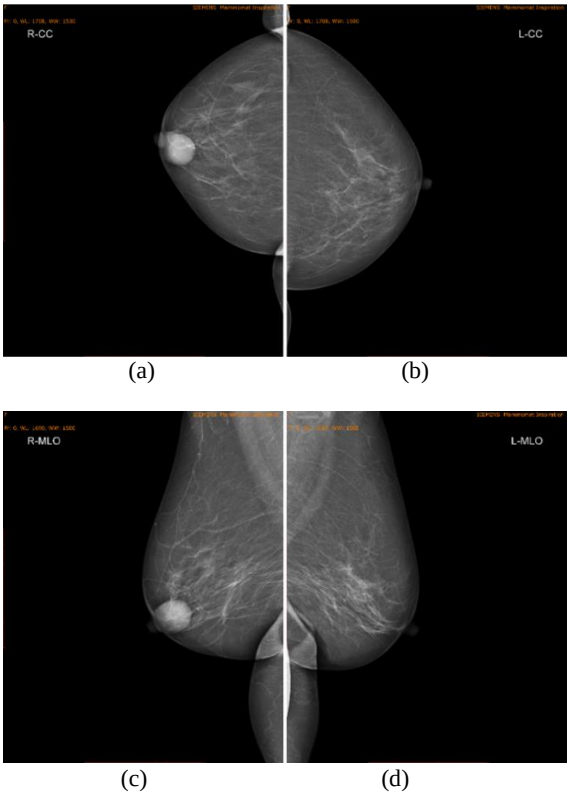

Figure 1. (a) RCC (b) LCC (c) RMLO (d) LMLO views of a case

Table 1. The distribution of the data used in the study in terms of BI-RADS category, density, and view (According to the distribution of findings)

BI-RADS	**3**	**4**	**5**	**-**
	530	481	215	-
Density	**A**	**B**	**C**	**D**
	5	153	998	70
View	**LCC**	**RCC**	**LMLO**	**RMLO**
	310	267	343	306

2.2. Image Pre-processing and ROI Extraction

All mammography images were pre-processed for the second and third scenarios. In the second scenario, a pre-processing method was presented to remove as much of the breast area as possible. Thus, the breast regions in the entire image were automatically cropped. In the third scenario, ROIs were cropped to sizes with dimensions that changed by 1.2 times, according to the bounding box coordinates provided in the VinDrMammo dataset. First of all, high-resolution mammography images with DICOM extension were converted to PNG format for all scenarios. For the second scenario (ROI1), an automated pre-processing pipeline was developed that only takes the breast area, as the mammography images have the text and a lot of black pixel backgrounds. Images were recorded in 3 channels. Therefore, conversion from color image to gray level was performed. Binarization was applied by finding the adaptive threshold value specific to the image with the OTSU thresholding method [40]. The holes in the object were filled and the binary regions with 50-pixel clusters were removed from the image. By finding the pixel areas of independent objects, the index of the object with the highest pixel area was obtained. Since the largest object with this index was the breast region, the smallest bounding box coordinates surrounding this region were saved. The largest object corresponding to these coordinates in the original image was cropped and saved as a new image. In order not to lose the mass region coordinates given in VinDr-Mammo, resize was not performed. This developed pipeline was looped and all images were cropped automatically. The developed pipeline is given in Figure 2 as a flow chart. Figure 3 pre-processing steps are given visually on mammography images. For the third scenario (ROI2), considering the bounding boxes in the VinDrMammo dataset, the relevant region of each image was cropped by a 1.2x ratio (This expression is not the zoom of the image, but how much the relevant coordinate points are expanded when cropping the ROI boundaries). As a

result, a new dataset was created with the truncated ROIs by enlarging the bounding box 1.2 times. The new coordinate values were calculated according to the original image and saved in YOLO format. The goal of the approach here is to calculate how the performance of the algorithm may change as the ROI region becomes smaller. Figure 4 shows the cropping of a mass ROI.

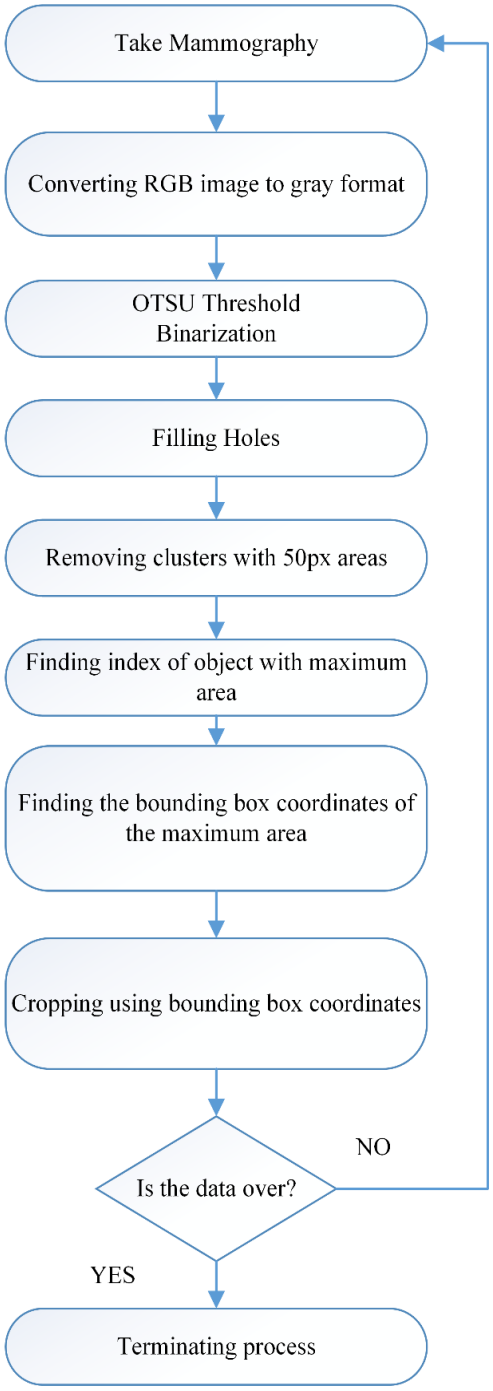

Figure 2. Pipeline developed to crop the breast area

2.3. YOLOv8 Network Settings

The YOLOv8 deep learning model was preferred for breast mass detection because it is one of the newest versions of the YOLO family. During the training stage, a high-performance computing environment was obtained by purchasing the Google Colab Pro version. The training process was carried out using the YOLOv8 model with the GPU and Tesla T4 graphics processing unit provided by Google Colab Pro. Model hyperparameters were set to epoch 600, optimization algorithm Stochastic Gradient Descent, mini-batch size 16. Other hyperparameters were left as default. The n model of YOLOv8 was downloaded from the Ultralytics repository, and transfer learning and fine-tuning operations were carried out. This model was a pre-trained network with 80 classes of output, normally trained with the COCO dataset. The classes in the "coco.yaml" file were deleted and replaced with the name "mass" to give a single class output. The data for the three scenarios were divided into 80% training, 10% validation and 10% testing. The bounding box in YOLO format and data were uploaded to the COLAB platform and the training process was started.

2.4. Performance Evaluation Metrics

Performance evaluation metrics were examined in two stages: training and testing. IoU (Intersection over Union) value is taken into account in the performance criteria during the training stage. This metric is a measure of how much the annotated region overlaps with the bounding box obtained by the algorithm. For IoU, 50% overlap is the critical limit. If the overlap is largely achieved, True Positive (TP), False Positive (FP), and False Negative (FN) values are calculated. Using these values, precision (Equation 1), recall (Equation 2), and F1-score (Equation 3) values of the training phase are obtained. Another metric for the training process is mAP (mean Average Precision). This value is calculated after determining the average precision (AP) value for each class. The AP value is the area under the precision-recall graph of the classes. mAP is the average of the AP values of all classes. The mAP .5 value represents the performance when the IoU is 50%. mAP .5: .95 is the average of the IoU threshold from 50% to 95% by calculating one by one with a step size of 0.05. The higher the AP and mAP values, the more successful the training. By using the weight file obtained as a result of the training, the detection, and localization of the masses were performed in test images. By evaluating these data, TP, FP, and FN values were calculated, and precision (Equation 1), recall

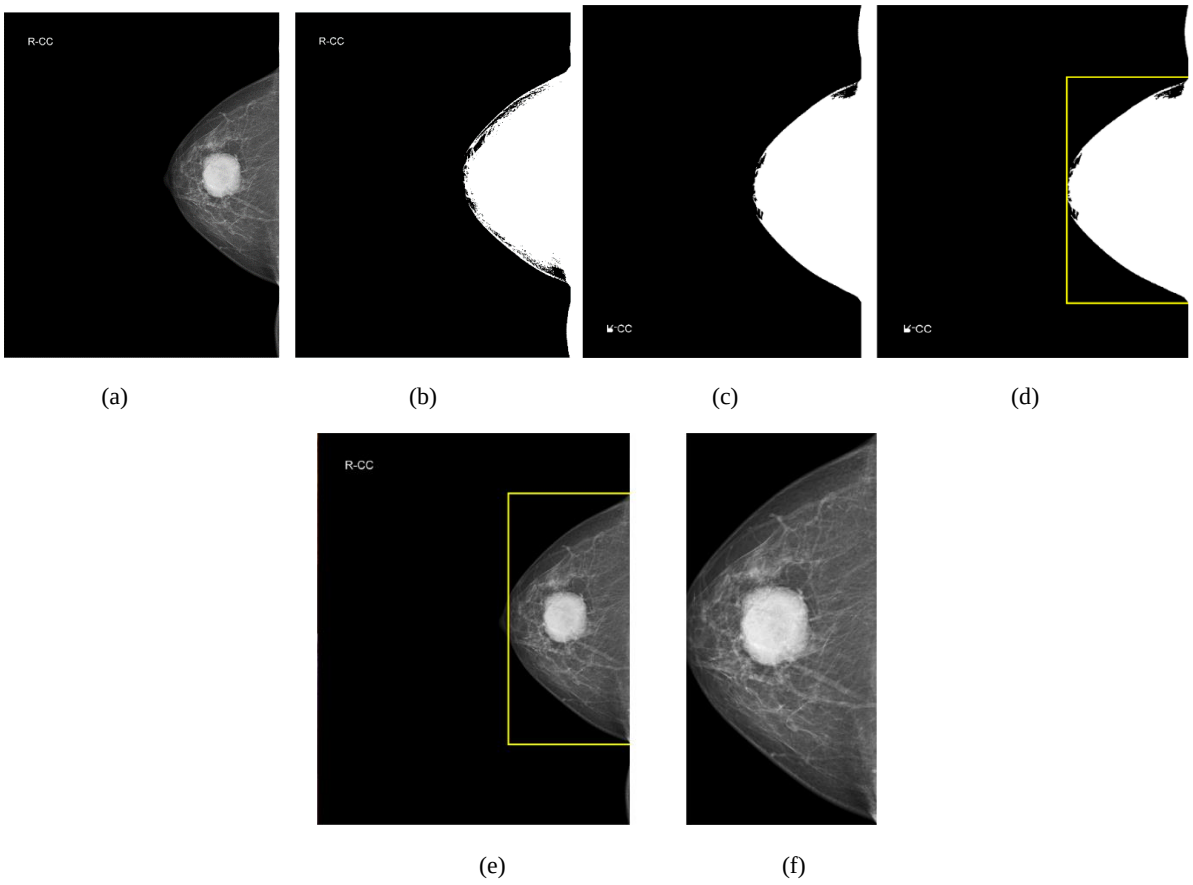

(a) (b) (c) (d)

(e) (f)

Figure 3. (a) Original mammography converted to gray level (b) OTSU Threshold and Binarization (c) Filling holes and removing 50-pixel areas (d) Finding maximum area, indexing and finding bounding box coordinates (e) Cropping using bounding box coordinates (f) Cropped mammography

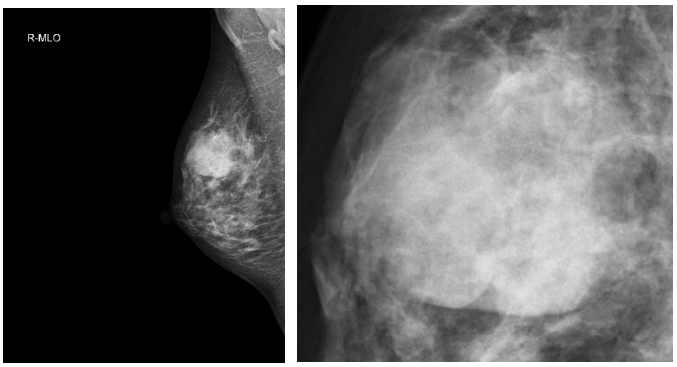

(a) (b)

Figure 4. (a) Original Mammography (b) Cropped Mass Region

(Equation 2), F1-score (Equation 3) values and test performance were evaluated.

$$precision = \frac{TP}{TP + FP} \quad (1)$$

$$recall = \frac{TP}{TP + FN} \quad (2)$$

$$F1 - score = 2 * \frac{Precision * Recall}{Precision + Recall} \quad (3)$$

3. Results and Discussion

3.1. Training and Testing Results

Training results for three scenarios are given in Table 2, and test results are given in Table 3. Figure 5 shows training graphs for different metrics by epoch progression for the three scenarios. When Table 2 was examined, it was observed that the values of training performance evaluation metrics increased as the evaluated region became smaller. Although 600 epochs of hyperparameter input were given for each scenario, the training was stopped by performing an early stopping operation on the system at the 88th epoch for raw data, the 71st epoch for ROI1, and the 102nd epoch for ROI2. This process was performed automatically by the system when there was no significant change in the last epochs. Thus, it reduced the training time. The pre-processing performed for ROI2 generally increased the performance values. Since mAP values were above the determined threshold values, it showed that the detection process was successful. It was observed that the graphical progress given in Figure 5 approaches zero for loss graphs and approaches one value for other metrics, indicating that the training process was progressing at appropriate values. The test results given in Table 3 were calculated by comparing the detection operations performed on mammography images with the ground truth labels. The precision value was obtained as 95.7% for raw data, 97.9% for ROI1, and 100% for ROI2. It has been determined that the mass regions detected by the model are largely accurate and that models trained by pre-processing increase the precision results. Recall value was obtained as 78.8% for raw data, 82.4% for ROI1, and 100% for ROI3. This metric shows how much of the mass regions the algorithm needs to detect. Thus, the results proved that as the ROI size decreased, the amount of FN decreased and therefore the recall value increased.

3.2. Visual Results

Detection and localization of mass on six test raw mammography images at different views in Figure 6, detection and localization of mass on six test ROI1 (Breast Region) mammography images at different views in Figure 7, detection of masses on eight ROI2 (Mass Region) mammography patches in Figure 8 are given as sample images from the visual results.

Table 2. Training Results

Scenario	Precision	Recall	F1-Score	mAP.5	mAP.5:.95	Training Time	Epoch
Raw Data	64.5	63.4	63.9	65.6	40.4	1.72 h	88/600
ROI1(Breast Region)	73.0	62.6	67.4	69.4	41.0	0.74 h	71/600
ROI2(Mass Region)	100	100	100	99.5	99.5	0.62 h	102/600

Table 3. Testing Results

Scenario	TP	FP	FN	Precision	Recall	F1-Score
Raw Data	90	4	24	95.7	78.8	86.4
ROI1(Breast Region)	94	2	20	97.9	82.4	89.4
ROI2(Mass Region)	114	0	0	100.0	100.0	100.0

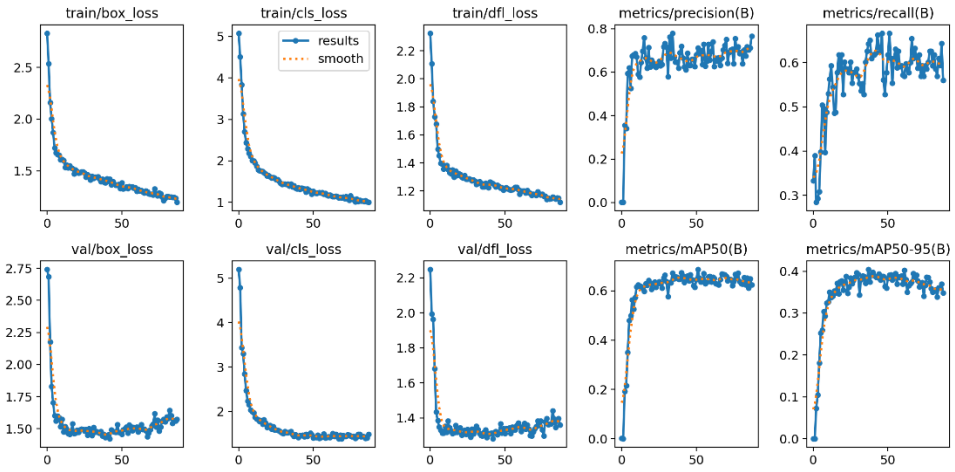

(a)

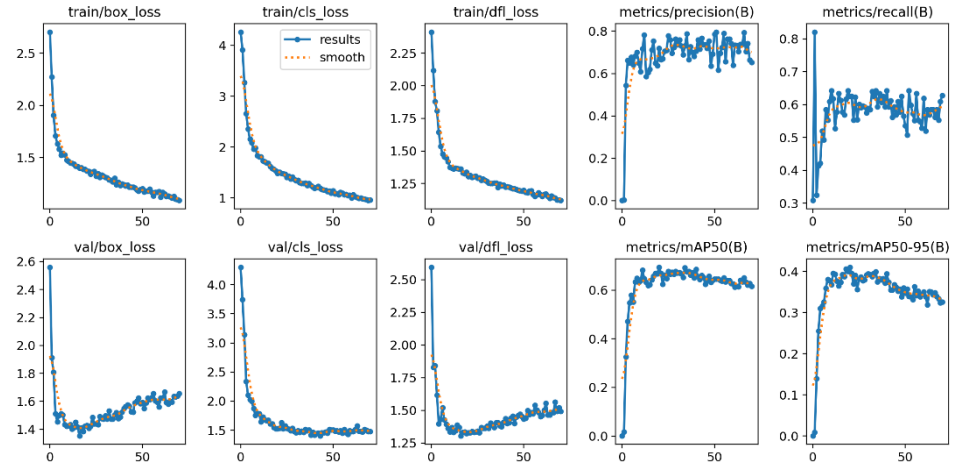

(b)

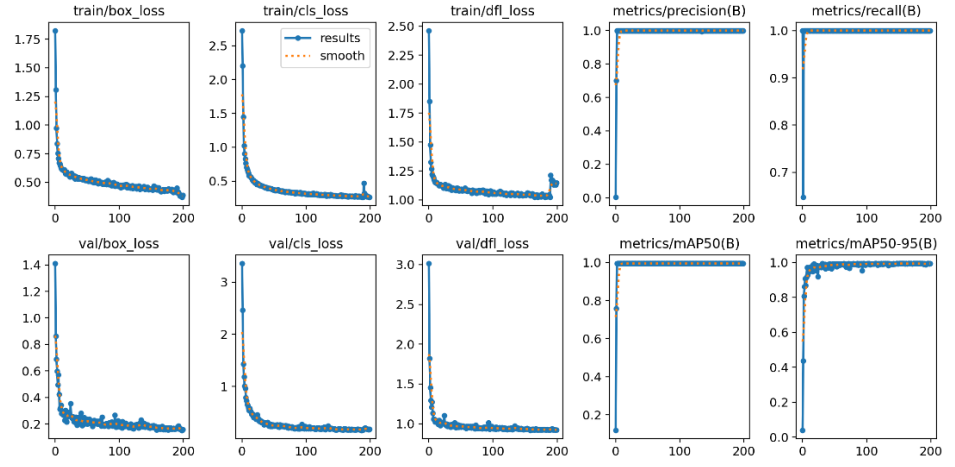

(c)

Figure 5. Training and validation graphs according to epoch progress (a) Raw data (b) ROI1 data (c) ROI2 data

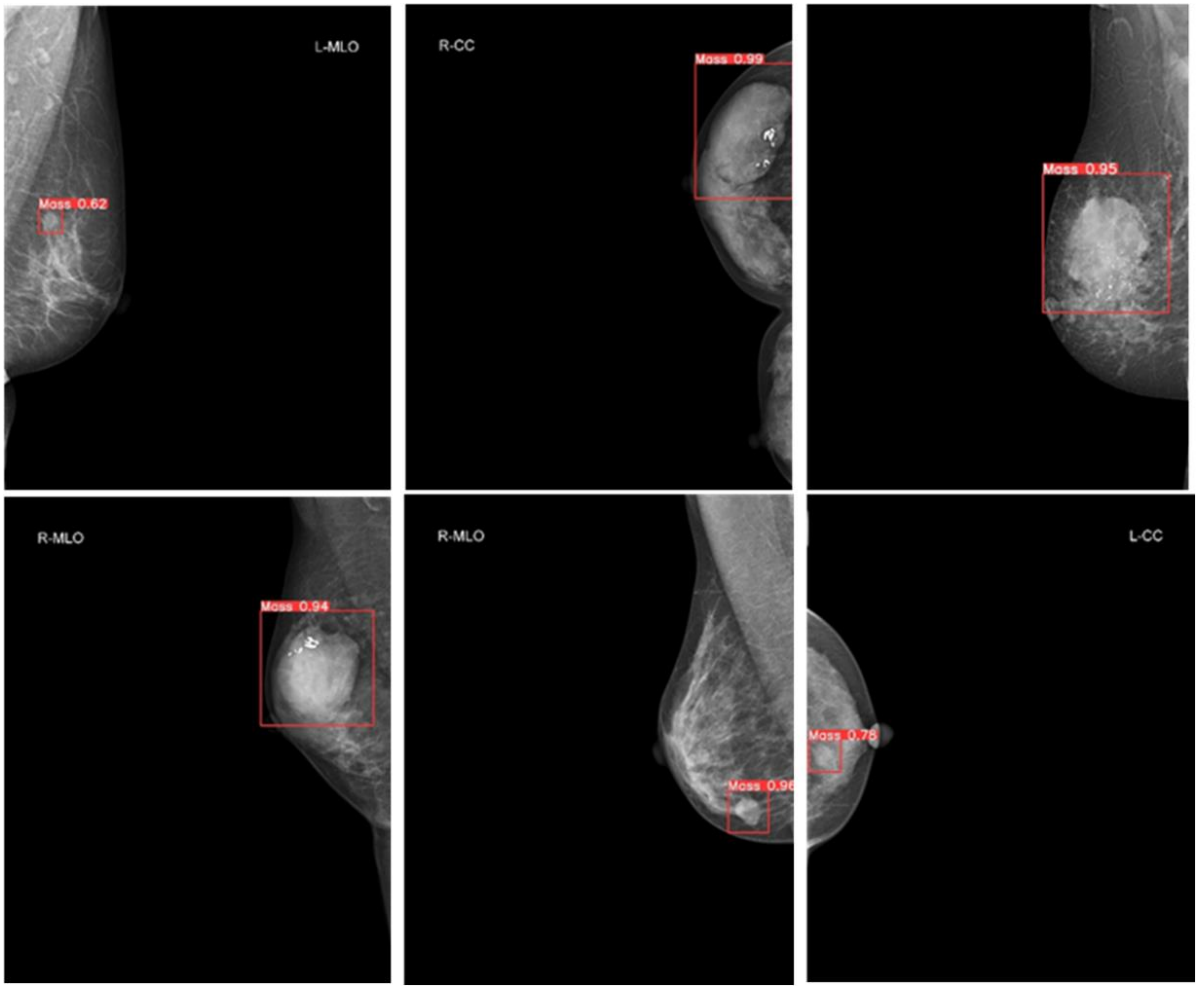

Figure 6. Visual results of mass detection on six raw test images

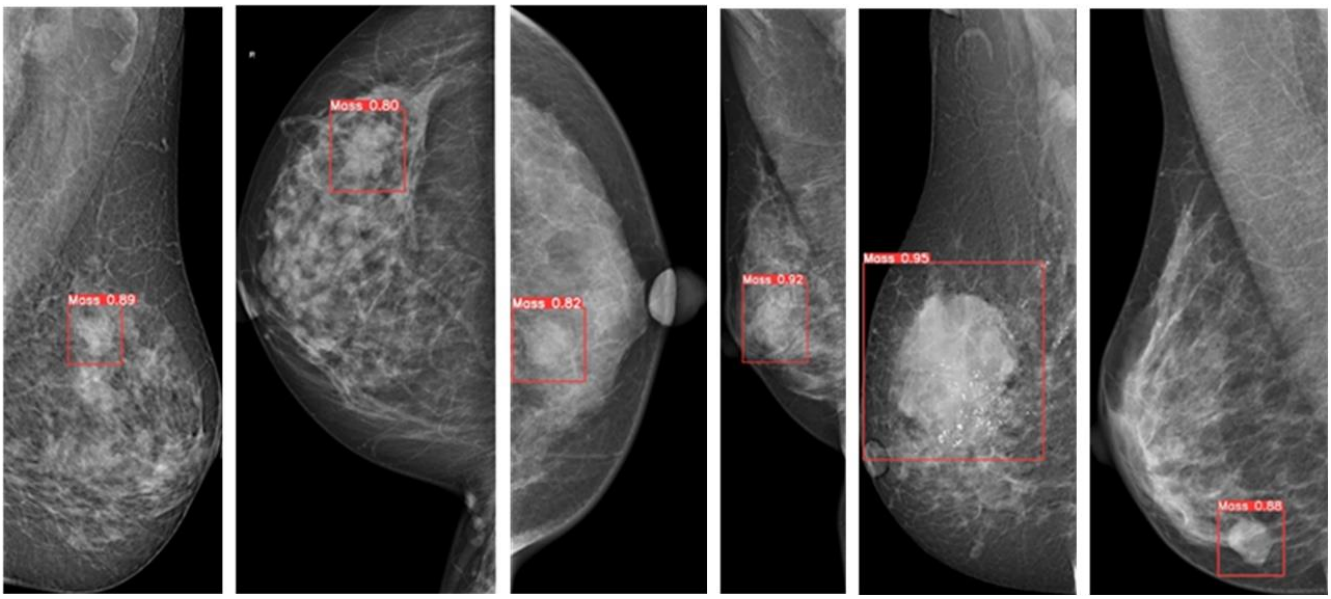

Figure 7. Visual results of mass detection on six ROI1 test images

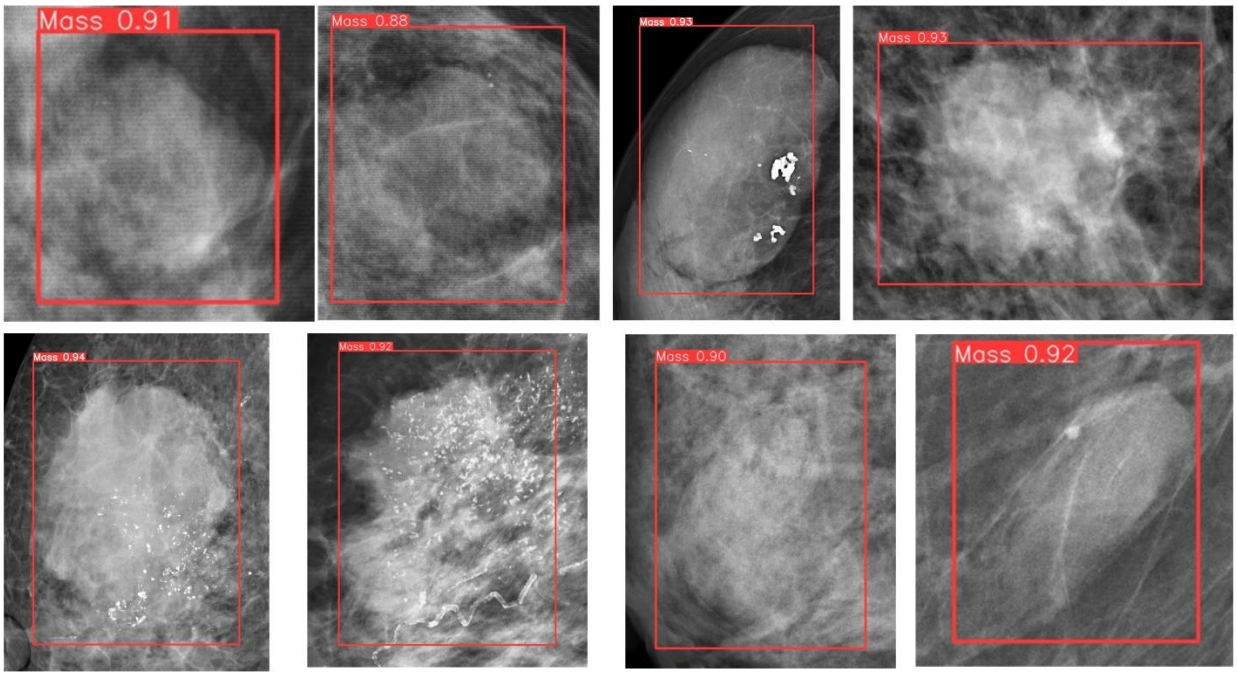

Figure 8. Visual results of mass detection on eight ROI2 test images

3.3. Discussion

Automated mass detection and classification of mammography images, usually using open-source datasets and sometimes privately collected datasets, is a hot topic studied in the literature [6-19]. The Digital Database for Screening Mammography (DDSM) dataset, the Mammographic Image Analysis Society Digital Mammogram Database (MIAS), and the INbreast dataset have been popularly used for years. It is stated that the low-resolution images in MIAS, one of the oldest databases, cause inaccurate training and performance. DDSM, which has low mammography quality and pixel-level contour labels, is not sensitive enough for segmentation and classification processes. Although the INBreast dataset releases high-resolution full-field digital mammography, the number of data is low [20-23]. The VinDr-Mammo dataset is a relatively new study and consists of 5000 cases and contains 20000 high-resolution images, each with four views. Laterality, size, view status, BI-RADS category, and breast density category information of the images are shared with researchers as finding annotations. The data were independently reviewed twice, and in case of discrepancy, they were evaluated by a third radiologist. The VinDrMammo dataset contains the symptoms and label information for skin retraction, suspicious lymph nodes, skin thickening, asymmetry, focal asymmetry, suspicious calcification, nipple retraction, architectural distortion, global asymmetry, and mass. Therefore, it has a richer structure than other databases, as it includes the number of data, the number of symptoms, finding annotation, and high-resolution images [24]. While many applications are using other databases, the number of studies conducted with VinDrMammo is relatively low [34, 35, 41-44]. Some studies using the VinDr-Mammo dataset applied the YOLO algorithm as a pre-processing tool to crop only the breast region from the image [35, 44]. There is one study that automatically detects the mass area from VinDr mammograms using YOLO [34]. Mahoro and Akhloufi determined the mass regions with YOLOv7 and YOLOv8 with different pre-processing, resize processes, and data augmentation, using 1029 labeled data from the VinDr Mammo dataset. Different pre-processing techniques were performed on mammograms with bilateral filter, median filter, and contrast-limited adaptive histogram equalization (CLAHE). Images resized to 640x640 pixels and converted to JPG format in DICOM were divided into 75% train, 22% validation, and 3% test. Data augmentation was performed during training with different transformations. In experiments conducted with CLAHE, median filter, bilateral filter, and raw data, the mAP values obtained for YOLOv7 were 0.51, 0.53, 0.42, 0.44, and for YOLOv8 were 0.61, 0.65, 0.61, 0.64, respectively (IoU=0.5). In the study, in which no pre-processing was performed to determine the area of interest of the breast region, the results were evaluated only on mAP, and the precision, recall, and F1-score values of the test results were not given. It has been stated that YOLOv8, which is a state-of-the-art model, gives better results in terms of

model architecture, speed, accuracy, and detection of small objects compared to YOLOv7. YOLOv8, one of the latest versions of the YOLO family, has a lot of new features provided to researchers by Ultralytics and offers a user-friendly GitHub repo. The Pytorch-based algorithm uses a dynamic head network strategy to increase its speed and accuracy compared to its competitors. Many studies have shown that YOLOv8 gives better results in terms of performance evaluation metrics than YOLOv7 [31, 45, 46]. In this study, mass areas were automatically detected with the YOLOv8 algorithm in three different scenarios using high-resolution mammography images. DICOM images were saved in PNG format to achieve high contrast. No filters or resizing were applied to mammograms, thus reducing the computational cost. Using the same set of hyperparameters, the experiments produced the following precision, recall, and F1-score values for the test data: 95.7%, 78.8%, and 86.4% for raw data, 97.9%, 82.4%, and 89.4% for ROI1, and 100%, 100%, and 100% for ROI3. One of the most significant advantages of this study was the ability to capture high-contrast images from mammography without applying any complex filters. The second advantage was the examination of the impact of the detection process when experiments were conducted with ROIs. As seen in Table 2 and Table 3, the success rates of performance metrics increased as processing was performed with ROIs compared to raw data.

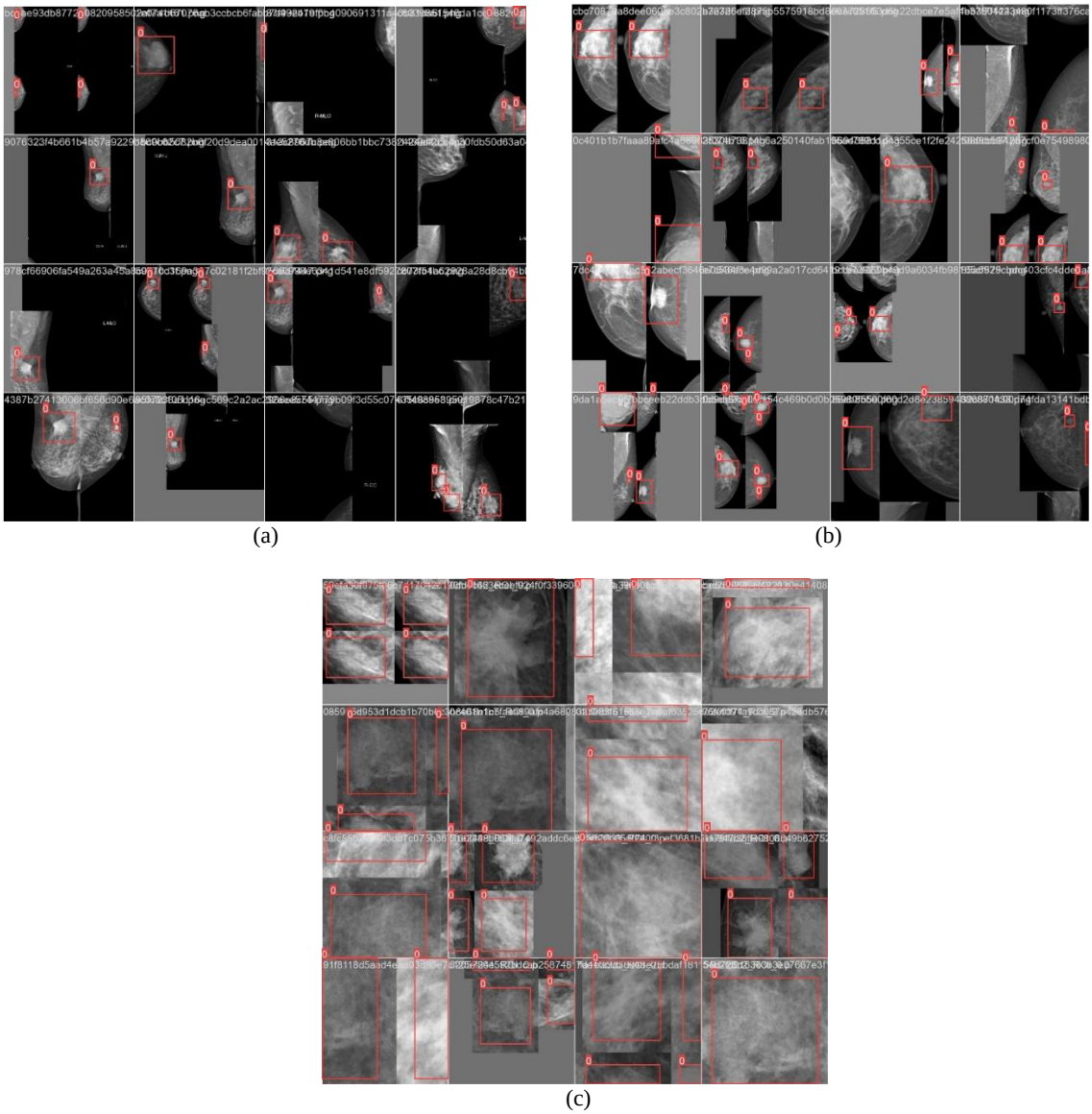

(a) (b) (c)

Figure 9. (a) Mosaic data augmentation for raw data (b) Mosaic data augmentation for ROI1 (c) Mosaic data augmentation for ROI2

In Figure 5, the training conducted with ROIs was shown to be more successful. While performance criteria may vary, as demonstrated in Figure 6, Figure 7, and Figure 8, the detection and localization of mass regions can be accurately determined. It has been determined that the performance evaluation results have increased with the developed automatic background subtraction pre-processing method. 100% success was achieved in the detection processes with ROI2 regions that were cropped by 1.2x. The third advantage was that, as seen in the data distribution provided in Table 1, high detection results were achieved despite the complex distribution of factors such as different BI-RADS, breast density, and views. One of the notable findings was that as the background, which did not contain meaningful information in the image, was removed, the accuracy results increased, demonstrating that higher results can be achieved with patch-based approaches. This may be due to the automatic mosaic data augmentation process implemented during the training of the YOLOv8 algorithm. This process was automatically carried out at the algorithm's input. During the training process, YOLOv8 was provided with images in mini-batches of 16. The training batch was designed as a mosaic through various scaling, resizing, and cropping operations. When examining the mosaic form in Figure 9a, it was evident that there were many black regions in the raw image, which negatively affected the algorithm's performance. As shown in Figure 9b, even with pre-processing, there were relatively black areas left due to the structure of the breast, which did not entirely cover the bounding box of the breast as a whole. In Figure 9c, the mosaic data augmentation form of the patch-based approach with 16 batches is demonstrated. Here, having only breast tissue and no black pixel background regions has positively influenced the performance metrics. As a result of such training, a precision and recall value of 100% was achieved on test data, and the algorithm detected mass in all patches. Another significant finding highlighted by this study was how patch-based approaches significantly improve results and the necessity of breaking down the image into as small patches as possible without background for detection processes. The limitation of this study is the irregularity in the distributions in the BI-RADS, density, and view categories in the data set. Having an equal number of examples in these categories can increase the results of performance evaluation metrics. However, since the VinDr-Mammo dataset was used as a benchmark, this study was performed according to the procedures shared in the database.

4. Conclusion and Suggestions

In this study, breast mass detection was performed in different scenarios using the VinDr-Mammo full-field digital mammography dataset and a deep-learning model. The results demonstrate that the deep learning model provides successful results in the detection and localization of masses in breast cancer. In future studies, applications for the detection of other anomalies in mammograms will be explored. AI methods have gained popularity in recent years for the detection, localization, grading, segmentation, and classification of anomalies in medical images. Therefore, the automated analysis of anomalies in medical images, presenting preliminary findings to doctors, is expected to be advanced software used in the future. The applications conducted in this study, which automatically identify and localize breast masses related to breast cancer, have the potential to be used as a computer-based decision support system, aiding doctors in the diagnostic process.

Acknowledgment

This study was supported by the Scientific Research Coordination Unit of Pamukkale University under project number 2023LÖKAP007.

Contributions of the authors

ASY and MÜÖ contributed to the organization of the data and the pre-processing. MÜÖ carried out the study and algorithm design. HİS and HBE wrote the code and calculated the performance criteria. All authors contributed equally to article writing and literature review.

Conflict of Interest Statement

There is no conflict of interest between the authors.

Statement of Research and Publication Ethics

The study complies with research and publication ethics

References

[1] M. Arnold *et al.*, "Current and future burden of breast cancer: Global statistics for 2020 and 2040," *The Breast*, vol. 66, pp. 15-23, 2022.

[2] L. Wilkinson and T. Gathani, "Understanding breast cancer as a global health concern," *The British Journal of Radiology*, vol. 95, no. 1130, p. 20211033, 2022.

[3] R. Ali, A. Sultan, R. Ishrat, S. Haque, N. J. Khan, and M. A. Prieto, "Identification of New Key Genes and Their Association with Breast Cancer Occurrence and Poor Survival Using In Silico and In Vitro Methods," *Biomedicines*, vol. 11, no. 5, p. 1271, 2023.

[4] M. Buda *et al.*, "Detection of masses and architectural distortions in digital breast tomosynthesis: a publicly available dataset of 5,060 patients and a deep learning model," *arXiv preprint arXiv:2011.07995*, 2020.

[5] V. Barros *et al.*, "Virtual biopsy by using artificial intelligence–based multimodal modeling of binational mammography data," *Radiology*, vol. 306, no. 3, p. e220027, 2022.

[6] Y. Yan, P.-H. Conze, G. Quellec, M. Lamard, B. Cochener, and G. Coatrieux, "Two-stage multi-scale breast mass segmentation for full mammogram analysis without user intervention," *Biocybernetics and Biomedical Engineering*, vol. 41, no. 2, pp. 746-757, 2021.

[7] I. Domingues and J. Cardoso, "Mass detection on mammogram images: a first assessment of deep learning techniques," in *19th Portuguese Conference on Pattern Recognition (RECPAD)*, 2013.

[8] R. Gayathri and K. Kasirajan, "Yolo Algorithm Based Breast Masses Detection And Classification Technique For Digital Mammograms," *Latin American Journal of Pharmacy*, vol. 42, no. 3, pp. 374-381, 2023.

[9] A. Mohiyuddin *et al.*, "Breast tumor detection and classification in mammogram images using modified YOLOv5 network," *Computational and mathematical methods in medicine*, vol. 2022, pp. 1-16, 2022.

[10] Z. Cao *et al.*, "Deep learning based mass detection in mammograms," in *2019 IEEE Global Conference on Signal and Information Processing (GlobalSIP)*, 2019: IEEE, pp. 1-5.

[11] M. A. Al-masni *et al.*, "Detection and classification of the breast abnormalities in digital mammograms via regional convolutional neural network," in *2017 39th annual international conference of the IEEE engineering in medicine and biology society (EMBC)*, 2017: IEEE, pp. 1230-1233.

[12] G. Ayana *et al.*, "Vision-Transformer-Based Transfer Learning for Mammogram Classification," *Diagnostics*, vol. 13, no. 2, p. 178, 2023.

[13] G. H. Aly, M. Marey, S. A. El-Sayed, and M. F. Tolba, "YOLO based breast masses detection and classification in full-field digital mammograms," *Computer methods and programs in biomedicine*, vol. 200, p. 105823, 2021.

[14] Y. Cui, Y. Li, D. Xing, T. Bai, J. Dong, and J. Zhu, "Improving the prediction of benign or malignant breast masses using a combination of image biomarkers and clinical parameters," *Frontiers in Oncology*, vol. 11, p. 629321, 2021.

[15] H. Zhang, Z. Xu, D. Yao, S. Zhang, J. Chen, and T. Lukasiewicz, "Multi-Head Feature Pyramid Networks for Breast Mass Detection," in *ICASSP 2023-2023 IEEE International Conference on Acoustics, Speech and Signal Processing (ICASSP)*, 2023: IEEE, pp. 1-5.

[16] Y. Yan, P.-H. Conze, M. Lamard, G. Quellec, B. Cochener, and G. Coatrieux, "Multi-tasking siamese networks for breast mass detection using dual-view mammogram matching," in *Machine Learning in Medical Imaging: 11th International Workshop, MLMI 2020, Held in Conjunction with MICCAI 2020, Lima, Peru, October 4, 2020, Proceedings 11*, 2020: Springer, pp. 312-321.

[17] M. A. Al-Masni *et al.*, "Simultaneous detection and classification of breast masses in digital mammograms via a deep learning YOLO-based CAD system," *Computer methods and programs in biomedicine*, vol. 157, pp. 85-94, 2018.

[18] Y. Su, Q. Liu, W. Xie, and P. Hu, "YOLO-LOGO: A transformer-based YOLO segmentation model for breast mass detection and segmentation in digital mammograms," *Computer Methods and Programs in Biomedicine*, vol. 221, p. 106903, 2022.

[19] B. Abhisheka, S. K. Biswas, and B. Purkayastha, "A comprehensive review on breast cancer detection, classification and segmentation using deep learning," *Archives of Computational Methods in Engineering*, pp. 1-30, 2023.

[20] I. C. Moreira, I. Amaral, I. Domingues, A. Cardoso, M. J. Cardoso, and J. S. Cardoso, "Inbreast: toward a full-field digital mammographic database," *Academic radiology*, vol. 19, no. 2, pp. 236-248, 2012.

[21] S. Singh and K. Bovis, "An evaluation of contrast enhancement techniques for mammographic breast masses," *IEEE Transactions on Information Technology in Biomedicine,* vol. 9, no. 1, pp. 109-119, 2005.

[22] M. P. Sampat, A. C. Bovik, G. J. Whitman, and M. K. Markey, "A model-based framework for the detection of spiculated masses on mammography a," *Medical physics,* vol. 35, no. 5, pp. 2110-2123, 2008.

[23] E. Song *et al.*, "Hybrid segmentation of mass in mammograms using template matching and dynamic programming," *Academic radiology,* vol. 17, no. 11, pp. 1414-1424, 2010.

[24] H. T. Nguyen *et al.*, "VinDr-Mammo: A large-scale benchmark dataset for computer-aided diagnosis in full-field digital mammography," *Scientific Data,* vol. 10, no. 1, p. 277, 2023.

[25] M. Ü. Öziç, M. Barstuğan, and A. Özdamar, "An autonomous system design for mold loading on press brake machines using a camera platform, deep learning, and image processing," *Journal of Mechanical Science and Technology,* pp. 1-9, 2023.

[26] F. Yuce, M. Ü. Öziç, and M. Tassoker, "Detection of pulpal calcifications on bite-wing radiographs using deep learning," *Clinical Oral Investigations,* vol. 27, no. 6, pp. 2679-2689, 2023.

[27] J. Redmon and A. Farhadi, "YOLO9000: better, faster, stronger," in *Proceedings of the IEEE conference on computer vision and pattern recognition*, 2017, pp. 7263-7271.

[28] J. Redmon and A. Farhadi, "Yolov3: An incremental improvement," *arXiv preprint arXiv:1804.02767,* 2018.

[29] A. Bochkovskiy, C.-Y. Wang, and H.-Y. M. Liao, "Yolov4: Optimal speed and accuracy of object detection," *arXiv preprint arXiv:2004.10934,* 2020.

[30] G. Jocher *et al.*, "ultralytics/yolov5: v3. 0," *Zenodo,* 2020.

[31] J. Terven and D. Cordova-Esparza, "A comprehensive review of YOLO: From YOLOv1 to YOLOv8 and beyond," *arXiv preprint arXiv:2304.00501,* 2023.

[32] D. G. Petrini, C. Shimizu, R. A. Roela, G. V. Valente, M. A. A. K. Folgueira, and H. Y. Kim, "Breast cancer diagnosis in two-view mammography using end-to-end trained efficientnet-based convolutional network," *Ieee access,* vol. 10, pp. 77723-77731, 2022.

[33] D. Anyfantis, A. Koutras, G. Apostolopoulos, and I. Christoyianni, "Breast Density Transformations Using CycleGANs for Revealing Undetected Findings in Mammograms," *Signals,* vol. 4, no. 2, pp. 421-438, 2023.

[34] E. Mahoro and M. A. Akhloufi, "Breast masses detection on mammograms using recent one-shot deep object detectors," in *2023 5th International Conference on Bio-engineering for Smart Technologies (BioSMART)*, 2023: IEEE, pp. 1-4.

[35] H. T. Nguyen, S. B. Tran, D. B. Nguyen, H. H. Pham, and H. Q. Nguyen, "A novel multi-view deep learning approach for BI-RADS and density assessment of mammograms," in *2022 44th Annual International Conference of the IEEE Engineering in Medicine & Biology Society (EMBC)*, 2022: IEEE, pp. 2144-2148.

[36] S. B. Tran, H. T. Nguyen, C. Phan, H. H. Pham, and H. Q. Nguyen, "A Novel Transparency Strategy-based Data Augmentation Approach for BI-RADS Classification of Mammograms," *arXiv preprint arXiv:2203.10609,* 2022.

[37] S. Magny, R. Shikhman, and A. Keppke, "Breast Imaging Reporting and Data System. 2022 Aug 29," *StatPearls [Internet]. StatPearls Publishing (Treasure Island, FL),* 2022.

[38] Y. Liu *et al.*, "High-temporal resolution DCE-MRI improves assessment of intra-and peri-breast lesions categorized as BI-RADS 4," *BMC Medical Imaging,* vol. 23, no. 1, p. 58, 2023.

[39] A. Vourtsis and W. A. Berg, "Breast density implications and supplemental screening," *European radiology,* vol. 29, pp. 1762-1777, 2019.

[40] N. Otsu, "A threshold selection method from gray-level histograms," *IEEE transactions on systems, man, and cybernetics,* vol. 9, no. 1, pp. 62-66, 1979.

[41] R. Walsh and M. Tardy, "A Comparison of Techniques for Class Imbalance in Deep Learning Classification of Breast Cancer," *Diagnostics,* vol. 13, no. 1, p. 67, 2022.

[42] S. B. Tran, H. T. Nguyen, C. Phan, H. Q. Nguyen, and H. H. Pham, "A Novel Transparency Strategy-based Data Augmentation Approach for BI-RADS Classification of Mammograms," in *2023 IEEE Statistical Signal Processing Workshop (SSP)*, 2023: IEEE, pp. 681-685.

[43] V. Sampaio and F. R. Cordeiro, "A Study on Class Activation Map Methods to Detect Masses in Mammography Images using Weakly Supervised Learning," in *Anais do XIX Encontro Nacional de Inteligência Artificial e Computacional*, 2022: SBC, pp. 437-448.

[44] H. N. Huynh, A. T. Tran, and T. N. Tran, "Region-of-Interest Optimization for Deep-Learning-Based Breast Cancer Detection in Mammograms," *Applied Sciences,* vol. 13, no. 12, p. 6894, 2023.

[45] B. Gašparović, G. Mauša, J. Rukavina, and J. Lerga, "Evaluating YOLOV5, YOLOV6, YOLOV7, and YOLOV8 in Underwater Environment: Is There Real Improvement?," in *2023 8th International Conference on Smart and Sustainable Technologies (SpliTech)*, 2023: IEEE, pp. 1-4.

[46] F. N. Ortataş and M. Kaya, "Performance Evaluation of YOLOv5, YOLOv7, and YOLOv8 Models in Traffic Sign Detection," in *2023 8th International Conference on Computer Science and Engineering (UBMK)*, 2023: IEEE, pp. 151-156.

Bitlis Eren Üniversitesi Fen Bilimleri Dergisi
BİTLİS EREN UNIVERSITY JOURNAL OF SCIENCE
ISSN: 2147-3129/e-ISSN: 2147-3188
VOLUME: 12 NO: 4 PAGE: 1226-1236 YEAR: 2023
DOI:10.17798/bitlisfen.1361043

Cargo Company Recommendation Study Based on Probabilistic Linguistic Term Set

Veysel ÇOBAN[1*], Sezgin Çağlar AKSEZER[2]

[1]*Bilecik Seyh Edebali University, Industrial Engineering Department only once.)*
[2]*Isık University, Industrial Engineering Department*
(ORCID: 0000-0002-7885-1935) (ORCID: 0000-0002-1150-7064)

Keywords: Decision making, Probabilistic Linguistic Term Set, Recommendation, Cargo service.

Abstract

The global economic structure is the main reason for changes in consumption habits and consumer behavior. Developing information technologies direct producers and consumers to e-commerce. Cargo services are an important link in the chain in the fast and effective operation of e-commerce. The growth in e-commerce has a driving force in the development of cargo services and cargo companies. Cargo companies can survive in global competition by being preferred by customers and increasing their number of customers. The change in the number of customers occurs by communicating the satisfaction or dissatisfaction with the cargo company to potential customers. This study deals with the preference levels of cargo companies serving in Turkey according to customer suggestions. The data obtained from the survey evaluations are processed and recommendation ranking calculations are made for cargo companies. Probabilistic Linguistic Term Sets (PLTS) are used to eliminate customer ambiguities in survey evaluations. Alternative cargo company recommendations are ranked based on the customers' past service experiences from cargo companies. Aras Cargo, MNG Cargo, PTT Cargo, Surat Cargo, UPS Cargo, Yurtiçi Cargo companies are evaluated according to price, personnel, speed, reliability and network attributes. The maximum deviation optimization method based on the Lagrangian function is used to calculate the weights of the cargo companies' attributes. The probabilistic linguistic cosine similarity method compares cargo companies pairwise under attributes and a similarity matrix is obtained for six cargo companies. The similarity matrix defines the alternative cargo company recommendation ranking based on customers' past experiences. UPS, SURAT and MNG cargo companies stand out as the most prioritized companies according to the evaluation results. The effects of attribute weights are observed by designing six different scenarios and it is observed that the differentiating attribute weights affect the recommendation ranking. Spearman correlation coefficient evaluation based on recommendation rankings indicates a high relationship between attributes.

1. Introduction

Consumer behavior keeps up with the changes in the globalizing economic system. E-commerce, which is a part of the global change process, helps customers to access products and services economically and quickly [1]. Recommendation systems enable consumers to reach the right service and product with past experience transfers. Collaborative filtering, content-based and hybrid recommendation methods are the most used methods in the traditional recommendation system. Collaborative filtering is the most common recommendation method and bases its evaluations on the similarities among items or users [2].

*Corresponding author: veysel.coban@bilecik.edu.tr
Received: 23.09.2023, Accepted: 02.12.2023

Recommendation systems in the literature deal with user preference movements based on offline and online data. Hwangbo et al. proposes a new called K-RecSys model based on the collaborative filtering recommendation system and applies this system on the click and sales data of a fashion product [3]. Zihayat et al. introduces the two-stage benefit-based news recommendation system and examines whether users' news clicks reflect users' real interests [4]. Lin et al.'s study applies a recommendation system in students' course selection based on course registration data in Chinese universities [5]. Abbasi-Moud et al. studies on the tourism recommendation system and reveals user preferences based on social network comments [6]. Liu et al. design a multi-modal transportation recommendation system in the perspectives of users, travel modes, time and location, and this model is promoted as a superior method of providing navigation service [7]. Cui et al. propose a new recommendation model developed with cuckoo search to provide faster and more accurate advice to users [8]. Nitu et al. develop an integrated personalized travel recommendation system with time-sensitive innovation weighting based on tweet data [9]. Wang et al.'s study proposes a collaborative filtering recommendation algorithm for hotels, and the validity of the model is checked with data collected from the website for ten hotels [10].

Cargo services, which have an important place in e-commerce, allow customers to reach products and services effectively, efficiently and with high satisfaction [11]. Customers are affected by the evaluations of their relatives or online users when choosing a company for cargo service, and their preferences are determined by these effects. Evaluations based on past experience are difficult to define by users with precise measurements and expressions. In addition, evaluations expressed in linguistic terms cause information to contain vagueness and fuzziness [12]. In this study, the importance and frequency levels of users' evaluations are expressed by using a set of PLTSs. Single and multiple linguistic term models have been developed to solve linguistic definition problems. Single linguistic terms that reflect the unhesitant expression of opinions are inadequate to describe hesitant and uncertain real-life expressions. Therefore, multiple linguistic terms are used to describe uncertain real-life expressions and resolve ambiguities in expressions. Hesitant Fuzzy Linguistic Term Set (HFLTS) is one of the widely used multi-linguistic methods for expressing ambiguous and complex evaluations [13]. PLTS proposed by Pang et al. assigns probabilities to linguistic terms of HFLTS to more accurately describe ambiguities [12]. The PLTS method used in different computing with words studies has proven its validity [10], [14], [15]. In this study, PLTS helps reflect the different importance of possible recommendation statements. PLTS is chosen as the mathematical tool to deal with hesitant and ambiguous statements in recommendation problems based on multiple attribute evaluations [12].

This identification method helps to reduce the level of incomplete and incorrect expression of hesitant information. PLTSs used in individual and group assessments have found application area in education, health and project studies [10], [14]. PLTSs method, which also finds application areas in recommendation studies, generates a solution in film and hotel recommendation problems [2].

The main motivation of this study is to create an alternative cargo company to meet the expectations of the users in the provision of cargo services, which constitute an important stage of e-commerce. This study aims to make a comparative evaluation for six common cargo companies in Turkey based on five key attributes in the evaluation and to develop a recommendation ranking for users. Linguistic evaluations of the users based on their past experiences are collected through an online survey and the linguistic evaluations of the users are converted into Probabilistic Linguistic Term Elements (PLTE). Evaluation expressions converted to PLTEs are used in the probabilistic linguistic cosine similarity method to calculate similarity between cargo companies. Cargo companies are compared according to their similarity values and recommendations are ranked according to the past usage characteristics of the users. The difference in the range of linguistic terms used by the probabilistic linguistic term method and the first use of this method in the cargo company recommendation study are determined as the original contributions of the study to the literature.

The study is organized under the following sections. Section Preliminaries discusses the basic concepts of PLTSs, the methods used in the recommendation model, and the recommendation model based on the PLTS approach. With the case study in Section Application, the recommendation model is applied in the courier recommendation ranking case study. The Discussion Section mentions comparative information about similar studies. In the Section Conclusion, evaluations are made about the validity of the model and the order of cargo proposals, and future studies are also mentioned.

2. Preliminaries

This section describes the PLTSs, which is the main assessment tool used in the study, the basic concepts of the study and the computational processes applied in the recommendation ranking study.

2.1. Probabilistic Linguistic Term Sets

PLTSs were developed by Pang [12] in order to reduce information fuzziness by including ambiguities and hesitancies in commonly used linguistic expressions in the decision-making process. A set of linguistic terms is defined as S= $\{s_\alpha | \alpha=-\tau,\ldots,0,\ldots,\tau\}$ where s_α defines the possible value of linguistic variable and τ is a positive integer. For example if τ is 1, linguistic term set can be defined as S=$\{s_{-1}$ =very low, s_0 = medium, s_1 = very high$\}$. The set of probabilistic linguistic terms is defined as [12]:

$$L(p) = \left\{L^i(p^i) | L^i \in S, p^i \geq 0, i = 1, \ldots, \#L(p), \sum_{i=1}^{\#L(p)} p^i \leq 0\right\} \quad (1)$$

where L^i corresponds to the ith term of the linguistic term set defined by #L(p) terms, and the probability of the ith term is denoted by p^i. If the sum of the probability values of the elements of the linguistic term set is equal to one, this set is called full PLTS. If the evaluation has complete information about the probabilistic distribution of possible linguistic terms, $\sum_{i=1}^{\#L(p)} p^i$ is calculated as 1. Otherwise, $\sum_{i=1}^{\#L(p)} p^i = 0$ indicates that no information is available about the probabilistic distribution of possible linguistic terms. This situation prevents the calculations and evaluation process. The realization of the $\sum_{i=1}^{\#L(p)} p^i < 0$ situation indicates that information loss will occur in the evaluation and that deviations will occur in the decision results. This is avoided by normalizing probabilities before computational operations as follows:

$$\acute{L}(p) = \left\{L^i(\acute{p}^i) | i = 1, \ldots, \#\mathrm{L(p)}\right\} \quad (2)$$

$$\acute{p}^i = \mathrm{p^i} / \sum_{\mathrm{i=1}}^{\#\mathrm{L(p)}} \mathrm{p^i} \quad (3)$$

If the term numbers of the two PLTSs are different $\left(\#L_1(p) \neq \#L_2(p)\right)$, equality is established between the term numbers of the set. The number of missing elements is added to the set with the smallest number of elements, and the probability values of these added elements are accepted as 0.

The distance between two PLTSs, $L_1(p) = \{L_1^i(p_1^i) | \, i = 1, \ldots, \#L_1(p)\}$ and $L_2(p) = \left\{L_2^i(p_2^i) \middle| \, i = 1, \ldots, \#L_2(p)\right\}$, is calculated as follows [12]:

$$\mathrm{d}\left(\mathrm{L_1(p), L_2(p)}\right) = \sqrt{\sum_{\mathrm{i=1}}^{\#\mathrm{L(p)}} \left(\mathrm{p_1^i r_1^i - p_1^i r_2^i}\right)^2 / \#\mathrm{L(p)}} \quad (4)$$

r_1^i and r_2^i refer to the sub-index values of the linguistic terms L_1^i and L_2^i, respectively. The distances satisfy the conditions $d\left(L_1(p), L_1(p)\right) = 0$ and $d\left(L_1(p), L_2(p)\right) = d\left(L_2(p), L_1(p)\right)$. The similarity measure is used to define the level of similarity between elements. Cosine similarity value (SIM), which is used as an important tool in decision-making problems, calculates the similarity measure between two vectors. The cosine similarity value between L_1 and L_2 PLTSs is calculated as follows [13], [16]:

$$SIM\left(\mathrm{L_1(p), L_2(p)}\right) = \frac{\sum_{i=1}^{\#\mathrm{L(p)}} \left(\tau^{(L_1^i p_1^i)/\tau} * \tau^{(L_2^i p_2^i)/\tau}\right)}{\sqrt{\left(\sum_{i=1}^{\#\mathrm{L(p)}} \left(\tau^{\frac{L_1^i p_1^i}{\tau}}\right)^2\right)\left(\sum_{i=1}^{\#\mathrm{L(p)}} \left(\tau^{\frac{L_2^i p_2^i}{\tau}}\right)^2\right)}} \quad (5)$$

Cosine similarity values between PLTSs satisfy the conditions SIM(L_1(p), L_1(p))=1 and SIM(L_1(p), L_2(p))=SIM(L_2(p), L_1(p)).

2.2. Problem Definition and Data Processing

The set $X = \{x_i | x_1, x_2, \ldots, x_m\}$ is used to define the six common cargo companies in Turkey that are covered in the cargo company recommendation study. The set of attributes that customers use to define the service they receive from shipping companies is defined as $A = \left\{a_j \middle| a_1, a_2, \ldots, a_n\right\}$. Customers who want to receive cargo service are guided by the experience and evaluations of other customers.

Users are requested to evaluate their experiences with cargo companies through a survey created with a Google form. Users make their evaluations by considering price, personnel approach, service speed, reliability and service network attributes [17], [18]. The seven-dimensional linguistic

term set, S={s_{-3}=very bad, s_{-2}=bad, s_{-1}=somewhat bad, s_0=moderate, s_1=somewhat good, s_2=well, s_3=very good}, is used to convey users' past experience. Probabilistic linguistic term set transformations are performed to statistically describe the linguistic views obtained from users' evaluations [19]. The number of repetitions of the expression in each evaluation of each service attribute expression $O_{s_\alpha}^j$ and the total number of repetitions of each attribute a_j are counted as O_{a_j}. Thus, the probability value (P^α) of the sub-index α of the linguistic term s_α, which defines the attribute terms, is calculated as [2], [15].

$$P^\alpha = O_{s_\alpha}^j / O_{a_j} \tag{6}$$

A probabilistic set of linguistic terms is obtained by calculating the probability values of all expressions. The view set of the i^{th} cargo service according to the j^{th} attribute is represented as L_{ij} (p). The implementation steps of the cargo company recommendation method are as follows:

Step 1: Formation of evaluation matrices of cargo companies: Cargo companies' factor-based evaluation information is explained with PLTS and the evaluation matrix is obtained.

$$P = \begin{bmatrix} L_{11}(p) & L_{12}(p) & \cdots & L_{1n}(p) \\ L_{21}(p) & L_{22}(p) & & L_{2n}(p) \\ \vdots & & \ddots & \vdots \\ L_{m1}(p) & L_{m2}(p) & \cdots & L_{mn}(p) \end{bmatrix} \tag{7}$$

where L_{ij} represents the evaluation information of cargo company x_i (i=1,2,…,m) according to the factor a_j (j=1,2,…,n).

Step 2: Determination of attribute weights: The attribute weights are determined using the maximum deviation method. The large deviation value of the attribute, which reflects the power of the discrimination ability, indicates that the weight of the attribute is also large. The degree of deviation, with w={w_j| j=1, 2,…, n} being the set of attribute weights, is calculated based on the distance between PLTS formula (Eq.4). The degree of deviation between the x_i cargo company and other cargo companies according to the a_j attribute is calculated as follows [20]:

$$d_{ij} = \sum_{k=1,k\neq i}^{m} d\left(L_{ij}(p), L_{kj}(p)\right) = \sum_{k=1,k\neq i}^{m} \sqrt{\sum_{l=1}^{\#L(p)} \left(p_{ij}^l r_{ij}^l - p_{kj}^l r_{kj}^l\right)^2 / \#L(p)} \tag{8}$$

The total degree of deviation for the a_j attribute is defined as:

$$d_j = \sum_{i=1}^{m} d_{ij} \tag{9}$$

The total degree of deviation between attributes according to the evaluation matrix is shown as follows [2], [21]:

$$d_P = \sum_{j=1}^{n} w_j d_j \tag{10}$$

The maximum deviation optimization model is created as follows:

$$mak\ d_P = \sum_{j=1}^{n} w_j \sum_{i=1}^{m} \sum_{k=1,k\neq i}^{m} d\left(L_{ij}(p), L_{kj}(p)\right) \quad \sum_{j=1}^{n} w_j^2 = 1, w_j \geq 0 \tag{11}$$

The Lagrangian function is used to solve the maximum deviation optimization model:

$$L(w,\lambda) = \sum_{j=1}^{n} w_j \sum_{i=1}^{m} \sum_{k=1,k\neq i}^{m} d\left(L_{ij}(p), L_{kj}(p)\right) + \frac{\lambda}{2}\left(\sum_{j=1}^{n} w_j^2 - 1\right) \tag{12}$$

The normalized attribute weights are calculated as:

$$w_j = \frac{\sum_{i=1}^{m}\sum_{k=1,k\neq i}^{m} d\left(L_{ij}(p), L_{kj}(p)\right)}{\sum_{j=1}^{n}\sum_{i=1}^{m}\sum_{k=1,k\neq i}^{m} d\left(L_{ij}(p), L_{kj}(p)\right)} \tag{13}$$

Step 3: The similarity matrix is created: Similarities between cargo companies are calculated by weighted similarity calculation method. First of all, the pairwise similarities between the cargo companies under each attribute are calculated according to the cosine similarity method (Eq.5) as follows:

$$SIM\left(L_{ij}(p), L_{kj}(p)\right) = \frac{\sum_{l=1}^{\#L(p)} \left(\tau^{(L_{ij}^{l} p_{ij}^{l})/\tau} * \tau^{(L_{kj}^{l} p_{kj}^{l})/\tau}\right)}{\sqrt{\left(\sum_{l=1}^{\#L(p)} \left(\tau^{\frac{L_{ij}^{l} p_{ij}^{l}}{\tau}}\right)^{2}\right)\left(\sum_{l=1}^{\#L(p)} \left(\tau^{\frac{L_{kj}^{l} p_{kj}^{l}}{\tau}}\right)^{2}\right)}} \quad (14)$$

where #L(p)=#L_{ij} (p)=#L_{kj} (p). The pairwise weighted similarity values between x_i and x_k cargo companies are calculated as follows according to the weights of the attributes:

$$SIM(x_i, x_k) = \sum_{j=1}^{n} w_j SIM\left(L_{ij}(p), L_{kj}(p)\right) \quad (15)$$

The similarity matrix between the cargo companies according to the pairwise weighted similarity values is defined as follows:

$$M = \begin{bmatrix} SIM(x_1,x_1) & SIM(x_1,x_2) & \cdots & SIM(x_1,x_m) \\ SIM(x_2,x_1) & SIM(x_2,x_2) & & SIM(x_2,x_m) \\ \vdots & & \ddots & \vdots \\ SIM(x_m,x_1) & SIM(x_m,x_2) & \cdots & SIM(x_m,x_m) \end{bmatrix} \quad (16)$$

$SIM(x_i, x_i)=1$ and $SIM(x_i, x_k)=SIM(x_k, x_i)$ conditions are met in the similarity matrix showing the similarity between the two cargo companies.

Step 4: Ranking of alternative cargo company recommendations for users. A recommendation ranking is created for past cargo company users based on customer expectations. The similarity matrix between companies that exceed the threshold value is taken into account in the recommendation ranking formation.

A case study is carried out by following the steps mentioned in this section. The flow chart of the application steps is shown in Figure 1.

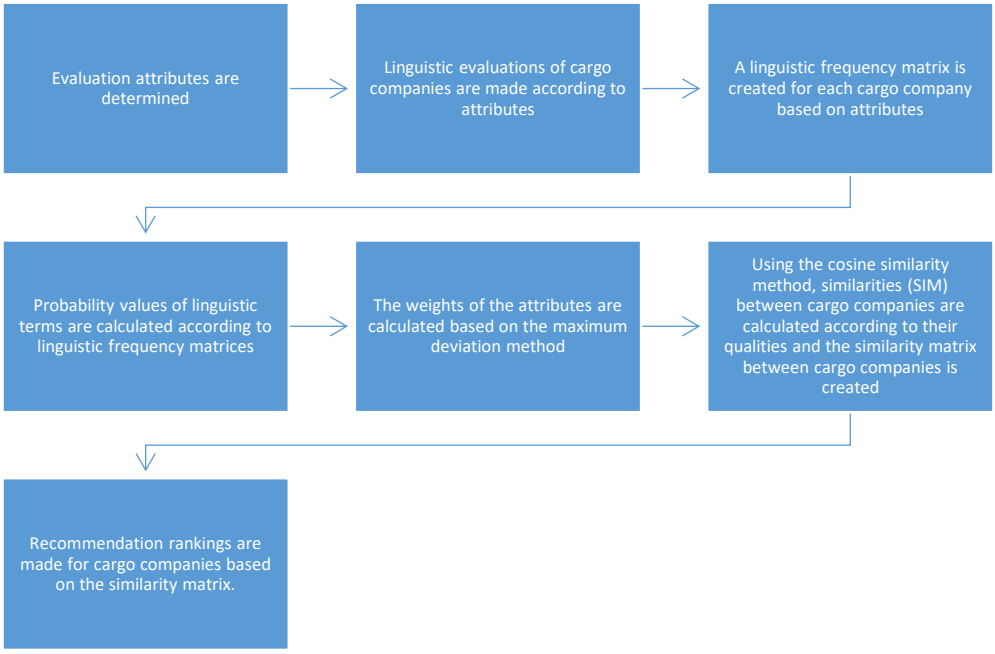

Figure 1. Flow diagram of the application steps

3. Case Application

In this section, a recommendation study is made for five common cargo companies in Turkey, taking into account the evaluations made by users based on the basic characteristics of cargo service. Common cargo companies covered in the study are as follows: Aras Cargo, MNG Cargo, PTT Cargo, Surat Cargo, UPS Cargo, Yurtici Cargo. The participants are asked to evaluate the cargo companies based on their experiences on price, personnel approach, speed, reliability and service network attributes with the survey defined in Google forms. The evaluation attributes of cargo companies are defined by considering the studies in the literature. The descriptions of the attributes are as follows:

- Price (a1): All service fees incurred in the process of receiving, safe transport and delivery of the cargo. Price varies according to delivery time, product sensitivity, product size and product weights [22]–[24].

- Personnel approach (a2): Verbal and nonverbal communication of the personnel in charge of the product delivery and purchase stages with the customer [23], [25], [26].
- Speed (a3): Cargo delivery is realized within the shortest time promised [22], [24], [27].
- Reliability (a4): The expectation that the product will be delivered in desired conditions, durable and clean [22], [27], [28].
- Service network (a5): Existence of a widespread branch network that facilitates the process of receiving and returning the product [17], [24], [27].

The set of cargo companies is shown as X = $\{x_1, x_2, x_3, x_4, x_5, x_6\}$ and the set of attributes is defined as A= $\{a_1, a_2, a_3, a_4, a_5\}$. A linguistic term set as S=$\{s_{-3}, s_{-2}, s_{-1}, s_0, s_1, s_2, s_3\}$ is defined for customers to evaluate cargo companies according to attributes. The number of evaluation terms for each cargo company is indicated by $Q_{s_\alpha}^{j}$ and the total number of evaluations by Q_{a_j} for each attribute a_j.

Table 1. Linguistic evaluation results of the survey

Cargo company	Attributes	Linguistic terms						
		s_{-3}	s_{-2}	s_{-1}	s_0	s_1	s_2	s_3
ARAS	a_1	6	8	2	15	7	13	6
	a_2	4	3	3	14	7	16	10
	a_3	5	2	4	11	8	15	12
	a_4	3	4	4	14	4	14	14
	a_5	3	2	5	12	8	15	12
MNG	a_1	4	6	2	15	12	14	4
	a_2	3	3	6	10	9	17	9
	a_3	3	0	6	14	12	16	6
	a_4	0	2	8	13	7	19	8
	a_5	0	2	7	12	10	18	8
PTT	a_1	12	5	9	10	6	12	3
	a_2	10	6	8	9	7	12	5
	a_3	22	8	9	9	5	3	1
	a_4	10	4	8	13	8	8	6
	a_5	8	7	5	11	10	9	7
SURAT	a_1	6	10	6	17	8	7	3
	a_2	4	7	7	13	8	11	7
	a_3	4	3	8	13	13	11	5
	a_4	2	5	5	17	10	12	6
	a_5	2	7	6	14	8	13	7
UPS	a_1	4	1	3	17	3	15	14
	a_2	1	0	2	15	8	18	13
	a_3	2	1	2	15	8	11	18
	a_4	0	0	2	13	10	13	19
	a_5	1	3	4	15	7	15	12
YURTICI	a_1	5	4	3	6	9	17	13
	a_2	1	1	2	9	11	16	17
	a_3	1	1	3	8	6	11	27
	a_4	0	1	1	12	5	14	24
	a_5	0	1	2	7	11	14	22

Step 1: Users making evaluations are expected to have past cargo usage experience. Experiences may have been gained from direct or indirect interaction with the cargo service. Users' personal information such as age, gender, education or income level is not requested when evaluating cargo companies. Users make their evaluations based on the linguistic terms as S=$\{s_{-3}$: very bad, s_{-2}: bad, s_{-1}: little bad, s_0: not bad/good, s_1: a little good, s_2:good, s_3:very good$\}$. The evaluation results of 57 users according to the seventh linguistic term scale are collected and shown in Table 1.

Step 2: According to the survey data obtained in Table 1, the probability value of the related linguistic term of each cargo company is calculated according to Eq.6 and PLTSs are defined for linguistic terms. For example, the probability values of the linguistic terms of the evaluations made for the price attribute (a_1) of ARAS Cargo Company (x_1) are calculated as P^{-3}=6/57=0.105, P^{-2}=0.140, P^{-1}=0.035, P^0=0.263, P^1=0.123, P^2=0.228, P^3=0.105.

The PLTS of the linguistic assessments of x_1 determined by a_1 is defined as: L_{11}=$\{s_{-3}(0.105), s_{-2}(0.140), s_{-1}(0.035), s_0(0.263), s_1(0.123), s_2(0.228), s_3(0.105)\}$. The PLTS of the linguistic evaluations of the cargo companies are calculated according to the qualifications and the evaluation matrix of the cargo companies is obtained as follows:

$$P = \begin{bmatrix} \left\{\begin{matrix} s^{-3}(0.105), s^{-2}(0.140), \\ s^{-1}(0.035), s^{0}(0.263), \\ s^{1}(0.123), s^{2}(0.228), s^{3}(0.105) \end{matrix}\right\} & \cdots & \left\{\begin{matrix} s^{-3}(0.05), s^{-2}(0.04), \\ s^{-1}(0.09), s^{0}(0.21), \\ s^{1}(0.14), s^{2}(0.26), s^{3}(0.21) \end{matrix}\right\} \\ \left\{\begin{matrix} s^{-3}(0.07), s^{-2}(0.11), \\ s^{-1}(0.04), s^{0}(0.26), \\ s^{1}(0.21), s^{2}(0.25), s^{3}(0.07) \end{matrix}\right\} & \cdots & \left\{\begin{matrix} s^{-3}(0), s^{-2}(0.04), \\ s^{-1}(0.12), s^{0}(0.21), \\ s^{1}(0.18), s^{2}(0.32), s^{3}(0.14) \end{matrix}\right\} \\ \vdots & \ddots & \vdots \\ \left\{\begin{matrix} s^{-3}(0.09), s^{-2}(0.07), \\ s^{-1}(0.05), s^{0}(0.11), \\ s^{1}(0.16), s^{2}(0.30), s^{3}(0.23) \end{matrix}\right\} & \cdots & \left\{\begin{matrix} s^{-3}(0), s^{-2}(0.02), \\ s^{-1}(0.04), s^{0}(0.12), \\ s^{1}(0.19), s^{2}(0.25), s^{3}(0.39) \end{matrix}\right\} \end{bmatrix}$$

Since the probability values of linguistic terms are obtained by normalizing in the evaluation matrix, there is no need to make a new normalization over the probability values.

Step 3: The weights of the attributes are calculated using the maximum deviation method. First, the distances between the PLTSs of the attributes are calculated using Eq.4 to observe the relationships between the cargo companies. For example, the distance for PLTSs L_{11} and L_{21}, which are defined according to the price (a_1) nature of Aras (x_1) and MNG (x_2) cargo companies, respectively, is calculated as follows:

$$d\left(L_{11}(p).L_{21}(p)\right) = \sqrt{\frac{\begin{matrix}\left((-3)*(0.105-0.07)\right)^2+\left((-2)*(0.140-0.105)\right)^2+\\ \left((-1)*(0.035-0.035)\right)^2+\left((0)*(0.263-0.263)\right)^2+\\ \left((1)*(0.123-0.211)\right)^2+\left((2)*(0.228-0.246)\right)^2\\ +\left((3)*(0.105-0.07)\right)^2\end{matrix}}{7}}$$

$$= 0.072$$

Relative deviation degrees and total deviation degrees of attributes According to Eq.8 and Eq.9 for each cargo company are shown in Table 2. The total degree of deviation between attributes according to Eq.10 is defined as:

$$d_P = 5.341w_1 + 4.701w_2 + 9.812w_3 + 7.029w_4 + 5.357w_5$$

Table 2. Deviation degrees of attributes

Attributes	Aras	MNG	PTT	Surat	UPS	YURTICI	d_j
Price	0.678	0.774	1.013	0.912	1.038	0.926	5.341
Personnel	0.572	0.596	1.060	0.766	0.745	0.962	4.701
Speed	1.190	1.338	2.500	1.346	1.389	2.049	9.812
Reliability	0.899	1.093	1.412	1.096	1.091	1.438	7.029
Network	0.662	0.807	1.069	0.792	0.659	1.368	5.357

The maximum deviation optimization model based on the total deviation degree is defined as:

$$maks\ d_P = 5.341w_1 + 4.701w_2 + 9.812w_3 + 7.029w_4 + 5.357w_5$$
$$w_1^2 + w_2^2 + w_3^2 + w_4^2 + w_5^2 = 1$$

The optimization model is solved by defining the Lagrangian function (L (w, λ)):

$$L(w.\lambda) = 5.341w_1 + 4.701w_2 + 9.812w_3 + 7.029w_4 + 5.357w5 + \frac{\lambda}{2}(w_1^2 + w_2^2 + w_3^2 + w_4^2 + w_5^2 - 1)$$

The partial derivatives of the Lagrangian function are taken according to the weights of the attributes and the Lagrange parameter λ:

$$5.341 + \lambda w_1 = 0$$
$$4.701 + \lambda w_2 = 0$$
$$9.812 + \lambda w_3 = 0$$
$$7.029 + \lambda w_4 = 0$$
$$5.357 + \lambda w_5 = 0$$
$$\frac{1}{2}\left(w_1^2 + w_2^2 + w_3^2 + w_4^2 + w_5^2 - 1\right) = 0$$

The solution of the Lagrangian function gives the Lagrangian parameter λ=-15 and the attribute weights 0.356, 0.313, 0.654, 0.469 and 0.357, respectively. Normalized values are defined as w_1=0.166, w_2=0.146, w_3=0.304, w_4=0.218, w_5=0.166.

Step 4: Similarities between cargo companies for each attribute are calculated using the cosine similarity method and a similarity matrix is created. For example, the cosine similarity values of Aras Cargo with other cargo companies under all attributes are defined in Table 3.

The weights of the attributes are included in the calculation process and the weighted similarity matrix is generated using Eq.15. For example, the weighted similar value between ARAS (x1) and MNG (x2) cargo companies is calculated as follows:

$$SIM(x_1, x_2) = 0.9997 * 0.166 + 0.9999 * 0.146 + 0.9986 * 0.304 + 0.9980 * 0.218 + 0.9991 * 0.166 = 0.9989$$

Table 3. Cosine similarity degrees for Aras Cargo Company

$SIM(L_{ij}(p), L_{kj}(p))$	MNG	PTT	Surat	UPS	YURTICI
	0.9997	0.9992	0.9995	0.9981	0.9988
	0.9999	0.9992	0.9996	0.9997	0.9987
ARAS	0.9986	0.9949	0.9985	0.9984	0.9916
	0.9980	0.9978	0.9979	0.9992	0.9970
	0.9991	0.9990	0.9992	0.9999	0.9970

The similarity matrix between all cargo companies is defined as:

$$M = \begin{array}{c} \\ ARAS \\ MNG \\ PTT \\ Surat \\ UPS \\ Yurtici \end{array} \begin{bmatrix} 1 & 0.9989 & 0.9975 & 0.9988 & 0.9990 & 0.9959 \\ 0.9989 & 1 & 0.9974 & 0.9996 & 0.9967 & 0.9915 \\ 0.9975 & 0.9974 & 1 & 0.9980 & 0.9951 & 0.9900 \\ 0.9988 & 0.9996 & 0.9980 & 1 & 0.9967 & 0.9915 \\ 0.9990 & 0.9967 & 0.9951 & 0.9967 & 1 & 0.9982 \\ 0.9959 & 0.9915 & 0.9900 & 0.9915 & 0.9982 & 1 \end{bmatrix}$$

The similarity matrix shows high similarity among cargo companies. A value of 1 in the matrix indicates the user's previous cargo preference. The matrix defines cargo company recommendations based on users' past preferences. For example, the order of recommendation for the customer using Aras Cargo Company is determined as UPS> MNG> Surat> PTT>Yurtiçi. The recommendation ranking table for all cargo companies is shown in Table 4.

While users' past preferences put forward Surat and UPS cargo companies as the most

recommended companies, the least recommended cargo companies are determined as Yurtici and PTT.

Table 4. Recommendation rankings for cargo companies

Rank	Aras (x_1)	MNG (x_2)	PTT (x_3)	Surat (x_4)	UPS (x_5)	Yurtici (x_6)
1	UPS	Surat	Surat	MNG	Aras	UPS
2	MNG	Aras	Aras	Aras	Y.ici	Aras
3	Surat	PTT	MNG	PTT	Surat	Surat
4	PTT	UPS	UPS	UPS	MNG	MNG
5	Y.ici	Y.ici	Y.ici	Y.ici	PTT	PTT

3.1. Sensitivity Analysis

Sensitivity analysis is applied for cargo companies in different scenarios to observe the effects of the weights of the attributes (a1: price, a2: personnel, a3: speed, a4: reliability, a5: network) on the recommendation system (Table 5). Weights are defined as 1/5 to consider attributes equal, and weight values are assigned as 1 to prioritize each attribute weight.

Table 5. Recommendation rankings for cargo companies in different scenarios

Aras (x_1)							MNG (x_2)							PTT (x_3)						
w_{Lagr}	1/5	a1	a2	a3	a4	a5	w_{Lagr}	1/5	a1	a2	a3	a4	a5	w_{Lagr}	1/5	a1	a2	a3	a4	a5
x5	x5	x2	x2	x2	x5	x5	x4	x4	x1	x1	x4	x4	x4	x4	x4	x1	x4	x4	x4	x4
x2	x2	x4	x5	x4	x2	x4	x1	x1	x4	x4	x1	x1	x5	x1	x1	x2	x1	x2	x1	x1
x4	x4	x3	x4	x5	x4	x2	x3	x3	x3	x5	x3	x3	x1	x2	x2	x4	x2	x1	x2	x5
x3	x3	x6	x3	x3	x3	x3	x5	x5	x6	x3	x5	x5	x3	x5	x5	x6	x5	x5	x5	x2
x6	x6	x5	x6	x6	x6	x6	x6	x6	x5	x6	x6	x6	x6	x6	x6	x5	x6	x6	x6	x6
Surat (x_4)							UPS (x_5)							Yurtici (x_6)						
w_{Lagr}	1/5	a1	a2	a3	a4	a5	w_{Lagr}	1/5	a1	a2	a3	a4	a5	w_{Lagr}	1/5	a1	a2	a3	a4	a5
x2	x2	x2	x2	x2	x2	x2	x1	x1	x6	x1	x1	x1	x1	x5	x5	x5	x5	x5	x5	x1
x1	x1	x1	x1	x1	x3	x5	x6	x6	x1	x2	x6	x6	x4	x1	x1	x1	x1	x1	x1	x5
x3	x3	x3	x3	x3	x1	x1	x2	x2	x2	x6	x4	x4	x2	x4	x2	x2	x2	x4	x2	x3
x5	x5	x6	x5	x5	x5	x3	x4	x4	x3	x4	x2	x3	x3	x2	x4	x3	x4	x2	x3	x4
x6	x6	x5	x6	x6	x6	x6	x3	x3	x4	x3	x3	x2	x6	x3	x3	x4	x3	x3	x4	x2

Since the attribute weights are equal to the attribute weights obtained in the study (w_{Lagr}), there is no change in the recommendation order. Only MNG and Surat cargoes have been replaced in the Yurtici cargo recommendation list. UPS and Yurtici cargo companies are mutually recommended companies based on the price priority evaluation. Aras cargo company is recommended for PTT and MNG, and MNG is the first recommended company for Aras and Surat cargo companies. The priority of personnel behavior is similar to the price priority of the first recommendation firm for Aras, MNG, Surat and Yurtici companies, while the following recommendation orders change. According to personnel priority, Surat is the first recommended company for PTT users, while Aras is the first recommended cargo company for UPS. In the speed-weighted evaluation, MNG and Surat cargo companies are determined as the priority recommendation company, while Aras Cargo Company is defined for UPS users and UPS Company for Yurtici users as the first recommendation. According to the reliability priority weighting, while the UPS Company is the first recommended company to Aras company users, the other company's recommendation rankings follow the speed-weighted recommendation ranking. According to the priority weighting of the service network, Aras is recommended for Yurtici cargo company users, while the recommendation rankings for other cargo companies are similar to the reliability recommendation rankings.

Relationships between attributes are compared with Spearman correlation coefficient values according to priority attributes recommendation rankings (Table 6).

Table 6. Relationship matrix between attributes according to recommendation order

Attributes	Price	Personnel	Speed	Reliability	Network
Price	1	0.9884	0.9848	0.9835	0.9771
Personnel	0.9884	1	0.9920	0.9902	0.9812
Speed	0.9848	0.9920	1	0.9959	0.9810
Reliability	0.9835	0.9902	0.9959	1	0.9846
Network	0.9771	0.9812	0.9810	0.9846	1

In general, the high correlation between attributes indicates that users attach importance to all attributes in service evaluation. According to the relationship matrix, speed attribute is highly correlated with reliability (0.9959) and personnel (0.9920) attributes. The weakest relationship is seen between price and network (0.9771).

4. Discussion

The recommendation system makes candidate suggestions by analyzing past customer behavior under multiple attributes. Customers can turn to alternative suppliers that suit their usage habits and preferences with the recommendation system. Recommendation systems are also used to solve decision-making problems based on production and service preferences [3], [4], [6]. The selection of alternative methods and vehicles in the transportation sector is considered as a decision-making problem, and studies commonly address air transportation problems [22]–[24], [28]. Additionally, the literature does not include a recommendation study for urban cargo services. Existing studies in the literature focus on cargo company selection problems and address the problems with decision-making methods.

Atmaca and Turgut's study aims to determine customers' selection criteria among cargo companies operating in Turkey [18]. The survey results based on 17 criteria reveal price, safe delivery of cargo, customer service and the company's corporate image as critical factors in customers' preferences for cargo companies. These factors are compatible with the price, reliability and personnel factors discussed in our study. Deste and Savaşkan's study deals with the selection of cargo companies in e-commerce businesses and emphasizes paying attention to price, experience, number of branches, delivery time, number of personnel, number of complaints, resolved complaint rate and reputation criteria [26]. These criteria are similar to the price, personnel, speed and network criteria mentioned in our study. Five cargo companies in Turkey (without specifying their names) are selected in the application part of the study and a preference ranking is made for the companies according to the VIKOR multi-criteria decision-making method. Boz et al.'s study deals with air cargo company selection under chaos conditions with the integrated bayesian BWM (Best-Worst Method) and WASPAS (Weighted Aggregated Sum Product Assessment) method [25]. Five main criteria (economic, social, logistics, location, quality) and 26 sub-criteria are considered for air cargo company selection, and all of the criteria defined in our study are indirectly similar to these sub-criteria. While speed and reliability were determined as the most important criteria in our study, in this study speed emerges as the most important criterion together with service cost, but the reliability criterion has a medium level of importance as product reliability. Asoğlu and Eren handle cargo company selection studies with Analytic Hierarchy Process (AHP), Technique for Order of Preference by Similarity to Ideal Solution (TOPSIS) and Preference Ranking Organization Method for Enrichment Evaluation (PROMETHEE) decision-making methods [17]. They evaluate ARAS, PTT, METRO, MNG, SURAT, UPS and YURTİCİ cargoes with on-time delivery, personnel approach, customer relations, reliability, solution generation, reasonable pricing and fast operation criteria. AHP analysis determines the most important criteria as appropriate pricing and on-time delivery, while the least important criteria are customer relations and personnel approach. While the on-time delivery criterion, which has the highest importance, overlaps with the speed criterion in our study, the customer relations and personnel approach criteria, which have the lowest importance, overlaps with the personnel criterion in our study. Although YURTICI is ranked first in the alternative cargo company ranking in this study, it appears as the last recommended company in our study. Differences arise from identifiable or latent effects such as the characteristics of the evaluation groups, the number of samples, and experience variability. However, UPS, ARAS and MNG companies, which follow YURTICI in the rankings, are determined as the first three most recommended companies in our study.

5. Conclusion and Suggestions

The change in global trade causes rapid changes in consumer expectations and behaviors. Especially, the corona pandemic period has caused a rapid and inclusive transformation in remote procurement and supply behaviors. This global change reveals the necessity of observing and evaluating user behavior of cargo service companies. This study aims to develop a method that enables users to rank alternative cargo companies based on their evaluations based on their past experiences. In addition, study evaluations allow cargo companies to be compared with each other on the basis of defined attributes.

In this study, Aras, MNG, PTT, Surat, UPS and Yurtici cargo companies are determined as the most preferred cargo companies by users in Turkey. User evaluations of cargo companies according to

price, personnel behavior, speed, reliability and network characteristics are collected with the Google form survey tool. Linguistic assessments collected from 57 participants are converted into PLTS and used in calculations. The attribute weights are calculated using the maximum deviation method and the Lagrangian function. Similarity values between cargo companies are calculated using PLTSs and using the cosine similarity method. A similarity matrix is created between the cargo companies by including the attribute weights in the similarity values calculations. The similarity matrix enables the identification of similarity between cargo companies and the order of priority for recommendation.

The primary recommended cargo companies for Aras, MNG, PTT, Surat, UPS and Yurtici companies are determined based on the similarity matrix as UPS, Surat, Surat, MNG, Aras and UPS, respectively. While Surat and UPS companies stand out in the recommendation list, PTT and Yurtici companies are not included in the primary recommendation. In addition, recommendation rankings are created in six different scenarios to observe the effects of attribute weights on recommendation rankings. Weightings that prioritize attributes change the recommendation order, while equal weighting does not show any significant change. Considering the recommendation rankings based on the scenarios that prioritize the attributes, the relations between the attributes are examined with the Spearman correlation coefficient values. While the results indicate high correlations among all attributes, speed appears to have higher associations with reliability and personnel behavior.

The insufficient number of questionnaires emerges as the most important limitation for this study. Improvement of the study with the increasing number of questionnaires and attributes may be included in the future study plans. In addition, the development of surveys with methods that allow users to make more clear evaluations can reduce the loss of information in the evaluation and calculation process. The method applied in the study can also be extended for different service sectors (such as accommodation, banking, and consultancy).

Contributions of the authors

Author 1 contributed to the study in the sections of definition of the problem, determination of evaluation and solution methods, survey study, evaluation of the data and explanation of the results; Author 2 contributed to the study in defining the problem and developing solution suggestions, evaluating the data obtained from the surveys and interpreting the results.

Conflict of Interest Statement

There is no conflict of interest between the authors.

Statement of Research and Publication Ethics

The study is complied with research and publication ethics

References

[1] A. Gülbaşı, "E-ticaret kullanıcılarına ait e-hizmet kalitesinin müşteri memnuniyeti üzerine etkisi", *Toplum Ekonomi ve Yönetim Dergisi*, vol. 3, no. 1, pp. 22–39, 2022.

[2] C. Cui, M. Wei, L. Che, S. Wu, and E. Wang, "Hotel recommendation algorithms based on online reviews and probabilistic linguistic term sets", *Expert Systems with Applications*, vol. 210, p. 118503, 2022.

[3] H. Hwangbo, Y. S. Kim, and K. J. Cha, "Recommendation system development for fashion retail e-commerce", *Electronic Commerce Research and Applications*, vol. 28, pp. 94–101, 2018.

[4] M. Zihayat, A. Ayanso, X. Zhao, H. Davoudi, and A. An, "A utility-based news recommendation system", *Decision support systems*, vol. 117, pp. 14–27, 2019.

[5] J. Lin, H. Pu, Y. Li, and J. Lian, "Intelligent recommendation system for course selection in smart education", *Procedia Computer Science*, vol. 129, pp. 449–453, 2018.

[6] Z. Abbasi-Moud, H. Vahdat-Nejad, and J. Sadri, "Tourism recommendation system based on semantic clustering and sentiment analysis", *Expert Systems with Applications*, vol. 167, p. 114324, 2021.

[7] Y. Liu, C. Lyu, Z. Liu, and J. Cao, "Exploring a large-scale multi-modal transportation recommendation system", *Transportation Research Part C: Emerging Technologies*, vol. 126, p. 103070, 2021.

[8] Z. Cui et al., "Personalized recommendation system based on collaborative filtering for IoT scenarios", *IEEE Transactions on Services Computing*, vol. 13, no. 4, pp. 685–695, 2020.

[9] P. Nitu, J. Coelho, and P. Madiraju, "Improvising personalized travel recommendation system with recency effects", *Big Data Mining and Analytics*, vol. 4, no. 3, pp. 139–154, 2021.

[10] X. Wang, Z. Xu, Q. Wen, and H. Li, "A multidimensional decision with nested probabilistic linguistic term sets and its application in corporate investment", *Economic Research-Ekonomska Istraživanja*, pp. 1–19, 2021.

[11] G. Duran, "Kargo hizmetlerinin tüketici davranışlarına etkisi üzerine bir uygulama", *Strategic Public Management Journal*, vol. 3, no. 5, pp. 109–123, 2017.

[12] Q. Pang, H. Wang, and Z. Xu, "Probabilistic linguistic term sets in multi-attribute group decision making", *Information Sciences*, vol. 369, pp. 128–143, 2016.

[13] J.-Y. Dong, Y. Chen, and S.-P. Wan, "A cosine similarity based QUALIFLEX approach with hesitant fuzzy linguistic term sets for financial performance evaluation", *Applied Soft Computing*, vol. 69, pp. 316–329, 2018.

[14] Y. Song and G. Li, "A large-scale group decision-making with incomplete multi-granular probabilistic linguistic term sets and its application in sustainable supplier selection", *Journal of the Operational Research Society*, vol. 70, no. 5, pp. 827–841, 2019.

[15] D. Liang, Z. Dai, and M. Wang, "Assessing customer satisfaction of O2O takeaway based on online reviews by integrating fuzzy comprehensive evaluation with AHP and probabilistic linguistic term sets", *Applied Soft Computing*, vol. 98, p. 106847, 2021.

[16] S. Luo, H. Zhang, J. Wang, and L. Li, "Group decision-making approach for evaluating the sustainability of constructed wetlands with probabilistic linguistic preference relations", *Journal of the Operational Research Society*, vol. 70, no. 12, pp. 2039–2055, 2019.

[17] İ. Asoğlu and E. Tamer, "AHP, TOPSIS, PROMETHEE yöntemleri ile bir işletme için kargo şirketi seçimi", *Yalova Sosyal Bilimler Dergisi*, vol. 8, no. 16, pp. 102–122, 2018.

[18] H. E. Atmaca and D. Tuğrul, "Kargo şirketi seçimine yönelik kriterlerin belirlenmesinde Türkiye genelinde bir saha araştırması", *Çukurova Üniversitesi İktisadi ve İdari Bilimler Fakültesi Dergisi*, vol. 19, no. 2, pp. 65–79, 2015.

[19] X. Gou and Z. Xu, "Double hierarchy linguistic term set and its extensions", in *Double Hierarchy Linguistic Term Set and Its Extensions*, Springer, 2021, pp. 1–21.

[20] S.-H. Lee, "Using fuzzy AHP to develop intellectual capital evaluation model for assessing their performance contribution in a university", *Expert systems with applications*, vol. 37, no. 7, pp. 4941–4947, 2010.

[21] B. C. Giri, M. U. Molla, and P. Biswas, "TOPSIS method for MADM based on interval trapezoidal neutrosophic number", *Neutrosophic Sets and Systems*, vol. 22, pp. 151–167, 2018.

[22] S.-H. Yoon and J.-W. Park, "A study of the competitiveness of airline cargo services departing from Korea: Focusing on the main export routes", *Journal of Air Transport Management*, vol. 42, pp. 232–238, 2015, doi: https://doi.org/10.1016/j.jairtraman.2014.11.004.

[23] S.-H. S. Huang and W.-K. K. Hsu, "Evaluating the service requirements of combination air cargo carriers", *Asia Pacific Management Review*, vol. 21, no. 1, pp. 1–8, 2016, doi: https://doi.org/10.1016/j.apmrv.2015.05.001.

[24] Y. Park, J. K. Choi, and A. Zhang, "Evaluating competitiveness of air cargo express services", *Transportation Research Part E: Logistics and Transportation Review*, vol. 45, no. 2, pp. 321–334, 2009, doi: https://doi.org/10.1016/j.tre.2008.09.004.

[25] B. Esra, S. Çizmecioğlu, and A. Çalık, "Kaos durumu altında hava kargo şirketi seçimi: Bütünleşik Bayesian BWM ve WASPAS çerçevesi", *Gazi Üniversitesi Mühendislik Mimarlık Fakültesi Dergisi*, vol. 38, no. 3, pp. 1586–1600, 2023.

[26] M. Deste and A. G. Savaşkan, "E-ticaret işletmelerinin kargo firması seçimi üzerine VIKOR yöntemiyle bir uygulama", *Uluslararası Anadolu Sosyal Bilimler Dergisi*, vol. 5, no. 1, pp. 4–21, 2021.

[27] A. Ulutaş, "SWARA tabanlı CODAS yöntemi ile kargo şirketi seçimi", *MANAS Sosyal Araştırmalar Dergisi*, vol. 9, no. 3, pp. 1640–1647, 2020.

[28] O. Kulak, A. Genç, and M. E. Taner, "A decision making tool considering risk assessment of sub-contracting agents for an air cargo shipment planning problem", *Journal of Air Transport Management*, vol. 69, pp. 123–136, 2018, doi: https://doi.org/10.1016/j.jairtraman.2018.02.005.

Bitlis Eren Üniversitesi Fen Bilimleri Dergisi
BİTLİS EREN UNIVERSITY JOURNAL OF SCIENCE
ISSN: 2147-3129/e-ISSN: 2147-3188
VOLUME: 12 NO: 4 PAGE: 1237-1247 YEAR: 2023
DOI:10.17798/bitlisfen.1375045

Pollen and Capsule Morphological Studies on Verbascum Hybrids (Scrophulariaceae) in Mardin, Turkey and Their Taxonomic Importance

Fatma MUNGAN KILIÇ[1], Murat KILIÇ[1*]

[1]*Department of Crops and Animal Production, Mardin Artuklu University, 47200 Mardin, Artuklu, Turkey*

(ORCID: 0000-0001-6858-3458) (ORCID: 0000-0002-6408-9660)

Keywords: Hybrid, Pollen, Capsule, SEM, *Verbascum*, Turkey.

Abstract

Verbascum (Scrophulariaceae, Lamiales), usually known as "Mullein", is widely distributed in Eurasia and North Africa, but the highest taxa diversity is in Anatolia, the southern Balkans, the Middle East, the Caucasus and northwestern Iran and is represented by approximately 360 species in the World. As hybridization is very dense in the genus *Vesbascum*, the high frequency of morphological variations has been intricated in species delimitation. In this study, pollen and capsule morphology of three hybrid *Verbascum* taxa [*Verbascum* × *calcicola* Hub.-Mor., *V.* × *kotschyoides* Hub.-Mor., and *V.* × *nusaybinense* Hub.- Mor.] were investigated. They are hybrids wild distributed in the province of Mardin in Southeastern Anatolia. Pollen slides were prepared according to the Wodehouse method, pollen and capsule morphologies were examined with microscope. In general terms, aperture types were tricolporate, but also tricolpate aperture types were observed. The shapes of the pollen grains were determined as oblate-spheroidal and subprolate. The sculpture was reticulate in all cases. The seeds not developed. The capsules are pubescent, densely covered by branched hairs, or loosely by glandular hairs, depending on taxa. The results of this study showed that morphological features, such as pollen shape, polar axis (P), equatorial diameter (E), aperture type, exine and intine thickness, colpus, and por measurement, show differences that can be taken into consideration in the systematic discrimination within the taxa. The capsule showed that substantial taxonomic insight can be gained from examining the capsule characteristics of *Verbascum*, particularly at the species level.

1. Introduction

The family Scrophulariaceae, mostly known as "figwort", contains about 62 genera and 1830 species and consists of herbaceous angiosperms and a shrub genus [1, 2]. *Verbascum* (Scrophulariaceae, Lamiales), usually known as "Mullein", is widely distributed in Eurasia and North Africa, but the highest taxa diversity is in Anatolia, the southern Balkans, the Middle East, the Caucasus and northwestern Iran and is represented by approximately 360 species in the world [3-7]. The gene center of this genus is Turkey with 257 species and 132 hybrids divided into 13 artificial groups [8-10]. The genus *Verbascum* is still not fully understood and new species are regularly described, especially in Turkey [11]. The endemism ratio of the genus is very high, with 202 endemic species (80%) [8-10, 12-14]. As hybridization is very dense in the genus *Verbascum*, the high frequency of morphological variations has been intricated in species delimitation [8, 15]. The taxonomy of *Verbascum* has been a source of controversy because there is so much interspecific hybridization. The genus is biennial or perennial, characterized by flowers with thyrsus or inflorescences and yellow flowers [1, 16]. *Verbascum* extracts, decoctions and infusions have long been used in traditional medicine. The leaves have been used as a diuretic, sudorific, expectorant, sedative and the flowers have mucolytic and expectorant

Corresponding author: muratkilic04@gmail.com
Received: 12.10.2023, Accepted: 08.12.2023

properties [17-19]. *Verbascum* is a taxonomically difficult genus and the infrageneric classification is informal and partly artificial. Moreover, identification of taxa also might be problematic because of the difficulties of providing a workable key. For this purpose, studies are being carried out by many scientists in Turkey and around the world regarding the systematics and morphology of *Verbascum* taxa [20].

There are many SEM studies based on the pollen morphology of the some *Verbascum* species taxa [15, 20-28]. SEM study based on pollen morphology of *Verbascum* hybrid taxa is only available on *V.* × *splendidum* by Aktas [29]. The capsule morphology of the genus *Verbascum* is known to have been studied only by Juan et al. [22] and Attar et al. [30]. Although there are studies of pollen morphology in Turkey, there are still deficiencies and unstudied taxa. In addition, studies on capsule morphology are not known in Turkey.

There is no palynologıcal micromorphology and capsule morphology record for *Verbascum* × *calcicola* Hub.-Mor. (*V. andrusii* x *V. laetum*), *V.* × *kotschyoides* Hub.-Mor. (*V. andrusii* x *V. kotschyi*), and *V.* × *nusaybinense* Hub.-Mor. (*V. geminiflorum* x *V. kotschyi*). This study was carried out to understand the relationships between the three hybrid *Verbascum* taxa distributed in Mardin province, to obtain useful comparative information, and to show the fine structure of pollen surfaces and the external morphology of pollen and capsules. Thus, it should be aimed to obtain data that will help the classification of the genus or provide a health evaluation.

2. Material and Method

The specimens belonging to three hybrid *Verbascum* taxa were collected from several localities in Mardin. Voucher samples were stored in the herbarium of the Department of Plants and Animal Production of Kızıltepe Vocational School, Mardin Artuklu University, Turkey. Collection locations, collector's number and the habitat of investigated samples studied for their morphology features are presented in Table 1. The taxonomic description of the plant was prepared according to Davis et al. [9] and Karavelioğulları [10].

For palynological investigations, all the pollen grains for LM and SEM by the standard methods described by Erdtman [31]. Pollen grains for LM examination were prepared following the standard procedure of Wodehouse [32]. They were observed in glycerin-water using a standard Isolab microscope. Thirty pollen grains per specimen were regarded as sufficient for the palynological analysis [32-34]. For SEM, pollen grains were removed by distilled water treatment, the air-dried, pollen grains were directly mounted on stubs using double-sided adhesive tape and it was covered with gold. The photomicrographs were taken with a ZEISS EVO 50 scanning electron microscope. The values of P (polar axis), E (equatorial diameter), Clg (colpus length), Clt (colpus width), Plg (porus length), Plt (porus latitude), Ex (exine thickness), and In (intine thickness) were measured, and the P/E ratio was calculated, Apt (aperture type), and Or (ornamentation) for 30 pollen grains were measured under light microscope. The terminology of the pollen follows that of Punt et al. [35]. The values are presented as minimum, maximum and mean, that is represented in Table 2.

Capsules were examined using an Isolab stereo microscope. In order to determine the average capsule sizes, 30 unripe capsules were measured. The terminology of the capsule follows that of Attar et al. [30].

Table 1. *Verbascum* taxa used for morphology studies and collected localities

Species	Collection areas and habitat	Collector	Collector's number

V. × *calcicola*	Turkey, C8 Mardin: Artuklu, roadside, slopes area, 37°23'06"N 40°39'39"E, 1130 m.	F. Mungan Kılıç M. Kılıç	*M.Kılıç 274* *M.Kılıç 399-2*
	Mardin: Artuklu, Mardin-Diyarbakır road, 26 km north of Mardin, roadside, calcareous slopes, 1039 m.	F. Mungan Kılıç M. Kılıç	*M.Kılıç 344-2*
	Mardin: Kızıltepe, roadside, rocky area, 37°16'14"N 40°38'57"E, 598 m.	F. Mungan Kılıç M. Kılıç	*M.Kılıç 248* *M.Kılıç 319*
	Mardin: Kızıltepe, roadside, rocky area, 37°16'26"N 40°38'41"E, 620 m.	F. Mungan Kılıç M. Kılıç	*M.Kılıç 375*
	Mardin: Mazıdağı, slopes area, 37°29'11"N 40°30'35"E, 990 m.	F. Mungan Kılıç M. Kılıç	*M.Kılıç 280*
	Mardin: Midyat, roadside, slopes area, 37°26'15"N 41°18'07"E, 928 m.	F. Mungan Kılıç M. Kılıç	*M.Kılıç 314-1* *M.Kılıç 403-2*
	Mardin: Midyat, roadside, slopes area, 37°27'54"N 41°04'59"E, 1030 m.	F. Mungan Kılıç M. Kılıç	*M.Kılıç 405-4*
	Mardin: Midyat, roadside, slopes area, 37°26'15"N 41°18'07"E, 928 m.	F. Mungan Kılıç M. Kılıç	*M.Kılıç 404-1*
	Mardin: Savur, roadside, rocky area, 37°31'18"N 40°54'26"E, 1070 m.	F. Mungan Kılıç M. Kılıç	*M.Kılıç 341-2* *M.Kılıç 410-1*
V. × *kotschyoides*	Mardin: Artuklu, roadside, slopes area, 37°17'07"N 40°46'32"E, 742 m.	F. Mungan Kılıç M. Kılıç	*M.Kılıç 332* *M.Kılıç 380-2*
	Mardin: Artuklu, roadside, rocky area, 37°13'22"N 40°58'23"E, 701 m.	F. Mungan Kılıç M. Kılıç	*M.Kılıç 363-1*
	Mardin: Derik, Derik-Mazıdağı road, 10 km after Derik, roadside, rocky slope.	F. Mungan Kılıç M. Kılıç	*M.Kılıç 279*
	Mardin: Kızıltepe, roadside, slopes area, 37°16'49"N 40°32'36"E, 721 m.	F. Mungan Kılıç M. Kılıç	*M.Kılıç 325*
	Mardin: Mazıdağı, Mardin-Diyarbakır road, 24 km from Çınar, roadside, calcareous slopes, 929 m.	F. Mungan Kılıç M. Kılıç	*M.Kılıç 345-2*
	Mardin: Midyat, roadside, slopes area, 37°27'54"N 41°04'59"E, 1030 m.	F. Mungan Kılıç M. Kılıç	*M.Kılıç 405-3*
	Mardin: Nusaybin, roadside, rocky area, 37°12'00"N 41°01'01"E, 756 m.	F. Mungan Kılıç M. Kılıç	*M.Kılıç 302*
	Mardin: Savur, roadside, 37°27'12"N 40°51'38"E, 940 m.	F. Mungan Kılıç M. Kılıç	*M.Kılıç 333-2*
	Mardin: Savur, roadside, rocky area, 37°32'47"N 40°53'35"E, 833 m.	F. Mungan Kılıç M. Kılıç	*M.Kılıç 339*
	Mardin: Savur, roadside, rocky area, 37°28'28"N 41°01'49"E, 1094 m.	F. Mungan Kılıç M. Kılıç	*M.Kılıç 343-2*

	Mardin: Yeşilli, roadside central median, 37°22'17"N 40°51'38"E, 1158 m.	F. Mungan Kılıç M. Kılıç	*M.Kılıç 307-1* *M.Kılıç 401-3*
V. × *nusaybinense*	Mardin: Artuklu, roadside, rocky area, 37°20'44"N 40°43'44"E, 834 m.	F. Mungan Kılıç M. Kılıç	*M.Kılıç 371-1* *M.Kılıç 388*
	Mardin: Nusaybin, roadside, creek edge, 37°08'11"N 41°04'44"E, 536 m.	F. Mungan Kılıç M. Kılıç	*M.Kılıç 300-3* *M.Kılıç 377-1*

3. Results and Discussion

In this study, various features of pollen and capsule structure of three hybrid *Verbascum* taxa were stated. The characteristics of pollen grains are summarized in Table 2 and shown in Figure 1. The morphological characters of the capsule grains, including their size, shape, and color are summarized in Table 3 and shown in Figure 2.

3.1. Pollen morphology

3.1.1. Size, symmetry and shape

The pollen grains of *Verbascum* are isopolar and radially symmetric. The pollens of the taxa are oblate-spheroidal and subspheroidal with the polar axis 10.11-16.52 μm and the equatorial diameter 5.24-16.48 μm. Their dimensions are smaller in *V.* × *nusaybinense* and larger in *V.* × *kotschyoides* (Table 2, Figure 1).

3.1.2. Apertures

The pollen grains of *Verbascum* are tricolporate (in *V.* × *calcicola* 13%, *V.* × *kotschyoides* 29%, and *V.* × *nusaybinense* 52% tricolpate). The colpus is length (7.49-12.64 μm) and width (2.21-4.94 μm), margins distinct, regular and ends acute. The porus is 2.77-5.38 μm in length and 2.30-5.02 μm in width. (Table 2, Figure 1).

3.1.3. Exine, intine and ornamentation

The exine thickness ranges from 0.54 to 1.50 μm. The intine thickness is 0.28-0.79 μm thin (Table 2). Exine sculpturing is reticulate in all investigated species (Table 2, Figure 1).

Table 2. Pollen morphological characters in taxa of *Verbascum* (μm)

Species	P min (mean) max	E min (mean) max	P/E ratio	Shape	Clg min (mean) max	Clt min (mean) max	Plg min (mean) max	Plt min (mean) max	Ex min (mean) max	In min (mean) max	Apt	Or
V. x *calcicola*	12.34 (14.06) 16.52	6.00 (8.85) 11.38	1.59	Subprolate	8.41 (10.78) 12.51	2.22 (3.17) 4.35	3.13 (3.93) 5.14	2.30 (3.11) 4.23	0.64 (0.84) 1.06	0.30 (0.46) 0.68	87% Tricolporate 13% Tricolpate	Reticulate
V. x *kotschyoides*	11.92 (13.69) 14.94	12.66 (14.67) 16.48	0.93	Oblate-spheroidal	9.42 (10.92) 12.64	2.80 (3.59) 4.94	3.70 (4.52) 5.38	2.80 (3.89) 5.02	0.75 (1.09) 1.50	0.40 (0.59) 0.79	71% Tricolporate 29% Tricolpate	Reticulate
V. x *nusaybinense*	10.11 (11.48) 13.61	5.24 (7.24) 8.69	1.59	Subprolate	7.49 (9.39) 11.85	2.21 (2.66) 3.68	2.77 (3.43) 4.32	2.58 (3.01) 3.68	0.54 (0.69) 0.87	0.28 (0.40) 0.56	48% Tricolporate 52% Tricolpate	Reticulate

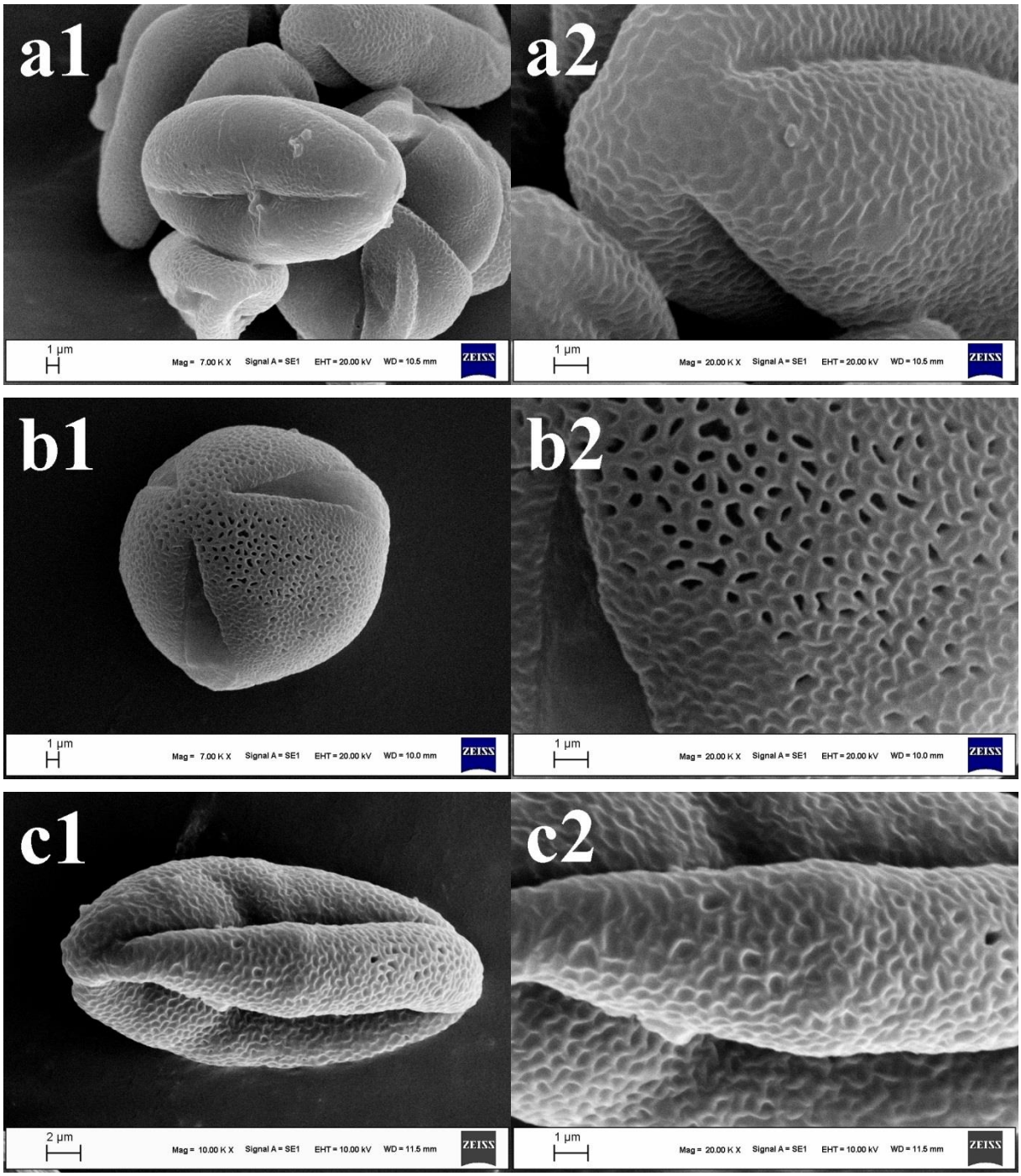

Figure 1. Scanning electron micrographs of pollen in taxa *Verbascum*. 1- General view, 2- Exine sculpturing. (a1-a2) *V.* x *calcicola* (*M.Kılıç 248*), (b1-b2) *V.* x *kotschyoides* (*M.Kılıç 325*), (c1-c2) *V.* x *nusaybinense* (*M.Kılıç 300-3*)

3.2. Capsule morphology

3.2.1. Capsule size

According to the measurements made, the dimensions vary between species from 1.86 to 3.61 mm in length and 1.47 to 3.26 mm in width. Their dimensions are

smaller in *V.* x *calcicola* and larger in *V.* x *nusaybinense* (Table 3, Figure 2).

3.2.2. Capsule shape

Oblong and ovate are the shapes of capsules observed among the studied taxa (Table 3, Figure 2).

3.2.3. Capsule colour

In this study there are three different capsule colour observed as light brown, brown, and dark brown (Table 3, Figure 2).

3.2.3. Apex of the capsules

The capsules have acute beak in *V.* x *kotschyoides*, acute beak to obtuse beak in *V.* x *calcicola* or truncated beak in *V.* x *nusaybinense* (Table 3, Figure 2).

Table 3. Capsule morphological characters in taxa of *Verbascum*

Species (Collecter number)	Length (mm) min (mean) max	Width (mm) min (mean) max	Colour	Shape	Hair
V. x *calcicola* (*M.Kılıç 375*)	1.86 (2.69) 3.61	1.78 (2.03) 2.34	Light brown	Ovate, oblong, often with acute beaks, and some with obtuse beaks	Densely stellata, branched, glandular
V. x *kotschyoides* (*M.Kılıç 332*)	2.10 (2.85) 3.38	1.47 (2.38) 3.26	Brown	Ovate, acute long beaks	Densely stellata, branched, sparsely glandular
V. x *nusaybinense* (*M.Kılıç 377-1*)	2.35 (2.95) 3.45	1.95 (2.22) 2.72	Brown-dark brown	Oblong, ovate, often with short obtuse beaks, and some with truncate beaks	Densely stellata, branched, sparsely glandular

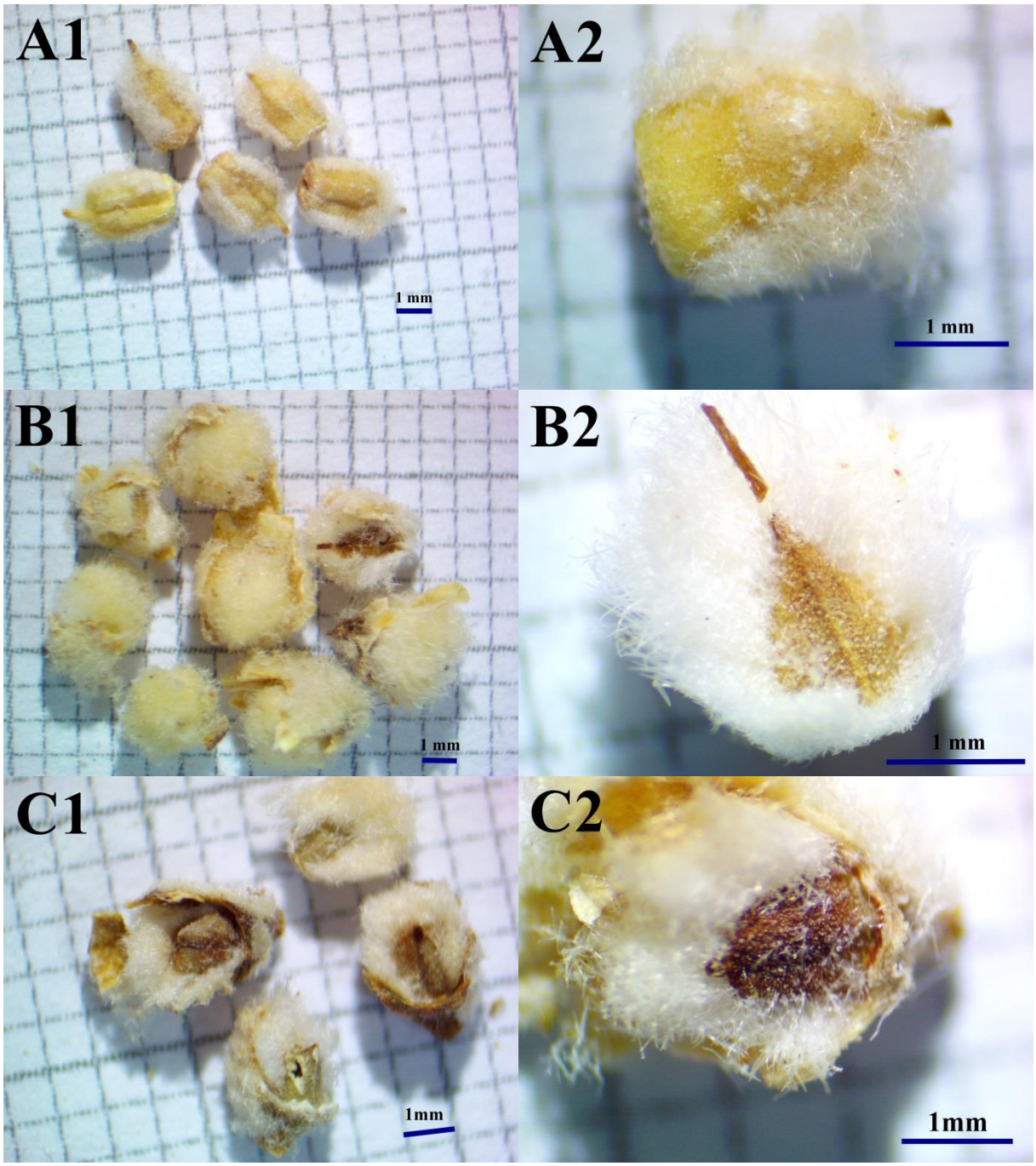

Figure 2. Stereo microscopy photographs of capsule in taxa *Verbascum*. 1- General view, 2- Close view. (A1-A2) *V.* x *calcicola*, (B1-B2) *V.* x *kotschyoides*, (C1-C2) *V.* x *nusaybinense*

4. Conclusion and Suggestions

Analyzes of pollen grains and capsules of the three hybrid *Verbascum* taxa studied for the first time in this study make them comparable to some of the other *Verbascum* members investigated.

The pollen of three hybrid *Verbascum* taxa isopolar and radially symmetric, oblate-spheroidal, subprolate, tricolporate (there is tricolpate), the exine exhibits a tectate structure and reticulate ornamentation. Baser [28], in his study on *Verbascum* (8 species), established the pollen grains as tricolporate and tricolpate. Aktas et al. [27] determined the pollen grain as tricolpate in their study on the endemic *Verbascum* species. Aktas [29] noted the pollen grain as tricolpate in his study on *Verbascum* x *splendidum* taxa. Özturk et al. [20] reported that there were tricolporate and tricolpate aperture types in their pollen study on *Verbascum*. Al-Hadeethy et al. [26] stated that the aperture types of

Verbascum species (20 species) were tricolporate. Çakir and Bagci [36] determined the tricolpate aperture types of *Verbascum* species in their study. Aperture type of *Verbascum* reported to have tricolporate aperture type [25, 37].

In the pollen of three investigated species determined oblate-spheroidal and subprolate shape. However, Aktas et al. [27] recorded the prolate pollen shape in the endemic *Verbascum* species examined. Aktas [29] stated that the pollen shape of the *V.* x *splendidum* he researched has subprolate. Nevertheless, Baser [28] recorded the prolate pollen shape in the *Verbascum* (8 species) taxa in the studied. Öztürk et al. [20] stated that pollen shapes were prolate-spheroidal and oblate-spheroidal in the taxa studied. Asmat et al. [25] determined that the pollen grains of *V. thapsus* was oblate-spheroidal. Kheiri et al. [37] determined that the pollen of *V. mucronatum* species was prolate-spheroidal. In addition, Al-Hadeethy et al. [26] observed the presence of prolate-spheroidal and oblate-spheroidal pollen in *Verbascum* (20 species). Morphological pollen traits observed through LM proved not very important in their taxonomic use, but sculpting examined by SEM was found to be more significant in the classification of taxa [28, 38].

Since exine thickness did not make a significant difference between the studied taxa, this character was ignored for taxonomic discrimination [26]. The results obtained from this study are compatible with studies on *Verbascum* [20, 25-28]. However, all taxa included in our study showed a reticulate exine sculptural pattern.

Capsules of the three hybrid *Verbascum* taxa are densely covered with stellate, branched, and more or less glandular hairs. In some *Verbascum* species distributed in Spain [22] and Iran [30], the capsules have a similar hair indumentum. Based on the available findings, one of the reliable features for classification in *Verbascum* is the indumentum of the capsule.

The results of this study predicted that it is the first study on capsule and pollen characteristics of three hybrid *Verbascum* taxa and will form a comprehensive taxonomic awareness, especially at the species level. The results of this study showed that morphological features, such as pollen shape, polar axis, equatorial diameter, aperture type, exine and intine thickness, colpus, and porus measurement, show differences that can be taken into consideration in the systematic discrimination within the taxa. The capsule showed that substantial taxonomic insight can be gained from examining the capsule characteristics of *Verbascum*, particularly at the species level. Based on the available findings, one of the reliable characteristics for grouping in *Verbascum* is the indumentum and shape of the capsule.

Acknowledgment

We wish to thank Scientific Investigation Project to Coordinate of Mardin Artuklu University (Project No. MAÜ.BAP.22.KMY.011) for financial support.

Contributions of the authors

MK and FMK planned the study. MK carried out fieldwork. All authors analyzed the data and provided comments on the study. MK wrote the manuscript. All authors read and approved the final manuscript.

Conflict of Interest Statement

The authors declare that they have no conflict of interest.

Statement of Research and Publication Ethics

The study is complied with research and publication ethics.

References

[1] E. Fischer. "Scrophulariaceae. In: J. W. Kadereit (ed), Flowering Plants Dicotyledons," *The Families and Genera of Vascular Plants*, *Paris*, vol.7 pp. 333-432, 2004.

[2] M. J. Christenhusz & J. W. Byng. "The number of known plants species in the world and its annual increase." Phytotaxa, vol.261 no.3, pp. 201–217, 2016.

[3] S. Murbeck. "Weitere Studien über die Gattungen Verbascum und Celsia," Acta Univ. Lund. vol. 2 no. 35, pp. 1-70, 1939.

[4] D. J. Mabberley. "Mabberley's plant book: a portable dictionary of plants, their classifications and uses," *Cambridge Univ. Press.*, 2008.

[5] M. I. Georgiev, K. Ali, K. Alipieva, R. Verpoorte & Y. H. Choi. "Metabolic differentiations and classification of *Verbascum* species by NMR-based metabolomics." *Phytochemistry*, vol.72 no.16, pp.2045–51, 2011.

[6] M. Riahi & F. Ghahremaninejad. "The tribe Scrophularieae (Scrophulariaceae): A Review of Phylogenetic Studies." *Hacquetia*, vol.18 no. 2, 2019.

[7] M. Hassler. "Synonymic Checklists of the Vascular Plants of the World. In: O. Bánki, Y. Roskov, L. Vandepitte, R. E. DeWalt, D. Remsen, P. Schalk, T. Orrell, M. Keping, J. Miller, R. Aalbu, R. Adlard, E. Adriaenssens, C. Aedo, E. Aescht, N. Akkari, M. A. Alonso-Zarazaga, B. Alvarez, F. Alvarez & Anderson, G. (eds), *Catalogue of Life Checklist* (Version 2021-08-06), 2021.

[8] A. Huber-Morath. "*Verbascum* L. In: P. H. Davis (ed.)," *Flora of Turkey and the East Aegean Islands*, *Edinburgh Univ. Press*, vol. 6 pp. 461-603, 1978.

[9] P. H. Davis, R. R. Mill and K. Tan. "Flora of Turkey and the East Aegean Islands (Suppl. 1)", *Edinburgh Univ. Press*, vol. 10. pp. 191-193, 1988.

[10] F. A. Karavelioğulları. "*Verbascum* L. In: A. Güner (ed.), Türkiye Bitkileri Listesi (Damarlı Bitkiler)," *Nezahat Gökyiğit Botanik Bahçesi ve Flora Araştırmaları Derneği Yayını, İstanbul,* pp. 850–870, 2012.

[11] F. Ghahremaninejad, M. Riahi, M. Babaei, F. Attar, L. Behcet & A. Sonboli. "Monophyly of *Verbascum* (Scrophularieae: Scrophulariaceae): evidence from nuclear and plastid phylogenetic analyses." *Australian Journal of Botany*, vol.62 no.8, pp. 638–46, 2015.

[12] T. Ekim. *Verbascum* L. In: Güner, A. (ed.), Flora of Turkey and the East Aegean Islands (Suppl. 2), Edinburgh Univ. Press. vol. 11, p. 193, 2000.

[13] F. A. Karavelioğulları. "A new record *Verbascum szovitsianum* Boiss. var. *szovitsianum* (Scrophulariaceae) from Turkey." *Biodicon.*, vol. 2, pp. 68–70, 2009.

[14] M. Firat. "*Verbascum zerdust* (Scrophulariaceae), a new species from Bitlis province (Turkey) belonging to section *Bothrosperma*." *Nordic Journal of Botany*, doi: 10.1111/njb.03649, 2022.

[15] F. A. Karaveliogullari, E. Yüce & B. Başer. "*Verbascum duzgunbabadagensis* (Scrophulariaceae), a new species from eastern Anatolia, Turkey." *Phytotaxa*, vol.181, pp. 47-53, 2014.

[16] B. Oxelman, P. Kornhall, R. G. Olmstead & B. Bremer. "Further disintegration of Scrophulariaceae." *Taxon*, vol. 54 no. 2, pp.411–25, 2005.

[17] J. B. Lust and M. Tierra. "The Natural Remedy Bible," *Simon and Schuster*, 2003.

[18] S. Vogl, P. Picker, J. Mihaly-Bison, N. Fakhrudin, A. G. Atanasov, E. H. Heiss, C. Wawrosch, G. Reznicek, V. M. Dirsch & J. Saukel. "Ethnopharmacological in vitro studies on Austria's folk medicine

- an unexplored lore in vitro anti-inflammatory activities of 71 Austrian traditional herbal drugs." *Journal of Ethnopharmacology*, vol.149 no.3, pp.750–71, 2004.

[19] V. Kaur & K. Upadhyaya. "Antibacterial activity of *Verbascum chinense* (Scrophulariaceae) extracts." *International Journal of Current Microbiology and Applied Sciences*, vol.5 no.4, pp. 578–84, 2016.

[20] A. Öztürk, K. B. Güney, B. Bani, K. Güney, F. A. Karaveliogullari, N. M. Pinar & T. Çeter. "Pollen morphology of some *Verbascum* (Scrophulariaceae) taxa in Turkey." *Phytotaxa*, vol.333 no.2, pp.209-218, 2018. https://doi.org/10.11646/phytotaxa.333.2.4

[21] J. P. Minkin & W. Hardy-Eshbaugh. "Pollen morphology of the Orobanchaceae and Rhinanthoid Scrophulariaceae." *Grana*, vol.28, pp. 1-18, 1989. https://doi.org/10.1080/00173138909431007

[22] R. Juan, I. Fernandez & J. Pastor. "Systematic consideration of microcharacters of fruits and seeds in the genus *Verbascum* (Scrophulariaceae)." *Annals of Botany*, vol.80, pp. 591-598, 1997. https://doi.org/10.1006/anbo.1997.0472

[23] F. Dane and G. Yılmaz. "Palynological study on some *Verbascum* L. species. The third international conference ″Falz Fein Reading", p. 151, 25-27 April 2002. Training University, Kherson, Ukraine.

[24] S. Kheyri. "Identification of breeding system of some species of *Verbascum* (Scrophulariaceae) in north-west of Iran on the basis of the ratio of pollen to ovule number." *Biological Journal of Islamic Azad University, Garmsar Branch*, vol.4, pp. 67-74, 2009.

[25] T. Asmat, M. A. Khan, M. Ahmed, M. Zafar, F. Manzoor, M. Munir, K. Akhtar, S. Bashir, T. Mukhtar, M. Ambreen & S. N. Abbasi. "Pollen morphology of selected species of Scrophulariaceae of District Dir Upper, Pakistan." *Journal of Medicinal Plants Research*, vol.5, pp. 6423-6428, 2011. https://doi.org/10.5897/JMPR11.723

[26] M. Al-Hadeethy, A. Al-Mashhadani, T. Al-Khesraji, S. Barusrux, H. Al-Jewari, P. Theerakulpisut & P. Pornpongrungrueng. "Pollen morphology of *Verbascum* L. (Scrophulariaceae) in Northern and Central Iraq." *Bangladesh Journal of Plant Taxonomy*, vol. 21, pp. 159-165, 2014. https://doi.org/10.3329/bjpt.v21i2.21355

[27] K. Aktas, C. Özdemir & B. Özdemir. "Morphology, Anatomy, Palynology and Seed Micromorphology of Turkish Endemic *Verbascum exuberans* Hub.-Mor. (Scrophulariaceae)." *Planta Daninha*, v38:e020191125, 2020.

[28] B. Baser. "Pollen and Seed Morphology of *Verbascum* Species (Group D) (*Scrophulariaceae*) in Turkey." *Fresenius Environmental Bulletin*, vol.30 no.7, pp. 8978-8987, 2021.

[29] K. Aktas. "Morphology, Anatomy, Palynology and Seed Micromorphology of Turkish Endemic *Verbascum* x *splendidum* Boiss. (Scrophulariaceae)." *Fresenius Environmental Bulletin*, vol.28 no.12, pp. 10004-10010, 2019.

[30] F. Attar, A. Keshvari, A. Ghahreman, S. Zarre & F. Aghabeigi. "Micromorphological studies on *Verbascum* (Scrophulariaceae) in Iran with emphasis on seed surface, capsule ornamentation and trichomes." *Flora*, vol. 202, pp. 169-175, 2007. https://doi.org/10.1016/j.flora.2006.04.001

[31] G. Erdtman. "Pollen Morphology and Plant Taxonomy: Angiosperms." *Chronica Botanica Co., Massachusettes, USA*, pp. 1-553, 1952.

[32] R. P. Wodehouse. "Pollen Grains, their structure, identification and significance in sci-ence and medicine." *Hafner Publishing Company, New York*, 1935.

[33] E. Cabi, B. Baser, A. Yavru, F. Polat, U. Toprak & F. A. Karaveliogulları. "Scanning electron microscope (SEM) and Light microscope (LM) studies on the seed morphology of *Verbascum* taxa

(Scrophulariaceae) and their systematic implications." *Australian Journal of Crop Science*, vol.5, pp. 660-667, 2011.

[34] S. Kheiri, M. Khayami & A. Mahmoudzadeh. "Micromorphological and anatomical studies of certain species of *Verbascum* (Scrophulariaceae) in West Azerbaijan, Iran." *Iran Journal of Botany*., vol.15, pp. 105-13, 2009.

[35] W. Punt, P. P. Hoen, S. Blackmore, S. Nilsson & A. Le-Thomas. "Glossary of pollen and spore terminology." *Review of Palaeobotany and Palynology*, vol.143, pp. 1-81, 2007.

[36] T. Çakir & E. Bagci. "A taxonomical study on the *Verbascum euphraticum* Bentham and *Verbascum melitenense* Boiss (Scrophulariaceae)." *Fırat University Journal of Engineering Science*, vol.18 no.4, pp. 445-58, 2006.

[37] S. Kheiri, M. Khayami, S. K. Osaloo & A. Mahmoodzadeh. "Pollen morphology of some species of *Verbascum* L. (Scrophulari-aceae) in Urmia." *Pakistan Journal of Biological Sciences*, vol.9, pp. 434-436, 2006.

[38] S. Pehlivan, B. Baser B & F. A. Karaveliogullari. "Pollen morphology of the genus *Verbascum* L. (Group A) in Turkey." *Biodicon*., vol.1, pp. 1-24, 2008.

Bitlis Eren Üniversitesi Fen Bilimleri Dergisi
BİTLİS EREN UNIVERSITY JOURNAL OF SCIENCE
ISSN: 2147-3129/e-ISSN: 2147-3188
VOLUME: 12 NO: 4 PAGE: 1248-1260 YEAR: 2023
DOI:10.17798/bitlisfen.1376430

Evaluation of November 23, 2022, Duzce Earthquake data with Ground Motion Prediction Equations

Ömer Faruk NEMUTLU[1*], Bilal BALUN[2]

[1]*Department of Civil Engineering, Bingöl University*
[2]*Department of Architecture, Bingöl University*
(ORCID: 0000-0001-7841-3911) (ORCID: 0000-0003-0906-4484)

Keywords: GMPE, Gölyaka, Earthquake, Past-Earthquake Assessment, Attenuation Relationship.

Abstract

An earthquake with a magnitude of 5.9 Mw occurred in Düzce (Gölyaka) on November 23, 2022. A rupture occurred on the Karadere Segment, a section of the North Anatolian Fault zone. According to the investigations, an 8 km section that was not broken in the 1999 Gölcük Earthquake was broken by this earthquake and caused the earthquake. Station number 8105, one of the stations of the Disaster and Emergency Presidency, measured the maximum ground acceleration of the earthquake as 0.6 g. This value is above the peak ground acceleration (PGA) value taken from the hazard map of the region. This earthquake in the Marmara region attracts the attention of researchers both because it is close to the 1999 Gölcük Earthquake and because there is an earthquake expectation in Istanbul and its surroundings. Researchers create ground motion prediction equations to predict the effects of future earthquakes. This study, it is aimed to compare 5 ground motion equations developed for Türkiye. PGA data were collected and compared with the 5 ground motion prediction equation (GMPE, or attenuation relationship) employed from the stations taking measurements from the earthquake, and the compatibility of the earthquake with the 5 existing models was investigated. As a result of the study, it was determined that the GMPEs prepared using the data in the region where the earthquake occurred showed a higher fit among these GMPEs. In addition, it has been observed that low PGA values at stations farther from the epicenter of the earthquake fit better with the curves obtained from the GMPEs. The number of data sets in GMPEs and the study area increase the possibility of estimating earthquake parameters. The data set for AR4 GMPE used in the study and the fact that the region taken into consideration is the region where the earthquake occurred increased the data-model compatibility. It was concluded that existing GMPEs should be updated to predict future earthquakes and their effects better.

1. Introduction

Northwest Marmara is one of the first regions that come to mind when earthquakes are mentioned in Türkiye. Two major earthquakes that occurred in 1999 changed Türkiye's perspective on earthquakes [1]. On November 23, 2022, at 04.08 local time, an earthquake with a 5.9 Mw occurred in Düzce Gölyaka epicenter. According to Disaster and Emergency Management Presidency (DEMA) data, the depth of the earthquake was announced to be 6.8 km below the ground. The visual showing the epicenter of the earthquake is demonstrated in Figure 1 [2, 3].
Magnitude and depth information of different centers collecting earthquake-related information are presented in the table below (Table 1).

* Corresponding author: ofnemutlu@bingol.edu.tr
Received: 15.10.2023, Accepted: 13.12.2023

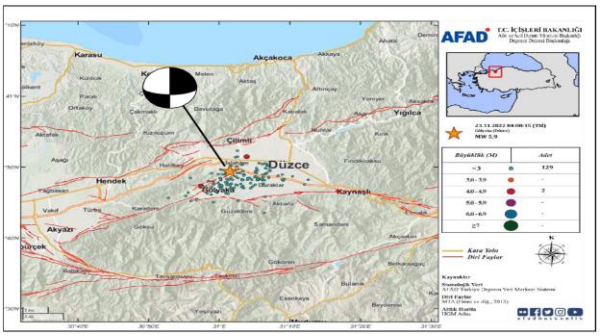

Figure 1. The epicenter of 5.9 M_w Gölyaka Earthquake [2, 3]

Table 1. Information for different centre [4].

Centre	Latitude	Longitude	Depth	Magnitude (M_w)
DEMA	40.823	31.025	6.81	5.9
KOERI	40.817	30.987	10.6	6.0
EMSC	40.820	30.990	11.0	6.1
USGS	40.836	30.983	10.0	6.1

DEMA: Disaster and Emergency Management Affairs

KOERI: Kandilli Observation Earthquake Research Institute

EMSC: European-Mediterranean Seismological Centre

USGS: United States Geological Survey

The earthquake occurred in the Karadere Segment [5], located on the North Anatolian Fault line, at the northeastern end of this segment. When the data obtained from the stations in the region were evaluated, the highest acceleration values were measured at station no. 8105. The acceleration measured by this station in the East-West direction is 0.60 g. The station is located in the center of Düzce. Turkey Earthquake Hazard Map [2 ,3] illustrates that the earthquake hazard of the region is clearly high. The map showing the earthquake hazard of the region is demonstrated in Figure 2. The PGA value from the Turkey Earthquake Hazard Map for the earthquake ground motion level at the point where the earthquake occurred is 0.593 g.

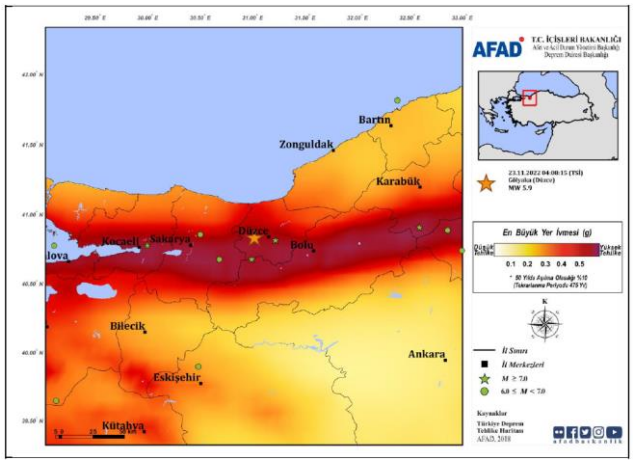

Figure 2. Seismicity of the study area [2, 3]

Post-earthquake studies are generally focused on evaluating earthquake-induced structural damage, examining earthquake records, evaluating ground properties, and comparing ground motion prediction equations [6-15]. In the literature, there is a study on the evaluation of ground motion prediction equations of the results of the 24 January 2020 Elazığ earthquake by Bayrak et al. [16]. In this study,

microtremor measurements were taken in the field after the earthquake. With these measurements, shear wave velocity and damage index parameters were obtained by empirical relations. Ground motion prediction equations and earthquake acceleration values were scrutinized and the most compatible model was determined. Özalp et al. [17] conducted evaluations about the source fault. It was stated that no surface fracture was observed in the study, and structural damage occurred in buildings located in areas suitable for ground enlargement around the Karadere segment. It was stated that the earthquake occurred when an 8 km section, which was not broken during the 1999 Izmit earthquake broke. There are also reports containing field observations and evaluations regarding this earthquake [2-4]. Equations in the literature as GMPEs are utilized to estimate the earthquake parameters that earthquakes will create according to a certain magnitude and distance, starting from the epicenter of the earthquake [18]. These GMPEs vary depending on the fault where the earthquake occurred, the soil conditions of the region, and the measured magnitude of the earthquake. For this reason, GMPEs are equations that reflect a specific region. Obtaining local GMPEs is important to accurately reflect the study area. Additionally, new regional PGA attenuation equations for vertical ground motion and accompanying seismic micro-zoning maps for this purpose were developed by Bulajic [19]. Both seismicity and earthquake scenarios studies were performed for the region where the study was carried out [20, 21].

In this study, the GMPEs prepared by the researchers for Türkiye in general or a specific region were employed. The greatest ground acceleration values at the stations recorded in the Düzce (Gölyaka) earthquake, which were taken into account in the study, were investigated together with the GMPEs. The compatibility of these ground acceleration values with 5 different ground motion prediction equations was evaluated. The results are explained with their justifications.

The main purpose of this study is to obtain the shortcomings and differences of the currently used ground motion prediction equations by evaluating the post-earthquake measurement data together with the ground motion prediction equations. This study examines the behavior of different ground motion prediction equations on actual earthquake data.

2. Estimation of Ground Motions

Within the scope of the study, stations taking measurements for the Gölyaka-Düzce earthquake were evaluated. The figure below shows the distribution of stations taking measurements after the earthquake (Figure 3). When the records taken from these stations are evaluated, there is no information about ground properties at some stations. For this reason, stations with existing ground information were selected and taken into account in the study. Records were taken from a total of 68 stations with available ground information. Information about the records is shown in Table 2 below. Table 2 includes the station code, latitude, longitude, acceleration values measured in 3 directions, Rjb distance, shear wave velocities and soil classification according to the soil classification presented in the Turkish Building Earthquake Code [22].

Table 2. Information about the records.

NO	Code	Longitude	Latitude	PGA_NS (g)	PGA_EW (g)	PGA_UD (g)	R_{jb} (km)	V_{s30} m/s	Site Class.	Site Class.-2
1	8109	31.0144	40.7810	0.27	0.36	0.24	5.94	183	C	Soft Soil
2	8106	31.1124	40.7671	0.35	0.38	0.23	12.87	338	C	Soft Soil
3	8101	31.1489	40.8436	0.30	0.31	0.26	14.01	282	C	Soft Soil
4	8102	31.1644	40.8342	0.22	0.42	0.25	14.98	280	C	Soft Soil
5	8104	31.1804	40.8611	0.36	0.37	0.23	17.17	395	B	Soil
6	8105	31.1520	40.9028	0.59	0.60	0.22	17.45	914	A	Rock
7	8108	31.2300	40.8613	0.11	0.12	0.07	21.10	487	B	Soil
8	1407	31.0028	40.5818	0.14	0.10	0.07	29.35	273	C	Soft Soil
9	8110	31.1428	41.0900	0.11	0.16	0.07	34.29	407	B	Soil

10	5406	30.6225	40.6703	0.074	0.073	0.03	41.45	272	UNKNOWN	Soft Soil
11	1403	30.7898	40.3984	0.05	0.07	0.02	54.33	472	B	Soil
12	1411	31.6175	40.6846	0.10	0.14	0.05	55.78	229	C	Soft Soil
13	5401	30.3801	40.7371	0.011	0.012	0.01	58.50	412	UNKNOWN	Soil
14	5403	30.2700	40.6908	0.02	0.03	0.01	68.56	215	C	Soft Soil
15	5404	30.2932	40.5191	0.08	0.06	0.04	73.91	381	B	Soil
16	4129	30.1122	40.7175	0.026	0.032	0.01	81.14	203	C	Soft Soil
17	4110	30.1525	41.0691	0.0073	0.0071	0.00	81.75	308	UNKNOWN	Soft Soil
18	4120	30.0274	40.7676	0.00014	0.00011	0.00	87.67	214	C	Soft Soil
19	4103	30.0250	40.7858	0.0129	0.0101	0.00	87.75	1013	A	Rock
20	4122	30.0263	40.7483	0.0166	0.0141	0.01	87.93	303	C	Soft Soil
21	1410	32.0370	40.7711	0.0125	0.0129	0.01	88.93	338	C	Soft Soil
22	4117	30.0267	40.6699	0.0152	0.0132	0.01	89.13	282	C	Soft Soil
23	1409	32.0638	40.7174	0.0279	0.0276	0.02	91.83	362	B	Soil
24	1405	32.0760	40.9381	0.0123	0.0148	0.01	92.67	365	B	Soil
25	4104	29.9700	40.6804	0.0047	0.0046	0.00	93.62	770	B	Rock
26	4105	29.9694	40.6744	0.0278	0.0165	0.02	93.79	289	C	Soft Soil
27	4125	29.9172	40.7665	0.0063	0.0062	0.00	96.93	826	A	Rock
28	4126	29.9149	40.7625	0.0176	0.0150	0.01	97.16	188	C	Soft Soil
29	4127	29.9047	40.7609	0.0107	0.0109	0.01	98.02	215	C	Soft Soil
30	1402	32.2059	40.7925	0.0100	0.0098	0.00	102.98	445	B	Soil
31	4112	29.8400	40.7245	0.0158	0.0145	0.01	103.81	352	UNKNOWN	Soft Soil
32	0601	31.9170	40.1608	0.0150	0.0141	0.01	108.41	340	C	Soft Soil
33	1101	29.9774	40.1411	0.0043	0.0047	0.00	120.19	901	A	Rock
34	4111	29.5888	40.6844	0.0110	0.0116	0.01	125.36	300	UNKNOWN	Soft Soil
35	2602	30.4973	39.7893	0.0108	0.0070	0.01	126.39	328	C	Soft Soil
36	3410	29.6082	41.1719	0.0077	0.0095	0.01	128.62	587	B	Soil
37	7802	32.5322	40.9563	0.0089	0.0073	0.01	130.97	393	B	Soil
38	7712	29.5088	40.6929	0.0063	0.0074	0.00	131.94	280	C	Soft Soil
39	2606	30.4558	39.7487	0.00003	0.00002	0.00	131.92	348	C	Soft Soil
40	2607	30.1460	39.8175	0.0050	0.0064	0.00	137.74	265	C	Soft Soil
41	4130	29.3879	40.7545	0.0064	0.0082	0.00	141.51	484	B	Soil
42	7801	32.6237	41.2046	0.0095	0.0053	0.01	144.07	530	UNKNOWN	Soil
43	7711	29.3271	40.6594	0.0121	0.0098	0.01	147.60	199	C	Soft Soil
44	2608	31.1830	39.5197	0.0030	0.0021	0.00	147.44	480	B	Soil
45	3418	29.2755	40.8146	0.0036	0.0043	0.00	150.74	1182	A	Rock
46	7709	29.3060	40.5642	0.01685	0.01693	0.01	151.08	382	B	Soil
47	1631	29.2993	40.4941	0.0097	0.0101	0.00	153.40	410	B	Soil
48	7710	29.2668	40.5900	0.0079	0.0099	0.00	153.80	358	UNKNOWN	Soft Soil
49	7708	29.2473	40.6576	0.0124	0.0117	0.01	154.31	196	UNKNOWN	Soft Soil
50	1619	29.2907	40.4224	0.0184	0.0148	0.01	156.37	348	C	Soft Soil
51	1610	29.5088	40.0671	0.0201	0.0122	0.01	156.95	252	C	Soft Soil
52	1635	29.2587	40.4496	0.0045	0.0048	0.00	158.06	570	B	Soil
53	2609	30.6966	39.4463	0.0049	0.0033	0.00	158.25	407	B	Soil

54	1803	32.8834	40.8149	0.0055	0.0056	0.00	159.90	348	C	Soft Soil
55	3405	29.1567	40.9111	0.00330	0.00329	0.00	160.96	1862	B	Rock
56	7707	29.0788	40.6381	0.0130	0.0081	0.00	168.68	312	C	Soft Soil
57	1630	29.1221	40.3630	0.0153	0.0090	0.00	172.00	301	C	Soft Soil
58	3407	29.0095	41.0582	0.0069	0.0033	0.00	174.87	595	B	Soil
59	3411	28.9761	41.0119	0.0051	0.0034	0.00	177.01	323	C	Soft Soil
60	1620	29.1296	40.1824	0.0051	0.0042	0.00	178.86	459	B	Soil
61	3413	28.9482	41.0943	0.0030	0.0025	0.00	180.56	452	B	Soil
62	1627	29.0752	40.2257	0.0123	0.0141	0.00	181.14	249	C	Soft Soil
63	4307	30.0143	39.4053	0.0033	0.0035	0.00	182.80	438	B	Soil
64	1622	29.0527	40.1960	0.0056	0.0045	0.00	184.20	448	B	Soil
65	1618	28.9282	40.3510	0.0032	0.0041	0.00	188.04	314	C	Soft Soil
66	1621	28.9756	40.2269	0.0049	0.0046	0.00	188.91	396	B	Soil
67	7706	28.8266	40.5131	0.0065	0.0095	0.00	191.93	277	C	Soft Soil
68	3415	28.7585	41.0273	0.0096	0.0125	0.01	195.34	283	C	Soft Soil

In this study, apart from the code [22] soil classification, another classification has been made in Figure 2, which will be Rock, Soil and Soft Soil as presented in Table 1, to make a common soil classification among the GMPEs. Again, in this triple classification, shear wave velocities were taken into account. For rock soil, Vs≥760 m/s, for soil, 360≤Vs≤760 m/s, for soft soil, Vs≤360 m/s. Ground properties are divided in Table 3.

Table 3. Ground properties for records

Soil Type	Number of Records
Rock	7
Soil	24
Soft Soil	37
Total	68

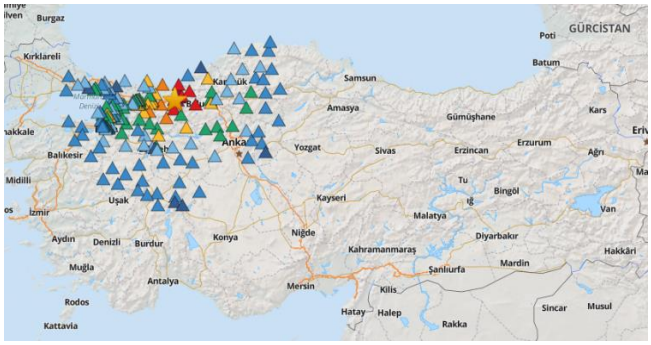

Figure 3. Distribution of stations

68 records to be used in the study were obtained from stations belonging to different soil classes. The distribution of earthquake records according to soil classes is presented in Table 3 above.

The highest acceleration values during the earthquake were measured at station no. 8105. An acceleration value of 0.60 g was obtained in the East-West direction. Acceleration time graphs for the 3 directions of the acceleration record are demonstrated in Figure 4. The PGA value for the location of station 8105 on the earthquake hazard map is 0.472 g. It appears that this value has been exceeded. This exceedance is also seen in the comparison of the spectra.

Ss and S1 values for the earthquake ground motion level, which has a 10% probability of being exceeded in 50 years as determined in the Turkish Building Earthquake Code [22], that is, a recurrence period of 475 years, were taken from the hazard map and the design spectrum for the DD-2 ground motion level was obtained. Since it is known that station no. 8105 is in the ZB soil class, the values obtained for the spectra were obtained for the ZB soil class. The response spectra of the East-West and North-South components for station 8105 are also presented in Figure 5. When looking at the comparison of these two spectra, the data of the station that measured the highest acceleration value during the earthquake shows that the regulation conditions were exceeded. It is seen that overshoot occurs especially in periods up to 0.5 s. This situation is expected to occur in low-rise buildings that suffer structural damage [17]. The data obtained from the Turkey Earthquake Hazard Map of station number 8105 is in Table 4.

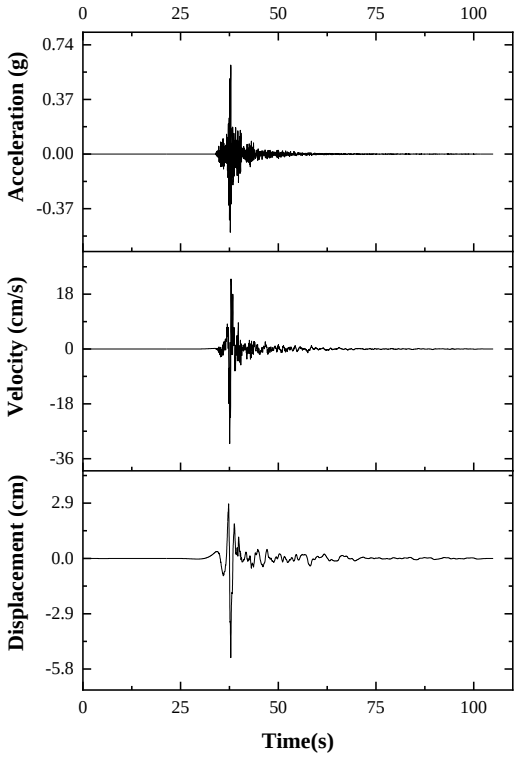

Figure 4. 8105 Stations Time Histories

3. Ground Motion Prediction Equations(GMPEs)

If accurate earthquake data is used, ground motion prediction equations can reflect the earthquake demand that may occur in a particular region. Attenuation relations are generally prepared for a specific region or city. They estimate earthquake parameters using magnitude and distance values as earthquake input. In general, the magnitude of the earthquake, the distance of the fault to the study area and the ground properties are the basic parameters of the GMPEs. These parameters may vary depending on the details of the study and the characteristics of the fault close to the study area. The most well-known GMPEs in the world are the GMPEs found in the NGA-West2 [24] project, which was prepared using the largest data set. Even though they are compatible with many regions of the world, the data sets are also regional in these equations. In Türkiye, there are ground motion prediction equations created regionally or for the entire country. The most well-known of these are the equations prepared by Özbey et al. [25], Kalkan&Gülkan [26, 27], Akkar et al. [28, 29]. For example, the ground motion prediction equations prepared by Özbey et al. are GMPEs prepared for North-West Marmara. In this attenuation relationship, 1999 Gölcük earthquake data were employed. The fault taken into consideration is the North Anatolian Fault. Within the scope of this study, 5 ground motion prediction equations prepared for the country and regionally were evaluated. Below, the equations of the decay relations and the explanation of the parameters are given respectively. Attenuation relations are named "AR" in this study, as well as the names of the authors.

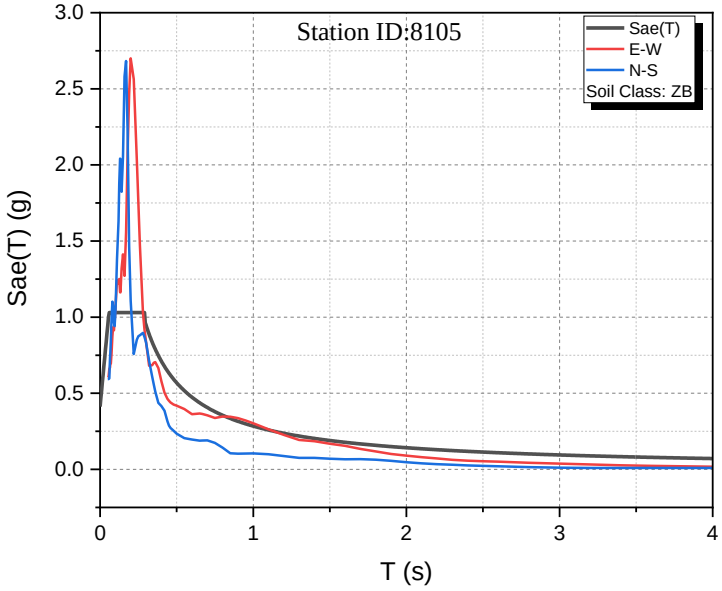

Figure 5. Comparison of Response and Design Spectra

Table 4. Parameter obtained from hazard map [23]

Latitude, Longitude	40.90278-31.15198
Station ID	8105 DEMA
Soil Class	ZB
S_s (Short period map spectral acceleration coefficient)	1.145
S_1 (Map spectral acceleration coefficient for a period of 1.0 seconds)	0.316
PGA (Peak ground acceleration (g))	0.472
PGV (Peak Ground Velocity (g))	29.291
F_s (Local ground impact coefficient for the short-period region)	0.900
F_1 (Local ground impact coefficient for a period of 1.0 seconds)	0.800
S_{DS} (Short-period design spectral acceleration coefficient)	1.030
S_{D1} (Design spectral acceleration coefficient for a period of 1.0 seconds)	0.253

3.1. AR1 (Özbey et al., 2004)

In the article titled an empirical GMPEs for Northwestern Türkiye ground motion using a random effects approach [25], researchers developed an GMPEs for Northwest Marmara. Analyzes were carried out using 195 different ground motion records of 17 earthquakes in the GMPEs prepared using Kocaeli and Düzce Earthquake data (Equation 1).

$$\log(Y_{ij}) = a + b(M_i - 6) + c(M_i - 6)^2 + dlog\sqrt{R_{ij}^2 + h^2} + eG_1 + fG_2 \quad (1)$$

G1 and G2 coefficients in the equation; It takes the values G1=0 and G2=0 for local soil classes A and B, G1=1 and G2=0 for local soil class C, and G1=0 and G2=1 for soil class D. The regression coefficients of the study are in Table 5. The soil classifications defined in the study are presented in Table 6. 4 different soil classes are grouped according to shear wave velocities.

3.2. AR2 (Kalkan and Gülkan, 2004)

In their study titled Site-Dependent Spectra Derived from Ground Motion Records in Türkiye [27], Kalkan and Gülkan developed this model by using 112 strong ground motion records of 57 earthquakes that occurred between 1976 and 2003. The ground motion prediction equation in the study is located below (Equation 2).

$$\ln Y = b_1 + b_2(M - 6) + b_3(M - 6)^2 + b_5 \ln r + b_v \ln(V_S/V_A)$$
$$r = \left(r_{cl}^2 + h^2\right)^{\frac{1}{2}} \quad (2)$$

The regression coefficients used in the study are presented in Table 7. We divided soil groups for recording stations in Türkiye into three categories: rock (with average Vs=700 m/sec), soil (Vs=400 m/sec), and soft soil (Vs=200 m/sec).

3.3. AR3 (Akkar and Çağnan, 2010)

In the study titled A Local Ground-Motion Predictive Model for Türkiye, and Its Comparison with Other Regional and Global Ground-Motion Models [28], a model for Türkiye in general was obtained. The results were compared with other GMPEs for Türkiye and equations valid worldwide. Italian and Türkiye data sets were utilized. The resulting equation is given below (Equation 3). The constant c1 is the reference magnitude.

$M \leq c_1$

$$\ln(Y) = a_1 + a_2(M - c_1) + a_4(8.5 - M)^2 + [a_5 + a_6(M - c_1)] \ln\sqrt{R_{jb}^2 + a_7^2} + a_8F_N + a_9F_R$$

$M \geq c_1$

$$\ln(Y) = a_1 + a_3(M - c_1) + a_4(8.5 - M)^2 [a_5 + a_6(M - c_1)] \ln\sqrt{R_{jb}^2 + a_7^2} + a_8F_N + a_9F_R \quad (3)$$

The regression coefficients in the study are presented in Table 8.

3.4. AR4 (Ulutaş et al., 2010)

An GMPE based on Turkish strong motion data and iso-acceleration map of Türkiye [30]. The curve that

Ulutaş et al. used the 5.8 Mw earthquake data set and obtained with this data set is given in Figure 8.

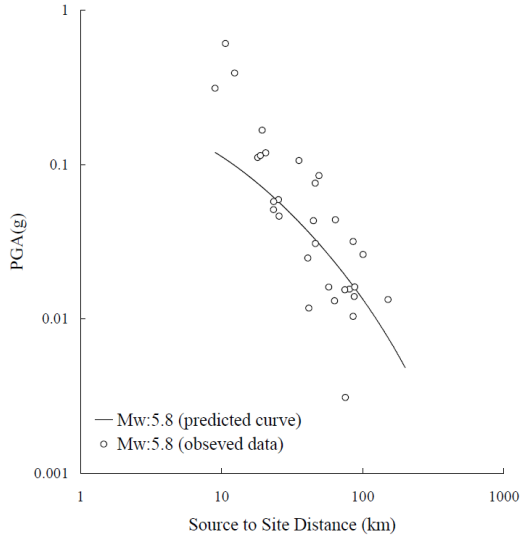

Figure 6. Proposed new GMPE plotted along with the 5.8 M_w data set for the study [25]

The ground motion prediction equation created in the study is given in Equation 4.

$$\log(PGV) = -2.12833 + 1.21448M - 0.08137M^2 - (2.46942 - 0.22349M)log\sqrt{R_{jb}^2 + 6.41443^2} + 0.20354S_S + 0.08484S_A - 0.05856F_N + 0.01305F_R \quad (4)$$

The regression coefficients in the study are in Table 9. In this study, therefore, three site conditions, namely rock, soil and soft soil sites, were considered.

3.5. AR5 (Akkar and Bommer, 2010)

Akkar and Bommer [29] developed the following Equation 5 for the Mediterranean, Europe and Middle East regions. It is stated that it is suitable for use in Türkiye.

$$\log(PSA) = b_1 + b_2M + b_3M^2 + (b_4 + b_5M)log\sqrt{R_{jb}^2 + b_6^2} + b_7S_S + b_8S_A + b_9F_N + b_{10}F_R + \epsilon\sigma \quad (5)$$

where SS and SA take the value of 1 for soft (Vs30 < 360 m/s) and stiff soil sites, otherwise zero, rock sites being defined as having Vs30 > 750 m/s.

Table 5. Regression coefficients [25]

Period(s)	a	b	c	d	h	e	f	$\sigma_{log(Y)}$
PGA	3.287	0.503	-0.079	-1.1177	14.82	0.141	0.331	0.260

Table 6. Definition of site classes in the attenuation models [25]

Site Class	Shear wave velocity
A	>750 m/s
B	360-750 m/s
C	180-360 m/s
D	<180 m/s

Table 7. Regression coefficients [27]

Period(s)	b_1	b_2	b_3	b_5	b_V	V_A	h(km)	σ_{lnY}
PGA	0.393	0.576	-0.107	-0.899	-0.200	1112	6.91	0.612

Table 8. Regression coefficients [23]

T(s)	a_1	a_2	a_3	a_4	a_5	a_6	a_7	a_8	a_9	σ*	τ*	σ_{Tot}*
PGA_{GM}	8.924	-0.513	-0.695	-0.185	-1.255	0.181	7.336	-0.021	0.018	0.652	0.516	0.832

Table 9. Coefficient of Regression

Period(s)	b1	b2	b3	b5	b_V	V_A	h	$\sigma_{ln(Y)}$
0(PGA)	-0.682	0.253	0.036	-0.562	-0.297	1381	4.48	0.562

5. Results

By using GMPEs and Gölyaka earthquake data in the previous part of the study, the harmony between GMPEs and real earthquake data was investigated in this section. Attention was paid to the limitations of GMPEs and the classification of ground properties.
Site conditions in the database reported from institutions are updated at different times based on new information and are constituted of three groups as rock,

soil, and soft soil thus GMPEs in this study employed different soil class assessments.
Figure 7-Figure 11 show that as the distance increases, a higher agreement is generally observed between GMPEs and earthquake data. As the distance gets closer, it is seen that the earthquake data remain above the data related to the GMPEs, that is, they take on higher values.

In the GMPEs that take into account different soil classes, it is seen that the lowest harmony between the curves and the data is in the graphs of rock soil. This is due to the low number of station data with rock soil characteristics.

In some GMPEs, soil classification is not considered. In this study, the AR3 attenuation relationship was prepared for rock soils. Therefore, the data used here are the data of all earthquake records. The reason why earthquake data is concentrated in some parts of the curves is that the PGA value corresponding to that region is obtained from more than one station.
It was determined that the highest harmony between curves and data between GMPEs for this study was observed in AR4. The GMPEs shows a certain harmony when the standard deviation is taken into consideration.

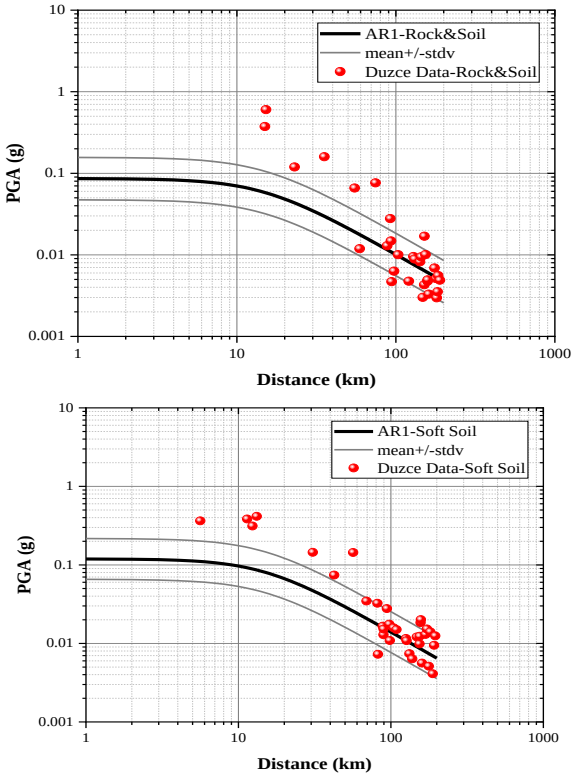

Figure 7. Comparison of AR1 and Gölyaka Earthquake's Data

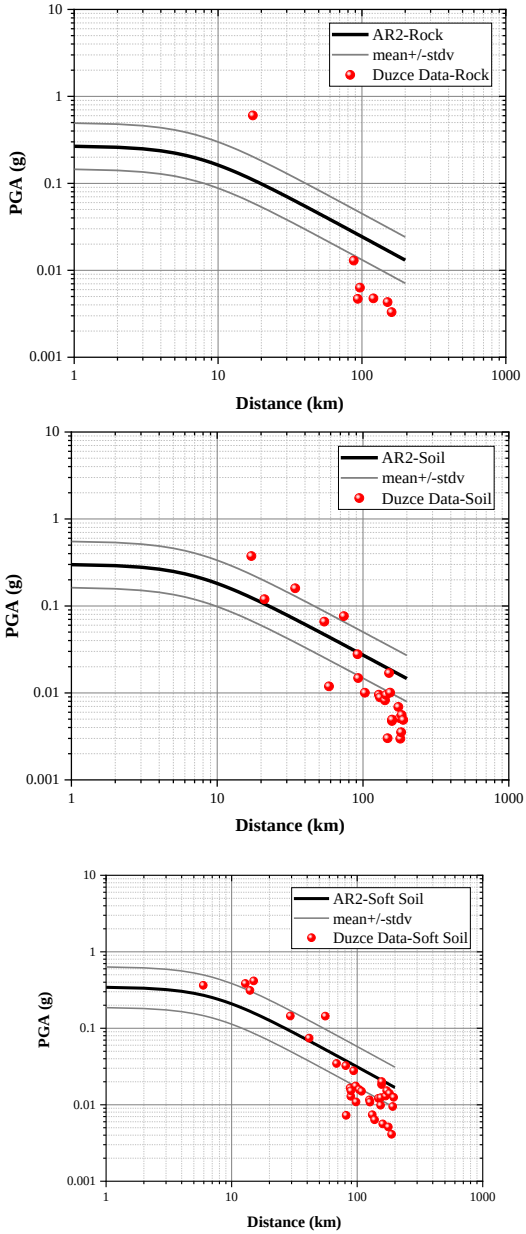

Figure 8. Comparison of AR2 and Gölyaka Earthquake's Data

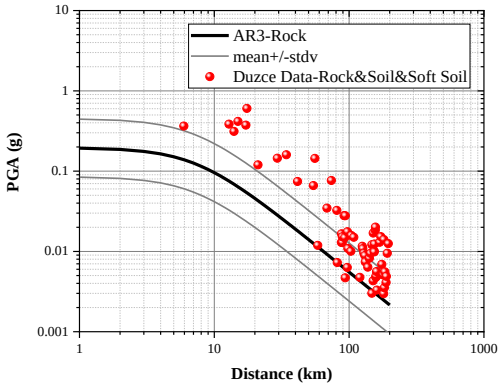

Figure 9. Comparison of AR3 and Gölyaka Earthquake's Data

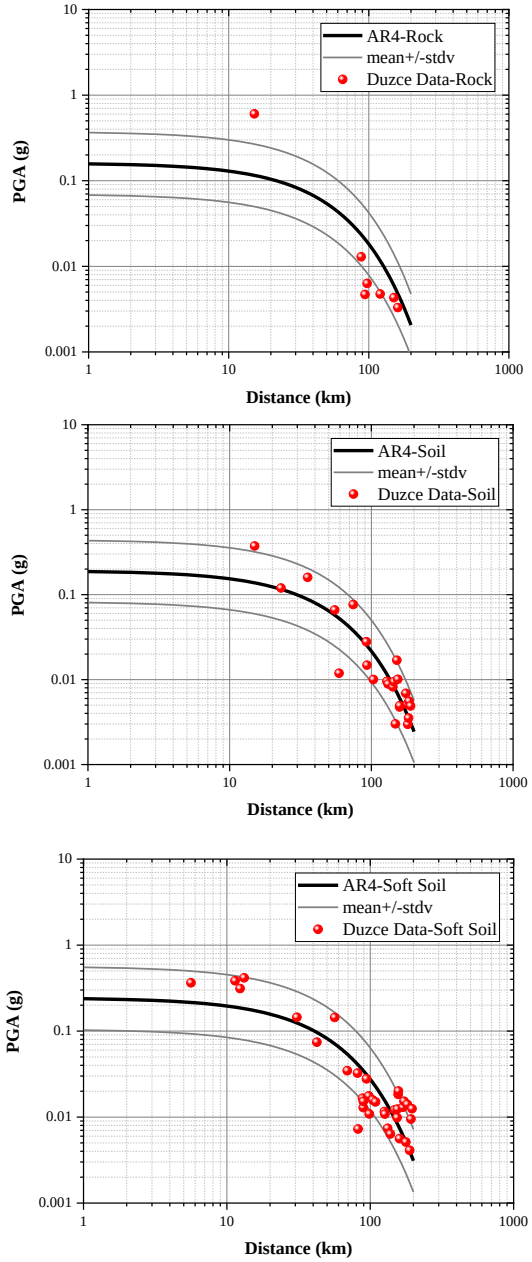

Figure 10. Comparison of AR4 and Gölyaka Earthquake's Data

In general, the compatibility of the 5 GMPEs with real earthquake data increases as the distance increases. It cannot be said that it predicts the PGA values measured more closely very well. It can be said that this is due to the small number of data by the decay relations. In addition, examining this harmony after earthquakes guide detailing the parameters in subsequent GMPEs The most important data that feeds the attenuation relations; are the measurement stations. The fact that these stations provide accurate information and are numerous increases the accuracy of the prepared prediction equations. The increasing station network in recent years will increase the accuracy of the GMPEs obtained in new studies.

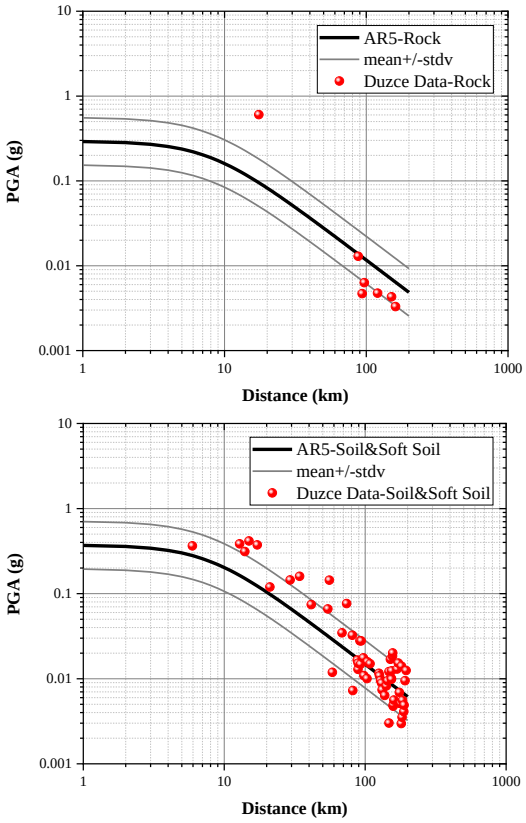

Figure 11. Comparison of AR5 and Gölyaka Earthquake's Data

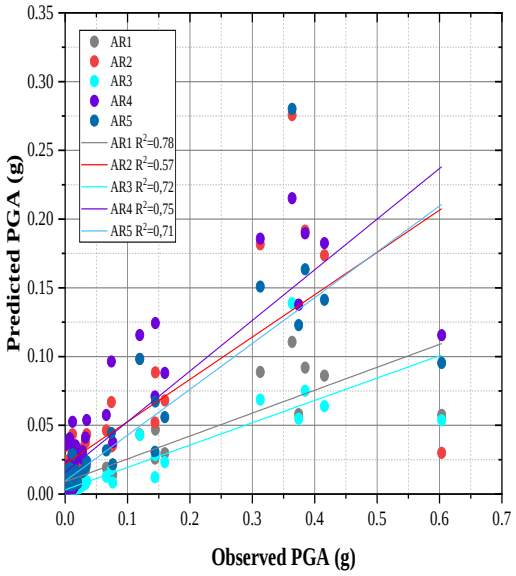

Figure 12. Correlation between Predicted PGA and Observed PGA

When the Observed and Predicted PGA values are compared (Fig.12), it is seen that the GMPEs except AR2 show similar compliance, even though the fits in

the curves of the attenuation relationships seem very different. With R2 correlations, it is seen that 4 equations have values above 0.70. Although the AR1 curve alone does not seem to have a very high fit, the highest fit between the predicted and predicted PGA's belongs to this GMPEs. However, high R2 values do not fully reflect high fit. It is seen that as the correlation approaches the y=x line, closer values can be estimated. When we look at the curve drawn for the AR4 equation, we see the best fit between predicted and observed in the y=x curve. Looking at Figure 10 and Figure 12, the highest agreement is found in AR4, the data set uses a wide range of data and was developed by considering the region where the Gölyaka earthquake occurred. Ulutaş's work focuses on the Marmara region.

6. Conclusions

Within the scope of the study, data on the 5.9 Mw earthquake that occurred on November 23, 2022, were investigated. Acceleration values obtained from the stations were evaluated with 5 different GMPEs developed for Türkiye. According to the results obtained from 5 different GMPEs the fits of the models were evaluated and interpreted. The results obtained within the scope of the study are given below.

• According to the results obtained in the study, 5 different GMPEs were evaluated. All the GMPEs are compatible with certain earthquake magnitudes. In general, the curves of the GMPEs remain below the real values by a standard deviation.

• As the distance increases, the actual earthquake data and the values predicted by GMPEs converge in regions where PGA values are low.

• The GMPEs called AR4 shows the highest fit in the study. The reason for this is that the data set utilized to obtain the GMPEs is large in number. Another reason is that the aim is to develop the GMPEs for the Marmara region. The fact that the Gölyaka earthquake remains within the region where the GMPEs is focused is effective in the high degree of harmony.

• The most important issue in obtaining GMPEs is the data set and the ground properties of the region. These need to be well-detailed and effective with the right approach. For this reason, existing GMPEs need to be improved and updated with new earthquake data to better reflect possible earthquakes.

Conflict of Interest Statement

There is no conflict of interest between the authors.

Statement of Research and Publication Ethics

The study is complied with research and publication ethics.

References

[1] H. Sezen, A. S. Whittaker, K. J. Elwood, and K. M. Mosalam, "Performance of reinforced concrete buildings during the August 17, 1999 Kocaeli, Turkey earthquake, and seismic design and construction practise in Turkey," *Eng. Struct*., vol. 25, no. 1, pp. 103–114, 2003.

[2] DEMA, "23 Kasım 2022 Gölyaka Duzce Depremine İlişkin Ön Değerlendirme Raporu,".2023 [Online]. Available: https://deprem.afad.gov.tr/assets/pdf/23kasim2022GolyakaDuzceMW59.pdf. [Accessed: Sept 2023]

[3] DEU-DAUM, "23 Kasım 2022 Mw 5.9 Gölyaka Düzce Depremi Ön Gözlem ve Değerlendirme Raporu," 2023. [Online]. Available: https://daum.deu.edu.tr/wp-content/uploads/2023/02/rapor_Duzce-DEU-DAUM.pdf [Accessed: Sept 2023]

[4] İMO, "23.11.2022 Gölyaka-Düzce Depremi Ön Değerlendirme Raporu" 2022. [Online]. Available: https://www.imo.org.tr/Eklenti/8115,golyaka-depremr-aporupdf.pdf?0&_tag1=D2A204FCD61ACD26AEB2AB1B4F74C5C48F66ED06 [Accessed: Sept 2023]

[5] Ö. Emre, "Active fault database of Turkey," Bull. Earthq. Eng., vol. 16, no. 8, pp. 3229–3275, 2018.

[6] E. Sayın, "24 January 2020 Sivrice-Elazığ, Turkey earthquake: geotechnical evaluation and performance of structures," *Bull. Earthq. Eng*., vol. 19, no. 2, pp. 657–684, 2021.

[7] Ö. F. Nemutlu, B. Balun, and A. Sarı, "Damage assessment of buildings after 24 January 2020 Elazığ-Sivrice earthquake," *Earthq. Struct*., vol. 20, no. 3, pp. 325–335, 2021.

[8] A. Doğangün, "Performance of reinforced concrete buildings during the May 1, 2003 Bingöl Earthquake in Turkey," *Eng. Struct*., vol. 26, no. 6, pp. 841–856, 2004.

[9] M. Bikçe, "Türkiye'de Hasara Ve Can Kaybina Neden Olan Deprem Listesi(1900-2014)," in 3.Türkiye Deprem Mühendisliği ve Sismoloji Konferansı, 2015, pp. 1–10, [Online]. Available: http://www.tdmd.org.tr/TR/Genel/pdf2015/TDMSK_084.pdf.

[10] O. K. Gül, "27 Aralık 1939 Erincan Depreminin Sivas ve İlçelerine Etkileri," *J. World Turks*, vol. 3, no. 2, 2011.

[11] M. Sunkar, "8 Mart 2010 Kovancılar-Okçular(Elazığ) Depremi;Yapı Malzemesi ve Yapı Tarzının Can ve Mal Kayıpları Üzerindeki Etkisi," *Türk Coğrafya Derg.*, no. 56, pp. 23–37, 2010.

[12] E. Işık, F. Avcil, A. Büyüksaraç, R. İzol, M.H. Arslan, C. Aksoylu, E. Harirchian, O. Eyisüren, E. Arkan, M.Ş. Güngür, M. Günay and H. Ulutaş, "Structural damages in masonry buildings in Adıyaman during the Kahramanmaraş (Turkiye) earthquakes (Mw 7.7 and Mw 7.6) on 06 February 2023". Engineering Failure Analysis, 107405, 2023.

[13] E. Arkan, E. Işık, E. Harirchian, M. Topçubaşı, F. Avcil, "Architectural Characteristics and Determination Seismic Risk Priorities of Traditional Masonry Structures: A Case Study for Bitlis (Eastern Türkiye)". *Buildings*, vol. 13, no. 4, p.1042, 2023.

[14] H. Bilgin, M. Nyarko-Hadzima, E. Işık, H.B. Özmen and E. Harirchian, "A comparative study on the seismic provisions of different codes for RC buildings". *Structural Engineering and Mechanics, An Int'l Journal*, vol. 83, no. 2, pp. 195-206, 2022.

[15] A. Büyüksaraç, E. Işık and Ö. Bektaş, "A comparative evaluation of earthquake code change on seismic parameter and structural analysis; a case of Turkey". *Arabian Journal for Science and Engineering*, vol. 47, no. 10, pp. 12301-12321, 2022.

[16] E. Bayrak, C. Ozer, H. Cakici, and M. E. Kocadagistan, "January 24, 2020 Sivrice (Turkey) Earthquake (Mw 6.8): Evaluation of Ground-Motion Prediction Equations and Microtremor Studies," *Turk Deprem Arastirma Derg.*, vol. 3, no. 2, pp. 125–148, 2021.

[17] S. Özalp, A. Kürçer, İ. Avcu ve Tayfun Güler Maden Tetkik ve Arama Genel Müdürlüğü, and J. Etütleri Dairesi, "23 Kasım 2022 Gölyaka (Düzce) Depremi (Mw 6,0) arazi gözlemleri ve kaynak faya ilişkin değerlendirmeler," Gölyaka (Düzce) Depremi, vol. 3, no. August 1999, pp. 61–79, 2023, [Online]. Available: https://www.mta.gov.tr/mtayerbilimleri/.

[18] M. Kutanis, "Sismik Tehlike Analizi," Sakarya, 2004.

[19] B.D. Bulajic, G. Pavic and M. Nyarko-Hadzima, "PGA estimates for deep soils atop deep geological sediments-An example of Osijek, Croatia". *Geomechanics and Engineering*, vol. 30, no. 3, pp. 233-246, 2022.

[20] E. Işık, Y.L. Ekinci, N. Sayil, A. Büyüksaraç and M.C. Aydin, "Time-dependent model for earthquake occurrence and effects of design spectra onstructural performance: a case study from the North Anatolian Fault Zone, Turkey". *Turkish Journal of Earth Sciences*, vol. 30, no. 2, pp. 215-234, 2021.

[21] L. Sabah, and H. Bayraktar, "Düzce Merkez ve İlçelerinin Deprem Senaryolarına Göre Karşılaştırmalı Olarak İncelenmesi". *Düzce Üniversitesi Bilim ve Teknoloji Dergisi*, vol. 8, no. 2, pp. 1695-1705, 2020.

[22] DEMA, "Turkey Seismic Code-2018 (TEC-2018)". 2018.

[23] DEMA, "Turkey Earthquake Hazard Map." Accessed: Oct. 12, 2022. [Online]. Available: https://tdth.afad.gov.tr/TDTH/main.xhtml.

[24] PEER, "Pacific Engineering Research Center Strong Ground Motion Database," 2021. http://ngawest2.berkeley.edu.

[25] C. Özbey, A. Sari, L. Manuel, M. Erdik, and Y. Fahjan, "An empirical attenuation relationship for Northwestern Turkey ground motion using a random effects approach," *Soil Dyn. Earthq. Eng.*, vol. 24, no. 2, pp. 115–125, 2004.

[26] E. Kalkan and P. Gülkan, "Empirical attenuation equations for vertical ground motion in Turkey," *Earthq. Spectra*, vol. 20, no. 3, pp. 853–882, 2004.

[27] E. Kalkan and P. Gülkan, "Site-dependent spectra derived from ground motion records in Turkey," *Earthq. Spectra*, vol. 20, no. 4, pp. 1111–1138, 2004.

[28] S. Akkar and Z. Çağnan, "A local ground-motion predictive model for Turkey, and its comparison with other regional and global ground-motion models," *Bull. Seismol. Soc. Am.*, vol. 100, no. 6, pp. 2978–2995, 2010.

[29] S. Akkar and J. J. Bommer, "Empirical equations for the prediction of PGA, PGV, and spectral accelerations in Europe, the mediterranean region, and the Middle East," *Seismol. Res. Lett.*, vol. 81, no. 2, pp. 195–206, 2010.

[30] E. Ulutas and M. F. Özer, “Empirical Attenuation Relationship of Peak Ground Acceleration for Eastern Marmara,” *Arab. J. Sci. Eng.*, vol. 35, no. 1A, pp. 187–203, 2010.

Bitlis Eren Üniversitesi Fen Bilimleri Dergisi
BİTLİS EREN UNIVERSITY JOURNAL OF SCIENCE
ISSN: 2147-3129/e-ISSN: 2147-3188
VOLUME: 12 NO: 4 PAGE: 1261-1274 YEAR: 2023
DOI:10.17798/bitlisfen.1376817

Enhancing Early Detection of Blood Disorders through A Novel Hybrid Modeling Approach

Pınar KARADAYI ATAŞ [1*]

[1] *Istanbul Arel University, Faculty of Engineering and Architecture, Department of Computer Engineering, Istanbul, Türkiye*
(ORCID: 0000-0002-9429-8463)

Keywords: applied statistic, statistical analysis and application, structural and functional data, machine learning.

Abstract
Blood disorders are such conditions that impact the blood's ability to function correctly. There is a range of different symptoms depending on the type. There are several different types of blood disorders such as Leukemia, chronic myelocytic leukemia, lymphoma, myelofibrosis, polycythemia, thrombocytopenia, anemia, and leukocytosis. Some resolve completely with therapy or do not cause symptoms and do not affect overall lifespan. Some are chronic and lifelong but do not affect how an individual life. Other blood disorders, like sickle cell disease and blood cancers, can be even fatal. There needs to be a capture of hidden information in the medical data for detecting diseases in the early stages. This paper presents a novel hybrid modeling strategy that makes use of the synergy between two methods with histogram-based gradient boosting classifier tree and random subspace. It should be emphasized that the combination of these two models is being employed in this study for the first time. This novel model is presented for the assessment of blood diseases. The results show that the proposed model can predict the tumor of blood disease better than the other classifiers.

1. Introduction

Providing accessible and reliable diagnosis is a fundamental problem for global healthcare systems [1]. Early diagnosis of blood diseases is critical for both successful treatment and the avoidance of misdiagnoses, which are sadly frequent in medical practice. A misdiagnosis may result in ineffective treatment strategies, postponed care, and in extreme circumstances, serious health decline. This is particularly important when discussing blood disorders because their symptoms might be mild and easily missed or confused with other illnesses [2]. An estimated 5% of outpatients in the US alone are given the incorrect diagnosis each year. Since one in three misdiagnoses of patients with major medical illnesses results in serious patient harm, it is estimated that 20% of patients with serious medical disorders receive incorrect diagnoses at the primary care level [3].

Improving the precision and scope of diagnostic processes is critical in the field of medicine, especially for blood disorders. A multidisciplinary approach is necessary to fully comprehend the patient's condition [4]. In order to augment the information currently available, more data is gathered during a diagnostic procedure from the patient's medical history, physical examination, and various diagnostic techniques, such as clinical laboratory tests. Laboratory tests are used to guide medical care as well as to confirm, rule out, classify, or monitor illnesses. [5]. The entire potency of laboratory test results is often overestimated since clinical laboratories often publish test results as individual numerical or categorical values, and clinicians typically focus on those values that fall outside of a given reference range.

* Corresponding author: pinaratas@arel.edu.tr
Received: 16.10.2023, Accepted: 04.12.2023

The development of advanced computational techniques has transformed the study and practice of medicine, providing new opportunities for the analysis of intricate health data [6]–[10]. For many years, medical datasets have been analyzed using machine learning techniques. [11]. It provides a number of essential tools for machine learning-based intelligent data analysis. Patient monitoring and other data gathering tools are now widely used in modern hospitals to gather data, which is then shared and kept in extensive information systems. These days, machine learning technology is ideal for identifying illnesses and evaluating medical data. Clinical data analysis reveals the molecular processes that underlie diseases and the ways in which risk factors impact their progression. Medical records in hospitals or their departments contain information about correct diagnosis. Patient data with the right diagnosis are loaded into a computer program and a learning algorithm is executed in medical machine learning studies. [11]. Machine learning (ML) has the potential to greatly improve the accuracy, efficiency, and dependability of systems intended for the diagnosis of particular illnesses[12].

Laboratory blood testing is the mainstay for the clinical diagnosis of hematological disorders; however, even the most skilled hematologist may overlook trends, outliers, or correlations among the myriad blood parameters that modern laboratories are now measuring [13], [14] . In contrast, this field of medicine is particularly interesting for machine learning applications because machine learning algorithms can manage hundreds of attributes (parameters) and can identify and utilize the interactions between these many attributes.

Machine learning has demonstrated potential in a number of areas related to medical practice, such as improving differential diagnosis, helping to choose the best course of treatment, offering prognostic estimates, lowering medical errors, and increasing overall effectiveness. Its uses in hematology are steadily growing in three main domains: image interpretation, diagnostic procedures, and predictive modeling.

Predictive modeling is one application of machine learning in hematology. A noteworthy study by [15] created a model to predict 100-day mortality after allogeneic hematopoietic stem cell transplantation (HSCT) using 28,236 acute leukemia patients from the European Society of Blood and Marrow Transplantation registry. This model was validated both internally and externally, showcasing machine learning's capacity to offer insightful information for crucial medical decisions.

An interpretable boosted decision tree model that performed better than the previous benchmark for outcome prediction was used in the model's creation. [16] used similar techniques to predict acute graft-versus-host disease (GVHD). Other groups have focused on creating techniques that use imaging and gene expression data to predict treatment response [17]. Artificial intelligence decision support solutions for oncology are already available. A model developed by [18] generates a list of probable diagnoses based on age, serial chemistry, and complete blood count laboratory values. These diagnoses are then fed into a support vector machine model. The aforementioned findings suggest several possible real-world uses for artificial intelligence.

IBM Watson for Oncology ranks and suggests treatment options based on patient and illness characteristics, published literature, available clinical trials, and the expertise of top oncologists. It uses the EMR's natural language processing and machine learning algorithms to achieve this [19]. Numerous techniques have been used to apply AI to improve the efficacy, practicality, or accuracy of diagnoses. It has been demonstrated that CNN-based techniques can reliably identify multiple myeloma based only on mass spectrometry data from peripheral blood [20].

Machine learning has great potential for the field of hematology as well as the larger medical community, even though it is still in its infancy [21]. This review intends to clarify important artificial intelligence (AI) concepts for readers who are not familiar with the field, examine the various hematology applications where AI has proven useful, and talk about the new difficulties that arise when incorporating AI into clinical practice. Moreover, the aim is to offer perspectives on how these cutting-edge technologies might influence clinical outcomes and patient care in the future [22]. Machine learning has been used in some research to forecast the number of instances of a specific disease in a given region based on historical data and present conditions [23]. Others have utilized machine learning to determine the most likely sources of an outbreak based on the pathogen's genetic makeup and infection pattern [24], [25]. Others have utilized machine learning to estimate an individual's risk of developing an infectious

disease based on their persona[15]l attributes and activities [26].

The use of machine learning in infectious illness prediction is a promising area of research with potential implications in public health, epidemiology, and clinical practice. However, there are substantial obstacles and constraints to utilizing machine learning in this context, such as the requirement for high-quality data, the complexity of the underlying phenomenon, and the risk of bias and overfitting [27].

Das and Tsanas et al. [28], [29] developed novel artificial intelligence-based methodologies for analyzing Parkinson's disease patients. Little et al. [30] proposed using speech signal information to distinguish Parkinson's disease. They discriminated between 23 Parkinson's disease patients and 8 healthy people. SVM is used to define both Parkinson's disease and healthy people. The proposed technique was found to be 91.4% accurate. Another survey [28] chose 132 elements based on dysphonic discourse indicators. Specular selection (FS) calculations such as LASSO, Relief, MRMR, and LLBFS[29].

A crucial component use in blood disease detection research, image datasets have certain drawbacks, including reliance on high-quality imaging and interpretive variability [31]–[36]. For image processing, these techniques also demand a substantial amount of processing power. On the other hand, our work offers clear benefits as it makes use of numerical data from laboratory tests. Subjectivity in image analysis is reduced when dealing with numerical data because they are more standardized and structured. They offer measurable metrics, which are essential for reliable diagnosis. This method also makes it simpler to integrate patient data with other sources, which supports diagnostic models that are more thorough. Additionally, models based on numerical data need less processing power, which makes them more accessible and useful in a range of clinical contexts. In hematology, this efficiency is essential for prompt and precise diagnosis, which results in more efficient treatment planning.

A method for monitoring blood pressure (BP), which is essential for identifying and averting health problems like hypertension and cardiovascular disorders, is presented in a study in the field [37] . With the use of CNN-LSTM and Photoplethysmography (PPG) signals, the study successfully divides blood pressure (BP) into three groups: normotension, prehypertension, and hypertension. It is noteworthy that it distinguishes between normotension and hypertension with a noteworthy accuracy of 66.76%, highlighting the potential of sophisticated techniques in continuous blood pressure monitoring.

Five machine learning models (RF, NB, LogR, SVM, and AdaBoost) were developed by Kim, T., et al. using a clinical database to predict persistent immune thrombocytopenia in pediatric ITP patients. The study comprised 969 juvenile patients with ITP, of which 332 had verified acute ITP and 253 had chronic ITP. In order to predict chronic ITP, 10-fold cross-validation was carried out using clinical (age, gender, race, ethnicity, presence of primary ITP) and laboratory variables (baseline platelet count, leukocyte count, lymphocyte count, eosinophil count, mean platelet volume, anti-nuclear antibody, immature platelet fraction, direct antiglobulin test, and immunoglobin levels). When it came to predicting chronic ITP, the 100-tree random forest model performed better than any other model (AUC: 0.795, accuracy: 0.737, precision: 0.738, F1-score: 0.671, and recall: 0.737). Naïve Bayes was the second-best performing model (AUC: 0.792, accuracy, 0.698, precision: 0.737, F1-score: 0.671, and recall: 0.698) [38]

Seven machine learning models were developed to predict hospital-acquired thrombocytopenia (HAT) post-surgery in the study by Cheng et al. These models included Gradient Boosting (GB), Random Forest (RF), Logistic Regression (LogR), XGBoost, Multilayer Perceptron, Support Vector Machine (SVM), and k-nearest Neighbors (k-NN). Adult ICU patients who had undergone surgery were enrolled in the study, with training and assessment divided 70-30. In roughly 13.1% of cases, thrombocytopenia occurred. The RF and GB models fared the best in internal validation, exhibiting high levels of specificity (79.1% and 73.7%, respectively) and sensitivity (79.3% and 73.6%, respectively), with no discernible differences between them. RF and GB had AUCs of 0.834 and 0.828, respectively [39]. In order to predict 30-day mortality in ITP patients with cerebral bleeding, Zhang, X.H. et al. [40] created ten machine learning algorithms (ML): SVM, k-NN, LogR, linear discriminant analysis, decision tree, RF, GB decision tree, AdaBoost, XGBoost, and light gradient boosting machine. In the training cohort, they carried out a 10-fold cross-validation, and they externally verified across 11 different centers. During internal validation, the SVM model performed better in predicting 30-day mortality (AUC: 0.879, F-1 score: 0.748, sensitivity: 0.600).

A crucial component of medical diagnostics, early identification of blood disorders has a major influence on patient outcomes [41]. Blood disorders can have a significant impact on general health and quality of life [42]. They include a broad range of conditions from anemia to leukemia. Early detection of these conditions is essential for the possibility of early intervention, which could reduce the severity of the illness and enhance the prognosis [43].

Unfortunately, there are a number of drawbacks to the current blood disorder diagnostic techniques [44]. Even though they work well, traditional blood tests frequently miss subtle symptoms of early-stage disorders or fail to present a complete picture of the patient's health. In addition, a number of blood disorders share symptoms with other illnesses, which could result in a delayed or incorrect diagnosis.

The gaps in the diagnostic procedures used today emphasize the need for more sophisticated and accurate detection techniques [45]–[47]. By facilitating prompt and focused treatments, an improved strategy for early detection lowers the risk of complications while also increasing the accuracy of diagnoses. Closing these gaps and improving patient care in the field of blood disorders requires the development and application of novel diagnostic tools. Through the introduction of a novel hybrid modeling approach that blends cutting-edge analytics with conventional diagnostic techniques, our research seeks to address these issues and provide a more effective and efficient pathway for the early detection of blood disorders.

In this study, prior research on blood condition was assessed for early detection critically, noting important constraints and the results attained in these investigations. Gaps in present diagnostic techniques are identified by this assessment, especially with regard to the detection of subtle and early-stage signs of blood diseases. By merging random subspace techniques with gradient boosting based on histograms, our research advances this subject through the introduction of a novel hybrid modeling methodology. By addressing the inadequacies of conventional diagnostic approaches, this novel methodology seeks to improve the accuracy and reliability of blood disease diagnosis. The theory was that specific hematological diseases like leukocytosis, anemia, and thrombocytopenia found in the values of blood test results would be enough for the novel hybrid predictive model to suggest a plausible diagnosis if it were trained on a large enough dataset of medical cases that included clinical laboratory blood tests. Two separate methodologies, the Random Subspace Ensemble method and the Histogram-based Gradient Boosting Classification Tree (HIST-GBCT) algorithm, are combined to create a novel methodology. To the best of knowledge, this combination has not before been investigated in the literature.

2. Material and Method

2.1. Dataset

The 4000 samples in the dataset are categorized into three distinct groups: 1232 samples relate to pediatric hematology cases, 1451 samples are from adult hematology patients, and the remaining 1232 samples are linked to different tumor types. Sensitive personal data, including names and IDs, has been removed from the dataset in order to respect privacy standards. A salient characteristic of our dataset is the 'Clinic Number,' which functions as the classification target label. The three groups are identified by this label: 80 stands for adult hematology cases, 95 for pediatric hematology cases, and 59 for tumor cases. The National Heart, Lung, and Blood Institute's (2016) guidelines were carefully followed in the selection of the dataset's features to ensure their applicability and coherence within the framework of oncology and hematological research. The features of the dataset are listed depending on (National Heart Lung Blood Institute site, 2016). The content of the dataset's columns is presented in Table 1.

Table 1. Data set content

Name	Definition
WBC	White blood cells
RBC	RED blood cells
Cupper	Cu
hgb	Hemoglobin
HCT	Hematocrit
MCV	Macrocytic Anemia:
MCH	Mean Corpuscular Hemoglobin
MCHC	Mean Corpuscular Hemoglobin Concentration
PLT	Platelet Count
RDW-SD	Red blood cell distribution width
RDW-CV	Red blood cell distribution width
PDW	platelet distribution width
MPV	Mean platelet volume
RDW-SD	Red blood cell distribution width
P-LCR	Platelet larger cell ratio
PCT	Procalcitonin
NEUT	Neutropenia

LYMPH	Lymphocytes	OUTPUT	Thrombocytopenia = 1
MONO	Mononucleosis		Normal = 2
EO	Eosinophil granulocyte		Leukocytosis = 3
BASO	Basophil granulocyte		
IG	Intravenous immunoglobulin		

2.2. Model background

Random Subspace Ensemble (RSE) is a machine learning technique used to improve predictive modeling by training several models on randomly selected subsets of the input characteristics. Each model in the ensemble focuses on a different subset of the available features, encouraging model variety. RSE tries to increase the overall model's robustness and generalization performance by merging predictions from several diverse models, making it particularly beneficial for high-dimensional datasets or when dealing with the curse of dimensionality. Ho et al. presented a classic integrated technique called random subspace in 1998 [52]. To generate the training subset, the algorithm is comparable to the bagging algorithm and is randomly selected by the original training set [52], [53]. The algorithm of the Random subspace is represented in Alg. 1.

Algorithm: Random Subspace Method

Input:

Training dataset: (*X_train*, *y_train*)
Number of base models: *n_estimators*
Maximum number of features to consider for each base model: max_features

Output:

List of base models: estimators
Initialize an empty list estimator to store the base models.
For *i* in range(*n_estimators*):

a. Randomly select a subset of features from the available features with a size not exceeding max_features. Let's call this subset selected_features.
b. Create a base model (e.g., decision tree classifier) and train it using the training data (*X_train*[:, *selected_features*], *y_train*).
c. Append the trained base model and the selected_features to the estimators list.
d. Return the list of estimators.

The Histogram-based Gradient Boosting Classification Tree (HIST-GBCT) is a supervised classification machine learning algorithm. It creates an ensemble of decision trees by enhancing their forecast accuracy iteratively. The use of histograms to efficiently represent and manipulate data during the training phase distinguishes HIST-GBCT. HIST-GBCT organizes data into bins or buckets rather than individual data points, reducing computing complexity and allowing for faster training. This method is very useful when working with huge datasets or high-dimensional feature spaces. The algorithm gradually refines its judgment bounds, resulting in a sophisticated classification model capable of successfully classifying new, previously unseen data points [54].

The outline of the mathematical formulation of Histogram-based Gradient Boosting:

Initialize the ensemble model as an empty function: $f_0(x) = 0$. For each boosting round m from 1 to M:

Step 1: Compute Negative Gradient

For Calculating the negative gradient of the loss function with respect to the current model's predictions

$$g_m(x_i) = \frac{dL\left(y_i, F_{m-1}(x_i)\right)}{dF_{m-1}(x_i)}, \text{for i} = 1,2,3,\dots,\text{N.} \quad (\mathbf{2.1})$$

Step 2: Fit a Base Learner

Fit a base learner to the negative gradients $g_m(x_i) = 0$ and discover the best structure for the tree (e.g., split points and leaf values). This is accomplished by minimizing a loss function, such as squared error in regression or deviation in classification.

$$Tree_m = argmin_{tree} \sum_{i=1}^{N} L\left(y_i, F_{m-1}(x_i) + tree(x_i)\right). (\mathbf{2.2})$$

Step 3: Update the Model

$$F_m(x) = y_i, F_{m-1}(x) + tree(x_i) + \eta. tree_m(x_i) \ (\mathbf{2.3})$$

Add the new tree to the ensemble model, weighted by a learning rate:

Step 4: Termination Check

Steps 1-3 must be repeated for a set number of boosting rounds M or until a convergence condition is fulfilled.

2.3. Proposed model

Figure 1 depicts the classification process with the whole flow of operations through the various stages. Two major operations were carried out in the preprocessing step to prepare the dataset for future analysis that represented under phase 1.

First, categorization was employed, which included converting non-numeric categorical information into a numerical format that can be used in machine learning models. This phase guarantees that the algorithms can work effectively with categorical data, contributing to the dataset's overall quality.

Accordingly, feature normalization was used. Normalization of features is an important step in data preprocessing. Scaling the numerical properties to a common range or distribution is involved. This normalization procedure guarantees that all features have a comparable influence on the modeling process, avoiding particular features from dominating the others due to scale disparities.

Furthermore, the dataset has been divided into two parts: the training set and the test set. The dataset was randomly divided into two subsets, with 70% going to the training set and 30% going to the test set. Because of the random split, both sets are representative of the whole dataset, allowing for robust model training and evaluation. This section is necessary for model training and evaluation. The training set is used to train machine learning models, while the test set is used to evaluate their performance and generalizability.

Under phase 2; the efficacy of a random forest-based method for selecting relevant features, thus enhancing data input quality, is being investigated. The Histogram-based Gradient Boosting Classification Tree (HIST-GBCT) technique is employed in an ensemble of random subspaces. This method allows us to efficiently classify the selected features, which contributes to better analysis accuracy.

In phase 3; a comprehensive set of experiments is carried out to demonstrate the efficacy of the proposed methods. These studies are designed to empirically show the benefits and efficacy of the chosen strategies.

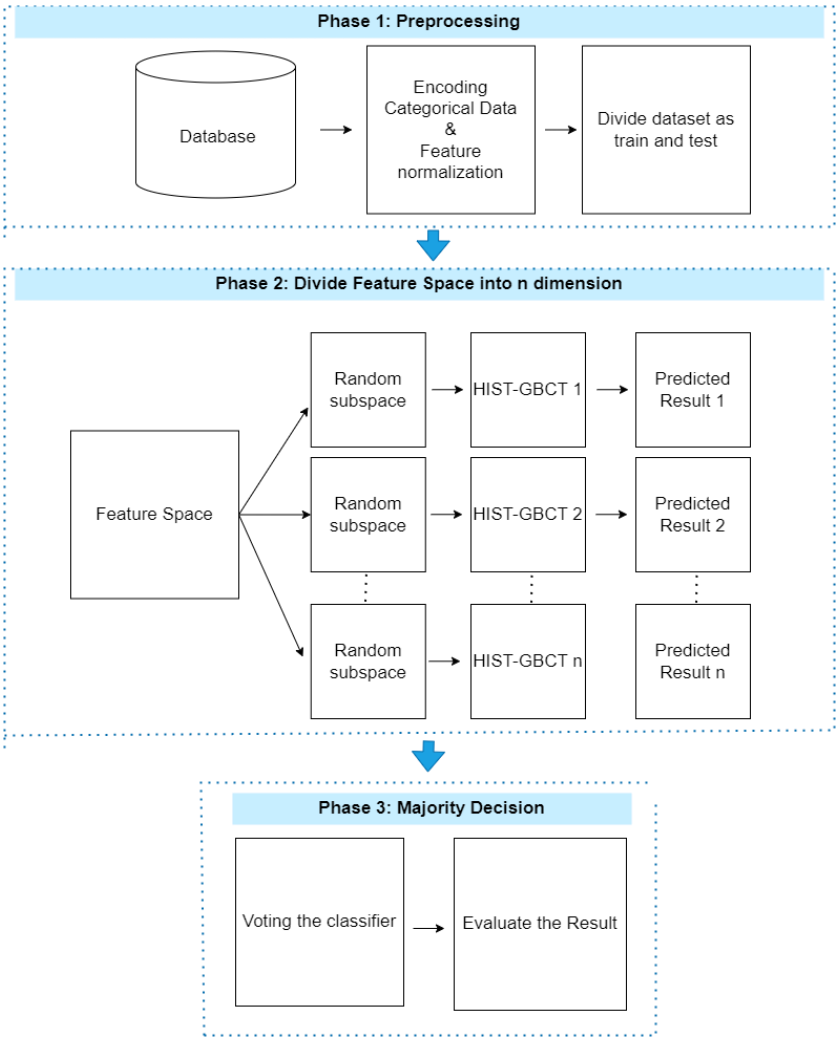

Figure 1. Illustration of the proposed workflow.

3. Results and Discussion

In this study, the focus is placed on the classification of patients with thrombocytopenia, leukocytosis, and individuals with normal hematological profiles by utilizing the proposed model. Following that, comparison analysis is performed by comparing the findings to those produced by established approaches such as logistic regression, Bernoulli Naive Bayes, SVM-linear, and k-Nearest Neighbors (kNN). Table 2 demonstrates unequivocally that the proposed model has greater predictive performance [55].

Table 2. Comparative Performance Analysis

Model Name	Accuracy	Precision	Recall	F1 score	AUC
Logistic Regression	0.842	0.841	0.802	0.799	0.694
Bernoulli Naive Bayes	0.641	0.638	0.575	0.516	0.800
SVM-Linear	0.635	0.631	0.623	0.490	0.771
KNN	0.820	0.819	0.741	0.755	0.721
Proposed Model	**0.896**	**0.894**	**0.864**	**0.862**	**0.967**

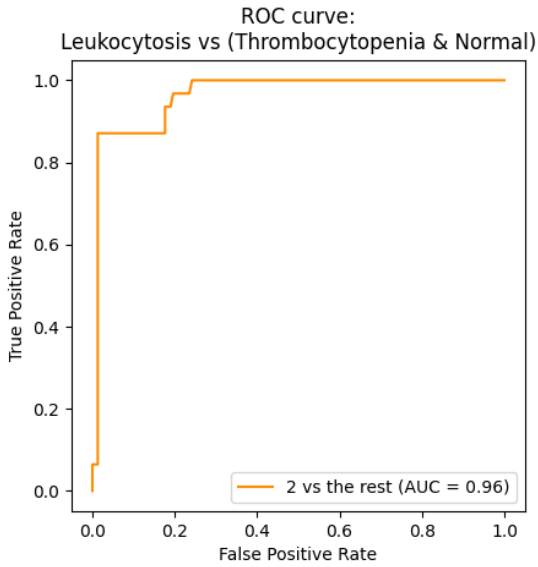

Figure 1. ROC curve for Leukocytosis vs (Thrombocytopenia and Normal).

Figure 1 shows the ROC curve displaying the classification of blood illnesses into two categories, those are 'Leukocytosis' (class_id=2) and 'Thrombocytopenia and Normal' (all other classes). Figure 2 depicts the ROC curve for classifying blood ailments into two groups: 'Thrombocytopenia (class_id=2) and 'Leukocytosis and Normal' (all other classes).

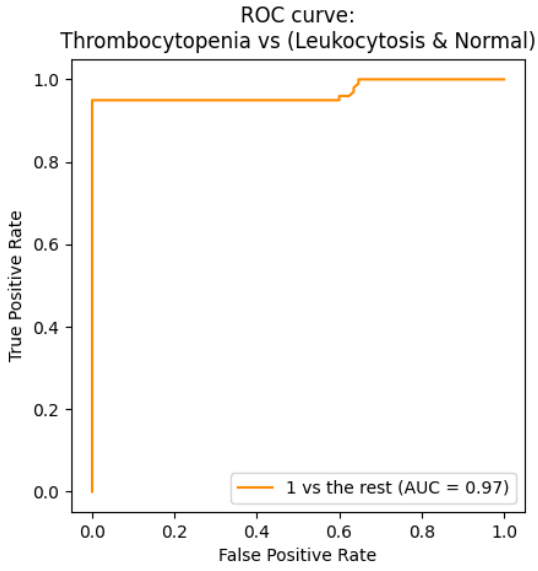

Figure 2. ROC curve for Thrombocytopenia vs (Leukocytosis and Normal).

The suggested technique regularly achieves superior ROC curve findings, suggesting its strong performance in accurately differentiating between Leukocytosis and 'Thrombocytopenia and Normal.' These excellent ROC curves highlight the method's usefulness in achieving high sensitivity and specificity, which are critical for accurate disease categorization.

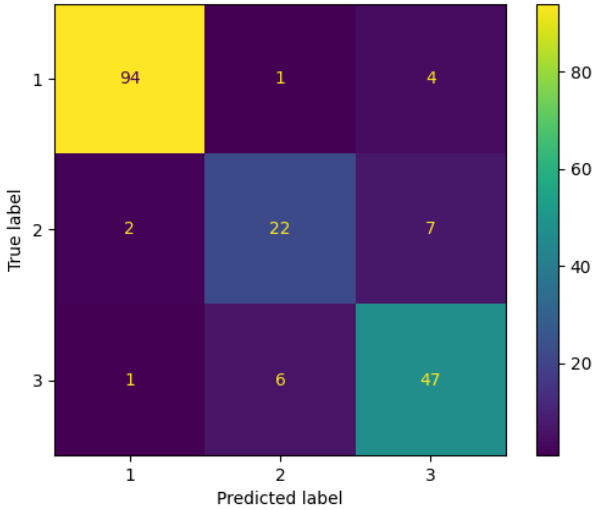

Figure 3. Confusion matrix results

Figure 3 illustrates the results of the confusion matrix. The high-performance confusion matrix demonstrates the several advantages of the technique. It emphasizes not just the model's ability to reliably identify examples, but also its ability to decrease misclassifications. As a result, diagnostic accuracy improves, false positives are minimized, and overall clinical decision support improves, ultimately contributing to more effective disease management and patient care.

Table 3 shows a comparative study of the performance of our suggested model on different sized datasets. Important performance indicators like training time, prediction time, accuracy, and memory utilization are highlighted in the table. Three different dataset sizes—small (800 rows), medium (1000 rows), and big (1400 rows)—are assessed using these metrics. The outcomes show how the model scales with increasing data quantity in terms of accuracy and efficiency, offering important information about how well-suited it is for various clinical circumstances and dataset complexity. The value of second is averaged.

Table 3: Performance Analysis of the Proposed Model for Varying Dataset Sizes

Dataset Size	Model	Training Time	Prediction Time	Accuracy	Memory Usage (Training)	Memory Usage (Prediction)
Small (1100 rows)	Proposed Model	10 seconds	1 second	83%	204 MB	50 MB
Medium (2200 rows)	Proposed Model	12 seconds	2 seconds	85%	411 MB	96 MB
Large (4000 rows)	Proposed Model	15 seconds	4 seconds	89%	622 MB	231 MB

In this paper, a novel hybrid modeling strategy was presented that takes advantage of the synergistic advantages of two different methods: the histogram-based gradient boosting classifier tree and the random subspace approach. The major goal was to develop a prediction model optimized for the assessment of blood disorders, with a particular emphasis on tumor detection.

Table 4 offers a thorough summary of the most important hematology-related studies that use machine learning methods. It contains each study's title, author names, scope, particular machine learning techniques employed, and key conclusions or contributions from each study. The table also highlights the progress and difficulties in applying machine learning to different hematological aspects by contrasting and comparing the methods and results of these studies. This compilation is a useful tool for learning about the state of machine learning applications in this important field of medical research as well as their future potential.

Table 4: Compilation and comparsion of Machine Learning Studies in Hematology

References	**Objective**	**Dataset**	**Method**	**Performance**
[48]	Predict acute lymphoblastic leukemia (ALL)	336 diagnosed children with ALL	Random forest algorithm	Accuracy: 0.829 AUC: 0.902
[49]	Predict chronic myeloid leukemia (CML)	Complete blood count records of 1623 people with CML	XGBoost and LASSO	AUC range: 0.87-0.96
[50]	Detection of leukemia and its types	220 blood smear images from healthy individuals and patients with leukemia	support vector machine	Accuracy: 0.80
[51]	Leukemia image segmentation	The Acute Lymphoblastic Leukemia Image Database	HSCRKMb/particle swarm optimization/K-means	Accuracy: 0.80
[17]	Prediction of complete remission of acute myeloid leukemia	473 bone marrow samples	K-nearest neighbor, support vector machine, and hill climbing	AUC :0.84
Proposed Model	**Prediction the tumor of blood disease**	**The 4000 samples for hematology**	**The Histogram-based Gradient Boosting Classification Tree with Random Subspace Method**	**Accuracy :0.896 Precision :0.894 Recall :0.864 F1 score:0.862 AUC :0.967**

The findings show that suggested model outperforms other classifiers in predicting blood disease tumors. This accomplishment highlights the study's approach potential therapeutic relevance and utility in assisting medical practitioners in the early detection of these crucial illnesses.

This study's methodology is unique in that it combines the Random Subspace Method with the Histogram-based Gradient Boosting Classification Tree. The goal of this special pairing, which hasn't been discussed in the literature before, is to maximize the advantages of both approaches. Although the Gradient Boosting based on Histogram provides a strong instrument for managing intricate data structures, the Random Subspace Method improves the model's capacity to generalize and function in various diagnostic situations. This technology offers a more sophisticated and useful tool for early blood problem diagnosis, marking a substantial shift from conventional diagnostic techniques.

It is worth noting that the encouraging results of this study pave the path for additional research and therapeutic applications. The accuracy and effectiveness of the model suggest that it could be a useful tool in the field of healthcare, particularly for the early diagnosis of blood diseases. However, it is critical to recognize the study's limitations, such as the size of the dataset and the necessity for real-world validation.

4. Conclusion

Blood disorders are a broad category of medical illnesses that can have a significant impact on the correct functioning of the circulatory system. This broad range of illnesses produces a variety of symptoms that can range from minor to severe, depending on the exact type and unique patient features. Among the many blood illnesses include leukemia, chronic myelocytic leukemia, lymphoma, myelofibrosis, polycythemia, thrombocytopenia, anemia, and leukocytosis. Understanding these illnesses is critical because they have a wide range of consequences, from those that can be adequately managed to those that can be fatal.

Early detection of blood problems is one of the most difficult challenges in the field of blood disorders. An accurate diagnosis is critical for commencing appropriate therapeutic interventions, which can have a major impact on patient outcomes. However, due to the intricacy of the underlying illness processes, detecting blood problems in their early stages can be extremely difficult.

In conclusion, the findings of the study show the utility of hybrid modeling strategies in the context of blood condition assessment, particularly tumor prediction. These findings lay the groundwork for future research efforts aimed at improving early detection, treatment, and overall outcomes for those affected by blood diseases.

Acknowledgement

This research did not receive any specific grant from funding agencies in the public, commercial, or not-for profit sectors.

Author's Contributions

Ethics *(mandatory)*

There are no ethical issues after the publication of this manuscript.

References

[1] H. Singh, A. N. D. Meyer, and E. J. Thomas, 'The frequency of diagnostic errors in outpatient care: estimations from three large observational studies involving US adult populations', *BMJ Qual. Saf.*, vol. 23, no. 9, pp. 727–731, Sep. 2014, doi: 10.1136/bmjqs-2013-002627.

[2] T. M. Ghazal, A. U. Rehman, M. Saleem, M. Ahmad, S. Ahmad, and F. Mehmood, 'Intelligent Model to Predict Early Liver Disease using Machine Learning Technique', presented at the 2022 International Conference on Business Analytics for Technology and Security (ICBATS), IEEE, 2022, pp. 1–5.

[3] M. L. Graber, 'The incidence of diagnostic error in medicine', *BMJ Qual. Saf.*, vol. 22, no. Suppl 2, pp. ii21–ii27, Oct. 2013, doi: 10.1136/bmjqs-2012-001615.

[4] J. J. Deeks, P. M. Bossuyt, M. M. Leeflang, and Y. Takwoingi, *Cochrane handbook for systematic reviews of diagnostic test accuracy*. John Wiley & Sons, 2023.

[5] T. Badrick, 'Biological variation: Understanding why it is so important?', *Pract. Lab. Med.*, vol. 23, p. e00199, Jan. 2021, doi: 10.1016/j.plabm.2020.e00199.

[6] A. Alanazi, 'Using machine learning for healthcare challenges and opportunities', *Inform. Med. Unlocked*, vol. 30, p. 100924, 2022.

[7] P. Sanchez, J. P. Voisey, T. Xia, H. I. Watson, A. Q. O'Neil, and S. A. Tsaftaris, 'Causal machine learning for healthcare and precision medicine', *R. Soc. Open Sci.*, vol. 9, no. 8, p. 220638, 2022.

[8] M. Javaid, A. Haleem, R. P. Singh, R. Suman, and S. Rab, 'Significance of machine learning in healthcare: Features, pillars and applications', *Int. J. Intell. Netw.*, vol. 3, pp. 58–73, 2022.

[9] S. Aminizadeh *et al.*, 'The applications of machine learning techniques in medical data processing based on distributed computing and the Internet of Things', *Comput. Methods Programs Biomed.*, p. 107745, 2023.

[10] A. Y. Gill, A. Saeed, S. Rasool, A. Husnain, and H. K. Hussain, 'Revolutionizing Healthcare: How Machine Learning is Transforming Patient Diagnoses-a Comprehensive Review of AI's Impact on Medical Diagnosis', *J. World Sci.*, vol. 2, no. 10, pp. 1638–1652, 2023.

[11] M. Shehab *et al.*, 'Machine learning in medical applications: A review of state-of-the-art methods', *Comput. Biol. Med.*, vol. 145, p. 105458, Jun. 2022, doi: 10.1016/j.compbiomed.2022.105458.

[12] K. Arumugam, M. Naved, P. P. Shinde, O. Leiva-Chauca, A. Huaman-Osorio, and T. Gonzales-Yanac, 'Multiple disease prediction using Machine learning algorithms', *Mater. Today Proc.*, vol. 80, pp. 3682–3685, 2023.

[13] R. J. Means Jr *et al.*, *Wintrobe's clinical hematology*. Lippincott Williams & Wilkins, 2023.

[14] M. Auerbach, 'Optimizing diagnosis and treatment of iron deficiency and iron deficiency anemia in women and girls of reproductive age: clinical opinion', *Int. J. Gynecol. Obstet.*, vol. 162, pp. 68–77, 2023.

[15] R. Shouval *et al.*, 'Validation of the acute leukemia-EBMT score for prediction of mortality following allogeneic stem cell transplantation in a multi-center GITMO cohort', *Am. J. Hematol.*, vol. 92, no. 5, pp. 429–434, May 2017, doi: 10.1002/ajh.24677.

[16] Y. Arai *et al.*, 'Using a machine learning algorithm to predict acute graft-versus-host disease following allogeneic transplantation', *Blood Adv.*, vol. 3, no. 22, pp. 3626–3634, Nov. 2019, doi: 10.1182/bloodadvances.2019000934.

[17] O. Gal, N. Auslander, Y. Fan, and D. Meerzaman, 'Predicting Complete Remission of Acute Myeloid Leukemia: Machine Learning Applied to Gene Expression', *Cancer Inform.*, vol. 18, p. 117693511983554, Jan. 2019, doi: 10.1177/1176935119835544.

[18] G. Gunčar *et al.*, 'An application of machine learning to haematological diagnosis', *Sci. Rep.*, vol. 8, no. 1, p. 411, Jan. 2018, doi: 10.1038/s41598-017-18564-8.

[19] J. L. Malin, 'Envisioning Watson As a Rapid-Learning System for Oncology', *J. Oncol. Pract.*, vol. 9, no. 3, pp. 155–157, May 2013, doi: 10.1200/JOP.2013.001021.

[20] M. Deulofeu *et al.*, 'Rapid discrimination of multiple myeloma patients by artificial neural networks coupled with mass spectrometry of peripheral blood plasma', *Sci. Rep.*, vol. 9, no. 1, p. 7975, May 2019, doi: 10.1038/s41598-019-44215-1.

[21] C. J. Haug and J. M. Drazen, 'Artificial intelligence and machine learning in clinical medicine, 2023', *N. Engl. J. Med.*, vol. 388, no. 13, pp. 1201–1208, 2023.

[22] S. A. Alowais *et al.*, 'Revolutionizing healthcare: the role of artificial intelligence in clinical practice', *BMC Med. Educ.*, vol. 23, no. 1, p. 689, 2023.

[23] S. Palaniappan, R. V, B. David, and P. N. S, 'Prediction of Epidemic Disease Dynamics on the Infection Risk Using Machine Learning Algorithms', *SN Comput. Sci.*, vol. 3, no. 1, p. 47, Jan. 2022, doi: 10.1007/s42979-021-00902-3.

[24] S. Roy, P. Biswas, and P. Ghosh, 'Spatiotemporal tracing of pandemic spread from infection data', *Sci. Rep.*, vol. 11, no. 1, p. 17689, Sep. 2021, doi: 10.1038/s41598-021-97207-5.

[25] R. B. Ghannam and S. M. Techtmann, 'Machine learning applications in microbial ecology, human microbiome studies, and environmental monitoring', *Comput. Struct. Biotechnol. J.*, vol. 19, pp. 1092–1107, 2021, doi: 10.1016/j.csbj.2021.01.028.

[26] S. Yadav, M. K. Singh, and S. Pal, 'Artificial Intelligence Model for Parkinson Disease Detection Using Machine Learning Algorithms', Biomed. Mater. Devices, Mar. 2023, doi: 10.1007/s44174-023-00068-x.

[27] J. A. Roth, M. Battegay, F. Juchler, J. E. Vogt, and A. F. Widmer, 'Introduction to Machine Learning in Digital Healthcare Epidemiology', Infect. Control Hosp. Epidemiol., vol. 39, no. 12, pp. 1457–1462, Dec. 2018, doi: 10.1017/ice.2018.265.

[28] R. Das, 'A comparison of multiple classification methods for diagnosis of Parkinson disease', Expert Syst. Appl., vol. 37, no. 2, pp. 1568–1572, Mar. 2010, doi: 10.1016/j.eswa.2009.06.040.

[29] A. Tsanas, M. A. Little, P. E. McSharry, and L. O. Ramig, 'Nonlinear speech analysis algorithms mapped to a standard metric achieve clinically useful quantification of average Parkinson's disease symptom severity', J. R. Soc. Interface, vol. 8, no. 59, pp. 842–855, Jun. 2011, doi: 10.1098/rsif.2010.0456.

[30] M. A. Little and L. O. Ramig, 'Suitability of dysphonia measurements for telemonitoring of Parkinson's disease', Nat. Preced., 2008.

[31] M. K. Gourisaria, S. Das, R. Sharma, S. S. Rautaray, and M. Pandey, 'A deep learning model for malaria disease detection and analysis using deep convolutional neural networks', Int. J. Emerg. Technol., vol. 11, no. 2, pp. 699–704, 2020.

[32] N. M. Deshpande, S. Gite, and R. Aluvalu, 'A review of microscopic analysis of blood cells for disease detection with AI perspective', PeerJ Comput. Sci., vol. 7, p. e460, 2021.

[33] D. N. Patil and U. P. Khot, 'Image processing based abnormal blood cells detection', Int. J. Tech. Res. Appl., vol. 31, pp. 37–43, 2015.

[34] R. Sigit, M. M. Bachtiar, and M. I. Fikri, 'Identification of leukemia diseases based on microscopic human blood cells using image processing', presented at the 2018 International Conference on Applied Engineering (ICAE), IEEE, 2018, pp. 1–5.

[35] P. K. Das, B. Nayak, and S. Meher, 'A lightweight deep learning system for automatic detection of blood cancer', Measurement, vol. 191, p. 110762, 2022.

[36] D. O. Oyewola, E. G. Dada, S. Misra, and R. Damaševičius, 'A novel data augmentation convolutional neural network for detecting malaria parasite in blood smear images', Appl. Artif. Intell., vol. 36, no. 1, p. 2033473, 2022.

[37] K. Gupta, N. Jiwani, and N. Afreen, 'Blood pressure detection using CNN-LSTM model', presented at the 2022 IEEE 11th International Conference on Communication Systems and Network Technologies (CSNT), IEEE, 2022, pp. 262–366.

[38] T. O. Kim et al., ‘Predicting Chronic Immune Thrombocytopenia in Pediatric Patients at Disease Presentation: Leveraging Clinical and Laboratory Characteristics Via Machine Learning Models’, Blood, vol. 138, p. 1023, 2021.

[39] Y. Cheng et al., ‘Using Machine Learning Algorithms to Predict Hospital Acquired Thrombocytopenia after Operation in the Intensive Care Unit: A Retrospective Cohort Study’, Diagnostics, vol. 11, no. 9, p. 1614, 2021.

[40] X.-H. Zhang et al., ‘P1652: Machine-Learning-Based Mortality Predıction of Ich In Adults With Itp: A Natıonwıde Representatıve Multicentre Study’, HemaSphere, vol. 6, no. Suppl, 2022.

[41] Y. Zhou et al., ‘Severe anemia, severe leukopenia, and severe thrombocytopenia of amphotericin B deoxycholate-based induction therapy in patients with HIV-associated talaromycosis: a subgroup analysis of a prospective multicenter cohort study’, BMC Infect. Dis., vol. 23, no. 1, p. 707, 2023.

[42] A. T. Johnsen, D. Tholstrup, M. A. Petersen, L. Pedersen, and M. Groenvold, ‘Health related quality of life in a nationally representative sample of haematological patients’, Eur. J. Haematol., vol. 83, no. 2, pp. 139–148, 2009.

[43] U. Jäger et al., ‘Diagnosis and treatment of autoimmune hemolytic anemia in adults: Recommendations from the First International Consensus Meeting’, Blood Rev., vol. 41, p. 100648, 2020.

[44] E. Franco, K. A. Karkoska, and P. T. McGann, ‘Inherited disorders of hemoglobin: A review of old and new diagnostic methods’, Blood Cells. Mol. Dis., p. 102758, 2023.

[45] E. Grudzińska and M. Modrzejewska, ‘Modern diagnostic techniques for the assessment of ocular blood flow in myopia: current state of knowledge’, J. Ophthalmol., vol. 2018, 2018.

[46] I. Voinsky, O. Y. Fridland, A. Aran, R. E. Frye, and D. Gurwitz, ‘Machine learning-based blood RNA signature for diagnosis of autism spectrum disorder’, Int. J. Mol. Sci., vol. 24, no. 3, p. 2082, 2023.

[47] S. Abd El-Ghany, M. Elmogy, and A. A. El-Aziz, ‘Computer-Aided Diagnosis System for Blood Diseases Using EfficientNet-B3 Based on a Dynamic Learning Algorithm’, Diagnostics, vol. 13, no. 3, p. 404, 2023.

[48] L. Pan et al., ‘Machine learning applications for prediction of relapse in childhood acute lymphoblastic leukemia’, Sci. Rep., vol. 7, no. 1, p. 7402, 2017.

[49] R. G. Hauser et al., ‘A machine learning model to successfully predict future diagnosis of chronic myelogenous leukemia with retrospective electronic health records data’, Am. J. Clin. Pathol., vol. 156, no. 6, pp. 1142–1148, 2021.

[50] P. Jagadev and D. H. G. Virani, "Detection of Leukemia and its Types using Image Processing and Machine Learning", 2017.

[51] H. Inbarani H., A. T. Azar, and J. G, ‘Leukemia Image Segmentation Using a Hybrid Histogram-Based Soft Covering Rough K-Means Clustering Algorithm’, Electronics, vol. 9, no. 1, p. 188, Jan. 2020, doi: 10.3390/electronics9010188.

[52] S. Kotsiantis, ‘Combining bagging, boosting, rotation forest and random subspace methods’, Artif. Intell. Rev., vol. 35, no. 3, pp. 223–240, Mar. 2011, doi: 10.1007/s10462-010-9192-8.

[53] J. Mielniczuk and P. Teisseyre, ‘Using random subspace method for prediction and variable importance assessment in linear regression’, Comput. Stat. Data Anal., vol. 71, pp. 725–742, Mar. 2014, doi: 10.1016/j.csda.2012.09.018.

[54] C. Bentéjac, A. Csörgő, and G. Martínez-Muñoz, ‘A comparative analysis of gradient boosting algorithms’, Artif. Intell. Rev., vol. 54, no. 3, pp. 1937–1967, Mar. 2021, doi: 10.1007/s10462-020-09896-5.

[55] F. Bulut, "Çok Katmanlı Algılayıcılar İle Doğru Meslek Tercihi", *Anadolu Univ. J. Sci. Technol.-Appl. Sci. Eng.*, vol. 17, no. 1, Apr. 2016, doi: 10.18038/btda.45787.

Bitlis Eren Üniversitesi Fen Bilimleri Dergisi
BİTLİS EREN UNIVERSITY JOURNAL OF SCIENCE
ISSN: 2147-3129/e-ISSN: 2147-3188
VOLUME: 12 NO: 4 PAGE: 1275-1288 YEAR: 2023
DOI:10.17798/bitlisfen.1379840

Last Mile Humanitarian Aid Delivery Model with Electric Vehicles to Disaster Areas

Mihrimah ÖZMEN[1]*, Rıza ÇELIK[1], Ülkü Nisa AYDOS[1], Melisa TEBER[1], Duygu Ceren AKTAŞ[1], Mehmet Fatih KAYA[2]

[1]*Erciyes University, Engineering Faculty, Industrial Engineering Department, Kayseri, Türkiye*
[2] *Erciyes University, Engineering Faculty, Energy Systems Engineering Department, Kayseri, Türkiye*

(ORCID: 0000-0002-2648-5865) (ORCID: 0009-0003-2518-4512) (ORCID: 0009-0008-7943-6662)
(ORCID: 0000-0002-0051-7603) (ORCID: 0009-0008-1467-060X) (ORCID: 0000-0002-2444-0583)

Keywords: Vehicle Routing Problem, Disaster, Last Mile Humanitarian Aid Delivery Model, Electric Vehicles

Abstract

Natural disasters that cause loss of life and property in Türkiye occur frequently. It is also very important to quickly deliver the necessary materials and equipment to people affected by these disasters. Therefore, in this study, Last Mile Humanitarian Aid Distribution with Electric Vehicles 0-1 Mixed Integer Mathematical Model is proposed due to the fuel problems that will be experienced during the disaster process. The proposed model calculates routes that minimize the total distance traveled by electric vehicles, while also considering their charging needs and energy consumption. Given the likelihood of power outages post-earthquake, the model prioritizes the use of solar-powered electric vehicle charging stations. 7 earthquakes with magnitudes between 4 and 5 occurred in Kayseri in 2023. In this study, an application was carried out for a possible earthquake close to the magnitude of the earthquakes that occurred in Kayseri in recent years. The application of this proposed model was demonstrated in an example of post-earthquake aid distribution using electric vehicles in Kayseri province. Distance data and consumed energy amounts for the Kayseri province example were entered into the model and solved in the CPLEX program. As a result, 3 identical electric vehicles met the demands and the total distance traveled by Vehicle 1 is 414.3 km, Vehicle 2 is 18 km and Vehicle 3 is 10.8 km. Additionally, the effectiveness of the use of energy-efficient electric vehicles in disaster management was evaluated in the article.

1. Introduction

Disasters are natural and human-induced events that can cause loss of life and property, affect the flow of life, and cause serious social and economic damage to society. Every year, millions of people in the world lose their lives due to disasters. For this reason, it is very important to take precautions against disasters and to provide timely aid to disaster victims in case of disasters.

* Corresponding author: *mihrimah@erciyes.edu.tr*
Received:23.10.2023, Accepted: 08.12.2023

Factors such as our country's geographical location and landforms lead to natural disasters. The Gölcük earthquake (1999), Van earthquake (2011), Izmir earthquake (2020), Elazığ earthquake (2020) and many such devastating earthquakes with high loss of life that occurred in the past years can be given as examples. It is the earthquake that occurred recently on February 6, 2023, in the Pazarcık and Elbistan districts of Kahramanmaraş, with a magnitude of 7.8 and 7.7, respectively, and affected 11 provinces. According to the Disaster and Emergency Management Presidency (AFAD), according to the latest data due to earthquakes, more than 50,000 people lost their lives, more than 108,000 people were injured, and more than 430,000 people had to leave their homes and the province they lived in and were resettled to other provinces.

Humanitarian aid logistics is the implementation of a planned and controlled approach from the starting node to the destination node, to reach the victims in an effectively planned manner in case of disaster and emergency, and to meet their needs at the right time and in the right place. Humanitarian aid logistics because of natural disasters is important to reduce the damage caused by the disaster as quickly as possible. In addition, this humanitarian aid logistics must be done quickly and at a low cost. Taking this into consideration, choosing the vehicles that provide logistics in this study as electric vehicles is very important in terms of cost savings and faster delivery, as well as preventing fuel problems that may occur since they can be supported by renewable energy. Another reason for choosing an electric vehicle in this study is prevent the use of harmful fossil fuels due to CO_2 release and greenhouse gases and emissions into the air.

Green logistics are logistics activities aimed at increasing economic efficiency by reducing transportation costs, reducing dependence on gasoline vehicles, and increasing environmental benefits. Countries are trying to integrate this understanding into society by enacting laws. For example, in Belgium, financial support is provided to people who want to buy an electric vehicle, and electric vehicles in the Flanders region are exempt from registration tax and ownership tax [1]. This kind of laws are very important for the adoption of the concept of green logistics.

It is extremely important to correctly route the electric vehicles we use in our study, which aims to ensure that the humanitarian aid distribution model is carried out at the lowest cost and in the shortest distance, considering the concept of green logistics. For this reason, in our study, a last-mile humanitarian aid distribution model was created to ensure optimal routing. The term 'last mile' is used because it represents the final direct transportation leg from the airport to the hospital.

A study was conducted on Kayseri, which we discussed in the context of the problem because it is situated near significant earthquake fault lines and is classified as a third-degree earthquake zone [2]. A mixed integer (0-1) mathematical model was created for last-mile humanitarian aid distribution with electric vehicles from Erkilet Airport to selected hospitals in Kayseri province. Solar charging stations in certain regions have been selected to meet the battery charging needs of electric vehicles. The model was solved in the CPLEX program and aid routes to hospitals were created in the shortest distance. In addition, the battery tracking of the vehicles is also monitored.

In Section 2, the literature on disasters and vehicle routing problems is presented. Section 3 provides an explanation of the methods employed. In Section 4, the proposed mathematical model for last-mile humanitarian aid delivery, utilizing 0-1 mixed-integer electric vehicles, is presented and elucidated. The developed model was applied to Kayseri province, and the results are detailed in Section 5. Section 6 covers scenario analysis, encompassing a broad spectrum of potential fluctuations and increases in patient demands, with subsequent presentation of results and discussion. Section 7 includes the results and recommendations.

2. Literature Review

Disaster is called a natural, technological, and human-origin event that causes material and moral damage to people and human-made artifacts and affects societies in the form of stopping or interrupting everyday life and

human activities [3-6]. The disasters that have occurred all over the world have caused great destruction and brought with them the necessary precautions and responsibilities as a result.

There is a lot of research conducted on disasters. For example, in Akin and Ordu [7] study on the COVID-19 pandemic, which recently occurred on Earth and caused the death of many people, a new simulation based on two-stage optimization has been developed to determine the shifts and numbers of nurses working for the Covid19 service in a Turkish Public Hospital. This study was performed in three stages. In the first stage, a simulation model was developed to determine the number of nurses required per week and scenarios based on increased patient activity. In the second stage, the first mathematical model was applied to determine the number of weekly shifts. In the third stage, fair nurse shift planning has been prepared for the pandemic service. With the model created as a result of the study, it has been observed that well-balanced planning was achieved among the nurses working in the COVID-19 service. This study is significant, as it will enable health managers to plan for personal needs during the next surges of the COVID-19 pandemic.

In another study about COVID-19, a Data Envelopment Analysis (DEA)-based model has been developed to evaluate the effectiveness of regions against a pandemic outbreak to better manage the fight against the epidemic by the relevant authorities and implement emergency action plans [8]. The DEA method has been used to measure the productivity scores of countries. DEA is an extremely popular technique that is applied to a wide range of sectors, including healthcare, education, agricultural culture, finance, and manufacturing services. It is a method that provides meaningful results for comparative performance. This method was utilized in the study to improve both reliable rankings of countries and health services. In the study, 16 countries have been selected that after the confirmed hundredth cases, undergo at least five weeks of continuous pandemic process. 16 DEA models have been developed for each week. The percentage of fertile countries decreased significantly from 43.75% in the first week to 25% in the fifth week. Unlike most European countries, China and South Korea have increased their effectiveness by implementing all the necessary measures after the first week. This study sheds light on the effectiveness of the policies adopted by the countries and the management strategies in the fight against the COVID-19 pandemic for the better by standing.

Another study conducted on the disaster in Turkey is on the emergency service network for the possible earthquake disaster in Istanbul [9]. The hybrid study includes artificial neural networks (ANN) to estimate the number of casualties and discrete event simulation to analyze the impact of the increase in patient requests in the emergency department after the earthquake. In the study, the five emergency service region networks that are estimated to have the highest injury rate after an earthquake in Istanbul were selected. The study consists of three stages. In the first stage, the earthquake casualty model is run for the next stage with ANN. In the second stage, the Earthquake Time Emergency Department Network Simulation Model creates the performance outputs of simulated emergency departments with the ANN outputs of the first stage. In the last stage, the simulation results are evaluated and produce some practical results for planning. The model has been run more than once because the region studied is large and there are stochastic variables. For each of the 432 scenarios, five repetitions were made with random numbers cause five repetitions are enough to make inferences. To compare the simulation scenarios, variance analysis (ANOVA) was performed with the Minitab program with a significance level of 5%. This study is important in terms of the lack of a study on emergency service simulation in earthquake disasters.

Disaster logistics is very important for emergency response to people in case of disaster and providing the materials they need. There are quite important studies on this topic in the literature. The selection of the ideal disaster warehouse location for disaster logistics made by Ergun et al (2020) is one of these studies [10]. In the study, the selection of the ideal disaster warehouse location in Giresun for disaster logistics was selected. The reason why the disaster storage place of the study was

established in Giresun is that floods and landslides occur frequently in the city. In addition, the fact that the districts in the inner parts of Giresun are close to the fault lines is one of the reasons for being chosen. The AHS method was used to determine the alternatives in the selection of the warehouse location. Later, the selection of the ideal disaster storage location was carried out by AHS-based MAUT and SAW methods. AHS is a mathematical approach used in decision making and measurement. The MAUT method is the method of finding the most useful alternative with quantitative and qualitative criteria. In the SAW method, the highest performing alternative is selected by sorting the alternatives first after matrix normalization. In the study, infrastructure was determined as the most important criterion for choosing the ideal disaster storage location for sustainable disaster logistics. Location is the main criterion, while you are the least important. It is an exemplary study because there is no such study in the literature reviews.

Another valuable study in disaster logistics is Tezcan et al (2021) [11]. In the study, temporary storage location selection and a multi-vehicle vehicle routing application were made after the disaster. The study was applied in Kırıkkale province. The reason why Kırıkkale was chosen is that it is the intersection of 43 provinces, the fact that there are large industrial enterprises located between Ankara and Kırıkkale increases the importance of the temporary warehouse to be established in the city in case of a possible earthquake other than Kırıkkale. The problem has been addressed in three stages. In the first stage, the alternative four districts and in the second stage, the alternative six locations were decided using the multi-criteria decision-making method. After the location of the temporary warehouse was determined, the route of food distribution was determined in the third stage. The methods used, AHP, FAHP, TOPSIS, PROMETHEE and VIKOR methods were used. In the first stage, when the districts were sorted, it was determined that the best location was Yahşihan district. In the second stage, it has been determined that the best alternative from six locations in Yahşihan district is the southern parking area. In the third stage, it is determined by which route the food will reach the disaster victims. The study provides convenience in post-disaster planning.

In their study, Küçük and Çavdur (2019) modeled and solved the distribution problem of post-disaster relief materials as a Time-Window Divided-Distributed Vehicle Routing Problem (ZPBD-ARP) [12]. Moreover, Cavdur et al (2016) [13], using the results of the model developed by the initial distribution problem is divided into smaller dimensional transport problems, which are solved as ZPBD-ARP. In the model developed by Cavdur et al (2016) [13], the locations of temporary facilities, the quantity, and the number of relief materials to be distributed to disaster victims are determined. The determined optimal amounts of relief material distribution, the amounts to be transported from the facilities to the disaster victims were taken as inputs to the model. In the study, the solution of the distribution problem after the disaster was provided by considering the data of the earthquake sample event in Bursa province. The ZPBD-ARP model was coded in Mathematical Programming Language (MPL) environment and decoded by Gurobi program. In the study, the route was designed to meet the potential maximum demand, considering the worst-case earthquake scenario.

The implementation of humanitarian aid logistics in a planned and controlled manner from the starting point to the destination to meet the needs of the victims of disasters and emergencies in an effectively planned manner and the right place to meet their needs at the right time and in the right place is called humanitarian aid logistics. Humanitarian aid logistics as a result of natural disasters is important to reduce the damage caused by disasters in the fastest way possible. In the study, electric vehicles were considered because fossil-fueled vehicles are expendable, high-cost, and quite harmful to the environment.

There are many studies in the literature on models that will enable vehicles to be rotated in the fastest way. When looking at electric vehicle routing problems (EARP), Çimen and Belbağ (2022) [14], one of the first studies to take into account the use of electric vehicles, contributes in terms of presenting a mixed integer linear programming-based solution

approach for solving the sustainable dynamic vehicle routing problem, in which electric vehicles are taken into account and demonstrating the applicability and value of the proposed method with the help of numerical analysis. This study, unlike other studies, wanted to draw attention to the issues of dynamic traffic density, electric vehicles, and social and environmental sustainability. In the results obtained with static and dynamic assumptions, it was seen that there is a faster delivery in the static case, and in future studies, it aimed to integrate issues such as time window or load capacity for dynamic parameters into the model, to enrich the literature on addressing different dynamic parameters such as changing or canceling demand points.

In another study conducted on EARP, a mixed integer linear programming model was proposed for a multi-use and time-window vehicle routing problem [15]. In the study, the relationship between the time window and vehicle capacity was questioned by constructing the model of 2 types of test classes. In each test class, the customers in type R problems are completely random, and in type C problems, the customers are concentrated in certain regions and placed. As a result of the study, it has been seen that the solution to the problem becomes easier as the restrictions on route times decrease. It has been found that RC-type problems have a higher Percentage Deviation Value compared to R and C-type problems.

The heterogeneous fleet method, which includes 8 different electric vehicles with different technical characteristics, was examined with EARP, which was considered by Desaulniers et al (2016) [16]. While the fuel capacities of vehicles are not included in the normal ARP, the charging capacities of vehicles, the amount of charge consumed at a unit distance, charging time, and battery capacity have been added as restrictions in EARP. Desaulniers et al (2016) [16] the studies carried out by Solomon also used the data set derived by Solomon for time-window vehicle routing. To test the validity of the first developed model, the model was run and developed the model. It has been observed that it has a shorter processing time compared to the model.

3. Methodology

3.1. Electric Vehicles

The rising population exacerbates energy and fuel-related challenges. Examining fossil fuel reserves reveals a limited 50-year supply [17]. Simultaneously, the detrimental impact of fossil fuels on the environment, including the release of greenhouse gases into the air, constitutes a significant drawback to their utilization. Another negative aspect of fossil fuel use is that fuel prices may increase depending on the dollar exchange rate in our country. As is widely known, vehicles, being crucial providers of transportation and logistics, rely on fuel or a propulsion system. Modern drive systems can be supplied by either electric vehicles with internal combustion engines or electric motors. Although it initially appeared more logical for the propelling force behind vehicle movement to be electric, the limited battery capacity and the absence of widespread charging stations necessary for electric vehicle charging made internal combustion engine vehicles more popular from the late 1800s to the early 2000s. In the early 2000s, with the spread of lithium batteries and the decrease in costs, electric vehicles entered our lives widely again. In this way, the damage caused by fossil fuels to the environment has been reduced over the years and vehicles have been moved efficiently with more efficient drive systems. The number of electric vehicles and stations in our country is increasing day by day. While this number was 1342 in the first three months of 2022, it became 4870 in the same period of 2023 (TUIK). The number of electric vehicles charging stations is 4498 according to the Electricity Market Regulatory Board. The number of electric vehicles in the world has exceeded 10 million (TURKSTAT). When looked at in this context, it is very important to make disaster, emergency, and other plans according to these systems that have become widespread in our country.

3.2. Renewable Energy Supported Charging Stations

Renewable energy: generally, covers the energy obtained from solar, wind, biomass, geothermal, and hydraulic energy sources. Since Kayseri province was considered as the subject of this study and Kayseri has a very high potential when sunshine hours were examined,

a model was developed by considering solar charging stations [18].

3.2.1 Solar Charging Stations

Solar energy is the energy released because of the fusion process in the core of the sun. Solar energy has an important place among renewable energy resources. Because it is known that the amount of energy is equal to 50 times the coal reserves and 800 times the oil reserves. We can produce more solar energy than Germany, which ranks first among the countries producing energy from the sun in the world. Electrical energy production by the photovoltaic method, which has an important place among solar energy production systems, is used more since it is cheaper than collector structures that provide production by thermal means. Photovoltaic solar cells consist of semiconductor materials and convert solar energy into electrical energy. The cells are connected, and a photovoltaic energy production system is created with solar panels, accumulators, converters, and various circuit elements. Solar charging stations also work in integration with these photovoltaic systems, appearing as an environmentally friendly method that reduces fuel costs [19].

3.3. Vehicle Routing Problem

Traveling Salesman Problem (TSP) is an optimization problem that returns to where it started after visiting all n nodes with known distances between each other at least once, and whose aim is to obtain the shortest route (minimum cost). TSP is classified as an NP-complete problem. Although TSP has many advantages, as the number of nodes increases, the probability of the resulting solution being optimal decreases. For this reason, various heuristic methods have been developed for a better solution. Some of these heuristics can be listed as: Ant Colony Optimization, Artificial Bee Colony Optimization, Genetic Algorithms, Particle Swarm Optimization, Tabu search, Differential Evolution, and Scatter Search algorithms. The traveling salesman problem method, which is used in many fields, especially logistics, still has a very important place today [20].

The vehicle routing problem is to ship products or services according to customers' needs in the logistics system. The vehicle routing problem consists of warehouses and customers. Products or services are sent from warehouses in the quantities requested by customers. While warehouses may be single, sometimes there may be more than one. In vehicle routing problems, when meeting the needs of customers, some targets are taken into consideration and the order in which distribution is more advantageous to the customers is preferred. Vehicle Routing Problem was first introduced to the literature by Dantzig et al (1959) [21]. This study focused on distributing gasoline to gas stations. In the study, the problem was solved with the aim of minimum transportation cost and minimum distance of the vehicle leaving a certain warehouse with certain constraints. After the studies of Dantzig and Ramser, studies were carried out on types of vehicle routing problems. (e.g., Cordeau et al., 2005 [22]). In the literature, the vehicle routing problem is known as an improved version of the traveling salesman problem.

4. Proposed Mathematical Model of Last Mile Humanitarian Aid Distribution with 0-1 Mixed Integer Electric Vehicles

In this study, a last-mile humanitarian aid distribution model with electric vehicles was proposed to meet the medical aid needs that may arise after the earthquake disaster in Kayseri. The assumptions of the proposed model are as follows:

• Hospitals will not be damaged after the earthquake occurs.
• In the event of an earthquake, power outages may occur. Therefore, if gas stations are unable to provide service, electric vehicles can be charged using solar charging stations.
•No other disaster will occur after the earthquake occurs.
•Electric vehicles will be available to receive medical aid from airports after the earthquake occurs.
• The roads that electric vehicles will use to deliver aid to hospitals will remain undamaged.

Indices
n: Airport and hospitals index
k: Hospitals index
l: Charging stations index
h: Airport index

t: All points index

Parameters
B: Vehicle battery capacity
vehicle_number: Number of vehicles
Cap: Vehicle material capacity

Clusters
C: Hospital cluster
DAC: All nodes cluster

CDD: Set of all nodes
Vehicle: Vehicle cluster
Charging: Set of charging stations
C1: Airport and hospitals cluster
q_i**:** i. hospital's request
RM_{ij}**:** Fuel consumption from node i to node j (kWh)
M_{ij}**:** Distance matrix of node i to node j (KM)

Decision Variables
u_i**:** Sub-route decision variable
$remaining\_fuel_{ijk}$**:** Decision variable showing the remaining fuel of vehicle k when it goes from node i to node j
x_{ijk}**:** k vehicle route decision variable $\begin{cases} 1, : \ 1, if\ vehicle\ k\ departs\ node\ i\ toward\ node\ j \\ 0, otherwise \end{cases}$
y_{ik}**:** $\begin{cases} 1, If\ vehicle\ k\ arrives\ at\ point\ i \\ 0, otherwise \end{cases}$
z_k**:** $\begin{cases} 1, if\ vehicle\ k\ is\ moving \\ 0, otherwise \end{cases}$
$current\_fuel_{ik}$**:** Current fuel value of vehicle k at node i

Min Z= $\sum_{i\in DAC} \sum_{\substack{j\in CDD \\ i\neq j}} \sum_{k\in arac} M_{ij} \times x_{ijk}$ *(1)*

Subject to

$\sum_{i\in DAC} \sum_{k\in vehicle} x_{ijk} = 1 \quad \forall_j \in C1, j \neq 1$ *(2)*
$\sum_{i\in DAC} \sum_{k\in vehicle} x_{jik} = 1 \quad \forall_j \in C1, j \neq 1$ *(3)*
$\sum_{\substack{j\in DAC \\ j\neq 1}} x_{1jk} \leq 1 \quad \forall_k \in vehicle$ *(4)*
$\sum_{\substack{j\in DAC \\ j\neq i}} x_{ijk} = \sum_{\substack{j\in DAC \\ j\neq i}} x_{ijk} \quad \forall_i \in DAC, \forall_k \in vehicle$ *(5)*
$u_j - u_i \geq 1 - M \times (1 - x_{ijk}) \quad \forall_{i,j} \in DAC \ i \neq j, i \neq 1, j \neq 1, \forall_k \in vehicle$ *(6)*
$\sum_{\substack{i\in DAC \\ i\neq 1}} x_{i1k} \leq 1 \quad \forall_k \in vehicle$ *(7)*
$\sum_{i\in DAC} \sum_{j\in DAC} x_{ijk} \leq t \times z_k \quad \forall_k \in vehicle$ *(8)*
$\sum_{i\in DAC} \sum_{j\in DAC} x_{ijk} \geq z_k \quad \forall_k \in vehicle$ *(9)*
$\sum_{j\in DAC} x_{ijk} + \sum_{j\in DAC} x_{jik} = 2 \times y_{ik} \quad \forall_i \in DAC, \forall_k \in vehicle$ *(10)*
$\sum_{\substack{i\in DAC \\ i\neq 1}} \sum_{\substack{j\in DAC \\ j\neq 1 \\ i<j}} x_{ijk} \leq \sum_{\substack{i\in DAC \\ i\neq 1}} y_{ik} - y_{zk} \quad \forall_z \in DAC, z \neq 1, \forall_k \in vehicle$ *(11)*
$\sum_{i\in DAC} \sum_{k\in vechicle} x_{iik} = 0$ *(12)*
$\sum_{i\in DAC} \sum_{j\in C} q_j \times x_{ijk} \leq Cap \quad \forall_k \in vehicle$ *(13)*
$x_{ijk} \geq 1 \Rightarrow current\_fuel_{jk} = B \times x_{ijk} \quad \forall_i \in DAC, \forall_j \in charging, , \forall_k \in vehicle$ *(14)*
$x_{ijk} \geq 1 \Rightarrow remaining\_fuel_{ijk} = B \times x_{ijk} \quad \forall_i \in DAC, \forall_j \in charging, \forall_k \in vehicle$ *(15)*
$remaining\_fuel_{ijk} = B - x_{ijk} \times RM_{ij} \quad \forall_i \in DAC, i = 1, \forall_j \in C, \forall_k \in vehicle$ *(16)*
$x_{ijk} \geq 1 \Rightarrow current\_fuel_{jk} = remaining\_fuel_{ijk} \quad \forall_i \in DAC, \forall_j \in C1, \forall_k \in vehicle$ *(17)*
$remaining\_fuel_{ijk} = current\_fuel_{jk} - x_{ijk} \times RM_{ij} \quad \forall_i \in DAC, i \neq 1, \forall_j \in DAC, j \notin charging, \forall_k \in vehicle$ *(18)*
$remaining\_fuel_{ijk} \leq RM_{jz} \Rightarrow x_{izk} = 1 \quad \forall_i \in DAC, \forall_j \in C, i \neq j, \forall_k \in vehicle, \forall_z \in Charging$ *(19)*
$current\_fuel_{ik} \geq \min(s \in charging)\ RM_{is} \quad \forall_i \in DAC, \forall_j \in DAC, \forall_k \in vehicle$ *(20)*
$current\_fuel_{ik} \leq B \quad \forall_i \in DAC, \forall_j \in DAC, \forall_k \in vehicle$ *(21)*
$remaining\_fuel_{ijk} \geq min(s \in charging)\ RM_{js} \quad \forall_i \in DAC, \forall_j \in DAC, \forall_k \in vehicle$ *(22)*
$remaining\_fuel_{ijk} \leq B \quad \forall_i \in DAC, \forall_j \in DAC, \forall_k \in vehicle$ *(23)*
$x_{ijk} \in (0,1) \quad \forall_i \in DAC, \ \forall_j \in DAC, \ \forall_k \in vehicle$ *(24)*
$z_k \in (0,1) \quad \forall_k \in vehicle$ *(25)*
$y_{ik} \in (0,1) \quad \forall_i \in DAC, \ \forall_k \in vehicle$ *(26)*
$u_i \in Z^+ \quad \forall_i \in DAC$ *(27)*
$remaining\_fuel_{ijk} \in R \quad \forall_i \in DAC, \forall_j \in DAC, \forall_k \in vehicle$ *(28)*

$$current\_fuel_{ik} \in R \qquad \forall_i \in DAC, \forall_k \in vehicle \qquad (29)$$

In the mathematical model, the objective function shown in equation (1) minimizes the total distance traveled. These are the constraints that ensure that (2) it must visit every node, while (3) it ensures that it leaves after visiting the nodes. (4) is the constraint that indicates that not all the tools in the tool set have to be used. Constraint (5) ensures that the vehicles entering a node and the vehicles leaving it are equal. (6) is the sub-round elimination constraint. Constraint (7) ensures the return to the warehouse. (8) limits the number of nodes it visits based on the number of exiting vehicles. Constraint (9) determines the lower limit based on the number of vehicles. Constraint (10) makes the sum of the number of vehicles entering and exiting the node equal to the number of vehicles. Constraints (11) and (12) ensure that the same node is not visited. Constraint (13) ensures that the vehicle does not exceed its cargo capacity. (14) is the constraint that makes the current charge value at the point equal to the battery capacity of the vehicle if the vehicle visits the charging point. Constraint (15) tracks the charge of the vehicle and shows the current charge value. Constraint (16) determines the remaining capacity of the battery as a result of the first step. (Such a constraint was added because a special situation occurred when the battery was at full capacity when leaving the warehouse in the first step.) Constraint (17) is the constraint that synchronizes the remaining charge of the vehicle with the current charge at the node. Constraint (18) determines the remainder as a result of the next step by taking the value of the previous node of the current one when it leaves the node where the remaining fuel value is entered and goes to the next node. Constraint (19) prevents the vehicle from stranding on the road by controlling the remaining fuel value of the vehicle. Constraint (20) determines the nearest charging stations that the vehicle can go to, considering its current value at the node. Constraint (21) ensures that the vehicle does not exceed the current charging battery capacity at the node. Constraint (22) ensures that the remaining charge of the vehicle is at least enough to get to the charging point. Constraint (23) ensures that the remaining fuel capacity is not exceeded. Constraints numbered (24-26) x, y and z can only take values 1 and 0. Constraints numbered (27-29) show the set elements.

5. Kayseri Province Application

In the problem under consideration, it is planned that the electric transit vehicle will provide the logistics. The capacity of this vehicle was determined as 600 units and distribution was made according to the demands of nine hospitals. Five solar charging stations were determined to meet the charging needs of electric vehicles. Information about the vehicle and charging station used in the application is included in Table 1.

Table 1. Electric vehicle and charging station power values used [23]

Vehicle Battery Capacity	68kWh
Solar Energy Supported Charger Power (Tomma Tech Commercial 120kW)	120 kW (DC)
Vehicle Charging Time 20%-80%	34 min

As shown in Table 1, Tomma Tech brand charging stations, capable of working in conjunction with solar energy, can charge the Ford E-Transit vehicle, with a battery capacity of 68kWh, to 80% in just 34 minutes. The data used in the study were obtained through the Google Maps program. A distance matrix was created on the map, indicating the distances from the airport, charging stations, and between hospitals in Kayseri province. The created distance matrix is given in Table 2. The fuel consumption matrix obtained by using the distance matrix is given in Table 3 below. The value in each cell is multiplied by 0.3 to calculate fuel burned by distance.

Table 2. Distance matrix

DISTANCES (KM)	Airport	Akkışla	Bunyan	Develi	Felahiye	Hacılar	İncesu	Kayseri State	Kayseri City	Talas	i1	i2	i3	i4	i5
Airport	0	85.9	44.3	50.6	50.6	17.5	36.4	5.4	9	13	5.9	5.6	11.5	29	21.4
Akkışla	85.9	0	52.9	121	70.1	92.4	116	80.3	85.6	83.6	81	77.6	88	104	69.9
Bunyan	44.3	52.9	0	90.5	55.9	55.5	79.1	43.4	48.6	46.5	44	40.7	51.1	67.1	33
Develi	50.6	121	90.5	0	93.1	33.9	54.4	44.4	52.3	39	41.2	43.6	51.8	20	55.5
Felahiye	50.6	70.1	55.9	93.1	0	66	87.5	53.9	57	57.1	52.6	49.6	59.4	75.7	48.9
Hacılar	17.5	92.4	55.5	33.9	66	0	33.7	11.9	19.3	15.5	13	15.3	16.6	16.7	26.4
İncesu	36.4	116	79.1	54.4	87.5	33.7	0	33.7	34.1	44.1	37	37.8	26.1	51.3	51
Kayseri State	5.4	80.3	43.4	44.4	53.9	11.9	33.7	0	9	11.1	2.1	4.9	8.3	25.2	15.3
Kayseri City	9	85.6	48.6	52.3	57	19.3	34.1	9	0	19.5	12.4	14.6	3,4	35.2	20.6
Talas	13	83.6	46.5	39	57.1	15.5	44.1	11.1	19.5	0	8.4	8.3	18.7	21.9	16.8
i1	5.9	81	44	41.2	52.6	13	37	2.1	12.4	8.4	0	2.8	11.3	24.4	14.5
i2	5.6	77.6	40.7	43.6	49.6	15.3	37.8	4.9	14.6	8.3	2.8	0	12.3	27.1	12.4
i3	11.5	88	51.1	51.8	59.4	16.6	26.1	8.3	3,4	18.7	11.3	12.3	0	32.4	24.1
i4	29	104	67.1	20	75.7	16.7	51.3	25.2	35.2	21.9	24.4	27.1	32.4	0	38.3
i5	21.4	69.9	33	55.5	48.9	26.4	51	15.3	20.6	16.8	14.5	12.4	24.1	38.3	0

Table 3. Fuel Consumption Matrix

FUEL CONSUMPTION	Airport	Akkışla	Bunyan	Develi	Felahiye	Hacılar	İncesu	Kayseri State	Kayseri City	Talas	i1	i2	i3	i4	i5
Airport	0	25.77	13.29	15,18	15,18	5.25	10.92	1.62	2.7	3.9	1.77	1.68	3.45	8.7	6.42
Akkışla	25.77	0	15.87	36.3	21.03	27.72	34.8	24.09	25.68	25.08	24.3	23,28	26.4	31.2	20.97
Bunyan	13.29	15.87	0	27.15	16.77	16.65	23.73	13.02	14.58	13.95	13.2	12,21	15.33	20,13	9.9
Develi	15,18	36.3	27.15	0	27.93	10,17	16.32	13.32	15.69	11.7	12.36	13.08	15.54	6	16.65
Felahiye	15,18	21.03	16.77	27.93	0	19.8	26.25	16,17	17.1	17,13	15.78	14.88	17.82	22.71	14.67
Hacılar	5.25	27.72	16.65	10,17	19.8	0	10,11	3.57	5.79	4.65	3.9	4.59	4.98	5.01	7.92
İncesu	10.92	34.8	23.73	16.32	26.25	10,11	0	10,11	10.23	13.23	11.1	11.34	7.83	15.39	15.3
Kayseri State	1.62	24.09	13.02	13.32	16,17	3.57	10,11	0	2.7	3.33	0.63	1.47	2.49	7.56	4.59
Kayseri City	2.7	25.68	14.58	15.69	17.1	5.79	10.23	2.7	0	5.85	3.72	4.38	1.02	10.56	6.18
Talas	3.9	25.08	13.95	11.7	17,13	4.65	13.23	3.33	5.85	0	2.52	2.49	5.61	6.57	5.04
i1	1.77	24.3	13.2	12.36	15.78	3.9	11.1	0.63	3.72	2.52	0	0.84	3.39	7.32	4.35
i2	1.68	23,28	12,21	13.08	14.88	4.59	11.34	1.47	4.38	2.49	0.84	0	3.69	8.13	3.72
i3	3.45	26.4	15.33	15.54	17.82	4.98	7.83	2.49	1.02	5.61	3.39	3.69	0	9.72	7.23
i4	8.7	31.2	20,13	6	22.71	5.01	15.39	7.56	10.56	6.57	7.32	8.13	9.72	0	11.49
i5	6.42	20.97	9.9	16.65	14.67	7.92	15.3	4.59	6.18	5.04	4.35	3.72	7.23	11.49	0

Table 4. Hospital Demands

Akkışla District State Hospital	5
Bünyan State Hospital	29
Develi State Hospital	66
Felahiye Integrated District Hospital	5
Hacilar Community Health Center	12
İncesu State Hospital	29
Kayseri State Hospital	410
Kayseri City Hospital	582
Talas Community Health Center	169

According to the AFAD, in 2023, Kayseri experienced a series of seven earthquakes ranging in magnitudes between 4 and 5. In response to the seismic activity, a study was conducted to develop a model for predicting potential earthquakes with magnitudes similar to those observed in recent years in Kayseri. The practical application of this proposed model was demonstrated through an example involving the distribution of post-earthquake aid using electric vehicles in the Kayseri province. Demands of hospitals are shown in Table 4. A commodity, such as a tent, needed by one in every thousand people affected by the disaster is taken as basis.

Therefore, the number of materials to be sent was determined by dividing the total population by thousand. The total demand for hospitals was determined as 1307, in direct proportion to the population of the districts considered. For example, while the population

of Akkışla district was 5563, the hospital demand was set at 5, following the same method for other districts. In the application, the distance data of the hospitals to each other, the airport, and the charging stations in Table 2 were used. In addition, the amount of fuel consumed by electric vehicles per 1 km to reach hospitals is determined in Table 3. At the same time, the demands of the hospitals and the capacity of the electric vehicle were specified in Table 4, ensuring that the materials were delivered by traveling the shortest distance.

The proposed Last Mile Humanitarian Aid Distribution Mathematical Model with 0-1 Mixed Integer Electric Vehicles was solved in the ILOG Cplex program for the Kayseri province application and the results were obtained. In practice, the total demand for 3 identical electric vehicles with a capacity of 600 and hospitals is 1307. In this case, the routes obtained by the model for 3 vehicles are given below.

Route of Vehicle 1: 1-7-4-14-6-10-12-3-2-15-5-1 and the total distance traveled by Vehicle 1: 414.3 km

Route of Vehicle 2: 1-9-1 and total distance traveled by Vehicle 2: 18 km

Route of Vehicle 3: 1-8-1 and total distance traveled by Vehicle 3: 10.8 km

Table 5. Routes obtained with the model for all vehicles.

Vehicle	Node i	Node j
1	1	7
1	7	4
1	4	14
1	14	6
1	6	10
1	10	12
1	12	3
1	3	2
1	2	15
1	15	5
1	5	1
2	1	9
2	9	1
3	1	8
3	8	1

The routes obtained as a result of the model are in Table 5, the current charge values at the nodes are in Table 6, and the route formed on the map is in Figure 1.

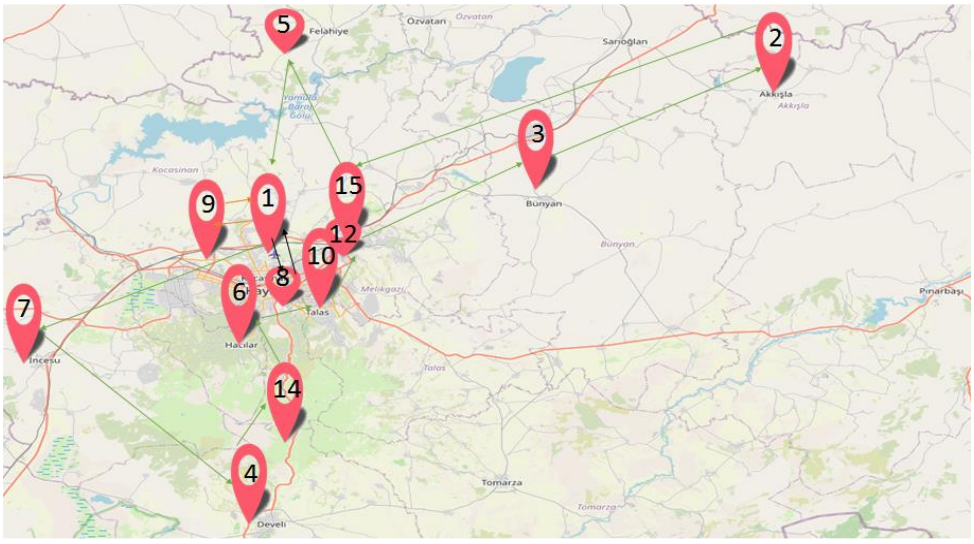

Figure 1. Representation of the route on the map

Table 6. Current Charge Values at the Point

All Nodes Cluster (DAC)	Vehicle (Size 3)		
	1	2	3
1	30.15	54.6	56.76
2	31.92	22,711	22,711
3	47.79	31,201	31,201
4	32.76	60	60
5	45.33	31,201	31,201
6	54.99	60	31,201
7	49.08	31,201	31,201
8	31,201	60	58.38
9	31,201	57.3	60
10	50.34	60	31,201
11	60	60	31,201
12	60	31,201	31,201
13	60	60	60
14	60	31,201	31,201
15	60	31,201	31,201

6. Results and Discussion

The objective of this research is to establish a Last Mile Humanitarian Aid Delivery Model utilizing electric vehicles for disaster areas. The significance of this research lies in addressing the critical aspect of last-mile humanitarian aid delivery, a phase often challenging to navigate due to its proximity to disaster-stricken areas. The utilization of electric vehicles introduces an eco-friendly and efficient approach to aid distribution, considering the potential benefits of reduced environmental impact and operational costs. The justification for employing electric vehicles in aid distribution will be explored, taking into account their potential for agility, reduced emissions, and lower operating costs compared to traditional vehicles.

In the literature, Kilic (2020) [24] optimized and compared the routing costs of electric and gasoline vehicles. Kabadurmus and Erdogan (2022) [25] addressed a dual-purpose time window green vehicle routing problem in their study, aiming to minimize carbon emissions.

The rationale behind the choice of Kayseri province as a case study is grounded in the recent seismic activity experienced in the region. The occurrence of multiple earthquakes with magnitudes between 4 and 5 underscores the importance of implementing an effective aid delivery system that can swiftly respond to the needs of affected communities. Furthermore, the study assesed the feasibility and practicality of the proposed model by considering real-life factors such as infrastructure, technology, and community engagement. By doing so, the study aims to provide insights into how the Last Mile Humanitarian Aid Delivery Model with Electric Vehicles can be implemented effectively in Kayseri and potentially serve as a benchmark for similar regions facing comparable challenges. This research endeavors to not only propose a Last Mile Humanitarian Aid Delivery Model tailored for Kayseri but also to establish a comprehensive justification for its adoption.

Finally, a sensitivity analysis was performed to assess the system's response to the broader spectrum of increased demand.

6.1. Sensitivity Analysis

In this section, a thorough scenario analysis was conducted, encompassing a wide range of potential fluctuations and increases in patient demands. Scenario analysis involves considering different possible situations or scenarios that could impact the system or process under investigation. In healthcare, scenarios could include changes in patient demographics, new disease outbreaks, changes in healthcare policies, or other factors that might influence patient demand. Fluctuations and increases in patient demand analysis likely involves exploring how the system responds to variations in the number of patients seeking healthcare services. This could be due to seasonal changes, unexpected events, or other factors that might lead to fluctuations or increases in patient demands. Sensitivity analysis is a technique used to understand how changes in one variable (in this case, patient demand) affect the outcomes of interest. It helps identify which factors have the most significant

impact on the system and which are less influential. The specific focus on the increase in patient demand suggests that the analysis is particularly interested in understanding how the system copes with higher-than-usual patient loads. This could involve assessing the capacity of healthcare facilities, the availability of resources, and the ability to adapt to sudden spikes in demand.

Different scenarios were defined a range of possible situations that could affect patient demand, considering both fluctuations and sustained increases. The demands of Kayseri State Hospital and Kayseri City Hospital were 410 and 582. In the scenario analysis, the demands of these hospitals were taken as constant so that they would not exceed the vehicle capacity of 600. In our mathematical model, constraint (13) ensures that the vehicle does not exceed its cargo capacity. Scenarios have been determined based on an increase in the demands of other hospitals from 5% to 50%. And these scenarios are listed in Table 7.

Each scenarios results were obtained from Proposed Last Mile Humanitarian Aid Distribution with Electric Vehicles 0-1 Mixed Integer Mathematical Model and results were given in Table 8.

Table 7. Scenarios of Kayseri Province Application

# Scenario	1	2	3	4	5	6
Demand	100%	105%	110%	115%	120%	150%
Akkışla	5	5.00	6.00	6.00	6.00	8.00
Bunyan	29	30.00	32.00	33.00	35.00	44.00
Develi	66	69.00	73.00	76.00	79.00	99.00
Felahiye	5	5.00	6.00	6.00	6.00	8.00
Hacılar	12	13.00	13.00	14.00	14.00	18.00
İncesu	29	30.00	32.00	33.00	35.00	44.00
Kayseri State	410	410	410	410	410	410
Kayseri City	582	582	582	582	582	582
Talas	169	177.00	186.00	194.00	202.00	254.00
objective function value (total distance)	443.1	443.1	443.1	443.1	443.1	443.1

Table 8. Routes obtained with the model for all vehicles and all scenarios.

# Scenario	Routes produced by the model for vehicles																**objective function value (total distance)**
1	Vehicle	1	1	1	1	1	1	1	1	1	1	1	2	2	3	3	443.1
	Node i	1	7	4	14	6	10	12	3	2	15	5	1	9	1	8	
	Node j	7	4	14	6	10	12	3	2	15	5	1	9	1	8	1	
2	Vehicle	1	1	1	1	1	1	1	1	1	1	1	2	2	3	3	443.1
	Node i	1	7	4	14	6	10	12	3	2	15	5	1	9	1	8	
	Node j	7	4	14	6	10	12	3	2	15	5	1	9	1	8	1	
3	Vehicle	1	1	1	1	1	1	1	1	1	1	1	2	2	3	3	443.1
	Node i	1	5	15	3	2	12	10	6	14	4	7	1	9	1	8	
	Node j	5	15	3	2	12	10	0	14	4	7	1	9	1	8	1	
4	Vehicle	1	1	1	1	1	1	1	1	1	1	1	2	2	3	3	443.1
	Node i	1	7	4	14	6	10	12	3	2	15	5	1	9	1	8	
	Node j	7	4	14	6	10	12	3	2	15	5	1	9	1	8	1	
5	Vehicle	1	1	1	1	1	1	1	1	1	1	1	2	2	3	3	443.1
	Node i	1	7	4	14	6	10	12	3	2	15	5	1	9	1	8	
	Node j	7	4	14	6	10	12	3	2	15	5	1	9	1	8	1	
6	Vehicle	1	1	1	1	1	1	1	1	1	1	1	2	2	3	3	443.1
	Node i	1	5	15	3	2	12	10	6	14	4	7	1	9	1	8	
	Node j	5	15	3	2	12	10	0	14	4	7	1	9	1	8	1	

According to the results, the model identifies different routes but maintains the same distance for all scenarios. These findings demonstrate the model's robustness in handling possible fluctuations and increases in patient demands. Scenario 1 presents the results based on the initial demand amounts without a demand increase. Other scenarios showcase the model's outcomes with demand increases of 5%, 10%, 15%, and, finally, 50%, respectively.

In Scenarios 2, 4, and 5, both the routes and distances are the same as in Scenario 1. In Scenario 3 and 6, the routes are identical, and their distances are the same as in Scenario 1.

7. Conclusion and Recommendations

Within the scope of this study, the issue of last-mile aid distribution after disaster was addressed with energy-efficient electric vehicles. Considering the problems encountered after the February 6 earthquake in our country, a 0-1 mixed integer last-mile humanitarian aid distribution model was developed. In the developed model, electric vehicles that can be charged at solar-powered stations were used, considering the power outages experienced after the disaster. The application of the proposed model was carried out with the example of Kayseri province. The model has 9 hospitals and 5 solar charging stations. The total demand for hospitals is assumed to be 1307. Erkilet Airport was chosen as the warehouse. Electric vehicles: 3 E-Transit vehicles with a battery capacity of 68 kWh and a material capacity of 600 units were preferred. Distance data and consumed energy amounts were entered into the model and solved in the CPLEX program. The model calculated the route for each vehicle that minimized the total distance. In the future, this study could provide support for our country to determine the most suitable routes for every natural disaster in every province and to provide immediate intervention and assistance without waiting in the event of a disaster. In the future, with meta-heuristic algorithms and artificial intelligence techniques, appropriate routes could be created for all provinces in case of natural disasters such as fire, flood, and landslide, and all kinds of humanitarian and medical aid will be provided to disaster victims in minimum time. In addition, these models could be expanded in our country and could set an example for other countries and the whole world could be prepared for possible disasters.

Acknowledgment

This work was supported by research grants from The Scientific and Technological Research Council of Türkiye (Project No: 121E406).

Thanks. This study was presented as a Graduation Paper at Erciyes University Industrial Engineering Department. We would like to thank the final paper jury for their valuable contributions.

We commemorate with mercy those who lost their lives in the earthquake of February 6, 2023.

Conflict of Interest Statement

There is no conflict of interest between the authors.

Statement of Research and Publication Ethics

The study is complied with research and publication ethics

References

[1] *Evbox.com*. [Online]. Available: https://evbox.com/en/learn/faq/incentives-buyingelectriccar. [Accessed: 25-Nov-2023].

[2] İ. A Gürbüz, B.aslan, "Kahramanmaraş Depreminde Hasar Tespit Çalışmaları Üzerine Bir Değerlendirme" *Çevre Şehir ve İklim Dergisi*, vol. 2, no. 4, pp. 180-195, 2023.

[3] Özey, R. (2006). *Afetler Coğrafyası*, Aktif Yayınevi, İstanbul

[4] O. Ergünay, *Türkiye'nin Afet Profili. TMMOB Afet Sempozyumu Bildiriler Kitabı*. Ankara, 2007.

[5] S.S. Durduran, A. Geymen, "Türkiye'de Afet Bilgi Sistemi Çalışmalarının Genel Bir Değerlendirilmesi", *Erciyes Üniversitesi 2. Uzaktan Algılama ve Coğrafi Bilgi Sistemleri Sempozyumu*,13-15 Ekim 2008, pp.1-9,

[6] T. Erkal and M. Değerliyurt, "Türkiye'de Afet Yönetimi," *Doğu Coğrafya Dergisi*, vol. 14, pp. 147–164, 2009.
[7] H. K. Akin and M. Ordu, "A Novel Simulation-Based Two-Stage Optimization Approach for Nurse Planning," *International Journal of Simulation Modelling (IJSIMM)*, vol. 21, no. 4, 2022.
[8] M. Ordu, H. Kirli Akin, and E. Demir, "Healthcare systems and Covid19: Lessons to be learnt from efficient countries," *Int. J. Health Plann. Manage.*, vol. 36, no. 5, pp. 1476–1485, 2021.
[9] M. Gul, A. Fuat Guneri, and M. M. Gunal, "Emergency department network under disaster conditions: The case of possible major Istanbul earthquake," *J. Oper. Res. Soc.*, vol. 71, no. 5, pp. 733–747, 2020.
[10] M. Ergün, S. Korucuk, and S. Memiş, "Sürdürülebilir Afet Lojistiğine Yönelik İdeal Afet Depo Yeri Seçimi: Giresun İli Örneği," *Çanakkale onsekiz mart Üniv. fen bilim. enst. derg.*, vol. 6, no. 1, pp. 144–165, 2020.
[11] B. Tezcan, H. M. Alakaş, E. Özcan, and T. Eren, "Afet Sonrası Geçici Depo Yeri Seçimi ve Çok Araçlı Araç Rotalama Uygulaması: Kırıkkale İlinde Bir Uygulama," *J. Polytech.*, vol. 26, no. 1, pp. 13-27, 2021.
[12] M. Köse Küçük and F. Çavdur, "Zaman Pencereli Bölünmüş-Dağıtımlı Araç Rotalama İle Afet Sonrası Yardım Malzemesi Dağıtımı Planlaması," *Uludağ Univ. J. Fac. Eng.*, vol. 24, no. 2, pp. 127–146, 2019.
[13] F. Cavdur, M. Kose-Kucuk, and A. Sebatli, "Allocation of temporary disaster response facilities under demand uncertainty: An earthquake case study," *Int. J. Disaster Risk Reduct.*, vol. 19, pp. 159–166, 2016.
[14] M. Çimen and S. Belbağ, "Elektrikli Araç Varsayımı Altında Sürdürülebilir Dinamik Araç Rotalama Problemleri: Karma Tamsayılı Doğrusal Programlama Tabanlı Bir Çözüm Algoritması," *3 sekt. Sos. Ekon. Derg.*, vol. 57, no. 3, pp. 1572-1592, 2022.
[15] Ç. Koç and İ. Karaoğlan, "Çok Kullanımlı Ve Zaman Pencereli Araç Rotalama Problemi İçin Bir Matematiksel Model," *Journal of the Faculty of Engineering & Architecture*, vol. 27, no. 3, pp. 569-576, 2012.
[16] G. Desaulniers, F. Errico, S. Irnich, and M. Schneider, "Exact algorithms for electric vehicle-routing problems with time windows," *Oper. Res.*, vol. 64, no. 6, pp. 1388–1405, 2016.
[17] J. Jannatkhah, B. Najafi, and H. Ghaebi, "Energy And Exergy Analysis of Combined Orc-Erc System for Biodiesel-Fed Diesel Engine Waste Heat Recovery," *Energy Conversion and Management*, vol. 209, 2020 .
[18] M. Oğuz and Ş. Akkurt, "Kayseri İlinin Yenilenebilir Enerji Potansiyeli" *Niğde Ömer Halisdemir Üniversitesi Mühendislik Bilimleri Dergisi*, vol. 6, pp. 362–374, 2017.
[19] F. Dinçer, "The analysis on photovoltaic electricity generation status, potential and policies of the leading countries in solar energy," Renew. Sustain. Energy Rev., vol. 15, no. 1, pp. 713–720, 2011.
[20] İ. Mumcu, E*lektrikli araçlar için güneş enerjisi ile çalışan şarj istasyonu ağı kurma* (Doctoral dissertation) 2019
[21] G. B. Dantzig and J. H. Ramser, "The truck dispatching problem," *Manage. Sci.*, vol. 6, no. 1, pp. 80–91, 1959.
[22] J.-F. Cordeau, M. Gendreau, G. Laporte, J.-Y. Potvin, and F. Semet, "A guide to vehicle routing heuristics," *J. Oper. Res. Soc.*, vol. 53, no. 5, pp. 512–522, 2002.
[23] "Ford E-Transit - Elektrikli Araç Modelleri," Com.tr. [Online]. Available: https://www.ford.com.tr/elektrikli-araclar/e-transit. [Accessed: 25-Nov-2023].
[24] K. Kılıç, "Elektrikli ve benzinli araç rota planlaması, maliyet optimizasyonu ve karşılaştırması," TOBB ETÜ Sosyal Bilimler Enstitüsü, ANKARA/TURKIYE, 2020.
[25] Ö. Kabadurmuş and M. S. Erdoğan, "Bi-objective Green Vehicle Routing Problem minimizing carbon emissions and maximizing service level," *Gazi Üniv. Mühendis.-Mimar. Fak. Derg.*, 2022.

Bitlis Eren Üniversitesi Fen Bilimleri Dergisi
BİTLİS EREN UNIVERSITY JOURNAL OF SCIENCE
ISSN: 2147-3129/e-ISSN: 2147-3188
VOLUME: 12 NO: 4 PAGE: 1289-1297 YEAR: 2023
DOI:10.17798/bitlisfen.1383335

Evaluating the Effect of Diameter-to-Length Ratio in Point Load Index Test on Predicting Uniaxial Compressive Strength

Deniz AKBAY[1*]

[1]*Çanakkale Onsekiz Mart University, Çan Vocational School, Department of Mining and Mineral Extraction, Çan, Çanakkale, Turkey*
(ORCID: 000-0002-7794-5278)

Keywords: Uniaxial Compressive Strength, Point Load Strength Index, Diameter-to-Length Ratio, Rock Material.

Abstract
Accurate determination of the strength properties of rock materials is very important in engineering projects. The most important parameter used to express the strength of rocks is the uniaxial compressive strength (UCS). However, in some cases it can be quite difficult to determine the UCS. For example, when it is difficult to obtain rock specimens of the required size for UCS testing, indirect methods such as point load strength and ultrasonic wave velocity are used to estimate UCS. If the UCS is determined incorrectly, this can lead to irreversible design errors, project delays and financial losses. PLI testing is performed on specimens of different shapes as well as on specimens of different sizes. This study investigates the ability of the values obtained as a result of PLI tests on specimens prepared with different diameter/length (D/L) ratios to predict UCS. For this purpose, PLI experiments were performed on seven different carbonate rocks prepared at different D/L ratios. The relationships between the obtained values and the UCS values of the rocks were analyzed. High correlations were obtained between PLI and UCS values and it was observed that D/L ratio has no significant effect on UCS estimation.

1. Introduction

In order to ensure the stability of structures in engineering projects, the strength properties of rock materials should be accurately determined in designs. The most commonly used mechanical parameters for demonstrating the strength properties of rock materials are the uniaxial compressive strength (UCS) and the point load strength index (PLI). These two parameters are commonly used as input for software used in the design of underground and surface engineering structures as well as tunnels. They also feature in numerous rock mass and excavation classification systems.

Rock specimens with the applicable dimensions must be used to determine the UCS according to the International Society for Rock Mechanics [1], [2]. However, the required size rock samples for UCS testing are very difficult to obtain in many cases, such as layered sedimentary rocks, schistosity metamorphic rocks and highly weathered rocks [2]. Therefore, indirect methods such as point load index (PLI) and ultrasonic wave velocity are used to estimate UCS. Incorrect determination of UCS can lead to errors in the design, which can damage the project [3]. There have been numerous studies on the correlations between UCS and PLI and more than 100 equations have been proposed to determine UCS values [4], [5]. To estimate the UCS, a wide range of coefficients from 3 to 71 must be multiplied by the PLI values of the rocks [6]. The reliability of PLI's UCS estimates is called into question due to this wide range of coefficients. There are several reasons for the wide coefficient range, including test method (specimen geometry), test apparatus and rock origin/type.

Determination of the PLI of rocks is a simpler, faster, and cheaper method when compared to the UCS. It is a method that can be used both in the field and laboratory without requiring specimen

*Corresponding author: denizakbay@comu.edu.tr
Received: 30.10.2023, Accepted: 04.12.2023

preparation or sampling whatsoever. Despite its advantages, errors arising from the equipment used and the operator are encountered during the determination of PLI. Loading speed and discrete loading, dial gauge (indicator) errors, conical platen geometry, distortion of conical platens from axis can be mentioned as some of these errors [6].

Core specimens (for both radial and axial testing), cut block specimens, or irregularly sized specimens may be used in the determination of the PLI. Due to this difference in available specimens, in order to obtain a unique PLI value for the rock specimen, a size correction must be applied. The size effect in the PLI test has been the subject of extensive investigations.

In their study, Franklin et al [7] found that PLI increased linearly as the length/diameter (L/D) ratio approached 1 in the diameter test and did not change much when L/D>1, while PLI decreased as the L/D ratio decreased in the axial test. Therefore, they suggested that the values obtained from axial tests should be corrected with a correction factor for size and shape effects. Wijk et al. [8] determined the tensile strength indirectly from the values obtained by performing PLI tests on granite and determined that the strength value decreases as the specimen volume increases. Al-Jassar and Hawkins [9] performed PLI tests on cube and core specimens of three different sizes and determined that the PLI values decreased as D (diameter=thickness) increased. Brook [10] carried out some tests on different limestone and sandstone specimens to determine the shape and size effect and emphasised the cross-sectional area. He argued that the 50 mm diameter correction factor proposed by Broch and Franklin [11] is difficult to apply in stratified rocks. Greminger [12] conducted experiments on four different rock types to determine how anisotropy affects the PLI due to shape and size effects. He recommended the use of 50 mm diameter specimens where possible, and where not, specimens with a minimum diameter of 30 mm that fulfil the $1 \leq L/D \leq 3$ condition. Forster [13] identified three basic problems for PLI (diametral testing in anisotropic rocks, specimen geometry for axial testing, and UCS/PLI relationship). He performed experiments on 7 different types of rocks with different length/diameter ratios and obtained similar results to previous studies. He stated that $0.5<L/D<1$ and D>30 mm for axial testing and proposed two different equations for the cases of D<50 mm and D>50 mm for axial testing. Broch [14] stated in his study that the method recommended by ISRM [15] should be used in the diametrical test and $0.5 D<L<D$ in the axial test. Brook [16], in his study, summarised the size and shape correction factors to date and made an evaluation. He used and defined the equivalent diameter expression. Abdallah [17] conducted PLI tests on unshaped (D=10-80 mm) and core (D=10-100 mm) specimens of different thicknesses for four different rock types. They determined that the PLI changed very sensitively in the experiments performed on specimens with a thickness below 10 mm, while there was no change in the specimens with a thickness above 70 mm, and it was independent of the size effect. As a result, they recommended $10 \text{ mm}<D<70 \text{ mm}$ (where D represents the distance between the conical platens). Chau [18], in his study, tried to determine the stress distributions in the specimen under tensile stress by PLI test. He emphasised that the tensile stress occurring in the middle of the specimens increases for $2L/D<1$, and remains roughly constant for $2L/D>1$. He found that the model he applied was consistent with the results obtained experimentally on marble, granite, and tuff. Wei et al. [19] determined that the widest rock has the lowest PLI for fixed L/D ratio and the thinnest specimen has the lowest PLI for fixed diameter value. In their study, Chau and Wei [20] found that circumferential stress is dominant in long cylinder specimens (L/D>7), while axial stresses are more intense in small specimens (L/D<4). They stated that the shape effect can be neglected when L/D=0.7. They suggested that specimens with large diameter values should not be used in the PLI test. Zacoeb and Ishibasi [21] recommended a diameter of 50 mm and an L/D ratio of 2 for the PLI test. Li et al. [22] stated that the height of the rock mass has a certain influence on the load point, whether the height is too large or too small has great effects. When using irregular specimens in the tests, they recommended the use of specimens with a height of 30 mm to 50 mm. Forbes et al. [23] through an experimental investigation of both axial and diametral PLI tests involving 374 specimens of Gosford sandstone. As a result of this investigation, they found that the PLI varies increasingly with specimen diameter for all investigated specimens at different length-to-diameter ratios. Masoumi et al. [24] compared the experimental results obtained in their study and concluded that the concept of "generalised size effect" was observed in which the strength decreases with increasing size in all rock types.

Studies in the literature have always sought answers to questions such as how PLI changes and how much it changes. However, in this study, the relationship between uniaxial compressive strength and PLI values obtained from specimens with different D/L ratios was also investigated. For this purpose, PLI experiments were performed on rock specimens prepared with different D/L ratios to

determine how the D/L ratio changes the PLI, and then the relationship between UCS and PLI values obtained from specimens prepared with different D/L ratios was examined.

2. Material and Method

2.1. Point Load Index

Core specimens (for diametrical and axial tests), cut block specimens, or irregular lump specimens can be used in the PLI tests. The required specimen dimensions according to the test types are given in Figure 1. The rock specimen, whose dimensions are measured and placed between the conical platens, is broken within a certain time (10-60 s) and the failure load is read from the load indicator. The load at which the rock is broken is recorded. If the test specimen is heterogeneous and anisotropic, the test is repeated 10 times. The lowest and highest two values are discarded. The arithmetic mean of the remaining six values is taken.

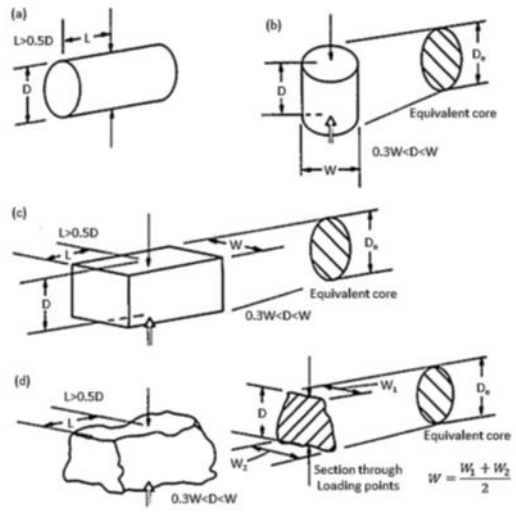

Figure 1. Specimen dimensions and limits for (a) diametral test specimen, (b) axial test specimen, (c) block specimen, and (d) an irregular lump [25].

ISRM [25] gives the types of failure modes for which the test should be considered valid or invalid in Figure 2. In particular, it is sufficient for the failure to be considered invalid if the failure surface does not pass through any loading point.

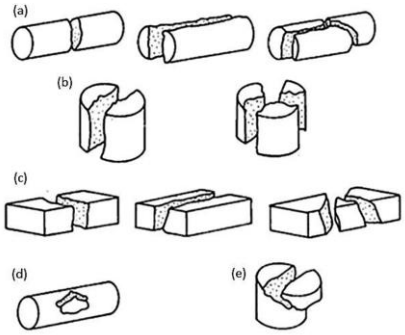

Figure 2. Failure modes for valid tests (a, b, c) and invalid tests (d, e) [25].

The After the test is completed, the uncorrected PLI is calculated by Equation 1:

$$I_s = \frac{P}{D_e^2} \qquad (1)$$

Where I_S is the uncorrected point loading strength (MPa), P is the failure load (kN, kgf, etc.) and D_e is the equivalent core diameter (mm). Equivalent core diameter is calculated by Equation 2 for diametrical specimens:

$$D_e^2 = D^2 \qquad (2)$$

Where D_e is the equivalent core diameter (mm) and D is the core diameter (mm). It is calculated by Equation 3 for axial test, block test, and irregular lumps:

$$D_e^2 = \frac{4 \times A}{\pi} \qquad (3)$$

Where D_e is the equivalent core diameter (mm) and A is the smallest cross-sectional area of the specimen passing through the contact points of the conical heads.

The value of I_S varies as a function of D in the diametral test and as a function of De in other types of tests. Therefore, the I_S value must be corrected for a standard core diameter (D=50 mm). The corrected $I_{S(50)}$ value is determined using a monogram (Figure 3) or graph (Figure 4) prepared for this purpose.

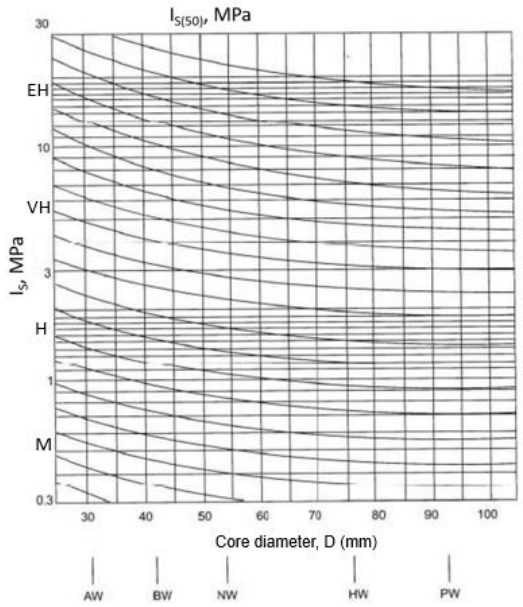

Figure 3. Corrected PLI determination nomogram [11] (M: Medium; H: High; VH: Very high; EH: Extremely high).

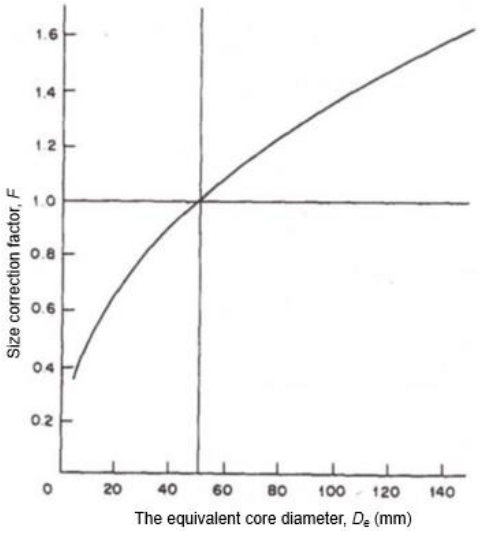

Figure 4. Size correction factor chart [25].

If there is no nomogram, the size correction factor is calculated by Equation 4 and the corrected PLI is calculated by Equation 5:

$$F = \left(\frac{D_e}{50}\right)^{0,45} \quad (4)$$

$$I_{s(50)} = I_s \times F \quad (5)$$

2.2. Experimental Study

In this study, seven different natural stones of sedimentary origin, which are generally used in building cladding and flooring applications, were used (Table 1). Some physical and mechanical properties were determined to characterise the rocks studied. All tests were performed according to the relevant standards recommended by the Turkish Standards Institute (TSE). Unit volume weight (UVW), water absorption percent by weight (WAW), apparent density (AP) of rocks were determined according to the EN 1925 [26]. The ultrasonic wave velocity (*Vp*) tests were measured on specimens cubical in shape having 70 mm edge length as specified in EN 14579 [27]. The UCS tests were conducted on specimens cubical in shape 50×50×50 mm as specified in the principles of EN 1926 [28] standard. The test results are presented in Table 1.

Table 1. Some physical and mechanical properties of the studied rocks

Specimen Code	Origin	Region	UVW t/m^3	AP %	WAW %	*Vp* m/s	UCS MPa
K-1	Sedimentary	Isparta	2.7	0.324	0.120	6168	155
K-2	Sedimentary	Antalya	2.7	0.267	0.099	6117	158
K-3	Sedimentary	Isparta	2.7	0.325	0.120	6154	122
K-4	Sedimentary	Burdur	2.7	0.409	0.151	6160	149
K-5	Sedimentary	Isparta	2.7	0.441	0.163	6286	98
K-6	Sedimentary	Afyon	2.7	0.425	0.157	6234	115
K-7	Sedimentary	Afyon	2.7	0.381	0.141	6258	117

UVW: unit volume weight; WAW: water absorption percent by weight; AP: apparent density; *Vp*: ultrasonic wave velocity; UCS: uniaxial compressive strength

Specimens for PLI tests with different D/L ratios were prepared according to the limit dimensions recommended by ISRM for specimens that can be used in PLI tests [25]. The specimens were placed in

the test apparatus as shown in Figure 5 for a simpler expression of the D/L ratio. Specimens with a diameter of 35 mm and a D/L ratio ranging from 0.39 to 1.08 were prepared for diametrical PLI test and specimens with a diameter of 35 mm and a D/L ratio ranging from 0.95 to 2.50 were prepared for axial PLI tests (Figure 6). PLI tests were applied on seven specimens for each test in accordance with the standard recommended by ISRM [25]. At the end of the tests, all specimens were broken in valid failure modes (Figure 7). The test results were presented in Table 2.

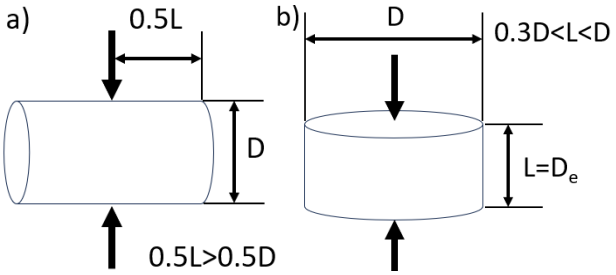

Figure 5. The specimen dimensions and limits for (a) diametral test specimen, (b) axial test specimen (modified from ISRM [25]).

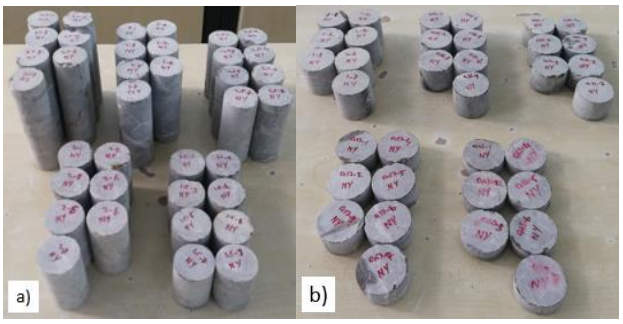

Figure 6. Specimens prepared for PLI tests a) diametral test, b) axial test.

Figure 7. Broken specimens after the PLI tests a) diametral test, b) axial test.

Table 2. The PLI values and D/L of the studied rocks

Specimen code	K-1		K-2		K-3		K-4		K-5		K-6		K-7	
Test type	D/L	PLI MPa	D/L	PLI MPa	D/L	PLI MPa	D/L	PLI MPa	D/L	PLI MPa	D/L	PLI MPa	D/L	PLI MPa
Diametral test	0.39	2.61	0.40	3.12	0.42	2.30	0.40	2.89	0.41	1.05	0.42	1.08	0.40	1.21
	0.55	4.10	0.57	4.10	0.55	3.21	0.56	3.70	0.53	1.41	0.55	1.59	0.55	1.94
	0.71	4.93	0.70	4.72	0.72	3.96	0.72	4.40	0.69	1.85	0.72	2.04	0.67	2.36
	0.79	5.36	0.78	5.46	0.83	4.65	0.82	4.94	0.78	2.28	0.81	2.39	0.80	2.98
	0.89	5.51	0.90	5.64	0.91	4.84	0.91	5.12	0.88	2.31	0.88	2.43	0.93	3.13
	1.04	5.46	1.06	5.62	1.02	4.83	1.08	5.10	1.05	2.33	1.04	2.45	1.05	3.08
Axial test	1.04	5.21	0.99	6.42	1.01	5.52	0.95	4.95	0.95	2.31	0.99	2.44	1.01	2.84
	1.21	4.74	1.23	5.81	1.21	4.82	1.20	4.60	1.23	2.04	1.25	2.10	1.20	2.50
	1.49	4.41	1.46	5.57	1.52	4.47	1.55	4.39	1.54	1.81	1.53	1.87	1.52	2.38
	1.82	4.13	1.82	4.58	1.82	3.59	1.84	4.23	1.76	1.47	1.85	1.40	1.83	2.02
	2.21	3.99	2.22	4.43	2.19	3.63	2.23	3.69	2.18	1.43	2.17	1.32	2.24	1.57
	2.50	3.67	2.39	4.10	2.41	3.12	2.40	3.68	2.38	1.20	2.40	1.05	2.39	1.47

3. Results and Discussion

The relations between PLI values and D/L ratios of the studied rocks were graphically investigated and the plots are shown in Figure 8 and Figure 9. In addition to the effect of D/L ratios, the correlations between PLI values and D/L ratios of the studied rocks were analyzed by simple regression. Significant relationships were found between PLI values and D/L ratios as expected. In diametral test, correlations vary between 0.92-0.97, and in axial test correlations vary between 0.96-0.99. In In Figure 8, the relationship between PLI and D/L ratios indicated that PLI values increased as the D/L ratios of the specimens became larger until D/L ratios of 1. It is observed that the PLI values almost do not change much after the critical D/L ratio of approximately 0.8. In other words, the PLI values increased as the D/L ratio of the specimens became larger—up to the critical D/L ratio of 0.8. After this value, PLI values did not change significantly as the D/L ratio approached towards 1. This ratio is also very close to the value D/L=1.0

ISRM's recommended upper limit for specimen's D/L ratio [25]. As can be seen in Figure 9, the PLI values have decreased as the D/L ratios increased. Moreover, PLI values were observed to increase as the specimen length (height) became near the specimen diameter. Therefore, the results indicated an apparent correlation between PLI and the length (height/thickness) of specimens.

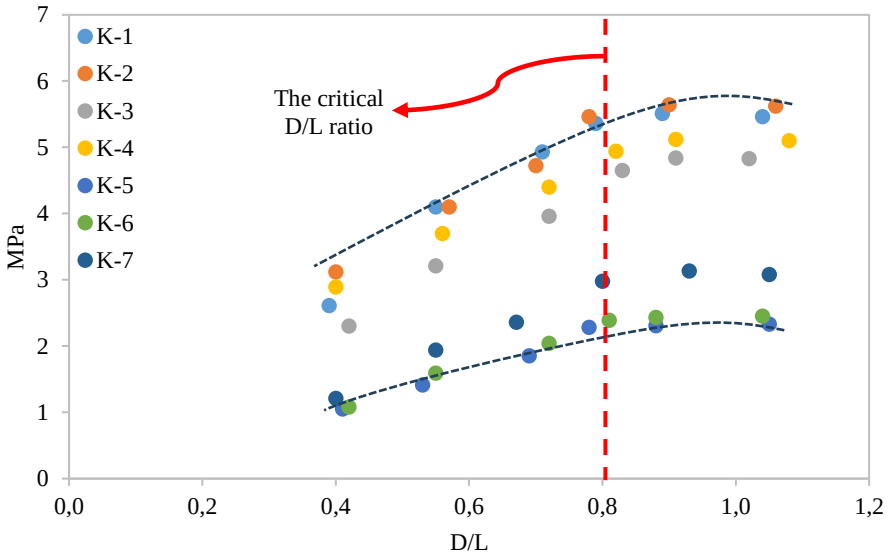

Figure 8. The relationships between the PLI and D/L ratios in diametral test.

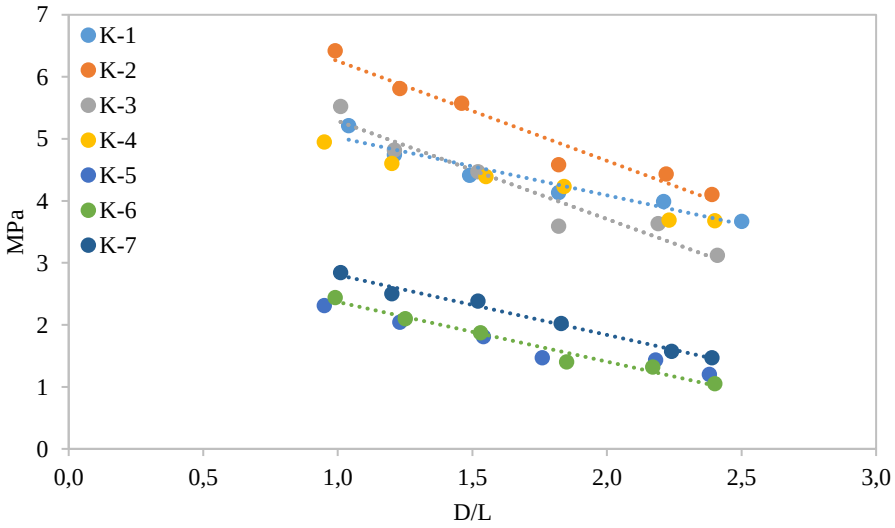

Figure 9. The relationships between the PLI and D/L ratios in axial test.

The study also examined the relationship between UCS and PLI. Similar results to those obtained in previous studies between UCS and PLI were obtained. Strong relationships with high correlation coefficients were found between UCS and PLI for both the diametral and axial tests. In diametral tests, linear relationships were determined between UCS and PLI values obtained from specimens prepared at different D/L ratios with correlation coefficients ranging from 0.91 to 0.94 (Figure 10). As a result of axial tests, correlations ranging from 0.84 to 0.91 were determined between UCS and PLI values obtained from specimens prepared at different D/L ratios (Figure 11). The correlations obtained from the diametral tests are slightly higher than the axial tests.

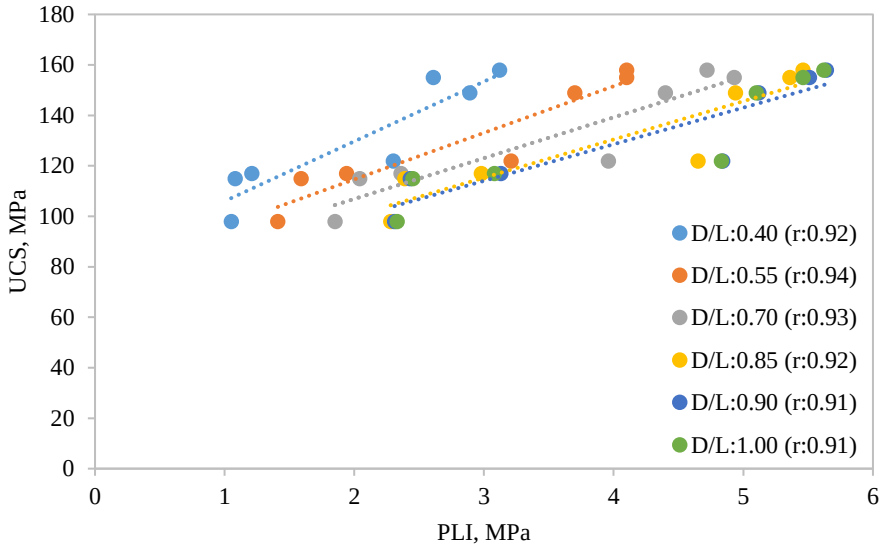

Figure 10. The relationships between the PLI and UCS in diametral test.

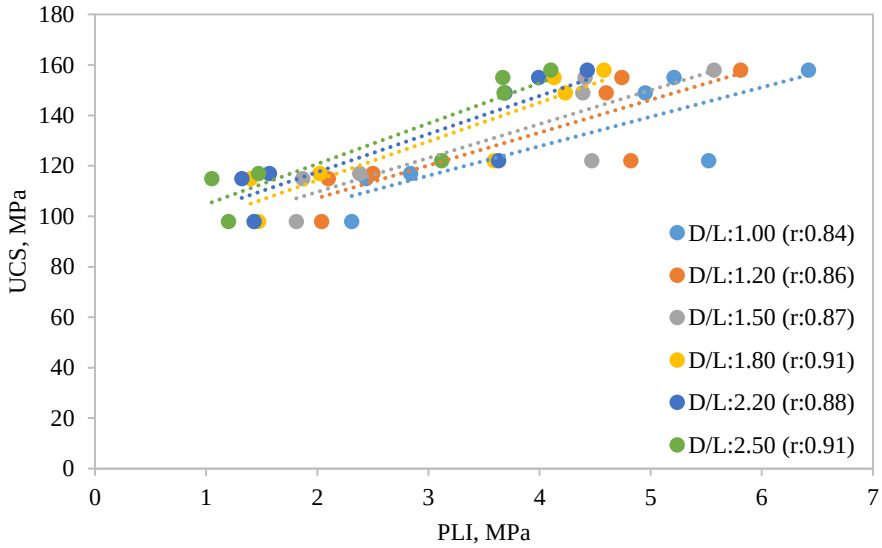

Figure 11. The relationships between the PLI and UCS in axial test.

4. Conclusion and Suggestions

The results obtained in this study show that the D/L ratio of the specimen significantly affects the determination of PLI values and is a parameter that should be taken into account in the evaluations of diametral and axial PLI tests.

It was determined that the PLI increased linearly as the D/L ratio approached 1.0 in the diametral test, and did not change much after 1.0, while the PLI decreased as the D/L ratio increased in the axial test, as stated by Franklin et al. [7] in their study.

The difference in the effect of the D/L ratio on the axial and diametral tests can be explained as diameter is a horizontal distance and length is a vertical distance in the axial tests whereas diameter is a vertical distance and length is a horizontal distance in the diametral tests. In the diametral test, the moment created by gravity due to the mass moving away from the centre as a result of neck elongation creates an additional tensile stress in the centre of the specimen in addition to the loading condition. Due to this extra stress, which is not read on the load indicator, the specimen breaks at low loads. As the D/L ratio approaches 1, in other words, as "L" approaches "D", the value of this extra stress decreases. Therefore, D/L=1 condition for diametrical test is the ideal D/L ratio.

In the axial test, for constant diameter, as the thickness increases, that is, as the length increases, the load required to break the specimen will increase, and as the thickness decreases, that is, as the length shortens, the load required to break the specimen will decrease. When examined in previous studies, the current size correction factor is not sufficient for this situation [21]. The main point to be considered here is that in order for the experiment to be considered valid, the failure must occur between 10-60 seconds as recommended by ISRM. In very long specimens, it takes more than 60 seconds for failure to occur, while in very short specimens it takes less than 10 seconds. In order to determine the ideal ratio, the stress distributions on the specimen at different length and diameter ratios should be analysed.

This study was carried out only on seven types of natural stones of carbonate origin and test specimens were prepared at six different D/L ratios. In future studies, the results of this study will become more meaningful if experiments are carried out on prepared specimens with more D/L ratios (especially the part in the range of D/L=0.8-1.0 can be increased) with rocks of different geologic origin.

When the relationships between the results obtained from the PLI tests on the specimens prepared at different D/L ratios and the UCS values of the rocks were analyzed, high linear relationships were determined for both diametral (r=0.91-0.94) and axial (r=0.84-0.91) tests. It was observed that PLI can be successfully used to predict UCS regardless of the D/L ratio. And also, it could be told that the correlations between the PLI values obtained as a result of the diametral tests only were slightly higher than the correlations between the PLI values obtained as a result of the axial tests.

The findings of this study may be specific to the tested rocks and may not be applicable to rocks of different origins or compositions. Further research is needed to validate the findings on a broader range of rock types.

Statement of Research and Publication Ethics

The study is complied with research and publication ethics.

References

[1] ISRM, *The complete suggested methods for rock characterization, testing and monitoring: 1974–2006.* London: Springer, 2007.

[2] A. Jamshidi, M. R. Nikudel, M. Khamehchiyan, R. Zarei Sahamieh, and Y. Abdi, "A correlation between P-wave velocity and Schmidt hardness with mechanical properties of travertine building stones," *Arab. J. Geosci*., vol. 9, no. 10, p. 568, Jul. 2016, doi: 10.1007/s12517-016-2542-3.

[3] M. Heidari, G. R. Khanlari, M. T. Kaveh, and S. Kargarian, "Predicting the uniaxial compressive and tensile strengths of gypsum rock by point load testing," *Rock Mech. Rock Eng*., vol. 45, no. 2, pp. 265–273, 2012, doi: 10.1007/s00603-011-0196-8.

[4] A. Jamshidi, "A Comparative Study of Point Load Index Test Procedures in Predicting the Uniaxial Compressive Strength of Sandstones," *Rock Mech. Rock. Eng*., vol. 55, pp. 4507–4516, Jul. 2022, doi: 10.1007/S00603-022-02877-W.

[5] D. Akbay, "Antalya-Kemer-Tekirova Karayolu Güzergâhinda Bulunan Altan Ayağ Tünelindeki (T3 Tüneli) Delik Delme Performans Analizi," M.S. thesis, Dept. Min. Eng., Süleyman Demirel Uni., Isparta, Türkiye, 2013.

[6] D. Akbay and R. Altındağ, "Reliability and evaluation of point load index values obtained from different testing devices," *J. South Afr. Inst. Min. Metall*., vol. 120, no. 3, pp. 181–190, 2020.

[7] J. A. Franklin, E. Broch, and G. Walton, "Logging the Mechanical Character of Rock," *Transactions of the Institution of Mining and Metallurgy*, vol. 80, no. A, pp. 1–9, 1971.

[8] G. Wijk, G. Rehbinder, and G. Lögdström, "The relation between the uniaxial tensile strength and the sample size for bohus granite," *Rock Mechanics Felsmechanik Mecanique des Roches*, vol. 10, no. 4, pp. 201–219, 1978, doi: 10.1007/BF01891959.

[9] S. H. Al-Jassar and A. B. Hawkins, "Geotechnical Properties of The Carboniferous Limestone of The Bristol Area The Influence of Petrography And Chemistry," in *4th ISRM Congr*., 2-8 September, Montreux, Switzerland, 1979, pp. 3–14.

[10] N. Brook, "Size Correction for Point Load Testing," *Int. J. Rock Mech. Min. Sci. Geomech.* Abstr., vol. 17, no. 2, pp. 231–235, 1980.

[11] E. Broch and J. A. Franklin, "The Point-Load Strength Test," *Int. J. Rock Mech. Min. Sci.*, vol. 9, pp. 669–697, 1972.
[12] M. Greminger, "Experimental studies of the influence of rock anisotropy on size and shape effects in point-load testing," *Int. J. Rock Mech. Min. Sci. Geomech. Abstr.*, vol. 19, no. 5, pp. 241–246, 1982, doi: 10.1016/0148-9062(82)90222-4.
[13] I. R. Forster, "The influence of core sample geometry on the axial point-load test," *Int. J. Rock Mech. Min. Sci. Geomech. Abstr.*, vol. 20, no. 6, pp. 291–295, 1983, doi: 10.1016/0148-9062(83)90599-5.
[14] E. Broch, "Estimation of strength anisotropy using the point-load test," *Int. J. Rock Mech. Min. Sci. Geomech. Abstr.*, vol. 20, no. 4, pp. 181–187, 1983, doi: 10.1016/0148-9062(83)90942-7.
[15] ISRM Comission of Laboratory Tests, "Suggested Methods for Determining Point-Load Strength, Document 1," Lisbon, 1973.
[16] N. Brook, "The equivalent core diameter method of size and shape correction in point load testing," *Int. J. Rock. Mech. Min. Sci. Geomech. Abstr.*, vol. 22, no. 2, pp. 61–70, 1985, doi: 10.1016/0148-9062(85)92328-9.
[17] T. Abdallah, "Towards a Realistic Methodology of Modelling a Rock Blasting Pattern," in *Türkiye XIII. Madencilik Kong.*, 1993, pp. 289–300.
[18] K. T. Chau, "Analytic solutions for diametral point load strength tests," *J. Eng. Mech.*, vol. 124, no. 8, pp. 875–883, 1998, Accessed: Nov. 23, 2017, doi/pdf/10.1061/(ASCE)0733-9399(1998)124:8(875)
[19] X. X. Wei, K. T. Chau, and R. H. C. Wong, "Analytic solution for axial point load strength test on solid circular cylinders," *J. Eng. Mech.*, vol. 125, no. 12, pp. 1349–1357, 1999, Accessed: Nov. 23, 2017. [Online]. Available: http://ascelibrary.org/doi/pdf/10.1061/(ASCE)0733-9399(1999)125:12(1349)
[20] K. T. Chau and X. X. Wei, "New analytic solution for the diametral point load strength test on finite solid circular cylinders," *Int. J. Solids. Struct.*, vol. 38, no. 9, pp. 1459–1481, 2001, doi: 10.1016/S0020-7683(00)00122-0.
[21] A. Zacoeb and K. Ishibashi, "Point Load Test Application for Estimating Compressive Strength of Concrete Structures From Small Core," *ARPN J. Eng. Appl. Sci.*, vol. 4, no. 7, pp. 46–57, 2009.
[22] J. K. Li, F. F. Li, and X. K. Wei, "The effect of specimen's height on the point load test," *Adv Mat Res*, vol. 848, pp. 108–111, 2014, doi: 10.4028/www.scientific.net/AMR.848.108.
[23] M. Forbes, H. Masoumi, S. Saydam, and P. Hagan, "Investigation into the effect of length to diameter ratio on the point load strength index of Gosford sandstone," in *49th US Rock Mechanics / Geomechanics Symp., San Francisco, CA, USA, 28 June-1 July*, 2015, pp. 1–11.
[24] H. Masoumi, H. Roshan, A. Hedayat, and P. C. Hagan, "Scale-Size Dependency of Intact Rock under Point-Load and Indirect Tensile Brazilian Testing," *Int. J. Geomech.*, vol. 18, no. 3, p. 04018006, Mar. 2018, doi: 10.1061/(asce)gm.1943-5622.0001103.
[25] ISRM, "Suggested Method for Determining Point Load Strength," in ISRM, U. R. and H. J.A., Eds., London: Springer, 1985, pp. 53–60.
[26] *Natural stone test methods - Determination of water absorption coefficient by capillarity*, TS EN 1925, TSE, Ankara. 2000. [Online]. Available: https://www.tse.org.tr/
[27] *Natural stone test methods - Determination of sound speed propagation*, TS EN 14579, TSE, Ankara. 2006. Available: https://www.tse.org.tr/
[28] *Natural stone test methods - Determination of uniaxial compressive strength*, TS EN 1926, TSE, Ankara. 2013. Available: https://www.tse.org.tr/

Bitlis Eren Üniversitesi Fen Bilimleri Dergisi
BİTLİS EREN UNIVERSITY JOURNAL OF SCIENCE
ISSN: 2147-3129/e-ISSN: 2147-3188
VOLUME: 12 NO: 4 PAGE: 1298-1309 YEAR: 2023
DOI:10.17798/bitlisfen.1383231

Novel Application of Pythagorean Fuzzy MCDM in Prioritizing Transportation Alternatives: Insights from Ankara for the Ministry of Transportation

Murat ETYEMEZ[1], Kürşat YILDIZ[1], Mehmet Akif YERLİKAYA[2*]

[1]*Gazi University, Graduate School of Natural and Applied Sciences, Traffic Planning and Implementation, Ankara, Turkey*

[2]*Bitlis Eren University, Faculty of Engineering and Architecture, Department of Mechanical Engineering, Bitlis, Turkey*

(ORCID: 0009-0008-5932-8760) (ORCID: 0000-0003-2205-9997) (ORCID: 0000-0003-3084-0257)

Keywords: Transportation Prioritization, Fuzzy CRITIC, Fuzzy Weighted Sum Method, Transportation Criteria, Transportation Planning

Abstract

This study underscores the importance of prioritizing transportation modes in Ankara, particularly given the pivotal role transportation holds in contemporary urban societies. Transportation directly shapes the socio-economic framework of metropolitan areas. To address the complexities of transportation in Ankara, the study introduces a hybrid approach by integrating the Fuzzy CRITIC (Criteria Importance Through Inter-Criteria Correlation) method with the novel Pythagorean Fuzzy Weighted Sum Method. This novel approach assesses the various transportation modes available in Ankara, taking into account pivotal criteria such as cost, duration, reliability, comfort, and flexibility. The hybridized methodology offers a systematic way to determine the weights of each criterion. Then, leveraging these weights, the performance of each transportation mode is calculated and ranked. This integrated approach proves to be a powerful analytical tool for addressing multi-criteria decision-making challenges, especially when confronted with uncertainty and intricate details. The outcomes of this research aim to serve as a cornerstone for the Ankara Ministry of Transportation and other key stakeholders. The insights derived can be pivotal for enhancing the existing transportation infrastructure or for the initiation of new, more efficient projects. This study highlights the effectiveness of hybrid decision-making methods for urban transportation, setting a benchmark for similar challenges. It presents a strategic, analytical approach to streamline Ankara's transportation, addressing its complex urban transport needs.

1. Introduction

In today's world, it is evident that transportation plays a critical role in the sustainable development of cities and meeting the needs of communities [1]. With rapidly growing populations, the expansion of city boundaries, and the increasing demand for effective transportation systems to support the daily lives of city residents, the need for efficient transportation is on the rise.

Transportation is a domain where economic, social, and environmental factors intersect, making it crucial to plan and manage transportation systems effectively in a city. Especially in large cities like capitals, they host complex transportation networks. Ankara, as the capital of Turkey, stands out as a prominent example in this regard [2].

In a city sprawled over a vast geographical area like Ankara, residents must have access to a wide variety of transportation options to meet their basic

* *Corresponding author: mayerlikaya@beu.edu.tr*
Received: 30.10.2023, Accepted:15.12.2023

needs, such as commuting to work, shopping, and entertainment. Different modes of transportation, including cars, public transit, bicycles, and walking, serve as vehicles for the daily mobility of city dwellers. However, each transportation mode comes with its unique advantages and disadvantages. For instance, individual car usage provides freedom and comfort but may lead to issues like traffic congestion and environmental impacts. Public transportation can reduce costs but may suffer from problems related to timing and reliability. Therefore, effective planning and management of transportation systems in cities become a complex task for decision-makers.

In today's urban landscapes, prioritizing transportation in cities like Ankara is critical for strategic city management. Our study introduces a sophisticated methodology to identify optimal transportation alternatives, combining Fuzzy CRITIC and Pythagorean Fuzzy Weighted Sum for multi-criteria decision-making. This approach comprehensively evaluates various transportation modes in Ankara, focusing on key criteria such as cost, duration, reliability, comfort, and flexibility, to align with the city's evolving needs.

Our research's outcomes not only serve as an analytical guidepost for refining Ankara's transportation strategies but also set a precedent for urban transportation planning in comparable global cities. In essence, this study accentuates the urgency of navigating and refining intricate transportation choices in rapidly expanding urban centers. By doing so, it paves the way for shaping sustainable, cost-effective, and socially cohesive transportation infrastructures that cater to contemporary urban demands.

The structure of this paper is organized as follows: Section 2 delves into an extensive literature review, setting the stage for our research. Section 3 introduces the innovative methodology applied in our study. Following this, Section 4 discusses the specific analytical approaches and techniques used. The paper culminates in Section 5, where we present our key findings, analyze the results, and discuss their implications for urban transportation planning in Ankara.

2. Literature Research

Transportation prioritization and decision-making embodies a structured process wherein cities or regions determine the most apt transportation modes or projects to fulfill their specific mobility needs. This is inherently a multi-criteria endeavor, which necessitates the holistic evaluation of various modes or projects based on designated criteria and objectives.

In the earlier explorations of this field, Çelik et al. [3] embarked on an investigation into the applications of Multi-Criteria Decision Making (MCDM) in the Turkish transportation sector. Their research underscored the efficacy of these methodologies in assessing a plethora of transportation options. Building on this foundational work, Özcan and Celebi [4] employed MCDM methodologies to pinpoint preferred transportation modes throughout Turkey. A subsequent study by Ertugay et al. [5] utilized a fuzzy MCDM approach, emphasizing urban transportation mode preferences in Istanbul and furnishing a systematic ranking of distinct transportation modes. Broadening the scope, Yazdani [6] offered an all-encompassing perspective on the deployment of MCDM methods within transportation systems, thereby elucidating their inherent potential in this realm.

Extending beyond mere transportation, the adaptability of MCDM methodologies in diverse sectors is noteworthy. For instance, Kahraman et al. [7] showcased the versatile nature of these techniques in an array of industries, particularly through their implementation of the fuzzy AHP method for supplier selection. Similarly, underscoring the expansive utility of MCDM, Demirel et al. [8] leveraged the Choquet integral for making decisions on warehouse location. Fast forward to 2021, Zhang et al. [9] accentuated the pivotal role of public transportation within the circular economy. Their innovative study probed into the influence of public participation on mass transit decisions. This was achieved through the integration of fuzzy preference relations and expansive group decision making methodologies. Their approach was distinct, clustering participants using similarity methods and subsequently dissecting decision-making preferences. In 2023, landmark studies continued to build on these foundations. Kraus et al. [10] underscored the importance of sustainable transportation, drawing inspiration from the European Green Deal. Their research introduced a novel methodology based on ISM-P and PROMETHEE, focusing on the evaluation of urban transportation by converging societal, environmental, and economic dimensions. In the same year, Wang et al. [11] proposed an evaluative model for assessing the resilience of urban multi-modal transportation systems (UMTS). Given the escalating complexity of urban growth and transportation networks, this model combined diverse transport modes, such as buses

and subways, with simulation and network techniques. A case study in Singapore further solidified the relevance of their proposed indicators.

In this research, we place a magnifying lens on Ankara's transportation dynamics, critically assessing and ranking existing modes using specialized fuzzy methodologies: Fuzzy CRITIC and Pythagorean Fuzzy Weighted Sum. What sets this study apart is its integrated approach, employing a fusion of these methodologies to delve deeper into Ankara's unique transportation milieu. By synergizing Fuzzy CRITIC with the Pythagorean Fuzzy Weighted Sum, our research provides a novel and holistic perspective, standing in contrast to traditional studies that primarily leverage singular methods. The resultant findings underscore not only the alignment with Ankara's distinct transportation necessities but also vouch for the potency of fuzzy methodologies when faced with intricate real-world challenges. In this endeavor, our work emerges as a beacon, offering pivotal insights that could shape strategic interventions in Ankara's urban transportation framework. Summarily, multi-criteria decision-making (MCDM) methodologies are spotlighted as formidable instruments, adept at navigating complex decision-making arenas in transportation and broader sectors.

3. Material and Method

This section delves into the analytical structures and techniques utilized throughout the research. Our study leans heavily on two pivotal methods: the Fuzzy CRITIC and the Pythagorean Fuzzy Weighted Sum. The former, Fuzzy CRITIC, was harnessed for the intricate task of weighting transportation modes, while the latter, Pythagorean Fuzzy Weighted Sum, was designated for computing the aggregate performance scores of the presented alternatives.

The allure of the Fuzzy CRITIC method in the domain of multi-criteria decision-making is primarily its adeptness at navigating the murky waters of uncertainties and nebulous data. Instead of a rigid reliance on precise numerical values, this method champions the use of fuzzy data sets, making it particularly apt for confronting and decoding the ambiguities inherent in real-world scenarios. Such an approach not only acknowledges the inherent uncertainties but also paves the way for generating outcomes that are both resilient and adaptive. This, in turn, arms decision-makers with robust insights, propelling them towards making judicious choices. Meanwhile, the Pythagorean Fuzzy Weighted Sum technique furnishes a coherent and impartial scaffold, adeptly catering to multi-criteria decision-making quandaries shrouded in uncertainties.

3.1. Intuitionistic Fuzzy Set

An Intuitionistic Fuzzy Set (IFS) is an extension of the traditional fuzzy set and is characterized by both a membership function and a non-membership function. Introduced by Atanassov in 1986, the IFS provides a more comprehensive representation for situations where the degree of membership and the degree of non-membership are not always complementary. Specifically, for any element x in a universe of discourse X, an IFS A in X can be represented as shown in Equation 1 [12]:

$$A = \{(x, \mu_A(x), \nu_A(x)) | x \in X\} \quad (1)$$

Where;

- $\mu_A(x)$ is the membership function of x in A.
- $\nu_A(x)$ is the non-membership function of x in A.
- $\mu_A(x) + \nu_A(x) \leq 1$ for every $x \in X$.

3.2. Pythagorean Fuzzy Sets

Pythagorean Fuzzy Sets (PFS) extend the concept of IFS by allowing the sum of the squared membership function and squared non-membership function to be less than or equal to one. This provides a broader scope in expressing uncertainties and is particularly useful in scenarios where there is an inherent hesitation or doubt about the membership of an element. Formally, a PFS A in X can be represented as shown in Equaiton 2 [12]:

$$A = \{(x, \mu_A(x), \nu_A(x)) | x \in X\}$$

with the condition: (2)

- $\mu_A(x)^2 + \nu_A(x)^2 \leq 1$ for every $x \in X$.

The introduction of Pythagorean Fuzzy Sets offers more flexibility in decision-making scenarios, especially in multi-criteria contexts. Zhang and Xu [12] notably extended the traditional TOPSIS method to incorporate the principles of PFS, enhancing the method's applicability to scenarios with vague or imprecise information 1.

3.3. Fuzzy CRITIC Method

Criteria are considered a vital source of information during the decision-making process. Objective weights, termed "objective weights," furnish significant insights to decision-makers. The CRITIC method is utilized to compute the objective weights of criteria considered in multi-attribute decision-making problems. The objective weight derived from this method synthesizes the contrast intensity of each criterion and the discrepancy between criteria. The criterion's contrast intensity is acknowledged as the standard deviation, and the correlation coefficient is employed to calculate the disagreement between criteria [13]. The Fuzzy CRITIC approach is an extended version of the CRITIC method under a fuzzy environment. In this section, this approach has been applied in a Pythagorean fuzzy setting. Pythagorean fuzzy sets, an extension of intuitionistic fuzzy sets, were developed by Yager and are characterized by a membership degree and a non-membership degree, ensuring that the sum of their squares is equal to or less than one. These sets introduce a novel assessment format, especially when depicting a query in the most accurate and realistic manner using both its positive and negative aspects. The steps of the Pythagorean Fuzzy CRITIC method are as follows [14]:

Step 1. Calculation of the degree of uncertainty: For each fuzzy value's degree of uncertainty, where pij (μij, vij) is the Pythagorean fuzzy value for the i.th alternative based on the j.th criterion, The Equation 3 is employed.

$$\Pi_{ij} = \sqrt{1 - \mu_{ij}^2 - v_{ij}^2} \tag{3}$$

$(i = 1, 2, ..., m; j = 1, 2, ..., n)$

and $0 \le (\mu_{ij})^2 + (v_{ij})^2 \le 1$ with the condition

Step 2. Calculation of score functions for each Pythagorean fuzzy value (pij): Using Equation 4, the score functions ($R = (r_{ij})_{m \times n}$) for each fuzzy value are determined.

$$r_{ij} = \mu_{ij}^2 - v_{ij}^2 - \ln(1 + \Pi_{ij}^2) \tag{4}$$

$(i = 1, 2, ..., m; j = 1, 2, ..., n)$

Step 3. Transformation of the R score matrix into an orthonormal Pythagorean fuzzy matrix (Normalization process): The transformation is executed using Equation 5.

$$r_{ij}^{'} = \begin{cases} \dfrac{r_{ij} - r_j^-}{r_j^+ - r_j^-}, & \textit{for benefit criteria}, \\ \dfrac{r_j^+ - r_{ij}}{r_j^+ - r_j^-}, & \textit{for cost criteria} \end{cases} \tag{5}$$

Where; $r_j^- = \min_i r_{ij}$ *ve* $r_j^+ = \max_i r_{ij}$

Step 4: Calculation of standard deviations for criteria: The calculation is performed using The Equation 6.

$$\sigma_j = \sqrt{\frac{\sum_{i=1}^{m} (r_{ij}^{'} - \bar{r}_j)^2}{m}} \tag{6}$$

Where;

$$\bar{r}_j = \frac{\sum_{i=1}^{m} r_{ij}^{'}}{m} \tag{7}$$

Step 5: Determination of inter-criterion correlation: The correlation value between the j.th and k.th criterion is computed using Equation 8.

$$\rho_{jk} = \frac{\sum_{i=1}^{m} (r_{ij}^{'} - \bar{r}_j)(r_{ik}^{'} - \bar{r}_k)}{\sqrt{\sum_{i=1}^{m} (r_{ij}^{'} - \bar{r}_j)^2 \sum_{i=1}^{m} (r_{ik}^{'} - \bar{r}_k)^2}} \tag{8}$$

$(k = 1, 2, ..., n; j = 1, 2, ..., n)$

Step 6: Calculation of the information amount for each criterion: The amount of information is determined using Equation 9.

$$c_j = \sigma_j \sum_{k=1}^{n} (1 - \rho_{jk}) \tag{9}$$

$(k = 1, 2, ..., n; j = 1, 2, ..., n)$

The larger it is, the more information it contains for a particular criterion, thus the weight of this evaluation criterion is greater than that of the others.

Step 7: Determination of criterion weights: The criterion weights (wj) are ascertained using The Equation 10.

$$w_j = \frac{c_j}{\sum_{j=1}^{n} c_j} \quad (10)$$

$(j = 1, 2, ..., n)$

The Pythagorean Fuzzy Weighted Sum Method is favored in areas requiring intricate decision-making based on uncertain information. This includes supply chain management, engineering design, product development, service quality assessments, and sustainability evaluations.

Decision-making processes often hinge on imprecise and incomplete information. The Pythagorean Fuzzy Weighted Sum Method facilitates a thorough analysis of these uncertainties, empowering decision-makers to make more informed and rational choices. The in-depth analysis provided by this method proves especially advantageous in decision-making scenarios under uncertainty.

3.4. Pythagorean Fuzzy Weighted Sum Method

The Pythagorean Fuzzy Weighted Sum Method was developed to address uncertainties and vague information in MCDM processes. This method amalgamates the traditional weighted sum approach with Pythagorean fuzzy numbers, providing a more holistic analysis. Key features of this method include:

- Flexibility: This method offers a more flexible approach in decision-making scenarios with uncertain information.
- Extensive Analysis: Data limited by conventional methods can undergo a broader analysis using Pythagorean fuzzy numbers.
- User-Friendly: Despite its mathematical foundations, the method remains comprehensible and user-centric in practical applications.

The steps of this method are:

Step 1. Formulation of Decision Matrix: Performance values of alternatives for each criterion, expressed in Pythagorean fuzzy numbers, are compiled into a matrix.

Step 2. Determination of Criterion Importance Levels: Using weights specified by the decision-maker, the relative importance of each criterion in the decision process is defined.

Step 3. Calculation of Weighted Total Scores: The weighted total scores for alternatives are calculated using the criterion weights and Pythagorean fuzzy numbers in the decision matrix as per Equation 11.

$$V(a) = \sum_{j=1}^{n} w_j \times \sqrt{\mu_{ij}^2 + v_{ij}^2} \quad (11)$$

Step 4. Ranking and Selection of Alternatives: Alternatives are ranked based on their calculated weighted total scores. The alternative with the highest score is recognized as the best option.

4. Application

In this section, we will address the application process and outcomes of the study conducted for the Ankara Ministry of Transportation. This study, taking the analysis of data pertaining to the central districts of Ankara as its basis, has been carried out with the aim to more effectively plan and optimize Ankara's transportation systems. The research evaluated six different transportation alternatives, namely "Institutional Shuttle," "Private Vehicle," "Public Transport," "Bicycle/Scooter/Walking," and "Taxi," utilizing the Fuzzy CRITIC and Fuzzy Weighted Sum methods. The decision matrix for each region utilized in this study is provided in Appendix-1. These decision matrices reflect the performance of each alternative in terms of every criterion for the districts of Ankara.

4.1. Data Collection and Analysis

The application process began with the collection of survey data from employees of the Ankara Ministry of Transportation. These surveys assessed six different transportation alternatives for each district of Ankara. Participants evaluated each method based on criteria such as cost, duration, reliability, comfort, and flexibility. To effectively interpret this data, linguistic expressions from respondents were translated into quantifiable measures using Pythagorean Fuzzy Numbers, as illustrated in Table 1.

This conversion was pivotal in processing the gathered survey data using the Fuzzy CRITIC method to obtain a criteria weight matrix. This matrix was instrumental in calculating performance scores. Within this text, Table 2 has been provided, which details the evaluations for the Çankaya district. Additional decision matrices for other districts are presented in Appendix-1. Using the Pythagorean Fuzzy Weighted Sum Method, performance scores were computed, assessing each alternative concerning each criterion, while taking into account the interrelationship between criteria.

4.2. Results and Discussion

When considering the performance scores specific to different regions of Ankara, it is essential to note that each region has its unique needs and priorities. These results indicate how each area evaluates various transportation alternatives and which alternatives they prioritize. The results have been ranked based on the total performance scores of each alternative. This ranking has identified the best alternative according to the given criteria weights. The criteria weights for each district, calculated using the Fuzzy CRITIC method, are provided in Table 3. The performance scores for each district, calculated using the Fuzzy Weighted Total method, are given in Table 4. In Figure 1, transportation preferences across various regions are represented by scores and rankings for each specific mode of transport. The findings are as follows:

Evaluation for Çankaya: The criterion with the highest weight in Çankaya is cost, indicating that residents of Çankaya primarily consider economic factors when determining transportation options. This could be due to Çankaya's central location and potentially higher living costs compared to other districts. The "Bicycle/Scooter/Walking" alternative has received the highest score in Çankaya, suggesting that the district's central location and infrastructure might be suitable for bicycle and scooter usage. However, the "Corporate Service" scored the lowest in this region, hinting that corporate services might not be suited to Çankaya's traffic or infrastructure. One of the critical criteria in Çankaya is the speed and efficiency of transportation.

Evaluation for Keçiören: In Keçiören, cost also has the highest weight, suggesting residents may prefer economically viable transportation options. We can infer that economical options, like public transport, might be frequently used. In Keçiören, while the "Bicycle/Scooter/Walking" alternative ranks first, "Private Vehicle" has the lowest score. The dense population and narrow streets in Keçiören might hinder private vehicle use, advocating for promoting public transportation and bicycle use in this region.

Evaluation for Sincan: The highest weight in Sincan is given to the comfort criterion. This implies that residents of Sincan prioritize comfort and convenience when choosing transportation options. In the Sincan region, "Bicycle/Scooter/Walking" scored the highest, but "Corporate Service" scored the lowest. The vast areas and industrial zones in Sincan might be ideal for bicycle transportation. However, attention should be paid to corporate services' inefficiency in this area.

Evaluation for Etimesgut: For Etimesgut residents, cost is the top priority. This may indicate a preference for economical transportation options. The "Bicycle/Scooter/Walking" alternative has the highest score in Etimesgut. Increasing bike lanes and parking spaces in this area can make transportation more sustainable.

Evaluation for Yenimahalle: In Yenimahalle, cost again has the highest weight. This indicates a preference for economical transportation options. While "Bicycle/Scooter/Walking" ranks first in Yenimahalle, "Taxi" ranks last, pointing to potential traffic congestion, making taxi transportation challenging.

Evaluation for Pursaklar and Altındağ: In both districts, the most important criterion is cost. This suggests a preference for economical transportation options. Both regions have given the highest scores to "Bicycle/Scooter/Walking." Promoting bicycle use in these regions can make transportation more environmentally friendly and economical.

Evaluation for Mamak: In Mamak, the highest weight is on flexibility. This indicates that residents of Mamak value flexibility and accessibility in transportation options. While "Private Vehicle" scored the highest in Mamak, "Taxi" scored the lowest. This hints at Mamak's vast areas being more suitable for private vehicle use.

Evaluation for Gölbaşı: For Gölbaşı residents, cost is the primary concern. This indicates a preference for economical transportation options. "Corporate Service" ranks first in Gölbaşı, whereas "Public Transportation" has the lowest score. The remote location of

Gölbaşı suggests that corporate services might be more effective.

In conclusion, in many districts, the cost criterion emerges prominently. This underscores that Ankara residents lean towards economical transportation options, indicating its significant city-wide importance. Nevertheless, since each district has its dynamics and requirements, transportation planning should be tailored accordingly. For instance, the prominence of flexibility in Mamak might be due to its topography, population density, or other specific conditions. Considering such nuances will aid in devising a more effective and efficient transportation plan. Lastly, tailoring transportation systems by acknowledging the distinct transportation needs and priorities of Ankara's different regions will assist in achieving the city's sustainability objectives. As each area has its unique infrastructure and needs, these results are crucial for developing region-specific transportation solution

Table 1. Linguistic Expressions and Their Equivalents as Pythagorean Fuzzy Numbers

Linguistic Expressions	**Pythagorean Fuzzy Number Equivalent**
Very High (VH)	(1; 0)
High (H)	(0.8; 0.2)
Medium high (MH)	(0.6; 0.4)
Medium (M)	(0.5; 0.5)
Medium Low (ML)	(0.4; 0.6)
Low (L)	(0.2; 0.8)
Very Low (VL)	(0; 1)

Table 2. Decision matrix of Çankaya region

Region / Criteria	Cost	Time	Security	Comfort	Flexibility
Institutional Shuttle	O	D	Y	O	O
Private Vehicle	O	ÇD	Y	ÇY	ÇY
Public Transport	ÇD	Y	D	D	D
Bicycle/Scooter/Walking	ÇD	Y	ÇD	ÇD	ÇD
Taxi	ÇY	ÇD	O	Y	Y

Table 3. Criteria weights for districts using Fuzzy CRITIC method

Region / Criteria	Cost	Time	Security	Comfort	Flexibility	**Total**
ÇANKAYA	0,230	0,206	0,218	0,186	0,160	1
KEÇİÖREN	0,250	0,206	0,167	0,209	0,168	1
SİNCAN	0,203	0,216	0,130	0,234	0,217	1
ETİMESGUT	0,307	0,182	0,154	0,178	0,179	1
YENİMAHALLE	0,298	0,155	0,227	0,156	0,164	1
PURSAKLAR	0,279	0,170	0,183	0,203	0,166	1
ALTINDAĞ	0,331	0,143	0,144	0,228	0,154	1
MAMAK	0,178	0,167	0,152	0,248	0,255	1
GÖLBAŞI	0,345	0,150	0,154	0,200	0,151	1

Table 4. Performance scores of districts using Fuzzy Weighted Total method

Region / Alternative	Institutional Shuttle		Private Vehicle		Public Transport		Bicycle/Scooter/Walking		Taxi	
	Score	Rank	Score	Rank	Score	Rank	Score	Rank	Score	Rank
ÇANKAYA	0,757	5	0,894	2	0,865	4	0,964	1	0,875	3
KEÇİÖREN	0,849	4	0,810	5	0,897	2	0,927	1	0,874	3
SİNCAN	0,746	5	0,756	4	0,785	3	0,801	1	0,792	2
ETİMESGUT	0,818	5	0,887	3	0,869	4	0,969	1	0,888	2
YENİMAHALLE	0,770	3	0,798	2	0,769	4	0,814	1	0,752	5
PURSAKLAR	0,834	4	0,837	3	0,821	5	1,000	1	0,970	2
ALTINDAĞ	0,821	5	0,892	3	0,864	4	0,910	2	0,950	1
MAMAK	0,879	3	0,924	1	0,830	4	0,885	2	0,807	5
GÖLBAŞI	0,870	1	0,828	4	0,725	5	0,867	3	0,868	2

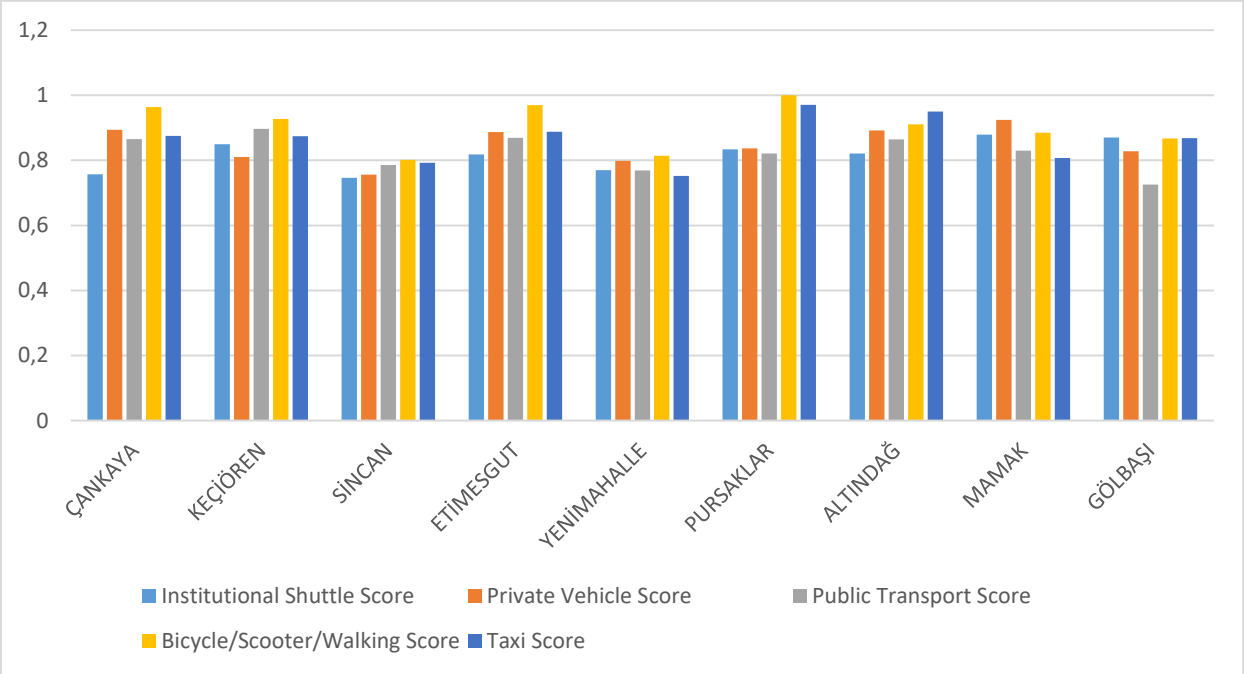

Figure 1. Performance of different transportation types across regions

5. Conclusion and Suggestions

In grappling with sustainable transportation challenges within Ankara's vast urban landscape, our research leveraged advanced fuzzy decision-making methodologies. The adoption of Fuzzy CRITIC and Pythagorean Fuzzy Weighted Sum methods revealed a clear preference for cost-effective transportation across the city, emphasizing the need to balance economic and environmental factors in urban planning. Our findings highlight regional variations in transportation preferences, reflecting the unique infrastructural and demographic characteristics of different districts. For example, the district of Mamak values transportation versatility, indicating a need for flexible transit solutions, while Gölbaşı's remote location shapes its distinct transportation preferences, contrasting with more central areas.

These insights underscore the necessity of customized transportation strategies for each district, considering their specific requirements and challenges. This study not only provides a comprehensive view of Ankara's transportation dynamics but also offers a blueprint for other cities with similar urban structures. Looking forward, the potential to apply these methodologies to cities with diverse landscapes and demographics is immense. Such approaches are crucial in guiding urban centers towards sustainable development, creating environments that balance livability with environmental responsibility.

As we move forward, further research could explore the adaptability of these methods to different urban contexts, potentially offering a versatile toolkit for urban planners globally. Our study sets the stage for a more nuanced understanding of urban transportation planning, advocating for strategies that are both environmentally sustainable and economically viable.

Conflict of Interest Statement

There is no conflict of interest between the authors.

Contributions of the authors

Each aouther has the same contribution to this study.

Statement of Research and Publication Ethics

The study is complied with research and publication ethic

References

[1] D. Banister, "The sustainable mobility paradigm," *Transport Policy*, vol. 15, pp. 73-80, 2008.
[2] K. T. Geurs and B. van Wee, "Accessibility evaluation of land-use and transport strategies: Review and research directions," *Journal of Transport Geography*, vol. 12, pp. 127-140, 2004.
[3] M. Çelik, S. Cebi, and C. Kahraman, "Multi-criteria decision making methods and their applications in the Turkish transportation sector," *Transport Reviews*, vol. 29, no. 4, pp. 467-496, 2009.
[4] T. Özcan and N. Çelebi, "Determination of the Transportation Mode Using Multi-Criteria Decision Making Methods: A Case Study for Turkey," *Transportation Research Procedia*, vol. 22, pp. 13-22, 2016.
[5] K. Ertugay and E. Eyol, "A Fuzzy MCDM Approach for Urban Transportation Mode Choice: A Case Study in Istanbul," *Procedia Computer Science*, vol. 120, pp. 569-576, 2017.
[6] M. Yazdani, "An overview of multi-criteria decision making methods in transportation systems," *Periodica Polytechnica Transportation Engineering*, vol. 43, no. 3, pp. 138-143, 2015.
[7] C. Kahraman, U. Cebeci, and Z. Z. Ulukan, "Multi-criteria supplier selection using fuzzy AHP," *Logistics Information Management*, vol. 16, no. 6, pp. 382-394, 2003.
[8] T. Demirel, N. Ç. Demirel, and C. Kahraman, "Multi-criteria warehouse location selection using Choquet integral," *Expert Systems with Applications*, vol. 37, no. 5, pp. 3943-3952, 2010.
[9] L. Zhang, J. Yuan, X. Gao, and D. Jiang, "Public transportation development decision-making under public participation: A large-scale group decision-making method based on fuzzy preference relations," *Technological Forecasting and Social Change*, vol. 172, pp. 121020, 2021, ISSN 0040-1625, https://doi.org/10.1016/j.techfore.2021.121020.
[10] L. Kraus, D. Wittowsky, and H. Proff, "Multi-method analysis to identify criteria interrelations for sustainability assessment of urban transportation services," *Journal of Cleaner Production*, vol. 412, pp. 137416, 2023, ISSN 0959-6526, https://doi.org/10.1016/j.jclepro.2023.137416.

[11] N. Wang, M. Wu, and K. F. Yuen, "A novel method to assess urban multimodal transportation system resilience considering passenger demand and infrastructure supply," *Reliability Engineering & System Safety*, vol. 238, pp. 109478, 2023, ISSN 0951-8320, https://doi.org/10.1016/j.ress.2023.109478.

[12] X. Zhang and Z.S. Xu, "Extension of TOPSIS to multiple criteria decision making with Pythagorean fuzzy sets," *International Journal of Intelligent Systems*, vol. 29, no. 12, pp. 1061-1078, 2014.

[13] D. Diakoulaki, G. Mavrotas, and L. Papayannakis, "Determining objective weights in multiple criteria problems: The CRITIC method," *Computers & Operations Research*, vol. 22, no. 7, pp. 763-770, 1995.

[14] M. A. Yerlikaya, "Belirsiz Sipariş Toplama Sistemlerinde Ürün Atama Kriterlerinin Pisagor Bulanık CRITIC Yöntemiyle Önceliklendirilmesi," in Bulanık Çok Kriterli Karar Verme Yöntemleri: MS Excel Çözümlü Uygulamalar, vol. 1, *Nobel Akademik Yayıncılık*, 2021, pp. 429-440.

APPENDIX 1. The decision matrix for each region

Table 5. Decision matrix of Keçiören region

Region / Criteria	Cost	Time	Security	Comfort	Flexibility
Institutional Shuttle	ÇD	O	Y	O	ÇD
Private Vehicle	Y	O	O	Y	ÇY
Public Transport	O	ÇY	ÇD	ÇD	D
Bicycle/Scooter/Walking	O	ÇY	ÇD	ÇD	ÇD
Taxi	ÇY	O	Y	Y	ÇY

Table 6. Decision matrix of Sincan region

Region / Criteria	Cost	Time	Security	Comfort	Flexibility
Institutional Shuttle	D	O	Y	O	O
Private Vehicle	Y	D	O	O	O
Public Transport	O	Y	O	D	D

Bicycle/Scooter/Walking	O	Y	D	D	D
Taxi	ÇY	D	O	O	O

Table 7. Decision matrix of Etimesgut region

Region / Criteria	Cost	Time	Security	Comfort	Flexibility
Institutional Shuttle	ÇD	O	O	O	D
Private Vehicle	Y	D	Y	ÇY	ÇY
Public Transport	D	Y	O	ÇD	ÇD
Bicycle/Scooter/Walking	ÇD	ÇY	ÇD	D	ÇY
Taxi	ÇY	O	D	D	ÇY

Table 8. Decision matrix of Yenimahalle region

Region / Criteria	Cost	Time	Security	Comfort	Flexibility
Institutional Shuttle	O	D	Y	Y	O
Private Vehicle	O	D	Y	ÇY	O
Public Transport	D	O	Y	O	O
Bicycle/Scooter/Walking	ÇD	O	O	O	D
Taxi	O	O	Y	Y	O

Table 9. Decision matrix of Pursaklar region

Region / Criteria	Cost	Time	Security	Comfort	Flexibility
Institutional Shuttle	Y	O	Y	Y	ÇD
Private Vehicle	O	O	Y	ÇY	ÇY
Public Transport	O	Y	Y	Y	ÇY
Bicycle/Scooter/Walking	ÇD	ÇD	ÇD	ÇD	ÇY
Taxi	ÇY	Y	ÇY	ÇY	ÇY

Table 10. Decision matrix of Altındağ region

Region / Criteria	Cost	Time	Security	Comfort	Flexibility
Institutional Shuttle	O	O	ÇY	Y	ÇD
Private Vehicle	Y	Y	Y	ÇY	ÇY
Public Transport	ÇY	Y	Y	D	O

Bicycle/Scooter/Walking	ÇD	Y	D	D	ÇY
Taxi	ÇY	Y	Y	ÇY	ÇY

Table 11. Decision matrix of Mamak region

Region / Criteria	Cost	Time	Security	Comfort	Flexibility
Institutional Shuttle	ÇD	O	ÇY	O	ÇD
Private Vehicle	Y	ÇY	O	ÇY	ÇY
Public Transport	O	ÇY	O	O	ÇY
Bicycle/Scooter/Walking	ÇY	ÇY	D	D	D
Taxi	ÇY	O	D	O	Y

Table 11. Decision matrix of Gölbaşı region

Region / Criteria	Cost	Time	Security	Comfort	Flexibility
Institutional Shuttle	ÇD	O	Y	O	ÇD
Private Vehicle	O	O	Y	ÇY	ÇY
Public Transport	O	Y	O	O	O
Bicycle/Scooter/Walking	ÇD	Y	O	D	Y
Taxi	Y	O	Y	ÇY	ÇY

Bitlis Eren Üniversitesi Fen Bilimleri Dergisi
BİTLİS EREN UNIVERSITY JOURNAL OF SCIENCE
ISSN: 2147-3129/e-ISSN: 2147-3188
VOLUME: 12 NO: 4 PAGE: 1310-1318 YEAR: 2023
DOI:10.17798/bitlisfen.1385330

Sex Ratio Estimation of Green Turtle Hatchlings in Kazanlı Beach, Türkiye

Onur CANDAN[1*]

[1]*Ordu University, Faculty of Arts and Sciences, Department of Molecular Biology and Genetics, 52200 Ordu, Türkiye*

(ORCID: 0000-0002-9254-4122)

Keywords: *Chelonia mydas*, Mediterranean Sea, Temperature-dependent sex determination, Thermal profiles, Sex ratio, Gonadal Histology.

Abstract

Sea turtles are distributed worldwide and have temperature-dependent sex determination. For hatchlings with a female:male ratio of 1:1, the pivotal temperature is usually around 29°C, with female hatchlings being observed at higher values and male ones at lower values. It is expected that wildlife threatened by global warming will be more severely affected, especially species that sex is determined by temperature. This study was carried out by measuring air, sand and nest temperatures during 2008 and 2009 nesting seasons at Kazanlı Beach, one of the largest nesting sites of *Chelonia mydas* (Green turtle) in the Mediterranean. Sand grain size was also measured, and gonads of dead hatchlings were examined histologically. Both sand (n=4) and nest (n=6) temperatures were above the pivotal temperature (between 29.1-31.6°C) in the study area. According to the estimation based on temperatures, hatchlings were female (♀>50%) biased. Of the hatchling samples, 75 were examined histologically. According to histological examination, the female:male ratio was 2:1. According to the direct examination and indirect estimation; the sex ratio of green turtle hatchlings in Kazanlı Beach, one of the highest hatchling producing nesting sites of the Mediterranean, was reported for the first time in this study. There is a need to fill the data gaps regarding sex ratios, especially for major beaches with high hatchling production. Knowing the temperature profiles in and around the nest and sex ratios of hatchlings is critical for the development of conservation measures for endangered sea turtles.

1. Introduction

Climate change is one of the most serious problems faced by wildlife. Human-induced climate change shows its effects at every stage of wildlife [1]. In species with temperature-dependent sex determination (TSD), it is reported that population sex ratios have started to change, especially in places where temperature increases are high [2]. Sea turtles, which are globally endangered except Natator depressus, are among the species with TSD. In order to understand the effects of global warming, it is critical to know the temperature values of the nesting site and the sex ratios of the hatchlings for the survival of these species [3]. Because it may be difficult for long-lived species such as sea turtles to adapt to the rate of temperature increase [4].

Studies on the impact of global warming on sea turtles have increased rapidly, especially in the last two decades [5]. Terrestrial studies and especially nest-hatchling studies are the easiest to conduct [6]. According to the sexual dimorphism index, curved carapace length is reported to be longer in females than males for sea turtle adults [7], but sexual dimorphism is not observed in hatchlings [8]. However, it has also been reported that female hatchlings are slightly heavier than males [9]. There are direct methods (gonadal histology [10] radio immuno-assay [11], gonad gross morphology [12]) and indirect methods (morphometrics [13], nest

*Corresponding author: onurcandan.phd@gmail.com
Received: 02.11.2023, Accepted: 14.12.2023

temperature [14], incubation duration [15]) to determine hatchlings' sex ratio. The methods and accuracy rates used for sex determination vary.

Histologic examination is the most accurate way to determine sex in hatchlings. However, it is necessary to develop non-invasive methods with high accuracy rather than methods that require hatchling sacrifice [15]. For green turtle hatchlings, the temperature at which the female:male ratio is equal is the pivotal temperature. Above this temperature, female hatchling development is observed, while below this temperature, male hatchling development is observed. The pivotal temperature for sea turtles is around 29°C [16].

The eastern Mediterranean coast of Türkiye, including Kazanlı Beach, hosts important nesting sites for green turtle. [17]. Since the high number of nests increases the number of hatchlings joining the population, Kazanlı Beach is an important nesting site for the survival of the green turtle in the Mediterranean. However, there is a gap in the data on sex ratios for this beach. In this study, temperature values in and around the nest (air, sand and nest temperatures) are presented. The sex ratios of green turtle hatchlings on Kazanlı Beach are given according to these temperature values and histological examination results. In addition to the temperature values, sex ratio of hatchlings was also estimated based on the incubation period.

2. Material and Method

2.1. Study Area (BEU-FBD-Main Title)

This study was conducted in 2008 and 2009 nesting season at Kazanlı Beach, located in Mersin province (Figure 1). The beach is divided into four sub-sections but just sub-sections K1, K2 and K3 were studied. Sub-section K-1 is approximately 2 km in length from the D-7 drainage channel to the poles in front of the Onur Site. The dunes behind the beach are 1-1.5 m high and covered with dense vegetation. The sandy area continues behind the dunes. There is a road separating the beach from the greenhouses at the back of the sandy area. The K-2 sub-section is ~1.7 km in length from the poles in front of Onur Site to the wastewater channel near High School building. There are various facilities within this section. The coast narrows from east to west in this sub-section. K-3 sub-section is ~0.47 km section from school building to Soda-Chromium factory.

2.2. Air, Sand and Nest Temperatures with Incubation Duration

Data loggers (Gemini Data Loggers-Tinytalk Part No: TK-0040) were placed at a suitable point on the beach at the beginning of the nesting season and recorded the sand temperature at a constant depth (50 cm) throughout the nesting season. Considering that this depth from the sand surface to the bottom of the nest is approximately 80 cm [18] and that some of this depth is covered by eggs, it was found appropriate to deploy the data-logger at a depth of 50 cm. When selecting the locations where these data loggers deployed, areas with dense nesting were preferred. The area where the nests are densed in Kazanlı Beach is 22 m from the sea on average.

A total of four sand temperature data loggers were placed in Kazanlı Beach, two in each season (one in each sub-section of K-1 and K-2). Due to intense erosion and tide line, no data-loggers were placed in the K-3 sub-section of Kazanlı Beach to measure sand temperature.

The device was programmed with its original software (GLM v.2.8). After programming, the data-logger was deployed in the beach sand and a total of 1500 measurements were taken with 120 minutes' interval.

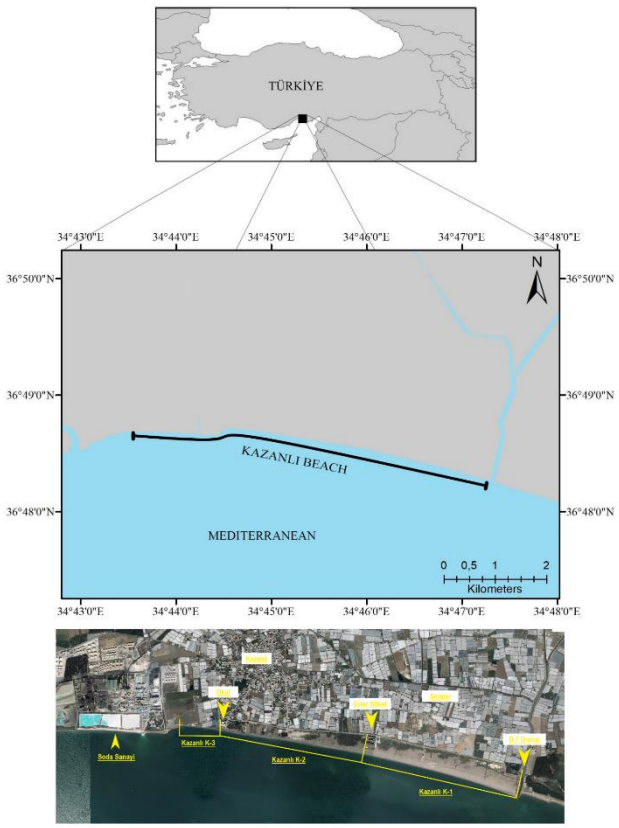

Figure 1. Site map and subsections.

Daily air temperature data for the 2008 and 2009 nesting seasons for Kazanlı Beach were obtained from the Turkish General Directorate of Meteorology. For Kazanlı Beach, Mersin station (Station Code: 17340) was chosen as the closest station to the area.

During the nesting period, the temperature data-logger was deployed into the centre of nest with two methods. The first method is after the female had laid the eggs in egg chamber reached a certain number (~ 50 eggs). In the second method, the datalogger was deployed after half of the eggs had been removed from the nest within 12 hours of egg laying. The time and date when the data logger was placed in the nest was recorded with the serial number of the device. These nests were caged against predation.

The data-logger was programmed with its original software and deployed in the nest. A total of 1500 measurements were taken at 60-minute' intervals during the incubation duration.

The nest temperature values were divided into three equal trimesters depending on the incubation duration [19]. The incubation duration is the time from the day the nest is laid to the day of the first hatchling emergence. Regression of the incubation period of the nests with histological results was calculated with gonad samples taken randomly. The regression equation was calculated by combining the data obtained for Kazanlı Beach with [20] Candan and Kolankaya (2016). Temperature differences between nesting seasons were evaluated by t-test.

2.3. Sand Sampling

When beach sand samples were taken, areas close to the sand temperature data loggers were preferred. A core was taken from the surface to the depth of the data logger with 10 cm diameter. The sand in the core was homogenized and tested. Thus, it was aimed to provide a comparison between beach temperature and sand grain structure. Samples were dried at 105 °C before grain size measurement. Sieving was performed on a Retsch shaker sieve at 60% shaking intensity for 10 minutes. Sand grain sizes were grouped into five different sizes (≥1.00 mm to ≤0.125 mm) and the results are presented as percentage.

2.4. Nest Parameters and Gonad Sampling

Hatchlings emerging from the eggs after the incubation period was over were identified by their tracks on the beach. The nests were uncovered for control after the completion of hatching, the number of hatchlings stucking in the nest (dead and alive), the number of hatchlings (empty eggshells), the number of damaged eggs and their embryonic development status were determined according to the Whitmore and Dutton [19]. The period from the day the nest was laid to the first hatchling emergence was calculated as the incubation duration. The number of eggs in the nest was recorded as the clutch size. The distance from the sand surface to the bottom of the nest was measured as nest depth. The distance from the nest to the high tide line was the distance from the sea.

Gonad samples were obtained from dead hatchlings and late-stage embryos found in the nest and/or on the beach (due to predation and sun exposure). The gonads were dissected as a complex together with the kidneys and placed in tubes with the nest number labels. Buffered para-formaldehyde (4%) prepared in advance for tissue fixation was added and the sample tubes were sealed via parafilm and stored at +4 °C until the histological preparation.

2.4. Histological examination and Sex ratios

The routine histologic procedures were applied to gonad samples after fixation. During this process, the specimens were vacuumed in paraffin passed through graded alcohol series. After these procedures, the tissues were embedded in paraffin blocks. Paraffin blocks were cut in 4μ and 5μ sizes (Thermo-Shandon Microtome) and stained with hematoxylin and eosin. The slides were covered with entellan for histological examination.

Histologic examination was performed with a light microscope (Leica). The criteria of [21]Yntema and Mrosovsky (1980) were used in the examinations. The primary follicle, medulla and thick cortex were used to identify the ovary, while a thin germinal epithelium, testicular cords and testicular tubules were used to identify the testis.

Sex ratios were calculated based on direct histological examination. The values in the literature were used for the calculation according to the regression equation (for details see [18]). According to the regression equation, values above 100% were accepted as 100%.

Table 1. Nest temperature, incubation duration and sex ratio estimation (WID: Whole incubation duration, MT: Middle Third, ID: Incubation duration)

		Temperature (ºC)			Sex ratio estimation (%♀) via		
Year	Nest No	WID	MT	ID (day)	WID	MT	ID
2008	K1	31.0	30.6	51	87.0	74.8	67.0
	K2	32.2	31.6	48	**100.0**	92.7	82.5
2009	K3	30.5	30.4	49	78.8	70.5	77.3
	K4	30.2	30.2	42	72.6	68.1	**100.0**
	K5	30.7	30.7	48	81.4	76.6	82.5
	K6	29.6	29.3	55	61.0	50.8	46.2

3. Results and Discussion

In Kazanlı Beach, which is one of the largest nesting sites for green turtles in the Mediterranean, it was determined that the hatchlings had a female biased (♀ ratio > 50%) sex ratio according to the results of air, sand and nest temperatures and histological examinations. However, there were differences between the values obtained in sex ratio estimation. Sex ratio estimates based on nest temperatures (whole incubation duration and middle third of incubation) differed by ~20% between seasons. However, the ratios are very close to each other based on incubation duration (Table 1). In the 2009 nesting season with higher sampling, it was calculated that a 1°C temperature increase shortened the incubation period by 5.7 days.

Air temperatures increase from June to August in both seasons. Except for June, air temperatures in the 2008 nesting season were higher than those in 2009 nesting season but difference is not significant (T-Value = 1,74 P> 0,05 DF = 241). The mean air temperature during the entire nesting season was 28.4 °C in the 2008 and 27.9 °C in the 2009 nesting season. July and August temperatures were above 29°C in both seasons (Table 2, Figure 2).

Table 2. Air temperature of Kazanlı Beach

Months	2008 nesting season		2009 nesting season	
	Mean ± SD	Min - Max	Mean ± SD	Min - Max
June	26.59 ± 1.61	23.6 - 29.0	26.95 ± 1.37	24.3 - 29.0
July	29.47 ± 0.57	28.4 - 30.4	29.03 ± 0.95	27.3 - 30.4
August	30.15 ± 0.58	28.4 - 31.5	29.55 ± 0.57	28.4 - 30.8
September	27.28 ± 2.42	22.1 - 30.3	26.10 ± 2.51	20.9 - 29.4
Overall	28.40 ± 2.10	22.1 - 31.5	27.93 ± 2.08	20.9 - 30.8

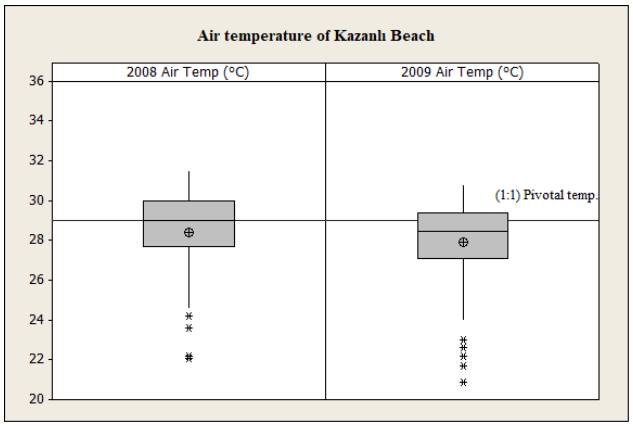

Figure 2. Air temperature of Kazanlı Beach in 2008 and 2009 nesting season.

Similar to the air temperatures, sand temperatures were also higher in the 2008 nesting season than 2009 nesting season. The difference between seasonal sand temperatures was significant (T-Value = 18,49 P< 0,005 DF = 3212). The mean sand temperatures in the K1 and K2 sub-sections of Kazanlı Beach were 30.1°C in the 2008 nesting season and 29.1°C in the 2009 nesting season. The average sand temperature was higher in the 2008 nesting season, as was the air temperature. The mean temperature values measured during the nesting season were above 29°C in both years (Table 3, Figure 3).

Table 3. Sand temperature (50 cm depth) of Kazanlı Beach at 2008 and 2009 nesting season

Subsection	2008 nesting season		2009 nesting season	
	Mean ± SD	Min - Max	Mean ± SD	Min - Max
K1	29.08 ± 0.76	27.2 - 30.6	29.41 ± 0.78	27.2 - 30.2
K2	31.15 ± 0.99	28.7 - 33.0	29.63 ± 0.68	27.9 - 30.2
Overall	30.11 ± 1.36	27.2 - 33.0	29.52 ± 0.74	27.2 - 30.2

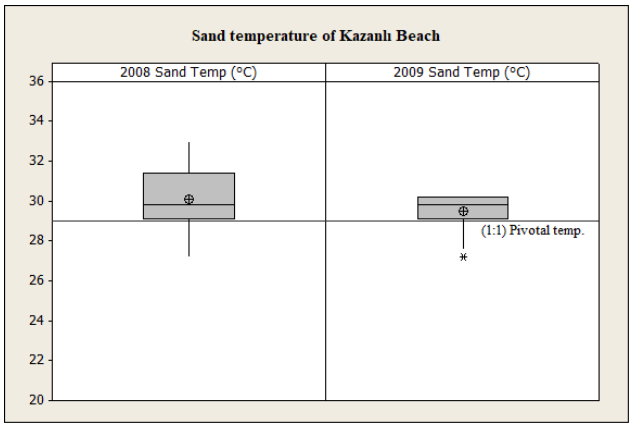

Figure 3. Sand temperature of Kazanlı Beach in 2008 and 2009 nesting season.

A total of six nests were equipped with temperature data loggers in both seasons. In the 2008 nesting season, the mean nest temperature was 31.6 °C and in the 2009 nesting season, the mean nest temperature was 30.2 °C. The difference of nest temperatures was significant between 2008 and 2009 nesting seasons (T-Value = 40,50 P< 0,005 DF = 3740). As with air and sand temperatures, the mean nest temperature in the 2008 nesting season was 1.4 °C higher than the mean nest temperature in the 2009 nesting season. The temperature values obtained in both seasons were between 29.6 - 32.2 °C. As in air and sand temperature, nest temperatures were also above 29 °C (Figure 4).

The differences between air, sand and nest temperatures for 2008 and 2009 nesting season were; (Tempnest - Tempair) 3.18 °C and 2.31 °C respectively, (Tempnest - Tempair) 1.47 °C and 0.72 °C respectively. Seasonal mean nest temperatures were higher than the surrounding sand and air temperatures (Table 1-3).

According to the histological examination, it was determined that the ratio of female:male was 2:1 (67% ovary, 33% testis) in 75 gonad samples in 2008 (n=29) and 2009 (n=46) (Table 4). In the 2008 nesting season at Kazanlı Beach, ovaries were observed in all 4 samples (100%) from nests with 45 - 49 days incubation duration, five ovaries and five testes were observed in 10 samples from nests with 50-54 days incubation duration. Testes (100%) were found in all 4 gonads that could be examined in the samples taken from the nest with 55-59 days incubation duration. In the nest with 60-64 days incubation duration, one of the six gonads examined had ovaries (16.7%) and rest of six had testes (83.3%). In the 2009 nesting season, there were fluctuations in the ratio of males to females depending on the incubation duration. During this season, only one hatchling was sampled from the nest with 45-49 days incubation duration, which was female. In 13 samples examined from nests with 50-54 days incubation duration, 10 ovaries (76.9%) and 3 testes (23.1%) were found, and in 8 samples collected from nests with 55-59 days incubation duration, 5 ovaries (62.5%) and 3 testes (37.5%) were found. No samples were collected from nests with 60-64 days incubation duration. In two samples collected from nests with incubation duration over 65 days, ovaries (100%) were detected. Of the 22 specimens with unknown incubation duration, 19 specimens had ovaries (86.4%) and 3 specimens had testes (13.6%). Although there is a difference between the sex ratios in percentage of the two seasons, this difference is not significant (T-Value = 1,37 P>0,05 DF = 10).

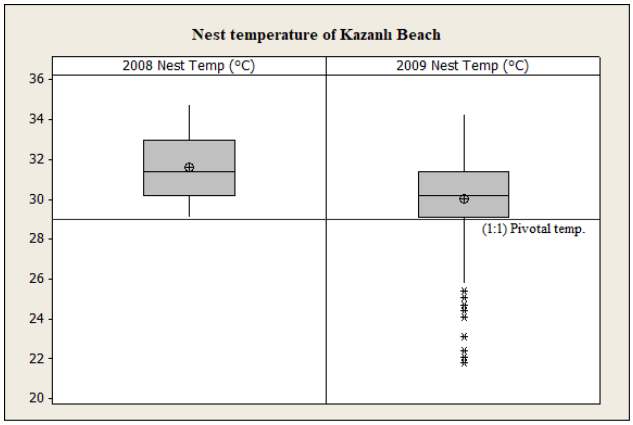

Figure 4. Nest temperature of Kazanlı Beach in 2008 and 2009 nesting season.

Table 4. Histological examination results of gonad samples

Sex		Nesting season 2008	2009	Overall
Female	n	13	37	50
	%	44.8	80.4	66.7
Male	n	16	9	25
	%	55.2	19.6	33.3

The sand grain size is coarser in the K-2 sub-section compared to K-1 sub-section. In sub-section K-1, sand is predominantly composed of 0.125 mm (56.93%) and 0.25 mm (37.25%) sized grains. In the other sub-section K-2, the proportion of 0.5 mm grains increased (16%) while the proportion of 0.125 mm grains (37.4%) decreased (Table 5).

Table 5. Histological examination results of gonad samples

	Grain size (mm)				
Subsection	1.00	0.50	0.25	0.125	<0.125
K1	0.40	2.40	37.25	56.93	3.02
K2	3.24	16.05	41.63	37.36	1.72

There are various conservation practices to ensure the survival of endangered species. Knowing the primary sex ratio of the species makes these conservation practices more effective in sea turtles, where sex is determined by hatching temperature [22]. Kazanlı Beach, which is the largest green turtle nesting area for both Türkiye and the entire Mediterranean basin, has been monitored for many years [23]. However, this is the first assessment of the sex ratio of green turtle hatchlings on this important beach has been reported here.

The sex ratio of green turtle hatchlings is between 67-100% [24]. According to the results of this study, the sex ratio of hatchlings was within the range of other studies. Kazanlı Beach, which is one of the areas producing high numbers of hatchling for the Mediterranean population, contributes to the population with a female bias. According to the results of histological examination of gonad samples for two nesting seasons, there was a difference between the seasons but not significant. Sex ratios show differences between seasons and beaches [25], [26]. However, the difference in this study is due to the limitation in sample numbers. When both seasons are evaluated together, the results of histological examination are calculated as 67% female.

It has been reported that the core region of a nest is hotter than the peripheral regions [27]. Effects such as non-uniformly distributed metabolic heating and sand grain size are likely to alter the temperature inside the nest. This temperature difference can affect sex determination when it occurs during the critical period. For this reason, the nest with 65 days incubation period, which is a limited sample, was completely female.

The most accurate way to determine sex of hatchling is histological examination [28]. However, this practice requires the sacrifice of hatchling, or leads to sample size limitations [29]. Therefore, it is necessary to develop accurate methods to estimate sex ratio. It has been reported that incubation duration is more accurate than other estimation methods [15]. In this study, predictions based on incubation duration showed close results between seasons.

Air and sand temperatures interact with nest temperatures. According to ecological niche modeling, temperature-related parameters (especially the mean temperature of warmest quarter) are among the factors affecting sea turtle nesting beach suitability [30]. An increase in air temperatures directly increases sand temperatures [31]. Nest temperatures are mostly higher than air and sand temperatures [18]. The fact that sand and nest temperatures are above 29 °C, which is the pivotal temperature for green turtles, clearly shows that Kazanlı Beach produces female biased hatchlings. By the end of the 21st century, air temperatures are projected to increase by 2 °C [32]. This global temperature increase is predicted to further increase female biased production. Moreover, it may also exceed the maximum temperature at which embryos can develop.

Considering the air, sand, and nest temperatures, 2008 nesting season was warmer than 2009 nesting season. There is a clear relation between air, sand, and nest temperatures [33], [34]. However, the highest values among these temperatures are observed in nest temperature. Because nest temperatures are not only affected by environmental temperature. Especially considering the contribution of metabolic heating produced by the developing embryos, nest temperatures are expected to be above the surrounding sand temperatures. It has been reported that a healthy developing embryo in green turtle nests increases the nest temperature by approximately 0.02°C [35].

Sand grain size is also among the factors affecting the temperature. When the sand grain size and temperature values in the two sub-sections are analyzed, the sand grain size in sub-section K2 is larger than K1 and the sand temperatures in K2 are higher than K1. As the sand grain size increases, its temperature increases. Thus, different temperatures can be observed on the same beach due to the effect of sand grain size.

When the relationship between nest temperature and incubation duration is analyzed, it is observed that the incubation duration shortens as the incubation temperature increases in both seasons. In laboratory-based studies, it was found that a 1°C temperature increase shortened the incubation period by 4.5 days [36]. However, there may be differences between laboratory-based results and results in the natural environment. The results obtained here are close to the literature, but the small sample size should also be taken into consideration.

4. Conclusion and Suggestions

There are many threats to wildlife. Global warming is among the most serious threats. All species will be affected by the global temperature increase. However, it can be assumed that the effects of global warming will occur in the shorter period on endangered species especially with TSD. Although it is thought that species will adapt to this temperature increase, as they have done in previous climatic changes, the rate of change may prevent this adaptation [37].

Climatic changes were considered to have dramatic impacts not only on hatchlings sex ratios but also nesting site suitability [38]. Practical applications such as measuring nest and sand temperatures and histological examination of dead hatchlings can be used to assess the effects of global warming on sex ratios in sea turtles. The results obtained at the local scale can be used to make global assessments. Therefore, it is of great importance to present data on temperature profiles and sex ratios in all nesting sites, especially in major ones.

Acknowledgment

I thank all volunteers from EKAD (Ecological Research Society). I also thank the anonymous reviewers for their careful reading of the manuscript and their constructive remarks, positive comments, and valuable contributions.**Statement of Research and Publication Ethics**

The study is complied with research and publication ethics

References

[1] J. W. Moore and D. E. Schindler, "Getting ahead of climate change for ecological adaptation and resilience," *Science* no. 376, pp. 1421–1426, 2022, doi: 10.1126/science.abo3608.

[2] H. P. Roberts, L. L. Willey, M. T. Jones, T. S. Akre, D. I. King, J. Kleopfer, ... and B. Zarate, "Is the future female for turtles? Climate change and wetland configuration predict sex ratios of a freshwater species," *Glob Chang Biol*, vol. 29, no. 10, pp. 2643-2654, 2023, doi: 10.1111/gcb.16625.

[3] F. J. Janzen, "Climate change and temperature-dependent sex determination in reptiles," *PNAS*, vol. 91, no. 16, pp. 7487-7490, 1994.

[4] R. B. Huey, L. Patridge and K. Fowler, "Thermal sensitivity of *Drosophila melanogaster* responds rapidly to laboratory natural selection," *Evol.*, vol. 45, no. 3, pp. 751-756, 1991, doi: 10.2307/2409925.

[5] N. J. Robinson, J. Aguzzi, S. Arias, C. Gatto, S. K. Mills, A. Monte, ... and P. S. Tomillo, "Global trends in sea turtle research and conservation: Using symposium abstracts to assess past biases and future opportunities," *Glob. Ecol. Conserv.*, vol. *47*, Article no. e02587, 2023, doi: 10.1016/j.gecco.2023.e02587.

[6] S. Catron, S. Roth, F. Zumpano, J. Bintz, J. A. Fordyce, S. Lenhart, ... and J. Wyneken, "Modeling the impacts of temperature during nesting seasons on Loggerhead (*Caretta caretta*) Sea Turtle populations in South Florida," *Ecol Modell*, vol. 481, Article no. 110363, 2023, doi: 10.1016/j.ecolmodel.2023.110363.

[7] B. J. Godley, A. C. Broderick, R. Frauenstein, F. Glen and G. C. Hays, "Reproductive seasonality and sexual dimorphism in green turtles," *Mar. Ecol. Prog. Ser.*, vol. 226, pp. 125-133, 2002, doi: 10.3354/meps226125.

[8] N. Valenzuela, D. C. Adams, R. M. Bowden and A. C. Gauger, "Geometric morphometric sex estimation for hatchling turtles: a powerful alternative for detecting subtle sexual shape dimorphism," *Copeia*, vol. 4, pp. 735-742, 2004, doi: 10.1643/CH-03-248R1.

[9] Ç. Kılıç and O. Candan, "Hatchling sex ratio, body weight and nest parameters for *Chelonia mydas* nesting on Sugözü beaches (Turkey)," *Anim Biodivers Conserv*, vol. 37, no. 2, pp. 177-182, 2014, doi: 10.32800/abc.2014.37.0177.

[10] R. King, W. H. Cheng, C. T. Tseng, H. Chen and I. J. Cheng, "Estimating the sex ratio of green sea turtles (*Chelonia mydas*) in Taiwan by the nest temperature and histological methods," *J. Exp. Mar. Biol. Ecol.*, vol. 445, pp. 140-147, 2013, doi: 10.1016/j.jembe.2013.03.016.

[11] J. Braun-Mc, S. P. Epperly, D. W. Owens, L. Avens, E. Williams and C. A. Harms, "Seasonal reliability of testosterone radioimmunoassay (RIA) for predicting sex ratios of juvenile loggerhead (*Caretta caretta*) turtles," *Herpetol.*, vol. 63, no. 3, pp. 275-284, 2007.

[12] S. A. Ceriani and J. Wyneken, "Comparative morphology and sex identification of the reproductive system in formalin-preserved sea turtle specimens," *Zool.*, vol. 111, no. 3, pp. 179-187, 2008, doi: 10.1016/j.zool.2007.07.007.

[13] B. Sönmez, E. Bağda, O. Candan and H. E. Yılmaz, "Sex determination in green turtle hatchlings: geometric morphometry and molecular sex markers," *NESciences*, vol. 4, no.1, pp. 42-54, 2019, doi: 10.28978/nesciences.522623.

[14] R. Calderón-Peña, R. Betancourt-Avila, E. Rodríguez-Fajardo, Y. Martínez-González and J. Azanza-Ricardo, "Sex ratio of the green sea turtle *Chelonia mydas* (Testudines: Cheloniidae) hatchlings in the Guanahacabibes Peninsula, Cuba," *Rev. Biol. Trop.*, vol. 68, no. 3, pp. 777-784, 2020, doi: 10.15517/rbt.v68i3.39033.

[15] M. H. Godfrey and N. Mrosovsky, "Pivotal temperature for green sea turtles, *Chelonia mydas*, nesting in Suriname," *Herpetol. J.*, vol. 16, no. 1, pp. 55-61, 2006.

[16] O. Türkozan and Y. Kaska, "Turkey," in *Sea turtles in the Mediterranean: distribution, threats and conservation priorities*, P. Casale and D. Margaritoulis, Eds., Gland, Switzerland: IUCN, 2010, pp. 257-293.

[17] O. Candan and D. Kolankaya , "Temperature Profiles And Sex Ratio Estimation For Green Turtle *Chelonia mydas* Hatchlings On Sugözü Beaches", *Hacettepe J. Biol. Chem.*, vol. 42, no. 4, pp. 531-536, 2014.

[18] C. L. Yntema and N. Mrosovsky, "Critical periods and pivotal temperatures for sexual differentiation in loggerhead sea turtles," *Can. J. Zool.*, vol: 60, no. 5, pp. 1012-1016, 1982, doi:10.1139/z82-141.

[19] O. Candan and D. Kolankaya, "Sex ratio of green turtle (*Chelonia mydas*) hatchlings at Sugözü, Turkey: higher accuracy with pivotal incubation duration," *Chelonian Conserv. Biol.*, vol. 15, no. 1, pp. 102-108, 2016, doi: 10.2744/CCB-1132.1.

[20] C. L. Yntema and N. Mrosovsky, "Sexual differentiation in hatchling loggerheads (*Caretta caretta*) incubated at different controlled temperatures," *Herpetol.*, vol. 36, no. 1, pp. 33-36, 1980.

[21] B. N. Reid and M. Z. Peery, "Land use patterns skew sex ratios, decrease genetic diversity and trump the effects of recent climate change in an endangered turtle," *Diversity Distrib.*, vol. 20, pp. 1425-1437, 2014, doi: 10.1111/ddi.12243.

[22] M. Kasparek, B. J. Godley and A. C. Broderick, "Nesting of the Green Turtle, *Chelonia mydas*, in the Mediterranean: a review of status and conservation needs," *Zool Middle East*, vol. 24, no. 1, pp. 45-74, 2001, doi: 10.1080/09397140.2001.10637885.

[23] L. A. Hawkes, A. C. Broderick, M. H. Godfrey and B. J. Godley, "Climate change and marine turtles," *Endang Species Res*, vol. 7, no. 2, pp. 137-154, 2009, doi: 10.3354/esr00198.

[24] N. Mrosovsky, S. R. Hopkins-Murphy and J.I. Richardson, "Sex ratio of sea turtles: seasonal changes," *Science*, vol. 225, pp. 739–741, 1984.

[25] E. A. Standora and J. R. Spotila, "Temperature dependent sex determination in sea turtles," *Copeia*, vol. 3, pp. 711–722, 1985.

[26] G. Vázquez Luna, R. Sanchez Trejo, R. Márquez Millan and R. Castro Melendez, "Temporal and spatial variation of the hatching temperature in transplanted *Lepidochelys kempi* nestings and their influence on teh sex ratio, egg survival and mortality," in *The Eighteenth International Sea Turtle Symposium* (Mazatlán: NOAA Technical Memorandum NMFS-SEFSC-436), 2000.

[27] M. Hamann, M.H. Godfrey, J.A. Seminoff, P.C.R. Barata, K.A. Bjorndal, A.B. Bolten, A.C. Broderick, L.M. Campbell, C. Carreras, P. Casale, M. Chaloupka, S.-K. Chan, M. Coyne, L.B. Crowder, C.E. Diez, P.H. Dutton, S.P. Epperly, N.N. FitzSimmons, A. Formia, M. Girondot, G.C. Hays, I.J. Cheng, Y. Kaska, R. Lewison, J.A. Mortimer, W.J. Nichols, R.D. Reina, K. Shanker, J.R. Spotila, J. Tomás, B.P. Wallace, Thierry M. Work, N. Zbinden, and B.J. Godley, "Global research priorities for sea turtles: informing management and conservation in the 21st century," *Endang Species Res*, vol. 11, no. 3, pp. 245-269, 2010, doi: 10.3354/esr00279.

[28] N. Mrosovsky, S. Kamel, A. F. Rees and D. Margaritoulis, "Pivotal temperature for loggerhead turtles (*Caretta caretta*) from Kyparissia Bay, Greece," *Can. J. Zool.*, vol. 80, no. 12, pp. 2118-2124, 2002, doi: 10.1139/z02-204.

[29] G. Arslan, A. Ertürk and O. Candan, "Predicting the distribution of green turtle nesting sites over the Mediterranean with outcoming climate driven changes," *J. Nat. Conserv.*, vol. 71, no.126320, 2023, doi: 10.1016/j.jnc.2022.126320.

[30] J. J. Lembrechts, J. van den Hoogen, J. Aalto, M. B. Ashcroft, P. De Frenne, J. Kemppinen, ... and D. S. Hik, "Global maps of soil temperature," *Glob Chang Biol*, vol. 28, no. 9, pp. 3110-3144, 2022, doi: 10.1111/gcb.16060.

[31] H. O. Pörtner, D. C. Roberts, M. Tignor, E. S. Poloczanska, K. Mintenbeck, A. Alegría, M. Craig, S. Langsdorf, S. Löschke, V. Möller et al., "Climate change 2022: impact, adaptation, and vulnerability" in *Contribution of Working Group II to the Sixth Assessment Report of the Intergovernmental Panel on Climate Change*. *Summary for Policymakers*, H.O. Pörtner, D.C. Roberts, M. Tignor, E.S. Poloczanska, K. Mintenbeck, A. Alegría, M. Craig, S. Langsdorf, S. Löschke, V. Möller, A. Okem and B. Rama Eds., Cambridge, UK, Cambridge University Press, 2023, doi: 10.1017/9781009325844.

[32] K. C. Santos, M. Livesey, M. Fish and A. C. Lorences, "Climate change implications for the nest site selection process and subsequent hatching success of a green turtle population," *Mitig Adapt Strateg Glob Chang*, vol. 22, pp. 121-135, 2017, doi: 10.1007/s11027-015-9668-6.

[33] C. T. Chu, D. T. Booth and C. J. Limpus, "Estimating the sex ratio of loggerhead turtle hatchlings at Mon Repos rookery (Australia) from nest temperatures," *Aust. J. Zool.*, vol. 56, pp. 57-64, 2008, doi:10.1071/ZO08004.

[34] B. F. Önder and O. Candan, "The feminizing effect of metabolic heating in Green Turtle (*Chelonia mydas*) clutches in the eastern Mediterranean," *Zool Middle East*, vol. 62, no. 3, pp. 239-246, 2016, doi: 10.1080/09397140.2016.1202927.

[35] N. Mrosovsky and C. L. Yntema, "Temperature dependence of sexual differentiation in sea turtles: implications for conservation practices," *Biol. Conserv.*, vol. 18, no. 4, pp. 271-280, 1980, doi: 10.1016/0006-3207(80)90003-8.

[36] S. S. Heppell, J. Wyneken and S. A. Heppell, "A morphologist, a modeler, and an endocrinologist consider sea turtle sex ratios in a changing climate. Some wine was involved," *Front. Ecol. Evol.*, vol. 10, no. 952432, 2022, doi: 10.3389/fevo.2022.952432

[37] A. D. Mazaris, C. Dimitriadis, M. Papazekou, G. Schofield, A. Doxa, A. Chatzimentor, O. Turkozan, S. Katsanevakis, A. Lioliou, S. Abalo-Morla, M. Aksissou, A. Arcangeli, V. Attard, H. A. El Hili, F. Atzori, E. J. Belda, L. B. Nakhla, A. A. Berbash, K. A. Bjorndal, A. C. Broderick, J.A. Camiñas, O. Candan, L. Cardona, I. Cetkovic, N. Dakik, G. A. de Lucia, P. G. Dimitrakopoulos, S. Diryaq, C. Favilli, C. M. Fortuna, W. J. Fuller, S. Gallon, A. Hamza, I. Jribi, M. B. Ismail, Y. Kamarianakis, Y. Kaska, K. Korro, D. Koutsoubas, G. Lauriano, B. Lazar, D. March, A. Marco, C. Minotou, J. R. Monsinjon, N. M. Naguib, A. Palialexis, V. Piroli, K. Sami, B. Sönmez, L. Sourbès, D. Sözbilen, F. Vandeperre, P. Vignes, M. Xanthakis, V. Köpsel and M. A. Peck, "Priorities for Mediterranean marine turtle conservation and management in the face of climate change," *J. Environ. Manage.*, vol. 339, no. 117805, 2023, doi: 10.1016/j.jenvman.2023.117805.

Bitlis Eren Üniversitesi Fen Bilimleri Dergisi
BİTLİS EREN UNIVERSITY JOURNAL OF SCIENCE
ISSN: 2147-3129/e-ISSN: 2147-3188
VOLUME: 12 NO: 4 PAGE: 1319-1336 YEAR: 2023
DOI:10.17798/bitlisfen.1386990

An Empirical Analysis of the Relationship Between Diabetes and Demographic, Socioeconomic and Built Environment Factors Across Turkish Cities

Ayşe Gül SOYDAN GÜRDAL[1*], Burcu Halide ÖZÜDURU[1]

[1] *Gazi University, Faculty of Architecture, Department of City and Regional Planning, Ankara, Türkiye*
(ORCID: 0000-0002-1786-4601) (ORCID: 0000-0002-8315-2303)

Keywords: Urban Planning, Urban Health, Built Environment, Spatial Autoregression, Diabetes

Abstract
Demographic, socioeconomic, and built environment factors of cities are considered among risk factors for many Noncommunicable Diseases (NCDs). Decreasing NCDs and supporting healthy, high-quality urban environments is one of the United Nations' Sustainable Development Goals (SDGs). In particular, diabetes is related to quality of life and physical activity, making the disease more responsive to built environment factors. This study examines the geographical distribution of diabetes disease rate and its risk factors across Turkish cities. Principal component analysis and spatial regression models are used for this purpose. It is observed that open green spaces with high accessibility can increase physical activity and thus have a reducing effect on diabetes prevalence. In addition, in cities with sufficient healthcare services per capita, diabetes prevalence is lower. On the other hand, private vehicle ownership can have an increasing effect on diabetes prevalence, and a high share of the elderly population can be another reason for high diagnosis. According to the study findings, planning settlements with high open green spaces prioritizing open green space development, public transportation and non-motorized vehicles, and accessible healthcare facilities can reduce diabetes risk factors by promoting physical activity and increased mobility along with a positive planning and design approach for public health. Elderly-friendly planning specifications need prioritization for some cities. This study presents evidence for the necessity of urban policies and public health strategies prioritizing health and physical activity in urban built environments.

1. Introduction

Noncommunicable diseases (NCDs) account for 74% of all deaths worldwide and are rapidly increasing [1]. 77% of NCD-related deaths occur in low and middle-income countries [1]. The United Nations' 2030 Sustainable Development Agenda aims to reduce premature deaths caused by NCDs by one-third by 2030 [2], [3]. In Turkey, NCD-related death rates are similar to countries in the WHO European Region, but the proportion of NCD-related deaths has increased from 68% in 2000 to 87% today [4]. This rate is higher than the global average.

NCDs result from long-term, genetic, physiological, environmental, and behavioral factors. The main types of NCDs include cardiovascular diseases (heart and vascular diseases, hypertension etc.), accounting for 44% of NCDs deaths; cancer at 23%; chronic respiratory diseases at 10%; and diabetes (including kidney disease caused by diabetes) at 5% [2]. While the risk of premature death from the four major NCDs has decreased globally from 2000 to 2016, the risk of premature death from diabetes has increased by 5% [5].

Type 2 diabetes is rapidly becoming a major public health issue worldwide [6], [7], [8], [9] and is the fourth most common NCDs globally; deaths from Type 1 and Type 2 diabetes account for 2% of all deaths, but in Turkey, it is approximately 3-3.5% [10], [2], [4]. It is estimated that by 2040, there will be 642

* *Corresponding author: aysegulsoydan@gazi.edu.tr*
Received: 06.11.2023, Accepted: 14.12.2023

million people (approximately 6% of the world's population) with diabetes worldwide [6], [8]. The majority of diabetes diagnoses (approximately 90%) are Type 2 diabetes [11], [12], [13]. Diabetes can cause serious damage to the kidneys and heart [6]. In Turkey, the prevalence of diabetes is increasing; in the National Burden of Disease Study (2004), the prevalence of diabetes in Turkey was approximately 5%. In the 2009 Turkish Adults' Heart Diseases and Risk Factors (TEKHARF) study, the prevalence of diabetes in the population over 35 was estimated to be 11.3%, with approximately 3.3 million people reported to have been diagnosed with diabetes [47]. While Type 2 diabetes is influenced by genetic factors, demographic, socioeconomic, and built environment risk factors are more influential for this disease than other NCDs [14], [15], [50]. Obesity and a physically inactive lifestyle are the most significant risk factors for the increasing rates of diabetes, as well as heart disease and cancer [8], [48]. Approximately 60% of Type 2 diabetes patients are described as obese [8], [49], [14]. Obesity is defined as excessive and abnormal fat accumulation leading to adverse health outcomes, with a body mass index (BMI) of $\geq$30 kg/m² [48]. It is estimated that by 2030, more than half of the world's population will be obese [48]. Obesity, like diabetes, as a significant modifiable risk factor, is related to physical activity and nutrition, both associated with urban planning, design, and built environment characteristics [16].

The built environment is a comprehensive structure that encompasses urban design, land use, transportation systems, and the physical surroundings. Urban design focuses on the arrangement of physical elements within a city, addressing the organization of public spaces and their functionality and attractiveness. Land use categorizes activities such as residential, commercial, office, and green spaces, expressing the distribution of activities in terms of location and intensity across the area. The transportation system includes the physical infrastructure and service levels of roads, as well as pedestrian and cycling paths [52]. Carmona categorizes built environment components into nine headings: spatial, morphological, contextual, visual, social, environmental, functional, perceptual, and sustainability, considering design and planning aspects [53]. This study interprets the relationship between built environment components and health through physical activity, land use functions, and urban air pollution.

Physical inactivity is the fourth most significant risk factor for noncommunicable diseases (NCDs) worldwide, contributing to approximately 3.2 million deaths [16]. Physical inactivity can influence the rates of diabetes and obesity [12], [17], [18], air pollution [13], [19], [6], leading them to increase. In a city, having a high level of walkability, cycling and green spaces can have a positive impact on reducing these rates [6]. To increase physical activity, individuals are recommended to engage in physical activities for at least 30 minutes on several days a week. [20]. While the rates of diabetes and obesity vary by geographical region, over 80% of diabetes patients live in low and middle-income countries [8], [13], [14], and the number of obese individuals is increasing in these countries [21]. Uncontrolled, car-centric urbanization in developing countries, along with a sedentary lifestyle and air pollution, is associated with the risk factor of physical inactivity, leading to an increase in obesity and Type 2 diabetes rates[9], [13], [19], [20].

The planning and design principles of cities are significant determinants of urban health, and factors such as residential density, the amount and accessibility of green spaces, the layout of walkable and cycle road networks, and air pollution features stand out. In England, a reverse relationship was found between obesity and residential density due to an increase in mixed land use and the likelihood of retail and workplace spaces in dense residential areas, suggesting that an increase in residential density results in a decrease in waist circumference measurements [22]. Density can be defined as "the amount of activity in an area" represented by population density, housing unit density, or employment density. High density represents compact land development, reducing dependence on motor vehicles by shortening the distance between starting and ending points [23]. It has a negative relationship with obesity because it increases the likelihood of physical activity.

The amount of green space has been associated with lower obesity and diabetes rates [6], [24]. Additionally, the accessibility of green spaces encourages an active lifestyle [25]. In a study, the amount of green space and the proximity of green spaces suitable for recreational use were found to promote physical activity within short distances [25], [26].

Walkability supports physical activity and has a reduction effect on both obesity and Type 2 diabetes prevalence. In cities with a specific residential density and high land use diversity, the level of walkability increases [27], [28], [29]. Besides residential density, intersection density, public transport density, and the number of parks within walking distance also increase physical activity [30].

Exposure to air pollution has been associated with glucose metabolism and biological outcomes,

leading to its relationship with diabetes prevalence [31]. Studies have found that greater exposure to air pollution and traffic density is associated with higher diabetes prevalence [6]. Air pollutants such as particulate matter PM10 [31], [34], PM2.5 [31], [33], nitrogen dioxide [31], [34], [35], and sulfur dioxide [34] have been found to increase diabetes prevalence.

Despite extensive research in this field, more studies are needed to understand the relationship between built environment factors and the prevalence of chronic diseases. Therefore, there is a need for additional research to uncover these relationships. There is no other national study that has developed a model to explain the relationship between NCDs and the built environment. This study is the first and only original work in the field within the context of Turkey. This article investigates the relationship between the prevalence of Type 2 diabetes and built environment characteristics, utilizing provincial-level data and considering other influencing factors. The study aims to reveal the geographical distribution in Turkey and examine prominent built environment features that impact such a chronic disease. Urban policies guiding the effects of these built environment features will undoubtedly play a significant role in creating healthy urban environments. Following the article's introduction section, the second section covers the data used and the methodology. The third section presents the findings and discussions, while the final section lists the results.

2. Data and Methodology

a. Database

The prevalences of obesity and Type 2 diabetes defined according to International Classification of Diseases (ICD) codes for 81 cities are obtained from the Turkish Ministry of Health; socioeconomic data were sourced from the Turkish Statistical Institute (TÜİK) and the Social Security Institution (SGK). Built environment indicators were obtained from Başarsoft Information Technologies Inc., and air quality data for the year 2019 were acquired from the Ministry of Environment, Urbanism, and Climate Change. The data obtained in the study are listed in Table 1. The study covers a population of individuals aged 15 and over, totaling approximately 64 million.

Table 1. Data Description

Health Variables	**Demographic and Socioeconomic Variables**	**Built Environment, Land Use, and Air Quality Variables**
Prevalence of Type 2 Diabetes in Individuals Aged 15 and Over (**DIA**)	Population Density (person/ha) (**Popdensity**)	Area of Parks per 1,000 People (m^2) (**Parks**)
Prevalence of Obesity in Individuals Aged 15 and Over (**OBS**)	The proportion of the Population aged 65 and over to the Total Population (**Pop65+**) (%)	Open green space per 1,000 People (m^2) (**Open green space**)
	Proportion of the Population with a Bachelor's Degree to the Total Population (**BachDeg**) (%)	Residential Area per 1,000 People (m^2) (**Residential Area**)
	Per Capita Gross Domestic Product (GDP) ($) (**GDP**)	Trade Area per 1,000 People (m^2) (**Trade Area**)
	Number of Private Cars per 1,000 People (**Number of Cars**)	Area of Health Services per 1,000 People (m^2) (**Health Area**)
	The ratio of Agricultural Sector Workers to the Total Employment in the City (**Agriculture**) (%)	Particulate Matter in the Air ($\mu g/m^3$) (**PM10**)
	The ratio of Industrial Sector Workers to the Total Employment in the City (**Industry**) (%)	

In the Turkey Nutrition and Health Survey (TBSA) 2017 study, the prevalence of diabetes was 12.5%, and the obesity prevalence was 27.8% [35]. In the Turkey Household Health Survey Noncommunicable Diseases Risk Factors Prevalence (STEPS) 2017 survey, the prevalence of diabetes was 11.1%, and the obesity prevalence was 28.8% [36]. Diabetes is 29.5% in rural areas and 70.5% in urban areas [37]. In this study's Database, the average prevalence of Type 2 diabetes is 5.95, and the obesity rate is 0.45[2] (Table 2).

The population density across Turkish cities shows that the least densely populated city is Tunceli, with 0.11 person/hectare, and the most densely populated city is Istanbul, with 28.40 person/hectare. According to the data, the percentage of the population aged 65 and over to the total population is an average of 13.36%. The city with the highest percentage is Sinop at 22.58%, and the city with the lowest percentage is Hakkari at 4.87%. The average percentage of the proportion of the population with a bachelor's degree to the total population is 14.1%. The city with the highest percentage is Ankara at 22.9%, and the city with the lowest percentage is Ağrı at 8.98%.

According to the 2019 data, the average annual Gross Domestic Product (GDP) per capita is $7,062.50. Based on this average, Turkey ranks 94th among all countries [38]. The highest GDP is observed in Istanbul, an industrial-focused city, with $16,791.00, while the lowest is in Diyarbakır at $431.00. There are 45 cities with GDP below the average.

The average percentage of people working in the agricultural sector to total employment is 1.57, and the industrial sector to total employment is 24.59. The city with the highest percentage of people working in the agricultural sector is Bolu at 5.43, and the city with the lowest percentage is Istanbul at 0.10.

Table 2. Descriptive Statistical Analysis

	N	Missing	Mean	Std. Deviation	Minimum	Maximum
DIA	81	0	5.95	2.55	0.76	11.13
OBS	81	0	0.45	0.43	0.02	2.66
Popdensity	81	0	1.30	3.19	0.11	28.40
Pop65+ %	81	0	13.36	3.85	4.87	22.58
BachDeg %	81	0	14.10	2.45	8.98	22.90
GDP ($)	81	0	7,062.50	2,841.40	431	16,791.00
Number of Cars	81	0	122.30	58.40	8	262
Agriculture %	81	0	1.57	0.93	0.10	5.43
Industry %	81	0	24.59	12.48	3.89	54.89
Park Area	81	0	1,967.60	1,132.80	104	5,022.40
Open Green Space	81	0	467,573.40	1,117,880.40	816.6	7,476,859.60
Residential Area	81	0	8,150.90	5,715.60	557.60	3,242.50
Trade Area	78	3	461.20	572.90	0	4,229.60
Health Area	81	0	930.60	300	400.40	1,721.10
PM10	80	1	101	88.62	0	452.20

[2] The reason for the difference between the Database obtained from the Ministry of Health and the TBSA 2017 study findings for Turkey is that TBSA involves personal measurements, and the Ministry of Health data presents individuals' self-reported diagnoses.

When it comes to the built environment data in terms of land use, on average, there is 1,967.60 m² of park area per 1,000 people and 467,573 m² of open green space per 1,000 people in each city. Similarly, there is an average of 8,150.90 m² of residential area, 461.20 m² of trade area, and 930.60 m² of health area per 1,000 people. Particulate matter (PM10) in the air, an important indicator of air quality, has an average level of 101 µg/m³. This level is well above the limit of 20 µg/m³ set by the World Health Organization for human health [51]. Regarding air quality, Hakkari has the lowest PM10 levels, while Istanbul has the highest at 452.20 µg/m³. There are 29 cities above the average, including Ankara, Kocaeli, and Izmir.

b. Method

In the study, first, the geographical distribution of the 2019 cross-sectional data for 81 cities was examined using thematic maps generated by GIS software. The level of spatial autocorrelations was specified with Moran's test. Moran's I statistic measures the degree of spatial dependency, examining how values diverge from the overall mean value across neighboring geographic units. The closer the Moran's I statistic is to +1, the more similar values are spatially dependent on each other, indicating positive spatial autocorrelation. If it is close to -1, it indicates negative spatial autocorrelation, where dissimilar values are clustered together. A value close to 0 indicates no spatial autocorrelation or randomness [39], [40] (Equation 1). Moran's I statistic for Diabetes prevalence is 0.39, indicating some spatial dependence for the variable DIA across cities (Figure 1).

$$I = \left(\frac{N}{\sum_i \sum_j w_{ij}}\right) x \left[\frac{\sum_i \sum_j w_{ij(y_i-\bar{y})(y_i-\bar{y})}}{\sum_i (y_i-\bar{y})^2}\right] \quad (1)$$

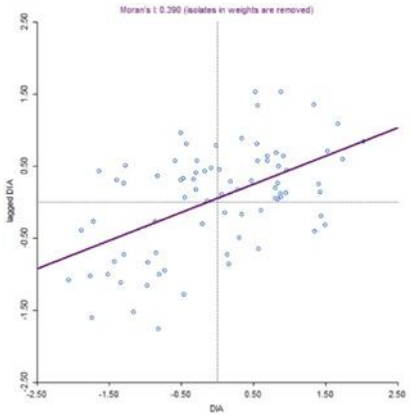

Figure 1. Moran's I statistic for Diabetes Prevalence

The spatial dependencies of various variables reflect the clustering tendencies. Cluster analysis was performed using the GeoDa program, and the LISA (Local Indicators of Spatial Association) analysis reveals the local clustering of the variables. Spatial dependencies are obtained for all cities and are calculated by dividing the differences between each region's value and the overall mean by the standard deviation. Spatial neighbor relationships are expressed using the spatial weights matrix "W" [41]. Equation (2) demonstrates the calculation of local indicators, where Xi is the observed value for each geographical unit from i to j, x is the mean value, s is the standard deviation, and Wij is the spatial weights matrix.

$$Local\ I = \frac{(x_i-\bar{x})}{S^2} \sum_j W_{ij}(x_j - \bar{x}) \quad (2)$$

In the second stage, Principal Component Analysis (PCA) [42] was used to understand the relationships between variables and reduce the number of selected variables. PCA is a statistical data reduction method that transforms study variables into fundamental features called principal components [42], [43]. This method helps reveal the similarities and differences between variables by using a few principal components [43].

In the third stage, regression models were set up to analyze the relationship between demographic, socioeconomic, and built environment variables with disease rates. Due to the high spatial dependence rates among variables at the provincial level, a spatial error model (SEM) was chosen as the most suitable model for regression analysis, and the findings of this model were presented. The spatial error model (SEM) is a

spatial regression model that solves spatial dependence issues in Ordinary Least Squares (OLS) models [44].

The OLS model can be expressed as shown in Equation (3):

$$y = \beta_0 + \sum_{i=1}^{k} \beta_i x_i + \varepsilon, \varepsilon \backsim \mathrm{N}(0, \delta^2) \quad (3)$$

The y in the model represents the dependent variable, which denotes disease rates. The x_i represents independent variables, including selected demographic, socioeconomic, and built environment factors. β_0 is the intercept, and β_i represents the parameter estimates for x_i. ε denotes the error term. The existence of spatial dependence in the error terms shows that the Spatial Error Model (SEM) was appropriately selected for this study.

$$y = X\beta + \lambda W u + \varepsilon, \varepsilon \backsim \mathrm{N}(0, \delta^2) \quad (4)$$

The SEM is represented by Equation (4). W is the spatial weights matrix of size NxN, and N is the number of geographic units in the study area, which is 81.

3. Findings

3.1 Distribution of Health Variables by Cities

The distribution of Type 2 diabetes prevalence (Figure 2(a)) shows that it is particularly high in the southeast of the Aegean, Western Black Sea, and Mediterranean regions. The average diabetes prevalence in Turkey is 5.94, while in Manisa (11.13), Zonguldak (10.40), and Aydın (10.23), it is approximately twice as high. The lowest rates are in Şırnak (0.75), Şanlıurfa (1.19), and Kars (1.49), mainly located in the Southeastern and Eastern Anatolian regions.

The geographical distribution of obesity prevalence (Figure 2(b)) shows that it is high in the Aegean and Western Black Sea regions. The average obesity prevalence in Turkey is 0.45, while in Bolu (2.65), Bartın (1.59), and Aydın (1.32), it is higher than average. The lowest obesity prevalences are observed in Ardahan (0.020), Bingöl (0.026), and Bayburt (0.033).

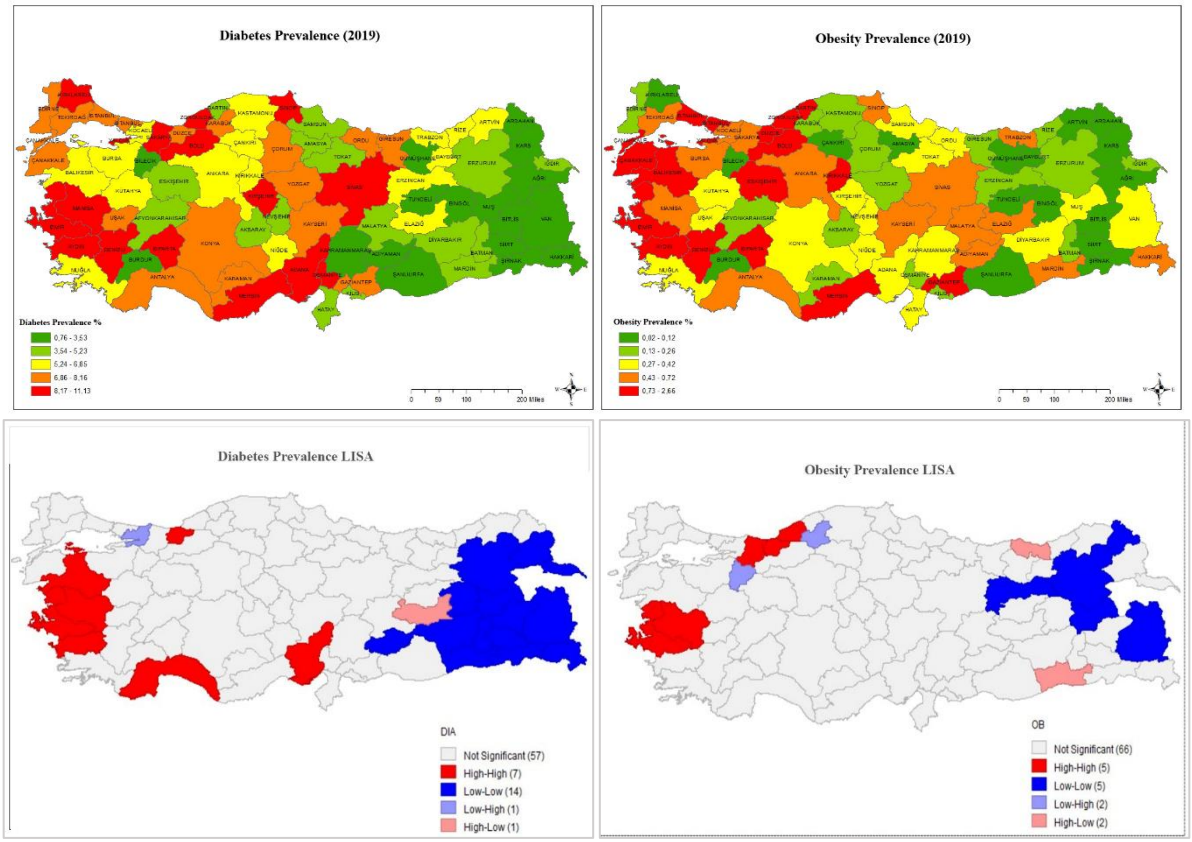

Figure 2. (a) Distribution of Type 2 diabetes prevalences by cities (Source: Ministry of Health, 2019), (b) Distribution of obesity prevalence by cities (Source: Ministry of Health, 2019), (c) Local spatial autocorrelation (LISA) analysis of Type 2 diabetes prevalence by cities, (d) Local spatial autocorrelation (LISA) analysis of obesity prevalence by cities.

LISA analysis reveals the spatial relationships of variables, as seen in Figure 2(c) and (d). In Figure 2(c), it is observed that the prevalence of type 2 diabetes is high and clustered in Aydın, Manisa, Izmir, Balıkesir in the Aegean region, in Antalya and Adana in the Mediterranean region, and Düzce in the Marmara region. In the Eastern Anatolian region, it is generally low and clustered. Kocaeli stands out as an outlier with significantly lower values than neighboring cities, and Elazığ stands out with significantly higher values than neighboring cities.

In Figure 2(d), it is evident that the prevalence of obesity is higher and clustered in Izmir and Manisa in the west, as well as in Düzce, Zonguldak, and Bartın in the north. In the east, it is recorded at low levels and clustered in Erzincan, Erzurum, Ardahan, Muş, and Van. Trabzon and Mardin have significantly higher prevalences than neighboring cities, while Karabük and Bilecik have lower prevalence than neighboring cities.

When comparing the geographical distribution of type 2 diabetes and obesity prevalence, similarities are observed in the Aegean and Eastern Anatolian regions. At the same time, differences are noted in the Mediterranean and Black Sea regions. Although obesity is a significant risk factor for diabetes, in Antalya, Adana, Düzce, and Elazığ, even if obesity prevalence is not high, a high prevalence of type 2 diabetes is observed. Obesity prevalence is varied and recorded at a high level in Sakarya, Zonguldak, Trabzon, and Mardin.

.

3.2 Distribution of Demographic Variables by Cities

When examining the distribution of population density by city (Figure 3(a)), it is observed that population density is higher in major cities, such as Istanbul, Ankara, and Izmir, as well as in coastal cities. In smaller cities, the proportion of the population aged 65 and over is higher (Figure 3(b)). In particular, in the North Aegean region (Çanakkale, Balıkesir), the Black Sea region (Sinop, Kastamonu), and in some cities in the Eastern Black Sea region (Giresun, Artvin), and the Central Anatolian region (Çankırı, Çorum, Tokat), this proportion is relatively high (between 16.38% and 22.58%). However, in the Southeastern Anatolian (Gaziantep, Şanlıurfa) and Eastern Anatolian (Van, Bitlis) cities, it is relatively lower (below 10.26%). The younger population (ages 15-34) predominantly resides in these regions.

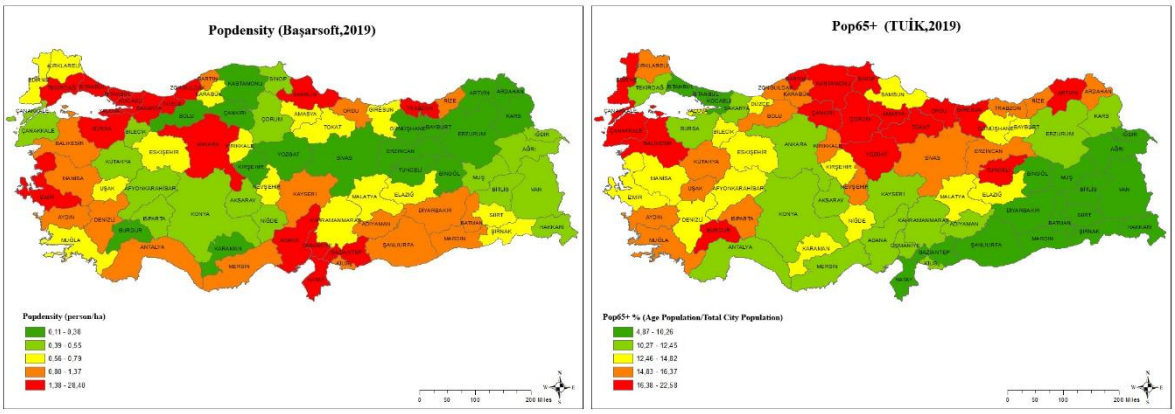

Figure 3. (a) Population density by city (Source: TÜİK, 2019), (b) The proportion of the population aged 65 and over to the total population by city (Source: Başarsoft, 2019).

3.3 Distribution of Socioeconomic Variables by Cities

To depict the socioeconomic status of the cities in the dataset, we chose variables associated with educational attainment. These variables encompass the percentage of the population holding a bachelor's degree, the per capita gross domestic product (GDP), the number of private cars per 1,000 individuals, and the proportion of the workforce engaged in the agricultural and industrial sectors relative to the total employed population.

When examining the geographical distribution of the proportion of the population with a bachelor's degree to the total population (Figure 4(a)), it is observed that in some cities in the Marmara Region (Istanbul, Kocaeli, Bursa, Çanakkale), Aegean Region (Izmir, Muğla), Mediterranean Region (Isparta, Antalya), Central Anatolia Region (Ankara, Eskişehir), Eastern Anatolia Region

(Malatya, Erzincan, Tunceli), and the Black Sea Region (Trabzon, Karabük), this proportion is relatively high (ranging from 15.85% to 22.92%).

The per capita gross domestic product (GDP) (Figure 4(b)) is high in industrialized regions and the western parts of the country. In particular, it is high in some cities in the Marmara Region (Istanbul, Kocaeli, Sakarya, Bursa, Bilecik, Çanakkale), Aegean and Mediterranean Regions (Manisa, Izmir, Muğla, Antalya), Central Anatolia Region (Ankara, Eskişehir), and in some cities in the Western Black Sea Region (Bolu) (ranging from $9,136 to $16,791). In contrast, it is low in all cities in the Southeastern Anatolia Region (except Gaziantep) and in some cities in the Eastern Anatolia Region (Bingöl, Muş, Ağrı, Kars, Van, Bitlis, Hakkâri) (ranging from $431 to $5,294).

The number of private cars per 1,000 people (Figure 4(e)) may indicate increased mobility and high income. In western parts of the country, car ownership is high, similar to the GDP distribution. It is high in larger cities in the Marmara Region (Istanbul, Çanakkale), Aegean Region (Izmir, Muğla, Kütahya, Uşak, Denizli), Antalya Region (Isparta, Burdur, Antalya), Central Anatolia, Western and Central Black Sea Regions (Ankara, Eskişehir, Nevşehir, Bolu, Amasya) (ranging from 172 to 262 cars per 1,000 people). In contrast, it is low in all cities in the Southeastern Anatolia Region (except Gaziantep), some cities in the Eastern Anatolia Region (Bingöl, Muş, Ağrı, Kars, Van, Bitlis, Hakkâri, Iğdır, Tunceli), and some cities in the Eastern Black Sea Region (Gümüşhane, Ardahan) (ranging from 8 to 65 cars per 1,000 people).

The variable of the percentage of people working in agriculture (Figure 4(c)) is high in some cities in the Mediterranean Region (Antalya, Mersin, Adana), the Aegean and Marmara Regions (Aydın, Muğla, Afyonkarahisar, and Balıkesir), the Central Anatolian and Black Sea Regions (Kırşehir, Yozgat, Amasya, Kastamonu, Sinop, Bolu, Artvin), and in some cities in the Southeastern and Eastern Anatolian Regions (Muş, Şanlıurfa) where agricultural production is high. On the other hand, the percentage of people working in the industrial sector (Figure 4(d)) is predominantly high in industrial areas, in particular, in the Marmara Region (Kocaeli, Sakarya, Düzce, Kırklareli, Tekirdağ, Bursa, Bilecik), the Aegean and Central Anatolian Regions (Manisa, Uşak, Denizli, Eskişehir, Karaman), and in some cities in the Mediterranean and Southeastern Anatolian Regions (Kahramanmaraş, Gaziantep) with rates ranging from 36.77% to 54.89%.

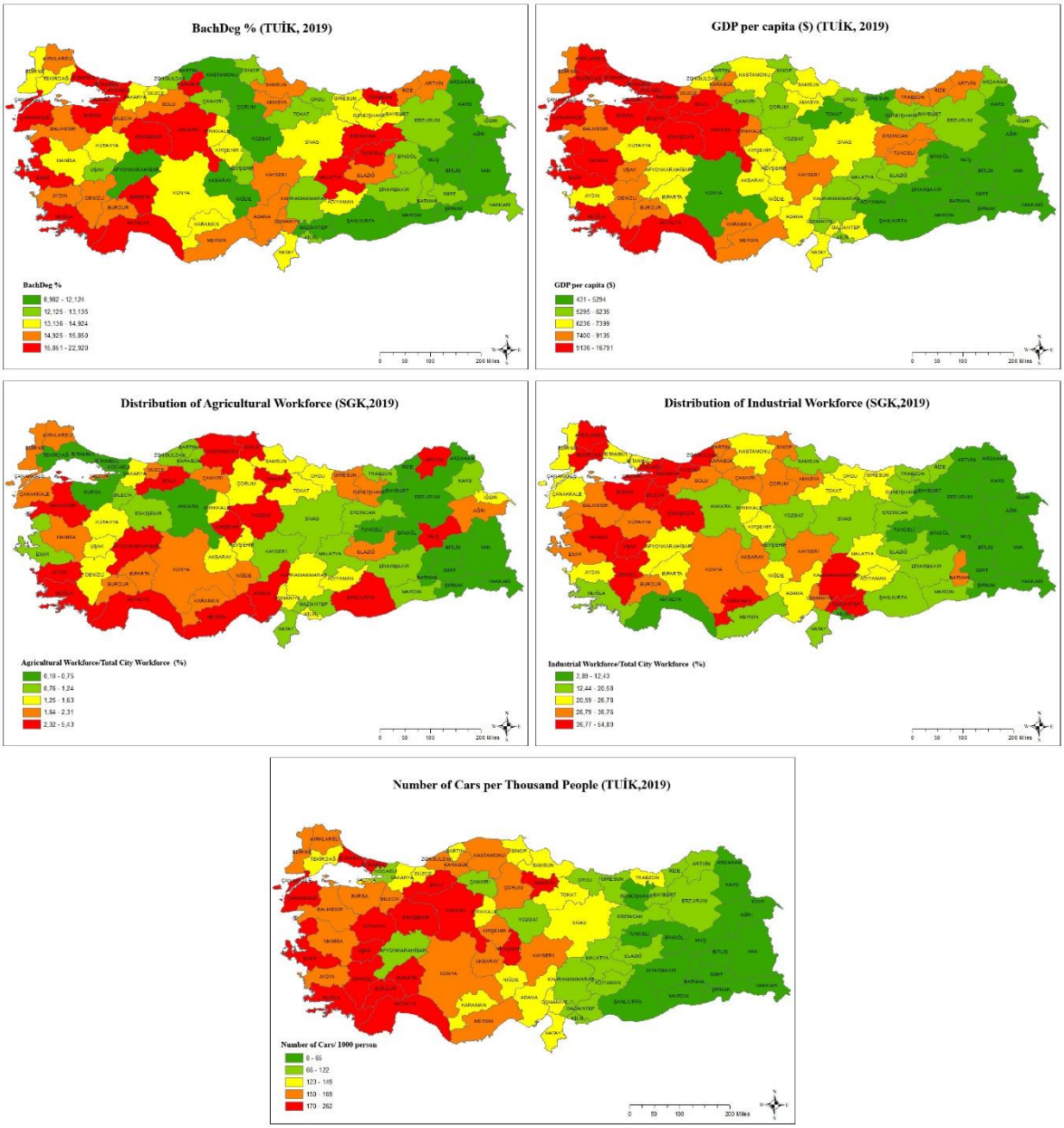

Figure 4. (a) Percentage of the population with bachelor's degree (Source: TURKSTAT, 2019), (b) Gross Domestic Product per capita ($) (Source: TURKSTAT, 2019), (c) Proportion of people employed in the agricultural sector to the total employment in the city (Source: SGK, 2019), (d) Proportion of people employed in the industrial sector to the total employment in the city (Source: SGK, 2019), (e) Number of private cars per 1,000 people (Source: TURKSTAT, 2019).

3.4 Distribution of Built Environment and Air Quality Variables by Cities

In the dataset, variables representing the built environment in cities include parks, open green spaces, residential areas, commercial areas, and health areas per 1,000 people, as well as air pollutants, such as Particulate Matter (PM10), responsible for air pollution. When examining the geographical distribution of area of parks per 1,000 people (Figure 5(a)), it is observed to be high (ranging from 2,847 to 5,022 square meters) in all cities in the Central Anatolia Region except for Yozgat, Sivas, and Çankırı. It is also high in some cities in the Central Black Sea Region (Çorum) and a few cities in the Aegean Region (Uşak, Denizli). The least area of parks per 1,000 people is observed in the eastern part of Turkey.

Open green spaces per 1,000 people (Figure 5(b)) are high (ranging from 581,442 to 7,476,860 square meters) in the Marmara Region (Edirne, Çanakkale), the Central Black Sea Region (Bartın, Kastamonu, Bolu, Gümüşhane, Artvin, Ardahan), the Mediterranean Region (Burdur, Antalya), and in some

cities in the Central Anatolia Region (Niğde). Open green spaces per 1,000 people represent large forest areas, parks, recreational areas and areas to be afforested.

In parallel with population density, the residential area per 1,000 people variable (Figure 5(d)) is high (ranging from 12,008 to 32,425 square meters) in cities in the Marmara Region (Tekirdağ, Edirne, Çanakkale, Balıkesir, Kocaeli, Sakarya, Düzce), the Aegean Region (Aydın, Muğla), Central Anatolia and Mediterranean Regions (Ankara, Antalya), and in some cities in the Southeastern and Eastern Anatolia Regions (Elazığ, Diyarbakır).

Trade area per 1,000 people (Figure 5(c)) is high in some cities in the Central Anatolia Region (Ankara, Konya, Aksaray, Nevşehir, Niğde), the Mediterranean Region (Isparta, Burdur, Mersin, Adana), the Marmara and Aegean Regions (Kırklareli, Edirne, Tekirdağ, Çanakkale, Kütahya), and in some cities in the Eastern and Southeastern Anatolia Regions (Erzurum, Batman). Data for the cities of Tunceli, Bayburt, and Ardahan is unavailable in the database.

.

The area of health services per 1,000 people (Figure 5(e)) is high (ranging from 1,228 to 1,721 square meters) in some cities in the Marmara and Aegean Regions (Bilecik, Kütahya), the Central Anatolia Region (Yozgat, Aksaray, Konya), the Central Black Sea Region (Bolu, Ardahan, Bayburt), the Mediterranean Region (Isparta, Kahramanmaraş), and in some cities in the Eastern Anatolia Region (Kars, Iğdır, Ağrı, Erzurum, Muş, Erzincan).

PM10 (Figure 5(f)), with a diameter of less than 10 μg/m3, represents coarse inhalable particles in air pollution data. PM10 values are derived from emissions released from traffic, residential heating, and industrial pollution. The areas with high pollution levels (ranging from 168.96 to 452.15 μg/m3) include cities with large industrial areas in the Marmara Region (Istanbul, Kocaeli, Bursa), in the Aegean Region (Izmir), and large cities, such as Ankara, Konya, and Kayseri in the Central Anatolian Region. Additionally, due to residential heating, high values are observed in some cities in the Black Sea Region (Çorum, Samsun, Amasya, Tokat, Ordu, Trabzon) and in some cities in the Eastern Anatolian Region (Erzurum, Ağrı, Iğdır).

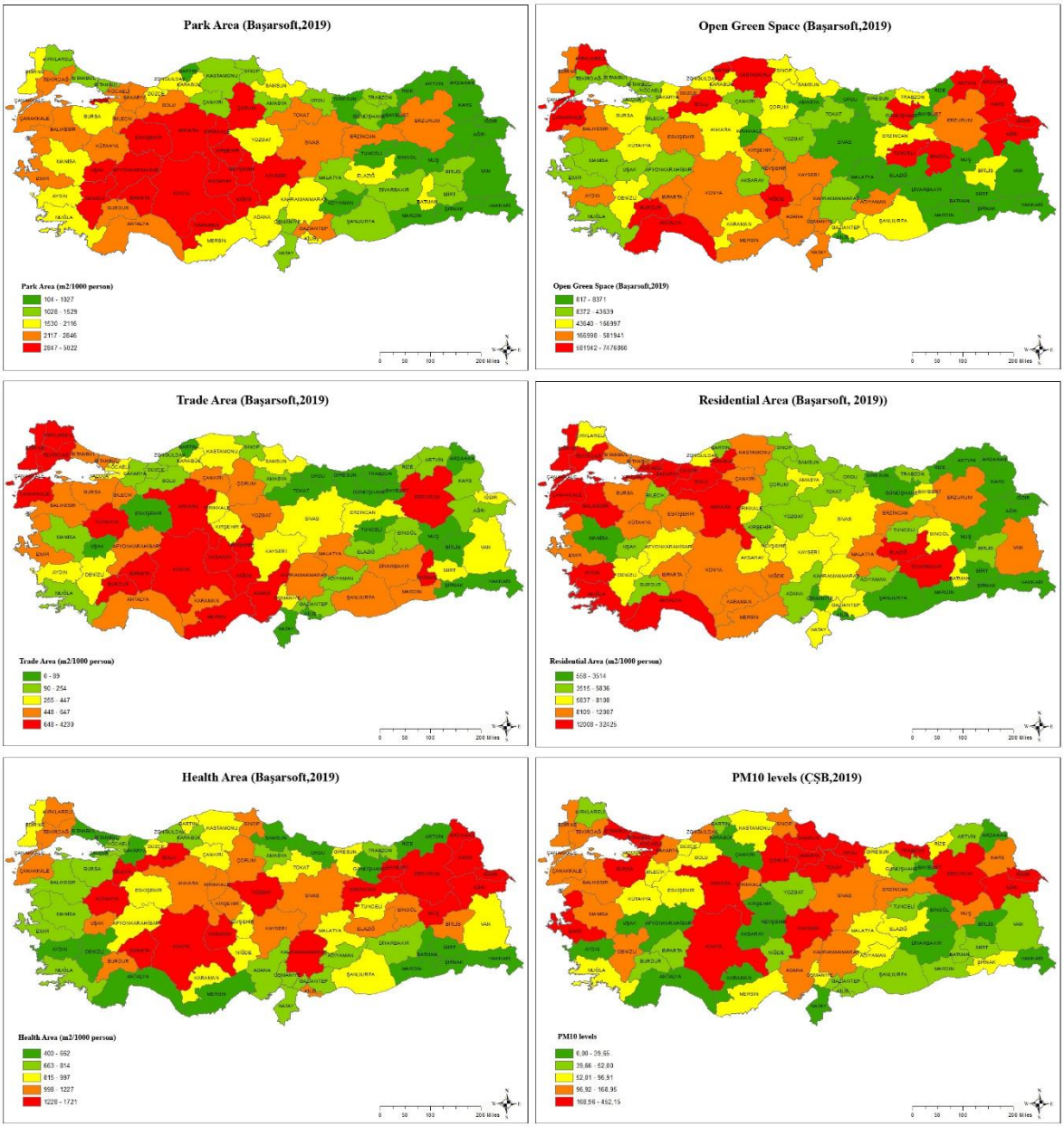

Figure 5. (a) Area of parks per 1,000 people (Source: Başarsoft, 2019), (b) Open green space per 1,000 people (Source: Başarsoft, 2019), (c) Commercial area per 1,000 people (Source: Başarsoft, 2019), (d) Residential area per 1,000 people (Source: Başarsoft, 2019), (e) Health area per 1,000 people (Source: Başarsoft, 2019), (f) Particulate Matter (PM10) in the air (Source: Başarsoft, 2019).

3.5 Principal Component Analysis (PCA)

Principal component analysis [42], [43] is used to examine the relationships across study variables and identify data suitable for regression models; the data is grouped into four components (Table 3). The first component is composed of health variables (DIA, OB), demographics, socioeconomic status of the population (Number of cars, Industry, and Agriculture %), and environmental variables (Residential area, parks). The second component includes demographic, socioeconomic status variables (Popdensity, GDP ($)), and the environmental variable PM10 value. The third component includes only the open green space variable, while the fourth component includes the environmental variables of the area of health services and trade areas. Kaiser-Meyer-Olkin (KMO) and Bartlett tests are examined for PCA validation. The Kaiser-Meyer-Olkin (KMO) test measures the sample adequacy, and a value greater than 0.60 is expected [45], [46].

In this study, the KMO value is 0.706, and the PCA explains a total variance of 70.6%. The significance value of the Bartlett test is also $p < 0.001$

(Table 3) [45]. Therefore, the data set is suitable for PCA, and the four components are used while selecting data for the following regression models.

Table 3. Principal Component Analysis

KMO and Bartlett's Test

Kaiser-Meyer-Olkin Measure of Sampling Adequacy.		.706
Bartlett's Test of Sphericity	Approx. Chi-Square	506,881
	df	105
	Sig.	.000

Rotated Component Matrix

	Component			
	1	2	3	4
Number of Cars	.857			
DIA	.813			
OBS	.625			
Industry %	.604			
Pop65+	.598			
Residential Area	.577			
Park Area	.550			
Agriculture %	.543			
Popdensity		.761		
PM10		.745		
GDP ($)		.680		
BachDeg %		.625		
Open green space			.843	
Health Area				.747
Trade Area				.527

Extraction Method: Principal Component Analysis.
Rotation Method: Varimax with Kaiser Normalization.

3.6 Spatial Regression Models

In the study, diabetes prevalence is the dependent variable, while other variables are treated as independent variables. Spatial regression analysis was conducted to analyze the relationships between the selected data based on PCA components. Given the spatial dependency of the geographical distribution of diabetes prevalence (Moran's I=0.39), five SEM regression models are constructed (Table 4). In SEM, the spatial weights matrix across 81 cities is included, accounting for the influence of spatial dependence between geographical units. The Adjusted R^2 values range from 0.37 to 0.58, and the significance levels of the models being $p < 0.001$ indicate that significant relationships exist in the models within the scope of the study.

In the selection of models that exhibit spatial dependence, the Akaike Information Criterion (AIC) value is also taken into account. A low AIC value is important in model selection. Model 5 has the lowest AIC value (332.69) and the highest R^2 value (0.58). Therefore, Model 5 is considered the model with the highest explanatory power within the scope of the study.

Table 4. Spatial Regression Models

	Model 1	Model 2	Model 3	Model 4	Model 5
Intercept	4.79 (10.63)	1.35 (1.45) [a]	0.92 (1.07)[b]	1.76 (1.98)	1.72 (1.80)
OBS	2.33 (4.23)	2.34 (4.41)	1.57 (2.96)	1.77 (3.58)	1.82 (3.66)
Popdensity		0.08 (1.18) [b]	0.06 (0.80) [b]		0.002 (0.02) [b]
Pop65+ %		0.25 (3.88)	0.11 (1.73) [a]	0.20 (3.08)	0.19 (3.11)
GDP ($)			-0.00003 (0.25) [b]		
Number of Cars			0.02 (2.85)	0.009 (1.49) [b]	0.011 (2.15)
Agriculture %			0.18 (0.73) [b]	0.17 (0.72) [b]	
Industry %			0.03 (1.43) [b]		0.007 (0.41)[b]
Park Area				0.0001 (0.81) [b]	
Open green space				-0.0000003 (-1.95)	-0.0000003 (-1.97)
Residential Area				0.00003 (0.09) [b]	0.000006 (0.15)[b]
Trade Area				0.0006 (1.77) [a]	0.0005 (1.62)[b]
Health Area				-0.0014(-2.18)	-0.0012 (-1.80)[a]
PM10				0.001 (0.84) [b]	0.001 (0.49) [b]

Model Statistics	**Model 1**	**Model 2**	**Model 3**	**Model 4**	**Model 5**
Adjusted R squared	0.371	0.424	0.525	0.569	0.578
P-value	0.001	0.001	0.001	0.001	0.001
Akaike information criterion	350.90	344.44	336.09	333.31	332.69
N	81	81	81	81	81

a Significant at 0.1 level (two-tailed).

b Not significant.

Table 5. Breusch-Pagan Test Statistics

Breusch-Pagan test statistics	**Model 1**	**Model 2**	**Model 3**	**Model 4**	**Model 5**
Degrees of freedom	1	3	7	10	10
Statistics	0.102	2.007	13.199	17.679	19.779
P-value	0.750	0.571	0.067	0.100	0.031

The strong relationship between diabetes and obesity prevalence is evident at the provincial level in Turkey [8], [11], [14]. Measuring the impact of demographic, socioeconomic, and built environment variables on diabetes, including the prevalence of obesity in the model, allows for a better understanding of the effect of other factors (demographic, socioeconomic, built environment) on diabetes. In models where diabetes prevalence at the provincial level is considered as the dependent variable (Model 1, Model 2, Model 3, Model 4, Model 5), it is observed that this variable shows a positive and significant relationship with the obesity rate.

In Model 2, there is a significant and positive relationship between the demographic variable of the 65+ population as a percentage of the total population and diabetes prevalence. According to Model 2, it can be inferred that a 1% increase in this variable could lead to a 0.25% increase in diabetes prevalence.

In Model 3, a significant and positive relationship was found between the number of cars per 1,000 people variable and diabetes prevalence, indicating car dependency for mobility and higher income levels. In cities with extensive road infrastructure, private vehicles are commonly used transportation modes (e.g., Ankara ranks first with 262 cars per 1,000 people); therefore, higher car ownership rates are observed. According to this model, a 1% increase in number of cars per 1,000 people could potentially lead to a 0.02% increase in diabetes prevalence.

Model 4 demonstrates a negative and significant relationship between the area of health services as a built environment variable and diabetes prevalence. This suggests that in cities with more

health facilities, residents may be able to take necessary precautions against diabetes before being diagnosed. An increase of 1% in health areas in a city may result in a 0.0014% lower diabetes prevalence.

The size of open green spaces plays a role in reducing diabetes prevalence, although at the provincial level, the marginal impact is low (i.e., 0.0000003%). As the open green space in square meters increases, diabetes prevalence decreases. On the other hand, having a higher proportion of trade area has an increasing effect on diabetes prevalence within a 10% confidence interval. The positive relationship between diabetes prevalence and trade areas could be associated with the size of the cities. Physical activity is generally high in cities with larger trade areas; however, nutrition status is also a notable risk factor for diabetes. The density of fast-food restaurants and the prevalence of supermarkets selling unhealthy and processed food products in trade areas might contribute to this outcome. However, it should be noted that heteroskedasticity is detected in this model based on the Breusch-Pagan test results (p=0.10) (Table 5). The presence of heteroskedasticity in the model affects the accuracy and reliability of the model and analysis. Therefore, for a model to be accepted, the significance level of the Pagan test is expected to be less than 0.05.

Model 5 is constructed with variables that have shown significant relationships in other models. According to Model 5, the obesity prevalence, the percentage of the 65+ population in the total population, the number of cars per 1,000 people, open green spaces, and areas of health services variables have shown significant relationships with diabetes prevalence within a 10% confidence interval. The presence of health services and open green spaces has a reducing effect on diabetes prevalence. In contrast, the percentage of the 65+ population in the total population and the number of cars per 1,000 people have an increasing effect on diabetes prevalence.

The three cities with the highest obesity rates are Bolu (2.65), Bartın (1.59), and Aydın (1.32). The three cities with the highest diabetes rates are Manisa (11.13), Zonguldak (10.40), and Aydın (10.23). Aydın is the third city where both diabetes and obesity rates are the highest. Zonguldak (1.25) is among the top five cities regarding obesity rates, and Manisa (0.71) is among the top twenty cities.

The models indicate that diabetes rates are associated with the percentage of the 65+ aged population. When examining this relationship, it is observed that Aydın (16.24) and Zonguldak (15.31) have a higher percentage of the elderly population. The national average for the percentage of the 65+ population in the total population is 13.00%. The number of cars per 1,000 people is also high in these cities. Access to healthcare services is important for diabetes patients for diagnosis and treatment. The models show that when the area of health services per 1,000 people increases, diabetes rates tend to decrease.

4. Conclusion

The relationship between the prevalence of diabetes and obesity and the built environment has been extensively studied in the literature. However, it is possible to reach different results based on local characteristics among countries. Particularly in developing countries, there is still a debate on which demographic, socio-economic, and built environment characteristics differentiate and influence the burden of health outcomes. On the other hand, evidence-based policies are developed for urban and public health interventions planned under Sustainable Urban Development Goals, particularly SDG3 – good health and well-being and SDG11 – Sustainable Cities and Communities. With the development of these policies, healthier and higher-quality living environments can be achieved within the context of sustainable urbanization.

The relationship between diabetes prevalence and physical activity is well-known [6], [12], [17], [18]. Studies in the literature have demonstrated an inverse relationship between green spaces and diabetes prevalence [6], [24], [25], [26]. This situation is associated with the opportunities that green spaces provide for physical activity. In this context, similar findings have emerged in this study regarding the relationship between diabetes prevalence and green spaces in Turkey. Therefore, there is a need to consciously emphasize that, according to the "3194 Law on Land Development Planning and Control," a minimum of 15 square meters of active green space per person is recommended throughout the city. According to the regulation, "active green space" includes larger green uses such as recreational areas, forest areas, areas to be afforested, fairgrounds, and festival areas, as well as urban parks, children's park areas, and recreational areas within the entire city. The open green space used in the study corresponds to the definition of active green space in the regulation. [54]. In the study,

the amount of open green space in 19 cities is below 15 m^2/person.

Similarly, the positive relationship between the size of healthcare facilities and diabetes prevalence in cities suggests that the presence of adequate healthcare facilities for diagnosis and treatment can be effective in reducing the disease. According to the Law on Land Development Planning and Control, the health square meter per person is a minimum of 1.50 in cities with a population of less than 500,000, while in cities with a population exceeding 500,000, it is at least 1.60 square meters [54]. In Erzurum (approximately 768,000 people), this value is 1.63, whereas in Kars (approximately 289,000 people), it is higher than the values specified in the regulation at 1.72 square meters. For the reduction of diabetes prevalence, the promotion of physical activity, and the creation of healthy cities, it is necessary to reevaluate and increase the per capita unit values in the regulation.

Balanced planning of mixed-use areas to reduce diabetes prevalence in Turkey, increasing access to affordable healthy food, making appropriate choices for the location of healthcare institutions, increasing the amount of open green spaces, ensuring accessibility, and enhancing opportunities for physical activity are necessary.

Additionally, the diabetes rate can be higher in cities with a high elderly population. In this case, increasing age-friendly built environment characteristics can effectively prevent the disease. The presence of healthcare facilities for diabetes patients and access to these institutions are of great importance. The SEM results show that as the number of vehicles per thousand people increases, diabetes prevalence also increases. As vehicle ownership increases, people can choose motorized mobility instead of active, non-motorized mobility, which leads to lower physical activity. Urban development in car-oriented cities should be redesigned to support physical activity through non-motorized vehicle access and infrastructure, public transportation systems, and the promotion of walkability and cycling.

There are certain limitations in the study. Health data in Turkey is obtained at the provincial level. To conduct detailed spatial studies, data should be obtained or generated at the neighborhood or community level. Similarly, air pollution data is available at the provincial level. Pollutants are not distributed equally across provincial boundaries. To better understand their effect on non-communicable diseases such as diabetes, more detailed analyses should be conducted in areas where pollutant concentrations occur. This way, the impact of air pollution values on NCDs, such as diabetes, can be measured for Turkey as well.

This study presents findings that can help determine the priorities for urban and public health plans, policies, and programs for health and physical activity-focused urban development in Turkey.

Acknowledgment

This study is derived from the doctoral thesis "The Impact of Built Environment Factors on Urban Health."

Contributions of the Authors

The authors' contributions to the paper are equal.

Conflict of Interest Statement

There is no conflict of interest between the authors.

Statement of Research and Publication Ethics

The study is complied with research and publication ethics

References

[1] Institute For Health Metrics And Evaluation, “Global Burden Of Disease Result”, [Online]. Available: Https://Vizhub.Healthdata.Org/Gbd-Results/. [Available:06.11.2023].

[2] World Health Organization, “Health Topics”, [Online]. Available: Https://Www.Who.İnt/Health-Topics/Noncommunicable-Diseases#Tab=Tab_1. [Available:06.11.2023].

[3] United Nation Turkey, “Sustainable Development Goals”, [Online]. Available: Https://Turkey.Un.Org/En/Sdgs/3. [Available:06.11.2023].

[4] T. S. Bakanlığı, “Türkiye Beslenme ve Sağlık Araştırması (TBSA),” Beslenme Durumu ve Alışkanlıklarının Değerlendirilmesi Sonuç Raporu Sağlık Bakanl. Yayın, No. 931, 2019.

[5] World Health Organization, "WHO Discussion Paper on The Development of an Implementation Roadmap 2023-2030 for The WHO Global Action Plan for The Prevention and Control of Ncds 2023-2030", WHO, Switzerland,2021.
[6] R. A. Defronzo et Al., "Type 2 Diabetes Mellitus," *Nat. Rev. Dis. Primer*, vol. 1, no. 1, pp. 1–22, 2015.
[7] A. D. Deshpande, M. Harris-Hayes, and M. Schootman, "Epidemiology of Diabetes and Diabetes-Related Complications," *Phys. Ther.*, vol. 88, no. 11, pp. 1254–1264, 2008.
[8] S. Chatterjee, K. Khunti, and M. J. Davies, "Type 2 Diabetes," *The Lancet*, vol. 389, no. 10085, pp. 2239–2251, 2017.
[9] Y. C. Chooi, C. Ding, and F. Magkos, "The Epidemiology of Obesity," *Metabolism*, vol. 92, pp. 6–10, 2019.
[10] S. Bakanlığı, "Sağlık İstatistikleri Yıllığı 2017," 2018, Accessed: Nov. 03, 2023. [Online]. Available: Https://Dspace.Ceid.Org.Tr/Xmlui/Handle/1/1561
[11] T. Dendup, X. Feng, S. Clingan, and T. Astell-Burt, "Environmental Risk Factors For Developing Type 2 Diabetes Mellitus: A Systematic Review," *Int. J. Environ. Res. Public. Health*, vol. 15, no. 1, p. 78, 2018.
[12] G. Seravalle and G. Grassi, "Obesity And Hypertension," *Pharmacol. Res.*, vol. 122, pp. 1–7, 2017.
[13] L. Chen, D. J. Magliano, and P. Z. Zimmet, "The Worldwide Epidemiology of Type 2 Diabetes Mellitus—Present And Future Perspectives," *Nat. Rev. Endocrinol.*, vol. 8, no. 4, pp. 228–236, 2012.
[14] A. B. Olokoba, O. A. Obateru, and L. B. Olokoba, "Type 2 Diabetes Mellitus: A Review Of Current Trends," *Oman Med. J.*, vol. 27, no. 4, p. 269, 2012.
[15] B. Fletcher, M. Gulanick, and C. Lamendola, "Risk Factors for Type 2 Diabetes Mellitus," *J. Cardiovasc. Nurs.*, vol. 16, no. 2, pp. 17–23, 2002.
[16] R. Ewing, G. Meakins, S. Hamidi, and A. C. Nelson, "Relationship Between Urban Sprawl and Physical Activity, Obesity, And Morbidity–Update and Refinement," *Health Place*, vol. 26, pp. 118–126, 2014.
[17] D. Thomas, E. J. Elliott, and G. A. Naughton, "Exercise For Type 2 Diabetes Mellitus," *Cochrane Database Syst. Rev.*, no. 3, 2006, Accessed: Nov. 03, 2023. [Online]. Available: Https://Www.Cochranelibrary.Com/Cdsr/Doi/10.1002/14651858.CD002968.Pub2/Abstract
[18] G. Lastra, S. Syed, L. R. Kurukulasuriya, C. Manrique, and J. R. Sowers, "Type 2 Diabetes Mellitus and Hypertension: an Update," *Endocrinol. Metab. Clin.*, vol. 43, no. 1, pp. 103–122, 2014.
[19] S. Rajagopalan and R. D. Brook, "Air Pollution and Type 2 Diabetes: Mechanistic İnsights," *Diabetes*, vol. 61, no. 12, pp. 3037–3045, 2012.
[20] V. S. Malik, W. C. Willett, and F. B. Hu, "Global Obesity: Trends, Risk Factors And Policy İmplications," *Nat. Rev. Endocrinol.*, vol. 9, no. 1, pp. 13–27, 2013.
[21] P. L. Valenzuela, P. Carrera-Bastos, A. Castillo-García, D. E. Lieberman, A. Santos-Lozano, and A. Lucia, "Obesity and The Risk of Cardiometabolic Diseases," *Nat. Rev. Cardiol.*, pp. 1–20, 2023.
[22] C. Sarkar, C. Webster, And J. Gallacher, "Residential Density and Adiposity: Findings From The UK Biobank," *Lancet*, vol. 390, Nn. Supplement 3, 2017.
[23] J. Feng, T. A. Glass, F. C. Curriero, W. F. Stewart, and B. S. Schwartz, "The Built Environment And Obesity: A Systematic Review of The Epidemiologic Evidence," *Health & Place*, vol. 16, no. 2, pp. 175-190, 2010.
[24] N. R. Den Braver, J. Lakerveld, F. Rutters, L. J. Schoonmade, J. Brug, And J. W. J. Beulens, "Built Environmental Characteristics and Diabetes: A Systematic Review And Meta-Analysis," *BMC Med.*, vol. 16, no. 1, p. 12, Dec. 2018, Doi: 10.1186/S12916-017-0997-Z.
[25] M. Neuvonen, T. Sievänen, S. Tönnes, And T. Koskela, "Access to Green Areas and the Frequency of Visits–a Case Study in Helsinki," *Urban Forestry & Urban Greening*, vol. 6, no. 4, pp. 235-247, 2007.
[26] F. De La Fuente et al., "Green Space Exposure Association with Type 2 Diabetes Mellitus, Physical Activity, and Obesity: A Systematic Review," *International Journal of Environmental Research and Public Health*, vol. 18, no. 1, p. 97, 2021.
[27] C. P. Durand, M. Andalib, G. F. Dunton, J. Wolch, and M. A. Pentz, "A Systematic Review of Built Environment Factors Related to Physical Activity and Obesity Risk: Implications for Smart Growth Urban Planning," *Obes. Rev.*, vol. 12, no. 5, May 2011, Doi: 10.1111/J.1467-789X.2010.00826.X.

[28] J. D. Mackenbach et Al., "Obesogenic Environments: A Systematic Review of The Association Between The Physical Environment and Adult Weight Status, The SPOTLIGHT Project," *BMC Public Health*, vol. 14, no. 1, p. 233, Dec. 2014, Doi: 10.1186/1471-2458-14-233.

[29] U. Bilal, A. H. Auchincloss, and A. V. Diez-Roux, "Neighborhood Environments And Diabetes Risk And Control," *Curr. Diab. Rep.*, vol. 18, no. 9, p. 62, Sep. 2018, Doi: 10.1007/S11892-018-1032-2.

[30] J. F. Sallis, E. Cerin, T.L. Conway, M.A. Adams, L.D. Frank, M. Pratt And N. Owen, "Physical Activity in Relation to Urban Environments in 14 Cities Worldwide: A Cross-Sectional Study", *The Lancet*, vol.387, no.10034, pp. 2207-2217, 2016.

[31] T. Honda, V. C. Pun, J. Manjourides And H. Suh, "Associations Between Long-Term Exposure to Air Pollution, Glycosylated Hemoglobin and Diabetes", *International Journal of Hygiene and Environmental Health*, vol. 220, no.7, pp. 1124-1132, 2017.

[32] M. Strak, N. Janssen, R. Beelen, O. Schmitz, I. Vaartjes, D. Karssenberg And G. Hoek, "Long-Term Exposure to Particulate Matter, NO2 and The Oxidative Potential Of Particulates And Diabetes Prevalence İn A Large National Health Survey". *Environment International*, vol. 108, pp. 228-236, 2017.

[33] H. Qiu, C. M. Schooling, S. Sun, H. Tsang, Y. Yang, R. S. Lee, And L. Tian, "Long-Term Exposure To Fine Particulate Matter Air Pollution and Type 2 Diabetes Mellitus in Elderly: A Cohort Study in Hong Kong", *Environment International*, vol.113, pp. 350-356, 2018.

[34] G. R. Aarthi, T. S. M.Begum, S.Al Moosawi, D.Kusuma, H.Ranjani, R. Paradeepa, and D. Fecht, "Associations of The Built Environment with Type 2 Diabetes in Asia: A Systematic Review", *BMJ Open*, vol.13, no.4, p. E065431, 2023.

[35] O. Raaschou-Nielsen et Al., "Long-Term Exposure to Traffic-Related Air Pollution and Diabetes-Associated Mortality: A Cohort Study," *Diabetologia*, Aug. 2012, Doi: 10.1007/S00125-012-2698-7.

[36] Ministry of Health, "National Household Health Survey in Turkey: Prevalence of Noncommunicable Disease Risk Factors, 2017 Final Report", World Health Organization, WHO, Ankara, 2017. Https://İris.Who.İnt/Handle/10665/342200

[37] T. S. Bakanlığı, *Türkiye Bulaşıcı Olmayan Hastalıklar ve Risk Faktörleri Kohort Çalışması* Sağlık Bakanl. Yayın, No. 1206, 2021.

[38] United Nation, "Basic Data Selection", [Online]. Available: Https://Unstats.Un.Org/Unsd/Snaama/Basic [Available:06.11.2023].

[39] R. Dubin, K. Pace, And T. Thibodeau, "Spatial Autoregression Techniques For Real Estate Data," *J. Real Estate Lit.*, vol. 7, no. 1, pp. 79–95, Jan. 1999, Doi: 10.1080/10835547.1999.12090079.

[40] B. H. Ozuduru, "Assessment of Spatial Dependence Using Spatial Autoregression Models: Empirical Analysis of Shopping Center Space Supply In Ohio," *J. Urban Plan. Dev.*, vol. 139, no. 1, pp. 12–21, Mar. 2013, Doi: 10.1061/(ASCE)UP.1943-5444.0000129.

[41] Anselin, L. "Local Indicators of Spatial Association—LISA". *Geographical Analysis*, vol. 27, no. 2, pp. 93-115, 1995.

[42] L. C. Messer Et Al., "The Development of A Standardized Neighborhood Deprivation Index," *J. Urban Health*, vol. 83, no. 6, pp. 1041–1062, Dec. 2006, Doi: 10.1007/S11524-006-9094-X.

[43] M. Greenacre, P. J. Groenen, T. Hastie, A. I. d'Enza, A. Markos, And E. Tuzhilina, "Principal Component Analysis," *Nat. Rev. Methods Primer*, vol. 2, no. 1, p. 100, 2022.

[44] C. Fang, H. Liu, G. Li, D. Sun, and Z. Miao, "Estimating The Impact of Urbanization on Air Quality in China Using Spatial Regression Models," *Sustainability*, vol. 7, no. 11, pp. 15570–15592, 2015.

[45] Ö. Çokluk, G. Şekercioğlu ve Ş. Büyüköztürk, Ş, *Sosyal Bilimler İçin Çok Değişkenli İstatistik: SPSS ve Lisrel Uygulamaları*, Vadi Grup Basım A.Ş, Ankara, Pegem Akademi Yayıncılık, 2021.

[46] Y. D. D. Ş. Büyüköztürk , "Faktör Analizi: Temel Kavramlar ve Ölçek Geliştirmede Kullanımı", *Kuram Ve Uygulamada Eğitim Yönetimi*, vol. 32, no. 32, pp. 470-483, Mar. 2002

[47] R. I. G. Holt, M. De Groot, and S. H. Golden, "Diabetes and Depression," *Curr. Diab. Rep.*, vol. 14, no. 6, p. 491, Jun. 2014, Doi: 10.1007/S11892-014-0491-3.

[48] A. Trikkalinou, A. K. Papazafiropoulou, and A. Melidonis, "Type 2 Diabetes and Quality of Life," *World J. Diabetes*, vol. 8, no. 4, p. 120, 2017.

[49] E. Agardh, P. Allebeck, J. Hallqvist, T. Moradi, and A. Sidorchuk, “Type 2 Diabetes Incidence and Socio-Economic Position: A Systematic Review and Meta-Analysis,” *Int. J. Epidemiol*., vol. 40, no. 3, pp. 804–818, 2011.

[50] M. Schetz et al., "Obesity in The Critically İll: A Narrative Review," *Intensive Care Med*., vol. 45, no. 6, pp. 757–769, Jun. 2019, Doi: 10.1007/S00134-019-05594-1.

[51] World Health Organization, “What Are The WHO Air Quality Guidelines?”, [Online]. Available: Https://Www.Who.İnt/News-Room/Feature-Stories/Detail/What-Are-The-Who-Air-Quality-Guidelines. [Available:06.11.2023].

[52] S. L. Handy, M. G. Boarnet, R. Ewing, and R. E. Killingsworth, "How the built environment affects physical activity: views from urban planning," *American journal of preventive medicine*, vol. 23, no. 2, pp. 64-73, 2002.

[53] M. Carmona, "Residential design policy and guidance: content, analytical basis, prescription and regional emphasis," *Planning Practice and Research*, vol. 14, no. 1, pp. 17-38, 1999.

[54] The Ministry of Environment, Urbanism, and Climate Change, “3194 Law on Land Development Planning and Control”, [Online]. Available: https://webdosya.csb.gov.tr/db/mpgm/icerikler/ek-2-tablo-17-mayis-20180214143000.pdf . [Available:24.11.2023].